Diagenesis in Rotliegend, Triassic and Jurassic clastic hydrocarbon reservoirs of the Central Graben, North Sea

Inorganic diagenetic processes and interactions with organic maturation products

Dissertation
zur Erlangung des akademischen Grades doctor rerum naturalium
(Dr. rer. nat.)

vorgelegt dem Rat der Chemisch-Geowissenschaftlichen Fakultät der
Friedrich-Schiller-Universität Jena

von Dipl.-Geol. Robert Lippmann

geboren am 12.06.1975 in Schlema

Gutachter:

1. Prof. Dr. Reinhard Gaupp
   Institut für Geowissenschaften der
   Friedrich-Schiller-Universität Jena

2. Prof. Dr. Rolando di Primio
   Geo-Forschungs-Zentrum Potsdam (GFZ)
   Sektion 4.3, Organische Geochemie

Tag der öffentlichen Verteidigung: 08. Februar 2012

Kurzfassung

Im Mittelpunkt der vorliegenden Arbeit stand die Untersuchung der diagenetischen Entwicklung von ausgewählten klastischen HPHT (Hochdruck-Hochtemperatur) Lagerstätten aus dem Rotliegenden, der Trias und dem Jura des Zentralgrabens der Nordsee. Im Fokus stand dabei die petrographische Analyse unterstützt von geochemischen Analysen und der numerischen Modellierung ausgewählter diagenetischer Prozesse. Hauptaugenmerk wurde auf die triassische Skagerrak Formation des Jade- und des Judy-Feldes aus dem UK-Sektor gelegt, da zu diesen beiden Lagerstätten das meiste Probenmaterial und die umfangreichsten Datensätze zur Verfügung standen.

Die Diagenese der triassischen Skagerrak Formation im Jade- und im Judy Feld (UK-Sektor) kann folgendermaßen zusammengefasst werden: Diagenese und Reservoireigenschaften sind stark faziesabhängig. Fluviatile Rinnen- und Schichtflutsandsteine haben die besten Reservoireigenschaften. Detritische Feldspäte und eodiagenetische Zemente wurden während der Mesodiagenese durch aggressive Fluide gelöst. Diese Fluide entstanden wahrscheinlich während der Alteration von Kohlenwasserstoffen innerhalb der Lagerstätte bei relativ flachen Versenkungstiefen. Die Lösungsprodukte wurden wahrscheinlich überwiegend während der Illitisierung von Smektit in den eingeschalteten Tonsteinen sowie während der lokalen Ausfällung von Fe-Karbonaten, Chlorit und Quarz in den Sandsteinen verbraucht. Der Quarzzement ist in den Sandsteinen nicht gleichmäßig verteilt, sondern zeigt eine Zunahme zu den Kontakten mit über- und unterlagernden Tonsteinen hin. Diese Verteilung kann mit der Smektit-zu-Illit-Umwandlung in den Tonsteinen und dem Export des überschüssigen SiO_2 in die Sandsteine erklärt werden. Die numerische Modellierung dieses Prozesses zeigte, dass diffusiver Massentransport über solch kurze Entfernungen möglich ist. Die Bildung von authigenem Chlorit und Ankerit steht im engen Zusammenhang mit der Reduktion von Hämatit/Goethit. Das Fehlen signifikanter Mengen faserigen Illites, trotz deutlicher K-Feldspatlösung, wird auf das Aufbrauchen der Feldspatlösungsprodukte während der Illitisierung von Smektit in den eingelagerten Tonsteinen und/oder auf eine frühe Kohlenwasserstofffüllung zurückgeführt. Eine externe Na^+-Quelle wird für die authigene Albitbildung nicht benötigt, vielmehr kann diese mit der Aufheizung der Sandsteine in ihren salinaren Formationswässern während der Versenkung erklärt werden. Kleinere Mengen an Na^+ könnten auch aus den Tonsteinen stammen, wie durch die Ergebnisse der diagenetischen Modellierung angedeutet wird. Der späte Aufbau von Überdruck in den Lagerstätten hat keine bedeutende Rolle in der diagenetischen Entwicklung gespielt, da die meisten Prozesses wesentlich früher stattfanden und die frühe Füllung mit Kohlenwasserstoffen die meisten späteren diagenetischen Reaktionen (mit Ausnahme von Quarzzementation) unterbunden hat.

Proben aus verschiedenen stratigraphischen Horizonten von acht Bohrungen aus dem norwegischen Sektor wurden zum Vergleich herangezogen.

Die eodiagenetischen Prozesse in den Triassedimenten der Bohrung NOR-E aus dem norwegischen Sektor waren insgesamt vergleichbar mit denen in feinkörnigen Lithologien des Jade- und des Judy-Feldes. Eine Ausnahme bildet die geringere Menge an K-Feldspatanwachssäumen. Die mesodiagenetischen Alterationen waren nicht so intensiv wie die in den zwei untersuchten UK-Feldern. Ursache ist vermutlich die geringere initiale Porosität in den Sedimenten der Bohrung NOR-E und die damit einhergehende geringere Porenwassermenge, die für den Massentransport zur Verfügung stand. Ein bemerkenswerter Unterschied ist die schwächer ausgeprägte Dolomitlösung und Ankeritneubildung, welche auf die fehlende Biodegradation der Kohlenwasserstoffe in Bohrung NOR-E zurückzuführen sein könnte. Die Füllung mit Kohlenwasserstoffen erfolgte hier erst bei größeren Versenkungstiefen.
Die untersuchten Triasproben aus der Bohrung NOR-C des norwegischen Sektors verdeutlichen die Diagenese in der Nähe einer Störungszone. Intensive K-Feldspatlösung wurde wahrscheinlich durch aggressive störungsgebundene Fluide verursacht. Ein deutlicher Unterschied zu den anderen triassischen Lagerstätten ist das Vorhandensein einiger Illitfasern und -blättchen sowie eine andere Chloritmorphologie (Fächer und Rosetten). Die Triassandsteine der Bohrung NOR-C waren wasserführend und das lokale Auftreten von geringen Illitmengen hier kann mit dem Fehlen einer frühen Kohlenwasserstofffüllung im Zusammenhang stehen.

Die untersuchten Sandsteine von zwei Rotliegendbohungen aus dem norwegischen Sektor der Nordsee waren wasserführend, aber eine Beeinflussung durch organische Reifungsprodukte erscheint wahrscheinlich. Der größte Unterschied zu den untersuchten Lagerstätten der Skagerrak Formation ist das pervasive Auftreten von porenfüllendem, permeabilitätszerstörendem, faserigem Illit. Andere mesodiagenetische Prozesse, wie Quarzzementation, Dolomitlösung oder Albitneubildung treten ebenfalls in der Trias auf. Authigener Chlorit war insgesamt relativ selten in den Rotliegend Sandsteinen.

Die Intra-Farsund-Sandsteine aus der Bohrung NOR-F (norwegischer Sektor) repräsentieren geringmächtige Sandsteine welche vollständig von Muttergesteinen umgeben sind. Sie boten eine gute Gelegenheit den Effekt von Fluiden mit organischen Reifungsprodukten auf die Diagenese von Sandsteinen zu untersuchen. Die Mesodiagenese der cm- bis dm-mächtigen Sandsteinlagen wird durch die direkte Nähe zu mächtigen, reifenden Muttergesteinen dominiert. Mesodiagenetische Alterationen beginnen hier mit der Umwandlung von detritischen Feldspäten in Kaolinit und Quarz. Ein großer Teil des Kaolinites wurde später wahrscheinlich durch Chlorit und ein kleiner Teil durch Dickit ersetzt. Die Phase der Chloritbildung wurde von pervasiver Ankeritzementation begleitet. Das Ersetzen von Kaolinit durch Chlorit kann durch sich verändernde Mineralstabilititäten mit zunehmender Temperatur im Zusammenhang mit der Smektit-zu-Illit-Transformation in den umgebenden Muttergesteinen erklärt werden. Die komplette Zementation des Porenraumes mit Ankerit und Quarz verhinderte wahrscheinlich weitere durchgreifende diagenetische Prozesse.

Die Bohrung NOR-G zeigt eine typische marine Eodiagenese. Der Einfluss meteorischer Wässer verursachte später bei flachen Versenkungstiefen die Lösung von Feldspäten, Kaolinitneubildung und Quarzzementation. Die darauf folgende mesodiagenetische Entwicklung ist durch Karbonat- und Quarzzementation zusammen mit etwas Illit-, Chlorit-, Barit- und Albitneubildung charakterisiert. Organische Reifungsprodukte könnten einige der mesodiagenetischen Prozesse (z.B. Karbonatzementation) beeinflusst haben. Die Füllung mit Kohlenwasserstoffen stoppte höchst wahrscheinlich eine ganze Reihe von diagenetischen Prozessen mit Ausnahme von Quarzzementation.

Die eodiagenetische Entwicklung in allen untersuchten Bohrungen zeigte eine starke Abhängigkeit von sedimentärer Fazies und dem Ablagerungsraum. Eodiagenetische authigene Phasen bildeten zusammen mit den detritischen Komponenten das Ausgangsmaterial für spätere Versenkungsdiagenese und wurden von dieser stark überprägt.

Die numerische Modellierung wurde benutzt, um verschiedene Szenarien zur Fluidentwicklung zu testen und das Verständnis diagenetischer Prozesse zu verbessern. Kein Einzelmodell war in der Lage alle beobachteten Veränderungen in der Sandsteinzusammensetzung während der Diagenese der Skagerrak Formation zusammen zu reproduzieren. Allerdings konnten wichtige Reaktionen in mehreren Modellen quantitativ rekonstruiert werden.

Auf diese Weise konnte gezeigt werden, dass die meisten mesodiagenetischen Reaktionen mit anderen über verschiedene Spezies, die während der einzelnen Prozesse verbraucht oder produziert werden, gekoppelt sind.

Mesodiagenetische Prozesse (wie z.B. Quarzzementation) sollten deshalb immer quantitativ und im Zusammenhang mit möglicherweise verbundenen Reaktionen betrachtet werden.

Die Modellierung der Diagenese konnte ebenfalls zeigen, dass die Infiltration von Kohlenwasserstoffen in eine Lagerstätte in der Lage ist eine Reihe von diagenetischen Alterationen auszulösen. Dazu gehören: Bleichung von Rotsedimenten, Lösung von Komponenten und Zementen, sowie Chlorit- und Karbonatneubildung. Alle Modellierungen konnten keinen oder nur einen sehr geringen Gewinn an Netto-Porosität nachweisen. Das bedeutet, dass die neugebildete Sekundärporosität meist mit einer volumetrisch gleichen Zementation an anderer Stelle verbunden ist.

Abstract

This study focused on petrographic analyses supported by geochemical investigations and diagenetic modelling, in order to investigate the diagenetic evolution of selected Rotliegend, Triassic and Jurassic HPHT (high pressure/high temperature) clastic reservoirs in the North Sea Central Graben. Focus was on the Triassic Skagerrak Formation of the Jade and the Judy Field in the UK sector, because most data and material was available from these two fields.

The studied diagenetic evolution of the Triassic Skagerrak Formation in the Jade and Judy Fields (UK-sector) can be summarized with following points: Facies is the main control for diagenesis and reservoir quality, with best reservoir properties observed in fluvial channel and sheetflood sandstones. Detrital feldspar grains and eodiagenetic cements were leached by aggressive fluids during mesodiagenesis. These fluids were probably associated with in-reservoir alteration of hydrocarbons at relatively shallow burial depth. The dissolution products were probably mainly consumed by illitization of smectite in interbedded mudstones and the local precipitation of Fe-carbonates, chlorite and quartz in the sandstones. Quartz cement is not distributed uniformly in the individual sandstone bodies, but shows an increase towards the contacts to over- and underlying mudstones. This distribution can be explained best by smectite-to-illite transformation in the interbedded mudstones releasing excessive SiO_2 into the sandstones. Diagenetic modelling can show that diffusive mass transport is possible over these short distances. The precipitation of authigenic chlorite and ankerite was probably associated with the reduction of hematite/goethite by hydrocarbons. The apparent lack of significant quantities of fibrous illite despite significant K-Feldspar dissolution is related to the preferred consumption of

feldspar dissolution products by illitization of smectite in adjacent mudstones and/or the early hydrocarbon fill of the reservoir. The formation of authigenic albite from dissolved K-feldspar requires no external Na^+ source and can be explained by heating the sandstone with its saline formation water during increasing burial. Minor contribution of Na^+ may also have been derived from mudstones as indicated by diagenetic modelling. The late overpressure development seems to have played no substantial role in (inorganic) diagenesis, since most volumetrically important processes occurred earlier and the early fill with hydrocarbons probably stopped diagenetic reactions, apart from quartz and minor ankerite cementation.

Samples from eight wells covering different stratigraphic units of the Norwegian sector were used for comparison.

Eodiagenetic processes in the Triassic core of well NOR-E from the Norwegian sector are comparable to those in finer grained lithologies of the Jade and Judy Fields, except for the minor occurrence of K-feldspar overgrowths. Mesodiagenetic alterations are not as intensive as in the two investigated fields from the UK-sector. This is probably related to the low initial porosity along with restricted amounts of pore water available for mass transport. A remarkable difference to the Jade and Judy Fields is the comparable lower amount of dolomite dissolution and ankerite formation, which may be related to the lack of biodegradation of hydrocarbons, because hydrocarbon charge occurred not until deep burial in well NOR-E.

The Triassic in well NOR-C of the Norwegian sector shows diagenesis close to a fault zone. Extensive K-feldspar dissolution was probably caused by aggressive fault related fluids. A significant difference to other Triassic reservoirs studied is the presence of few illite fibres/flakes and a different morphology of the authigenic chlorite (rosettes or fans) here. The Triassic in well NOR-C was found to be water-bearing and the presence of local minor illite is attributed to the lack of a hydrocarbon fill.

Sandstones in the two studied Rotliegend wells were found to be water-bearing, but an influence of organic maturation products is likely. The most significant difference to the studied Skagerrak Formation reservoirs is the partly pervasive occurrence of pore-filling permeability destroying fibrous/flaky illite. Other mesodiagenetic processes, such as quartz cementation, dolomite dissolution and albite formation occur also in the Triassic. Authigenic chlorite is not as abundant in the Rotliegend sandstones.

The Intra-Farsund sandstones from well NOR-F in the Norwegian sector represent thin sandstones completely enclosed into source rocks. They provided a good opportunity to study the effect of source rock maturation related fluids on sandstone diagenesis. The mesodiagenesis of the thin (cm to dm-thick) Intra-Farsund sandstone layers is dominated by the close relationship to thick maturing organic rich source rocks. Mesodiagenetic alterations started with the breakdown of detrital feldspar grains into kaolinite and quartz. A large part of the kaolinite was probably later replaced by authigenic chlorite and a minor part by dickite. Chloritization and chlorite neoformation was accompanied by pervasive ankerite cementation. The replacement of kaolinite by chlorite can be explained by changing mineral stabilities with increasing temperature along with smectite-to-illite transformation in the surrounding source rocks. Diagenesis ceased most likely with complete occlusion of interstital pore space by ankerite and quartz cement, leaving only small amounts of microporosity.

Well NOR-G shows a typical marine eodiagenesis. Meteoric water influx caused feldspar dissolution along with kaolinite and quartz cementation probably later after shallow burial. The mesodiagenetic evolution is characterized by carbonate and quartz cementation together with minor illite (but not as widespread as in the Rotliegend samples), chlorite, barite and albite precipitation. Organic maturation products may have influenced some mesodiagenetic processes, such as carbonate cementation. The reservoir is filled with hydrocarbons today. This hydrocarbon fill has terminated most diagenetic processes, excepting quartz cementation.

Eodiagenesis in all studied settings was dependent on sedimentary facies and depositional environment. Eodiagenetic authigenic phases together with detrital components provided the framework for later burial diagenesis and were overprinted by it.

Diagenetic modelling was used to improve the understanding of diagenetic processes and to test fluid evolution scenarios. No single model of this study is able to reproduce all observed changes in sandstone mineralogy during diagenesis in the Skagerrak Formation, but important mesodiagenetic changes can be reconstructed quantitatively. Diagenetic modelling shows that most mesodiagenetic reactions are linked to others via various species which are produced or consumed during the individual processes. Mesodiagenetic processes (such as quartz cementation) should therefore not be considered separately but examined quantitatively in the context of all possibly linked reactions.

Diagenetic modelling can also show that the infiltration of hydrocarbons is able to trigger a number of mesodiagenetic reactions, such as bleaching of red beds, dissolution of grains and cements as well as chlorite formation and carbonate cementation. All models show no or only a very small gain in net-porosity. Therefore, all secondary porosity created was most likely plugged elsewhere by authigenic phases.

Acknowledgments

I am particularly grateful to my supervisor Prof. Dr. Reinhard Gaupp for his valuable advices, guidance and encouragement over all the years. He initiated and helped to accomplish this project with his support during all the time.

I thank the German Research Foundation (DFG) for funding this work in the framework of the DFG-SPP 1135 “Dynamics of sedimentary systems under varying stress regimes: The example of the Central European Basin”. My thanks go also to the industry partners ConocoPhillips (UK) and Norsk Hydro (now Statoil), who provided core material, thin sections and internal reports for this work.

This work has greatly benefited from inspiring discussions with Dr. Robert Ondrak (GFZ Potsdam) and Dr. Robert Schöner (University Erlangen-Nürnberg), who contributed in a fundamental way to my understanding of diagenesis and diagenetic modelling. So, my sincere thanks go to them. I thank also Dr. Rolando di Primio and Dr. Volkmar Neumann from the GFZ in Potsdam for successful collaboration and their help in all questions concerning basin modelling.

Special thanks go to all members of the sedimentology group in Jena, especially to Dr. Thomas Voigt, Goska Rusek and Ivonne Kamradt for their help and the great time I had in Jena. Sigrid Bergmann and Frank Linde are acknowledged for their careful preparation of numerous samples at the Institute of Earth Sciences in Jena. I thank also Ursula Rudakoff for performing the XRD-measurements.

I am grateful to all scientists from other institutions, who allowed me to use their analytical equipment and shared their knowledge with me. So, I thank especially Dr. Willi Brand (MPI Jena) for his support and the opportunity to use (and to play with) his laser extraction system for stable isotope analyses. Many thanks go also to Dr. Andreas Kronz (University Göttingen) who helped me during the electron microprobe measurements in Göttingen. Dr. Jens Götze (University Freiberg) supported me with hot cathodoluminescence microscopy and Dr. Michael Joachimski (University Erlangen-Nürnberg) with stable isotope analyses. Dr. Günther Völksch (Department of Glass-Chemistry, Jena) assisted during the SEM-investigations. Dr. Ralf Irmler gave me support during my attempts to carry out a non-destructive analysis on a micro X-Ray diffractometer at the department of geography in Jena. I thank also Dr. Andreas Bauer (Karlsruhe), who did not hesitate to answer my e-mails with questions about clay mineralogy.

I thank my family and friends for backing me all the time, especially my mother and my father for their support and guidance. Last but not least, I am deeply indebted to my wife Andrea and my children for their patience and for all the holidays and weekends they gave me for this work. This work is dedicated to them.

Finally, I like to thank all those who are interested in this work and helped to improve it.

Contents

Appendix

Keywords

North Sea, Central Graben, Diagenesis, Diagenetic modelling, Skagerrak Formation, Ula Formation, Farsund Formation, Rotliegend Group

Abbreviations and definitions

BEI	backscatter electron image
BHT	bottom hole temperature
BSR	bacterial sulphate reduction
CL	cathodoluminescence
DST	Drill Stem Test
EDX	energy dispersive X-ray spectroscopy
EMP	electron microprobe
Fm	formation
GDT	gas down to
GOR	gas oil ratio
Gp	group
GWB	The Geochemist's Workbench$^{\mathrm{TM}}$ (modelling software)
GWC	gas-water contact
HWC	hydrocarbon-water contact
HPHT	high pressure high temperature
kaolin	the term kaolin in this study is used to describe kaolin-group minerals (i.e. kaolinite, dickite and nacrite)
max.	maximum
Mb	member
MD	measured depth
molality	number of moles per kilogram solvent
Mst	mudstone
mudstone	the term mudstone is used in the context of this study for siliciclastic mudstones and not for carbonate textures sensu Dunham (1962).
NBS19	International standard for oxygen and carbon isotopes of carbonates
PDB	Belemnitella americana of the Peedee-Formation (international standard for oxygen and carbon isotopes of carbonates)
RFT	repeat formation test
Ro	vitrinite reflectance in oil
SEM	scanning electron microscope
SEI	secondary electron image
Sst	sandstone
TSR	thermochemical sulphate reduction
TVD	true vertical depth
TVDSS	true vertical depth sub-sea
UK	United Kingdom
V-PDB	Vienna PDB (international standard for oxygen and carbon isotopes of carbonates, used as secondary standard calibrated on PDB to give the isotopic composition relative to PDB, as V-PDB)
vol.%	volume percent
WDS	wavelength dispersive X-ray spectroscopy
wt.%	weight percent
XRD	X-ray diffraction analysis

$$\delta^{18}\mathrm{O} = \left(\frac{\left(^{18}\mathrm{O}/^{16}\mathrm{O}\right)_{\mathrm{sample}}}{\left(^{18}\mathrm{O}/^{16}\mathrm{O}\right)_{\mathrm{standard}}} - 1 \right) \cdot 1000$$

$$\delta^{13}\mathrm{C} = \left(\frac{\left(^{13}\mathrm{C}/^{12}\mathrm{C}\right)_{\mathrm{sample}}}{\left(^{13}\mathrm{C}/^{12}\mathrm{C}\right)_{\mathrm{standard}}} - 1 \right) \cdot 1000$$

1 Introduction

The present PhD-study was part of the FLINT (Mineral-Fluid Interactions) project oft the DFG-SPP[1] 1135 “Dynamics of sedimentary systems under varying stress regimes: The example of the Central European Basin”. The FLINT-project had the objective to reconstruct the diagenetic evolution of the reservoir rocks and the compositional evolution of the reservoir fluids in deep overpressured basinal settings of the North Sea Central Graben. High pressure-high temperature (HPHT) reservoirs like the Jade and Judy Fields located in block 30 of the UK-sector are a common feature of the central North Sea. The investigated Triassic sandstones, for instance, are buried to depths between 3.5 and 5.3 km and have present day temperatures up to 194 ° C. These reservoirs experienced high overpressures during the rapid burial in Cenozoic times. They contain wet gas condensates and black oil today. Such deeply buried reservoirs received growing interest from the petroleum industry during the last decades due to their significantly high porosities relative to their present burial depths (e.g. Jade Field - up to 25% at 4.8 km, Jones et al., 2005).

Organic geochemical analyses and 3D basin modelling with focus on reservoir fluid evolution and overpressure development were performed at the GFZ Potsdam by V. Neumann (Neumann, 2007; di Primio & Neumann, 2008) and a short summary of his work is given in section 4.

The study presented here focused on petrographic analyses aided by geochemical investigations and diagenetic modelling, in order to study the diagenetic evolution of HPHT clastic reservoirs of Rotliegend, Triassic and Jurassic age in the North Sea Central Graben.
The major objective was to provide a detailed documentation of the petrography together with datasets for diagenetic modelling. These data should be used to find the dominant diagenetic processes, identify their driving forces and assess possible interactions in the selected reservoir sandstones quantitatively. Special attention should be paid to processes probably involving organic maturation products.

Sample material was available from different depositional settings including Triassic fluvial sediments, Rotliegend aeolian sandstones and Jurassic marine deposits. The inter-bedding of sandstones with mudstones in the Triassic Skagerrak Formation allowed to evaluate mass transport and interactions of diagenetic processes between different lithologies. Thin sandstones intercalated into hick mature source rocks of the Upper Jurassic Farsund Formation provided the opportunity to study the influence of organic maturation products directly.
Most material was available from the Triassic Skagerrak Formation (see section 2). Therefore the main focus of the study was on two Triassic HPHT fields (Judy and Jade) in the UK sector of the Central Graben. Samples from the Rotliegend, Triassic and Jurassic of the Norwegian sector were used for comparison.

This thesis is divided into four major parts. Part one (section 1 to 4) contains general information to methodology, sample material and the working area. The summary of the basin modelling study of V. Neumann is also included here. The second part (section 5 and 6) comprises the detailed description of petrography and geochemical data. Focus of this part is documentation of the data. Third part (section 7) is the description of the numerical diagenetic models and their results. The discussion and interpretation of all data and modelling results together is purpose of the fourth part (section 8 to 11).

---

[1] Deutsche Forschungsgemeinschaft Schwerpunktprogramm

2 Material and methodology

2.1 Material and working areas

The present study is based on samples from core material, thin sections and internal reports provided by the industry partners ConocoPhillips and Norsk Hydro (now Statoil). All samples are derived from major reservoir and source rock horizons in the Central Graben of the North Sea (Table 2.1). Material from 15 different wells was included.

Table 2.1: Overview of wells and available material used for this study. The column "core meter" shows the lengths of the cored section, and the columns "no. of samples" and "material" show how much and which type of material was available from this cored section. Code names of wells used by Neumann (2007) are given for comparison with results of the basin modelling study.

Well	Code used by Neumann (2007)	Stratigraphy	Age	Total core meter	No. of samples	Material
Norwegian sector (Quadrant 1 and 2)						
NOR-A	-	Rotliegend	Permian	9	5	samples
NOR-B	Hydro 305	Rotliegend	Permian	30	8	samples
NOR-G	Hydro 169	Rotliegend	Permian	-	3	cuttings
NOR-C	Hydro 289	Oxfordian sands	Jurassic	2	2	samples
NOR-C	Hydro 289	Skagerrak Fm	Triassic	14	10	samples
NOR-D	Hydro 181	Oxfordian sands	Jurassic	28	11	samples
NOR-E	Hydro 303	Skagerrak ?	Triassic	10	7	samples
NOR-F	Hydro 171	Farsund Fm	Jurassic	12	11	samples
NOR-G	Hydro 169	Ula Fm	Jurassic	18	9	thin sections
UK sector						
30/2c-4		Skagerrak Fm	Triassic	64	43	samples
30/7a-6		?	Jurassic	59	2	thin sections
30/7a-7		Skagerrak Fm*	Triassic	62	23	thin sections
30/7a-P7		Skagerrak Fm	Triassic	107?	3	thin sections
30/7a-8		Skagerrak Fm*	Triassic	99	13	thin sections
30/7a-9		Skagerrak Fm*	Triassic	55	20	thin sections
30/7a-11z		Skagerrak Fm	Triassic	?	30	thin sections

* and some samples from overlying strata (see Appendix 2.2 for details)

Small sized broken core samples (matchbox size) were provided from six of the wells by the partners and only well 30/2c-4 could be sampled by the author. The restricted sample size and the small amount of material limited possible examination methods. Thin sections were provided by the industry partners from cores of the other seven wells.

The locations of the wells in the UK sector are shown in Fig. 2.1. One of the wells (30/2c-4) is located in the Jade Field and the six other in the Judy Field. A detailed description of the Fields is given in section 5. The cores cover predominantly different intervals of the Triassic Skagerrak Formation. Material for other analyses than point-counting and optical microscopy was only available from well 30/2c-4. A few thin sections from overlying strata (Jurassic, Cretaceous and Tertiary) were available additionally for some wells of the Judy Field and used for comparison.

The location of the studied wells in the Norwegian sector is not plotted in Fig. 2.1 for confidentiality reasons. They are situated in quadrants 1 and 2. Small samples from cores of six of these wells, covering Rotliegend, Triassic and Upper Jurassic sediments, were available for this study. Thin sections were provided for the Upper Jurassic interval of well NOR-G and ditch cuttings for the Rotliegend interval of the same well. No useful petrographic information concerning diagenetic evolution could be obtained from these cuttings, due to strong deformation and bit metamorphism. Two 3D data sets were available for the basin modelling (see boundaries in Fig. 2.1), carried out by V. Neumann within the scope of the FLINT project at the GFZ Potsdam (Neumann, 2007).
An extended list of samples and applied methods can be found in Appendix 1. True vertical depths sub-sea (TVDSS) were calculated for samples from wells where deviation data were available. For the other samples only measured depth values (MD) are given.

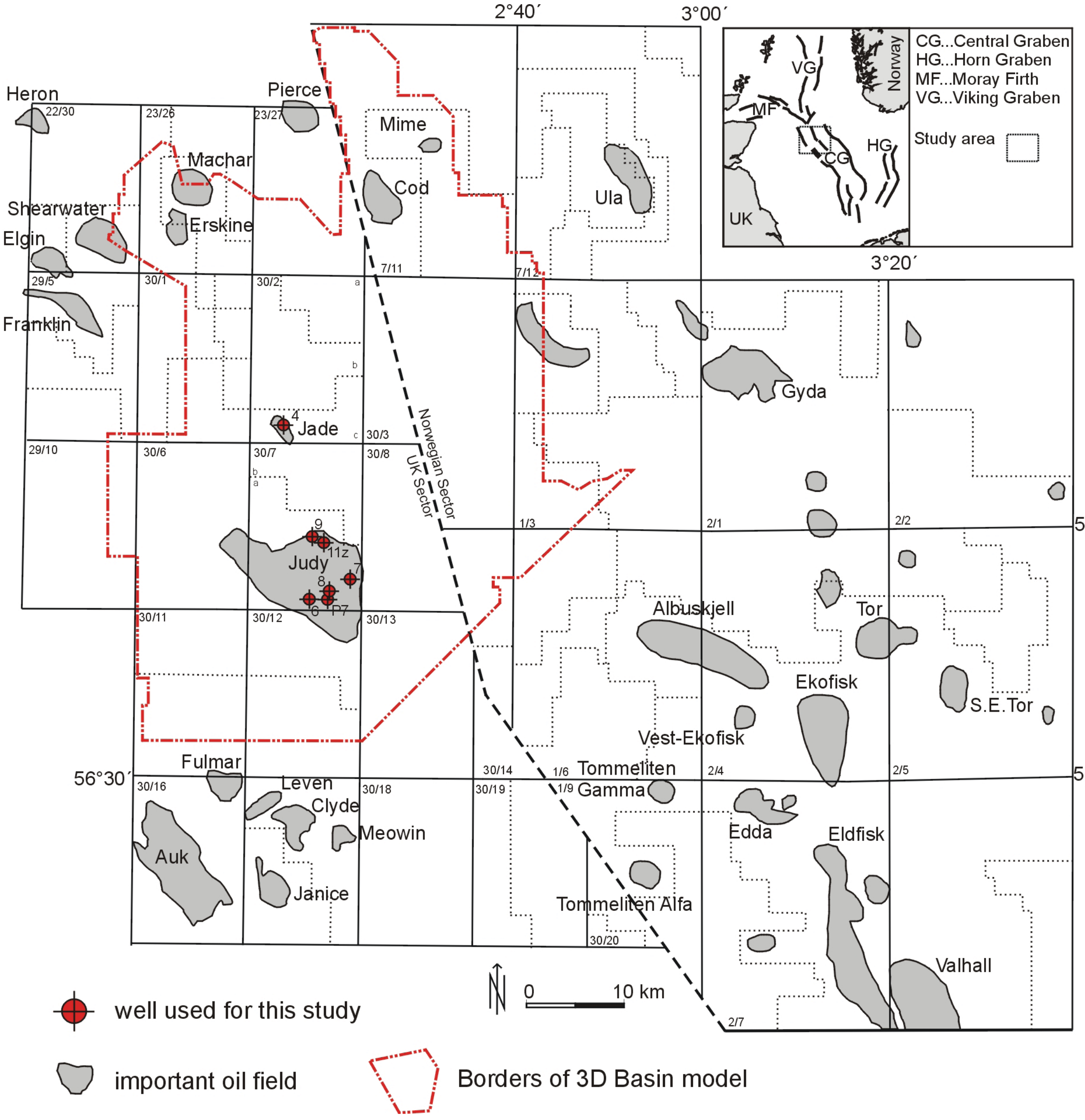

Fig. 2.1: Working area in the North Sea Central Graben showing investigated wells and the boundaries of the 3D basin model in the UK sector. The used wells from the Norwegian sector are located in quadrant 1 and 2 and the area of the Norwegian sector 3D basin model is situated in a block of quadrant 2. These data could not be plotted for confidentiality reasons.

2.2 Thin section preparation, optical microscopy and point-count analysis

Thin sections were prepared from the available core material additional to the thin sections provided by the industry partners in order to examine detrital and authigenic mineralogy as well as the textural relationship of authigenic phases. Blue dyed epoxy resin (Araldid 2020 + Sudan blue 670) was used for impregnation to allow a better visualization of porosity. Carbonate bearing thin sections were half side stained with Alizarin Red and potassium ferricyanide for the differentiation between calcite, dolomite and ankerite. Some of the thin sections provided by the industry partners were additionally stained with sodium cobaltnitrite for K-feldspar identification. Optical microscopy was carried out on a ZEISS Axioplan 2 microscope equipped with a HITACHI HV-C20 digital camera for photo documentation. Polished thin sections were prepared from selected samples for microprobe analysis and cathodoluminescence microscopy. Paragenetic sequences were derived using the textural relationship between different authigenic phases observed by optical microscopy, backscatter electron images (BEI) and scanning electron microscopy (SEM).

Point-count analyses were carried out on 179 thin sections in order to quantify the mineralogical composition. They are mostly based on 300 and sometimes on 600 counts per thin section. Quality of quantitative data derived from point-count analysis depends mainly on the number of counted points (see Fig. 2.2 for uncertainty). The number of 300 counted points was selected for most of the thin sections as the best choice between minimizing the statistical failure and reducing expenditure of time. Values in the petrographic tables (Appendix 2) are given in volume percent of whole rock including porosity. The error of point-count values is larger in thin sections containing two lithologies. In such cases the different domains of the thin section were counted separately.

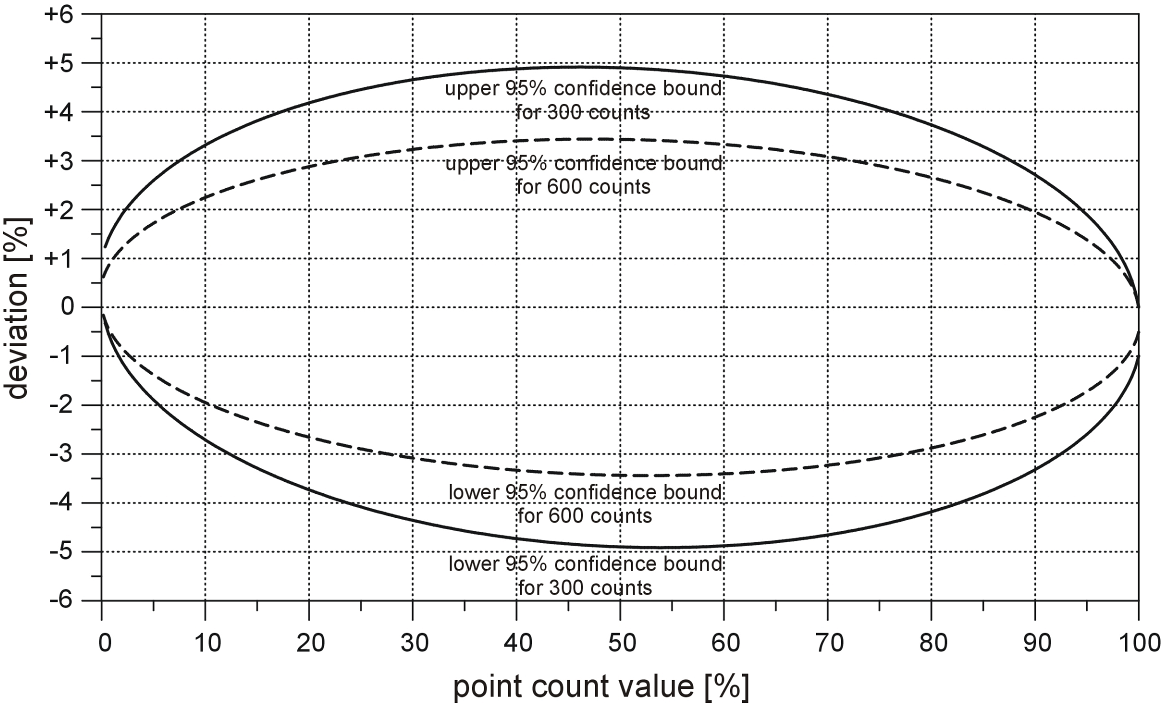

Fig. 2.2: Uncertainty of point-count data shown as 95% confidence interval for a total of 300 and 600 counts respectively. The deviation from counted value is plotted against the corresponding value in percent. The bounds were calculated after Howarth (1998).

Quartz overgrowths can only be quantified accurately by point-counting when the detrital grains are clearly outlined by a dust rim or a coating mineral. This was not always the case. If such dust rims (or coatings) are missing the result is more ambiguous. To overcome this problem it was attempted to use cathodoluminescence microscopy for the quantification of authigenic quartz. However, this method was restricted by the bright luminescence of frequently appearing detrital K-feldspars and carbonate cements.

The amount of fibrous and platy clay minerals is not easy to quantify accurately by point-count analysis. Their content is usually overestimated on the one hand and the amount of point-count porosity is underestimated in such samples due to the microporosity hidden between the single sheets or plates on the other hand. A similar effect may occur in samples with thin hematite coatings which were not cut perpendicular to the surface and which appear to be thicker than they are.

Pores with diameters smaller than the thickness of thin section could not be quantified accurately by optical microscopy. The thickness of thin sections lies around 28 µm and thus pores with a smaller diameter are referred as micropores in the context of this work. Such micropores occur for instance inside of leached feldspars and between fibrous or platy clay minerals (see sections 5 and 6 for example photographs).

Helium porosity values measured at routine plugs were available for some wells from internal industry reports and could be used for this study. This allowed to estimate the amount of microporosity in some of the samples. The difference between helium porosity values and point-count derived porosities is demonstrated in Fig 2.3 for samples from wells 30/2c-4[1], NOR-F and NOR-G. Helium porosity values are generally higher than those measured by point-counting (see Fig. 2.3). The difference between helium porosity and point-count porosity is especially noticeable in samples with relatively low porosity values, such as the Jurassic Intra-Farsund sandstones and finer grained samples from argillaceous sandflat facies (AS) in the Triassic Skagerrak Formation (see sections 5 and 6 for detailed facies description). Such samples had usually nearly no visible macropores and the whole measured helium porosity seems to be represented by small microspores located between detrital and authigenic clay minerals and inside of partly leached grains respectively.

Samples with a high content of fibrous or platy clay minerals like authigenic illite or chlorite contain also a high proportion of microporosity.

Bulk point-counted porosities are close to helium porosity values in samples from the best reservoir facies, which is represented by fluvial channel facies (FC) in the investigated Triassic wells and by upper shoreface facies (USF) in the samples from the Upper Jurassic (see Fig. 2.3).

Secondary porosity was estimated using textural criteria (see section 5 for details). Voids formed by plucking during the process of thin section preparation can easily be misinterpreted as being dissolution voids in this context. The differentiation between such pores and completely leached grains is not always possible. Such pores without mineral relicts were therefore counted separately as “oversized pores”.

---

[1] Samples from the 30/2c-4 well were not always taken exactly on the plug positions. On positions where the sample has been taken between two plugs, the helium porosity value of the nearest plug position in the same sedimentary body was assigned to the sample (routine plugs were sampled every 1 ft/30.48 cm).

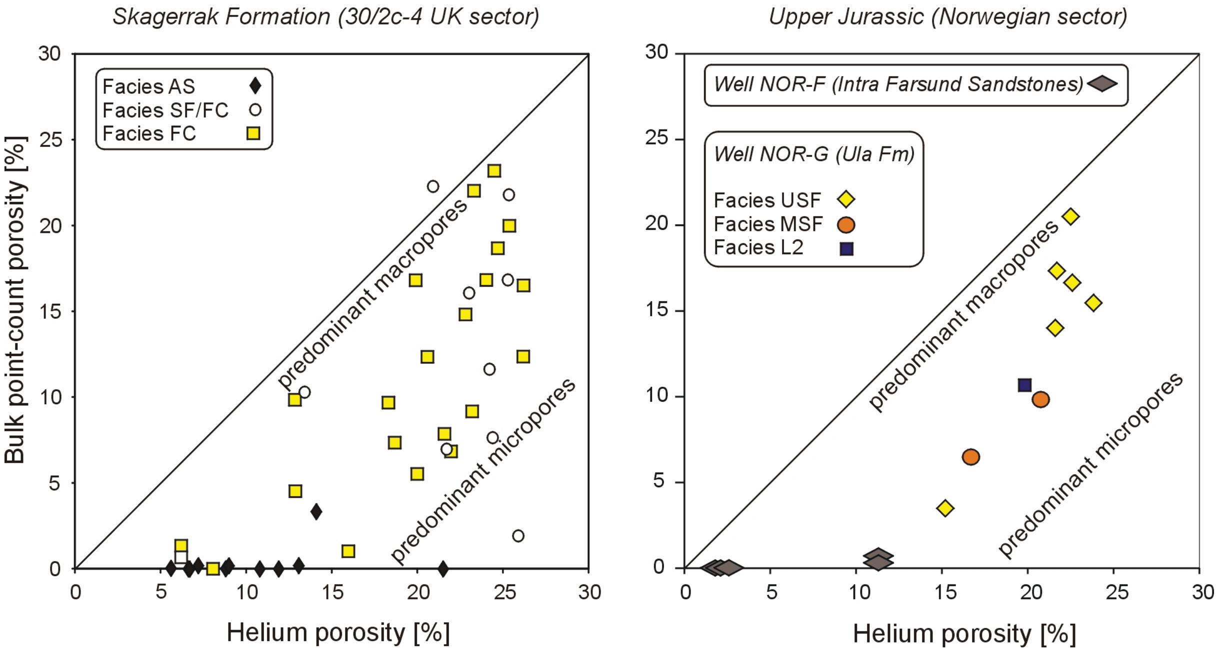

Fig. 2.3: Point-count porosity vs. Helium porosity from samples of wells 30/2c-4, NOR-F and NOR-G. Only minor visible porosity was observed in samples from the finer grained argillaceous sandflat facies (AS) and in intra Farsund sandstones. Most of the porosity is microporosity in such samples and can not be quantified by point-counting. In coarser cleaner sandstones (e.g. fluvial channel facies – FC, sheetflood facies – SF and upper shoreface facies - USF) much of the porosity is macroporosity and the values of point-counting are more equal to helium porosity.

Grain sizes were measured directly on random lines using a MINOX petroscope by quantifying the long diameter on 100 grains per thin section. It must be considered that the direct measurement in thin sections gives only the apparent grain size owing to random sectioning (Harrel & Eriksson, 1979). The measured values were converted to the phi scale:

$\phi = -\log_2 d$ (d...diameter in mm) (2.1)

A linear scale would overemphasize large and underemphasize small grain sizes (McManus, 1996 and references therein). Average values of this apparent grain sizes were calculated back to the linear scale for better imagination and documented in the tables of Appendix 2. Average grain sizes calculated in this way are generally a little bit smaller than average grain sizes calculated from the mm-values directly.

Sorting was estimated using comparison plates from Beard & Weyl (1973), since sorting was needed in context of this study particularly to estimate the initial porosity for the Houseknecht (1987)-diagram. Sphericity and rounding were estimated using comparison plates from Krumbein & Sloss (1963).

Two different approaches were used for the estimation of the degree of mechanical compaction. The first method was published by Houseknecht (1987) using the intergranular volume. The intergranular volume gives information about the degree of compaction for samples with identical initial porosity. The initial porosity is unknown, but can be estimated for samples with comparable sorting and grain size using published data of artificially mixed sands (e.g. Beard & Weyl, 1973).

Another approach using the nature of grain contacts was used for comparison with the intergranular volumes to avoid the problem of the unknown initially porosity.

For the estimation of the degree of mechanical compaction by the type of grain contacts the dominant grain contacts of 100 grains from clast supported samples were quantified in some of the wells (see table appendix 6). An extended description of grain contact types and the change of dominant types with increasing depths of burial can be found for instance in Taylor (1950). For better visualisation of the main grain contact type in diagrams the "level of compaction" was calculated using following formula:

$$loc = \sum_{i=0}^{5} \frac{Xi}{n}\, i \tag{2.2}$$

loc…level of compaction
n…...total number of counted grains
Xi.…number of grains with corresponding contact type in the plane of thin section for: X0 = floating grains (grains with no contact in thin section), X1 = point contacts, X2 = short longitudinal contact (< ½ grain lengths) , X3 = long longitudinal contact (> ½ grain lengths) , X4 = concave convex contact, X5 = sutured contact

2.3 Electron microprobe analysis

15 of the polished thin sections were carbon coated and analysed with a JEOL JXA 8900 RL electron microprobe device (EMP) equipped with five wavelength dispersive spectrometers (WDS) at the department of geochemistry at the University of Göttingen. Focus of the analysis was the qualitative and quantitative determination of mineral chemistry, especially of feldspars, carbonates and clay minerals. Backscatter electron images (BEI) were made from typical textures. Operation conditions during quantitative analysis were an acceleration voltage of 15 kV, a measurement beam current of 12 nA for carbonates and of 15 nA for silicates. The electron beam during the measurement had a diameter of 10 µm for carbonates and a diameter of 5-10 µm for silicates. The different standards, which have been used for carbonate and silicate analysis are summarized in Table 2.2. An energy dispersive spectrometer system (EDX) was used for quick qualitative determination of mineral composition of components, which could not be identified by optical microscopy. The results of the quantitative measurements are summarized in the tables of Appendix 3. Cations in the structural formula were calculated after (Bulach, 1970).

Table 2.2: Standards for silicate and carbonate program at EMP

	Silicates		**Carbonates**	
Compound	Standard	wt. %	Standard	wt. %
SiO_2	Wollastonite	51.51	Wollastonite	51.51
Na_2O	Albite	11.74		
CaO	Wollastonite	47.74	Calcite	56.04
K_2O	Sanidin	14.18		
FeO	Hematite	89.72	Siderite	59.08
Al_2O_3	Al_2O_3	99.99		
MgO	MgO	99.99	Dolomite	22.04
TiO_2	TiO_2	100.00		
SrO	Celestine	56.41	Strontianite	67.67
MnO	Rhodonite	42.44	Rhodonite	42.44
BaO	Celsian	38.77	Baryte	65.69

2.4 X-ray diffraction analysis

11 rock samples, mainly mudstones, were selected from well 30/2c-4 in order to identify the mineralogical composition, especially of the clay minerals. The analyses were carried out on a SEIFERT FPM XRD 7 device with following configuration: Cu-Kα radiation at 40 kV and 40 mA, 2θ in 0.02° steps between 4° and 70° for bulk rock samples and between 4° and 40° for the fraction < 2 µm. Bulk samples were powdered carefully in a mortar and coated in a 0.5 mm sheet on the sample carrier for the qualitative determination of bulk rock composition.

The fraction smaller than 2 µm of the mudstones was separated after crushing by gravity settling and analysed under air-dried conditions, glycol solvated and after heating to 550°C for two hours.

Mineral phases were identified by comparison with the powder diffraction file of the International Centre for Diffraction Data.

A non destructive analysis was carried out additionally on a micro X-Ray diffractometer (AXS-Bruker D8-Discover) at the department of geography in Jena, in order to identify authigenic clay minerals in the pore space of sandstones, since not enough material was available for the separation of (predominantly authigenic) clay minerals from the sandstones. However, the quality of these XRD data was relatively poor with only the detrital minerals generating suitable peaks for identification. Thus, this method brought no advantages compared to the powder diffractometry results for this study.

2.5 Scanning electron microscopy

In order to study typical textures, habit of minerals, pore geometries and surface morphologies a ZEISS DSM 940A scanning electron microscope (SEM) operated with 20 kV and 0.01-0.1 nA for image acquisition and ~ 0.3 nA for energy dispersive spectrometer system (EDX) was used at the department of glass chemistry in Jena. Four samples were coated with carbon prior to the measurement to avoid the build-up of electrical charge. Working distance was between 6 and 25 mm. One of these samples and four other samples (see Appendix 1 for details) were sent to the University of Warszawa for higher resolution and better quality SEM images which were made by Marek Wróbel with a JEOL JSM-6380LA SEM.

2.6 Stable isotope analysis of carbonates

Samples with a relatively high content of authigenic carbonate were selected after petrographic examination for the analysis of stable carbon and oxygen isotopes at carbonates. The samples were grinded and the measurements were carried out by Prof. Dr. M. Joachimski at the University of Erlangen using the following procedure: The powder was reacted with 100% phosphoric acid (density >1.9, see Wachter & Hayes, 1985) at 75°C using a Kiel III online carbonate preparation line connected to a THERMO-FINNIGAN 252 mass spectrometer. All values are reported in per mil relative to V-PDB by assigning a δ^{13}C-value of +1.95‰ and a δ^{18}O-value of -2.20‰ to NBS19. Reproducibility was checked by replicate analysis (3 times) of laboratory standards and is better than ±0.04‰ (1σ) for δ^{18}O- and ±0.03‰ for δ^{13}C-values. The oxygen isotopic compositions of dolomite and ankerite were corrected using the fractionation factor for dolomite published by Rosenbaum & Sheppard (1986).

The measurement of bulk sample isotopic composition is problematic since different carbonate generations in a sample can not be considered separately. The problem requires an analytical method which has a spatial resolution down to the micrometer range and allows to analyse the sample in-situ. It was attempted to fix this problem for carbon isotopes in samples of the well 30/2c-4 by carbon isotope analyses via an UV-laser system. Therefore, the laser extraction system of the Max-Planck-Institute for Biogeochemistry Jena was used. The system consists of a Nd:YAG 266 nm UV-laser (MERCHANTEK-NEW WAVE, USA) coupled with an isotope ratio mass spectrometer (DELTA$^+$XL, FINNINGAN MAT, Germany). For a detailed description of the analytical system see Schulze et al. (2004) and Wieser & Brand (1999). The carbonaceous compounds were volatilised by the laser energy mainly to CO and in parts to CO_2 (personal communication, W. Brand, P. Linke). In a combustion furnace behind the sample chamber all the gas was converted to CO_2 and analysed by the isotope ratio mass spectrometer.

The dimension of the craters caused by the laser depended on the used focus, energy and the sample material. These three parameters have been adjusted to narrow the crater size on the one hand and release enough material to produce suitable signal amplitudes on the other hand. Figure 2.4 shows the reproducibility against signal amplitude.

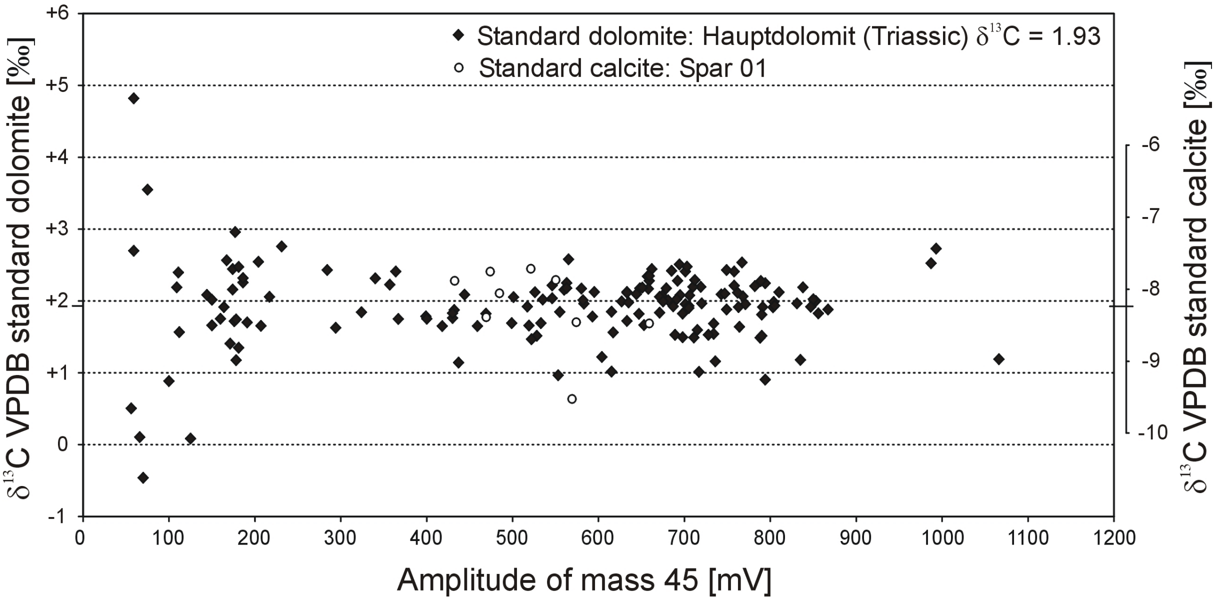

Fig. 2.4: Reproducibility of δ^{13}C-values for the used dolomite standard against the amplitude of the signal. Measurements at a second calcite standard were plotted additionally for comparison. Signal amplitudes lower than 150 mV spread over a wider range and such values are less reliable and should be used with care.

Diameters of craters were measured directly after the sample was removed from the holder and the depths of penetration after cutting some of the samples perpendicular. The depth of the craters exceeded the diameter significantly. In pure carbonate (dolomite standard) the craters had a width of 50 to 120 µm and a depth of 400 to 600 µm. Crater size in carbonate cemented sandstone samples was generally smaller, because the feldspar and quartz framework grains resisted the laser better than pure carbonates. However, this effect produced also lower signal amplitudes in the sandstone samples with the same laser settings. Standard deviation of repeated measurements on the dolomite standard is 0.58‰ for all signal amplitudes and 0.38‰ for amplitudes higher than 150 mV (see Fig. 2.4). Therefore, only values with signal amplitudes higher than 150 mV should be used for further interpretation. Subsequent to the measurement thin sections were prepared from the samples to determine the petrography around the analysed spots. However, the crater depth was larger than average authigenic mineral crystal size and it could not be excluded that a second carbon source was affected by the laser beam. So, spatial resolution was generally not suitable to differentiate between carbonate cement generations. Additional problems were caused by the occurrence of bitumen in some of the samples. Therefore, at least three different carbon sources must be considered when interpreting the data.

2.7 Cathodoluminescence microscopy

For the investigation of textural relationship between diagenetic phases, especially carbonates, a hot-cathode cathodoluminescence (CL) microscope (HC1-LM) equipped with a KAPPA 961-1138 CF 20 CXC digital camera at the University of Freiberg was used. To prevent the build-up of electrical charge, the investigated 3 polished thin sections from well 30/2c-4 were coated with carbon. Working conditions were: $<10^{-6}$ bar vacuum, acceleration voltage of 14 kV, and a current density of 10 μA/mm². Width of the electron beam was defocused ~ 5 mm. In the affected area the epoxy resin was thermal altered after a few seconds of electron beam treatment. The amount of quartz cement was very difficult to estimate due to the bright luminescence of frequently appearing detrital K-feldspars and carbonate cements.

3 Regional geology of the working area

This chapter gives a general overview of the geological development of the North Sea with emphasis on the investigated reservoir horizons in the Central Graben area. A more detailed geology of the investigated fields and wells is given in the petrography sections 5 and 6.
A huge amount of literature exists about the relatively complex geologic development of the North Sea basin as the result of a long exploration and research history. The text of section 3 was composed using mainly following sources: Bassett (2003), Bishop (1996), Bruce & Stemmerik (2003), Coward (1995), Coward et al. (2003), Erratt et al. (1999), Fisher & Mudge (1998), Gatliff et al. (1994), Glennie (1998), Glennie & Underhill (1998), Goldsmith et al. (1995), Goldsmith et al. (2003), Gowers et al. (1993), Pooler & Amory (1999), Spencer et al. (1996) and Ziegler (1990). All information in the following text comes from these articles unless other citations are given in the text.
A graphical summary of stratigraphy and geologic development of the central North Sea area is given in Fig. 3.1.

3.1 Pre-Permian

The basement of the North Sea consists of several continental blocks which were amalgamated during the Caledonian orogenic cycle (see basement map in Fig. 3.2). Today the North Sea is situated on the collision zone between the three main blocks Laurentia, Baltica, and Avalonia (Zanella et al., 2003).
Three main tectonic episodes occurred in the North Sea area from Cambrian to Carboniferous: The Athollian (former Grampian) Orogeny from about 460 to 450 Ma, the Acadian Orogeny around 400 Ma and the Variscan Orogeny from 400 to 300 Ma (see Coward et al., 2003 and references therein for details). They formed the framework for the following Mesozoic structural evolution.

Laurentia and Baltica existed as discrete continents after the break up of Rodinia. The Avalonian microplate detached from the north of Gondwana, probably in early Ordovician times, and drifted northwards, closing the southern Iapetus Ocean between Avalonia and Laurentia. The eastern part of Avalonia collided with Baltica in the Late Ordovician (Ashgill), closing the Tornquist Sea between Avalonia and Baltica. This caused metamorphism up to amphibolite facies on the Mid North Sea High. The Caledonian collision between Laurentia and Baltica started during the Ordovician. The southern Iapetus Ocean was finally closed during Silurian to Early Devonian. Tectonic activity between these three plates seems to have continued until the Mid Devonian.
It is widely accepted that the southern Iapetus suture on the British Isles, the northern Iapetus suture and the Tornquist suture form a triple junction somewhere in the North Sea. The exact position is unknown. It is located probably within the Central Graben north of the Mid North Sea High. The plate movements and accretions left rigid cratonic blocks and between the blocks zones of weakness, which seem to be important for later structural and stratigraphic evolution. Structural inheritance is a major feature of the geologic evolution of the North Sea.

Fig. 3.1 (next page): Summary stratigraphic column for the Central Graben area. Stratigraphic units covered by this study are marked yellow. The column was composed using the following references: Chronostratigraphy and lithostratigraphy - Menning & Commission (2002); Eustatic sea level from Triassic to Cenozoic - Haq et al. (1987); Eustatic sea level from Devonian to Permian - Veevers & Powell (1987); Lithology - Bruce & Stemmerik (2003), Cayley (1986), Erratt et al. (1999), Glennie et al. (2003), Goldsmith et al. (1995) and Oakman & Partington (1998).

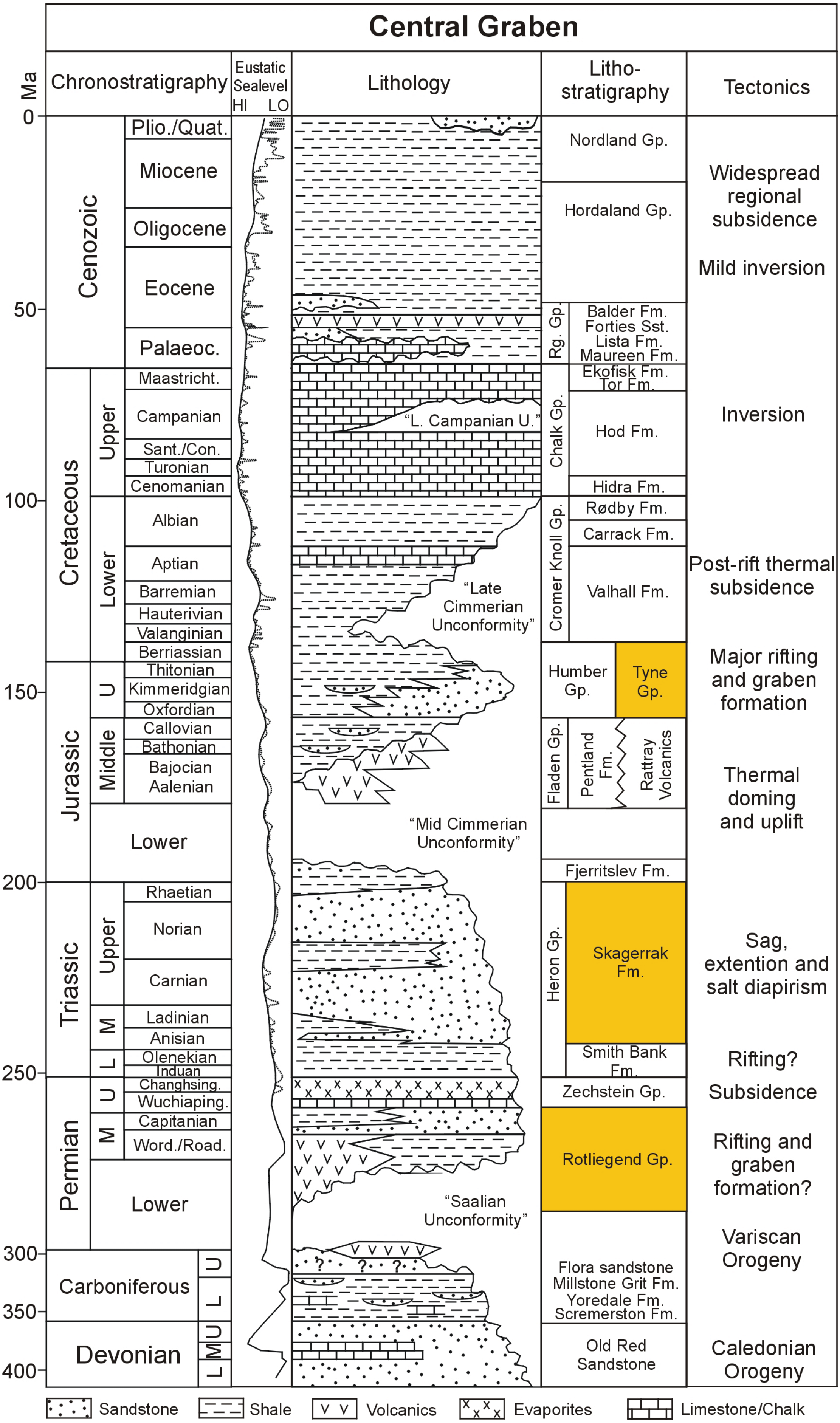
Central Graben
Ma
Chronostratigraphy
Eustatic Sealevel
HI LO
Lithology
Litho-stratigraphy
Tectonics
0
50
100
150
200
250
300
350
400
Cenozoic
Plio./Quat.
Miocene
Oligocene
Eocene
Palaeoc.
Cretaceous
Upper
Maastricht.
Campanian
Sant./Con.
Turonian
Cenomanian
Lower
Albian
Aptian
Barremian
Hauterivian
Valanginian
Berriassian
Jurassic
U
Thitonian
Kimmeridgian
Oxfordian
Middle
Callovian
Bathonian
Bajocian
Aalenian
Lower
Triassic
Upper
Rhaetian
Norian
Carnian
M
Ladinian
Anisian
L
Olenekian
Induan
Permian
U
Changhsing.
Wuchiaping.
M
Capitanian
Word./Road.
Lower
Carboniferous
U
L
Devonian
U
M
L
"L. Campanian U."
"Late Cimmerian Unconformity"
"Mid Cimmerian Unconformity"
"Saalian Unconformity"
?
Nordland Gp.
Hordaland Gp.
Rg. Gp.
Balder Fm.
Forties Sst.
Lista Fm.
Maureen Fm.
Chalk Gp.
Ekofisk Fm.
Tor Fm.
Hod Fm.
Hidra Fm.
Cromer Knoll Gp.
Rødby Fm.
Carrack Fm.
Valhall Fm.
Humber Gp.
Tyne Gp.
Fladen Gp.
Pentland Fm.
Rattray Volcanics
Fjerritslev Fm.
Heron Gp.
Skagerrak Fm.
Smith Bank Fm.
Zechstein Gp.
Rotliegend Gp.
Flora sandstone
Millstone Grit Fm.
Yoredale Fm.
Scremerston Fm.
Old Red Sandstone
Widespread regional subsidence
Mild inversion
Inversion
Post-rift thermal subsidence
Major rifting and graben formation
Thermal doming and uplift
Sag, extention and salt diapirism
Rifting?
Subsidence
Rifting and graben formation?
Variscan Orogeny
Caledonian Orogeny
Sandstone
Shale
Volcanics
Evaporites
Limestone/Chalk

]

The formation oft the mega continent Laurussia came to an end with the final closure of the Iapetus ocean at the end of Caledonian orogeny. Large pre-Permian continental sedimentary basins (Orcadian Basin and Midland Valley Graben) were located in the northern North Sea area. Thick clastic sequences of fluvial and lacustrine origin accumulated here. These deposits are referred to as Old Red Sandstone. Red bed sedimentation took also place in the central North Sea from the Devonian until the early Carboniferous. The southern margin of the Old Red continent bordered on the Rheic Ocean. A transgression from this ocean, following the northern Iapetus suture, led to the deposition of marine carbonates in Mid Devonian times. Such carbonates were found in the Auk and Argyll Fields in the central North Sea. This embayment seems to match with the later Central Graben and shows the repeated inheritance of older structural elements, as mentioned above.

The collision of Gondwana with the southern margin of Laurussia initiated the Variscan Orogeny in Lower Carboniferous times. The Rheic ocean was finally closed in the Late Carboniferous. The super continent Pangaea had formed during the Variscan plate cycle. Tectonic activities in Lower Carboniferous times caused the initiation of subsiding basins and grabens. One of them was the Midland Valley Graben, where subsidence was linked to igneous activity. Lower Carboniferous sedimentation seems to have been strongly affected by this synsedimentary tectonic activity.

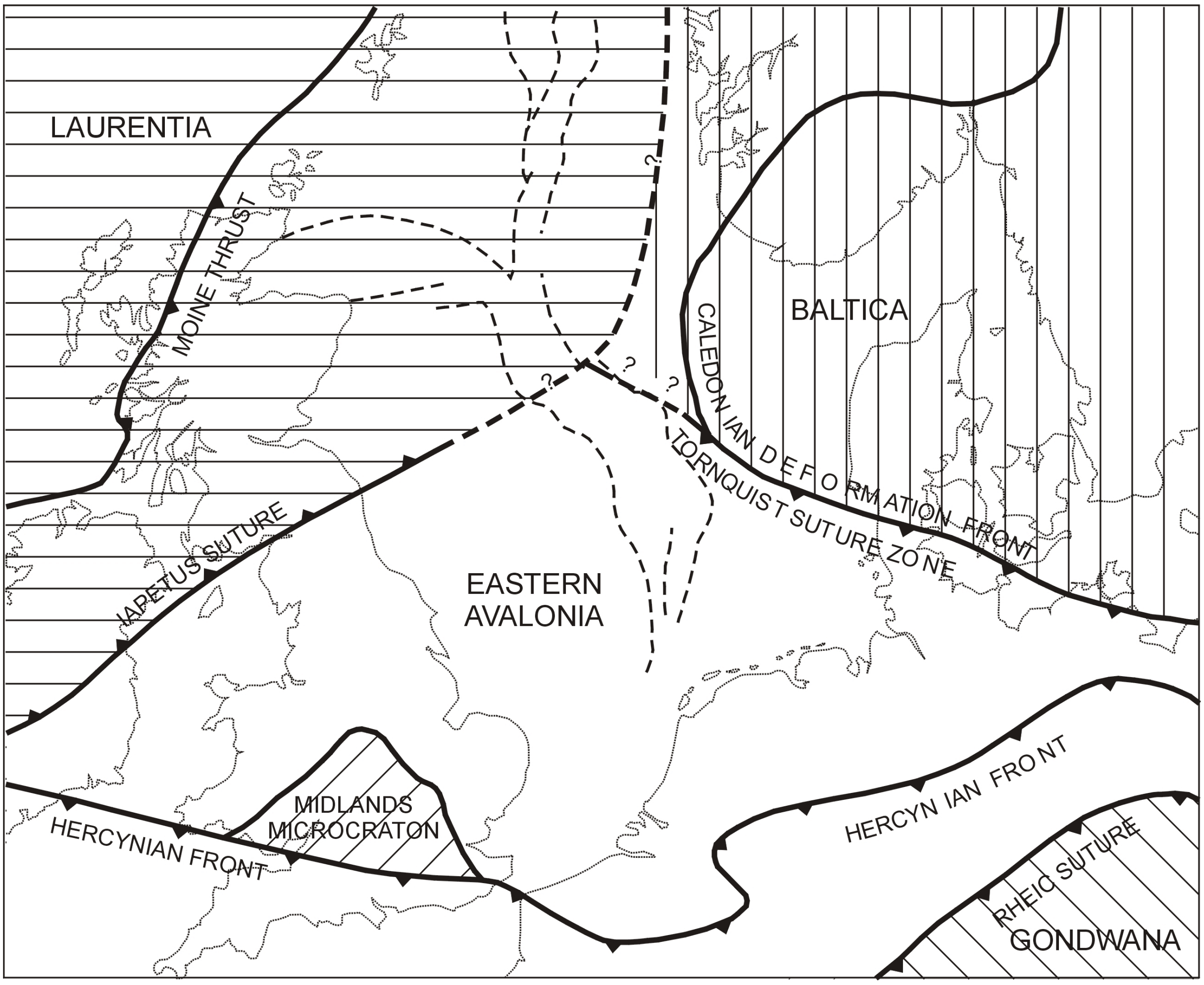

Fig. 3.2: Sketch map of the North Sea basement (slightly modified after Zanella et al., 2003).

Marine shelf sedimentation prevailed meanwhile in the southern parts of the North Sea which formed the southern margin of the Old Red Continent in Devonian and Early Carboniferous times. These sedimentary patterns changed with the development of the Variscan foreland basin after the docking of Gondwana. Thick coal measures were deposited in a rapidly subsiding foreland basin in front of the Variscan mountain belt in Westphalian times. These coal deposits are important hydrocarbon source rocks in the southern North Sea and adjacent areas.

The occurrence of Carboniferous deposits in the central and northern North Sea seems to be restricted to separated small basins (Spencer et al., 1996). However, only a small number of wells have reached Carboniferous strata in the central North Sea and thus this system remains poorly understood. The Carboniferous is divided into Scremerston, Yoredale and Millstone Grit Formations in the Central Graben and on the Mid North Sea High (see Bruce and Stemmerik, 2003 and references therein). The succession starts with sandstone dominated fluvial red beds at the boundary to the Devonian. The red beds were replaced by sediments of more deltaic character in the Mid Visean and followed by marine influenced sediments (Yoredale) in Late Visean and Early Namurean. The Upper Carboniferous Flora Sandstone occurs isolated in UK quadrant 31. It was dated as Westphalian B or Stephanian.

The Mid North Sea High was uplifted after Variscan foreland basin development in Late Carboniferous times. The uplift was possibly caused by magmatic unterplating, since intense Late Carboniferous intrusive activity occurred in this region (Coward, 1995 and Coward et al., 2003). Another explanation for the uplift may be local thickening of crust due to the reworking of the Iapetus and Tornquist sutures during the Variscan plate cycle (Coward et al., 2003).

3.2 Permian

The North Sea was situated mostly in an intraplate setting from Permian until today. Palaeozoic plate accretion changed over to continental extension during the Permo-Triassic and brought a major change in the tectonic regime. Two large regions of subsidence, separated by the Mid North Sea - Ringkøbing Fyn High, formed in the Permian. These two subsiding areas are referred to as the Northern and Southern Permian Basins (Fig. 3.3).

The patterns formed by these two basins were overprinted by rifting in the Central and Viking Graben system, which was probably initiated in the Permo-Triassic in an attempt to create a Proto-Atlantic. However, the exact starting time of the rifting is under discussion, ranging from Carboniferous to Triassic (see discussion in Cornford, 1994). The rift system had cut the Northern and Southern Permian Basin as well as the Mid North Sea High. It consists of several grabens. Important elements are the Viking and Central Grabens as areas of high subsidence. Major Permian subsidence occurred also outside the Central and Viking Grabens, e.g. in the Horn-Bamble-Oslo and North German systems of grabens as well as in the Moray Firth Basin.

A large east-west trending mountain chain developed during the Variscan orogeny south of the North Sea area. The climate north of these mountains was semi arid to arid and a desert established. Mainly clastic sediments of fluvial, aeolian and sabkha origin were deposited under these conditions in Rotliegend times.

The Lower Rotliegend south of the working area in the Central Graben consists mainly of volcanic rocks of the Karl Formation. These rocks are composed of basalts and tuffs with interbedded mudstones. Aeolian and fluvial sediments, sourced from the Caledonides, were deposited in the working area during the Upper Rotliegend. Two main facies types can be differentiated: A sequence mostly composed of aeolian and fluvial sandstones, which has been termed Auk Formation, and a lake or sabkha facies association, composed of siltstones and shales, which is referred to as Fraserburgh Formation (Fig. 3.4). Fraserburgh shales seem to occur in the deeper subsided graben areas at palaeo-morphological lows.

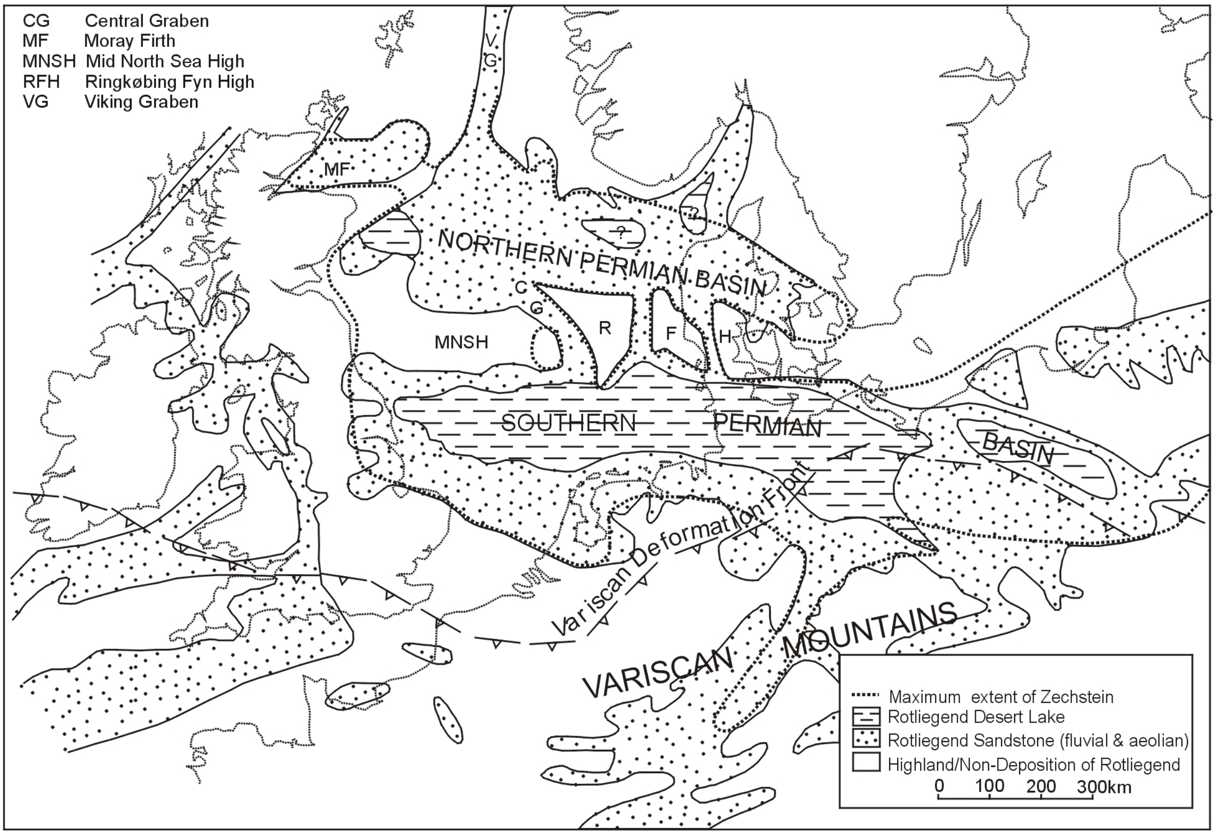

Fig. 3.3: Simplified facies distribution of the Rotliegend in NW Europe and the maximum extent of the succeeding Zechstein (Glennie, 2001).

The wind in the Northern Permian Basin came from northwest or northerly directions, as indicated by aeolian dune sands (Glennie, 1998 and Coward, 2003).
The rapid subsidence in both Permian basins exceeded the rate of sedimentation in the Late Permian and the deepest basin parts lay probably some 200-300 m below the sea level at this time (Glennie & Underhill, 1998). Desert lakes developed in the depressions which were affected by short-term marine ingressions in Rotliegend times (Legler & Schneider, 2008).

The deep, low-lying continental basin was flooded by the marine Zechstein transgression and the Zechstein sea extended across northern and central Europe, filling both Permian basins. This major transgression was probably initiated by a glacio-eustatic rise in sea level connected to the end of a glaciation phase in Gondwana (e.g. Glennie, 1998). The transgression came from the north using a seaway to the Arctic Ocean, that was created by rifting in the Faeroes-East Greenland region associated with some rifting in the northern North Sea. After initial minor reworking of uncemented Rotliegend sands during the flooding, an about one meter thick sapropelic shale was deposited under anoxic conditions (Taylor, 1998 and references therein). The shale is termed Kupferschiefer (copper shale) and can be found in the Southern and Northern Permian Basins, in the Moray Firth and in the Viking Graben, but appears to be absent from parts of the highs (Taylor, 1998).
After deposition of the Kupferschiefer, carbonates, sulphates, halite, potassic salts and fine-grained siliciclastic sediments were accumulated in a giant evaporitic salt basin. This basin was characterized by high evaporation rates and limited water supply under arid climate conditions. The Zechstein sequence is composed of five major depositional cycles showing glacio-eustatic sea level fluctuations. Each cycle started with the incursion of normal seawater and was followed by an increase of salinity, sometimes probably culminating in complete evaporation. Zechstein sediments were deposited in circular arranged facies patterns in every

cycle with thick evaporites in the basin centre and carbonates to clastic deposits at the margins. Gradual transgression of the Mid North Sea High occurred also during Zechstein times. No salt deposition has been observed from the Viking Graben north of the Beryl Embayment.

The later halokinetic movement of Zechstein salt was important for the post-Permian structural development in the Central North Sea (see Hodgson et al., 1992 and Bishop, 1996).

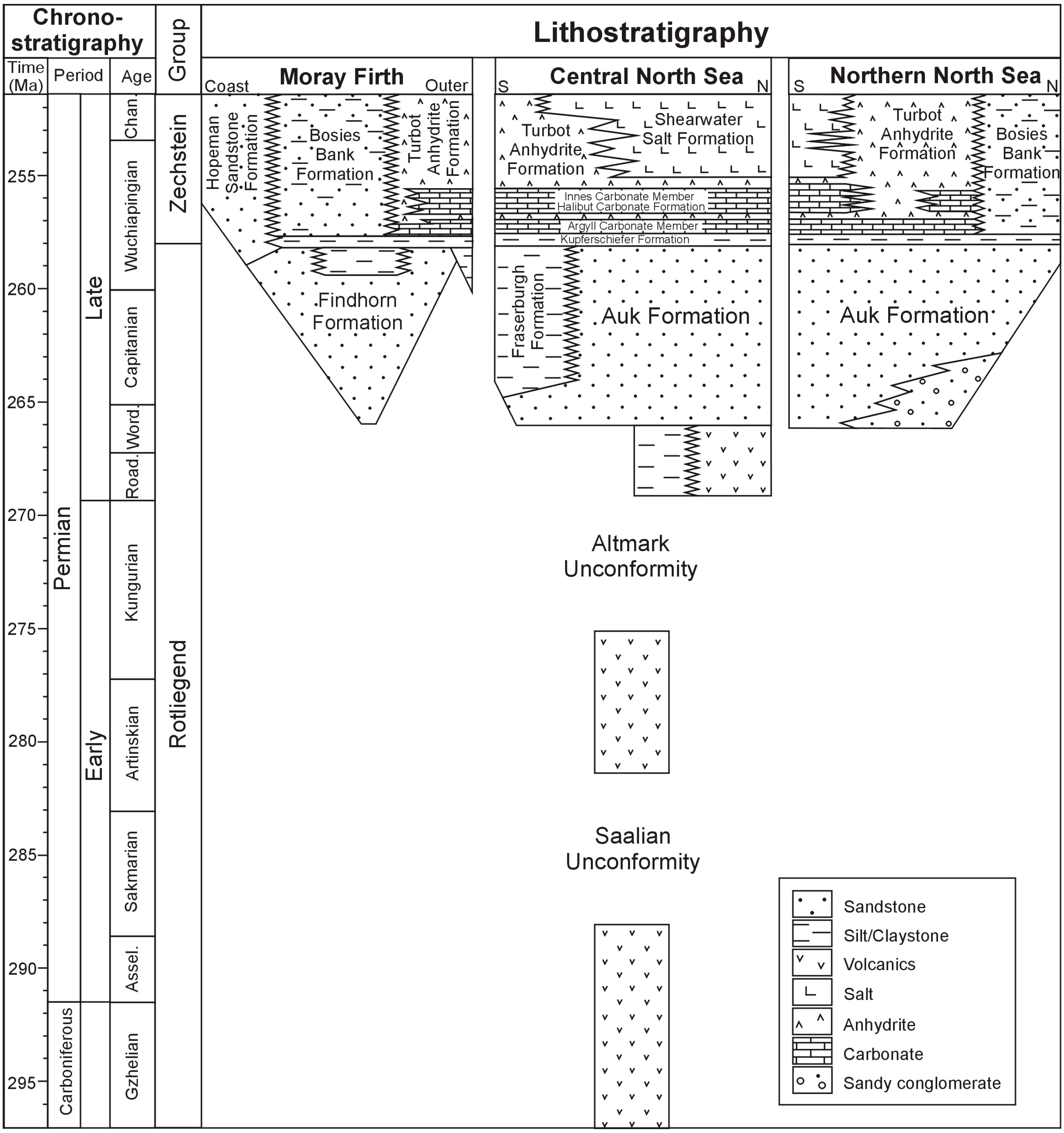

Fig. 3.4: Permian stratigraphic correlation chart for the central North Sea and adjacent areas (modified after Glennie et al. (2003).

3.3 Triassic

The important features of the Triassic in the Central North Sea are the deposition of red beds influenced by the movement of underlying Permian salt and a probable early rifting phase.

While it is currently under discussion if the Viking and Central Graben system was initiated in Permian or even in Carboniferous times, it is widely accepted that the grabens have existed in the Triassic. The north trending Graben system crossed mainly the Northern Permian Basin and the Mid North Sea Ringkøbing Fyn High. The rifting was probably followed by subsidence in the Central and Viking Grabens in Late Triassic to Early Jurassic. Other rapidly subsiding areas were located in the southern Central and Horn Grabens, where Triassic sediments have accumulated with a thickness of about 4000 m.

The sedimentary conditions returned to continental during the Triassic and mainly red beds were deposited in the whole Northern Permian Basin. The Muschelkalk transgressions reached most likely the central North Sea area via the Central Graben (Fig. 3.5a).

The Triassic succession in the central North Sea is composed of basal fluvial to lacustrine Smith Bank mudstones followed by Skagerrak Formation sandstones and mudstones (Fig. 3.5b). Broad floodplains had developed between marginal fans and the deepest basin parts. Sediments were deposited predominantly in small basins formed by the withdrawal of underlying Zechstein salt in the central North Sea (Smith et al., 1993 and Fisher & Mudge, 1998). These depressions, called pods, were located between nearly north-south trending salt ridges, which developed over Permian age faults in areas with active salt movement (Hodgson et al., 1992).

Many of these mini-basins developed across the Central Graben and were filled with ephemeral lake sediments. These lakes were surrounded by floodplains with fluvial channels. The typical Skagerrak Formation facies associations were deposited in this environment. Much of the coarser clastic material was sourced from the Fenno-Scandian Craton at eastern margin of the basin (Fisher & Mudge, 1998). Thick successions of coarse clastic material belonging to the Skagerrak Formation can also be found in the Egersund and North Danish basins.

Large parts of the Triassic sediments in the Central Graben were most likely removed by erosion associated with the following Jurassic thermal doming.

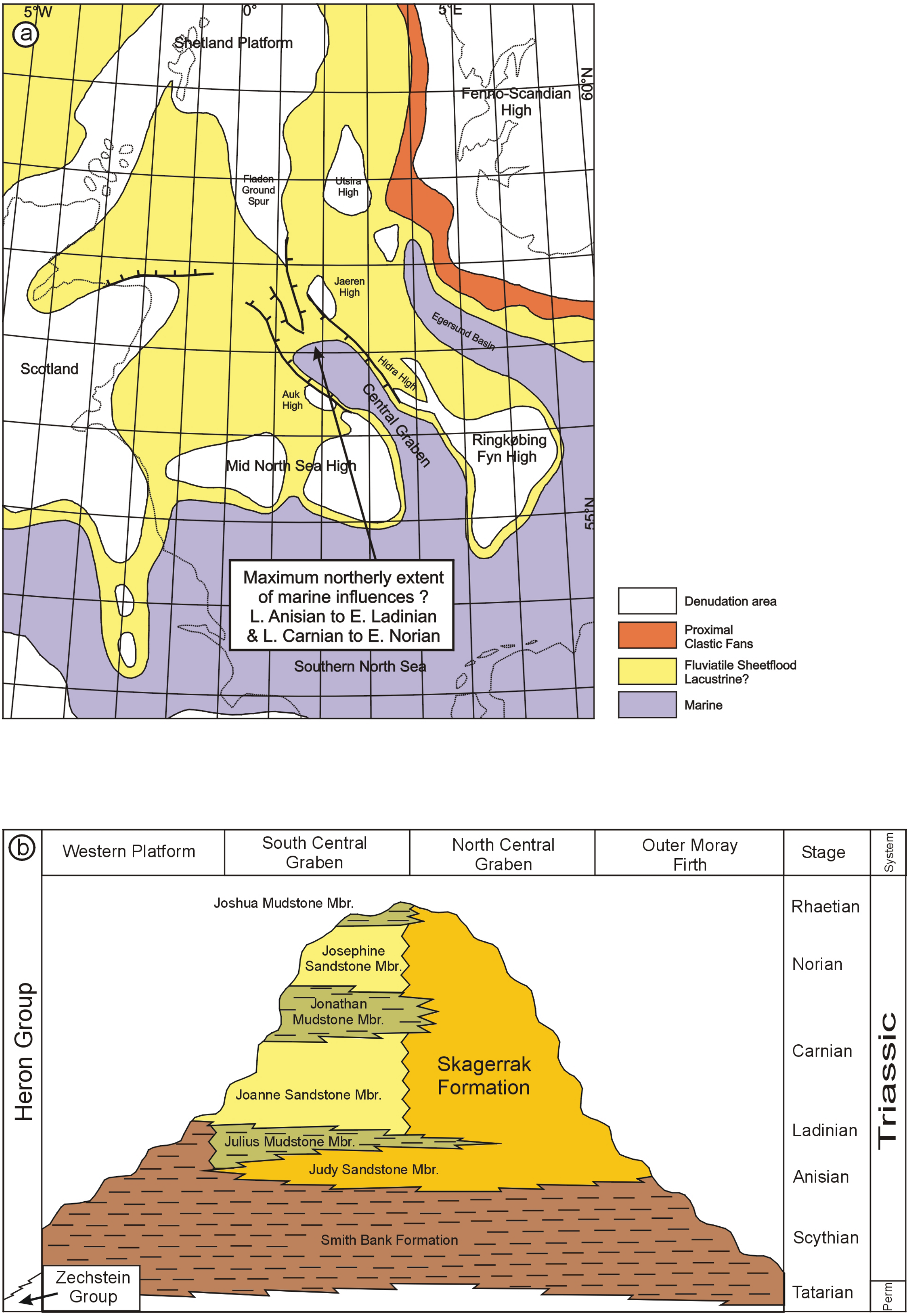

Fig. 3.5: Generalized Triassic palaeogeography (a) and stratigraphy (b) for the central North Sea area (after Goldsmith et al., (1995).

3.4 Jurassic

The terrigenous sedimentation of the Triassic changed gradually to marine and complete flooding occurred during the Early Jurassic. Thermal subsidence took place probably until the Toarcian. Much of the Lower Jurassic sequence was eroded because of domal uplift in the Middle Jurassic. Therefore, Lower Jurassic sediments are only locally preserved. They are referred to as the Gassum and Fjerritslev Formations.

The boundary between Middle and Lower Jurassic is marked by the widespread Mid Cimmerian Unconformity in the central North Sea. This stratigraphic break documents a phase of doming and uplift in early Middle Jurassic times. The uplifted area extended over a distance of 700 km in north-south direction from the southern Viking Graben into the southern North Sea, and over about 1000 km in east-west direction from England to Denmark. Parts of the Central Graben emerged with the dome and Triassic and older strata were eroded, in the centre of the dome locally down to the basement. The erosion products were accumulated as deltaic sequences (e.g. Brent Group) in adjacent basins (e.g. Viking Graben), which continued to subside.

Sedimentation in the Central Graben started again in middle Bajocian and Bathonian times, initially in tectonically induced half grabens and later more widespread, but confined to the graben. Sediments of this period belong to the coal bearing Pentland (UK) or Bryne (Norway) Formation, which overlie the Mid-Cimmerian Unconformity (Fig. 3.6). A marked angular unconformity with the underlying Triassic is absent within the deep graben areas of the central North Sea (Erratt et al., 1999).

The regional updoming of the central North Sea was accompanied by volcanic activity at the triple junction between Viking Graben, Central Graben and Moray Firth. These volcanic rocks cover a large area and have at the centre a thickness of circa 1500 m (Ziegler, 1990). They are termed Rattray Volcanic member and Ron Volcanic member respectively and belong to the Pentland Formation.

The main rift system developed during the Middle and Late Jurassic resulting in the extension of the Arctic Rift from the Barent Sea to the southern North Sea.

The first marine incursion in the Central Graben came from the north during the latest Bathonian and the regional transgression occurred in the early Callovian. The rift system was flooded and deep water conditions were gradually established in sub-basins during the late Callovian and Oxfordian. The Upper Jurassic succession is divided in Haugesund, Farsund and Mandal Formations in the Norwegian sector and in Heather and Kimmeridge Clay Formation in the UK sector (see Fig. 3.6). Rifting occurred in several pulses (Davies et al., 1999). The major phase of extentional activity began in middle Oxfordian to early Kimmeridgian. Marine conditions were established over much of the North Sea during the Kimmeridgian (Underhill, 1998) and a great part of the Central Graben formed a deep water trough. Whereas the Heather shale (Callovian to Oxfordian) was deposited under relatively oxic bottom water conditions in the Central Graben, stagnant bottom water conditions started to develop in some sub-basins later during early Kimmeridgian.

The earlier basin fabric was overprinted in the late Kimmeridgian to Tithonian during a change in the extensional tectonic style. The former East-West directed extension became Northeast-Southwest dominated (see Erratt et al., 1999 for more details) and a number of different structural changes were caused in the working area. They include the formation of the Søgne Graben, the rotation of the platform east of the Grensen Nose to form south westerly dipping fault blocks, intense rotational movements on the Hidra High, a renewed footwall uplift of the Auk Horst, collapse of parts of the Fulmar platform, and the uplift of the Josephine Ridge as the eastern remnant of this preexisting platform (see map of the structures in Fig. 3.8 and Erratt et al., 1999 for details).

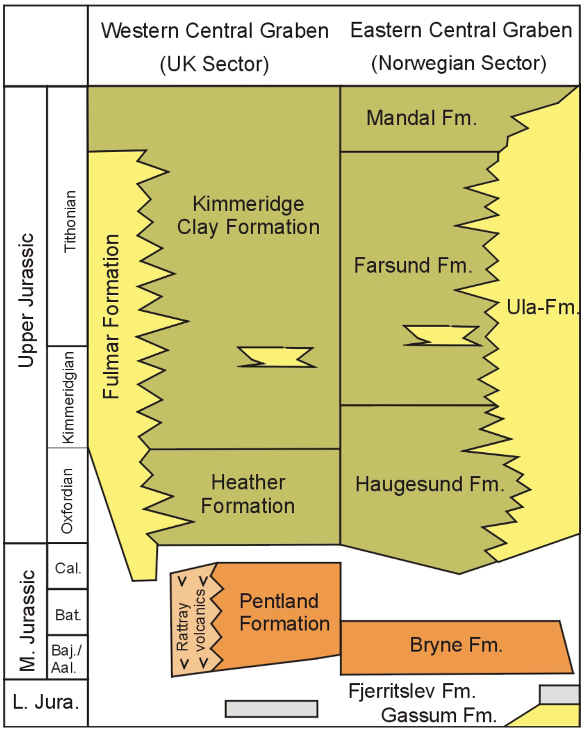

Fig. 3.6: Jurassic lithostratigraphy for the Central Graben. Modified after Fraser et al. (2003), Underhill (1998) and Simon Petroleum Technology limited (1994).

Accelerated subsidence during the late Oxfordian and Kimmeridgian led to deepening in all three rift arms and in Kimmeridgian times a major deep water trough has formed over the whole Central Graben. Disaerobic to anaerobic conditions prevailed at the sediment water interface from late Kimmeridgian to the Tithonian, and more locally until the Lower Cretaceous (Beriasian). Upper Jurassic organic rich mudstones and marls were accumulated under these conditions in the deep water basin, forming the most important source rocks of the region. The Late Jurassic succession can reach a thickness exceeding 1000 m in the Central Graben at its north-western border fault in the area of the Gannet Field. Callovian to latest Jurassic sediments in the northern parts of the Danish Central Graben have even a thickness of some 4000 m along the border fault of the Ringkøping High (Ziegler, 1990).

Shoreface sediments were deposited initially inside the active graben margins and later widespread across the platform areas, when the flanks of the grabens and the adjacent highs became gradually flooded in Oxfordian to late Kimmeridgian times.

These deposits are referred to as the Fulmar Formation (see also Fig. 3.6) on the western margin of the Central Graben (UK sector) or Ula Formation and Oxfordian Sands, respectively on the eastern margin (Norwegian sector). They form important reservoir rocks in the region. Continuing withdrawal of Permian salt led to the grounding of Triassic pods and the creation of accommodation space for Upper Jurassic sands on the platforms. The deposition occurred in an evolving pod-interpod network (Erratt et al., 1999). The shoreface facies retreated further to the basin margins in latest Jurassic after the ongoing flooding of the platforms. Organic rich mudstone sedimentation at this time was only locally interrupted by mass flow deposits caused by the instability of the graben margins.

Rifting intensified again in the North Sea from the Late Jurassic to the Early Createaceous, causing the Late Cimmerian rifting pulse. The rate of crustal extension and tectonic movements abated in the North Sea grabens after the Late Cimmerian rifting and most of the faults cease upwards in Early Cretaceous sediments of the Viking and Central Grabens.

The relief created by the rotated fault blocks was covered later by thick Cretaceous and Cenozoic sequences. The development of major salt domes started after differential loading with sediments in the main areas of Late Jurassic rifting and continues until today.

3.5 Cretaceous

The sedimentation from Early Cretaceous until present day was mostly controlled by thermal subsidence. Deep water shales were deposited over the relief which had developed during the Late Cimmerian rifting pulse starting in Early Cretaceous. The resulting unconformity is termed the Base Cretaceous Unconformity. Early Cretaceous sediments can reach a thickness between 250 and 500 m in the Central Graben (see Ziegler, 1990). They form a major seal for hydrocarbon accumulations and overpressure cells.

Sedimentation conditions remained marine during the whole Cretaceous. Pelagic Chalk was deposited widespread in the North Sea area, covering also the Mid North Sea High after a further eustatic rise in sea level. Cenomanian to Danian Chalk sequences have maximum thickness of up to 2000 m in the Central Graben and thin out over the Graben margins. Chalk mass-flow accumulations, derived from the graben margins, were deposited in the Central Graben in Maastrichtian to Danian times.

Tectonic inversion occurred in separate pulses from Hauterivian to Palaeocene. In the Central Graben inversion affected mainly Jurassic troughs, like the Feda Graben.

However, the precise nature of the inversion in the working area is only poorly documented (Gowers et al., 1993), and the different events seem to be very local, like the intense inversion observed along the Lindesnes Ridge. The reason for the inversion movements was intraplate compression, probably in context of the events which resulted in the opening of the North Atlantic. Compressional forces from North-West to South-East seem to have dominated in the North Sea until the present day, as indicated by borehole break-out data (Glennie & Underhill, 1998).

3.6 Cenozoic

The Cenozoic history of the North Sea Basin was dominated by regional subsidence as a result of post rift thermal relaxation of the lithosphere, and its isostatic adjustment to water and sediment loading (Ziegler, 1990). Thick sedimentary sequences have accumulated especially in the grabens. The sedimentary patterns were influenced by the effect of eustatic sea level fluctuations.

Clastic dominated deposition started after the end of chalk accumulation in late Danian times. Mainly deep water mudstones accumulated in parts of the Central Graben and in much of the North Sea area in late Paleocene and Eocene. Coarser clastic detritus was supplied into the North Sea basin from the Shetland Platform and the Scottish Mainland, forming major deltaic systems. Both sediment source areas were gradual uplifted in late Maastrichtian to Danian. The deltaic sediments were shed from the British Isles in a broad front into the North Sea Basin. Deep water fans interfinger with fine clastic accumulations where the delta systems have overstepped the graben margins in the Viking and Central Graben. The Late Paleocene sandstone sequence can reach a thickness up to 400 m in the Central Graben. The Paleocene and early Eocene sandstones form important reservoirs for hydrocarbons in the Central and the Viking Graben (e.g. Forties and Montrose).

The opening of the Atlantic in early Eocene times was predated by intense volcanic activity in the Scotland-East Greenland region. The widespread deposition of an (for stratigraphic correlation) important tuff marker horizon was associated with this activity.

The supply of clastic material from the Shetland Platform and the Scottish Mainland abated in early Eocene times in connection with a regional transgression. In late Eocene and Oligocene the deltas prograded again into the Viking Graben and to a lesser extent in northern parts of the Central Graben, caused by renewed uplift of the British Isles (Ziegler, 1990). Marine sedimentation continued to early Pleistocene times.

The thickness of Cenozoic strata increase in general from the margins of the North Sea towards the grabens in the centre. They can reach a thickness exceeding 3.5 km (see section in Fig. 3.7).

The subsidence of the Central Graben is still in progress. The average sedimentation rates of 14 m/my in the Palaeocene and 23 m/my in the Eocene-Miocene have accelerated to 100 m/my in the Pliocene-Pleistocene and to 148 m/my in the Quaternary (see Cornford, 1994 and references therein).

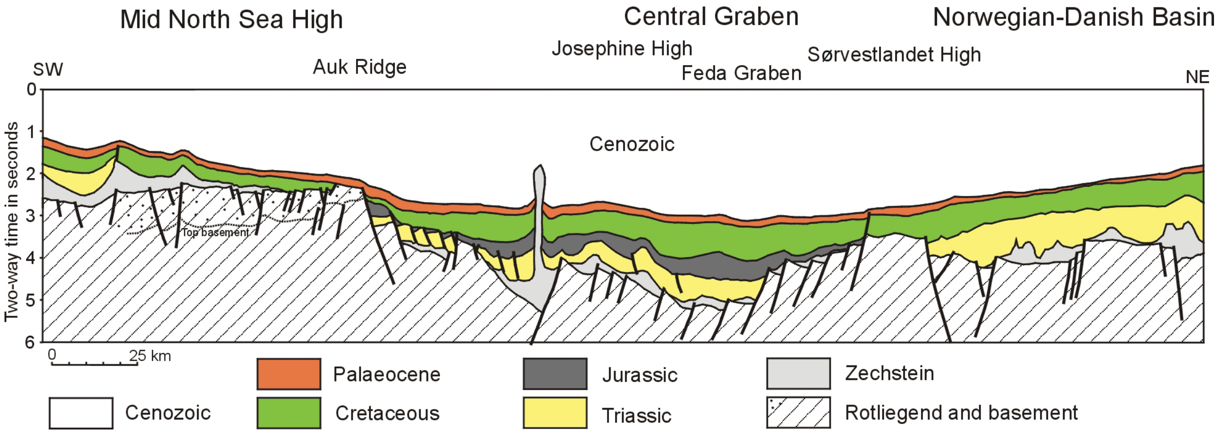

Fig. 3.7: Regional cross section across the working area derived from seismic data (redrawn after Zanella & Coward, 2003).

3.7 Structural units in the Central Graben

As seen in the previous sections, the present day structural units were formed mainly during the late Jurassic to early Cretaceous fragmentation phase. The individual structures are buried under thick Cretaceous and Cenozoic strata. An overview over the main structural elements below the Base Cretaceous Unconformity in the working area is given in Fig. 3.8. The configuration within the Central North Sea is very complex. The Central Graben is divided into a number of sub-grabens, intrabasinal highs and flanking terraces. The size of the individual structures lies between four and ten kilometres. The Central Graben is divided into an East- and a West Central Graben by the Forties Montrose High horst block in the North and by the Josephine High in the working area. The outer margin of both graben parts are flanked by marginal platform areas. The predominant fault direction is NW-SE.

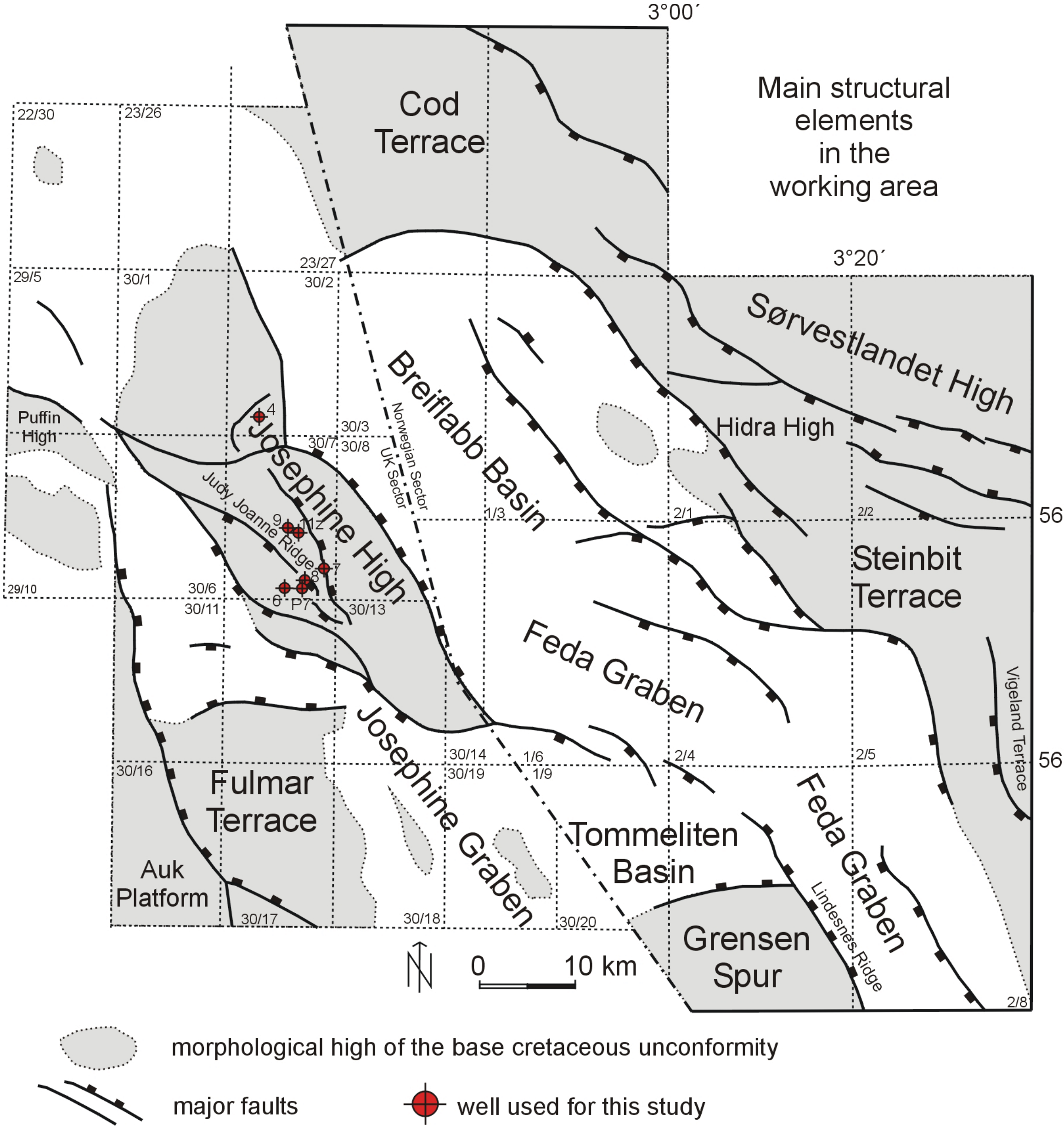

Fig. 3.8: Overview over main structural elements in the working area: Deeper graben areas (Feda Graben, Breiflabb Basin and Josephine Graben) are surrounded by platform areas like the Fulmar Terrace, the Cod Terrace and the Steinbit Terrace. The Josephine High forms an important intrabasinal high. Wells in the Norwegian sectors are not plotted, since their position is confidential. Following sources were used to compose this figure: Simon Petroleum Technology limited (1994), Saga-Petroleum (1994), Goldsmith et al. (2003) and Penge et al. (1999).

3.8 Hydrocarbon plays

The Central Graben hydrocarbon plays can be divided in pre-rift, syn-rift and post-rift relative to the main rifting event in the Upper Jurassic (Spencer et al., 1996).
The seals are often located in the same formation like the reservoir. The seal rock for the chalk reservoirs for example, is the same Upper Cretaceous and basal Tertiary chalk, but in an impermeable facies and Upper Jurassic sandstones are sealed by the Upper Jurassic mudstones of the Mandal and Farsund Formations (Cornford, 1994). Nevertheless, the main regional seals for Mesozoic reservoirs are provided by Upper Jurassic and Cretaceous shales and marlstones (Isaksen, 2004).

The source rock potential of the Devonian is generally restricted to the occurrence of organic rich lacustrine laminated mudstones, or laminites in the Orcadian basin (Marshall & Hewett, 2003). Fluvial and aeolian sandstones of the Mid and Upper Old Red act as reservoir rocks and they are locally impregnated by dead oil (Glennie & Underhill, 1998 and references therein). While the Carboniferous coals provide the main source rock for the southern North Sea gas province, the Carboniferous of central and northern North Sea has only limited importance as source rock, due to the apparent lack of thick coal bearing strata (Bruce & Stemmerik, 2003). The Permian Kupferschiefer (copper shale) is not thick enough to be a credible source rock (Taylor, 1998).

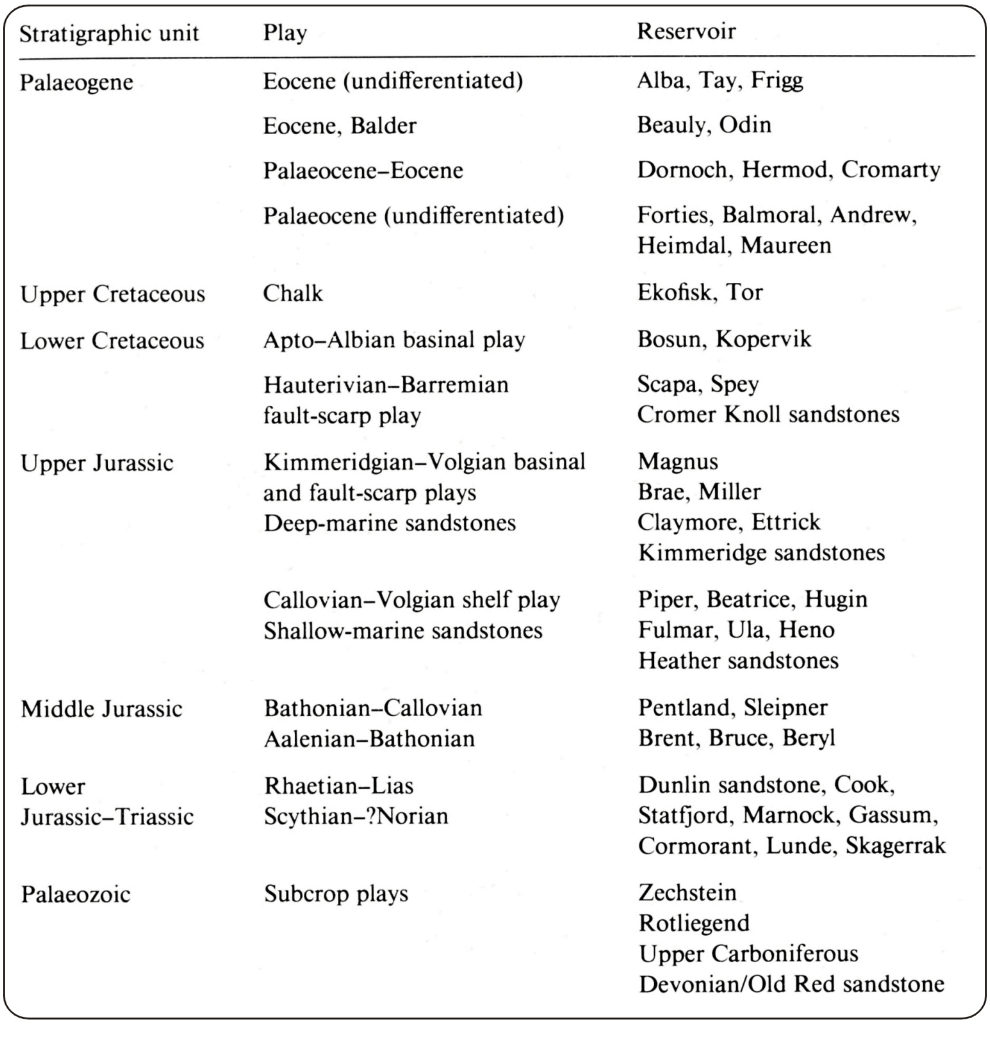

Stratigraphic unit	Play	Reservoir
Palaeogene	Eocene (undifferentiated)	Alba, Tay, Frigg
	Eocene, Balder	Beauly, Odin
	Palaeocene–Eocene	Dornoch, Hermod, Cromarty
	Palaeocene (undifferentiated)	Forties, Balmoral, Andrew, Heimdal, Maureen
Upper Cretaceous	Chalk	Ekofisk, Tor
Lower Cretaceous	Apto–Albian basinal play	Bosun, Kopervik
	Hauterivian–Barremian fault-scarp play	Scapa, Spey Cromer Knoll sandstones
Upper Jurassic	Kimmeridgian–Volgian basinal and fault-scarp plays Deep-marine sandstones	Magnus Brae, Miller Claymore, Ettrick Kimmeridge sandstones
	Callovian–Volgian shelf play Shallow-marine sandstones	Piper, Beatrice, Hugin Fulmar, Ula, Heno Heather sandstones
Middle Jurassic	Bathonian–Callovian Aalenian–Bathonian	Pentland, Sleipner Brent, Bruce, Beryl
Lower Jurassic–Triassic	Rhaetian–Lias Scythian–?Norian	Dunlin sandstone, Cook, Statfjord, Marnock, Gassum, Cormorant, Lunde, Skagerrak
Palaeozoic	Subcrop plays	Zechstein Rotliegend Upper Carboniferous Devonian/Old Red sandstone

Fig. 3.9: Overview of plays and associated reservoirs in the central and northern North Sea (Johnson & Fisher, 1998).

The Late Jurassic organic rich succession is source rock for a large part of the hydrocarbons in the central and northern North Sea, as described in the Jurassic section of this chapter. The Upper Jurassic Mandal, Farsund and Haugesund Formation shales are important for the studied settings in the Norwegian sector and the Heather and Kimmeridge Clay Formations for the Jade and Judy Fields in the UK sector. The accumulation of this important source rocks is owed to the combination of high sedimentation rates of fine-grained siliciclastic material, high planctonic productivity in the near surface water, and development of anoxic environment at the sediment water interface (Cornford, 1994).

Additional hydrocarbons may come from the Middle Jurassic Pentland Formation (Isaksen, 2004).

The oil in the southern North Sea (Netherland and German fields) comes from another Jurassic source rock, the lower Jurassic Posidonia shale, which is not present in the study area (e.g. Johnson & Fisher, 1998).

Fig. 3.9 gives an overview of the plays and their main reservoir rock in the central and northern North Sea. Important reservoirs are located for instance in the Rotliegend Auk Formation, the Triassic Skagerrak Formation, The Upper Jurassic Ula and Fulmar Formations, the Cretaceous Chalk and different sandstones in the Palaeogene.

4 Burial history and basin modelling

The burial history of reservoirs and potential source rocks is one essential factor for the understanding of diagenetic processes. Most important parameters are the evolution of temperature versus time and the timing of potential fluid flow events. Both can be derived, at least partly, from 3D basin modelling.

Burial history reconstruction and basin modelling was accomplished within the scope of the FLINT project by V. Neumann at the GFZ Potsdam and published in his PhD thesis (Neumann, 2007) and in di Primio & Neumann (2008). The content of the following burial history and basin modelling section summarizes aspects of this work, which are important for the interpretation of diagenetic changes. The text of this section was mainly derived from Neumann (2007) and references therein.

3D digital map sets (consisting of 14 depth maps for each working area), well reports and extensive data for organic geochemical analysis were provided by the industry partners (see also section 2 and Neumann, 2007). Thermal history was reconstructed using published geological data and calibrated with data from several wells. A relatively large set of vitrinite reflectance (Ro) and temperature data was supplied by industry partners for the Norwegian sector (Fig. 4.1). A smaller data set was available for the UK sector (Fig. 4.1). The distribution of maturity and temperature versus depths is illustrated in Fig. 4.1. Retardation of maturity, as frequently reported for overpressured settings, occurred in one well only and no retardation effects were observed in the majority of calibration wells.
Input parameters and boundary conditions for the models are described in detail in Neumann (2007). Numerical modelling was performed using the basin modelling software PetroMod™ (vs. 8.0) from IES GmbH, Germany.

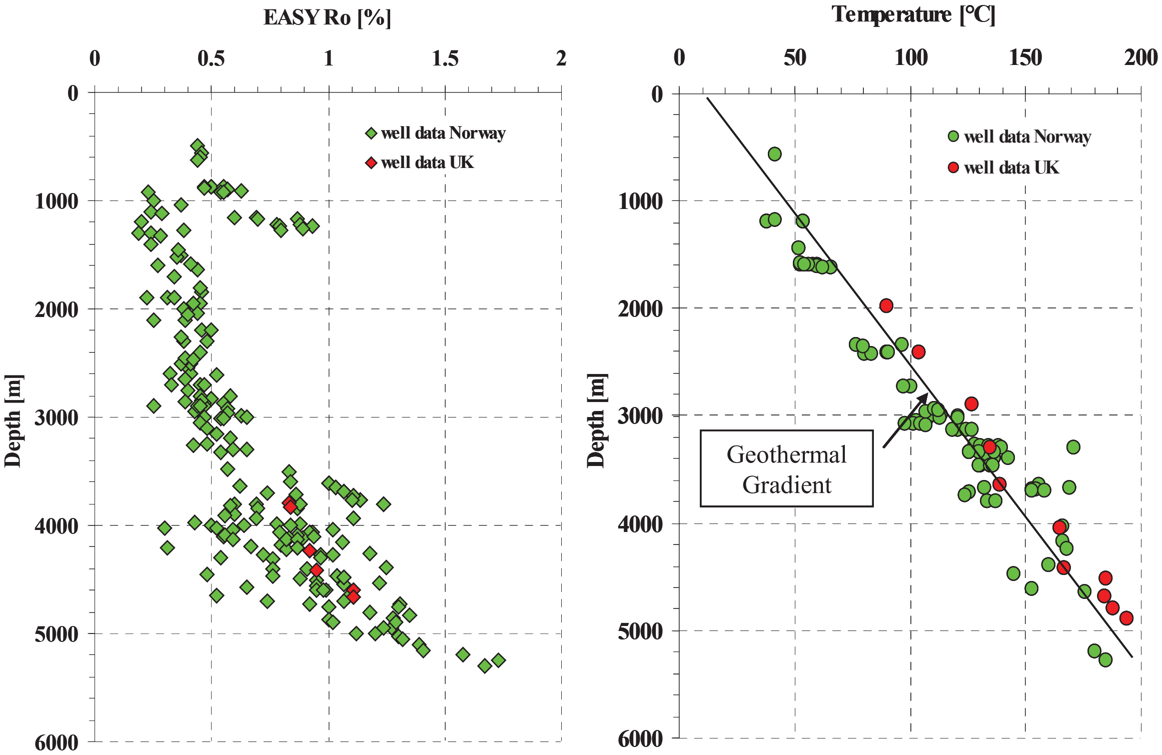

Fig. 4.1: Available thermal calibration data (temperature, maturity - % Ro) for both study areas (Neumann, 2007).

Hydrocarbon compositions and physical properties predicted by modelling using conventional compositional kinetic models showed a clear discrepancy to the observations in both study areas. Therefore user defined compositional kinetic models were used to reproduce the observed fluid composition and physical properties through time more accurately (for details see Neumann, 2007).

4.1 Pressure history modelling

Highly overpressured reservoirs are typical for the central North Sea. A number of mechanisms for the generation of overpressure in sedimentary basins were discussed in recent publications (e.g. Isaksen, 2004 or di Primio & Neumann, 2008). Most important for the Central Graben are disequilibrium compaction and gas generation, both in combination with lateral pressure transfer.

Pressure history was modelled and calibrated with pressure data from a number of wells. Available pressure calibration data (RFT pressure measurements) for both study areas are given in Fig. 4.2.

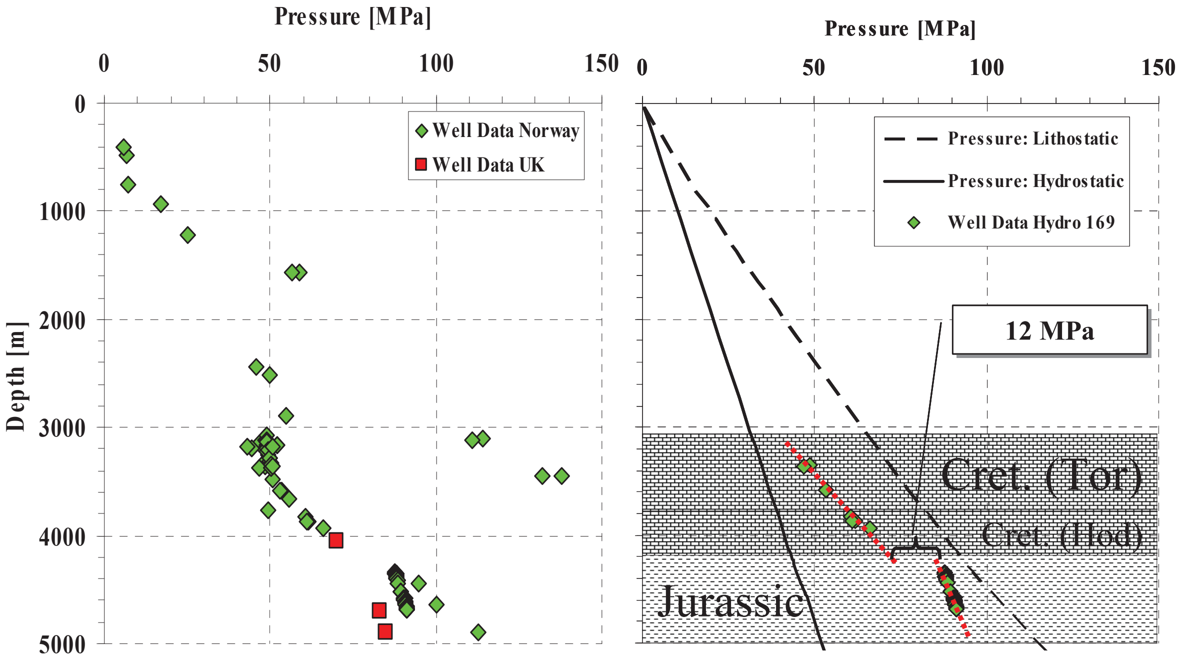

Fig. 4.2: Available pressure calibration data (RFT pressure measurements) for both study areas (left). Example from one well (right): A pressure transition zone occurs at about 4200 m TVDSS. Below this zone lies the overpressured Cretaceous-Jurassic section (Neumann, 2007).

Pressure modelling could help to evaluate the origins for the observed overpressure. Modelling of disequilibrium compaction alone using default lithologies resulted in relatively low overpressures and was not able to reproduce the observed pressure distribution (Fig. 4.3, green line). A better calibration to pressure measurements was possible after modifying the lithology of seals (Fig. 4.3, blue line) in order to increase the effect of disequilibrium compaction (see Neumann, 2007 for details). Using this configuration the onset of overpressure was modelled to occur at 90 Ma and the pressure increased nearly gradually to the present day value of about 40 MPa above hydrostatic conditions in the Jurassic Bryne Formation of well NOR-G (Hydro 169, see Fig. 4.3) in the Norwegian sector.

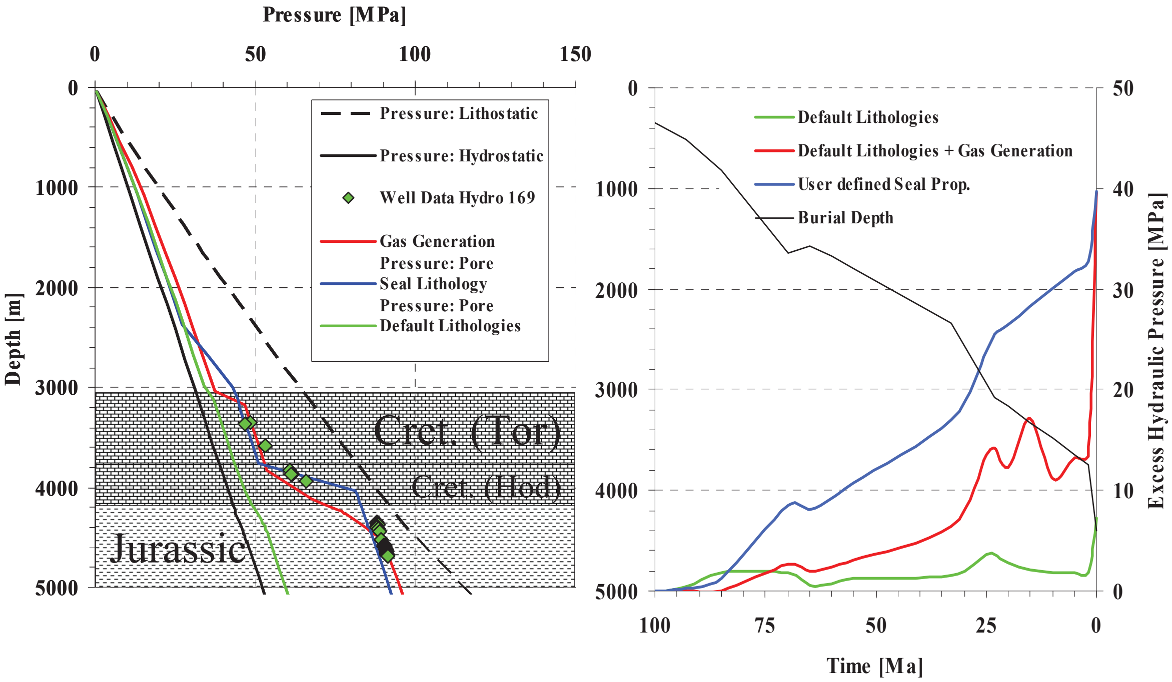

Fig. 4.3: Modelling of pressure evolution for the Norwegian sector (displayed for the position of well Hydro 169 = well NOR-G). Two modelled scenarios can reproduce the final pressure distribution: Disequilibrium compaction with user defined seal properties and gas generation (Neumann, 2007).

The modelling of gas generation as overpressure mechanism resulted also in a good match to measured data. The calculated pressure increase (Fig. 4.3, red line) was more moderate compared to the disequilibrium compaction model during most of the burial history. Present high overpressure is related in the gas generation model to the late rapid burial phase, which led to accelerated gas generation (see Neumann, 2007 or details).

Modelling of both mechanisms was able to reproduce the observed recent pressures, but it is not likely that one mechanism is exclusively responsible. The generation and preservation of overpressure by pure disequilibrium compaction requires very low permeabilities (10^{-9} mD) in the sealing strata. Overpressure generation by gas generation alone needs unreasonable amounts and properties of the generated gas (see Neumann, 2007 for details).

Therefore, pressure development was finely modelled as mixed from different origins, consisting of lateral pressure transfer, gas generation and disequilibrium compaction. The overpressure generated by the later one increased slightly compared to default lithologies by modification of mechanical properties of the sealing chalk (see Neumann, 2007 for details).
The combined model was additionally able to reproduce palaeo-pressure and temperature data, in contrast to the pure disequilibrium model. Such data, derived from fluid inclusions, were published for the Judy Field by Swarbrick et al. (2000) and Aplin et al. (2000). The good match of modelled pressures and temperatures with measured data can be seen as evidence for the influence of both mechanisms for overpressure generation. Nevertheless, this interpretation is in contrast to Swarbrick et al. (2000), who modelled the pressure history of the Judy Field and explained most of the overpressure by disequilibrium compaction as result of the rapid burial from late Tertiary until present. Lateral pressure transfer and gas generation were also modelled and had only minor effects in their model. Other volume change mechanisms like smectite dehydration, smectite to illite transformation and aquathermal pressuring were estimated additional by Swarbrick et al. (2000) and may have contributed also only minor amounts of overpressure (< 1.0 Mpa).

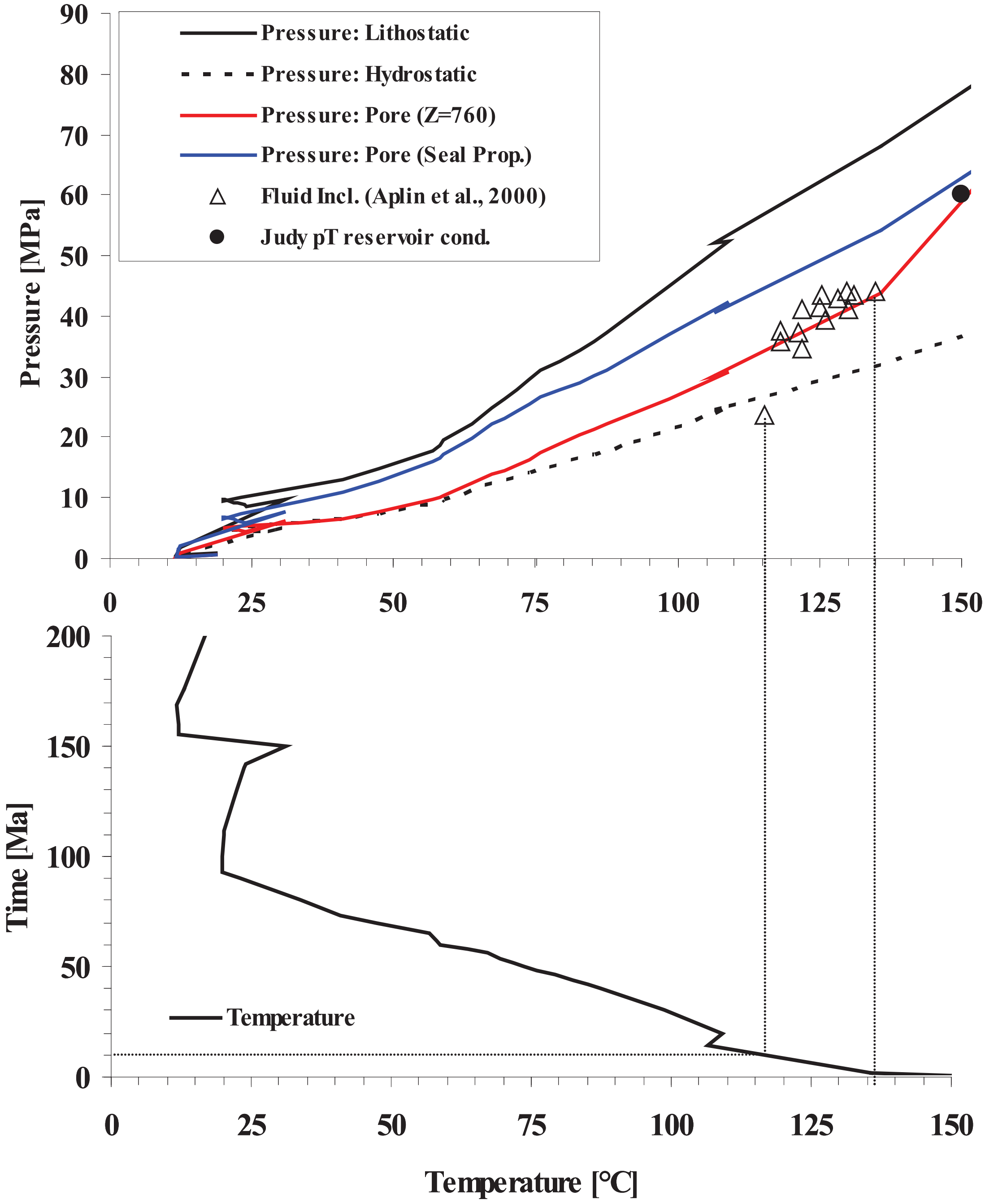

Fig. 4.4: Pressure vs. temperature evolution through time for the Judy Field. The black line illustrates the lithostatic pressure evolution; the black-dotted line shows the hydrostatic pressure evolution. The blue line shows the results for the pore pressure evolution based on pure disequilibrium compaction. The red graph describes the pore pressure evolution using the combined gas generation and disequilibrium compaction model (Neumann, 2007).

The combined model was finally used to model the pressure history of both working areas. Only few calibration data were available for the UK-sector. Two example wells, one for every modelled area, are shown in Fig. 4.5.

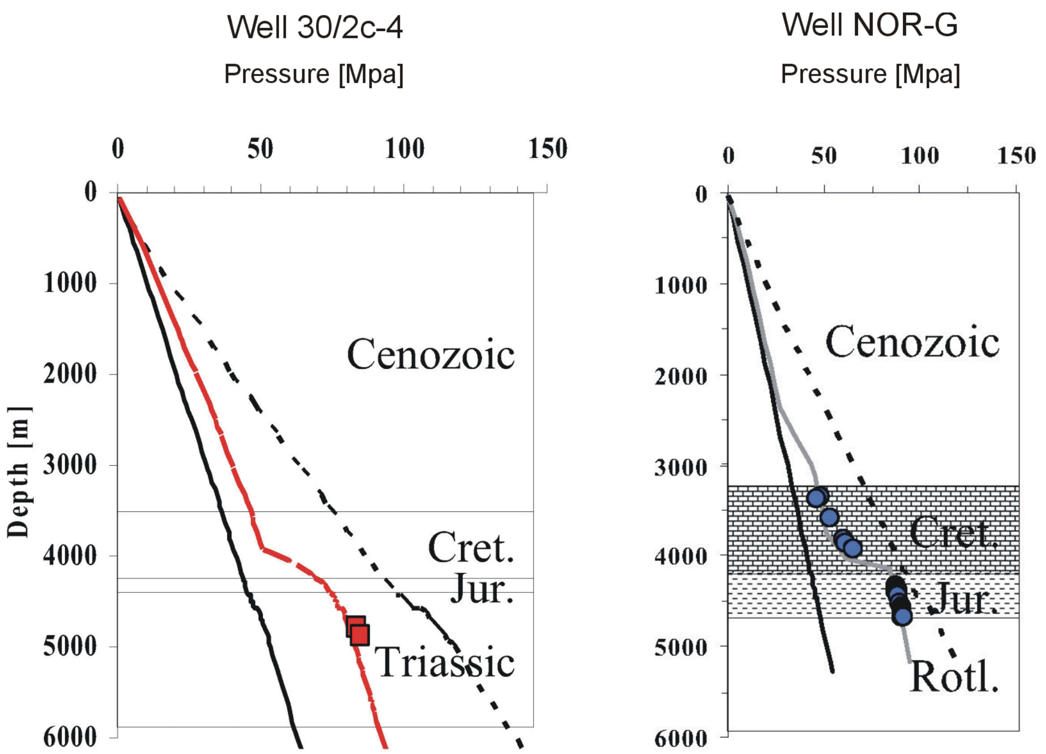

Fig. 4.5: Pore pressure calibration data compared to modelled results for two example wells: Well 30/2c-4 (Jade Field, UK-sector) and well NOR-G (Hydro 169, Norwegian sector). Solid black line = calculated hydrostatic pressure, dotted black line = calculated lithostatic pressure, coloured line = modelled pore pressure distribution (Neumann, 2007).

4.2 Burial history and hydrocarbon charge - UK-sector

The burial history of the UK-sector working area shows slightly different pattern for structural highs and deeper basinal areas.

The basin modelling shows only moderate initial burial rates on structural highs (Fig. 4.6 – well 30/2c-4). Thermal decay occurred throughout the Early Cretaceous associated with slowly increasing subsidence rates following the Jurassic rifting on the highs. Burial accelerated in the Late Cretaceous and high subsidence rates last until today. The Jade Field is presently at maximum temperature, with measured 188°C in the upper part of the reservoir section (4698 m TVDSS) and 194°C at 4930 m TVDSS (see Fig. 4.6 for burial history of the Jade Field and Neumann (2007) for detailed DST data).

The burial history of deeper basinal areas (pseudo well Fig. 4.6) differs mainly in the Cretaceous from that of the structural highs. While early Mesozoic subsidence rates were comparable low, the increase in burial rate started already in the Early Cretaceous. Subsidence history from Upper Cretaceous until today is again comparable to the situation on structural highs. Maximum recent temperatures were modelled with up to 300°C at the top of the source rock interval for the deepest part in the southwest of the study area.

Organic geochemical data (Gas chromatography and stable isotopes) indicate that the Upper Jurassic Heather and Kimmeridge Clay Formations are the primary source rocks and that a minor contribution may also have come from the Middle Jurassic Pentland Formation (Neumann, 2007).

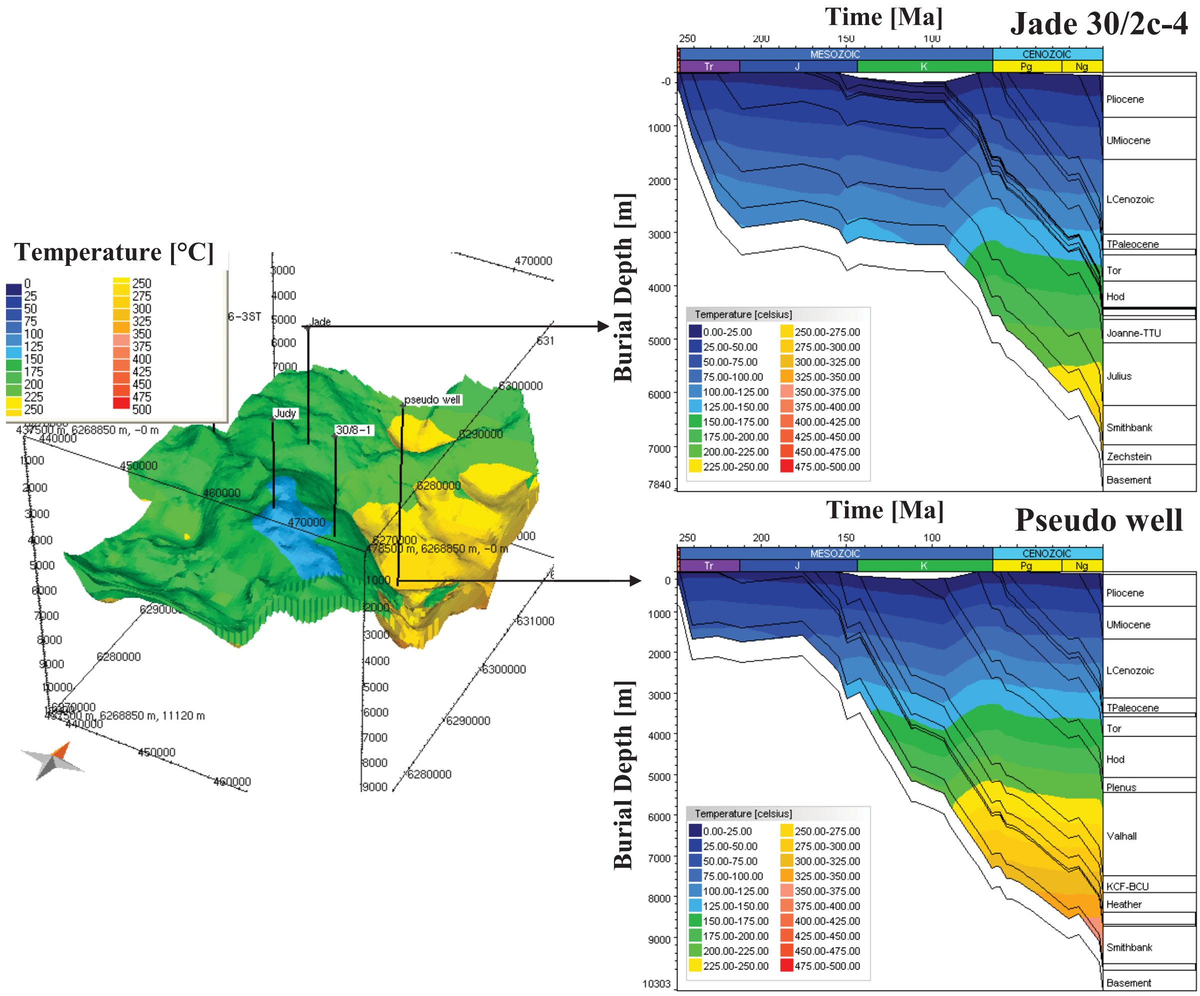

Fig. 4.6: Burial history and thermal evolution of the Kimmeridge Clay Formation of the Jade well 30/2c-4 and a pseudo well location at the deepest section of the UK study area (Neumann, 2007).

4.2.1 Maturation and filling history - published compositional kinetic models

First generation of hydrocarbons in the deepest basinal areas was predicted for the late Early Cretaceous (Aptian-Albian), approximately 120-110 Ma ago, by the Vandenbroucke compositional kinetic models.

An earlier 2D basin modelling study from Jones et al. (2005) calculated the onset of hydrocarbon generation and migration in Jade Field for the Late Cretaceous.

Source rock maturation increased during the faster burial phase in Late Cretaceous. Main charging and high overpressure in the Jade Field was associated with the rapid Late Pliocene and Pleistocene burial.

The first accumulation of hydrocarbons in Triassic reservoirs of the **Jade Field** was predicted by modelling results for the late Early Cretaceous (Albian), at approximately 100 Ma. This is very early in the burial history and the top of the Jade Structure was only at 450 m depth with temperatures below 30°C. Temperatures in the kitchen area southeast of the Jade Field reached ~100°C at this time.

The low palaeo-temperatures in the reservoir during hydrocarbon infiltration increased the risk of biodegradation of oil and gas significantly. The first hydrocarbons in the Skagerrak Formation reservoir of the Jade Field consisted of a two-phase system (gas and oil), with dominance of the vapour phase.

Additional kitchen areas on the flanks of the deeper basinal settings became mature with further burial. Higher maturity gas-richer fluids diluted the initial charge hydrocarbons in the reservoir, as the deeper buried source rocks reached the gas window.

Organic geochemical data show that the recent gas condensates in the Jade Field have already reached a high level of thermal maturity. Petroleum composition seems to be rather controlled by the effect of mixing with a fresh charge than by temperature induced in-reservoir alteration of petroleum.
Organic geochemical data do not point to biodegradation as important mechanism for the reservoir fluids encountered in the Jade Field today (see Neumann, 2007 for details). However, it cannot be excluded that the later dilution with higher mature hydrocarbons may have masked an earlier biodegradation signature. The early hydrocarbon emplacement at low temperature and the local occurrence of solid bitumen is evidence for biodegradation (Neumann, 2007).

The two tested hydrocarbon fluids from Jade well 30/2c-4 have different gas oil ratios (GOR). The observed difference can be best explained by compartmentalization of the reservoir column by interbedded mudstone layers. Other mechanisms like thermodynamic equilibrium, gravity segregation, or thermal cracking are unlikely to be responsible for the observed GORs (see Neumann, 2007 for details).

The modelling results indicate that the **Judy Structure** was sourced from eastern and western basins, and additional from Jade Field via lateral up-dip migration following the axes of the ridges in a fill-spill manner (Fig. 4.7). The filling history of the Judy Field is comparable to the Jade Field notwithstanding the charge from two source areas: Early (100 Ma) first accumulation took also place at shallow burial (300 m TVDSS) and low reservoir temperatures (< 30°C). Late Cretaceous burial was associated with enhanced gas generation and dilution of existing reservoir fluid, similar to the Jade Field.

However, the conventional kinetic models were not able to reproduce the observed fluid compositions and physical properties, neither for the Jade Field, nor for the Judy Field.

4.2.2 Maturation and filling history - user-defined compositional kinetic models

User-defined compositional kinetic models (see Neumann, 2007 for details) were assigned to the source rocks in the basin model. The start of source rock maturation was predicted by these models slightly later than by the conventional kinetic models, at 125 Ma. Filling histories using the user-defined kinetic models were comparable to the published compositional models: First charge of the **Jade** structure occurred during the Early Cretaceous at shallow burial depth (530 m TVDSS) and at low reservoir temperatures (T ~ 40°C). The reservoir contained a saturated two-phase system of oil and gas after the first charge. The influx of gas richer fluids, derived from higher mature source rocks, during further burial diluted the hydrocarbons in the reservoir and led to the increase of GOR. Onset of overpressure and enhanced gas generation in the Late Cretaceous caused a switch from light oil (saturated two-phase fluid) to gas condensate (under saturated phase), as encountered in the Jade Field recently. The filling history of the Judy Field is generally comparable to that of the Jade Field, with the difference that the first charge occurred at 80 Ma.

4.3 Calculation of fluid volumes derived from sediment compaction (UK sector)

Fluid volumes expulsed during compaction of sediments can be estimated from 3D basin modelling data simply by calculating the porosity loss for a defined volume versus time.

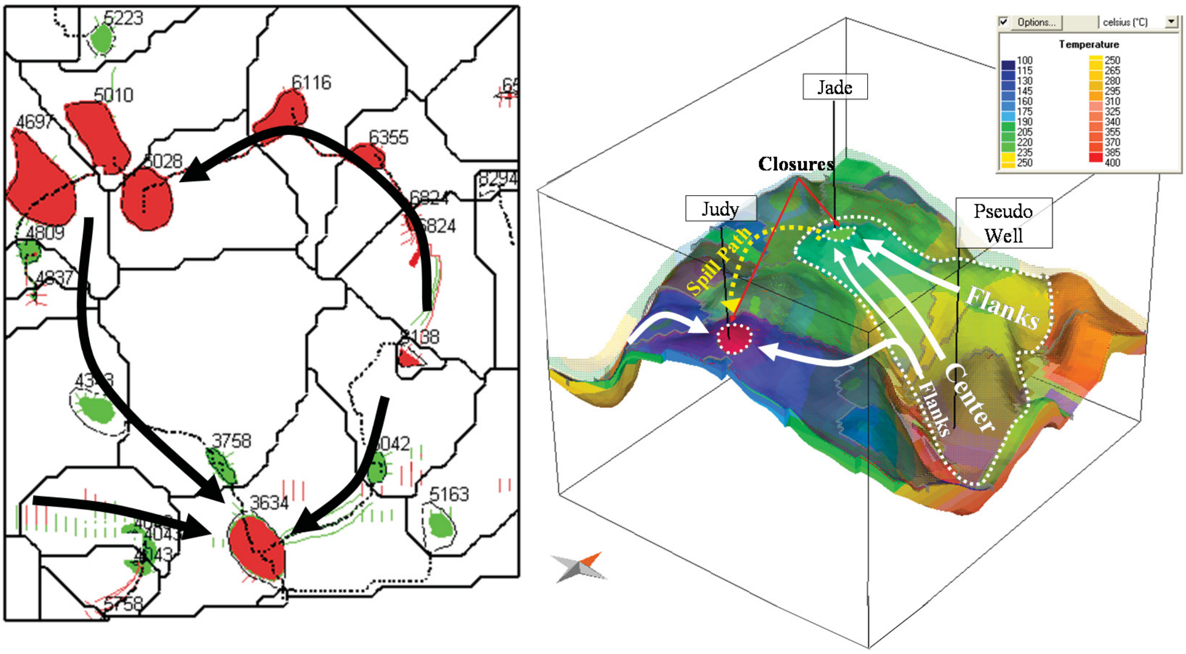

Fig. 4.7: Left: Present day drainage areas of the Joanne Sandstone layer (UK sector). The green areas represent oil accumulations, the red areas gas accumulations; the black arrows show migration paths of the hydrocarbons. Right: 3D view. White arrows are potential hydrocarbon migration pathways. Topography shows the Triassic Joanne sandstone (temperature overlay). The dark grey polygons are the individual drainage areas. The white dotted polygon outlines the kitchen area for the Jade Field. The yellow dotted arrow shows the spill path from Jade Field to the Judy Field (Neumann, 2007).

The drainage area for the Jade Field (based on the present day topography) was calculated with the PetroCharge tool of the PetroMod™ software (see Neumann, 2007 for details) in order to derive hydrocarbon migration history (Fig. 4.7).
Porosity loss during time was calculated by R. di Primio (GFZ Potsdam) for this drainage area to get a maximum amount of water, which may have passed the Jade Structure in a focused fluid flow scenario.

Calculated expelled fluid volumes for different stratigraphic layers in the Jade Field drainage area are given in Fig. 4.8. However, a number of restrictions must be considered interpreting and using these data: The flow path model of PetroCharge is simplified and based on the assumption that flow occurred within a carrier against a defined surface (e.g. a regional seal), and that the flow is generally up-dip. It is not very likely that fluid flow followed this simple mechanisms and it is also not likely that all compactional fluids from the Jade Field drainage area were focused through the Jade Structure. A large part of the fluids escaped most likely via faults or through the sealing horizons without reaching the Jade structure. Nevertheless, the calculated volumes can give an idea about maximum amounts and timing of fluid flow induced by the compaction of sediments. The calculated fluid volumes were used for diagenetic modelling (see section 7).

ⓐ Burial history Jade Field (well 30/2c-4)

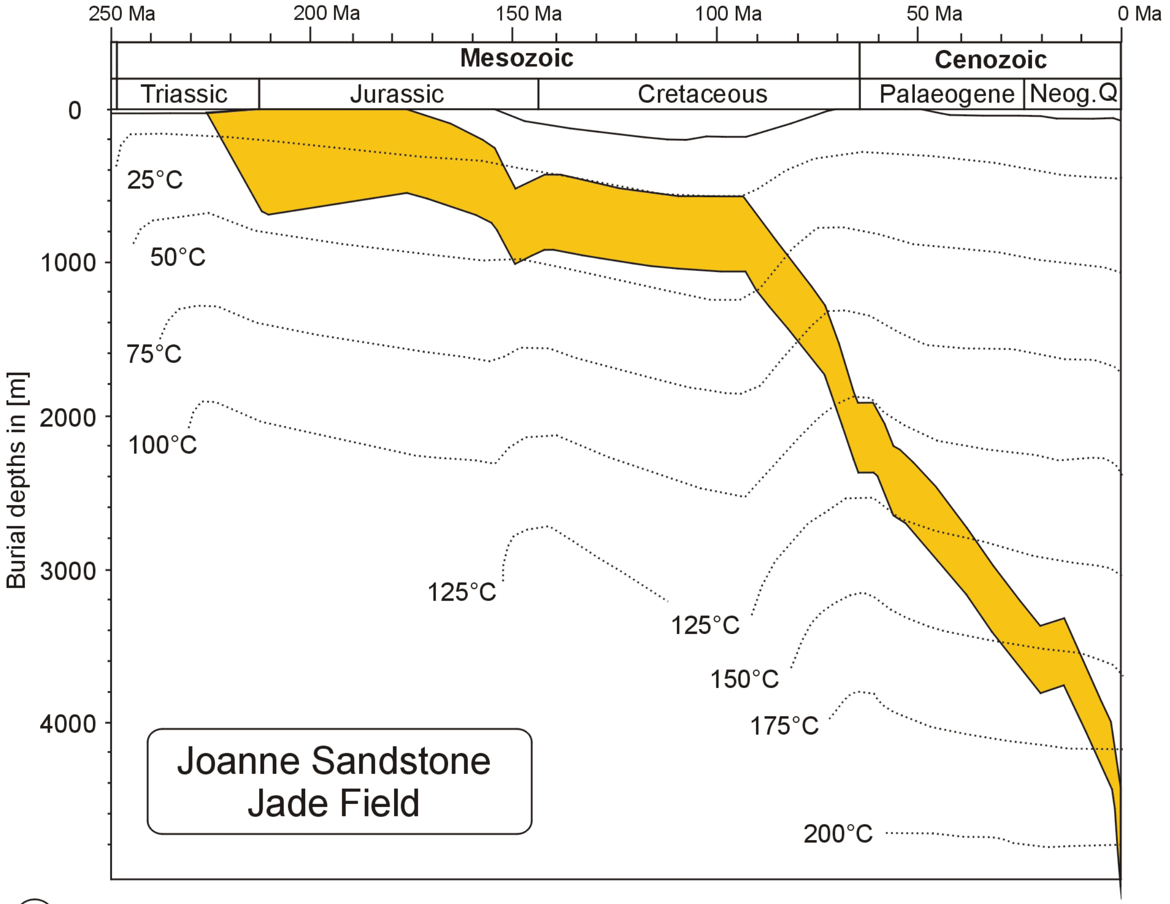

ⓑ Fluid volumes expelled from the drainage area of the Jade Field

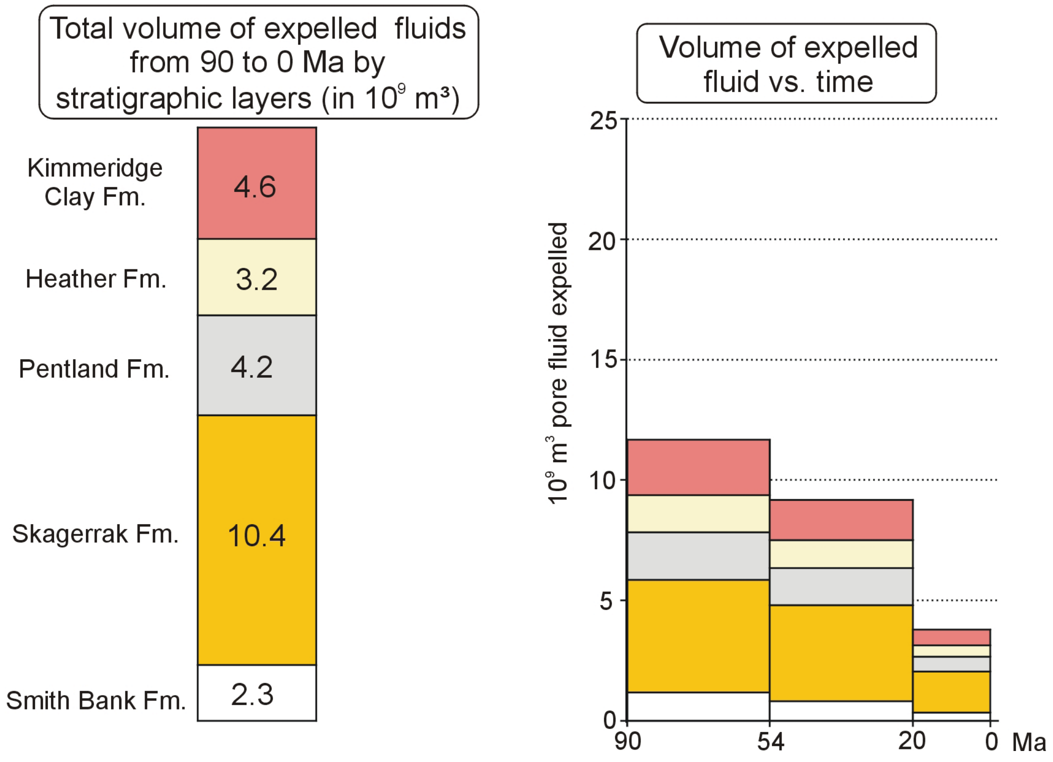

Fig. 4.8: Burial history of the Joanne Sandstone in the Jade Field (a) and fluid volumes (b), which can be potentially expelled by compaction of sediments from different stratigraphic layers in the Jade Field drainage area.

4.4 Burial history and hydrocarbon charge - Norwegian sector

Thermal development and burial history of the working area in the Norwegian sector is generally comparable to the 30 km westward-located UK sector working area. Two example wells are shown in Fig. 4.9. They are both at their maximum burial depths and highest temperatures today. Source rocks in the Norwegian working area are the Mandal, Farsund and Bryne Formations (for stratigraphic relationship see section 3).

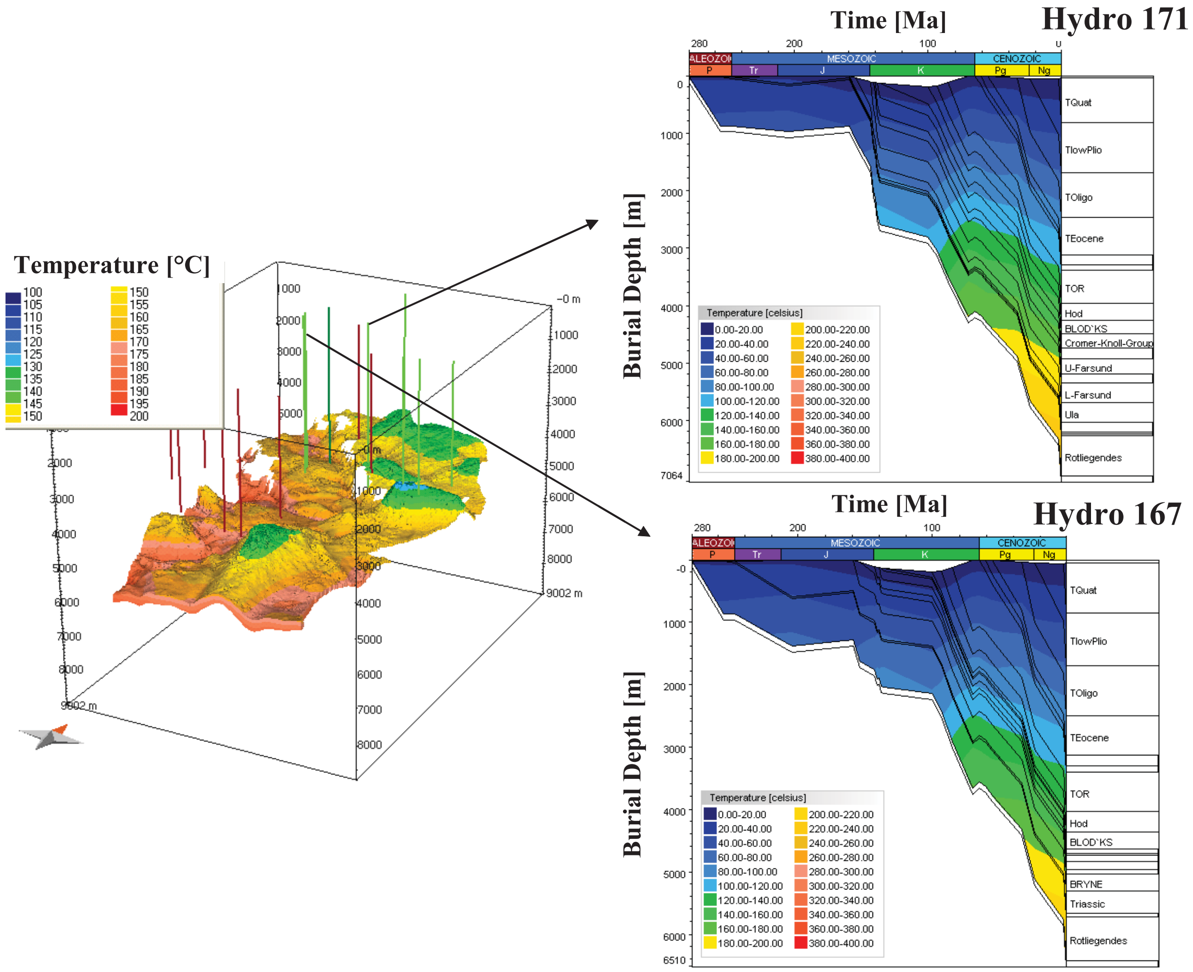

Fig. 4.9: Burial history and thermal evolution of the Mandal Formation at two locations in the northern part of the Norwegian study area (Neumann, 2007).

One important clastic reservoir studied in the Norwegian working area is provided by the Late Jurassic (Oxfordian) sandstones of the Ula Formation, encountered by well NOR-G (well Hydro 169 in Neumann, 2007). They have pressure-temperature conditions comparable to the Triassic reservoirs in the UK model.

The first hydrocarbon charge calculated by the Vandenbroucke kinetic models occurred approximately 70 Ma ago. This is clearly later than in the Triassic reservoir of the UK sector. The difference is caused by lower burial rates in the Norwegian kitchen area associated with later maturation of organic matter. During the first infiltration of hydrocarbons the structural top of the Oxfordian Sands reservoir was at 1500 m depths, with temperatures between 80 and 90°C. These relatively high temperatures inhibited biodegradation. The reservoir contained initially a saturated two-phase system with a predominance of oil over gas, in contrast to the Jade structure where gas was the predominant initial phase.

The user-defined compositional kinetic models calculated first hydrocarbon generation from the Bryne Formation at 80 Ma. The reservoir was at 1500 m depths at this time and reached relatively high reservoir temperatures (80-90°C). The reservoir contained a saturated two-phase system at the beginning. The GOR increased during further burial due to the infiltration of more gas rich fluids from deeper kitchen areas, which became mature with time. The onset of overpressure in Late Cretaceous was associated with enhanced gas generation and led to the switch from light oil (saturated two-phase fluid) to gas condensate (under saturated phase), like in the Jade Field.

The major difference between the filling histories of Oxfordian Sands in the Norwegian study area and Triassic reservoirs in the UK study area is the later hydrocarbon charge, at higher temperatures (~80 – 90°C), in the Oxfordian Sands.
During the early burial history of the reservoirs hydrocarbons occurred as two phase systems, with the highest proportion of gas in the shallowest and coolest reservoirs. Overpressure was responsible in all modelled cases for the under-saturation of reservoir fluids during later burial history.

5 Triassic fields in the UK sector: Petrography and diagenesis

The majority of samples used in this study was taken from cores of the Triassic Jade and Judy Fields in the UK-sector. They cover fluvial dominated intervals of the Joanne and Judy Sandstone Members of the Skagerrak Formation. The structural setting, stratigraphy, sandstone petrography and diagenetic evolution of the two fields is similar, therefore both Fields were treated together in this section. The study area is situated in the southern UK Central Graben in Block 30 (Fig. 2.1). Both Fields are located on an intra-basinal horst structure referred to as the Josephine High (Fig. 3.8). The Josephine High has the same orientation as the graben boundaries, and separates the Central Graben in an eastern and a western part. The main fault systems in the area have also the predominant NNW-SSE direction. Thick mature to over-mature source rock sequences of Jurassic age lie adjacent to the high structure and acted as hydrocarbon kitchen. Both fields have a burial history which is typical for the Central Graben region (see section 4). Early Mesozoic subsidence provided the accommodation space for the reservoir sandstones and was followed by gradual subsidence in the early Cretaceous subsequent to the Jurassic rifting phase. Burial accelerated during late Cretaceous and early Tertiary. The burial rate increased further during the accumulation of thick Cenozoic fine grained sequences reaching maximum values of about 500 m/Ma (Swarbrick et al., 2000) during the last 3 Ma. This late rapid burial led to the formation of significant overpressure.

5.1 Jade Field

The Jade Field (UK Block 30/2c) lies in the northern part of the north-westerly striking Josephine High (Fig. 2.1 and 3.8). An detailed description of the Jade Field is given in Jones et al. (2005) and only the main points of this article are summarized here. The Jade structure, which contains the reservoir in the central horst block, consists of three, northwest to southeast dipping, tilted fault blocks (Fig. 5.1a). The reservoir itself has an extension of 3.25 km by 1 km (Fig. 5.1c). The crest of the reservoir is in 4359 m TVDSS and the gas water contact (GWC) is in 5026 m TVDSS in the Judy Sandstone Member of the Triassic Skagerrak Formation. The gas water contact in the Joanne Sandstone Member was not reached and hydrocarbons were encountered down to 5308 m (Fig. 5.1b).

The Judy Sandstone Member in the Jade Field is composed of more than 300 m stacked fluvial sandstones, mudstones and lacustrine claystones, comparably to the overlying Joanne Sandstone Member. The Judy sandstone was not cored in the Jade Field, but cores from the Judy Field show a poorer reservoir quality and finer grained sandstones than the Joanne Sandstone.

The main reservoir is formed by the Joanne Sandstone Member and separated from the Judy Sandstone Member by the Julius Mudstone Member (Fig. 5.1a, b). It comprises approximately 400 m of interbedded fluvial sand- and mudstones with some lacustrine shale layers. Samples for this study were derived from a 64 m cored section of the Joanne Sandstone Member recovered from well 30/2c-4. The sandstones have relatively high porosities and permeabilities considering their present day depths of burial. The top of the Triassic sequence is formed by the Jonathan mudstone overlying the Joanne Sandstone Member. However, this mudstone layer is discontinuous since it was removed by erosion in the crest of the structure (Fig. 5.1a, b). So, the Base Cretaceous Unconformity cuts the Joanne Sandstone unit here. Jurassic sequences were also eroded over the Jade horst structure and the Triassic is unconformably overlain by the Cretaceous Hod Formation (see generalized stratigraphic column in Fig. 5.1d).

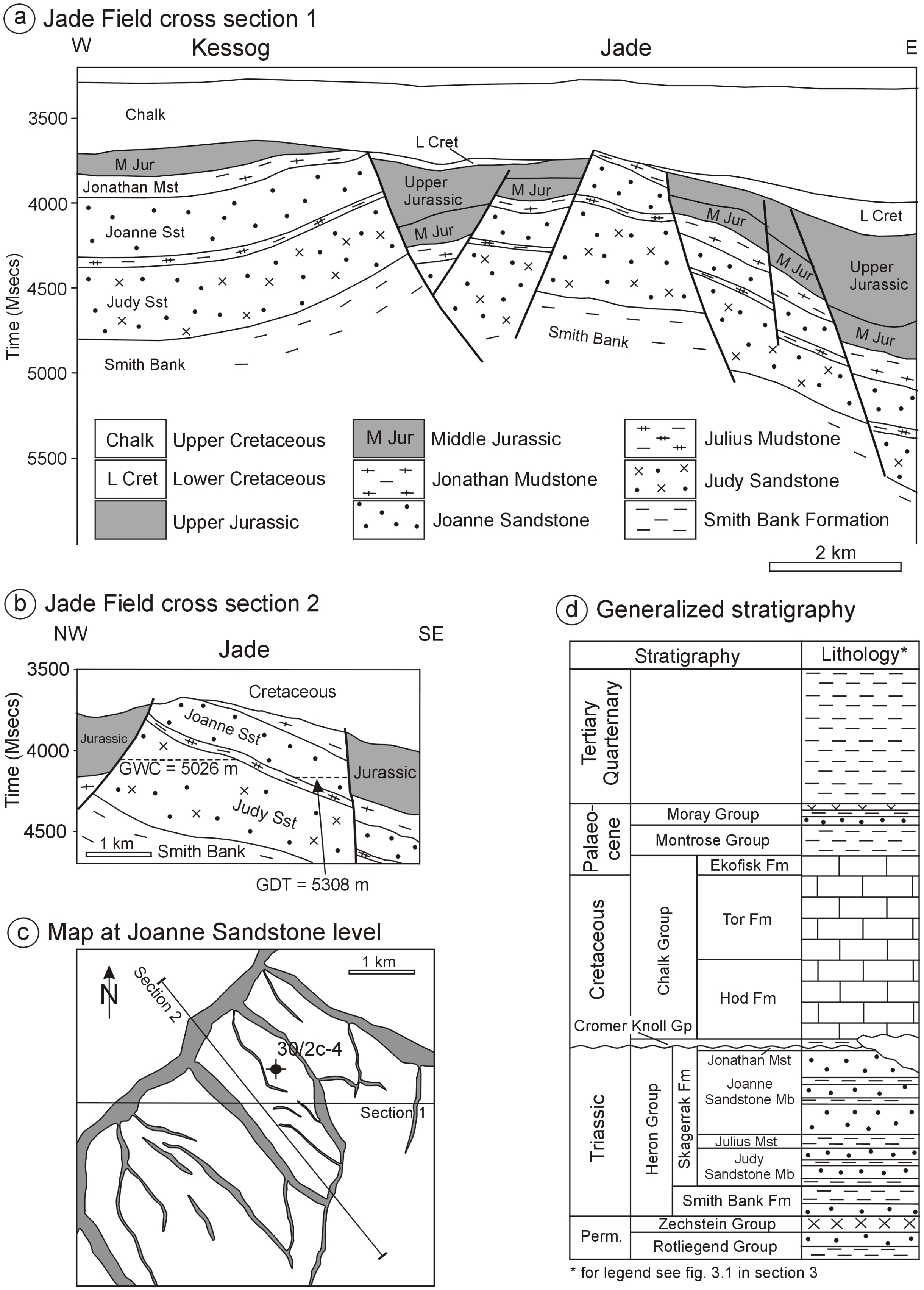

Fig. 5.1: The Jade Field: Interpreted seismic lines over the structure (a, b), structural map with main faults at the Joanne Sandstone level and the location of the well 30/2c-4 used for this study (c), and a generalized stratigraphic column of the Jade Field (d). All figures are modified after Jones et al. (2005).

The reservoir contains gas condensates with pressures exceeding 85 MPa and temperatures higher than 188°C (Neumann, 2007), allowing the classification as high pressure high temperature (HPHT) setting. The structure is bounded on three sides by faults which are interpreted to form lateral seals (Fig. 5.1c). The fourth side is closed by the southeast dipping of the structure (Palmer & Kelman, 1997). Top seal is formed partially by the Jonathan Mudstone, and by the Hod Formation where the Joanne Sandstone is cut by the Base Cretaceous Unconformity.

The primary source rocks of the hydrocarbons in the Jade Field are most likely the Heather and Kimmeridge Clay Formations with possible minor contributions from the Middle Jurassic Pentland Formation (see also section 4 and Neumann, 2007).

5.2 Judy Field

The following text about the Judy Field was derived from Goldsmith et al. (2003), Keller et al. (2005), Lines & Auld (2004) and Swarbrick et al. (2000) and summarizes aspects important for this study.

The Judy Field (UK Block 30/7a) is also located on the Josephine High, but in a shallower position (at around 3500 m depths) than the Jade Field. It lies approximately 15 km southeast of the Jade Structure (see Fig. 2.1).

The Judy structure containing the Judy Field is composed of several tilted fault blocks forming a horst structure below the Base Cretaceous Unconformity at the crest of the Josephine High. The Joanne salt pillow is located at the western margin of the Judy Horst. The Field is separated by WNW and NNW trending faults (Fig. 5.2b). These faults extend up to the Base Cretaceous and lead to the compartmentalization of the Field in a mosaic pattern.

Pore pressures in the pre-Cretaceous may exceed 60 Mpa (di Primio & Neumann, 2008). Repeated formation test (RFT) pressure data show that the magnitude of overpressure is comparable in the pre-Cretaceous aquifer across the Field at about 24 Mpa in the water phase (Swarbrick et al., 2000). This suggests the existence of a common aquifer over much of the Field and for most of the wells (Keller et al., 2005). However in detail, the situation is more complex. The single fault compartments are poorly communicating. One fault block in the east of the field seems to be isolated and is 2.8 Mpa more overpressured than the rest of the field (Swarbrick et al., 2000). The aquifer pressures in wells 30/7a-9 and 30/7a-11z, which are located in the northern compartment, seem to differ from the southern part of the field (Keller et al., 2005). The overpressure in the Judy Field was most likely caused by a combination of lateral pressure transfer, gas generation and disequilibrium compaction (see section 4 and Neumann, 2007).

Reservoir temperatures published by Swarbrick et al. (2000) for a not specified well are around 148°C.

Diverse petroleum accumulations occur at the crest of the individual tilted fault blocks without a common hydrocarbon-water contact (HWC) across the Field (Fig. 5.2.a). The main reservoirs are the Joanne Sandstone Member and the Judy Member of the Skagerrak Formation. Fluvial channel- and sheetflood sandstones have the best reservoir properties, whereas argillaceous sandstones and lacustrine mudstones form layers of poor reservoir quality, similar to the Jade Field. The stratigraphic situation is also generally comparable to the Jade Field (see Fig. 5.2c). Triassic strata are locally overlain by Upper Jurassic Heather and Kimmeridge Clay Formations (see Fig. 5.2a). But in most parts the Triassic is truncated by the Base Cretaceous Unconformity and covered by the Valhall Formation (Lower Cretaceous) on the flanks and by the Hod and Tor Formations (Upper Cretaceous) at the crest of the structure. Top seal of the structure is formed by the Cretaceous Hod Formation.

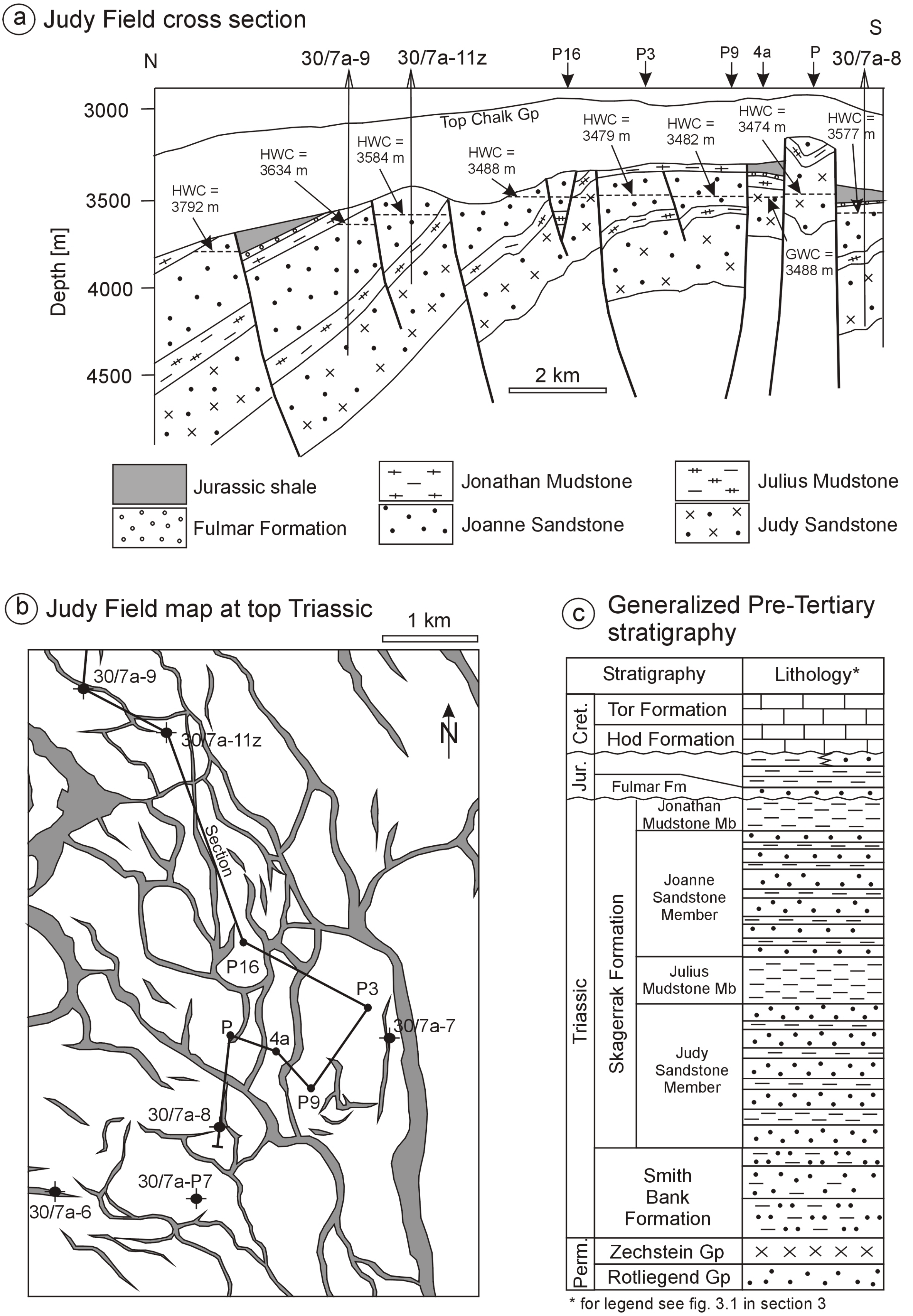

Fig. 5.2: The Judy Field: North-south cross section (a) modified after Keller et al. (2005), structural map with fault patterns at the top Triassic and the location of the wells used in this study (b) redrawn after Goldsmith et al. (2003), and a generalized Pre-Tertiary stratigraphic chart for the Judy area (c) modified after Keller et al. (2005).

The sealing capacity of the Upper Jurassic shales seems to be limited in the Judy Field. A study of Lines & Auld (2004) could show that hydrocarbons in the Triassic and the Chalk are geochemically very similar, indicating that hydrocarbons have leaked from the Triassic into the Chalk (see also Keller et al., 2005).

The hydrocarbons of the Judy Field have been sourced from adjacent thick Upper Jurassic shales (Kimmeridge Clay and Heather Formations). The compartments of the Field contain different hydrocarbon types. Geochemical analysis indicate at least three different source areas. The majority of fluids (gas condensates and volatile oils) were sourced from the northeast (e.g. well 30/7a-9, 30/7a-11z). The black oil encountered in the southern compartments in wells 30/7a-8 and P7 came from the southwest. The eastern fault block, containing gas condensates in well 30/7a-7, has a kitchen in the east (Keller et al., 2005).

5.3 Sedimentology and facies of the Skagerrak Formation

The Triassic Skagerrak-Formation in the Central Graben is composed mainly of fluvial channel and sheetflood sandstones with interbedded playa and lacustrine mudstones, deposited from Anisian to Rhaetian (Goldsmith et al., 1995).

The major depocentre in the area was formed probably by the eastern trough of the Central Graben, an extensive N-S trending braid plain in Triassic times, with drainage patterns along the graben axis (Fisher & Mudge, 1998). The thickness of the Skagerrak Formation deposits varies between some tens of meters up to hundreds of meters due to syndepositional salt movement, which resulted in the development of mini basins (termed pods) separated by salt walls (Smith et al., 1993 and Fisher & Mudge, 1998). Relatively isolated pods were prevalently observed in the southern Central Graben, on the West Central Shelf and the Jaeren High, whereas more continuous structures are more common in the northern Central Graben (Goldsmith et al., 2003).

Three extensive mudstones separate the Skagerrak Formation in the southern Central Graben into three sandstone units, the Judy, the Joanne and the Josephine Sandstone Member (see Fig. 3.5 in section 3). These three mudstone intervals are interpreted as marine incursions from the south and can be correlated with deposits of the Muschelkalk, Keuper and Rhaetian marine transgression of the southern North Sea. However, evidence for marine influence remains poor (Goldsmith et al., 2003 and Goldsmith et al., 1995). Triassic sediments were deposited in an arid to semi-arid environment in the northern trade-wind zone (Goldsmith et al., 2003). Precipitation was probably seasonal and was accompanied by short lived sheetfloods, which terminated in shallow saline playa lakes (Fisher & Mudge, 1998).

The sandstone members consist of stacked braided fluvial channel and sheetflood sandstones with interbedded argillaceous floodplain and lacustrine deposits. The fluvial systems seems to had formed a network of ephemeral streams, which dewatered probably towards the south into a braid plain or temporary lake (Goldsmith et al., 2003; Goldsmith et al., 1995).

The sandstone members contain five main facies associations according to internal industry data and Goldsmith et al. (2003) and the following description is derived from these sources. They represent a fluvial to sheetflood dominated environment interdigitated with a lake margin, as well as alluvial fans adjacent to fault bounded basin margins. In the investigated wells only four of these facies associations are present, the alluvial fan deposits are missing.

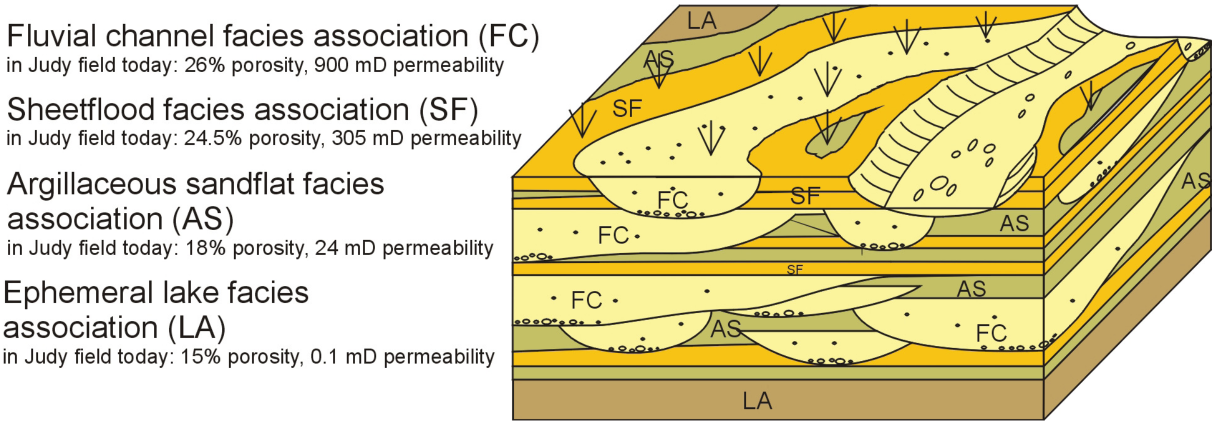
Fluvial channel facies association (FC)
in Judy field today: 26% porosity, 900 mD permeability

Sheetflood facies association (SF)
in Judy field today: 24.5% porosity, 305 mD permeability

Argillaceous sandflat facies association (AS)
in Judy field today: 18% porosity, 24 mD permeability

Ephemeral lake facies association (LA)
in Judy field today: 15% porosity, 0.1 mD permeability

Fig. 5.3: Schematic spatial relationship of facies associations of the Triassic Skagerrak Formation in the study area. Reservoir properties are average core values for the Judy Field taken from Goldsmith et al. (2003). Note the relationship between macro- and microporosity discussed in section 2 (Fig. 2.3) especially for the facies AS and LA. Most of the porosity in the finer grained facies (AS, LA) is microporosity in contrast to the coarser grained facies, where most of the porosity is macroporosity (FC, SF).

The **fluvial channel facies association (FC)** comprises very fine- to fine- or locally medium-grained, cross-bedded or massive sandstones with argillaceous layers. The base of individual channel-fill sequences is commonly formed by conglomerates containing eroded mudstone clasts and reworked dolocrete nodules. The top of the channel fill units is often formed by burrowed, mottled argillaceous sediments, representing channel abandonment. The **sheetflood facies association (SF)** consist of sheetflood sandstones which occur either as discrete beds or more commonly as thicker stacked and amalgamated units. These sediments are interpreted as ephemeral sheetflood deposits. They are usually unconfined with only little channel formation. The sheetflood sediments are often associated with sandstones of the fluvial channel facies. The **argillaceous sandflat facies association (AS)** represents fine-grained, mainly argillaceous sediments containing micaceous, burrowed sandstones and silty mudstones with common dolocrete nodules and scarce continuous dolocrete horizons. Initially developed lamination is often disturbed by bioturbation. The finer grained argillaceous sediments of the AS-facies association are interpreted to represent relatively low energy, inter-channel and more distal sandflat settings. The **ephemeral to perennial lake facies association (LA)** consists of thin, burrowed and bioturbated, silty lacustrine or ephemeral lake mudstones together with interbedded thin bioturbated sandstones. They are interpreted as deposits from suspension within shallow ephemeral lacustrine environment. They can form stratigraphic intra-reservoir barriers to fluid flow.

Reservoir structure is a layer cake of fluvial channel and sheetflood sand rich layers and mudstone dominated intervals (Fig. 5.3). Lateral connectivity of the channels is good but vertical connectivity is restricted by the argillaceous layers. Thicker mudstones from the LA- and AS-facies serve as sealing horizons (see also Jones et al., 2005).

5.4 Detrital composition

The sediments of the sandstone members in the Triassic Skagerrak Formation, investigated here, vary between pure sandstones (mainly in the facies associations FC and SF) and pure mudstones (mainly in the facies association LA). Fluvial channel and sheetflood sandstones have relatively low mud contents (average 1.2 vol.% in Jade Field and 1.5 vol.% in Judy Field), in contrast to the argillaceous sandstones of the facies association AS with up to 81.5 vol.% mud (average 42.9 vol.% in Jade Field and 10.9% in Judy Field – dependent on sampling[1]). Typical textures of a fluvial channel sandstone, an argillaceous sandstone and a mudstone from well 30/2c-4 are shown in Fig. 5.4.

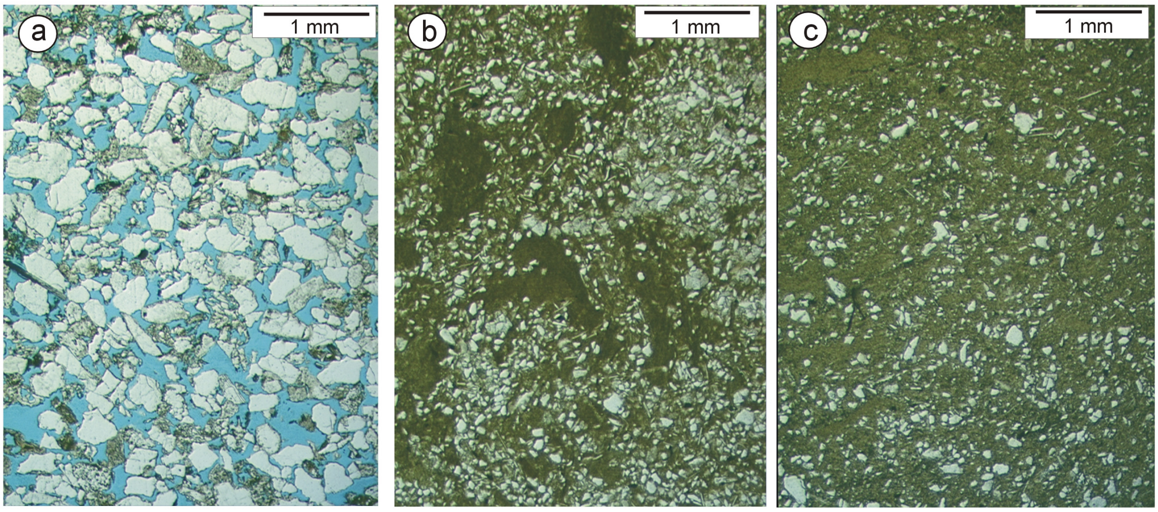

Fig. 5.4: Typical texture of a fluvial channel sandstone of the facies association FC (a, sample 15655.3), an argillaceous sandstone (b, sample 15628) and a mudstone with quartz grains (c, sample 15722.2) of the facies association AS. Note the higher content of detrital mud and the lack of macroporosity in the samples from the argillaceous sandstone samples.

Monocrystalline quartz in strained and unstrained varieties is commonly the dominant detrital phase (see Table 5.1 for average values of the detrital composition and Appendix 2.2 for detailed values). Polycrystalline quartz is also abundant. All sandstones contain a high proportion of feldspar. Plagioclase is sub-ordinate to K-feldspars. Microprobe analyses gave a Na-rich composition for the plagioclase from all grains investigated of well 30/2c-4 (Appendix 3.2). A minor amount of perthite occurred in the samples. Schistose fragments and quartz-feldspar aggregates occur in minor proportions. The quartz-feldspar aggregates show rarely a granophyric texture. Remains of volcanic fragments are very rare consisting of clay matrix with relictic feldspar ledges. Lithics are more common in coarser grained sandstones of facies FC/SF than in the finer grained sand- and mudstones of facies AS and LA (Fig. 5.5). This seems to reflect a grain size effect: Rock fragments are mainly composed of quartz and feldspars and in finer grained samples the lithics are separated into these components.

---

[1] The lower mean value in Judy Field appears not to represent a generally lower mud content in facies association AS in the Judy Field, but rather an effect of other sampling strategy. Thin sections from Judy Field were provided by the industry partner and contain mainly the sand-rich layers from the facies association AS.

Table 5.1: Average detrital composition of samples from the Jade and Judy Fields in volume percent of whole rock. The values given in the table are averages and the range of values (in brackets) from point count values derived from Appendix 2.2.

Field	Jade		Judy	
Facies	AS	FC/SF	AS/SF	FC/SF
Quartz	20.5 (4.5...35.5)	24.1 (15.8...30.0)	26.7 (13.0...38.0)	23.3 (8.7...37.0)
K-Feldspar (uncorroded)	11.9 (0.5...26.3)	14.0 (7.7...23.3)	12.3 (3.3...21.0)	12.3 (2.0...23.3)
K-Feldspar (corroded)	1.0 (0...4.0)	6.0 (0.7...13.8)	4.8 (0...11.7)	5.4 (0...10.7)
Plagioclase	0.3 (0...1.3)	1.9 (0...4.5)	3.3 (0.3...9.7)	3.6 (0...8.0)
Polyquartz	2.5 (0.2...6.8)	7.7 (2.7...14.0)	2.6 (0.3...9.3)	4.0 (0.3...11.3)
Metamorphics	0.3 (0...1.7)	1.3 (0.2...3.3)	0.7 (0...1.7)	1.1 (0...2.3)
Qz-Fsp-aggregates	0.2 (0...0.8)	1.1 (0...3.5)	0.7 (0...2.7)	1.4 (0...5.0)
Mudstone clasts	0.3 (0...3.5)	0.3 (0...4.0)	1.3 (0...9.3)	2.5 (0...39.3)
Detrital dolomite nodules	<0.1 (0...0.2)	0.4 (0...7.3)	<0.1 (0...0.3)	1.8 (0...31.0)
Light mica	3.0 (0.5-7.3)	1.5 (0...5.3)	3.0 (0.3...8.0)	1.6 (0...5.3)
Biotite	0.1 (0...1.0)	-	0.4 (0...4.3)	0.1 (0...1.0)
Chlorite	0.5 (0...1.0)	0.3 (0...1.0)	1.6 (0...4.7)	0.8 (0...4.7)
Detrital mud	42.9 (0...81.5)	1.2 (0...13.5)	10.9 (0...49.7)	1.5 (0...23.0)
number of analysis	15	35	29	41

Micas are common in all samples, but they occur in higher quantities in the argillaceous facies (Table 5.1). They consist mainly of muscovite. Biotite can be found in well 30/2c-4 of the Jade Field only in traces but is more common in samples from the Judy Field. Parts of the biotites are altered to chlorite, but primary chlorite is also present. Heavy minerals occur only in traces consisting of zircon, rutile, tourmaline, apatite, and spinell. In addition to the clasts derived from the source areas, minor intra-formational mudstones and reworked carbonate nodules occur in most of the sandstone samples. The percentage of these intraclasts can increase up to 31 vol.% in conglomerates at the base of fluvial channels.

The detrital composition today does not represent the initial depositional composition. One fourth to one third of the detrital K-feldspars are partly leached in fluvial channel and sheetflood sandstones and up to 4.7 vol.% of present day porosity can be attributed to feldspar grain dissolution in these sandstones. Some of the rock fragments (especially the feldspar-rich) show dissolution of the feldspatic parts.

The average grain sizes range from mud to coarse pebbles with a dominance of fine- to very fine-grained sand. Rounding ranges from angular to subrounded and sorting is well to moderate in sandstones, while moderate to poor in bioturbated mudstones and siltstones with higher mud contents. Sandstone samples were classified after McBride (1963) in Fig. 5.5 and most of them plot in the Arkose field.

The clay minerals in the argillaceous sands and the mudstones of the deeper Jade well (30/2c-4) consist only of illite and chlorite (see Appendix 4.2 for XRD-patterns). A small amount of illite-smectite mixed layer clay minerals was described in an internal industry report for samples from shallower wells of the Judy Field in addition to chlorite and illite (McDougall & Kimber, 1994). Furthermore, the clay assemblage in shallow Triassic basin margin sequences is known from a number of studies to be dominated by smectite and illite/smectite mixed layer clays (Taylor, 1978; Spark & Trewin, 1986; Burley & MacQuaker, 1992; Glasmann & Wilkinson, 1993 and Weibel, 1999). In general, smectites are very common in modern and Cenozoic red beds in arid environments (Walker et al., 1978) and therefore, it can be assumed that smectites were also precursors of some present clay minerals in the studied Triassic rocks.

The major source area of clastic material was most likely the Fenno-Scandian Shield. The material came probably from active fault zones flanking the Norwegian mainland. Other provenance areas were probably the Scottish Highlands, and with local minor contributions the Auk and Hidra Highs as well as the Fladen Ground Spur (Goldsmith et al., 1995).

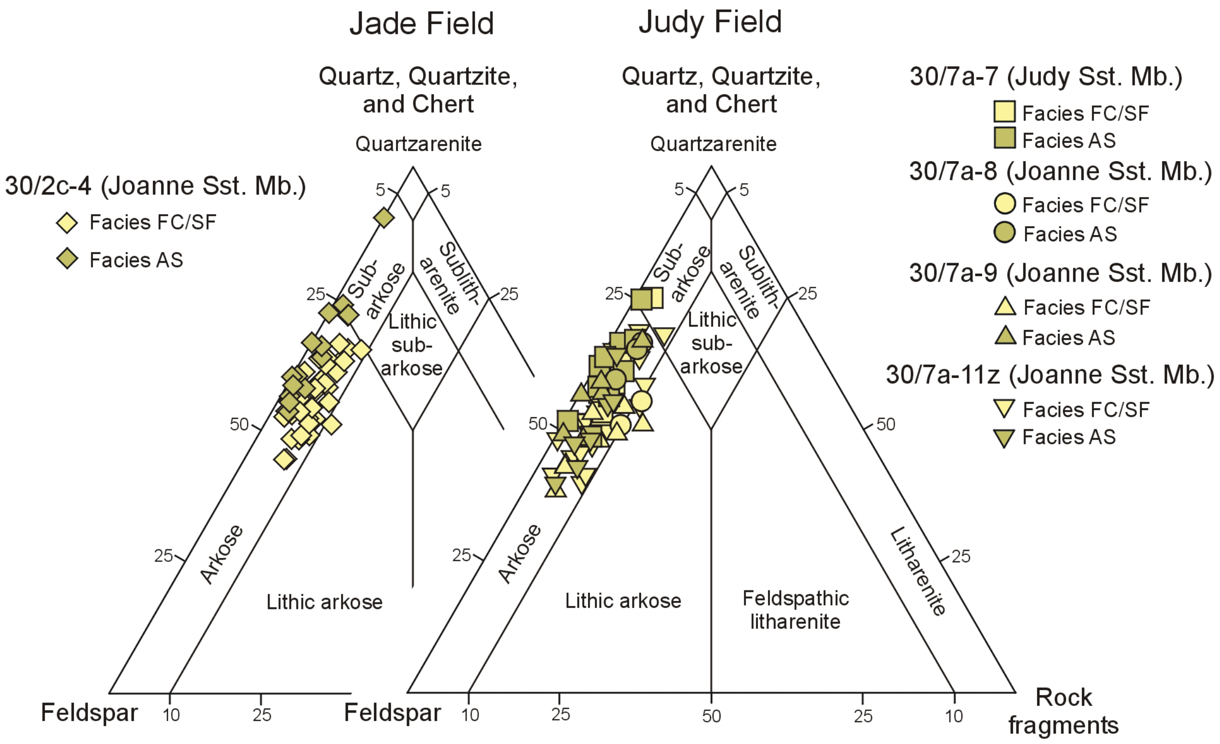

Fig. 5.5: Recent sandstone composition for Jade and Judy Field samples after McBride (1963). Sandstones of the fluvial channel and sheetflood facies associations (FC/SF) have a higher content of rock fragments than samples of the facies association AS. Most of the samples plot in the Arkose Field (Note: Feldspar leaching is not considered and the primary feldspar content was higher).

5.5 Authigenic phases and their occurrence

The occurrence of authigenic phases seems to be mainly controlled by depositional facies. In general, fluvial channel and sheetflood sandstones of facies FC and SF show a greater variety of diagenetic phenomena, probably due to their higher intergranular volume and better permeability for diagenetic fluids than finer grained silt- and mudstones of facies AS and LA. The main authigenic phases are dolomite, K-feldspar, quartz, and chlorite. Ankerite, siderite, calcite, albite, anatase, sulphides, bitumen, illite and hematite occur as minor phases.

Many of the detrital feldspar grains in facies FC/FS have well developed **K-feldspar** overgrowths (Fig. 5.6a-c), rarely forming pore-filling cements. Microprobe analyses show that these overgrowths consist of relatively pure K-feldspar (Appendix 3.2). The host grains are sometimes completely dissolved and only the overgrowth remained, indicating a higher resistance of the newly precipitated feldspar against dissolution. K-feldspar is one of the major authigenic phases in fluvial channel and sheetflood sandstones with average amounts around 6 vol.% and a maximum content of up to 13.5 vol.%. The highest amounts seems to be restricted to sand bodies with high initial porosities. The distribution is constant across the individual sandstone bodies, in contrast to quartz cements which show an increase towards over- and underlying mudstones. Argillaceous sand- and mudstones of the facies association AS show generally lower average contents of K-feldspar overgrowths (average 0.4 vol.% in Jade). The abundance of K-feldspar overgrowths is comparable in the Joanne Sandstone Member of Jade and Judy Fields, but seem to be lower in the Judy Sandstone Member of well 30/7a-7.

K-feldspar appeared relatively early in the diagenetic sequence and is commonly found overgrown by quartz. However, K-feldspar overgrows and thus post dates other eodiagenetic phases (e.g. grain-coating clays, dolomite, leucoxene/anatase and hematite coatings). Usually, the K-feldspar overgrowths are composed only of one generation, but at some grains a second generation was observed (Fig. 5.6b).

A texturally different type of authigenic K-feldspar was found in nearly pure mudstones of well 30/2c-4 as tiny (10-20 µm) pseudo-rhombic aggregates associated with chlorite and quartz (Fig. 5.6d). These K-feldspar-chlorite-quartz aggregates occur as irregular patches of mm size. The texture indicates an authigenic origin, either the replacement of detrital grains or neoformation. No relictic grain boundaries could be observed making neoformation more likely.

Authigenic **albite** can be found as single 10 to 60 µm sized euhedral crystals within dissolved K-feldspar grains (Fig. 5.6e-f) or as patchy replacement of detrital K-feldspar. Euhedral albite was not observed in the pore space between the grains in the samples investigated. Microprobe analyses indicate a nearly pure albite (Appendix 3.2). Authigenic albite is more common in higher permeable fluvial channel and sheetflood sandstones than in argillaceous deposits. In general, the amount of albite is low and only single "albitised" K-feldspar grains were found. Not every leached K-feldspar grain is associated with neoformed albite. The amounts of authigenic albite vary between average contents of ~ 0.5 vol.% in facies associations FC and SF, and ~ 0.1 vol.% in the facies association AS of the Jade Field. Textural relationship to other authigenic phases remains uncertain because the occurrence of authigenic albite is restricted to the interior of K-feldspar grains. However, the growth of euhedral albite crystals must have taken place coeval or after the dissolution of K-feldspar.

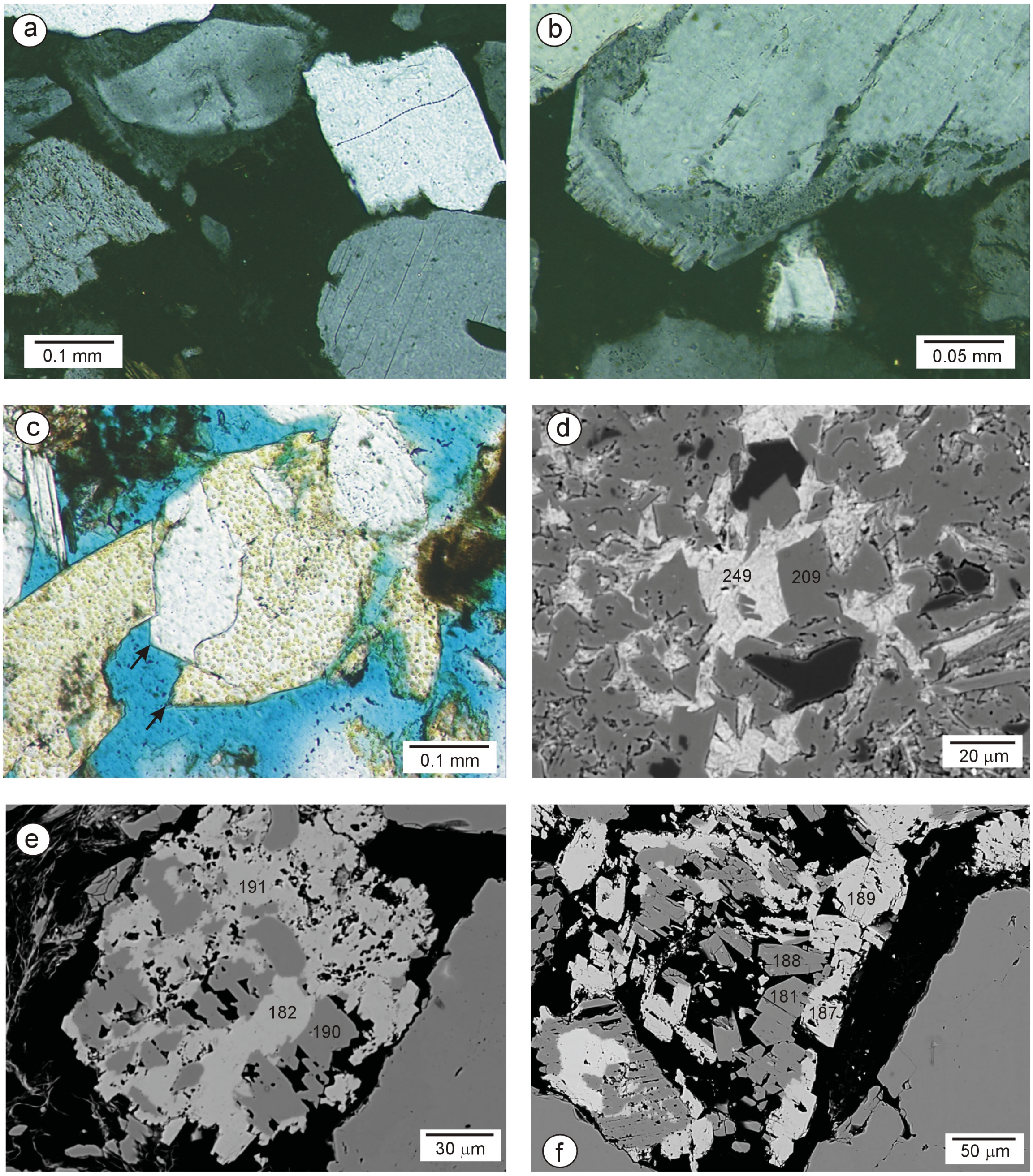

Fig. 5.6a: K-feldspar overgrowth on K-feldspar grains (sample 15615, well 30/2c-4, crossed polarisers); **b**: Two generations of K-feldspar overgrowths (sample 15615, well 30/2c-4, crossed polarisers); **c**: K-feldspar and quartz overgrowths (arrows) on a rock fragment. The yellow dots are the result of staining with sodium cobaltnitrite for K-feldspar identification. Porosity is blue dyed. Note that authigenic quartz engulfs the K-feldspar overgrowth from the left grain (sample 11510, well 30/7a-11z, plane polarised light); **d**: K-feldspar (grey), chlorite (light grey) and quartz (dark grey to black) aggregates in a mudstone. The numbers give the related analysis in Appendix 3 (sample 15768.5, well 30/2c-4, BEI micrograph); **e, f**: Neoformation of euhedral albite crystals (dark grey) in a leached K-feldspar grain (light grey). The grain in Fig. 5.6f shows a higher remaining porosity. Numbers give the related analysis in Appendix 3 (both BEI micrographs from sample 15616, well 30/2c-4).

Nonferrous dolomite occurs in different textural varieties: 1.) microspar or small single rhombic subhedral to euhedral crystals, separately or in dolomite nodules mainly in the argillaceous facies; 2.) coarser dolomite crystals, which can form a pore filling blocky dolomite spar cements.
The small rhombi of the first type vary in size between 10-50 µm in mudstones of the argillaceous facies. Larger rhombi in nodules were also point-counted to this type. It was observed that these small rhombi sometimes form clusters and on a larger scale nodules (Fig. 5.7a). Nevertheless, many nodules have a microspar texture (Fig. 5.7b-c). The individual dolomite nodules can reach sizes up to cm-scale and rarely merge to continuous layers. Authigenic dolomite in the nodules was observed to be very corrosive against framework grains, hence inside the nodules the grains are intensely corroded or completely replaced (Fig. 5.7c). The timing of this dolomite growth must be very early, since such nodules were found as rounded reworked intra-clasts in coarser grained sandstones. Dolomite nodules and small rhombi occur prevalently in the argillaceous sandstones of the facies association AS (average 5.1 vol.% in Judy Field and 6.4 vol.% in Jade Field). Average dolomite nodule contents are generally lower in fluvial channel and sheet flood sandstones (average 3.1 vol.% in Jade Field and 1.5 vol.% in Judy Field). Dolomite nodules can be found commonly near the top of amalgamated sandstone layers here. Microspar and small rhombi were also found to form a grain rimming cement, but this type is extremely rare and was detected only in one sample from a dolocrete layer of well 30/7a-9 (Fig. 5.7e).

The second main dolomite variety can be distinguished texturally from the first type. It consists of coarser patchy distributed rhomb-shaped subhedral to euhedral crystals (> 50 µm, see Fig. 5.7h), which can aggregate to blocky pore filling dolomite spar cements (Fig. 5.7d). This dolomite type is (in contrast to the nodules and small rhombi) dominant in porous sandstones of the facies associations FC and SF (4.4 vol.% in Jade Field and 2.5 vol.% in Judy Field). The pore filling dolomite occludes an intergranular volumen of around 34 vol.% in one sample (15715, well 30/2c-4) of the Jade Field, indicating a relatively high porosity and low degree of compaction at the time of precipitation. In the finer grained sandstones of the facies association AS this cement type is restricted to areas with higher initial porosities. The average content ranges from 0.2 vol.% in the Jade Field to 0.6 vol.% in the Judy Field. Dolomite crystals of this type often use existing dolomite nodules and reworked dolomite nodules in channel bottom conglomerates as a nucleation sites. So, they can be found frequently forming a coarser zone around the nodules. In one sample (15747, well 30/2c-4), covering the contact between sandstone and mudstone, small dolomite bands were found in the sandstone directly adjacent to the mudstones.

Fig. 5.7a (next page): Dolomite nodule composed of coarser crystals. Some of them have a rhombic shape. The yellow dyed grains are K-feldspars after staining with sodium cobaltnitrite (sample 11573, well 30/7a-11z, plane polarised light); **b**: Dolomite nodule with microspar texture and coarser rhomb-shaped crystals. Note the magnification is twice of that in Fig. 5.7a (sample 15604, well 30/2c-4, crossed polarisers); **c**: Many quartz grains inside a dolomite nodule with microspar texture have etched surfaces caused by corrosion during dolomite precipitation (sample 15608, well 30/2c-4, plane polarised light); **d**: A sample dominated by pore filling-, and partly clast replacing dolomite spar cement (sample 15715, well 30/2c-4, crossed polarisers); **e**: A rare type of dolomite cementation – grain rims composed of tiny crystals (sample 12160.4, well 30/7a-9, plane polarised light); **f**: Patchy cementation with calcite close to a fracture (sample 11519, well 30/7a-11z, plane polarised light); **g**: Ankerite (A) overgrowth on non-ferrous dolomite (D). Note the zonation of the dolomite (sample 15715, well 30/2c-4, BEI micrograph); **h**: Ankerite (A) overgrowth on a dolomite crystal. Numbers give the related analysis in Appendix 3 (sample 15715, well 30/2c-4, BEI micrograph).

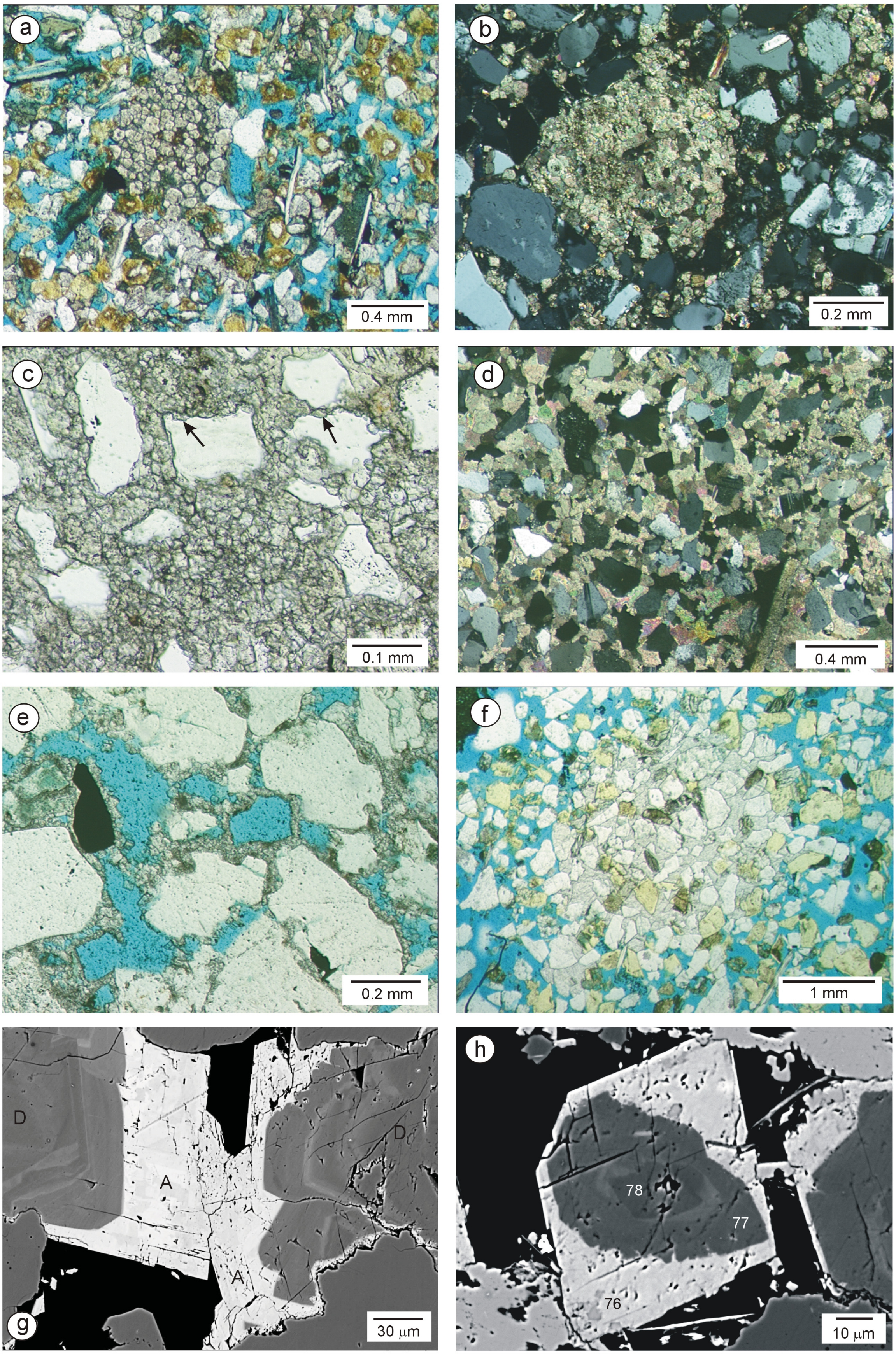
a
0.4 mm
b
0.2 mm
c
0.1 mm
d
0.4 mm
e
0.2 mm
f
1 mm
g
D
A
D
A
30 µm
h
78
77
76
10 µm

The non-ferrous dolomites in the Jade Field consist of nearly pure dolomite (see Fig. 5.8 for average composition) with a relatively low content of manganese (MnO average 0.82, max. 3.11 wt.%) and iron (FeO < 0.48 wt.%, see Appendix 3.1). One sample from well 30/7a-9 contained dolomite in nodules with a higher iron content (**ferrous dolomite**, FeO up to 5.12 wt.%). This ferrous dolomite was textural comparable to the nonferrous dolomite in the nodules from the Jade Field.

Backscatter electron images showed zonation in the non-ferrous dolomite (Fig. 5.7g-h). Brighter zones have a higher content of manganese (up to 3.11 wt.%) and iron than the darker zones. Non-ferrous dolomites can show dissolution traces (e.g. Fig 5.7h) mainly in fluvial sandstones with high porosities (see also part secondary porosity).

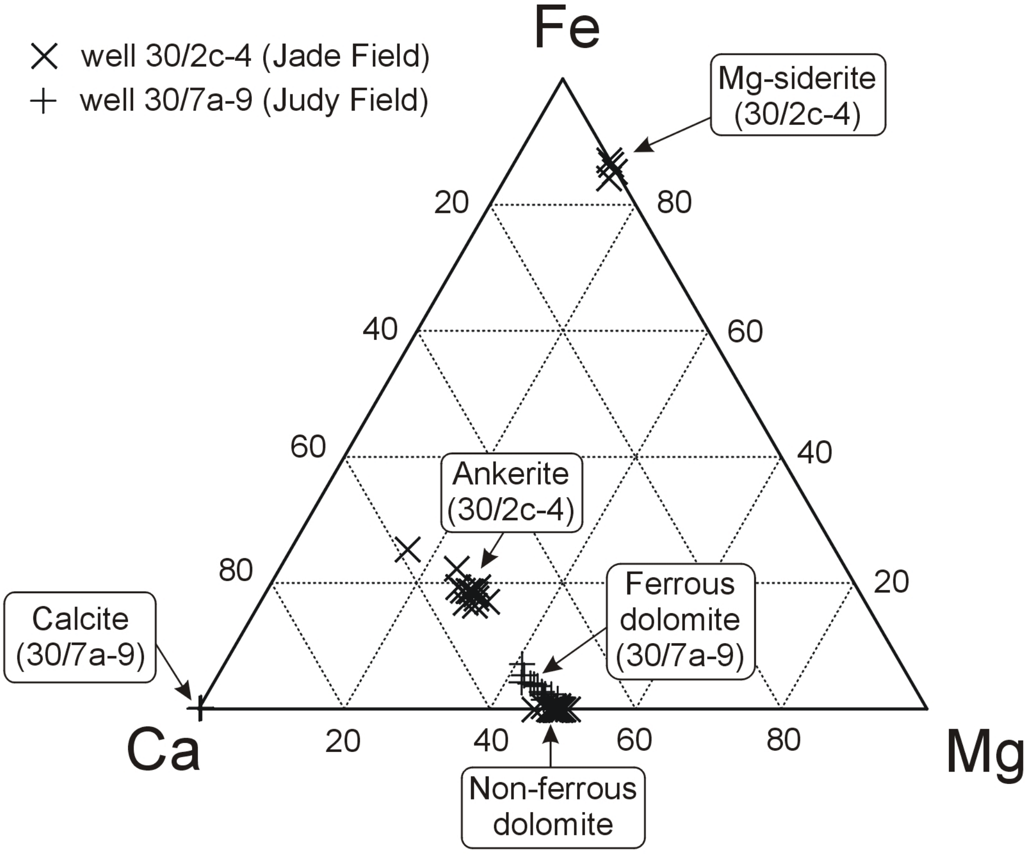

Composition of authigenic carbonates in the Skagerrak Formation

Mineral	Typical composition	No. of analyses
Calcite:	$Ca_{1.98\text{-}2.00}Mg_{0.00\text{-}0.01}Fe_{0.00\text{-}0.01}Mn_{0.01\text{-}0.02}(CO_3)_2$	3
Non-ferrous dolomite:	$Ca_{0.94\text{-}1.07}Mg_{0.90\text{-}1.01}Fe_{0.00\text{-}0.03}Mn_{0.00\text{-}0.08}(CO_3)_2$	38
Ferrous dolomite:	$Ca_{0.96\text{-}1.04}Mg_{0.76\text{-}0.91}Fe_{0.05\text{-}0.13}Mn_{0.01\text{-}0.05}(CO_3)_2$	9
Ankerite:	$Ca_{1.00\text{-}1.10}Mg_{0.30\text{-}0.60}Fe_{0.32\text{-}0.48}Mn_{0.03\text{-}0.13}(CO_3)_2$	12
Mg-siderite:	$Fe_{1.61\text{-}1.67}Mg_{0.25\text{-}0.28}Mn_{0.03\text{-}0.04}Ca_{0.00\text{-}0.03}(CO_3)_2$	4

Fig. 5.8: Composition of authigenic carbonates in samples of the Skagerrak Formation from Jade and Judy Fields derived from EMP measurements.

Ankerite occurs often as overgrowth on larger non-ferrous dolomite rhombi (Fig. 5.7g-h). Isolated ankerite crystals in the pore space were observed relatively seldom. Ankerite can also occur inside the rare pores of dolomite nodules. The average ankerite content in the investigated samples was relatively low. The highest amounts were found in sandstones of the facies associations FC and SF in the Jade Field (average 1.1, up to 7.7 vol.%). The average content is lower in samples from the same facies associations in the Judy Field (average 0.4, up to 2.3 vol.%). Argillaceous sandstones (AS) in both Fields show very low (average 0.1 vol.%) contents of ankerite.

The edges of non-ferrous dolomite, overgrown by later ankerite, are commonly corroded prior or coeval to ankerite precipitation (Fig. 5.7h). The ankerite has iron contents between 11.7 and 16.7 wt.% FeO and higher manganese contents than the non-ferrous dolomite (MnO average 2.17, max. 4.55 wt.%) in samples from the Jade Field. A mineral formula calculated from electron microprobe measurements and the Ca-Mg-Fe ternary diagram is given in Fig. 5.8. Ankerite has usually no zonation in backscatter electron images, in contrast to the non-ferrous dolomite. However, patchy areas inside of ankerite overgrowths, which appear brighter in the backscatter electron image, have a higher iron content than the rest of the ankerite crystal. The ankerite analysis with the highest iron content (no. 50 in Appendix 3.1) came from such a patchy area.

The formation of ankerite clearly postdates the non-ferrous dolomite. The textural relationship to quartz is not clear as the ankerite can be found overgrowing quartz cement or be overgrown by quartz cement. This can be interpreted as a short cementation event of ankerite during a longer lasting quartz cementation period. Ankerite appears to be completely unleached and all edges are sharp in the samples investigated.

Mg-siderite (see Appendix 3.1 for analysis and Fig. 5.8 for typical composition) was detected in a nearly pure mudstone sample (15768.5) of well 30/2c-4 (Jade Field). Mg-siderite occurs as mm to sub-mm sized reddish brown coloured concretions, which give the sample a dotted surface. The content of this Mg-siderite in the sample is relatively low (2.2 vol.%).

Calcite and **ferrous calcite** were found only in the Judy Field occurring as patchy cementation around fracture zones (Fig. 5.7f) and in the fractures itself. The calcite and ferrous calcite outside of the fractures forms poikilotopic cements. These cements consist of large crystals including several grains, in contrast to the typical texture of ankerite and nonferrous dolomite, which are composed of a mosaic of single crystals. This cement type is volumetrically only locally important. It was found only in well 30/7a-P7 and the both wells from the northern fault compartment (30/7a-9 and 30/7a-11z) of the Judy Field. The amount varies between 0.3 and 6.7 vol.% for calcite and between 0.3 and 21.3 vol.% for ferrous-calcite (see Appendix 2.2). Analysis of the calcite from well 30/7a-9 showed a nearly pure calcite with small amounts of manganese (up to 0.54 wt.% MnO) and iron (up to 0.24 wt.% FeO, see Fig. 5.8 and Appendix 3.1 for details).

Stable isotopes of carbonates in well 30/2c-4 (Jade Field)

As mentioned in the section “material and methods”, two different methods were used for the analysis of stable isotope ratios of carbonates at samples of well 30/2c-4. The results of the phosphoric acid method are plotted in Fig. 5.9a. A major issue was that at least three carbonate generations, distinguishable by petrographical means, occurred commonly together in the investigated samples (see description of carbonate textures). These are: dolomite in nodules, dolomite as large rhombi or pore filling cement (dolomite spar), and ankerite. Only the dolomite nodules were found separately, without contamination by the other phases, in some samples (15584, 15628, 15665, 15739). All other samples contained two or three carbonate types and thus the measured δ^{13}C- and δ^{18}O-values from these samples represent the mixing of isotopically different carbonates. The samples containing only dolomite nodules have δ^{13}C-values ranging from –7.97 to –9.14 ‰ V-PDB and δ^{18}O-values between –1.33 and –2.80 ‰ V-PDB (see Fig. 5.9, Appendix 5.1 for single values and Appendix 2.2 for the content of carbonate phases). The samples dominated by the dolomite spar type have comparable δ^{13}C-values, and by ~ 2 ‰ lighter δ^{18}O-values than the nodules. The values of sample 15655.3 seem to be most suitable to reconstruct the ankerite isotopic composition, since around 80 vol.% of the carbonate in the sample is ankerite. The other two samples with ankerite as the main carbonate phase (15716, 15752) have a lesser relative content of ankerite (45-51 vol.% of the carbonates in the sample) and plot closer to the dolomite spar in the diagram in Fig. 5.9. Pure ankerite seems to have δ^{13}C-values around –4 ‰ V-PDB and δ^{18}O-values around –10 ‰ V-PDB as indicated by the composition of sample 15655.3 and the mixing-trend indicated by all ankerite bearing samples (Fig. 5.9a).

It was attempted to fix the problem of different carbonate generations in some samples via UV laser system for the δ^{13}C-values (see values in Appendix 5.2). The areas affected by the laser were unfortunately too large to get signals from individual ankerite or dolomite spar crystals. The main problem was the depth of the craters ranging from 400 to 600 µm (compare this with the size of dolomite spar and ankerite crystals in Fig. 5.7g-h). Eventually, only the δ^{13}C-values of spots in dolomite nodules could be measured accurately and they are consistent with the values measured by the phosphoric acid method (see Fig. 5.9b). The δ^{13}C-values of all other spots show an depletion in ^{13}C. This seems to be an effect of the bitumen in the samples[2]. Bitumen was detected by optical microscopy at the surface around the analysed spots in many of the samples with the lightest δ^{13}C-values (see Fig. 5.9b). The spots, where bitumen dominated at the surface, have δ^{13}C-values down to –20 ‰ V-PDB.

---

[2] The problem of the bitumen effect is restricted to the UV-laser system analysis, since the CO_2 released by the reaction with phosphoric acid is derived almost completely from the carbonates, while the laser volatilises all carbon bearing compounds.

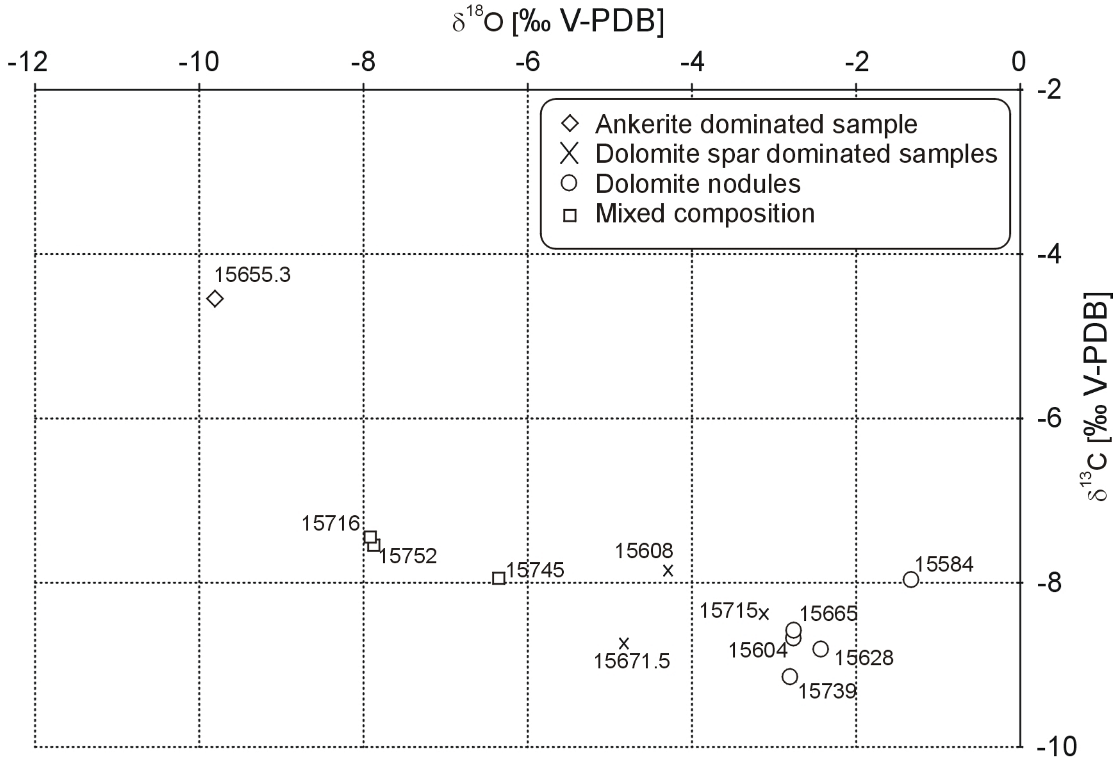
ⓐ Phosphoric acid method

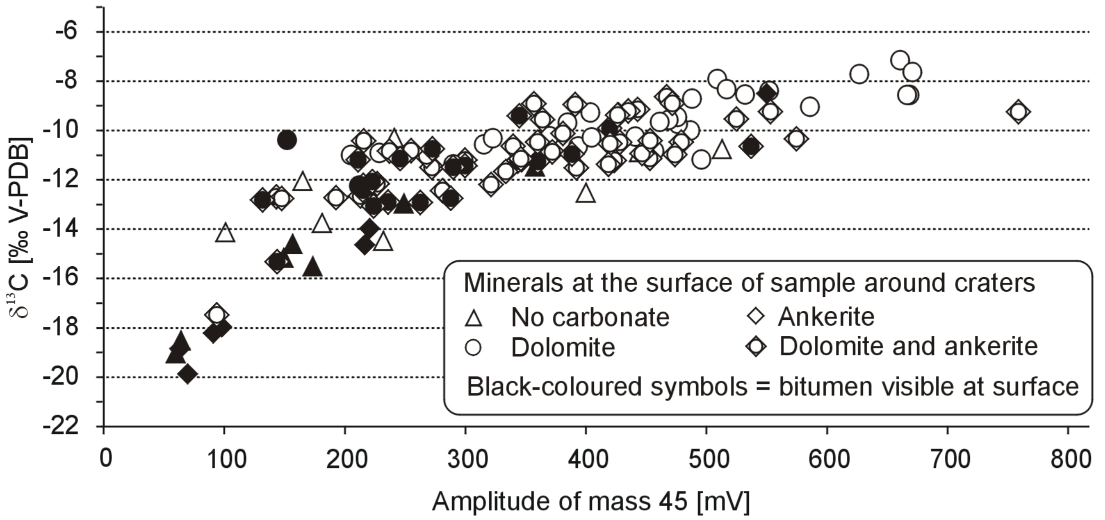
ⓑ UV-laser system

Fig. 5.9a: Stable isotope analyses of carbonates analysed using the phosphoric acid method for bulk samples of well 30/2c-4 (Jade Field). Most of the samples contain a mixture of at least three different carbonate generations (explanation see text); **b**: δ^{13}C-values of different spots measured via UV-laser system at four samples from well 30/2c-4 (Jade Field). The values are plotted against the amplitude of mass 45 for estimation of measurement accuracy (reproducibility of δ^{13}C-values can be found in Fig. 2.4). No clear differentiation can be made between different authigenic carbonates. However, the δ^{13}C values of dolomite measurements with a high signal amplitude are in consistence with samples analysed by the phosphoric acid method.

Quartz cements form commonly syntaxial overgrowths around detrital quartz grains (Fig. 5.10a-b). These overgrowths can amalgamate to pore-filling quartz cements. Such intense cementation can be observed on mm-scale within the sandstones directly adjacent to mudstones (Fig. 5.10c-d). The overgrowths appear predominantly in fine- to medium-grained sandstones in fluvial channel and sheetflood deposits (average contents 3.6 vol.% in Jade Field and 2.2 vol. % in Judy Field). Authigenic quartz shows an increase in quantity towards mudstone layers in the individual sandstone bodies between two mudstones layers (Fig. 5.11). Quartz cement volumes up to 25 vol.% can be observed in completely cemented zones directly at the contact to the mudstone on thin section scale. The argillaceous sandstones in facies association AS have much lower average contents of authigenic quartz (e.g. 0.1 vol.% in Jade Field).

Average amounts of quartz cements seem to increase with burial depth in sandstones of facies association FC and SF (see Fig. 5.12). So, the deeper buried Jade Field well 30/2c-4 has higher average authigenic quartz contents than the Judy Field wells. Samples from well 30/7a-7, covering the Judy Sandstone Member show higher quartz cement contents than samples from the Joanne Sandstone Member at comparable depths of burial (see Fig. 5.12). However, this observation should not be over-interpreted since only seven samples were available from the facies associations FC and SF of well 30/7a-7.

The amount of authigenic quartz was difficult to quantify exactly by optical microscopy. Cathodoluminescence microscopy could not be used, due to the bright luminescence of frequently appearing K-feldspars and carbonates, which outshine the quartz.

It was observed that authigenic quartz engulfs, and hence postdates early nonferrous dolomite, feldspar overgrowth, chlorite plates and leucoxene/anatase. As discussed previously, the timing relative to ankerite remains uncertain. Fluid inclusions in quartz cement are very rare and small. Therefore, no fluid inclusion micro-paleothermometry could be carried out. However, one of the rare fluid inclusions in the quartz cement was found to be fluorescent (personal communication R. di Primio). That indicates that it contains hydrocarbons. Bitumen stained clay minerals occluded by quartz cements can be found in samples of well 30/2c-4 in the Jade Field in the contact zone to the mudstones. Quartz cements have overgrown bitumen in some samples of the Judy Field while in other samples of the Judy Field bitumen can be found post-dating quartz overgrowths. According to these observations the timing of quartz cementation seems to be later than most other authigenic phases and it seems to have lasted over a longer period during which precipitation of ankerite and infiltration of bitumen occurred as shorter events.

Fig. 5.10a (next page): Syntaxial overgrowth of authigenic quartz (sample 15616, well 30/2c-4, plane polarised light); **b**: Syntaxial overgrowths of quartz. Note the leached surface of the K-feldspar overgrowth at bottom left (sample 15615, well 30/2c-4, SEI); **c**: Quartz cemented area (S1) and dolomite cemented zone (S2) at the contact between sandstone and mudstone (M). A close up view of the quartz cemented zone (S1) is given in **d** (c, d sample 15747, well 30/2c-4, plane polarised light); **e**: Authigenic chlorite type I as green coatings around the grains (sample 14348, well 30/7a-P7, plane polarised light); **f**: authigenic chlorite type II as small euhedral plates stained by bitumen. The single crystal growing into the pore space is anatase (sample 15680, well 30/2c-4, plane polarised light); **g**: Chlorite coatings of type I (CC), and euhedral chlorite plates of type II (CE) partly engulfed by a later quartz cement (sample 15654.5, well 30/2c-4, SEI); **h**: Euhedral chlorite plates of type II (sample 15654.5, well 30/2c-4, SEI).

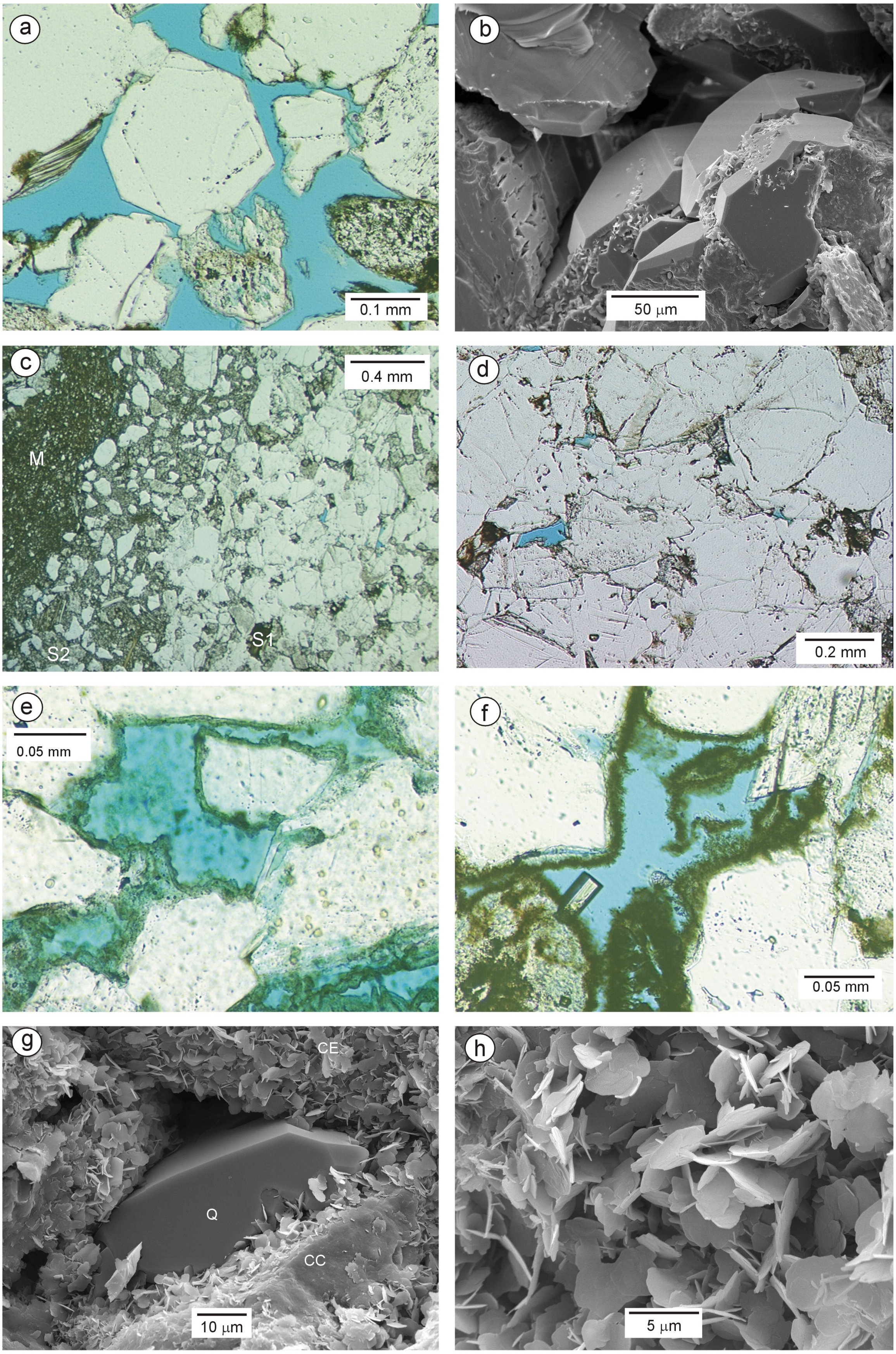
a
0.1 mm
b
50 µm
c
0.4 mm
M
S2
S1
d
0.2 mm
e
0.05 mm
f
0.05 mm
g
CE
Q
CC
10 µm
h
5 µm

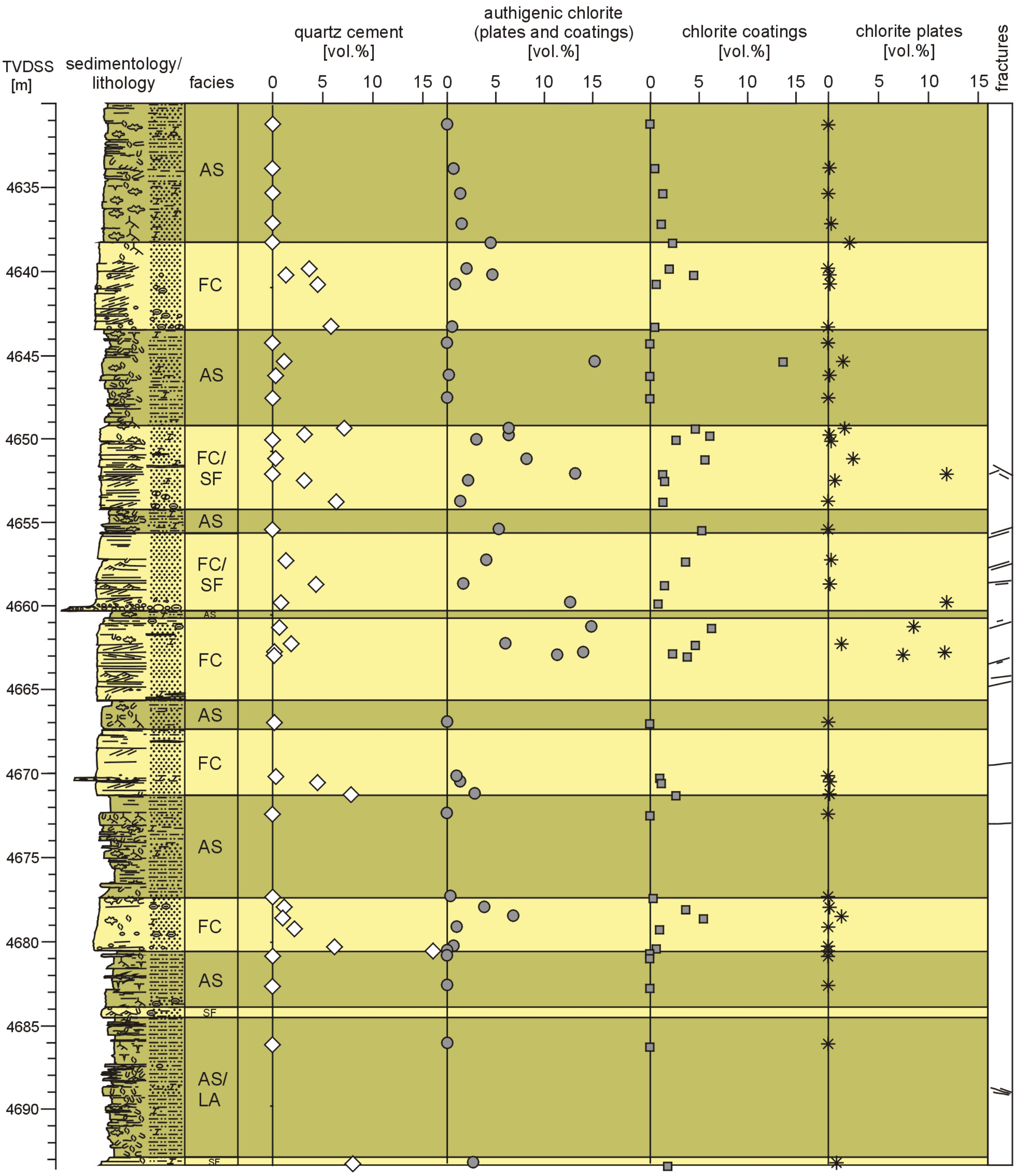

Fig. 5.11: Distribution of quartz cement and authigenic chlorite in the well 30/2c-4 (Jade Field). The abundance of quartz cement increases towards over or underlying sandstone/mudstone contacts (see sandbody at ~ 4657 m). The content of chlorite coatings (type I) is higher in the upper part of the individual sandstone layers. Euhedral chlorite plates (type II) occur mainly near fractures. The columns sedimentology, lithology, facies and fractures are taken from Kimber & Mathieson (1997).

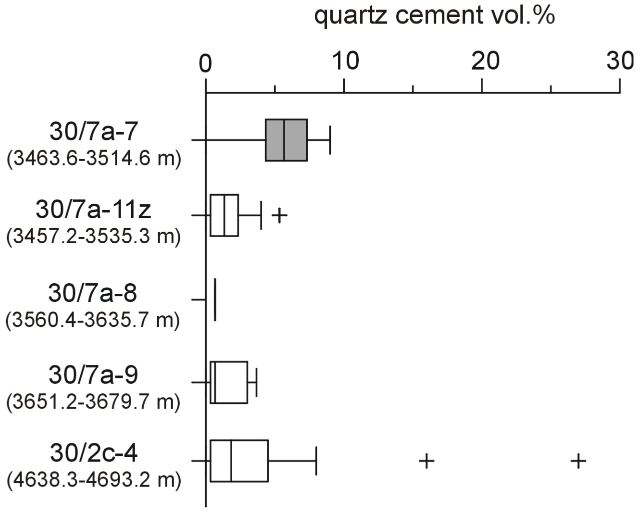

Fig 5.12: Average contents of quartz cement in sandstones from the facies associations FC and SF. The average authigenic quartz content seems to increase with depth of burial in the Joanne Sandstone Member (white). The samples from well 30/7a-7 are derived from the Judy Sandstone Member of the Skagerrak Formation and the samples from the other wells from the Joanne Sandstone Member (see text for discussion).

Different textural types of **Illite** are locally present in minor amounts. The most common type occurs as grain replacement, which may also be of detrital origin (average contents 1.6 vol.% in Judy Field and 2.1 vol.% in Jade Field facies associations FC/SF). Authigenic illite in moulds of dissolved feldspars can be present, but is generally rare. Tangential illite coatings can occur instead of chlorite coatings locally in some finer grained argillaceous samples. The grain-coating clay minerals are dominantly composed of chlorite in fluvial channel and sheetflood sandstones, while grain-coating illite is very rare. Pore-filling, permeability destroying, meshwork of fibrous/flaky illite as observed in Rotliegend samples of this study and also known from other Rotliegend and Jurassic wells was not detected in any sample of the Jade and Judy Fields.

Different textural types of authigenic **chlorite** can be distinguished. Type I consists of tangential grain coatings or rims around detrital grains in a more or less continuous irregular layer (Fig. 5.10e). The layers can have varying thickness. Faint geopetal structures were observed in some thin sections from the Judy Field. Chlorite type I is common in wells of both Fields and has an average abundance of 1.9 vol.%. Some argillaceous sandstones can have contents of up to 13.7 vol.%. The distribution of grain coating chlorite shows often an increase towards the top of single or amalgamated sandstone bodies (compare Fig. 5.11). The chemical composition measured by electron microprobe gave an iron rich composition. The formula calculated from analysis no. 248 is given as example:

chlorite I: $Mg_{3.14}Fe_{4.98}Al_{3.07}Si_{6.09}Al_{1.91}O_{20}(OH)_{16}$ (5.1)

The second type (type II) was observed mainly in well 30/2c-4 of the Jade Field. The highest amounts (up to 11.8 vol.%) were located close to fracture zones in the core (Fig. 5.11). Type II consists of small euhedral plates growing more or less radially from pore walls into the pore space (Fig. 5.10f-h). These small platelets have a size of approximately 5 µm. Microprobe analysis of these plates are not very accurate due to the small size of the single platelets.

However, they also yield iron rich compositions, comparable to type I. A formula calculated from the best analysis (no. 245) is:

chlorite II: $Mg_{3.71}Fe_{5.18}Al_{2.75}Si_{5.77}Al_{2.23}O_{20}(OH)_{16}$ (5.2)

In higher permeable samples chlorite type II is always intensely coated by bitumen (Fig. 5.10f). Nucleation of the euhedral chlorite on a former tangential chlorite is sometimes visible (Fig. 5.10g).

Chlorite type III represents a chlorite inside of detrital grains following the fissility of feldspars. This type occurs frequently together with type I, but is restricted to detrital grains in the argillaceous facies (4.3 vol.% in the facies association AS of well 30/2c-4). A transition between chlorite type III inside of a clast and the grain coating around seems to be common.

Chlorite type IV occurs only in nearly pure mudstones associated with K-feldspar and quartz in patchy aggregates (see Fig. 5.6d). This chlorite is also iron rich. A formula calculated from one of the analyses (no. 249) is:

chlorite IV: $Mg_{3.11}Fe_{6.29}Al_{2.49}Si_{5.69}Al_{2.31}O_{20}(OH)_{16}$ (5.3)

Leucoxene/anatase occurs as replacement of heavy mineral grains in nearly every sample. In some cases small euhedral anatase crystals can be found growing into pore space (Fig. 5.10f). In other situations, there is an optically not resolvable mass of leucoxene. In general, the amounts are low (<1 vol.%), but in some heavy mineral rich layers leucoxene/anatase can reach values up to 3.8 vol.%. Microprobe analyses gave a chemical composition of nearly pure TiO_2. In the paragenetic sequence it could be observed that leucoxene/anatase is engulfed by quartz and dolomite and thus predates these phases.

Hematite grain coatings could be found preserved in carbonate cement patches and nodules and beneath K-feldspar overgrowths (Fig. 5.13a). Hematite can also occur in fractures of grains, surely as relict of source area weathering or oxidation during the transport. Some of the carbonate cemented spots in mudstones samples from well 30/2c-4 are reddish brown, while the rest of mudstone is coloured dull green. Completely reddened horizons occur locally in wells 30/7a-8 and 9 from the Judy Field. The reddening of the entire Skagerrak Formation was described for not investigated wells (30/12b-2 and 3) by Goldsmith et al. (1995). Hematite is very rare in samples from well 30/2c-4 (up to 0.3 vol.% in facies associations FC and SF and up to 0.8 vol.% in facies association AS), but more common in the wells from the Judy Field (up to 2 vol.% in facies associations FC and SF and up to 14 vol.% in facies association AS). However, the exact quantification of authigenic hematite by point counting is difficult, since hematite is commonly associated with clay mineral coatings.

Fig. 5.13a (next page): Grain coating hematite (red) preserved beneath carbonate cement. Note that the grains outside of the carbonate cemented zone have no hematite coatings indicating later bleaching (sample 11627, well 30/7a-11z, plane polarised light); **b**: Authigenic euhedral pyrite (light grey) in a fracture (sample 15654.5, well 30/2c-4, BEI micrograph); **c**: Massive "tarry" bitumen (sample 11291, well 30/7a-7, plane polarised light); **d**: Authigenic chlorite plates coated by bitumen? (sample 15615, well 30/2c-4, SEI); **e**: Secondary porosity (arrow) in a leached K-Feldspar (sample 15716, well 30/2c-4, plane polarised light); **f**: Leached eodiagenetic dolomite (D) covered by later ankerite (A) overgrowth (sample 15680, well 30/2c-4, BEI); **g**: Typical texture of a fluvial channel sandstone with secondary porosity due to cement dissolution. Larger cement dissolution pores (P) exist adjacent to closer compacted areas (arrows) in the same thin section (sample 15655.3, well 30/2c-4, plane polarised light); **h**: Typical texture of a sandstone not affected by cement dissolution. Note the distribution of closer compacted areas (arrow) and authigenic dolomite (sample 15752, well 30/2c-4, crossed polarisers).

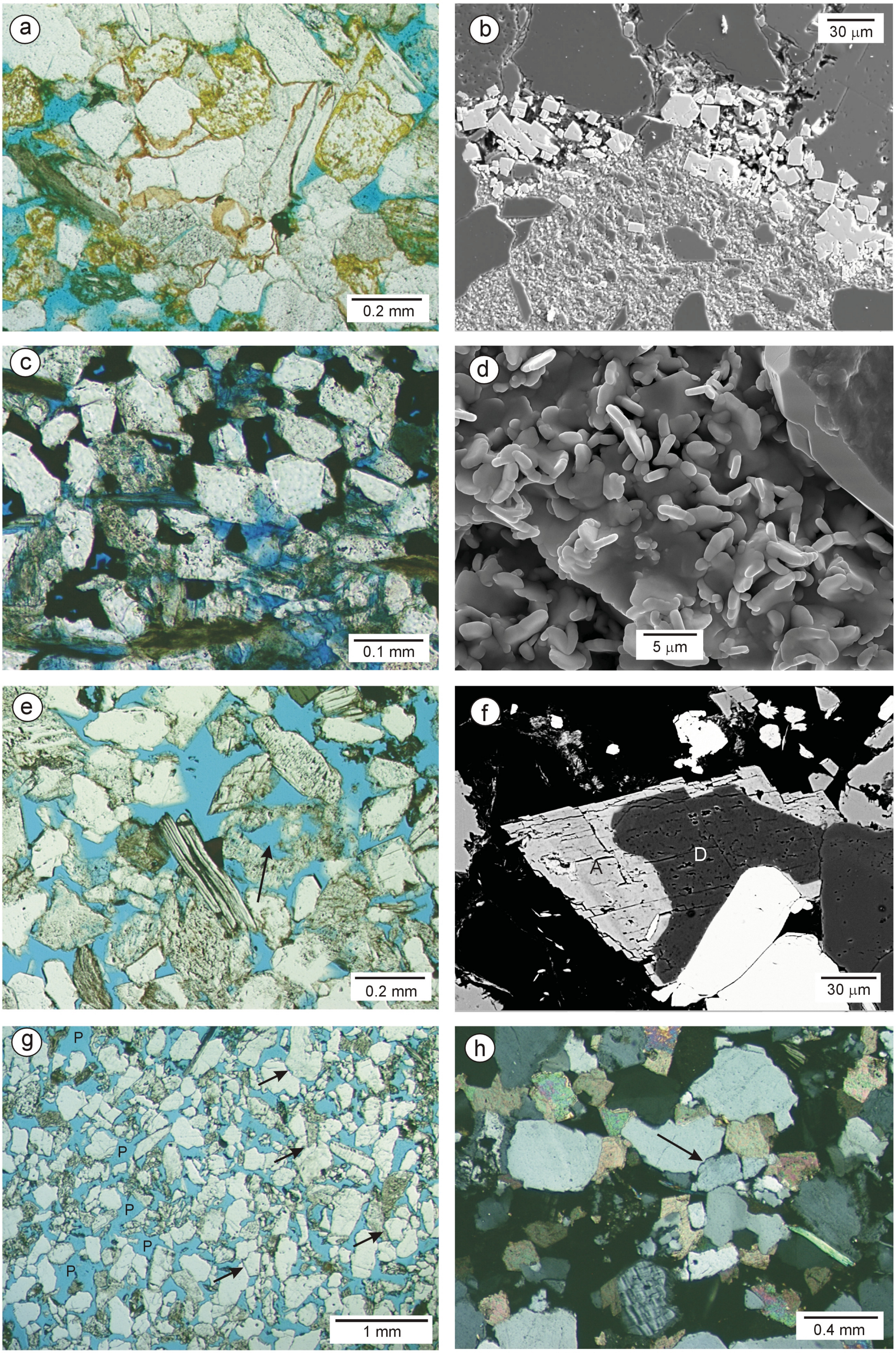
a
0.2 mm
b
30 µm
c
0.1 mm
d
5 µm
e
0.2 mm
f
A
D
30 µm
g
P
P
P
P
P
1 mm
h
0.4 mm

Preservation of hematite beneath K-feldspar overgrowths was only observed in wells from the Judy Field.

The present occurrence of hematite restricted to protected areas under K-feldspar overgrowths or inside of dolomite nodules is evidence for bleaching as result of iron oxide reduction. The occurrence of hematite was most likely more extensive during early diagenesis, and only the hematite in protected areas survived later bleaching.

The timing of bleaching appears to postdate dolomite and K-feldspar formation, but precedes quartz cementation, since no hematite was preserved beneath quartz cements. If hematite and chlorite occur together (which is very seldomly the case) than chlorite encloses hematite. A similar observation was made by Taylor (1978), which shows that hematite staining developed prior to the formation of chlorite (or its precursor).

Different **sulphides** were found in small amounts (average < 0.1 vol.%) in the samples. Patchy early diagenetic pyrite can occur rarely inside of dolomite nodules. Mesodiagenetic euhedral pyrite was found mainly as cubes in fracture zones (Fig. 5.13b) and single euhedral galenite crystals were found in the pore space of well 30/2c-4 (and verified by EDX analysis). Sulphates were found to be volumetrically not important, since they were detected only in traces in some sandstones samples from both fields in the form of authigenic barite.

Different types of **bitumen** occur in the thin sections from both fields. These types can be distinguished by optical microscopy, but need not necessarily to be linked to different hydrocarbon charges or compositions. The first bitumen type intensely impregnates clay minerals (mainly chlorite) and seems to consist of very thin coatings. This bitumen staining gives the clay minerals a brownish colour in thin section and is very common in well 30/2c-4 of the Jade Field. The staining of clay minerals was not observed so frequently in samples from the Judy Field. Intense bitumen staining of chlorite occurs mainly in channel and sheet flood sandstones of the Jade Field. Patchy bitumen staining was found only in the higher permeable areas of argillaceous sandstones, while it is completely absent in pure shales.

Bitumen can also occur as thick massive “tarry” crusts (Fig. 5.13c). This type can be found prevalent in the finer grained beds (mainly facies association AS) filling the former higher permeable parts in well 30/2c-4.

5.6 Secondary porosity

Different types of secondary porosity were observed in the investigated samples of the Skagerrak Formation. Optical microscopy allows to distinguish three types of secondary porosity: grain dissolution porosity, oversized pores and cement dissolution porosity (Fig. 5.14). However, identification of secondary porosity in thin sections can be difficult and quantification is ambiguous. Grain dissolution porosity is relatively easy to identify in most cases, but quantification of cement dissolution in thin sections remains a matter of interpretation (and speculation). Some of the problems of petrographic observations are illustrated by Giles (1997) and Taylor et al. (2010).

One fourth to one third of the detrital K-feldspars in the fluvial channel and sheet flood sandstones shows leaching traces and up to 4.7 vol. % of the K-feldspars were probably completely leached (see Fig. 5.13e for typical textures). Feldspar dissolution was observed mainly in the fluvial channel and sheet flood sandstones (average 1.3 vol.% in the deeper Jade Field, and 2.5 vol.% in the shallower Judy Field). Only few feldspar grains are leached in the finer grained facies. In the case of completely lacking grains it is sometimes difficult to decide if this porosity is due to leaching or caused by the rip up of grains during thin section preparation. Therefore, such pores where count separately as oversized pores (Fig. 5.14b).

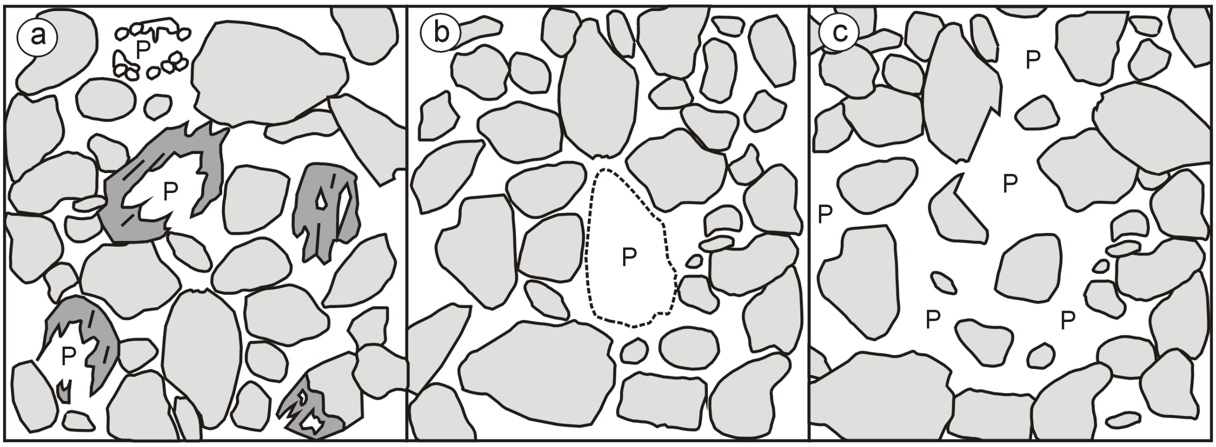

Fig 5.14: Different types of secondary porosity observed in samples of the Skagerrak Formation. **a**: Leaching of detrital grains (feldspars, feldspar bearing lithics and heavy minerals); **b**: Oversized pore; **c**: Cement dissolution porosity.

It was attempted to quantify cement dissolution voids using textural characteristics during point-counting. Pores interpreted as cement dissolution pores are usually intergranular macropores. They are often larger than other pores and located in patchy areas with a lesser degree of compaction than other areas around (Fig. 5.14c). Some of the grains in such patches seem to have no contacts or only point contacts to their neighbours (in thin section plane), in contrast to surrounding areas where predominantly long und concave-convex contacts are developed (Fig. 5.13g). Such inhomogeneous compaction pattern were interpreted as result of cement dissolution. However, it must be considered that similar patterns can be produced by another effect: Usually, the overburden load is transmitted by individual grains in thin section scale and not all grains are load bearing. Hence, so called stress transmission strings are developed with column like areas of higher compaction (see Giles et al., 2000 for details). It is not always possible to differentiate between these two pattern. Nevertheless, BEI-images showed clear evidence for cement dissolution (e.g. Fig. 5.13f) and dolomite corrosion was also reported from other Skagerrak Formation reservoirs, for instance from the Gannet Field (see Purvis, 1990).

Cement dissolution pores occur mainly in fluvial channel and sheet flood sandstones with point-counted amounts between 0 and 9.7 vol.% of bulk rock. The average for the facies associations FC and SF is 1.6 vol.% in the deeper Jade Field and 3.4 vol.% in the shallower Judy Field. The amount of cement dissolution pores is negligible in argillaceous sandstones. The composition of the leached cement is not entirely clear, but evidence points to dolomite. It can be observed that dolomite was leached before ankerite had precipitated on backscatter images (Fig. 5.13f)

5.7 Compaction and porosity loss

The Skagerrak Formation sandstones in the Judy and Jade Fields have relatively high porosities considering their present depth of burial. Investigated samples from fluvial channel and sheetflood sandstones (FC and SF) of the deeper Jade Field have average point-count porosities of 10.4 vol.% with values ranging from 0.7 to 23.2 vol.%. The average point-count porosities of samples from the same facies associations in the shallower Judy Field is nearly twice of that from Jade Field with 21.5 vol.% (values ranging from 1.0 up to 33.7). Measured helium porosities[3] are often higher, since they comprise macro- and microporosities (see

---

[3] Helium porosity versus permeability plots can be found in Jones et al. (2005) for the Jade Field and in Goldsmith et al. (2003) for the Judy Field.

section 2). The relationship between different types of point-counted macroporosity and depth for all Skagerrak Formation samples is given in Fig. 5.15a.

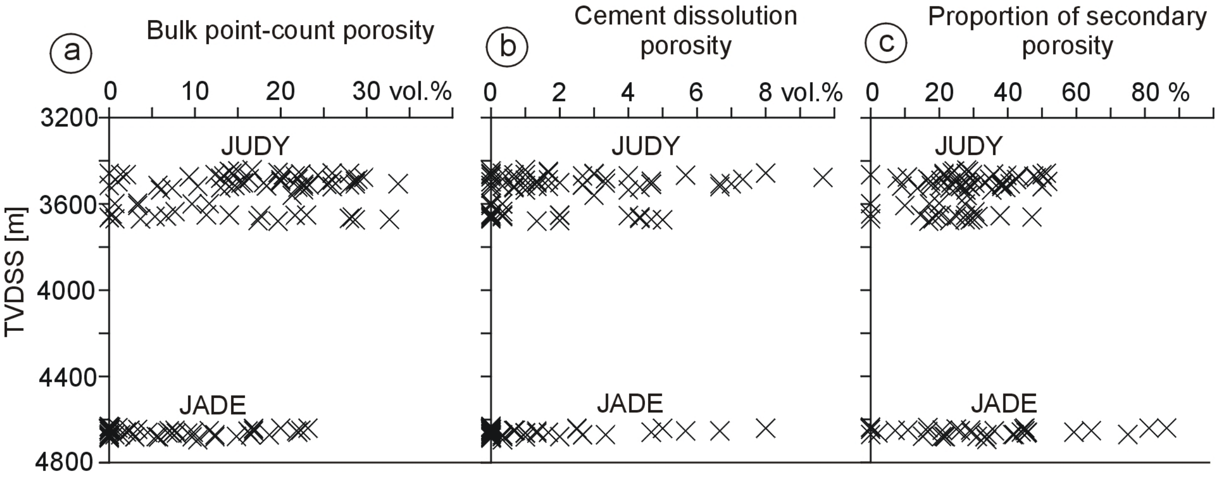

Fig. 5.15: Porosity depths trends. **a**: Point-count macroporosity versus depths for all Skagerrak Formation samples; **b**: Cement dissolution porosity versus depths; **c**: Proportion of secondary porosity (clast dissolution, oversized pores and cement dissolution voids) from bulk point-count porosity versus depths.

Information about the nature of porosity loss can be derived from the diagram intergranular volume (IGV) versus cement after Houseknecht (1987). It is necessary to know the initial porosities to estimate the degree of compaction and cementation using this approach. Initial porosities were estimated by comparison with data from artificially mixed sands published by Beard & Weyl (1973). Initial porosities of sands with the same average grain sizes and sorting as the sandstones from the fluvial channel and sheetflood facies of the Skagerrak Formation vary between 41.9 and 44.7 % for dry loose and between 33.9 and 39.1 % for wet packed sands. The highest measured intergranular volume is that of the completely dolomite cemented sample in well 30/2c-4. With a value of 45 vol.% this intergranular volume suggests initial porosities in the range of the highest value for dry loose sands. However, the content of dolomite may be overestimated here since differentiation between grain replacing dolomite and pore filling dolomite was difficult. Nevertheless, all samples from fluvial channel and sheetflood sandstones are plotted in Fig. 5.16a using 45 % as initial porosity.

Samples from the shallower Judy Field have generally higher intergranular porosities and appear to have slightly higher intergranular volumes (IGV). Some samples from the Jade Field are stronger affected by cementation. One part of the porosity loss was caused by (mainly early) cementation and another part is attributed to mechanical compaction (Fig. 5.16). However, different intergranular volumes are not automatically the result of different degrees of mechanical compaction. Such differences can also be the effect of varying sorting and grain shape (compare with Ehrenberg, 1995 and references therein). Therefore, the form of dominant grain contacts (as sorting and grain shape independent parameter) was estimated additionally, and quantified using the procedure described in section 2. Intergranular volumes can be correlated to the dominant type of grain contacts (Fig. 5.18a), and thus they seem to represent rather the degree of mechanical compaction than variations in sorting and grain shape, respectively.

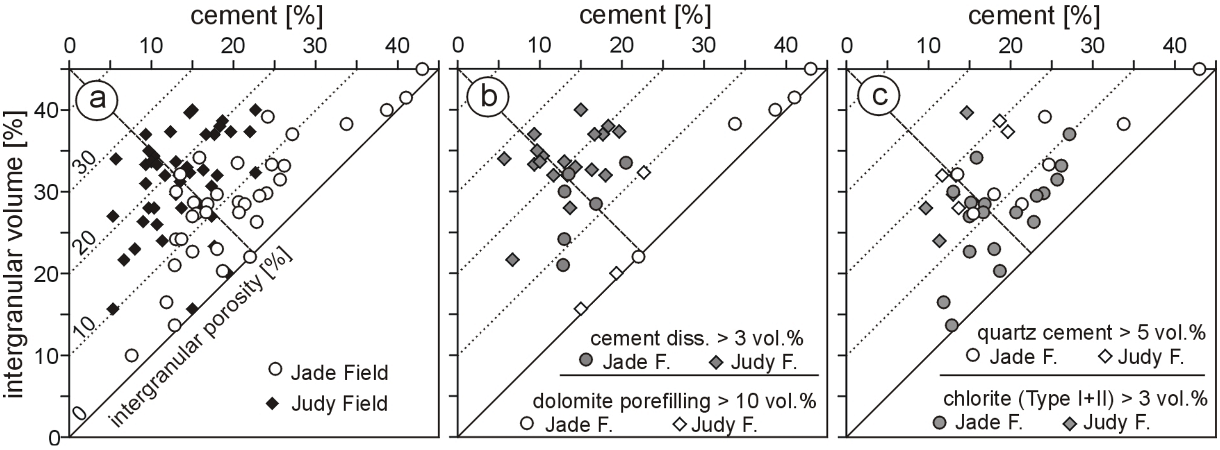

Fig. 5.16: Intergranular cement volume plotted against intergranular volume after Houseknecht (1987) for samples of the facies associations FC and SF from the deeper Jade- and the shallower Judy Field; **a**: all samples; **b**: samples with a volume of cement dissolution voids > 3 % and samples with high amounts of early diagenetic pore filling dolomite; **c**: samples with authigenic chlorite > 3 vol.% and samples with relatively intense quartz cementation.

The impact of cement dissolution is illustrated in Fig. 5.16b. Samples with a higher degree of cement dissolution voids and samples with a high amount of pore filling dolomite cement are selected from those in Fig. 5.16a and displayed separately. It is not surprising that samples with a high amount of dissolution voids have lesser cement contents and higher intergranular porosities. They have also a slightly lower intergranulare volume than samples with intense early diagenetic cementation.

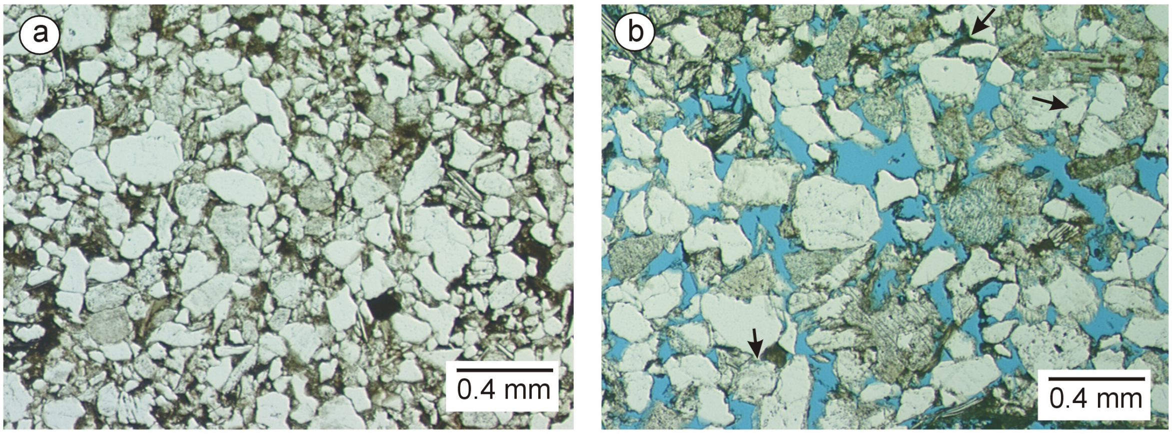

Fig. 5.17: Different compaction textures in sandstones with comparable grain sizes from the Jade Field. **a**: Sample 15598 (facies association AS, 4635.4 m TVDSS). All macroporosity is destroyed by mechanical compaction; **b**: Sample 15716 (facies association FC, 4670.5 m TVDSS). Relatively high intergranular porosity. Note the more compacted patches (arrows), which have a degree of compaction comparable to Fig. 5.17a.

The effect of quartz cementation and authigenic chlorite is shown in Fig. 5.16c and in Fig. 5.18. A decline in the degree of mechanical compaction (expressed as level of compaction) with increasing quartz cement can be observed up to 4 vol.% of authigenic quartz (Fig. 5.18e). Samples with more quartz cement seem to show no further decline. Samples with a higher quartz cement content retain higher intergranular volumes and partly higher intergranular porosities than most of the other samples and especially more than samples with a very high content of authigenic chlorite (see Fig. 5.16c). Intense quartz cementation was only observed in sandstones very close to mudstone layers. Minor quartz overgrowths as observed in many samples seem to have a positive effect in the preservation of high porosities by stabilizing the grain framework. Authigenic chlorite is known to prevent quartz cementation (e.g. Pittman et al. 1992), but seems not to be the main controlling mechanism for the formation of quartz here (see also the discussion in section 9).

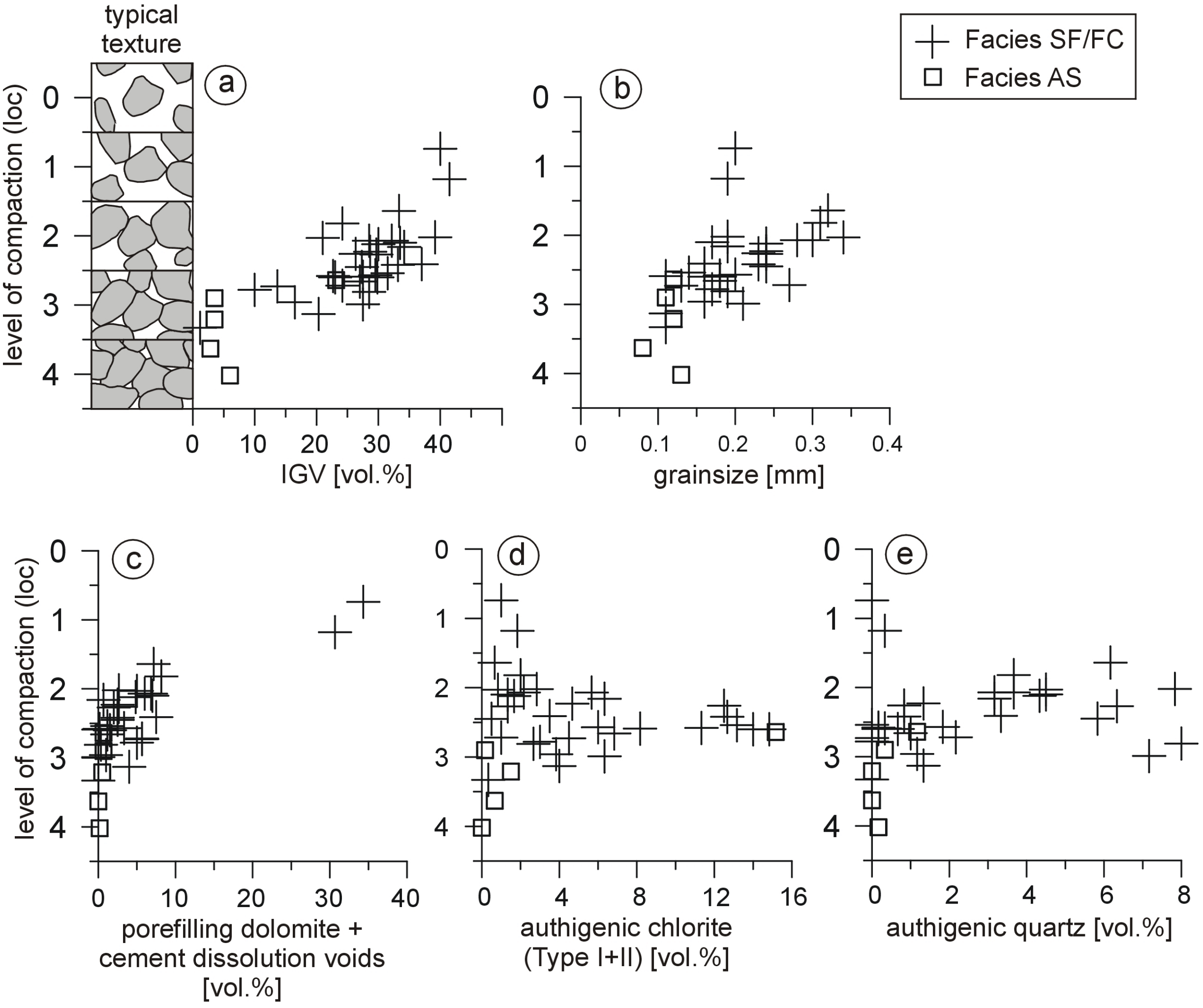

Fig. 5.18: Mechanical compaction estimated by the quantification of grain contact types and plotted as level of compaction (loc, definition see chapter 2) versus IGV, grainsize (note, the both samples with lowest loc are nearly completely dolomite cemented), summation of porefilling dolomite and cement dissolution voids (to estimate the effect of early cement), authigenic chlorite (type I +II) and authigenic quartz for grain supported samples of well 30/2c-4.

The relationship between authigenic chlorite (type I and II) and degree of compaction is illustrated in Fig. 5.18d and Fig. 5.16c. Samples with a very high content of intergranular authigenic chlorite (type I and II) seem to be more affected by mechanical compaction than many samples with a lower content. Samples of the facies association AS have generally a higher degree of mechanical compaction (Fig. 5.18b). Some of the samples with chlorite coatings show also a higher degree of grain-to-grain contact dissolution in thin section (e.g. 15704, well 30/2c-4).

Samples with a different degree of mechanical compaction were found at nearly the same burial depths (Fig. 5.17). This seems to be at least in some samples related to grain size (see Fig. 5.18b), but can also be observed in samples with comparable grain sizes from different facies associations (Fig. 5.17). However, it must be noted that samples with a relatively low level of compaction contain also patches which are more compacted (Fig. 5.17, arrows). This observation can be used as evidence for the mechanisms of intergranular porosity preservation: at least a part, if not the most of the present day porosity was preserved by a former pore filling phase, which did not occupy all pores (as indicated by more compacted parts). That could have been an eodiagenetic cement or a hydrocarbon phase which invaded only higher permeable lithologies.

5.8 Paragenetic sequence and timing

The paragenetic sequence was derived using textural observations of authigenic phase relationships. The paragenetic sequences show only minor differences between the Judy and the Jade Fields. Both Fields lie in different burial depths today. A schematic summary for both Fields is given in Fig. 5.19. Main differences between the two Fields are: The occurrence of higher amounts of euhedral chlorite (type II) in the Jade Field, the intense staining of this chlorite by bitumen only in the Jade Field, the occurrence of hematite beneath K-feldspar overgrowths which was observed only in the Judy Field, and calcite and Fe-calcite which were found only in some wells of the Judy Field.

Some phases (hematite and chlorite type I) were interpreted to have precursor minerals (see interpretation section 9).
Reconstruction of absolute timing or depth for the diagenetic reactions is difficult and highly speculative due to the lack of exact time or temperature markers. The sandstones have no cements suitable for isotopic age dating which can be separated and primary fluid inclusions in the quartz cements are too rare and too small for palaeo-thermometry measurements. A fluid inclusion study of Swarbrick et al. (2000) at secondary fluid inclusions was able to determine the healing of fractures by quartz cements at 115-136°C in the Judy Field. This data can be used to date the fracturing event, but gives no information about start or end of quartz cementation. Only bitumen can be used as marker and the timing of bitumen formation in the diagenetic sequence can be compared to the results from basin modelling. 2D basin and charge modelling from Jones et al. (2005) at two seismic lines indicated that hydrocarbon generation and migration began in the Late Cretaceous. The 3D basin modelling study of Neumann (2007) using user-defined compositional kinetic models predicted a first accumulation of hydrocarbons in the Jade structure in Early Cretaceous and in the Judy Field in Late Cretaceous (see also section 4). The reservoirs were at relatively shallow depth at this time (e.g. Jade 530 m TVDSS) and under low temperature conditions (T ~ 40°C) with a significant risk of biodegradation. Under the assumption that the observed bitumen was a result of biodegradation, it can be used as a time marker (see detailed discussion in section 9).

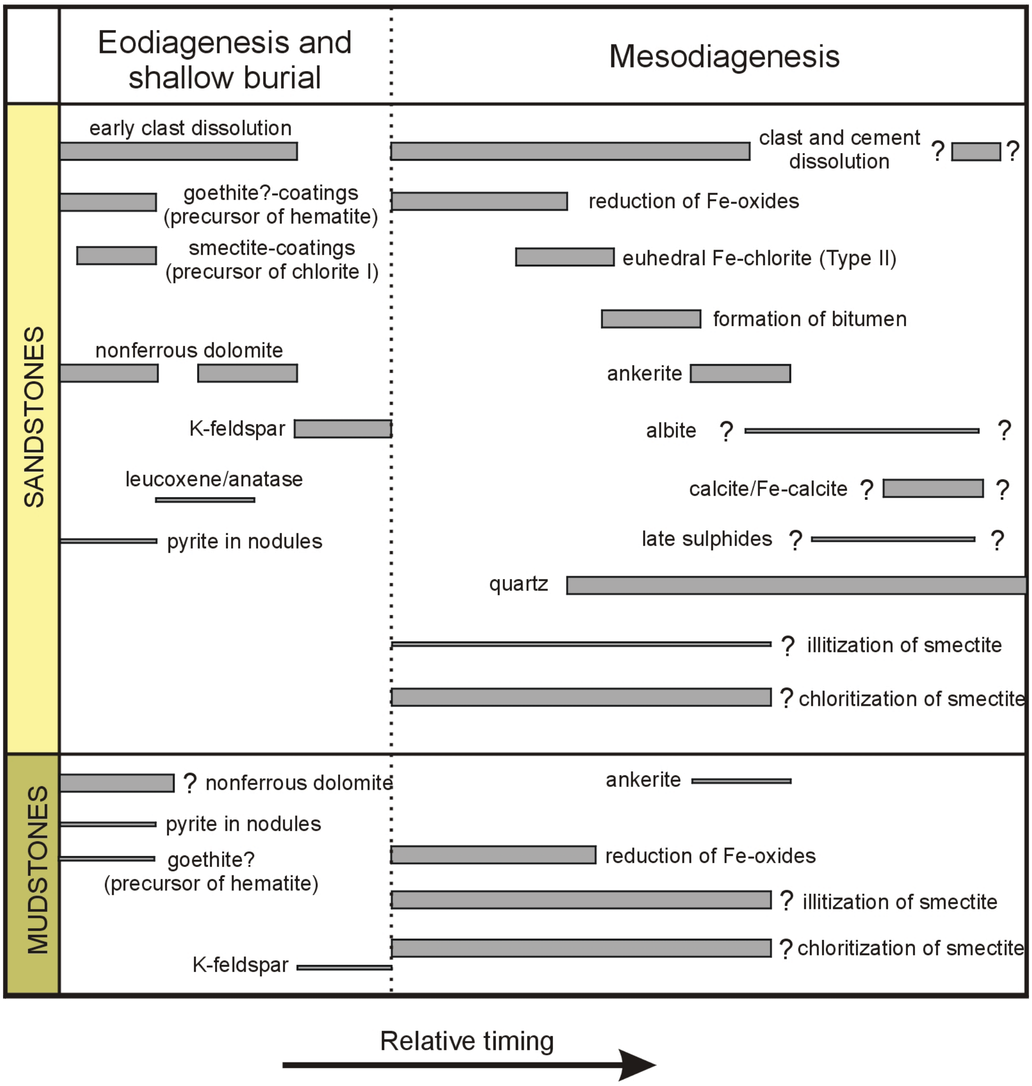

Fig. 5.19: Paragenetic sequence for the Skagerrak Formation in the Jade and Judy Field. Important authigenic phases (and diagenetic processes) are marked with thick bars and minor phases with thin bars.

6 Norwegian sector: Rotliegend, Triassic and Jurassic

Samples from eight wells in the Norwegian sector of the central North Sea were available for this study. They cover a relatively wide stratigraphic range from Rotliegend to Upper Jurassic. The wells were drilled into different structures located in quadrants 1 and 2.

Generally, the amount of sample material was relatively low per well (see section 2 and Appendix 1) and no detailed petrographic studies could be carried out. Final well reports and some special reports supplied by Norsk Hydro were available, additionally to the sample material. The material was used mainly for comparison of diagenetic evolution in different clastic reservoirs with the Skagerrak Formation in Jade and Judy Fields of the UK-sector. Burial history data from the basin modelling study of Neumann (2007) were available for some of the studied wells (see section 4.4).

6.1 Rotliegend wells: Petrography and diagenesis

Samples from the Rotliegend in the Norwegian sector of the North Sea were available from three wells (NOR-A, NOR-B, NOR-G) located in quadrants 1 and 2. The ditch cuttings from well NOR-G were unfortunately too much strained and destroyed by bit metamorphism and therefore useless for the reconstruction of diagenetic history.

The total amount of sample material from the other two wells was relatively low (5 and 8 samples) and so only limited conclusions could be made.

6.1.1 <u>Well NOR-A</u>

The well was drilled in a large north-eastwards dipping rotated fault block located on the eastern inner margin of the Central Graben. The well position is situated between the two basin modelling areas and this well was not included in the 3D basin models.

The structure was most likely formed during tectonic movements from Middle/Late Jurassic to Early Cretaceous (Norske-Shell, 1985).

The well penetrated 81 m of water-bearing Rotliegend sandstones between 4769 an 4850 m before it reached total depth. Only faint hydrocarbon indications (0.04-0.10% C_1, traces of C_2 near the top) were encountered while drilling in the Rotliegend section (Norske-Shell, 1985).

Ditch cuttings from the upper 25 m of the Rotliegend were whitish pale coloured and from the lower part dominantly reddish brown. The cored section from 4805 to 4814 m contained predominantly horizontal or cross-bedded, fine- to medium-grained well sorted mostly reddish coloured sandstones. The bedding was outlined by differences in grain size. Good porosities (up to 25%), but low permeabilities were reported from core measurements by Norske-Shell (1985).

The sandstones are interpreted to be dominantly of aeolian origin and stratigraphically equivalent to the Auk Formation in the UK sector of the central North Sea.

<u>Detrital composition of Rotliegend sandstones in well NOR-A</u>

The sandstone grains are subangular to rounded. Monocrystalline quartz in strained and unstrained form is the main detrital component (51.3…55.3 vol.%). Polycrystalline quartz is also relatively abundant (4.0…9.3 vol.%). Rock fragments occur dominantly as quartz feldspar aggregates (1.0…2.7 vol.%). Clasts of metamorphic origin are only subordinate. Volcanic rock fragments and mudstone intraclasts occur occasional. The total amount of rock fragments is around 10 vol.%. The feldspar content is relatively low (7.0…8.6 vol.%) compared to the Triassic Skagerrak Formation sandstones and consists mainly of K-feldspar (5.7…7.0 vol.%). A part of the feldspars is corroded, but feldspar leaching porosity occurs only in amounts lower than 1 vol.% (Appendix 2.1). Thus the present detrital composition represents nearly the composition during deposition. The sandstones can be classified as Subarkoses (Fig. 6.1a) after McBride (1963).

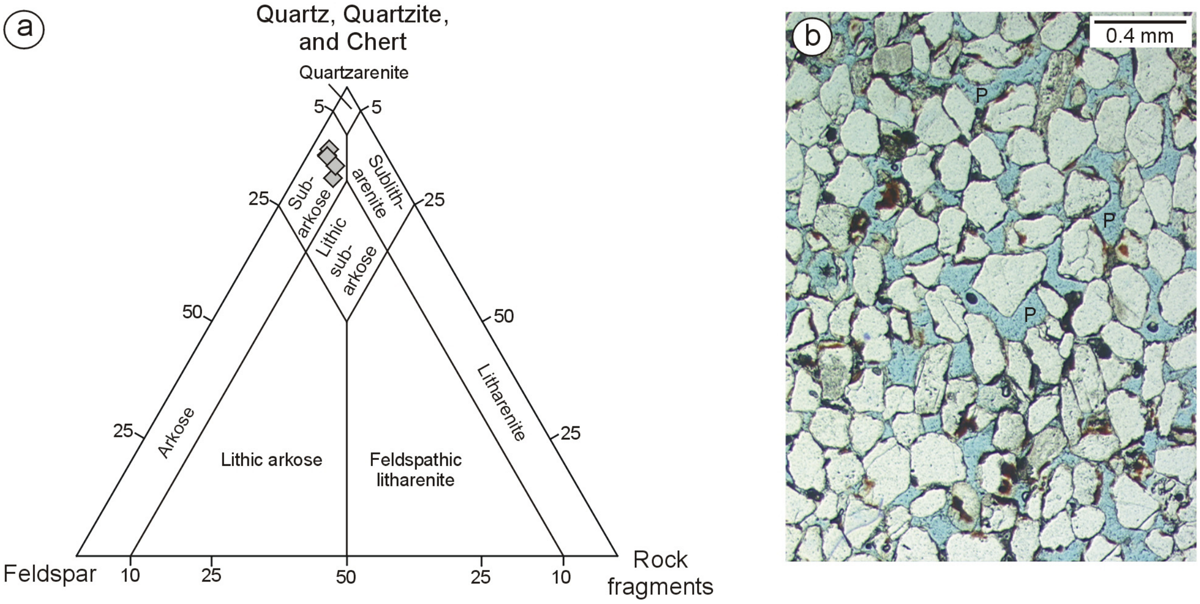

Fig. 6.1a: Sandstone composition according to McBride (1963) for the Rotliegend samples from well NOR-A. The sandstones plot in the subarkose field. **b:** Typical texture of a Rotliegend sandstone sample (4810.9) from well NOR-A. Note the large pores (P) and the stronger compacted areas between them.

Pore types and porosity in Rotliegend sandstones of well NOR-A

Point counted macroporosities lie between 3.7 and 10.3 vol.% and consist predominantly of intergranular macropores reduced from their original size by compaction (2.3…5.0 vol.%) and cement dissolution pores (1…5 vol.%). Large nearly uncompacted oversized pores (0…1 vol.%) and feldspar dissolution voids (traces...0.7 vol.%) occur also (see section 5.6 for detailed description of secondary porosity types). A relatively large amount of microporosity occurred between individual illite flakes (Fig. 6.4e, f). This porosity could not be quantified separately in all cases and was counted partly as illite meshwork (see also section 2).

Authigenic phases and diagenesis in Rotliegend sandstones of well NOR-A

Following authigenic phases were found in samples from well NOR-A: hematite (0…10.3 vol. %), illite meshwork (5.0…11.3 vol.%), illite coatings (0…1 vol.%), dolomite with Fe-dolomite overgrowths (2…5 %), quartz (0.3…4.3 vol. %), halite (0…0.7 vol.%), K-feldspar overgrowths (traces), albite (traces), barite (traces) and leucoxene (traces).

Fig. 6.2a, b (next page): Illite coatings (IC) caused a high amount of grain-to-grain contact dissolution. Note the leached feldspar (L) grain and the dolomite (D) crystals (sample 4812.1, well NOR-A, plane polarised light (a), crossed polarisers (b); **c:** Leached feldspar grain with faint overgrowths (arrow) (sample 4812.1, well NOR-A, plane polarised light); **d:** Hematite in grain indentations (arrow) indicating an inherited nature. The feldspar grain shows leaching traces (sample 4810.9; well NOR-A, plane polarised light); **e, f:** Patchy quartz cement. Note the "floating" grain (arrow) enclosed by authigenic quartz, which consists of merged overgrowths (sample 4812.1, well NOR-A, plane polarised light - e, crossed polarisers - f); **g:** Quartz overgrowths and patchy distributed hematite (sample 4812.1, well NOR-A, plane polarized light); **h:** Quartz overgrowths in a bleached part of the same sample. Note the remains of former hematite (arrow) in grain indentations (sample 4812.1, well NOR-A, plane polarized light).

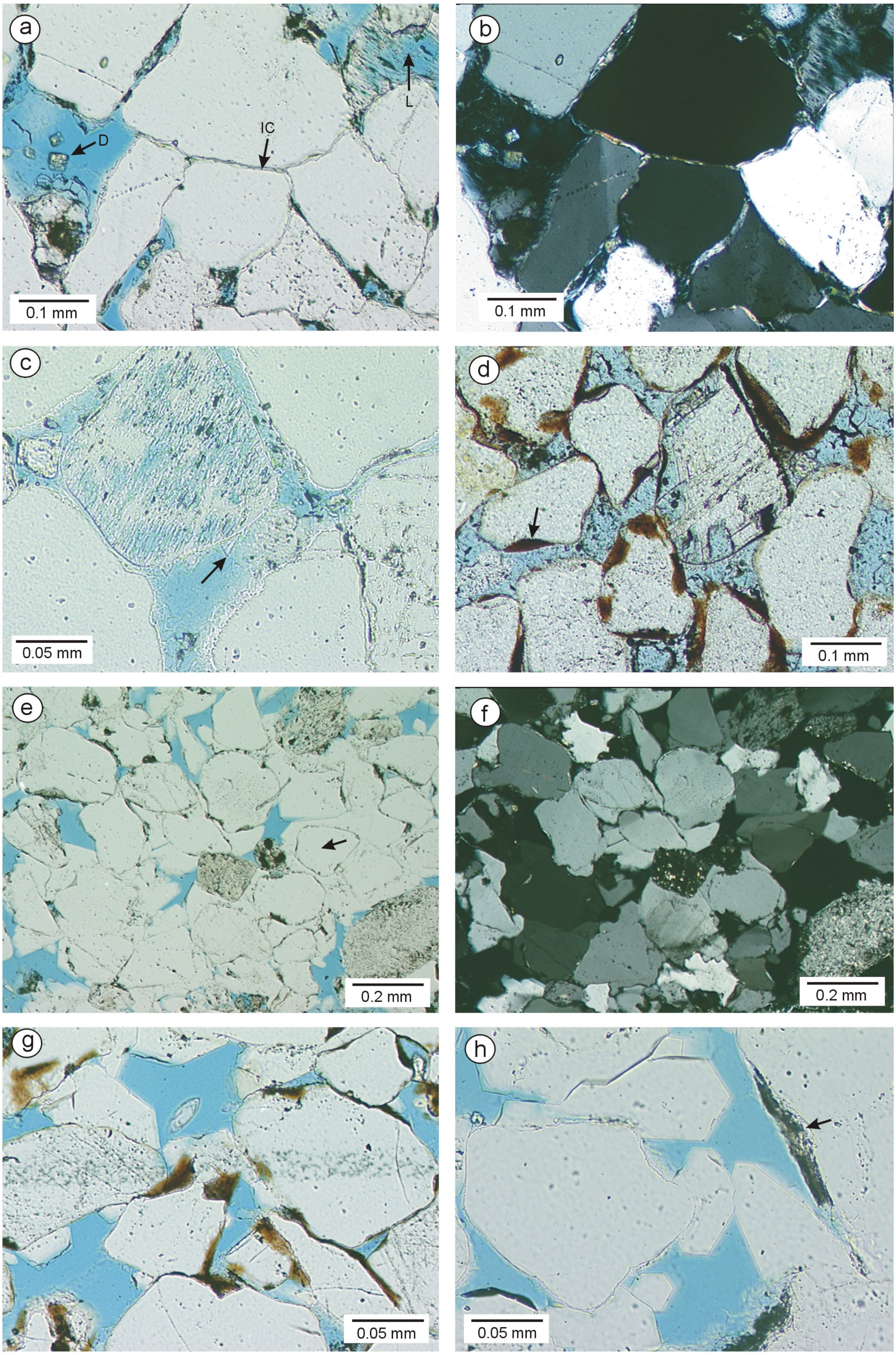
a
D
IC
L
0.1 mm
b
0.1 mm
c
0.05 mm
d
0.1 mm
e
0.2 mm
f
0.2 mm
g
0.05 mm
h
0.05 mm

Early diagenesis started probably with grain coating hematite and illite (Fig. 6.6). The **hematite** staining is intense. But the point count values are probably too high due to the effect of obliquely cut surfaces. The largest proportion of hematite in coarser lamina occurs in grain indentations (Fig. 6.2d), indicating an inherited nature. Nevertheless, thin neo-formed coatings exist too. Thicker hematite coatings were found mainly in finer grained layers.

Illite coatings occur occasionally and locally in small patches with abundant coated grains, especially in bleached areas. However, a part of the grain-coating illite may be masked by hematite in the red parts. Grain-to-grain contact dissolution is partly enhanced in areas with abundant illite coatings (Fig. 6.2a, b).

Leucoxene was observed commonly forming aggregates of tiny crystals, which outline sometimes the shape of former grains (Fig. 6.5d).

Authigenic **K-feldspar** can be found rarely, forming overgrowths on some of the feldspar grains (Fig. 6.2c). The amount of K-feldspar overgrowths is generally negligible compared to the Triassic Skagerrak Formation sandstones.

Two types of authigenic **quartz** were observed in samples of well NOR-A. A relatively **early quartz** cement (quartz I) is often developed as sub-mm to mm sized patches of silica, which contain several grains and consist of merged syntaxial overgrowths. The quartz cement patches preserve partly a high intergranular volume (up to ~40%) and they can be found mainly in coarse sand stripes (Fig. 6.2e, f). The early quartz was found to be overgrown by fibrous illite.
A **later quartz** (quartz II) was found engulfing illite fibres (Fig. 6.4g). However, it can not be decided if two distinct quartz generations exist, or one cementation episode was interrupted by illite precipitation.

Non-ferrous **dolomite** occurs mainly in the form of scattered tiny rhombi or as relicts in larger pores in well NOR-A. The dolomite relicts indicate the former existence of pore filling dolomite like in well NOR-B.
Fe-dolomite with iron contents between 3.60 and 4.13 wt.% FeO (see Appendix 3.1 and Fig. 6.3) is present in the form of overgrowths on non-ferrous dolomite crystals (Fig. 6.4h). The Fe-dolomite engulfs partly fibrous illite and can be observed growing into feldspar dissolution pores (Fig. 6.4h). This textural relationship indicates a precipitation post feldspar dissolution and illite meshwork formation (Fig. 6.6).

Authigenic **barite** is very seldom and was found only in one sample. It occurs as pore filling cement occupying a relatively high intergranular volume. Relative timing remains uncertain.

Bleaching was observed locally in a centimetre sized part of one sample of well NOR-A (4812.1) and whitish pale colours were reported from the upper 25 m of the Rotliegend section (Norske-Shell, 1985). Early diagenetic hematite is completely missing in the bleached part of the sample. The grains are covered instead by grain coating illite and by an optical not resolvable mass in the grain indentations (Fig. 6.2h). The bleaching seems to have already occurred before the onset of significant quartz cementation, since no hematite was preserved in the quartz cement patches of the bleaches area in contrast to other samples were hematite was engulfed by quartz crystals.

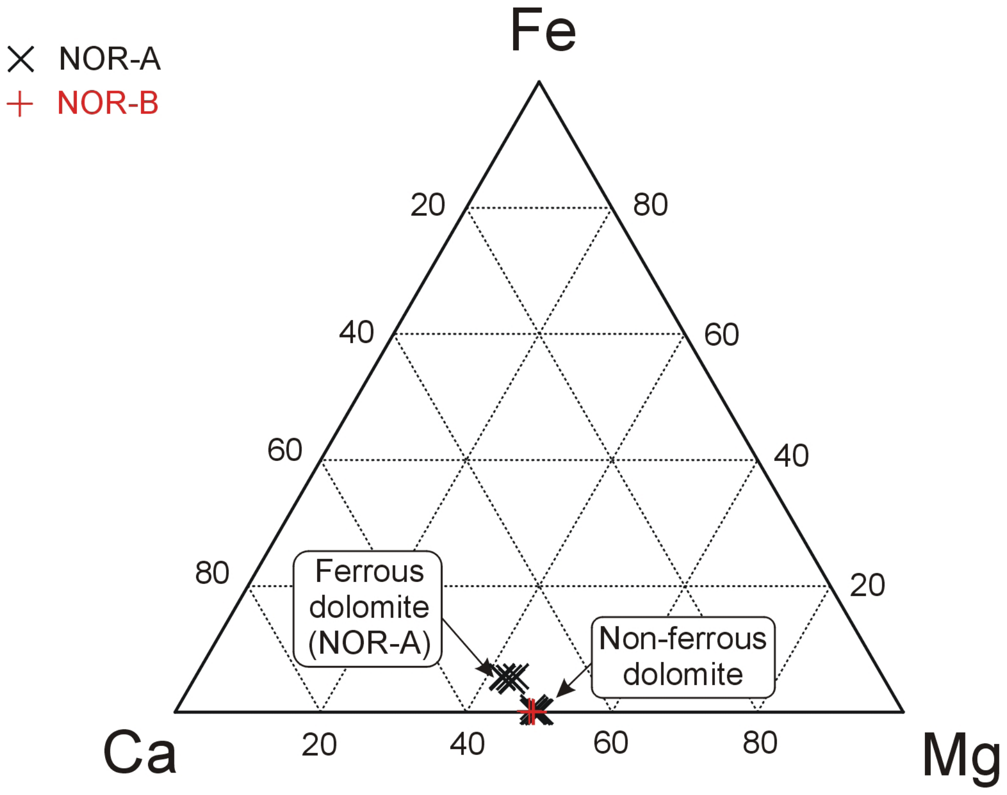

Composition of authigenic carbonates in Rotliegend sandstones

Mineral	**Typical composition**	**no. of analyses**
Non-ferrous dolomite:	$Ca_{0.93\text{-}1.00}Mg_{0.91\text{-}1.00}Fe_{0.00\text{-}0.02}Mn_{0.01\text{-}0.04}(CO_3)_2$	13
Ferrous dolomite:	$Ca_{0.90\text{-}1.00}Mg_{0.79\text{-}0.84}Fe_{0.09\text{-}0.11}Mn_{0.03\text{-}0.07}(CO_3)_2$	6

Fig. 6.3: Composition of authigenic carbonates in Rotliegend sandstones of well NOR-A and NOR-B derived from EMP measurements (Appendix 3.1).

Dissolution of feldspar is relatively common in the form of corroded detrital feldspars with microporosity (one-fourth to one-fifth of K-feldspar grains). Up to 0.7 vol.% of the macroporosity is of secondary origin due to feldspar leaching (Fig. 6.2a, 6.4a-c). A part of the feldspar dissolution porosity was later occluded by authigenic albite (Fig. 6.5a).

Cement dissolution is indicated by relatively large pores in higher compacted areas (Fig. 6.1b, Fig. 6.4a, 6.5c, see section 5.6 for detailed explanation of cement dissolution textures). Relicts of leached dolomite were found in some of these pores (Fig. 6.5c). Such cement dissolution pores make up between 1 to 5 percent of sample volume and have a relatively high proportion of the present porosity. They are irregular distributed indicating a former patchy developed cement.
A part of the feldspar grains was certainly corroded during weathering in the source area, transport or eodiagenesis. However, the main dissolution event occurred probably during mesodiagenesis subsequent to the main phase of mechanical compaction. This is indicated by uncompacted feldspar relicts (Fig. 6.4a-c) and by larger pores between higher compacted areas (Fig. 6.1b). A relatively late timing is also suggested by the observation that

hematite/clay rims, outlining former feldspar grains, were not affected by mechanical compaction (Fig. 6.4a).

Pervasive fibrous/flaky **illite** can be found in every sample of well NOR-A. The illite is usually composed of larger irregular flakes (Fig. 6.4e) which occlude the pore space with a meshwork leaving only micropores between the single flakes. The flakes grew from the pore margin into the centre. The individual flakes are composed of amalgamated fibres, which partly extent over the edges (Fig. 6.4f). The effect of this illite type for permeability is very destructive, as indicated by measurements on routine plugs (high porosities and low permeabilities, Norske-Shell, 1985).
This illite type was observed to be engulfed by a late quartz cement (Fig. 6.4g) which commonly occurs as syntaxial overgrowths on quartz grains.

Neo-formation of authigenic **albite** inside of leached K-feldspar grains (Fig. 6.5a) was observed in low amounts. Authigenic albite was relatively pure in contrast to detrital albite grains which contained partly a low amount of calcium (see Appendix 3.2 analyses 110-134).

Patchy occurrences of optical isotropic aggregates in some pores (Fig. 6.5b) were proven to be **halite** via SEM-EDX. Halite post-dates fibrous illite and quartz and seems to be an artefact from vaporising formation water after core recovery. However, it must be considered that late diagenetic halite cements are possible. They are known, for instance, from Triassic sandstones in Denmark (Laier & Nielsen, 1989) and a diagenetic origin can be not completely excluded.

Fig. 6.4a (next page): Feldspar dissolution pore (F) outlined by a hematite (and clay) rim and oversized pores (P). Note the deformation of the quartz grain by the former feldspar grain (arrow) and the denser packed areas (C) around the larger pores (sample 4812.1, well NOR-A, plane polarised light); **b:** Relict of a leached K-feldspar (sample 4812.8, well NOR-A, SEI); **c:** Leached feldspar grain with illite fibres inside, which postdate the dissolution (sample 4805.6, well NOR-A, plane polarised light); **d:** Illite fibres in the pore space (sample 4812.1, well NOR-A, plane polarised light); **e, f:** Pore filling illite flakes. The individual flakes are composed of amalgamated fibres (f), which extent partly over the edges (sample 4812.8, well NOR-A, SEI); **g:** Late quartz engulfing fibrous illite (sample 4812.1, well NOR-A, plane polarised light); **h:** Fe-dolomite (F) overgrowing earlier dolomite. Note that the Fe-dolomite formed after feldspar leaching (sample 4812.1, well NOR-A, BEI).

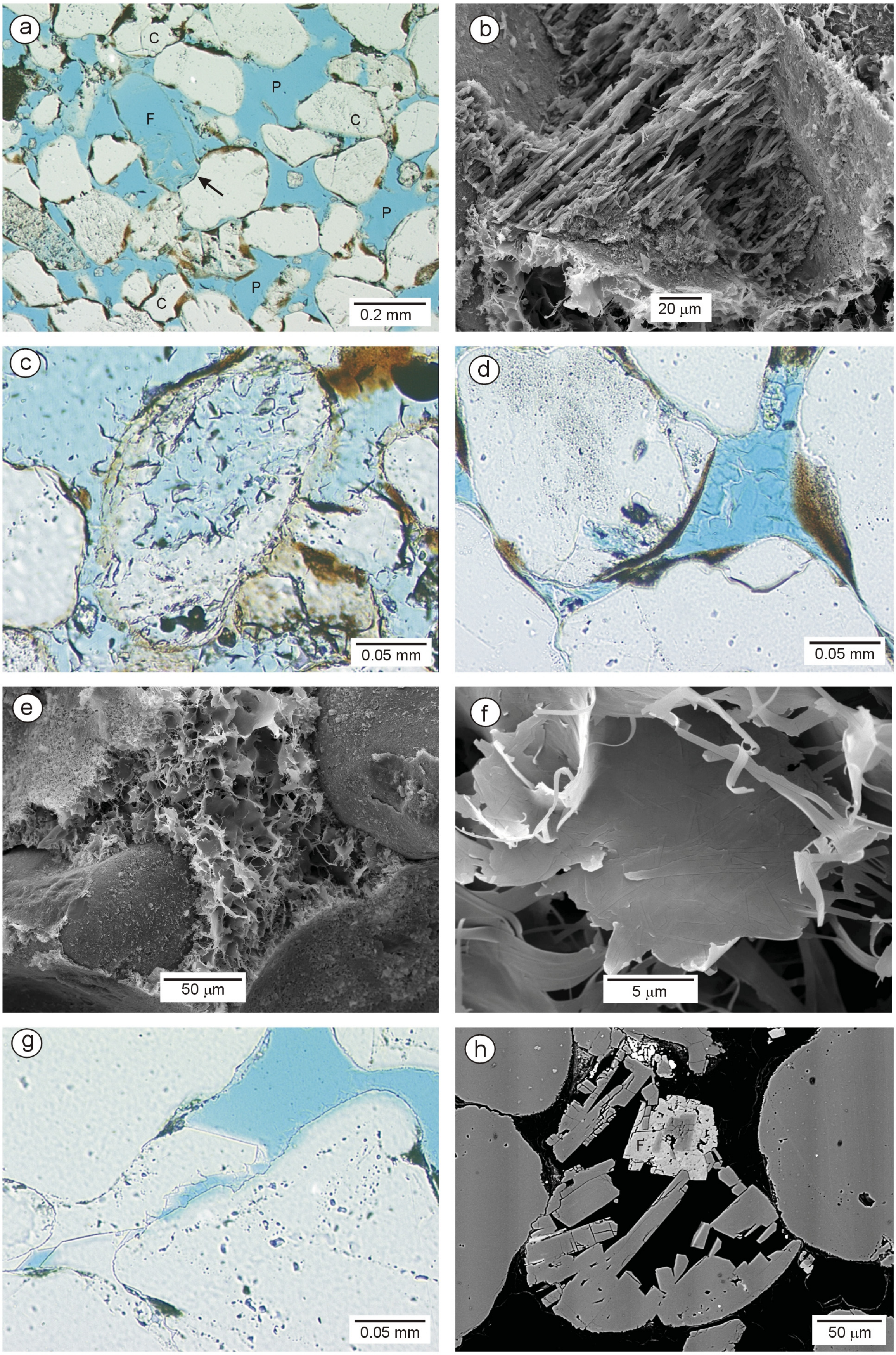
a
C
P
F
C
P
P
C
0.2 mm
b
20 µm
c
0.05 mm
d
0.05 mm
e
50 µm
f
5 µm
g
0.05 mm
h
F
50 µm

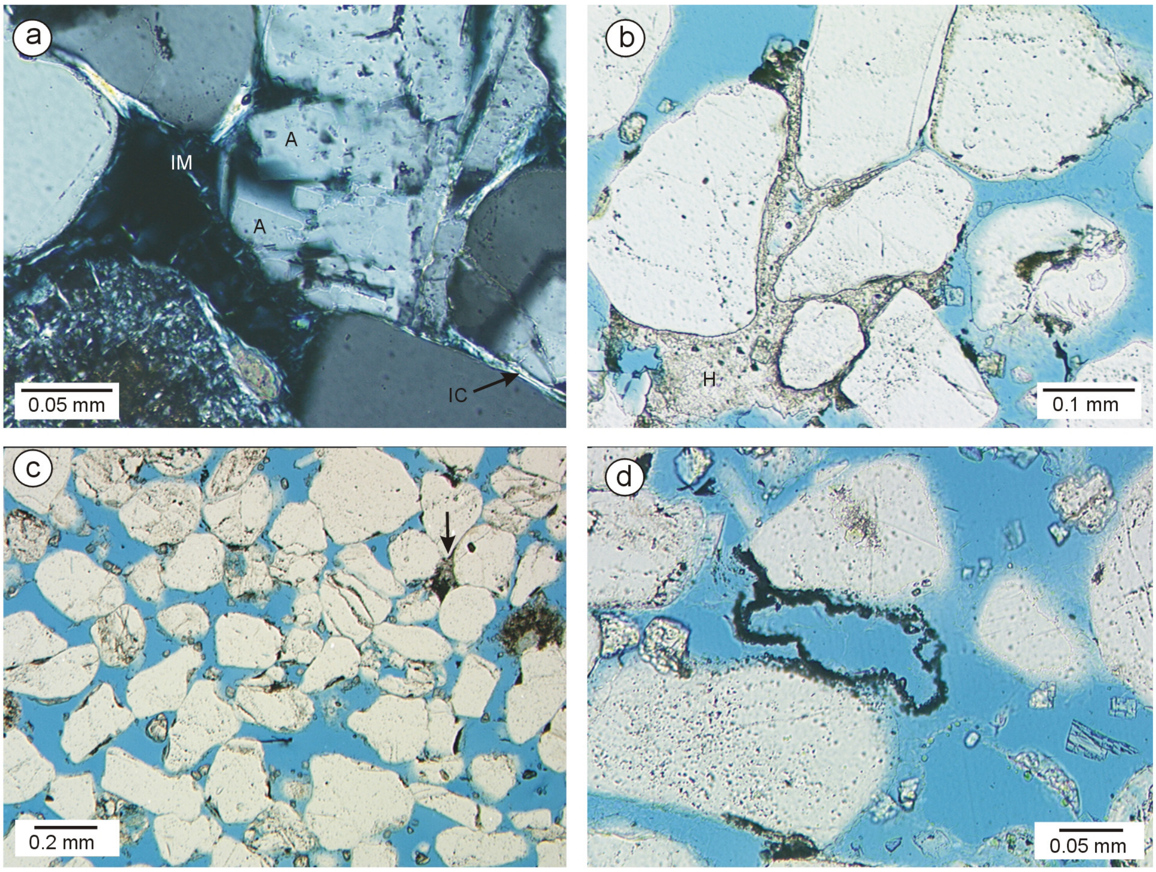

Fig. 6.5a: Authigenic albite (A) inside of a leached feldspar grain. Note the illite coatings (IC) between the grains and the illite meshwork (IM) in the pore space (sample 4812.1, well NOR-A, crossed polarisers); **b:** Halite (H) masses in some pores (sample 4812.1, well NOR-A, plane polarised light); **c:** More compacted areas (arrow) and large pores with dolomite relicts indicating cement dissolution (sample 4812.1, well NOR-A, plane polarised light); **d:** Tiny leucoxene crystals outlining a former grain – note the high porosity with relictic dolomite (sample 4812.1, well NOR-A, plane polarised light).

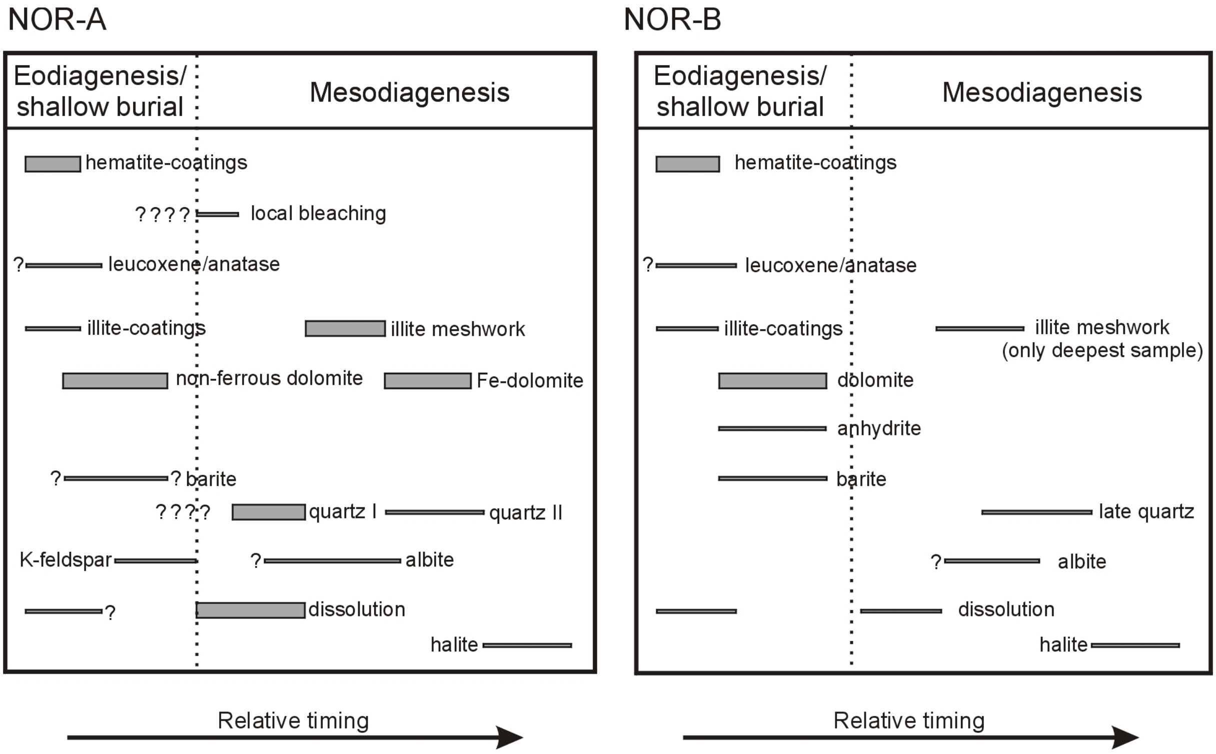

Fig. 6.6: Paragenetic sequences for the Rotliegend sandstones in well NOR-A and well NOR-B as indicated by observed phase relationship. Important authigenic phases are marked with thick bars and minor phases with thin bars.

6.1.2 Well NOR-B

The well was drilled in a fault bonded structure mapped at base Zechstein Group level on the Hidra High in a distance of ~ 15 km from well NOR-A. The well is, like well NOR-A, located between the two basin modelling areas.

The well reached 25 m fine-grained Rotliegend sediments (mudstones, siltstones and very fine-grained sandstones) at 5084 m depth and penetrated under this unit 356 m of thick aeolian sandstones (Auk Formation equivalent) from 5109 m to total depth (Kvadsheim & Aga, 1985; Sutherland et al., 1985). The Rotliegend was found water-bearing and no significant hydrocarbon shows were encountered in the whole well, but trip gas[1] composed of methane was reported from the Rotliegend sandstone sequence (Kvadsheim & Aga, 1985). The lack of significant hydrocarbons in the Rotliegend was interpreted by Kvadsheim & Aga (1985) to be caused by the absence of Carboniferous source rocks.

Reservoir conditions of 150-160°C and 81-84 MPa were encountered in the Rotliegend sandstones (Kvadsheim & Aga, 1985; Sutherland et al., 1985).

The Auk Formation equivalent unit consists of thick aeolian sandstones with few minor interbeds of dark grey mudstone. The sandstones are fine- to medium-grained and moderately to well sorted with subangular to rounded grains. The colour is reddish brown in the upper part, but turns pale red to milky white downwards (Kvadsheim & Aga, 1985).

Four cores were cut in the Auk Formation equivalent sandstone unit between 5115.05 m and 5165.0 m. Eight samples from these cores were available for this study. The cored sandstones were massive and horizontally bedded with occasional cross-bedding (Kvadsheim & Aga, 1985). Average sandstone core porosity is 15 % (12…24 %) and permeabilities range from 0.1 to 100 mD. Most permeability values lie between 0.1 and 1 mD.

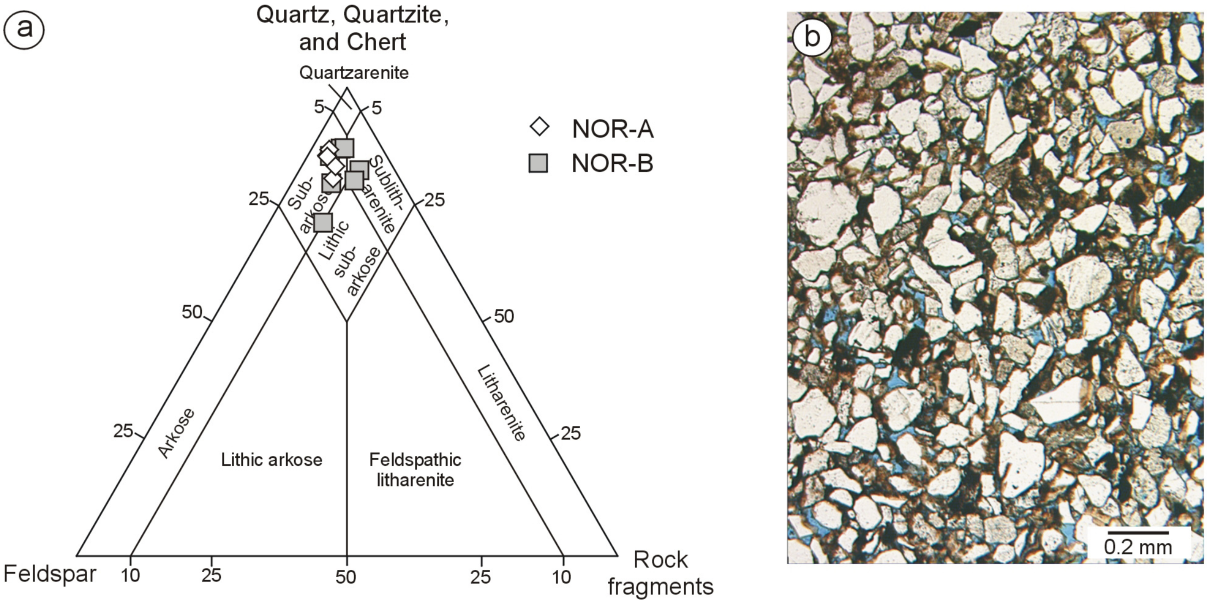

Fig. 6.7a: Sandstone composition according to McBride (1963) for the Rotliegend samples from well NOR-A and NOR-B. The sandstones plot in the Subarkose and Sublitharenite fields; **b:** Typical texture of a Rotliegend sandstone sample (5119.4) from well NOR-B.

---

[1] Gas entering the wellbore after shutting down the mud pump

Detrital composition of Rotliegend sandstones in well NOR-B

Monocrystalline quartz is the main detrital component (37.7…56.7 vol.%). Polycrystalline quartz (6.0…11.7 vol.%) is also abundant. Some of the sandstones are richer in rock fragments than the samples from well NOR-A (Fig. 6.7a). This may be due to the closer proximity to the source area of the Fenno-Scandian Shield. The rock fragments are dominantly composed of quartz feldspar aggregates (1.0…3.3 vol.%). Metamorphic lithoclasts, like slates, occur in relatively low amounts (0.3…3.7 vol.%). Volcanic rock fragments are more frequent than in well NOR-A (0…1 vol.%). Mudstone intraclasts are present in some samples in amounts up to 2.3 vol.%. The total content of rock fragments is around 14 vol.%. Different micas occur in traces.

The detrital feldspar content varies between 4.3 and 12.0 vol.% and consists dominantly of K-feldspar (3.0…8.3 vol.%). The fraction of the feldspars grains with corrosion traces is lower than in well NOR-A. Feldspar leaching porosity is generally lower than 1 vol.% (Appendix 2.1). Thus, the present detrital composition is not significantly different from the composition after deposition. The sandstones plot in the Subarkose and Sublitharenite fields of the McBride (1963) diagram (Fig. 6.7a). The data points scatter wider than those from well NOR-A.

Pore types and porosity in Rotliegend sandstones of well NOR-B

Thin section macro-porosities lie between 5.3 and 15.0 vol.% and consist of primary intergranular pores (5.0…13.7 vol.%), large nearly uncompacted oversized pores (up to 1 vol.%) and grain dissolution pores (up to 0.7 vol.%). Cement dissolution pores can make up to 2 percent of sample volume (see section 5.6 for detailed description of secondary porosity types).

Authigenic phases and diagenesis in Rotliegend sandstones of well NOR-B

The following authigenic phases were found in the investigated samples from well NOR-B: hematite (6.7…20.0 vol. %), dolomite (0.3…7.3 %), illite meshwork (0…7.3 vol.%), illite coatings (0…0.7 vol.%), quartz (0…0.7 vol. %), halite (traces), anhydrite (traces), barite (traces), albite (traces) and leucoxene (traces).

Hematite occurs in the form of grain coatings and is present in every sample of well NOR-B (Fig. 6.8c, d). The hematite staining is intense, but point count values given in Appendix 2.1 are too high due to the effect of obliquely surfaces in thin section. Thicker hematite crusts occur mainly in finer grained layers. The mass of hematite in coarser lamina is located in grain indentations, indicating an inherited nature.

Illite coatings were commonly stained with hematite and could only locally be differentiated from hematite coatings by optical microscopy.

Leucoxene was found occasional as aggregates of tiny crystals sometimes outlining the shape of former grains. Single anatase crystals were observed relatively seldom in pore space.

Dolomite is commonly present as patchy pore filling cement in well NOR-B (Fig. 6.8a), preserving a high intergranular volume (between 30-40%) in these patches. The dolomite is non-ferrous and no Fe-dolomite like in well NOR-A was found in well NOR-B (see also Fig. 6.3). The pore filling dolomite cement is more frequent in coarser lamina. A faint zoning was detected in the dolomite crystals using backscatter electron images (6.8b).

Small (~ 50 µm) dolomite rhombi can also occur. But they are relatively rare. Grain displacing dolomite or dolomite-barite blasts[2] (0.3 to 0.5 mm) were found in one finer grained sample (5126.70). Dolomite was observed enclosing early diagenetic hematite.

Barite and **anhydrite** are relatively rare and occur in the form of larger isolated pore filling crystals or as replacement of single grains commonly in close association with dolomite cement (SB-Type according to Gaupp, 1996). Barite was found together with dolomite forming larger blasts (0.3 to 0.5 mm) in finer grained samples.

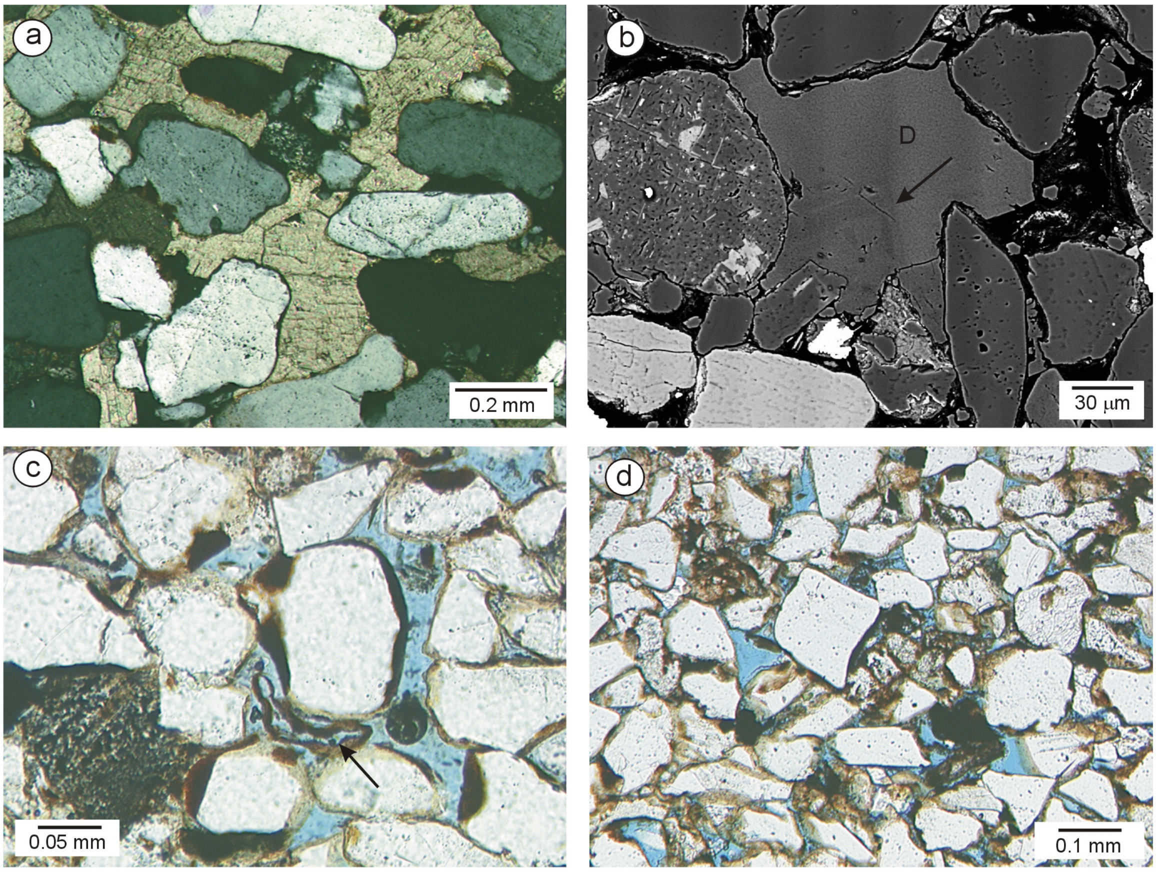

Fig. 6.8a: Authigenic dolomite. Note the large intergranular volume, which indicates an early diagenetic origin (sample 5115.4, well NOR-B, crossed polarisers); **b:** Pore filling dolomite with faint zoning (arrow) in well NOR-B (sample 5119.4, BEI); **c:** Compacted grain rim (arrow) indicating early leaching (sample 5124.6, well NOR-B, plane polarised light); **d:** Hematite coated grains (sample 5119.4, well NOR-B, plane polarised light)

Authigenic **illite** in the form of fibres and flakes around the pore margins or as pore filling meshwork was found only in the deepest sample (5164.6) in remarkable amounts. Illite meshwork is here not as common as in well NOR-A. Fibrous illite occurred only locally in very few pores in shallower samples, indicating a replacement of former feldspar grains. SEM-EDX measurements at some illite fibres in sample 5119.4 indicated the presence of some authigenic **chlorite** crystals between the illite flakes. However, the amount seems to be negligible and chlorite could not be identified by optical microscopy.

Authigenic **albite** is seldom and occurs in the form of neo-formed crystals in leached K-feldspar grains.

---

[2] It is also possible that these “blasts” represent rounded fragments of reworked cement-layers

Dissolution of feldspar is not as common as in well NOR-A. Some of the feldspar grains are corroded and sometimes the feldspar leaching porosity is filled by authigenic illite flakes in the deepest sample. Grain rims composed of clay minerals and hematite outlining former grains were found occasional[3]. Some, but not all, of these rims are compacted (Fig. 6.8c) indicating a pre-compaction dissolution.

Cement dissolution is indicated by relatively large pores in higher compacted areas and is also not as common as in well NOR-A (Appendix 2.1). Cement dissolution pores were mainly found in coarser grained lamina and were absent in some finer grained samples. The oversized cement dissolution pores have a shape comparable to the patchy pore filling dolomite cement. In one of the samples (5164.6) corroded dolomite cement was found in pores directly adjacent to oversized cement dissolution pores. Cement dissolution pores were later filled by authigenic illite meshwork in the deepest sample.

The content of authigenic **quartz** is generally lower than one percent of sample volume and not as high as in well NOR-A. Authigenic quartz occurs mostly in the form of syntaxial overgrowths on quartz grains which were observed partly enclosing illite fibres.

Halite was observed filling fissures in one sample 5119.4. This halite seems to postdate all other authigenic phases and is thought to be an artefact from vaporising formation water after core recovery. However, late diagenetic cementation can also not be ruled out (see above).

---

[3] The mineralogical composition of the leached grains is unknown and it could have been also an other chemical unstable phase than feldspar

6.2 Triassic wells: Petrography and diagenesis

Two of the wells from the Norwegian sector covered Triassic strata. Ten samples were available from the Triassic section in well NOR-C and seven samples from well NOR-E. Due to the relatively low amount of sample material, a detailed petrographic work as in the UK-sector was not performed. Nevertheless, this material was useful for comparison, since one of these wells (NOR-E) encountered extreme pressure and temperature conditions (see below).

6.2.1 Well NOR-E

Well NOR-E is located at the eastern margin of the Feda Graben ~ 40 km east south-east of the Judy Field between the two basin modelling areas. Objective of well NOR-E was to test the hydrocarbon potential of Jurassic sandstones on the southern flank of a faulted dip closure in a larger roughly NNW-SSE striking flower structure created by late Jurassic movements (KPUI/1, 1993). The well found indication of hydrocarbons in Upper Jurassic sandstones of Oxfordian age and was drilled 108 m down into Triassic strata to a total depth of 5565 m. The well encountered HPHT conditions with pressures close to fracture pressure (around 112 MPa at 5400 m in the Oxfordian sandstones) and BHT of 190°C (KPUI/1, 1993).

Triassic sediments were penetrated by well NOR-E directly under the Oxfordian sands. They consisted predominantly of brown to reddish brown and light grey mudstones in the upper part. The lower part was more sandy with interbedded brown to brown grey, very fine- to medium-grained sandstones (KPUI/1, 1993).

A bottom hole core was cut in the Triassic section from 5555 to 5565 m. A description of this core was available from Prestholm & Walderhaug (1994): The cored interval is composed of thin grey fine- to medium-grained sandstones interbedded with grey to dark grey faint laminated mudstones. A reddish colour was reported from a heterolithic interval between 5561.00 and 5561.25 m. The encountered sandstone beds are relatively thin (up to 10 cm thick) and horizontally laminated. They often show fining upwards trends into mudstones and have sharp lower boundaries. The mudstones are horizontally to wavy laminated and occasional bioturbated. Mudstone clasts up to 5 cm were observed in the sandstones. Porosities range from 3.0 to 9.8 % and permeabilities are lower than 0.2 mD in conventional core analysis (KPUI/1, 1993).

The Triassic sediments were interpreted to represent accumulations in the distal part of a braid plain by Prestholm & Walderhaug (1994).

Detrital composition of Triassic samples in well NOR-E

Many of the samples are composed of argillaceous sandstones with thin mudstone lamina (in these cases only the sandstone part was quantified by point-counting). The sandstones are fine-grained and well to moderately sorted with subangular to subrounded grains. The argillaceous sandstones in well NOR-E were texturally comparable to argillaceous sandstones (facies AS) from Jade and Judy Fields of the UK-sector.

Detrital phases in the investigated sandstone samples are dominated by monocrystalline quartz (30.3…43.3 vol.%). Polycrystalline quartz (3.7…7.0 vol.%) is also common. Rock fragments are mainly composed of metamorphic lithoclasts (0.3…6.7 vol.%) and quartz feldspar aggregates (2.7…5.7 vol. %). Volcanic rock fragment occur occasional. Mudstone intraclasts were found in amounts up to 2 vol.% and reworked dolomite nodules composed of dolomite microspar in traces. Some samples are relatively mica rich with up to 6.3 vol.% muscovite, up to 1.0 vol.% detrital chlorite and traces of biotite. Some sandstone layers in the argillaceous sandstones have a relatively high content of detrital clay matrix (up to 11.7 vol.%). Feldspars are present predominantly in the form of K-feldspar (5.0…10.7 vol.%). Plagioclase is relatively rare (up to 1 vol.%). Perthitic feldspar grains were found relatively seldom (see Appendix 3.2 for EMP-analyses). Some of the feldspar grains were partly corroded. Most of the sandstone samples from well NOR-E can be classified as lithic Subarkose (Fig. 6.10a) according to McBride (1963).

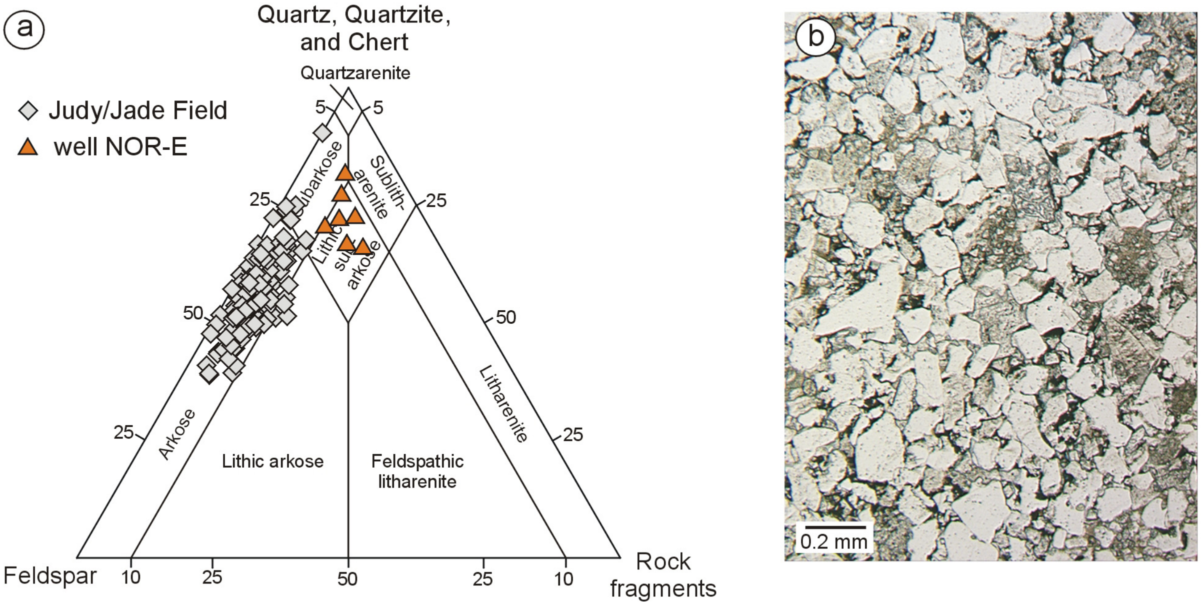

Fig. 6.10a: Detrital composition of Triassic samples from well NOR-E according to McBride (1963). The samples plot predominantly in the Lithic Subarkose field. Triassic samples from Judy and Jade Field in the UK-sector are plotted for comparison; **b:** texture of a Triassic sandstone (5564.35, probably facies SF - see section 5.3 for Skagerrak Fm. facies) from well NOR-E. Note the high degree of cementation and compaction with no remaining visible porosity.

The rocks in well NOR-E have a significantly lower feldspar content than samples of Triassic age investigated from Judy and Jade Field in the UK-sector (see Fig. 6.10a). The Triassic samples from well NOR-E are rather comparable to Rotliegend sandstones from wells NOR-A and NOR-B according to their detrital composition (see also Fig. 6.6a). There are different possibilities to explain this apparent inconsistency: 1.) The rocks contained no fossils and were not dated by biostratigraphy – it may be that they are not of Triassic but of Rotliegend age and the Mid Cimmerian Unconformity has cut down to Rotliegend rocks here. However, this not supported by petrographic pattern: chlorite rich argillaceous sands and the texture of the samples are rather comparable to Skagerrak Formation facies SF and AS in the UK sector; 2.) The main source area of the 40 km distant Judy and Jade Fields may have been different – and/or the rocks of well NOR-E have recycled Rotliegend sediments; and 3.) The more distal depositional facies may have contained more mineralogical mature grains and therefore the feldspar content is lower. A different source area along with local occurrence of a higher proportion of recycled Rotliegend material seems to be the most likely scenario. However, for a detailed discussion additional petrographic data of Triassic rocks from adjacent wells are required.

Fig. 6.11a (next page): Small dolomite rhombi sometimes amalgamating to nodules (sample 5558.4, well NOR-E, plane polarised light); **b:** larger dolomite crystals (D). Note the pore filling late quartz (arrow) and the relatively dense packing of grains (sample 5564.35, well NOR-E, plane polarised light); **c:** Ankerite (A)? crystals and bitumen (B) staining (sample 5556.45, well NOR-E, plane polarised light); **d:** Hematite relicts (H) enclosed into dolomite cement and a later bitumen (B) impregnation (sample 5564.35, well NOR-E, plane polarised light); **e:** Chlorite coated grains (arrow) in facies AS (sample 5559.35, well NOR-E, plane polarised light); **f:** Small euhedral chlorite plates (sample 5564.35, well NOR-E, plane polarised light); **g:** Bitumen (B) in a former migration pathway (sample 5564.35, well NOR-E, plane polarised light); **h:** Late quartz cement (Q) overgrowing bitumen and enclosing a carbonate (C) crystal (sample 5564.35, well NOR-E, plane polarised light).

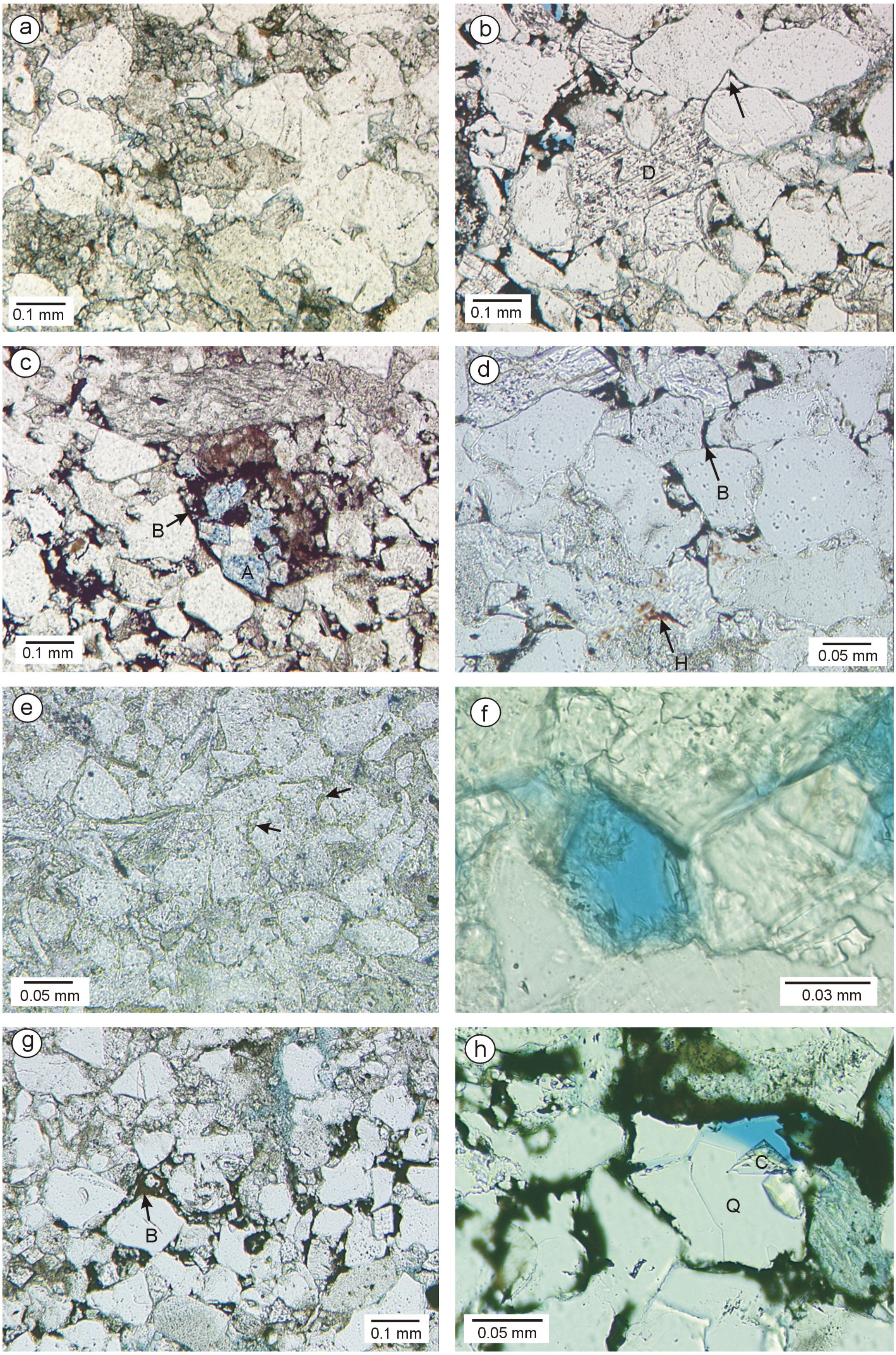
a
0.1 mm
b
D
0.1 mm
c
B
A
0.1 mm
d
B
H
0.05 mm
e
0.05 mm
f
0.03 mm
g
B
0.1 mm
h
C
Q
0.05 mm

Pore types and porosity in Triassic samples of well NOR-E

The investigated sandstones are tight due to intense dolomite cementation and mechanical compaction. Only very small amounts of macroporosity relicts were detected in thin sections (0…0.3 vol.%). The largest proportion of the measured core porosity seems to be related to micropores between detrital clay minerals. This is also supported by the low permeability values. The observed remaining macropores consisted of intergranular pores strongly reduced in size by compaction, some probably artificial oversized pores and feldspar dissolution pores.

Authigenic phases and diagenesis in Triassic samples of well NOR-E:

Following authigenic phases were found in the Triassic sandstones of the investigated samples of well NOR-E: dolomite (14.7…33.3 vol.%), bitumen (0…14.3 vol.%), chlorite coatings (0…9.7 vol.%), quartz (0…3.7 vol.%), chlorite intraclast (0…3 vol.%), chlorite plates (traces), K-feldspar (traces), hematite (traces), leucoxene/anatase (traces) and ankerite (traces).

Dolomite is the prevalent authigenic phase in samples of well NOR-E. It is commonly present in the form of small (10–50 µm) rhombi sometimes forming clusters or amalgamating to grain replacing nodules, which are partly composed of dolomite microspar (Fig. 6.11a). Dolomite can also occur in the form of larger rhombi (> 100 µm) and pore filling crystals (Fig. 6.11b). Authigenic dolomite was sometimes observed to replace grains.

Ankerite/or Fe-dolomite identified by staining with potassium ferricyanide was found only in traces in some of the samples in the form of single larger rhombi, small clusters of rhomb shaped crystals (Fig. 6.11c) or overgrowths on non-ferrous dolomite.

Leucoxene is present in traces frequently in the form of optical not resolvable masses or aggregates composed of tiny crystals. It seems to replace heavy mineral grains.

Authigenic **chlorite** occurs in different forms and is more common in the argillaceous sandstones (facies AS). The grains in facies AS are often coated by an irregular rim of green chlorite comparable to the type I chlorite described in section 5.5. Grain replacing chlorite (Type III – see section 5.5) occurs also predominantly in the finer grained facies AS. Irregular aggregates of tiny (5–10 µm) euhedral chlorite plates (Fig. 6.11f) were found occasional in the remaining pores of one sample (5564.35). They were found to have overgrown dolomite and seem to be comparable to chlorite II in Skagerrak Formation sandstones from Jade Field (see section 5.5).

K-feldspar overgrowths were found seldom on some of the K-feldspar grains. The overgrowths are commonly corroded.

Hematite relicts occur occasional enclosed into authigenic dolomite crystals or inside of detrital grains in the most samples (Fig. 6.11d). The occurrence of hematite enclosed into dolomite cements indicates a former more extensive presence. Moreover, a reddish colour was reported for a heterolithic interval of the core by Prestholm & Walderhaug (1994). Other parts of the sequence may also have been once red coloured. Most of the hematite was most likely removed by later **bleaching** and hematite remained only where it was protected by dolomite or inside of grains. This observation is comparable to the occurrence of hematite in Skagerrak Formation samples from Jade and Judy Fields in the UK-sector (see section 5.5).

Bitumen is a major authigenic phase in some of the samples and makes up to 14.3 vol.% there. It occurs commonly in sheetflood sands or coarser grained sandstone layers with a lower detrital mud content in the argillaceous sands. Sometimes it is pervasively developed and sometimes restricted to former migration pathways with lesser dolomite cementation (Fig. 6.11g), which are now completely compacted. Bitumen forms thick "tar like" crusts with a dark greenish black colour. It impregnates authigenic dolomite as well as leucoxene and was also found in some feldspar dissolution pores. Bitumen crusts were observed to be overgrown by later quartz cement (Fig. 6.11h) and partly by late diagenetic carbonates, probably ankerite[1].

Late authigenic **quartz** was found in amounts up to 3.7 vol.% in the sheetflood sandstones. It is rare in argillaceous sands and seems to be completely missing in the mudstone parts. Quartz encloses frequently bitumen and dolomite cements.

Dissolution of feldspar is relatively rare and no indications for cement dissolution were observed in the investigated thin sections.

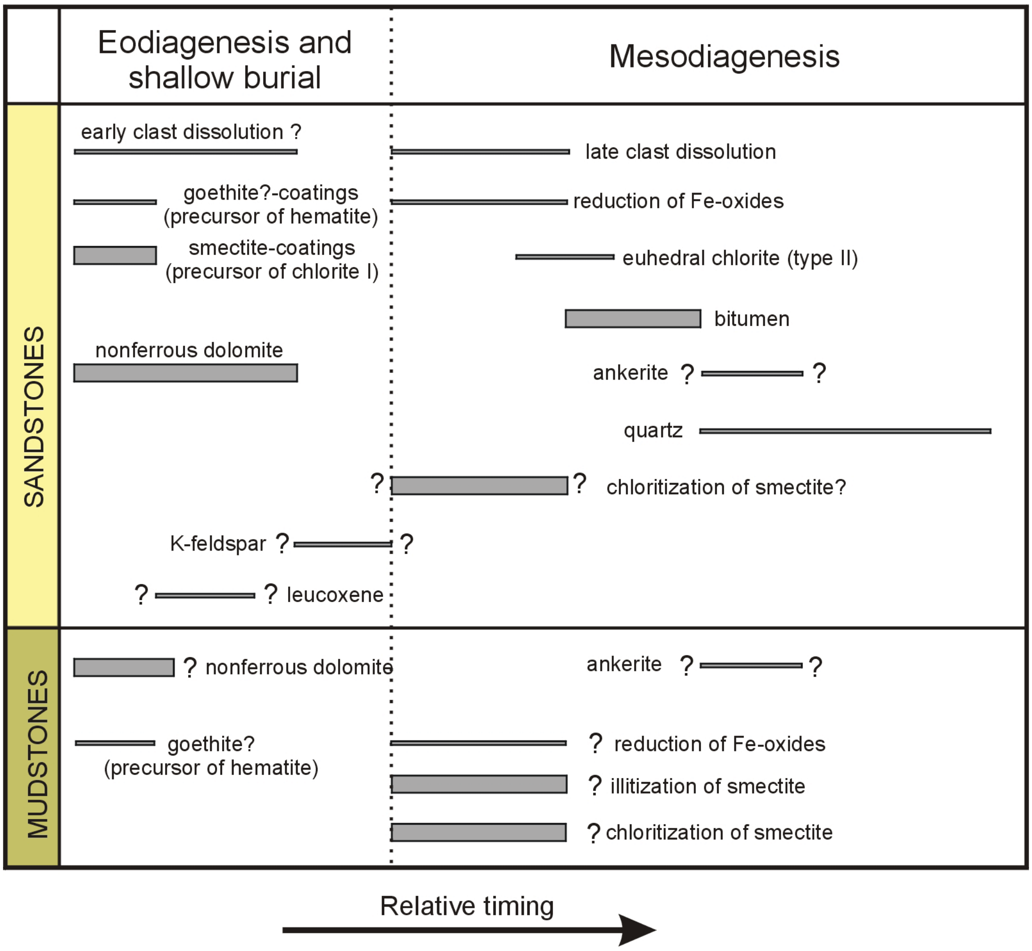

Fig. 6.12: Paragenetic sequence for the Triassic sandstones in well NOR-E as indicated by textural relationship in thin section. Important authigenic phases and processes are marked with thick bars and minor phases or processes with thin bars. Some of the processes like chloritization and illitization of smectite, or the goethite precursor of hematite were interpreted analogue to Triassic sediments of the Jade and Judy Fields (see section 5).

---

[1] Not all of the thin sections were stained for carbonate identification

6.2.2 Well NOR-C - Triassic

The well was drilled into a structural trap with dip closure elements located on the Steinbit Terrace at the eastern margin of the Central Graben. Jurassic sandstones of Oxfordian age were the primary target of the well and encountered at 4559 m TVDSS (Jysereid et al., 1994). However, the thickness of the Upper Jurassic reservoir was reduced by faulting to 5 m and 114 m of Triassic Skagerrak Formation sediments were penetrated below the fault.
Bottom hole temperatures (BHT) up to 165°C and formation pressures up to 93 MPa (at ~ 4600 m) were encountered by well NOR-C.
Two cores with a total length of 16 m were cut and contain 1.6 m of Oxfordian sandstones and 14.4 m of Triassic sediments (Prestholm & Walderhaug, 1994). Two samples from the Oxfordian sandstones and 10 samples from the Skagerrak Formation were available for this study.

Triassic Skagerrak Formation in well NOR-C
The Triassic section is composed of light grey and red brown very fine- to coarse-grained sandstones and siltstones, interbedded with thicker mudstone bands and thin carbonate layers (Jysereid et al., 1994). The Skagerrak Formation was found to be water-bearing and no oil shows were reported from this interval. However, some gas discharging from the cores was observed (Jysereid et al., 1994).

A core description from Prestholm & Walderhaug (1994) was available for the Skagerrak Formation of well NOR-C: The cored section consists of two major fining upward units. The lower unit is approximately six meter thick and composed of fine-grained sandstones associated with silt-rich mudstones. Some of the beds show sedimentary structures like climbing ripple cross-lamination, horizontal bedding and low-angle cross-stratification. Very-fine-grained sandstones in the upper part of this unit contain larger mudstone clasts and reworked dolomite nodules. Bioturbation was reported from finer grained sediments.
The lower unit is interpreted to comprise mainly the sheetflood (SF) and argillaceous sandflat (AS) facies associations[2].
The upper unit (approximately 10 m thick) of the cored Triassic section is composed of 0.6 to 1.0 m thick beds of medium- to coarse-grained sandstones showing fining upward trends with mudstones and very fine-grained sandstones developed at the top (Prestholm & Walderhaug, 1994). Larger mudstone and dolocrete clasts, were predominantly found at the base of the individual commonly erosively based beds. The sandstones show horizontally bedding, low-angle and through cross-lamination, respectively. Current ripple lamination or bioturbation traces were reported from the finer grained intervals (Prestholm & Walderhaug, 1994).
This unit is interpreted to comprise mainly the sheetflood (SF) and fluvial channel (FC) facies associations.
The cored Triassic sediments are interpreted to have been accumulated in a fluvial braid plain environment (Prestholm & Walderhaug, 1994).

Nodular dolocrete is partly developed in the cored Triassic succession (Jysereid et al., 1994). Some of the samples were intensely affected by tectonics, as shown by the occurrence of deformation bands.
Core porosities range from 7.7 to 21.2 % and permeabilities from 0.02 to 12.7 mD (Jysereid et al., 1994).

---

[2] This interpretation was derived from comparison with facies types of Jade and Judy Field in the UK-sector.

Detrital composition of Triassic sandstones in well NOR-C

Most of the investigated samples are fine-grained, partly mud- and mica-rich sandstones. They represent probably the argillaceous sandflat facies association, finer grained sheetflood sands and channel abandonment sediments, respectively. One sample was medium-grained with relatively low mud content and represents most likely a sheetflood or fluvial channel sandstone[3]. The investigated sandstones are moderately sorted and have subangular to subrounded grains.

Most of the grains consist of monocrystalline quartz (32 to 42 vol.%). Polycrystalline quartz is present in amounts between 2.7 and 15.0 vol.%.

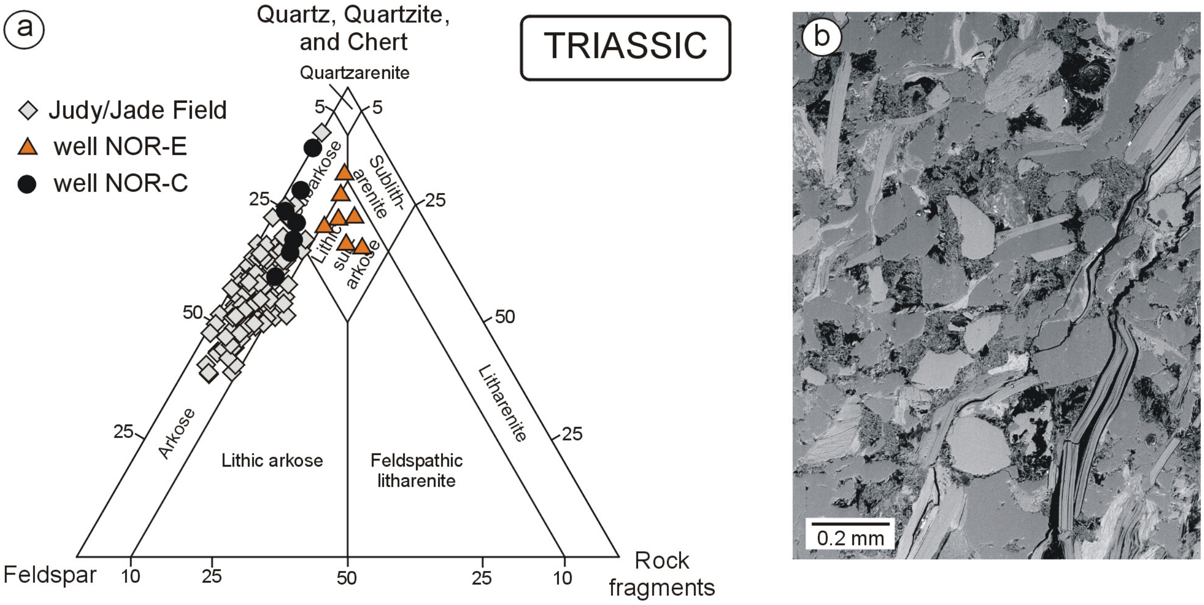

Fig. 6.13a: Present sandstone composition according to McBride (1963) of the Triassic samples from well NOR-C. The samples plot in the arkose and subarkose fields; **b:** Texture of a Triassic sandstone from well NOR-C (sample 4579.50, BEI).

Triassic sandstones of well NOR-C have a feldspar content ranging from 14.3 to 21.3 vol.%. Thus, they are feldspar richer than the Upper Jurassic sandstones of the same well (compare also Fig. 6.13a with Fig. 6.17a). K-feldspar is the dominant feldspar type (11.7…18.7 vol.%) and plagioclases occur subordinate (1.3…4.3 vol.%). The largest part of the feldspar grains is corroded and feldspar dissolution pores were found in amounts up to 5 vol.% in the samples investigated. This is evidence for a higher feldspar content during deposition.

Rock fragments are composed of metamorphic lithoclasts (0.3…2.7 vol.%), quartz feldspar aggregates (up to 1.7 vol.%) and sedimentary rock fragments (up to 0.7 vol.%).

Especially the fine-grained sandstones are locally mica rich (up to 14.4 vol.%) and have a high content of detrital mud (up to 25.3 vol.%).

Triassic sandstones of well NOR-E can be classified as Arkose or Subarkose (Fig. 6.13a) according to McBride (1963). They are comparable to quartz richer Triassic sandstones from Jade and Judy Field and have a significantly higher feldspar content than the sandstones from well NOR-E (see Fig. 6.13a).

---

[3] No core logging could be performed for this study and facies interpretation was derived from sediment texture and available information from internal industry reports

Pore types and porosity in Triassic sandstones of well NOR-C

Point counted macroporosity ranges from 0.3 to 13.3 vol.% in the Triassic sandstones investigated. The one dolocrete sample has no visible macropores. Observed macropores consist of intergranular pores (0.3 to 10.3 vol.%), feldspar dissolution pores (0.3 to 5.0 vol.%), oversized pores (up to 0.3 vol.%) and traces of cement dissolution pores. Measured core porosities by conventional core analyses reported by Jysereid et al. (1994) are higher and range from 7.7 to 21.2 %. Hence, a relatively high amount of microporosity seems to exist. This is supported by the relatively low permeability values (0.02 to 12.7 mD). Most of the micropores are probably located inside of leached feldspar grains (Fig. 6.15a, b) or between clay minerals (Fig. 6.14e-h). However, it should also be considered that the core porosity values reported by Jysereid et al. (1994) and the point count macroporosities were not measured at the same samples.

Authigenic phases and diagenesis in Triassic sandstones of well NOR-C

Following authigenic phases were observed in the investigated sandstones of the Triassic Skagerrak Formation in well NOR-C: Quartz (0…7.7 vol.%), dolomite (0…80 vol.%), K-feldspar (0…2 vol.%), leucoxene (0…0.7 vol.%), euhedral chlorite plates (0…3 vol.%), chlorite coatings (0…0.7 vol.%), illite coatings (0…0.3 vol.%), fibrous illite (0…0.3 vol.%), pyrite (0…0.3 vol.%), barite (traces) and hematite (traces).

Quartz is the volumetrically most important authigenic phase in the investigated Triassic sandstones of well NOR-C with up to 7.7 vol.%. Prestholm & Walderhaug (1994) reported even point count values up to 13 vol.% for one Triassic sandstone sample from well NOR-C. Authigenic quartz occurs mostly as syntaxial overgrowth (Fig. 6.15b) on detrital quartz grains. Theses overgrowths merge sometimes to pore filling cements. Quartz overgrowths were found occasional to grow into secondary dissolution pores. Authigenic quartz was also observed to enclose and thus postdate feldspar overgrowths (Fig. 6.14a) and euhedral chlorite plates.

Authigenic **dolomite** is present in different forms in the investigated Triassic samples of well NOR-C. Sample 4585.5 is composed to 80 vol.% of tiny (50 µm and smaller) partly rhomb shaped dolomite crystals, which occasional enclose hematite (Fig. 6.14c). This sample is interpreted to represent a part of a dolocrete layer. Some samples contain scattered partly corroded larger (~ 100–300 µm) dolomite crystals. Pore filling dolomite (Fig. 6.14b) cement was observed in sample 4587.2 (not point counted). The pore filling dolomite occludes a relatively high intergranular volume indicating an early timing of precipitation similar to the non-ferrous dolomite in the Skagerrak Formation of the UK-sector.

Fe-carbonates (probably Fe-dolomite or ankerite) were observed in the form of overgrowths on non-ferrous dolomite in the stained thin section (5590.50). The occurrence of iron rich carbonates was also reported by Prestholm & Walderhaug (1994) for the cored Triassic interval of well NOR-C.

Fig. 6.14a (next page): K-Feldspar overgrowths (F) enclosed by later quartz (Q) cement (sample 4578.4, well NOR-C, plane polarised light); **b:** Leached feldspar grains, partly with authigenic barite (white) (sample 4584.65, well NOR-C, BEI); **c:** Dolomite crystals with hematite traces in the dolocrete (sample 4585.5, well NOR-C, plane polarised light); **d:** Aggregates of euhedral chlorite (CP) plates (sample 4582.45, well NOR-C, plane polarised light); **e:** Euhedral chlorite plates (CP) and quartz (Q) cement (sample 4589.6, well NOR-C, SEI); **f:** Chlorite plates (CP) in rosette form (sample 4589.6, well NOR-C, SEI); **g:** Authigenic illite flakes and fibres overgrowing a detrital mica (sample 4589.6, well NOR-C, SEI); **h:** Illite fibres grow from chlorite plates (CP) into pore space (sample 4589.6, well NOR-C, SEI).

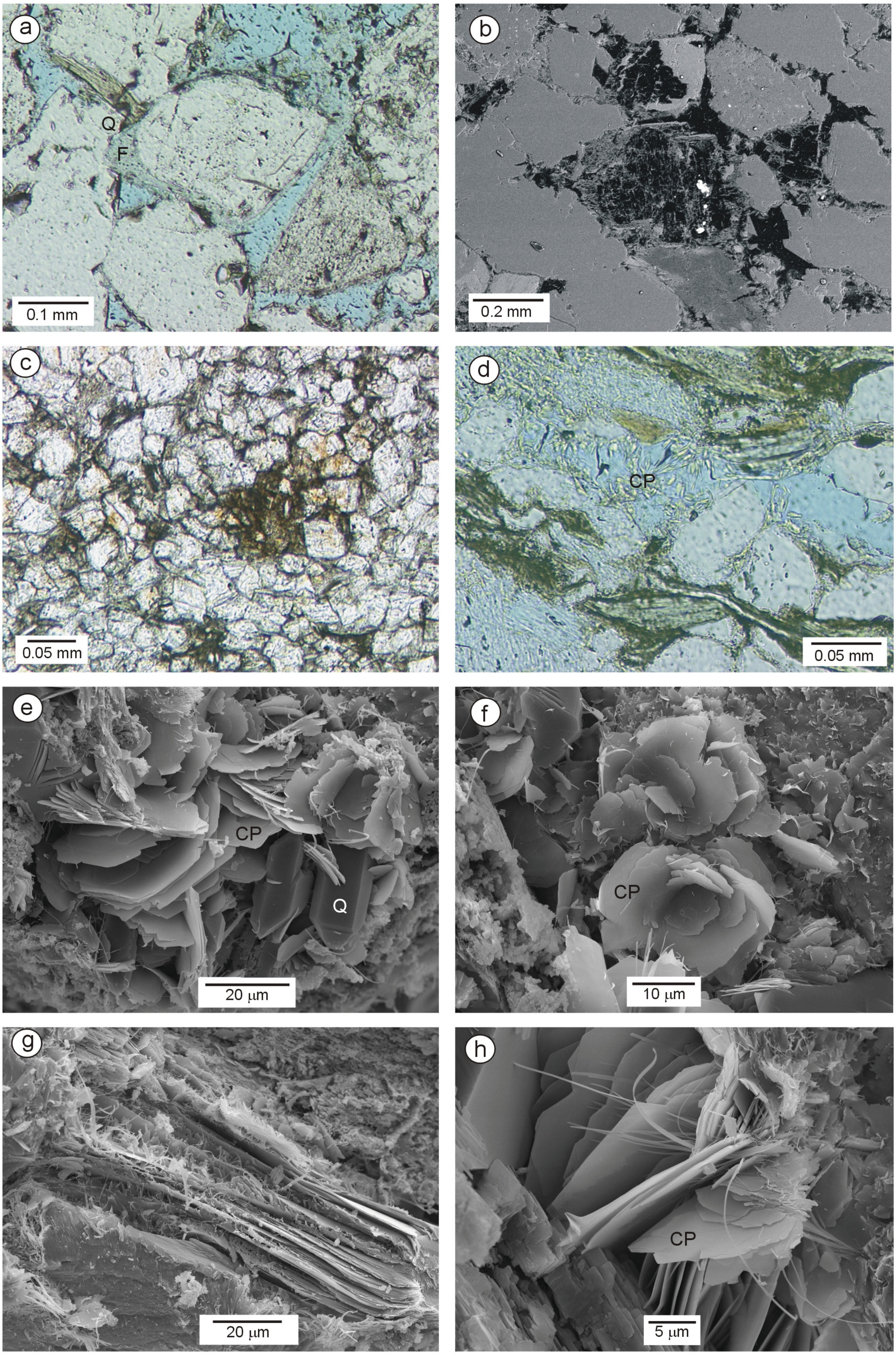
a
Q
F
0.1 mm
b
0.2 mm
c
0.05 mm
d
CP
0.05 mm
e
CP
Q
20 μm
f
CP
10 μm
g
20 μm
h
CP
5 μm

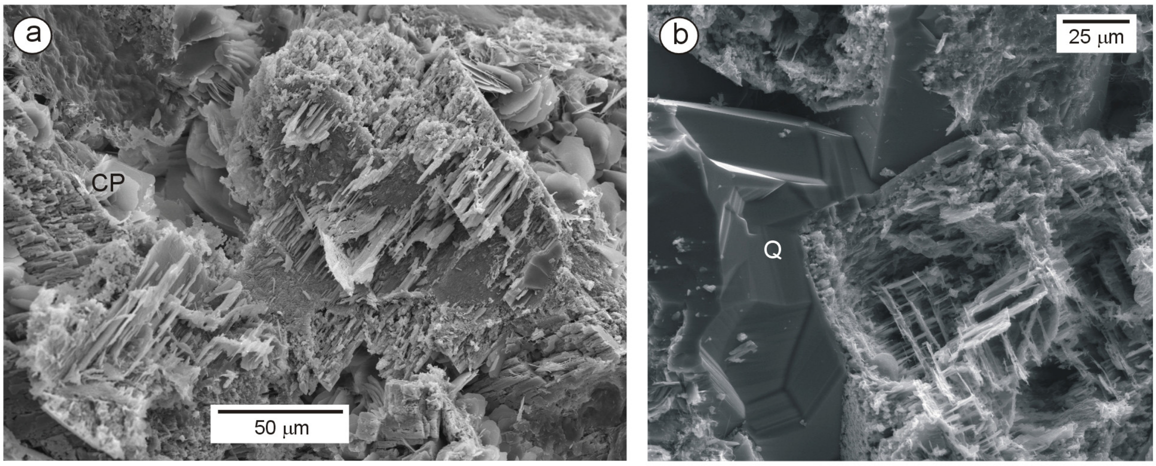

Fig. 6.15a: Leached feldspar with microporosity and chlorite (CP) plates (sample 4589.6, well NOR-C, SEI); **b:** Leached feldspar partly enclosed by authigenic quartz (Q) in sample 4589.6 (well NOR-C, SEI).

Authigenic **K-feldspar** was found as partly intensely corroded overgrowths on detrital K-feldspar grains. The K-feldspar overgrowths were observed to be enclosed into later quartz cements (Fig. 6.14a).

Authigenic **pyrite** was found as single cemented spots with ~ 0.3 mm diameter in some of the samples. These pyrite patches enclose some grains and pyrite occupies a relatively large intergranular volume indicating an early timing. In the dolocrete sample (4585.50) small amounts of pyrite and hematite could be observed in one thin section.

Hematite was found in traces enclosed into authigenic dolomite only in the dolocrete sample (Fig. 6.14c). It is possible that hematite was former more extensive developed like in the other Triassic wells. This is supported by the observation of optical not resolvable masses under quartz overgrowths like in the bleached part of Rotliegend sample 4812.1 in well NOR-A.

Leucoxene occurs in the form of optical not resolvable masses or aggregates of tiny crystals probably replacing former heavy mineral grains.

Authigenic **chlorite** is present in the form of more or less continuous grain coating rims (chlorite type I, see section 5.5) or more common as euhedral chlorite plates with a size between 10 and 30 µm. Chlorite inside of clasts (chlorite type III, see section 5.5) was also observed.
The authigenic chlorite plates from Triassic sandstones of well NOR-C are larger than the euhedral chlorite plates observed in the other studied Triassic wells (NOR-E, 30/2c-4 and the Judy Field wells), which have usually a size between 5 and 10 µm. The authigenic euhedral chlorite in the Triassic section is petrographically more comparable to the chlorite plates that were found in overlying Jurassic sandstones. Euhedral chlorite occurred in the Triassic section as few more or less fan shaped aggregates in single pores (Fig. 6.14d, e and h), as rosettes (Fig. 6.14f), or in the form of irregular pore filling masses composed of a number of partly radial arranged euhedral chlorite plates.

The chemical of composition of the euhedral chlorite plates was measured by electron microprobe analysis and gave an iron rich composition. The formula calculated from analysis no. 234 is given as example:

chlorite plates: $Mg_{3.16}Fe_{5.43}Al_{3.10}Si_{5.42}Al_{2.58}O_{20}(OH)_{16}$ (6.1)

This chemical composition is comparable to the authigenic chlorite plates (type II) in well 30/2c-4.
Authigenic chlorite plates were occasional found in feldspar dissolution pores, or enclosed by later quartz cement and partly overgrown by illite fibres (Fig. 6.14h).

Authigenic **illite** occurs occasional in the form of fibres growing from chlorite plates into pore space (Fig. 6.14h) or as tiny flakes (Fig. 6.14g). Authigenic illite was also observed in feldspar dissolution pores. However, authigenic illite is volumetrically not so important and pervasive pore occluding meshwork like in well NOR-A was not observed. Only few isolated pores were filled by illite, indicating the replacement of grains. Grain coating **illite** was found relatively seldom.

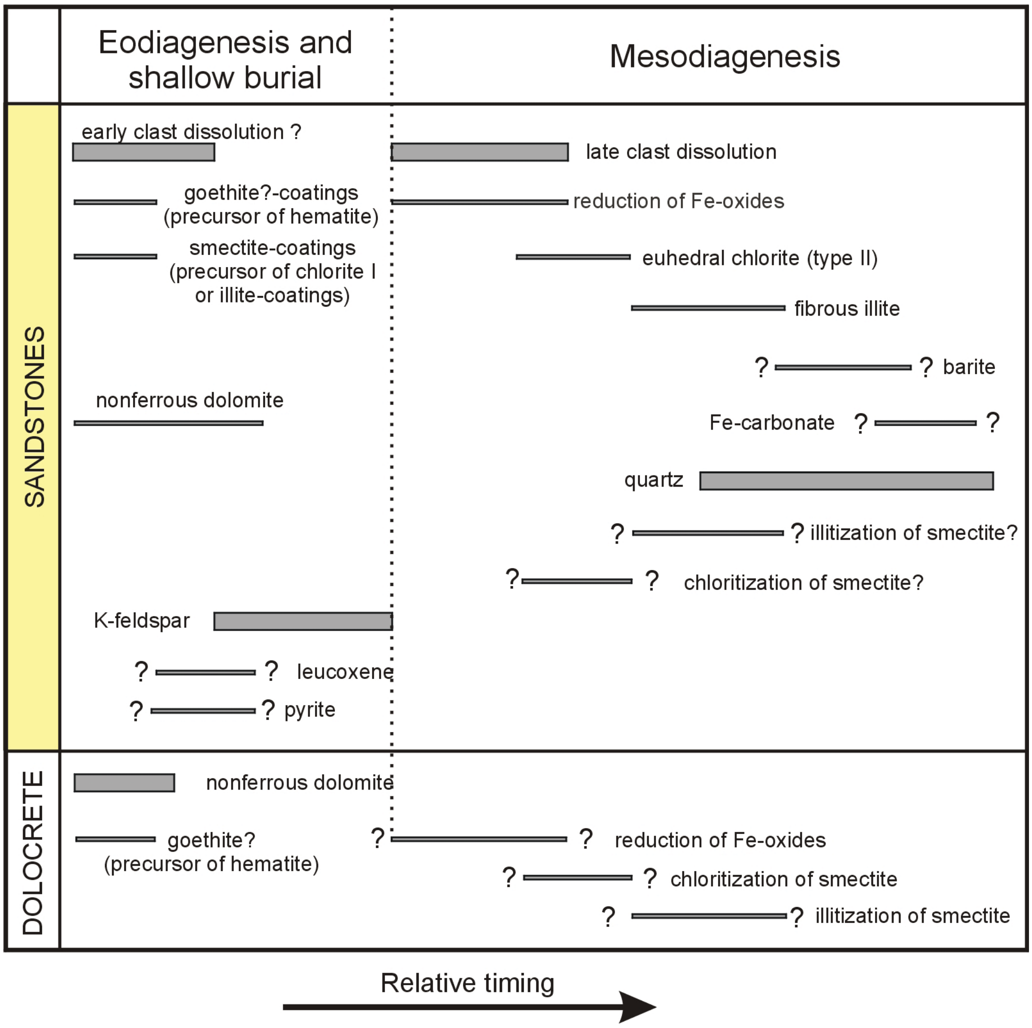

Fig. 6.16: Paragenetic sequence for the Triassic sandstones in well NOR-C as indicated by textural relationship in thin section. Important authigenic phases and processes are marked with thick bars and minor phases or processes with thin bars. Some of the processes like chloritization and illitization of smectite, or the goethite precursor of hematite were interpreted analogue to Triassic sediments of the Jade and Judy Fields (see section 5).

Authigenic **barite** was found in traces inside of leached feldspar grains like in the overlying Jurassic sandstones (Fig. 6.14b).

Relatively intensive feldspar **dissolution** was observed in the investigated Triassic sandstones of well NOR-C. Most of the detrital feldspar grains and authigenic overgrowths are corroded and point-counted feldspar dissolution pores make up to 5 vol.%. Values up to 14.3 vol.% of point counted feldspar dissolution porosity were reported by Prestholm & Walderhaug (1994) for Triassic sandstones from well NOR-C. Inside of the corroded feldspars exists a high amount of microporosity (Fig. 6.15a, b). Some of the leached feldspar grains are squeezed and seem to have been affected by mechanical compaction subsequent to leaching, while others remain relatively uncompacted in spite of the unstable framework in some of the leached feldspar grains (see Fig. 6.15b). Cement dissolution pores were found only in traces.

6.3 Jurassic wells: Petrography and diagenesis

6.3.1 Well NOR-C - Upper Jurassic (Oxfordian) Sandstones

The general setting of well NOR-C and the Triassic interval is described in section 6.2.2.

The Upper Jurassic sediments of well NOR-C consist of olive green and brownish grey very fine- to medium-grained sandstones and contained a small hydrocarbon accumulation (Jysereid et al., 1994).

A core description for the 1.6 m long Upper Jurassic section was available from Prestholm & Walderhaug (1994): This interval is composed of well sorted commonly bioturbated grey fine-grained sandstones with occasional very faint sedimentary structures and the trace fossils *Planolites* and *Zoophycus*. Small (1 to 3 mm) mudstone fragments are common.

The depositional environment was interpreted by Prestholm & Walderhaug (1994) to have been shallow marine to offshore.

Reservoir quality of Upper Jurassic sandstones in well NOR-C is poor and the rocks were intensely fractured by faulting (Jysereid et al., 1994). Conventional core porosities range from 12.5 to 20.3 %, permeabilities from 0.076 to 0.532 mD and the log derived water saturation has an average of 65 % (Jysereid et al., 1994). The two investigated samples showed deformation bands and stylolites.

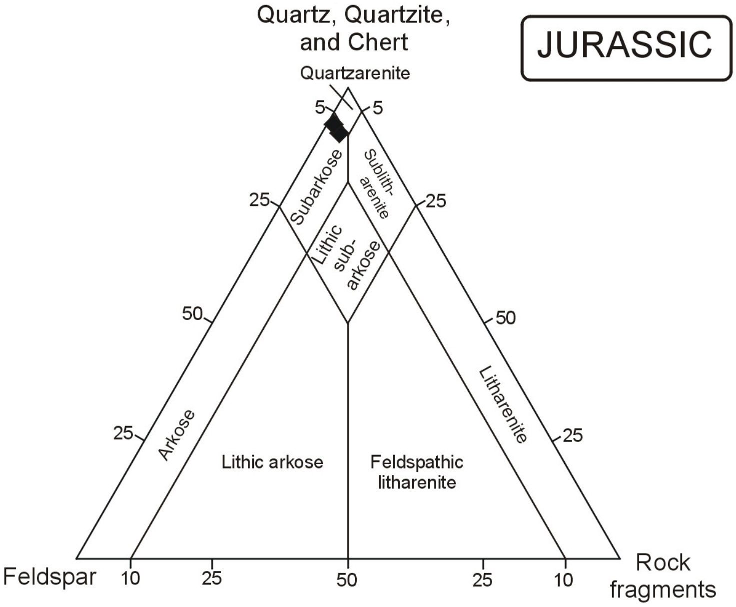

Fig. 6.17: Present composition of Jurassic sandstones from well NOR-C according to McBride (1963). Both sandstones plot in the Subarkose field.

Detrital composition of Upper Jurassic sandstones in well NOR-C

The two investigated samples from the Upper Jurassic interval of well NOR-C consist of fine-grained well sorted sandstones with subangular to subrounded grains. A part of the angularity may be attributed to syntaxial quartz overgrowths (see also Jysereid et al., 1994). Monocrystalline quartz (58.7…65.7 vol.%) is the predominant detrital phase in both sandstone samples. Polycrystalline quartz (7.3…10.0 vol.%) is also fairly common. Rock fragments, predominantly composed of quartz feldspar aggregates, occur subordinate in amounts between 1.0 and 2.3 vol.%. The total feldspar content is relatively low (4.7…5.3 vol.%) and consists predominantly of K-feldspar. The plagioclase content is lower than one volume percent. Most feldspar grains are corroded and a large part of the point-counted porosity is the result of feldspar dissolution (1.0 to 1.3 vol. % of bulk rock). Light mica can occur in amounts up to one volume percent and other micas in traces. Both samples contain detrital matrix clay (2.7 and 7.3 vol. % respectively). The Jurassic sandstones of well NOR-E can be classified as Subarkose (see Fig. 6.17) according to McBride (1963). Nevertheless, the samples plot relatively close to the Quartzarenite field.

Pore types and porosity in Upper Jurassic sandstones of well NOR-C

Point-count porosity is relatively low with values of 2.7 and 4.4 vol. %, respectively compared to the measured core porosities. The point counted porosity is composed of intergranular macropores and feldspar leaching pores. Most of the measured core porosity seems to be microporosity, probably in partly leached feldspar grains and between clay minerals. However, it must be considered that core porosity values from Jysereid et al. (1994) and point-count porosities were not measured at the same samples. The grain framework is clearly supported by merged quartz overgrowths.

Authigenic phases and diagenesis in Upper Jurassic sandstones of well NOR-C

Following authigenic phases were found in the two investigated Jurassic sandstone samples from well NOR-C: Quartz (7.7…9.3 vol.%), dolomite and Fe-carbonates (traces to 6 vol.%), euhedral chlorite (traces to 0.7 vol. %), pyrite (0…0.3. vol. %), barite (0…0.3 vol.%), ferrous carbonate (traces) and bitumen (traces).

Quartz is the dominant authigenic phase in well NOR-C with 7.7 and 9.3 vol.%, respectively. Quartz cement volumes up to 20 % were reported for a clean Upper Jurassic sandstone sample without detrital clay matrix by Prestholm & Walderhaug (1994) from this well. Authigenic quartz occurs as syntaxial overgrowths which can sometimes merge to pore-filling cements (Fig. 6.18a). Quartz cement is more common in cleaner sandstone parts with a lesser mud content and forms partly intensely cemented patches. Authigenic quartz was observed engulfing sometimes authigenic euhedral chlorite, seldom bitumen and occasional Fe-dolomite.

Authigenic **dolomite** is developed as euhedral rhombi (size 50 to 150 µm) which occur scattered or form clusters (Fig. 6.18b). Dolomite is also occasional present as pore-filling microspar. Authigenic dolomite was found to replace clasts and inside of feldspar dissolution pores.

Fe-carbonates are as common as dolomite and were found in the form of isolated rhomb shaped crystals, crystal clusters or as overgrowths on non-ferrous dolomite. Fe-carbonates can occur in primary pores which are significantly reduced in size by compaction or in enlarged secondary pores. Fe-carbonates were observed to overgrow authigenic quartz in places.

Stable isotopes of carbonates were measured at the sample with the highest carbonate content (4575.55). The sample has a $\delta^{18}O$ value of –10.55 ‰ and a $\delta^{13}C$ value of –5.50 ‰. It must be considered that two different carbonate phases are present in the sample and that this isotopic signature represents a mixture of both.

Authigenic **chlorite** is present in Upper Jurassic sandstones of well NOR-C mainly in the form of scattered clusters composed of euhedral plates with a size between 10 and 30 µm. The chlorite platelets occur commonly as irregular aggregates in some of the pores, partly also in the pores of leached feldspar grains. Authigenic chlorite plates were found to be enclosed into later quartz cement.

Prestholm & Walderhaug (1994) reported the occurrence of poorly developed green chloritic clay rims on some grains in Upper Jurassic sandstones of well NOR-C. Grain coating chlorite was also observed in the same stratigraphic horizon in the adjacent well NOR-D.

K-feldspar overgrowths were found very seldom. They are commonly intensely corroded and it may be that they are inherited from eroded Triassic sandstones in the source area.

Authigenic **pyrite** was found in framboidal form or as crystal aggregates mainly in finer grained clay rich parts of the sandstones. Pyrite framboids were observed inside of leached feldspar grains and partly enclosed by dolomite cement.

Authigenic **barite** occurs occasional inside of corroded feldspar grains.

Brown coloured **bitumen** staining was found frequently in the thin sections. It was more abundant in or adjacent to cataclastic deformation bands.

Feldspar **dissolution** is very common in the two samples from Jurassic sandstones of well NOR-C. The largest part of the feldspar grains is at least partly leached and 30 to 40 % (1.0 to 1.3 % of sample volume) of the point counted porosity is feldspar dissolution porosity. Feldspar dissolution related microporosity seems to be relatively high as indicated by the difference between point counted porosity and porosity measured at core plugs.

Most of the feldspar dissolution seems to have occurred coeval or subsequent to grain framework stabilization by beginning quartz cementation, since corroded feldspar remains appear relatively uncompacted. Nevertheless, eodiagenetic leaching can not completely ruled out.

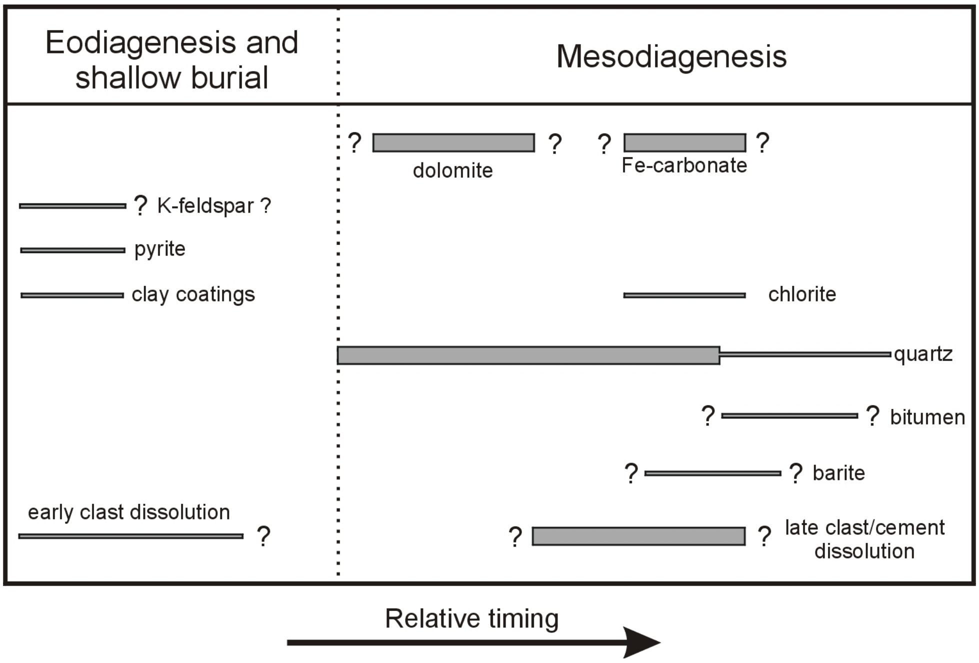

Fig. 6.18: Paragenetic sequence for the Upper Jurassic sandstones in well NOR-C and NOR-D as indicated by textural relationship in thin section. Important authigenic phases and processes are marked with thick bars and minor phases or processes with thin bars.

6.3.2 Well NOR-D

Well NOR-D was drilled as a sidetrack of well NOR-C in order to find a better reservoir since most of the main reservoir of Oxfordian age was removed by faulting in well NOR-C (Jysereid et al., 1994).

Three cores with a total length of 28.15 m were cut from well NOR-D. They cover the upper part of a approximately 50 m thick silty and sandy Upper Oxfordian sequence (Prestholm & Walderhaug, 1994). The cored section is composed of several 3 to 7 m thick coarsening upward sequences which are interpreted to represent marine sediments showing a shallowing trend from offshore to inner shelf/lower shoreface (Prestholm & Walderhaug, 1994). The lower part of such sequences is composed of argillaceous fine-grained sandstones and siltstones with intense bioturbation. The upper part of the coarsening upward sequences consists of mainly fine- to medium-grained, bioturbated sandstones with shell debris rich intervals (Prestholm & Walderhaug, 1994).

The sediment petrography of investigated sandstone samples from well NOR-D is overall comparable to the Upper Jurassic samples from well NOR-C. Rare vermicular kaolinite was found enclosed by quartz cement very seldom in one sample (4612.1) of well NOR-D. Nevertheless, the large proportion of feldspar leaching is not associated with kaolinite neoformation. Three carbonate cemented sandstone samples from well NOR-D were used for stable isotope analysis. All samples contained Fe-carbonates and dolomite in roughly the same proportion as indicated by potassium ferricyanide staining.

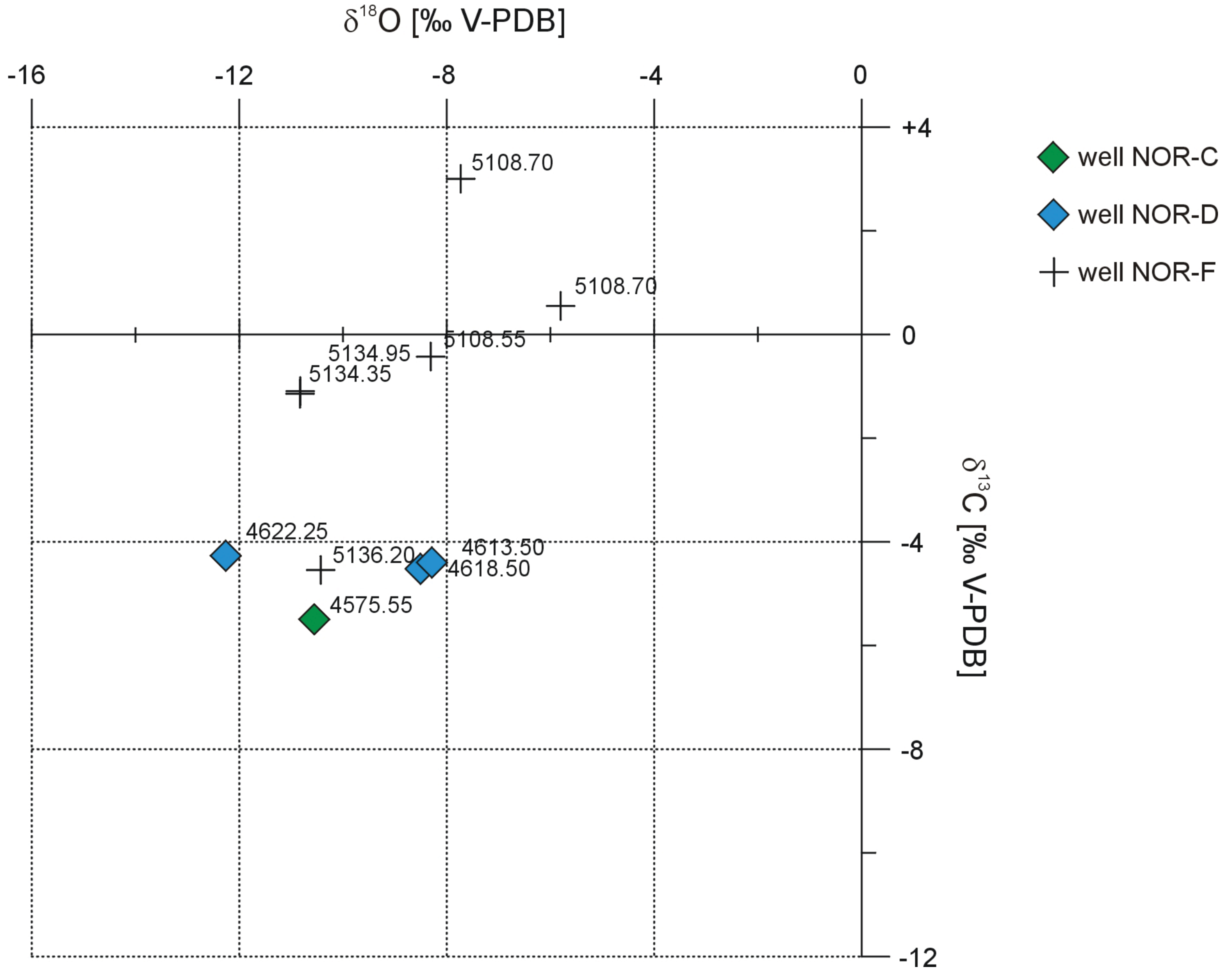

Fig. 6.19: Stable isotope analysis of carbonates via phosphoric acid method at samples of well NOR-C and NOR-D. Most of the samples contain a mixture of different carbonates (dolomite and Fe-carbonates).

6.3.3 Well NOR-F – Farsund Formation and Intra-Farsund Sandstones

The Intra-Farsund sandstones of well NOR-F provide a good example for sandstone diagenesis close (or better inside) of a source rock.

Well NOR-F is one of the two wells in the Norwegian sector covered by the 3D basin model of Neumann (2007) and the well is coded there as well Hydro 171.
Well NOR-F is located relatively close to well NOR-G (approximately 5 km westwards) in a structural deeper position. The well was drilled nearly vertical down to 5310 m (MD) and ended in Upper Jurassic sediments of the Farsund Formation (Tyne Group).

The Farsund Formation (Lower Kimmeridgian to Lower Thitonian) in well NOR-F is predominantly composed of organic rich shales with some interbedded thin fine- to medium-grained, commonly carbonate cemented sandstone beds and minor fine-crystalline limestone layers (Saga-Petroleum, 1994). The sandstone content is increasing towards the base of the unit.

Two conventional cores were cut in the Upper Jurassic Farsund Formation. Core 1 (5105 to 5114 m MD) contained nine metres of black shale. The 3.15 m long core 2 (5134 to 5137.15 m MD) was composed of black shale alternating with thin (cm- to dm-thick) light grey sandstone layers and lenses. Five samples were available from core one and six samples from core 2 for this study.
Conventional core analyses were provided by Saga-Petroleum (1994) for core 2 and showed permeabilities between <0.04 and 0.148 mD and porosities between 1.8 and 11.3 %.
Hydrocarbons were reported from log evaluation of Intra-Farsund Sandstones close to core 2. The deepest part of the Farsund Formation encountered by well NOR-F was found to be water-bearing (Saga-Petroleum, 1994).

A bottom hole temperature of 162°C was measured at 5160 m (MD) and a pressure of 94.4 MPa at 5151 m (MD) (Saga-Petroleum, 1994). Comparable reservoir conditions are likely for the cored intervals.

Detrital composition of Jurassic samples from well NOR-F

Three lithologies are represented by the investigated samples: Black shales, fine crystalline carbonates (only in core 1) and sandstones (only in core 2).
The five samples from core 1 consist of laminated black shales and fine-crystalline carbonates (micrite/microspar). Core 1 contains decimetre-thick zones with mm- to cm-thick Fe-carbonate cemented fractures.
The six samples from core 2 cover predominantly fine- to medium-grained light grey sandstones. One of the samples is composed of black shale.

The black shales are commonly laminated and contain a low amount of silt-sized quartz grains and mica (Fig. 6.20a).
The carbonates are predominantly composed of calcite with minor proportions of dolomite. They have a micrite/microspar matrix with coarser crystalline spots (probably replacing microfossils) and dark brown organic carbon-rich clay flasers (Fig 6.20c). Framboidal pyrite is ubiquitous. Some of the samples contain irregular patches impregnated with brown bitumen. Scattered quartz silt grains are common.

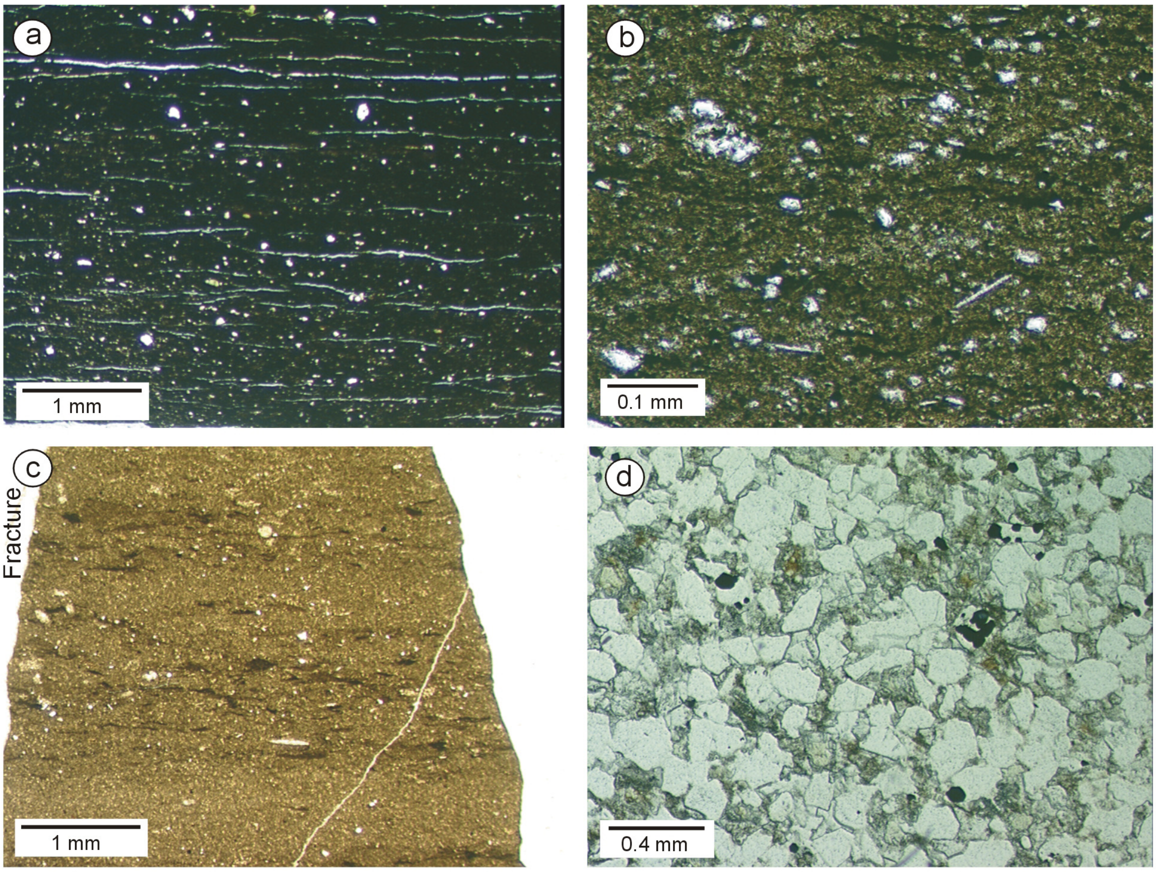

Fig. 6.20: Typical textures of samples from the Farsund Formation in thin section. **a:** Black shale with quartz silt (sample 5109.4, well NOR-F, plane polarised light); **b:** Mudstone part of sample 5136.85 (well NOR-F, plane polarised light); **c:** Fine-crystalline carbonate (sample 5113.65, well NOR-F, plane polarised light); **d:** Carbonate cemented sandstone (sample 5136.27, well NOR-F, plane polarised light).

The sandstones are light grey fine- to medium-grained, well sorted and have predominantly subrounded grains.

The present detrital composition of the sandstones from well NOR-F is overall comparable. They are quartz-rich and plot in the Sublitharenite, Subarkose and Quartzarenite fields of the McBride (1963) diagram (see Fig. 6.21). However, it must be considered that the present feldspar content reflects not the original composition. A notable number of feldspar grains was destroyed during diagenesis and replaced by authigenic clay.

The main detrital phase in the sandstones is monocrystalline quartz (31.3 to 50.3 vol.%). Rock fragments make up between 8 and 13.7 percent of sample volume. Polycrystalline quartz is the volumetrically most important rock fragment (6 and 9.7 vol.%). Metamorphic rock fragments (0…1.3 vol.%), quartz feldspar aggregates (0.3…2.0 vol.%), volcanic (up to 0.3) and sedimentary rock fragments (<0.7 vol.%) occur only subordinate in the sandstones of well NOR-F. The total feldspar content (1.3…3.7 vol.%) is relatively low and represented by plagioclase (1.0…2.3 vol.%) and K-feldspar (0…2.3 vol.%). EMP analyses of some feldspar grains are given in Appendix 3.2. The primary feldspar content seems to have been higher, as indicated by the replacement of grains with authigenic clay minerals. The mica content in the sandstones is relatively low (<0.7 vol.%).

The sandstones contain frequently thin discontinuous layers, lenses and patches of detrital clay or black shale. The proportion of such layers can make up to 35.7 vol.%. However, in cases were the sandstone part of a sample was large enough to be point-counted separately, only the sandstones composition was reported in Appendix 2.3. Some of the sandstones contain a remarkable amount of disperse intergranular clay matrix. Glauconite can occur in minor amounts in the sandstones.

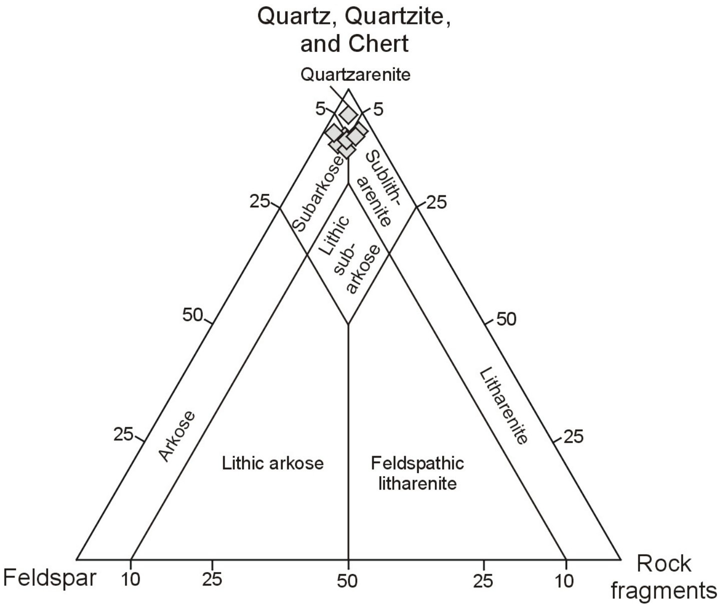

Fig. 6.21: Present detrital composition of Upper Jurassic sandstones from well NOR-F according to McBride (1963). The samples are quartz-rich and plot in the Subarkose, Sublitharenite and Quartzarenite fields. Note, that only the present composition is displayed and that the primary detrital feldspar content was most likely higher (see text).

Pore types and porosity in Jurassic samples of well NOR-F

The investigated samples are completely tight and only scarce visible pores are present. Either the pores in the sandstones are occluded by iron-rich carbonate cement or the porosity was reduced by compaction and quartz cementation. Thus, point-count porosities are very low (up to 0.7 vol.%).

The remaining pores are predominantly secondary grain dissolution pores. Sometimes euhedral quartz crystals and other diagenetic minerals were observed to grow into these pores and therefore it can be excluded that they are artificial.

However, Saga-Petroleum (1994) reported higher porosities between 1.8 and 11.3 % from conventional core analyses. Either the higher porosities were measured at plugs from more porous sandstone layers or the porosity is predominantly microporosity between clay minerals which is not visible in microscope. The low permeability values (<0.04 to 0.148 mD) suggest the latter.

Authigenic phases and diagenesis in Jurassic samples of well NOR-F

The black shales, fine-crystalline carbonates and mudstone parts in the sandstones showed only few authigenic phases visible in optical microscope: Pyrite (up to 21 vol.%), relatively coarse dolomite/ankerite crystals (up to 0.3 vol.%) and bitumen traces.

Zones with sub-millimetre- to centimetre-thick fractures which are filled with iron-rich carbonates were observed in the fine-grained lithologies of core 1.

More authigenic phases were found in the investigated sandstones of well NOR-F: Ankerite (0...22.6 vol.%), clast replacing carbonates (0.3...14.3 vol.%), dolomite (0...3.7 vol.%), kaolinite (0...12.7 vol.%), chlorite (0...7.7 vol.%), quartz (1.0...6.3 vol.%), pyrite (0.3...5.0 vol.%), bitumen (0...5.3 vol.%), albite (up to 0.3 vol.%) and calcite (traces).

The investigated sandstones can be petrographically divided into two groups: Tight pervasively carbonate cemented sandstones and tight intensely compacted sandstones with quartz cement, a relatively high amount of clay matrix and only few scattered carbonate cement crystals.

Ankerite is the main authigenic phase in the carbonate cemented sandstones. It is present as a pervasive pore-filling and grain replacing cement (Fig. 6.24b). Ankerite was observed to enclose and postdate authigenic kaolinite and quartz. However, quartz was also found to overgrow ankerite (see also the diagenetic sequence in Fig. 6.26). Authigenic ankerite was analysed via EMP and the composition is given in Fig. 6.22.
Authigenic **dolomite** occurs as individual scattered crystals and sometimes also grain replacing. Authigenic **calcite** is scarce in the sandstones.

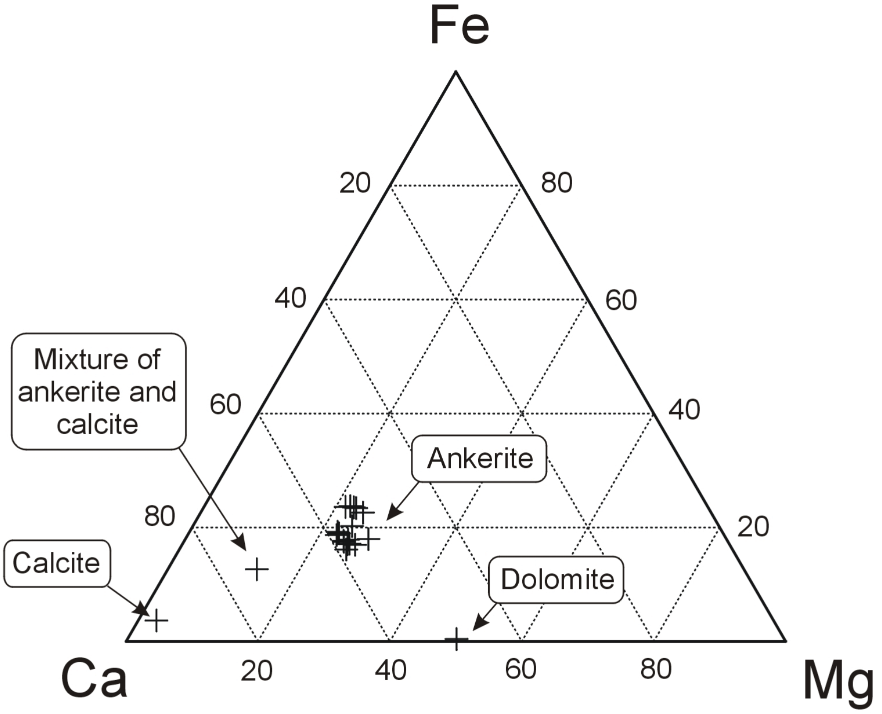

Composition of authigenic carbonates in well NOR-F

Mineral	Typical composition	No. of analyses
Dolomite:	$Ca_{0.98}Mg_{0.98}Fe_{0.01}Mn_{0.01}(CO_3)_2$	1
Calcite:	$Ca_{1.88}Mg_{0.06}Fe_{0.07}(CO_3)_2$	1
Ankerite:	$Ca_{1.03\text{-}1.18}Mg_{0.40\text{-}0.55}Fe_{0.32\text{-}0.47}Mn_{0.00\text{-}0.01}(CO_3)_2$	17

Fig. 6.22: Composition of authigenic carbonates in two samples from sandstones of the Farsund Formation in well NOR-F derived from EMP measurements. The data point between ankerite and calcite represents probably no single mineral composition but most likely a mixture analysis of adjacent ankerite and calcite crystals. The analysed calcite spot seems to comprise also some ankerite.

Stable isotopes were analysed at carbonate bearing samples from well NOR-F using the phosphoric acid method for bulk samples. The fracture filling carbonate was analysed after mechanical separation from sample 5108.7. The results are given in Appendix 5.1 and displayed in Fig. 6.23.

The two calcite microspar samples have δ^{18}O-values of –4.2 and –6.7 ‰ V-PDB and δ^{13}C-values of -0.4 and +0.6 ‰ V-PDB, respectively.

The two sandstone samples cemented with ankerite and dolomite are close to each other with δ^{18}O-values of –10.8 ‰ V-PDB and δ^{13}C-values of –1.1 ‰ V-PDB. The ankerite cemented sandstone has the lowest δ^{13}C-value with –4.5 ‰ V-PDB and a δ^{18}O-value of –10.4 ‰ V-PDB, comparable to the ankerite and dolomite cemented sandstones. The fracture filling iron rich carbonate has with +3.0 ‰ V-PDB the highest δ^{13}C-value. The δ^{18}O-value of the fracture cement lies with –7.7 ‰ V-PDB between the two microspar values. For the discussion of the isotope values see section 8.

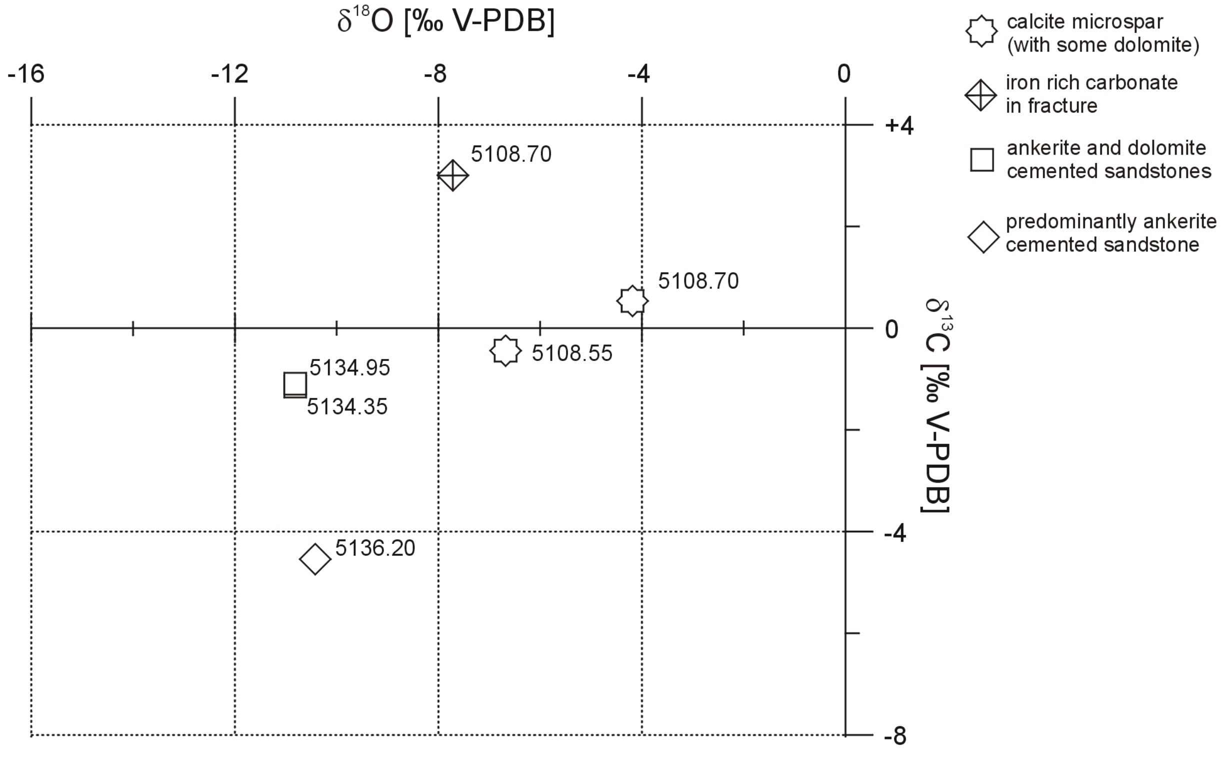

Fig. 6.23: δ^{18}O- vs. δ^{13}C-values from samples of well NOR-F. Some of the samples comprise a mixture of different carbonates.

Authigenic **kaolinite** is abundant in sample 5136.85. This sample represents a small (8 mm thick) sandstone lens enclosed completely into organic rich mudstones. Kaolinite occurs as replacement of grains and in the form of pore filling vermicular aggregates in this sample. Kaolinite is more scarce in the other samples where more authigenic chlorite is developed.

Authigenic kaolinite was found in the form of vermiform aggregates of pseudohexagonal crystals outlining former grains (Fig. 6.24e, f) and as more irregular clay aggregates (Fig. 6.24d) which also indicate a grain replacement. Authigenic kaolinite is frequently stained with bitumen. The relatively coarse plates visible in SEI (see Fig. 6.24f) indicate that a certain part (if not all) of the kaolinite may has been transformed into dickite.

Authigenic **chlorite** was observed in the thicker (of the cm- to dm-thick) sandstone layers in the Farsund Formation of well NOR-F. The chlorite is often associated with diagenetic ankerite and occurs in the form of coarse faint green coloured fans or as irregular aggregates (Fig. 6.25a-f). The fans are composed of up to ~ 50 µm sized platelets.
Chlorite replaces usually grains or occurs in grain dissolution pores (Fig. 6.25a-f). Sometimes feldspar remains (or authigenic albite) are present between the chlorite aggregates (Fig. 6.25d). Chlorite seems to replace kaolinite pseudomorphous in some of the samples as indicated by a faint vermiform of the chlorite. The chemical composition was measured by electron microprobe analysis and gave an iron rich composition. The formula calculated from analysis no. 230 is given as example:

Fe-chlorite: $Mg_{2.34}Fe_{5.55}Al_{3.57}Si_{5.42}Al_{2.58}O_{20}(OH)_{16}$ (6.2)

Authigenic chlorites from Upper Jurassic Farsund Formation sandstones have higher aluminium contents than analysed Triassic authigenic chlorites (see Appendix 3.3). This can also be seen as additional evidence for a kaolinite precursor.

Authigenic **quartz** occurs as syntaxial overgrowths on quartz grains or as euhedral neo-formed crystals in grain dissolution pores (Fig. 6.24c, Fig. 6.25e). The syntaxial overgrowths commonly interlock and form pore filling quartz cements (Fig. 6.24b). This process can create small (sub-mm) patchy completely silica cemented areas. Clear boundaries between the quartz grains and the cement were not always visible. This complicated the quantification by point-count analysis.
Authigenic quartz encloses diagenetic ankerite and is enclosed by ankerite. This indicates that at least a part of the quartz predates and another part postdates ankerite formation. Bitumen was observed to cover partly quartz overgrowths, but bitumen stained clay minerals were also enclosed into later authigenic silica. These observations can be explained by a longer quartz cementation period which was interrupted by bitumen and ankerite formation (Fig. 6.26).

Authigenic **pyrite** is ubiquitous in the samples from well NOR-F. It occurs commonly as small euhedral crystals or crystal aggregates in the sandstones (Fig. 6.24g) and in framboidal form in blacks hales, mudstones and fine-crystalline carbonates. Pyrite seems to be very early in the diagenetic sequence since it is often enclosed by a number of authigenic phases. However, the evaluation of phase relationships was complicated by the fact that pyrite displaces partly detrital grains.

Bitumen is common as brown patchy or pervasive staining of clay rich areas. It can also occur in the form of a liquid like dark brown bitumen between clay mineral aggregates or in remaining pores.

Authigenic **albite** is scarce and was observed in the form of tiny crystals (Fig. 6.25e) in grain dissolution pores.
K-Feldspar overgrowths were observed only at one grain in one sample (5135.6) and they are most likely inherited from a Triassic sediment source.

The **leaching** of detrital grains is indicated by isolated pores outlining the former grain shape. These secondary pores contain usually authigenic phases such as aggregates of quartz, chlorite and albite. Many grains were completely replaced by kaolinite or chlorite without any secondary porosity visible in optical microscope.

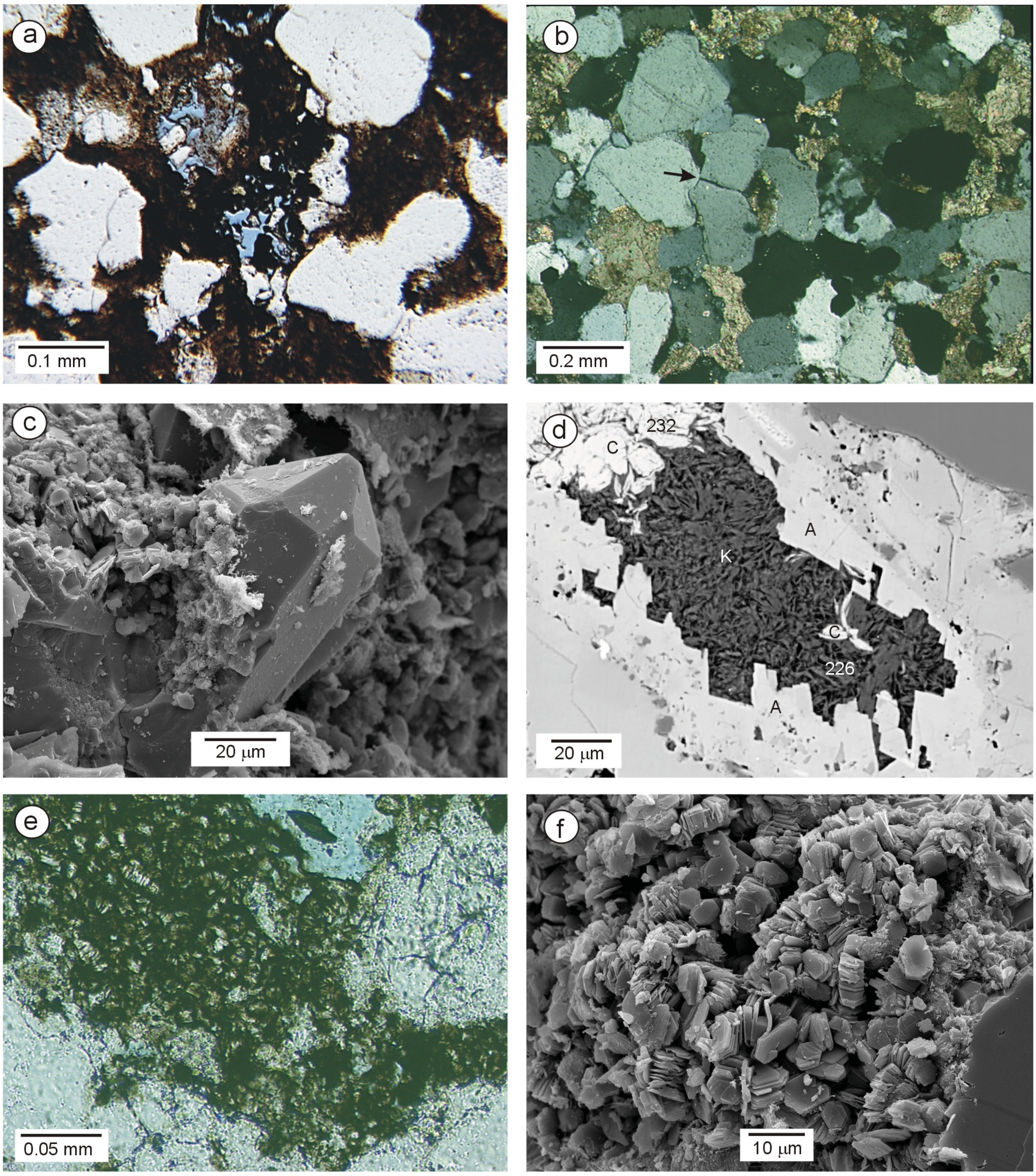

Fig. 6.24a: Remaining porosity (sample 5134.35, well NOR-F, plane polarised light); **b:** Ankerite and quartz (arrow) cemented tight sandstone (sample 5135.6, well NOR-F, crossed polarisers); **c:** Euhedral authigenic quartz growing into one of the few remaining larger pores (sample 5136.85, well NOR-F, SEI); **d:** Grain replacing kaolinite (K) and chlorite (C). Note the ankerite (A) crystals. Numbers give the related analyses in appendix 3 (sample 5136.2, well NOR-F, BEI); **e:** Grain replacing kaolinite (sample 5134.35, well NOR-F, plane polarised light); **f:** Authigenic kaolinite/dickite. Note the microporosity between the platelets (sample 5136.85, well NOR-F, SEI).

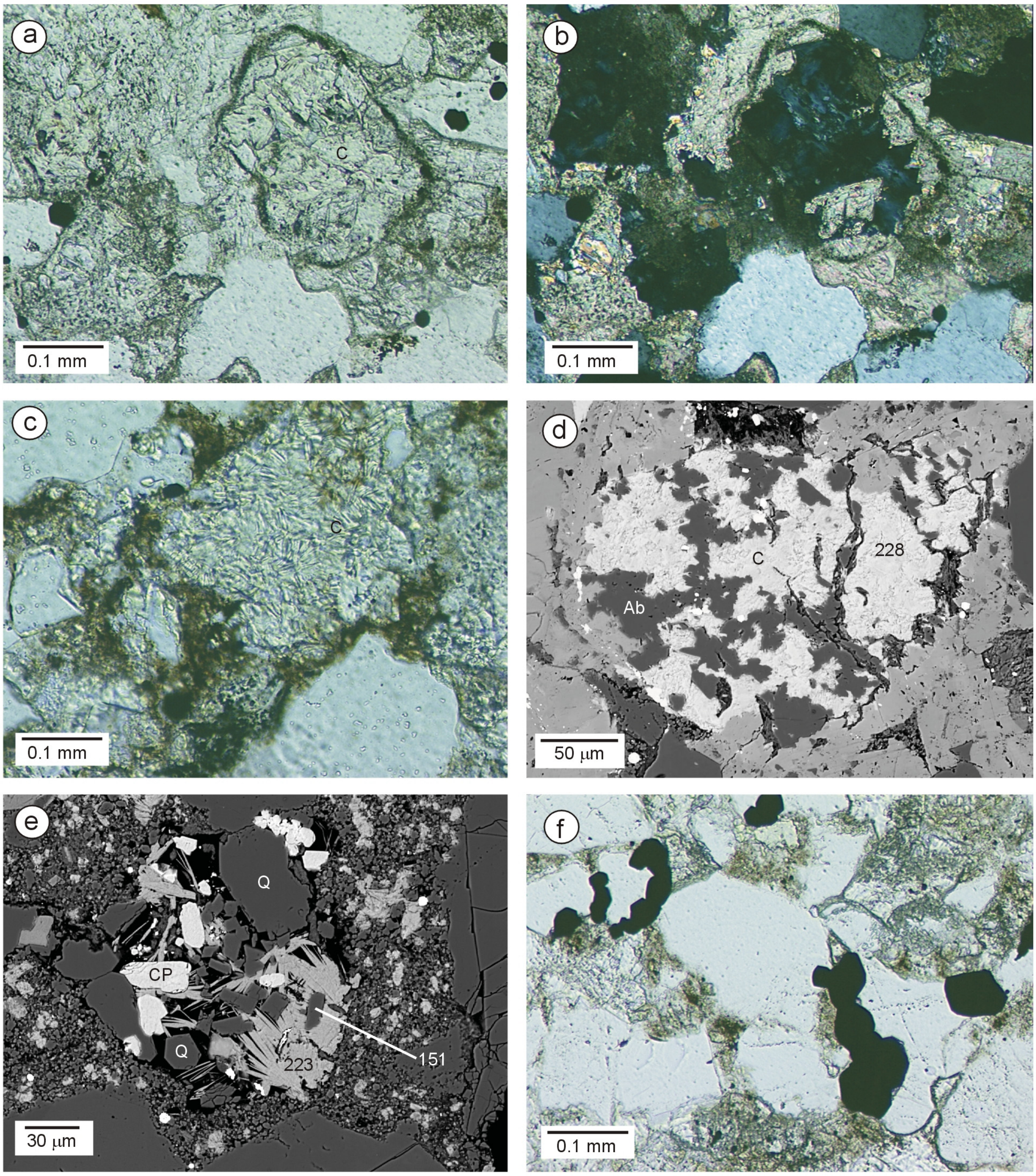

Fig. 6.25a, b: Feldspar? grain replaced by authigenic chlorite (C) and carbonate (sample 5134.95, well NOR-F, a: Plane polarised light, b: Crossed polarisers); **c:** Grain replacing chlorite (C). Note the patchy brown bitumen staining (sample 5136.2, well NOR-F, plane polarised light); **d:** Grain replacing chlorite (C) and albite (Ab). The Number gives the related analysis in appendix 3 (sample 5136.2, well NOR-F, BEI); **e:** Aggregate of chlorite (223), quartz (Q), albite (151) and calcium phosphate (CP). The Numbers give the related analyses in appendix 3 (sample 5136.2, well NOR-F, BEI); **f:** Euhedral authigenic pyrite crystals (sample 5136.2, well NOR-F, plane polarised light).

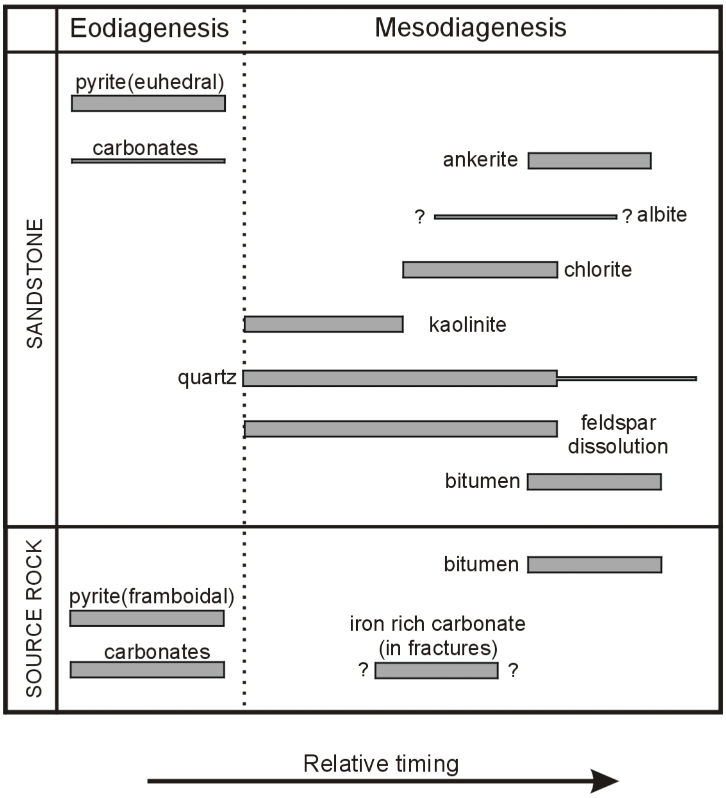

Fig. 6.26: Paragenetic sequences for the investigated Farsund Formation samples from well NOR-F as indicated by observed phase relationship in thin sections and BEI. Important authigenic phases and diagenetic processes are marked with thick bars and minor phases with thin bars.

6.3.4 Well NOR-G – Upper Jurassic lower Ula Formation (Oxfordian)

Well NOR-G is one of the two wells inside of the Norwegian sector 3D basin modelling area of Neumann (2007) and the well is referred there as well Hydro 169.

The well was drilled into a rotated fault block located at a terrace between the Hidra High and the Feda Graben.
It reached the approximately 50 m thick hydrocarbon-bearing lower Ula Formation sandstones at 4340 m MD (4295 m TVDSS) under 150 m shale of the Upper Jurassic Farsund- and Haugesund Formations (De Boer et al., 1992). These organic rich shales are expected to form a thick, robust seal across the structure (Bray, 1992) and act probably as primary hydrocarbon source (De Boer et al., 1992; Jensen et al., 1992; Rose, 1994).
The well reached a total depth of 5258 m and terminated in a Rotliegend mixed volcanic unit (De Boer et al., 1992).

Significant quantities of hydrocarbons were encountered in Upper Jurassic lower Ula Formation sandstones (De Boer et al., 1992). The Ula Formation consists of marine clastic sediments on the graben edge in the Norwegian sector. Sediments in a equivalent position in the UK-sector are known as Fulmar Formation. Nine covered thin sections provided from the industry partner were available from this unit.
Hydrocarbons were also found in the Middle Jurassic Bryne Formation and indicated by log interpretation in low and downward diminishing concentrations in Rotliegend sandstones (Rose, 1994). The Triassic Skagerrak Formation was absent (De Boer et al., 1992). A test of the Rotliegend sandstones produced mainly water with minor amounts of hydrocarbons (De Boer et al., 1992). Three ditch cutting samples were available from the Rotliegend, but too much affected by bit-metamorphism for detailed petrographic investigations and therefore only the nine thin sections from the lower Ula Formation were evaluated in this study.

The Ula Formation of well NOR-G is erosively truncated and comprises fine- to medium-grained sandstones, argillaceous sandstones and silty mudstones. The interval is interpreted to be composed of transgressive, nearshore, shoreface or lagoonal sediments (Bray, 1992).

A detailed description and interpretation of Jurassic facies in well NOR-G was available from (Bray, 1992): The basal part of the Ula Formation is composed of stacked nearshore and transgressive sandstones (Facies T). This interval is overlain by offshore mudstones (Facies O). A shoreface sequence was deposited over these mudstones (Facies LSF, MSF, USF) and lagoonal sediments (Facies L1, L2) are developed in the uppermost part of the Ula Formation. A summary of Jurassic facies is given in Table 6.1. The shoreface and lagoonal sediments were partly cored and the investigated thin sections were made from samples taken from this 18 m core. The core covers the upper part of the hydrocarbon bearing, sandstone dominated lower Ula Formation and contains massive partly bioturbated sandstones, locally with faint horizontal to wavy discontinuous lamination, wave ripples and shell debris (see Fig. 6.31).

Table 6.1: Facies scheme for the Jurassic of well NOR-G (slightly modified after SIMON-ROBERTSON – in Bray, 1992).

Facies association	Facies code	Facies description	Interpretation of depositional environment	Sediment body geometry
Facies association J: Basinal marine sediments	M	Silty locally calcareous mudstones	Deep water basinal mudstones (Farsund Fm. in well NOR-G)	The mudstones are expected to form a thick, robust seal across the structure
Facies association U: Marine shelf sediments	L1	Interbedded mudstones and very fine to fine grained sandstones with bivalves, gastropods and restricted microbiota	Deep lagoonal mudstones with thin, washover sheet sandstones	Interbedded lobate sheetlike sandstones and mudstones are interpreted to be laterally persistent over at least a part of the structure
	L2	Fine grained, locally argillaceous sandstones, forming an erosively based massive, possibly coarsening-upward sequence. Carbonaceous fragments common. Bivalve and gastropod fragments locally present	Shallow lagoonal sediments representing either a lagoon shoreface or fluvially supplied mouthbar	Shallow lagoonal sandstones form broad lenticular to sheetlike units which can extent over field scale as indicated by similar environments
	USF	Clean, fine to medium grained, moderately well sorted sandstones locally with thin, muddy drapes forming massive to locally fining-upward sequences	Clean, relatively coarse, well sorted upper shoreface sediments possibly cut by tidal inlets	The relatively coarse, clean sandstones will form a sheetlike composite sandbody. This facies interdigitates with Facies MSF and may contain discontinous lenses of MSF sandstones
	MSF	Very fine to fine grained, variably argillaceous sandstones, partly flaser bedded and locally burrowed	Below wave-base, tidally influenced middle shoreface sediments	This facies will form a broadly sheetlike unit and can contain elongate, lenticular developments of USF sandstones (tidal inlets and associated ebb tidal deltas)
	LSF	Very fine grained, argillaceous and/or micaceous, burrowed and bioturbated sandstones	Lower shoreface sediments	Probably sheetlike sandbodies
	O	Variably silty and sandy mudstones possibly interbedded with thin argillaceous sandstones	Offshore mudstones representing a relative sea-level high-stand	Offshore mudstones are expected to form field wide permeability barriers
	T	Interval of stacked, blocky to coarsening-upward sandstones forming the base of the marine sequence	Stacked transgressive and nearshore sediments deposited during a phase of shoreface aggradation	The transgressive sandstones form a composite sand sheet. Thickness and facies is related to unconformity topography
Facies association MJ: Alluvial plain sediments	MJ	Heterolithic sequences of fining-upward sandstones, thin discrete sandstones, mudstones and coals	Alluvial plain traversed by channels	Elongate, lenticular fluvial channel sandstones, locally stacked into thicker, more laterally extensive sandbodies, interbedded with persistent mudstones, coals and thin lobate to sheet like sandstones

The lower Ula Formation has an average porosity of 13.8% derived from wireline log data (De Boer et al., 1992). Measured core porosities range from 2.3 to 24.4 % and horizontal permeabilities from < 0.04 to 1530 mD (Bray, 1992). A water saturation of 10.8% derived from DST-measurements was reported by De Boer et al. (1992). Wireline log data show a downward increase in water saturation from close to zero in the uppermost sand unit of the Ula Formation at 4351 m to typically 50 % towards the base of the Bryne Formation, which underlies the lower Ula Formation (De Boer et al., 1992).

A wellhead sample analysed by Core-Laboraties (1992) was dominantly composed of methane (71.7 mol.%) with smaller proportion of ethane (8.5%), propane (3.9%) and other hydrocarbons. The sample had a CO_2 content of 2.7 mol.%.
87.4 MPa and 160°C were reported as average reservoir conditions for the Upper Jurassic lower Ula Formation by De Boer et al. (1992).

Detrital composition of Jurassic samples in well NOR-G
Nine covered thin sections from shallow lagoonal (L2), upper shoreface (USF) and middle shoreface facies (MSF) were provided by the industry partner. Most of the thin sections (6) are from the main reservoir facies – the upper shoreface facies (USF). One thin section is from the shallow lagoonal facies (L2) and two thin sections are from the middle shoreface facies (MSF) – see Appendix 2.3 for details.

The investigated samples are composed of moderately well to very well sorted, very fine- to medium-grained sandstones with varying mud content. The grains are generally subangular to rounded. Most sandstones of the main reservoir facies USF are clean with relatively low mud contents (0…1.2 vol.%). However, the uppermost sample of the upper shoreface facies (USF) has a relatively high content of detrital clay (27.7 vol.%), which is not typical for this facies. This thin section is derived from the top of the USF interval and directly overlain by deep lagoonal sediments of facies L1. The detrital mud was most likely mixed in the former cleaner sandstone by bioturbation. This is also suggested by the sediment texture. The two investigated sandstones of the middle shoreface facies have a mud content of 2.5 and 8.3 vol.%, respectively. The shallow lagoonal facies sample is composed of a very fine-grained sandstone with 4.0 vol.% mud.
The present detrital composition of all investigated Jurassic samples from different facies of well NOR-G is comparable, and they can be classified according to McBride (1963) as Quartzarenites (see Fig. 6.27a), reflecting a mineralogically mature composition.
Monocrystalline quartz (52.0…62.2 vol.%) is the main detrital phase in all samples. Polycrystalline quartz occurs in amounts between 2.8 and 6.7 vol.%. Rock fragments are predominantly composed of quartz-feldspar aggregates and metamorphic rock fragments. They are relatively scarce (0.3 vol.% and lower).
The total feldspar content is low (0.2…1.5 vol.%) and consists predominantly of corroded K-feldspar grains. The observed plagioclase content is generally lower than one volume percent.
The bulk content of detrital feldspar decreases with increasing depth in the cored interval (Fig. 6.31). The primary detrital feldspar content was most likely higher. This is indicated by the presence of feldspar dissolution pores (1.8…4.5 vol.%) which are partly outlined by clay coatings, and the occurrence of authigenic phases like kaolinite, illite and albite in such secondary pores.
Detrital sheet silicates are dominated by muscovite (up to 3.3 vol.%). Biotite and detrital chlorite are also present in some of the samples (up to 0.5 vol.%). Minor components include also shale intraclasts (up to 0.2 vol.%) and heavy minerals (up to 0.5 vol.%).
Plant remains occurred seldom in the investigated thin sections and bivalve shells were reported by Prestholm & Walderhaug (1994) from the core.

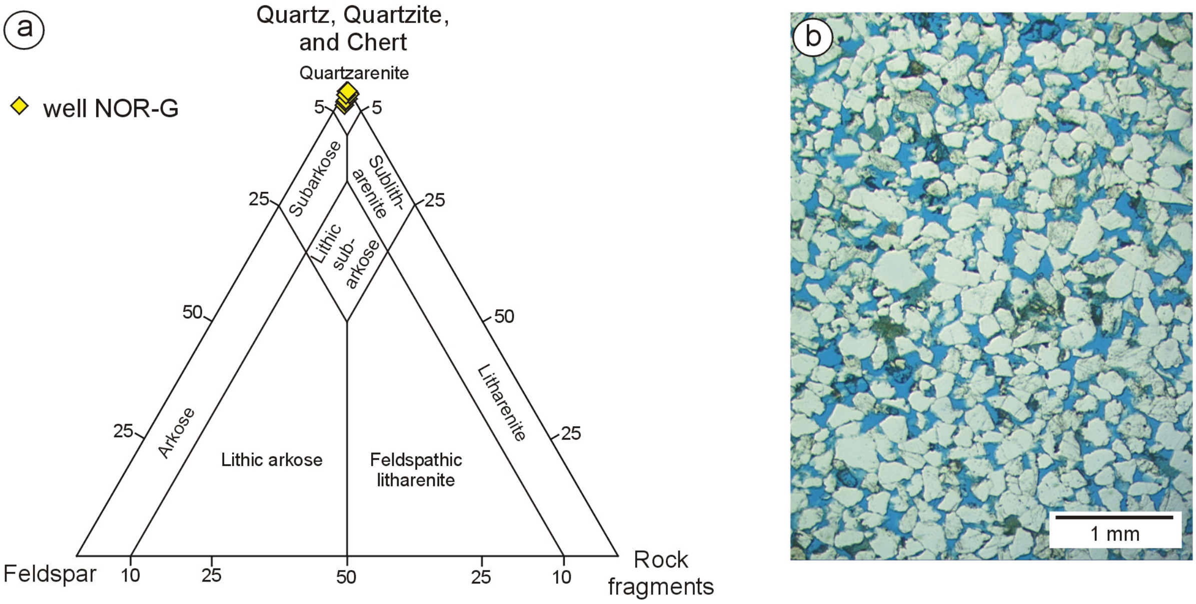

Fig. 6.27a: Present detrital composition of Upper Jurassic samples from well NOR-G according to McBride (1963). All samples plot in the Quartzarenite field. Note, that only the present composition is displayed and the primary detrital feldspar content was most likely higher (see text); **b:** Texture of a typical upper shoreface sandstone (thin section 14260.1, facies USF) from well NOR-G.

<u>Pore types and porosity in Jurassic samples of well NOR-G</u>

The observed bulk point counted porosity ranges from 3.5 to 20.5 vol.% with the highest values in samples from the upper shoreface facies (USF). The lowest value comes from the uppermost sample of the upper shoreface facies with the high mud content.

Prestholm & Walderhaug (1994) reported porosities close to zero percent from a pervasive carbonate cemented sample of well NOR-G.

The observed macropores consist predominantly of intergranular pores (0.3 to 18.2 vol.%) and feldspar dissolution pores (1.8 to 4.5 vol.%). Secondary pores in rock fragments (up to 0.5 vol.%) were found in minor proportions. Oversized pores (up to 0.7 vol.%) and cement dissolution pores (traces) occur also subordinate.

Measured core porosities range from 2.3 to 24.4 % and permeabilities from <0.04 to 1530 mD (Bray, 1992). Best reservoir properties were reported by Bray (1992) from the coarsest cleanest and best sorted sandstones of the upper shoreface facies (USF). Reservoir quality becomes poorer with increasing detrital clay content and decreasing grains size (Bray, 1992). This is also supported by the data of this study (see Fig 6.28).

Micropores occur mainly in detrital and authigenic clay aggregates as well as in corroded feldspars.

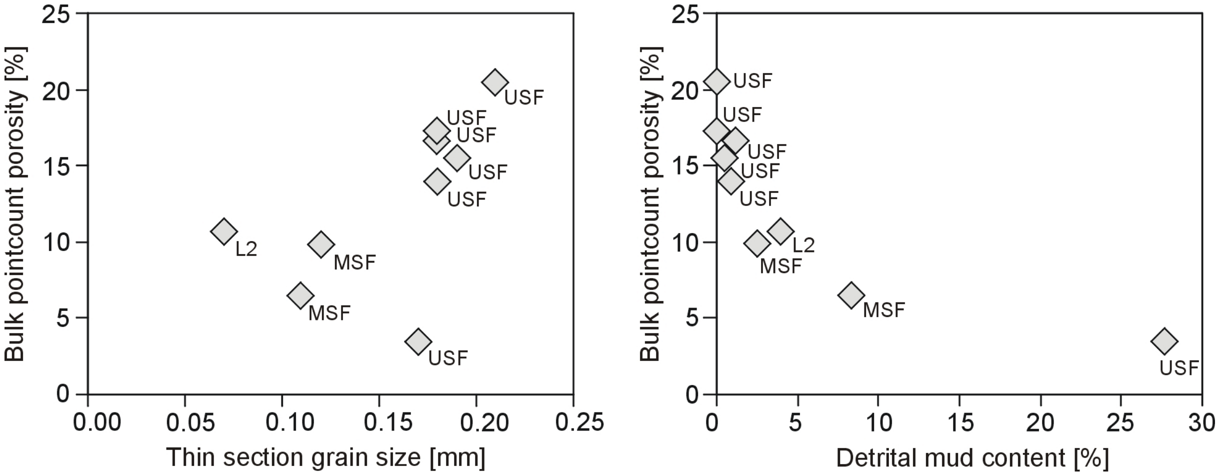

Fig. 6.28: Bulk point-count porosity of the samples from well NOR-G plotted against thin-section grain size and detrital mud content. Facies of the samples is given as label. Highest porosities were observed in coarse clean sandstones of facies USF.

<u>Authigenic phases and diagenesis in Jurassic samples of well NOR-G</u>

Following authigenic phases were found in the investigated samples of well NOR-G: quartz (0.7…13.3 vol.%), bitumen (0…5.3 vol.%), pyrite (0.8…3.2 vol.%), kaolinite (0.3…3.0 vol.%), chlorite coatings (0.2…1.3 vol.%), illite coatings (0…1.5 vol.%), dolomite (0…0.5 vol.%), ankerite/Fe-dolomite (0…1.3 vol.%), albite (up to 0.2 vol.%), barite (0…0.2) and illitic clay flakes (mainly grain replacing) in traces.

Authigenic **quartz** is the volumetrically most important diagenetic phase in most of the samples and occurs predominantly in the form of syntaxial overgrowths (Fig. 6.29e). The content of authigenic quartz is highest in relatively coarse and clean sandstones of facies USF (Fig. 6.31). These overgrowths enclose usually clay coatings, pyrite, dolomite, kaolinite and partly the illitic clay flakes. Quartz overgrowths were frequently observed to be covered by bitumen. However, in some few cases bitumen seems to be partly overgrown by late quartz. Quartz cements were observed to occlude secondary porosity by growing into feldspar dissolution pores. Therefore, at least a part of the authigenic quartz seems to postdate (or be coeval to) the feldspar dissolution. The partly high amount of quartz cement played most likely an important role in the stabilization of the grain framework against mechanical compaction prior the onset of significant overpressure (Bray, 1992). In some of the samples few quartz overgrowths were observed to be enclosed into dolomite. These overgrowths may be inherited or can represent an relatively early phase of quartz cementation.

Bitumen is an volumetrically important authigenic phase in some of the samples (up to 5.3 vol.%). It occurs locally in patches of "tar like" pore lining crusts (Fig. 6.29f) sometimes with tiny fractures (due to shrinkage?). Staining of clay minerals with brownish bitumen is also very common. Bitumen seems to be relatively late in the diagenetic sequence (Fig. 6.30) and was found only seldom to be overgrown by authigenic quartz. A local fracture fill with bitumen was reported by Bray (1992).

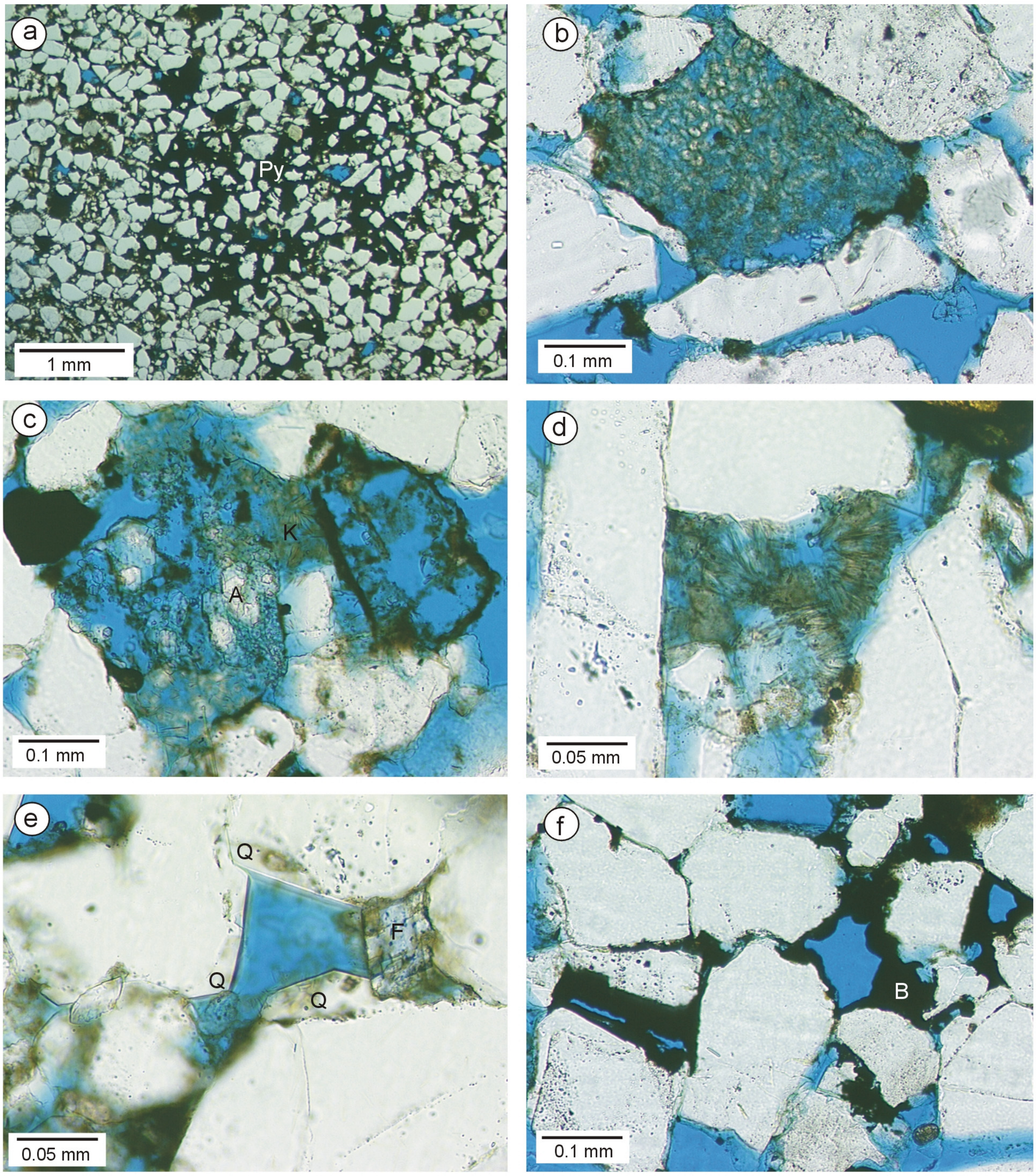

Fig. 6.29a: Pyrite (Py) cemented patch. Note the relatively high intergranular volume (sample 14246, facies USF, well NOR-G, plane polarised light); **b:** Former feldspar grain replaced by authigenic kaolinite (sample 14254, facies USF, well NOR-G, plane polarised light); **c:** Two leached grains – The form of the right one is outlined by a clay rim and filled with diffuse illitic clay flakes and the left one is partly replaced by authigenic albite (A). Note the kaolinite (K) between the two grains (sample 14249.2, facies USF, well NOR-G, plane polarised light); **d:** Kaolinite booklets (sample 14249.2, facies USF, well NOR-G, plane polarised light); **e:** Syntaxial quartz overgrowths (Q) and Fe-carbonate (F) in sample 14269 (facies MSF, well NOR-G, plane polarised light); **f:** Thick pore lining bitumen crusts (sample 14260.1, facies USF, well NOR-G, plane polarised light).

Authigenic **pyrite** was observed in all samples as grain replacing and pore filling cement. It occurs in different forms: Millimetre-sized cement patches, which preserve a high intergranular volume, were present in some of the samples (Fig. 6.29a). Scattered pyrite framboids are also very common. Pyrite was also found in the form of tiny euhedral cube shaped crystals together with framboids in clay rich layers.

The large intergranular volume in the cement patches and the framboidal form point to an early diagenetic origin.

Bray (1992) reported additional a fracture filling pyrite in association with bitumen from the core material of well NOR-G. This pyrite is probably of late diagenetic origin and syngenetic with bitumen.

Authigenic **kaolinite** was found in all samples in the form of scattered aggregates of vermiform kaolinite booklets composed of stacked platelets (Fig. 6.29b, d). The highest amounts were found in samples of the upper shoreface facies (see Fig. 6.31). Kaolinite is commonly replacing former feldspar grains and the kaolinite aggregates outline the former grain shape. However, authigenic kaolinite was sometimes also observed to fill individual pores completely (Fig. 6.29c).

Remarkable is the existence of two different sizes of kaolinite platelets. Some of the aggregates are composed of booklets with finer (~ 10 – 15 µm) and some with coarser (~ 20 – 30 µm) plates.

Kaolinite appears to be locally illitized and probably also partly chloritized.

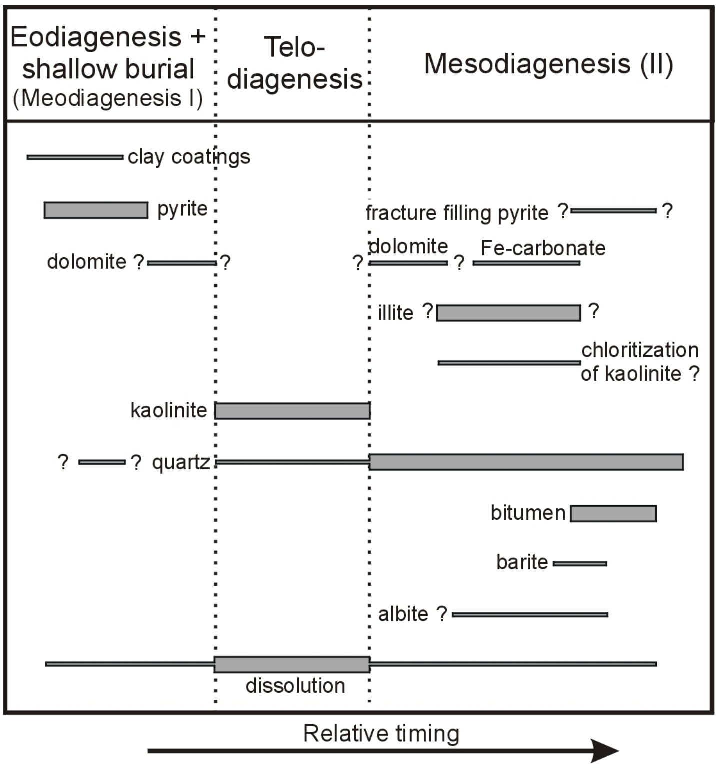

Fig. 6.30: Paragenetic sequence for Upper Jurassic sandstones in well NOR-G as indicated by phase relations observed in thin sections. Important authigenic phases and diagenetic processes are marked with thick bars and minor phases with thin bars.

Scattered grains with **illite coatings** are present in most of the samples in minor amounts. The content of illite coatings seems to increase with increasing depth. **Grain coating chlorite** was also found in relatively low amounts in all samples. Clay coatings are enclosed by a number of other cements and seem to be very early in the diagenetic sequence. They may be at least partially inherited.

Authigenic **illite** occurs in the form of diffuse flakes usually inside of feldspar dissolution pores (Fig. 6.29c). This illite forms no clear fibres or meshworks like the late illite in the Rotliegend wells NOR-A and NOR-B. The illite here is not pervasively scattered throughout the pore space, but occurs in isolated aggregates of diffuse flakes commonly as replacement of former feldspar grains. This type of illite was counted as replacement of grains in Appendix 2.3.
The timing of illite formation is not certain, but seems be relatively late following the main phase of feldspar dissolution (Fig. 6.30). The illitic clay flakes were found to be enclosed into late quartz cements and stained with bitumen.

Dolomite and Fe-dolomite were observed in minor amounts as individual scattered rhomb shaped crystals and inside of feldspar remains. The dolomite crystals showed partly leaching traces in some of the samples. Fe-dolomite enclosed partly kaolinite booklets and was found sometimes postdating quartz overgrowths but also enclosed into quartz cements.
Grey carbonate-cemented intervals were described by Prestholm & Walderhaug (1994) and a locally extensive cementation with pore-filling and grain replacing Fe-dolomite (up to 29 vol.%) was reported for one sample of the middle shoreface facies from well NOR-G by Bray (1992). Prestholm & Walderhaug (1994) found Fe-calcite in half of their investigated samples from Jurassic core material of well NOR-G. This Fe-calcite was described as scattered crystals in secondary pores and in one sample as poikilotopic cement with 28.7 volume percent. However, the sample with the poikilotopic cement is very close to the sample with the extensive pore filling Fe-dolomite mentioned by Bray (1992) and both studies seem to describe the same authigenic phase. Unfortunately, no sample from this interval was available for this study and all of the provided thin section were covered by glass. Thus, the presence of Fe-calcite/Fe-dolomite could not be proven by EMP or SEM-EDX.

Authigenic **albite** crystals were found in traces in some of the samples inside of leached feldspar grains (Fig. 6.29c).

Diagenetic **barite** is very seldom and was observed only in one sample. Barite overgrows authigenic quartz and the timing of barite seems therefore to be relatively late.

Traces of feldspar **dissolution** are ubiquitous**.** Only minor amounts (0.2 to 1.5 vol.%) of the original detrital feldspars remained. Feldspar dissolution pores make up between 1.8 and 4.5 vol.%, and many former feldspars are replaced by kaolinite, illite and albite, respectively. Secondary pores were also found in the feldspatic parts of rock fragments.
The dissolution of cements was not as intensive. Oversized pores (up to 0.7 vol.%) and cement dissolution pores (traces) occur only subordinate. Nevertheless, dolomite crystals show partly leaching traces.
The timing of the leaching event was probably relatively early in the diagenetic sequence (Fig. 6.30), most likely subsequent to shallow burial. However, additional late dissolution can not be excluded.

Fig. 6.31 (next page): Detrital feldspar content, authigenic kaolinite, replacement of grains, secondary porosity, point-count porosity, authigenic quartz and thin section apparent grain size versus depth for Upper Jurassic sandstones in well NOR-G. For explanations see text. The columns sedimentology, lithology and facies were taken from Bray (1992) and slightly modified.

Well NOR-G: Ula Formation (Oxfordian)

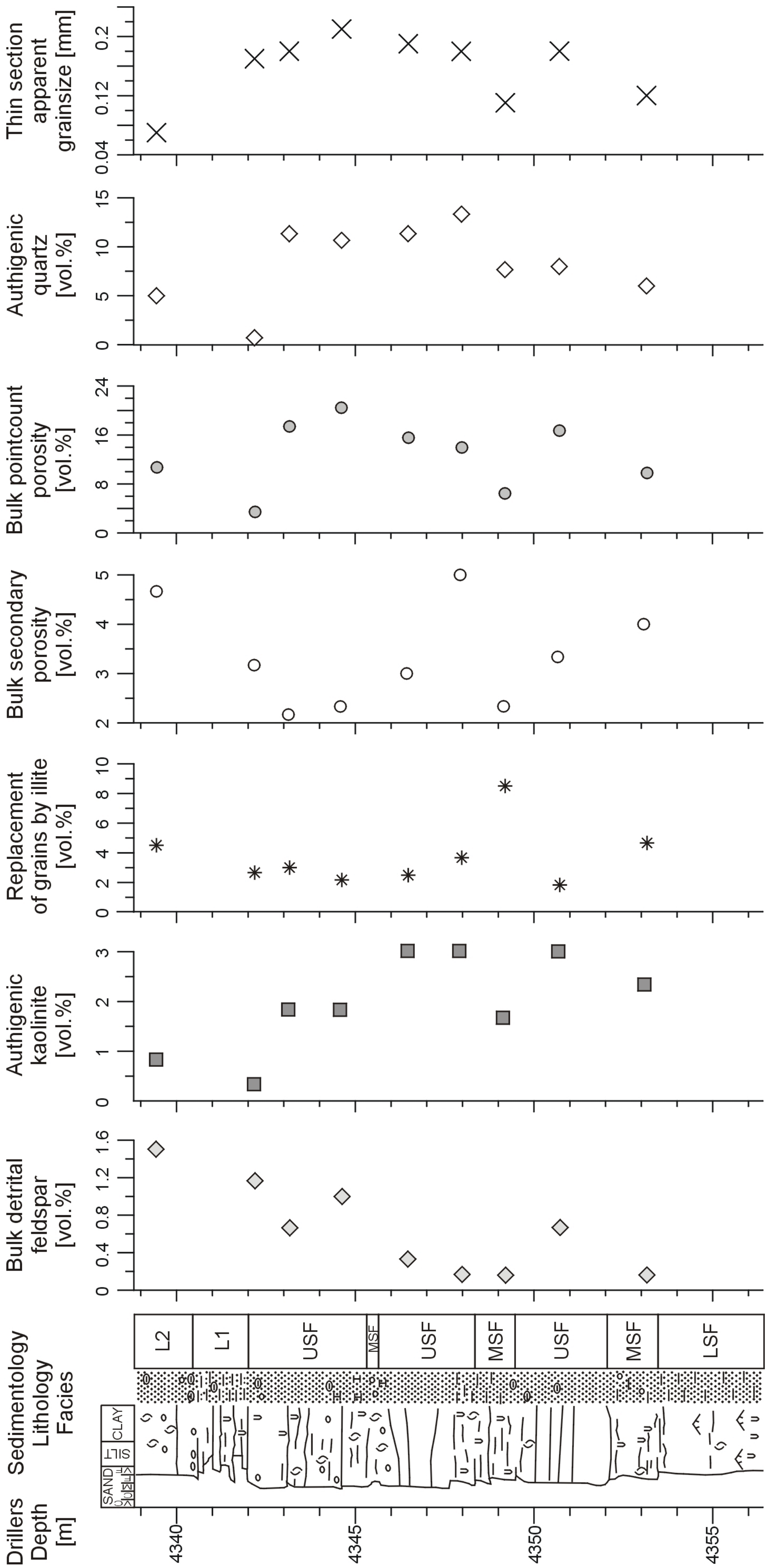

7 Numerical modelling of diagenesis

Numerical modelling was used to test different conceptual models for the diagenetic evolution of the Triassic Skagerrak Formation. These models were formulated using the interpreted compositional changes derived from petrographic observations and geochemical analyses (section 5). The changing stability of mineral assemblages was estimated by the calculation of thermodynamic equilibrium using commercial software.

Main target of diagenetic modelling was to show ways to reproduce some or all of the observed diagenetic changes, in order to develop a better understanding of processes in the studied system. Focus of modelling was the Triassic Skagerrak Formation, since here most information was available concerning formation water chemistry and sediment petrography.
It was tried to get a final system which is comparable to the present days formation water and petrographic composition. However, geochemical modelling is currently not able to reproduce all of the occurring changes (Brosse et al., 2003).

Eodiagenesis occurred at low temperatures and most likely in an open system with fluid exchange. Most of the reactions are kinetically controlled under these conditions and probably do not reach the equilibrium state (Worden & Burley, 2003). Kinetic constants are relatively poorly known for higher salinity waters, and amount and composition of infiltrating eodiagenetic waters is completely unknown. Therefore, modelling focused on mesodiagenetic changes, where equilibrium models could be applied more easily and the reactions are probably less dominated by kinetics (see section 7.2.1).

7.1 Modelling software

The program REACT (part of the software package Geochemist´s Workbench® Standard Release 6.0 from RockWare Inc.) was used to calculate different reaction paths. Reaction equations given in this section were produced with help of the RXN program (also part of Geochemist´s Workbench). Thermodynamic data were taken from the LLNL (Lawrence Livermore National Laboratories) data set provided with Geochemist´s Workbench in the thermo.dat file. Since no thermodynamic data for ankerite was included in the original database, a dataset of the ferrodolomite ($CaFe(CO_3)_2$) end-member of the ankerite solid solution series taken from D.M. Kirste (Australian National University) was added. It must be considered that pure ferrodolomite was hitherto not observed in nature (Deer et al., 1992) and this composition represents not the ankerite observed. However, using this mineral is closer to the "real" system than having no other iron bearing carbonate but siderite. The results of the presented models can be improved by running them again with thermodynamic data for ankerite with the observed composition.
The missing "mole vol." entry of ripidolite in the thermo.dat file was set to 211.680 cc (similar to chamosite) in order to calculate volumes of this mineral from the model runs.
An detailed description of the algorithms and the equations used by REACT can be found in Bethke (1996).

Reactive transport modelling of sandstone mudstone interactions was carried out by R. Ondrak (GFZ-Potsdam) using the software CrunchFlow (C. I. Steefel – Lawrence Berkeley National Laboratory/USA). Results of this modelling are given in the section sandstone mudstone interactions.

7.2 Limitations

A geochemical model can only represent a simplified system and the results of numerical simulation may not completely reproduce the diagenetic changes observed exactly. However, geochemical modelling can be used to learn more about the processes leading to diagenetic changes.

Some limitations must be considered when interpreting the modelling results. Thermodynamic are compiled from different sources. They vary considerable in quality, due to different measurement conditions and extrapolations. Error margins were commonly not reported in compiled datasets (Bethke, 1996).

Thus, the result of a geochemical model depends largely on the used thermodynamic database and the minerals included in this database. This is illustrated in Fig. 7.1: Stability fields and occurring minerals vary in models using different databases. This leads to different stable mineral assemblages using the same water chemistry, temperature and pressure.

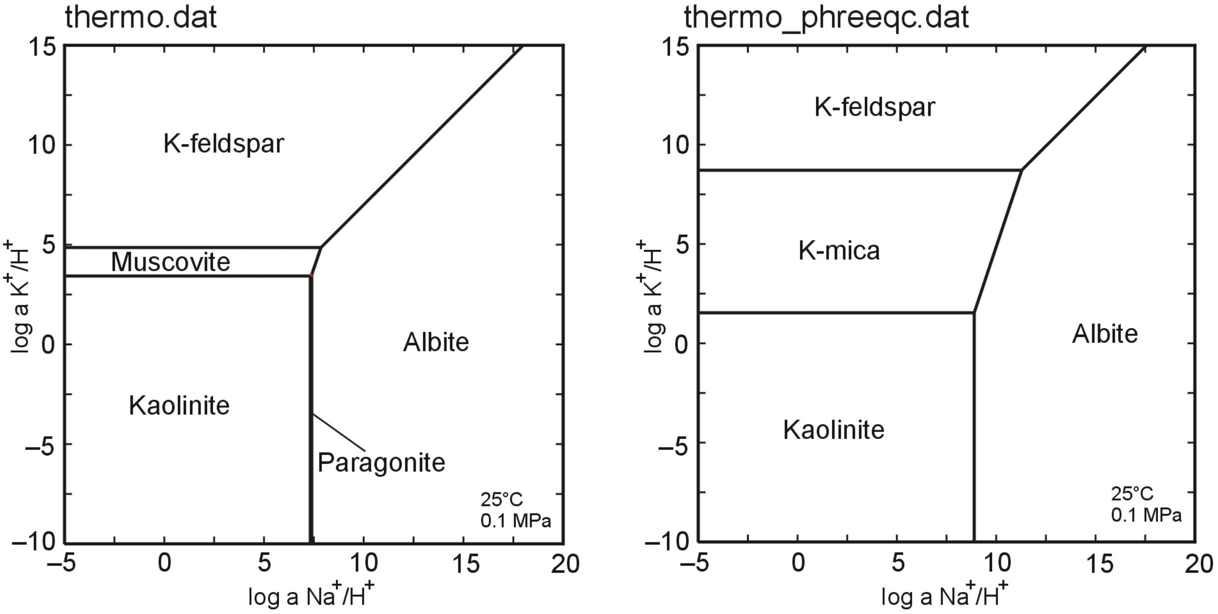

Fig. 7.1: Comparison of stability fields of minerals calculated using different thermodynamic datasets in a sandstone composed of K-feldspar and quartz (temperature 25°C, pressure 0.1 MPa). The stability field of a mineral depends on the thermodynamic dataset used for modelling. The field for Muscovite (illite) for instance, is much smaller if the LLNL database (thermo.dat) is used at same conditions compared to the PHREEQ C dataset.

The number of minerals and aqueous species in the database is limited and some effects are not considered, for instance the formation of aluminosilicate polymers in super-saturated solutions as described by Faimon (1996). Further more, the database contains only clearly defined end-members or minerals with fixed composition from solid solutions series (Bethke, 1996; Kirste et al., 2004) and the precipitation of a solid solution with an evolving composition can not be represented (Brosse et al., 2003). This is a major problem in the studied system, because no ankerite and no chlorite could be reproduced with the measured composition.

In addition to the limited number of minerals in the database, the model can only contain minerals up to the limit imposed by the phase rule. That means that the system can not have more phases than independent components (see Bethke (1996) for details).

Activity coefficients were calculated by the program REACT using the so called "B-dot" model as an modified form of the Debeye-Hückel equation (Bethke, 1996). The model predicts activities of Na^+ and Cl^- ions in concentrations up to 3 molal, and activities of other species to ionic strengths up to about 0.3 to 1 molal with reasonable accuracy (Bethke, 1996). The ionic strength exceeds 3 molal significantly in some formation water samples from the Skagerrak Formation (analyses no. 1 to 3). The B-dot equation is not valid for such high salinities and another activity model would normally be required, which can be applied at higher ionic strength (Fig. 7.2). This problem could be solved theoretically using virial activity models (semi-empirical equations – sometimes referred to as the "Pitzer equations"). Coefficients for the Harvie-Møller-Weare activity model are supplied with the software in the Thermo_hmw.dat database file. But this method has two major drawbacks, which makes it not useful for the modelling of diagenesis in deeper burial siliziclastic settings. First the method treats only solutions in the Na-K-Mg-Ca-H-Cl-SO_4-OH-HCO_3-CO_3-CO_2-H_2O system with no alumina and silica, and second the temperature is restricted to 25°C only (Bethke, 1996).

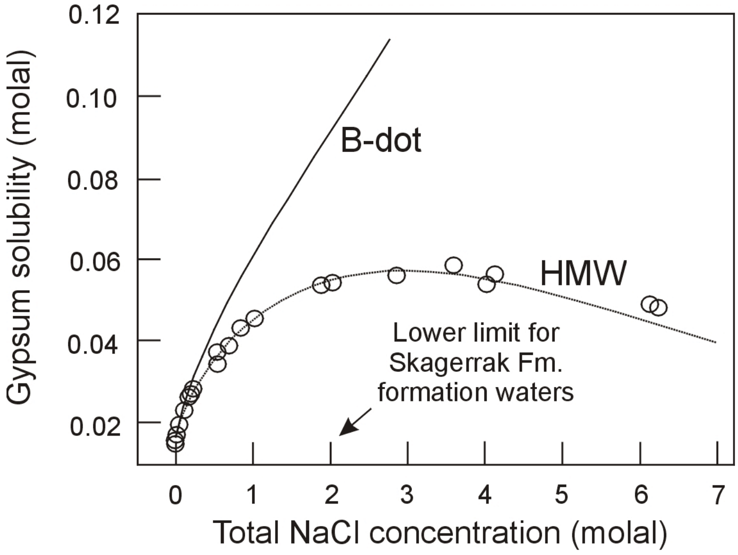

Fig. 7.2: Solubility of gypsum at 25°C at different NaCl concentrations calculated using the Harvie-Møller-Weare and B-dot activity models; experimental data are shown by circles (modified according to Bethke, 1996). The lower limit of NaCl concentrations in waters from the Skagerrak Formation is shown by the arrow.

7.2.1 Kinetics

Thermodynamic models can be used to describe systems were equilibrium is attained, but many geological processes are rather controlled by reaction rates, and can only be understood in terms of kinetics (Rimstidt & Barnes, 1980). For instance, many natural waters are known to be supersaturated at low temperatures (Bethke, 1996) and the rock matrix is not in equilibrium with the pore fluids, especially in low temperature systems (Giles et al., 2000).

However, equilibrium models are still common use because kinetic constants are ill defined for geological systems. Rate constants measured in laboratory represent the conditions of the experiment and may be far away from natural systems. The rate constants are usually determined in deionised water or in diluted solutions. They may differ significantly in solutions with higher ionic strength, like the formation waters of the Skagerrak Formation. Reactive surfaces are poorly known for the studied systems and quantification can be further complicated by clay mineral and oxide coatings (Bethke, 1996 and Xu et al., 2000), as well as by the change in surface area during ongoing dissolution.

Due to these uncertainties, especially the dissolution rates at higher ionic strengths, kinetic effect were not considered in most of the presented models. Only the modelling runs from R. Ondrak used kinetics.

7.2.2 Other effects

There are other important diagenetic effects which can not be considered using REACT. For instance, the modelling approach does not consider mechanical stress and associated dissolution at stylolites and grain contacts. This is an important source for silica leading to quartz cementation during deep burial diagenesis (see section 11 discussion). Porosity loss due to mechanical compaction can also not be considered.

Seeing these limitations, it is not to expect that the given geochemical models can provide a correct replication of all occurring processes. Nevertheless, it can be used to improve the understanding of diagenetic processes and their driving forces.

7.3 Input data

7.3.1 Formation water composition

Formation water analyses must be interpreted with care, because they are relatively prone to different changes, such as the contamination with fluids from other intervals, dilution by water condensed from a gas phase during cooling, loss of CO_2 and other gases during pressure depletion, or the precipitation of minerals during ascent and cooling (Bethke, 1996; Giles, 1997; Warren & Smalley, 1993). Especially the Fe and HCO_3^- values must be taken with care, because of the loss of iron by precipitation of iron hydroxides at contact with atmospheric oxygen and the loss of CO_2 due to degassing during pressure depletion.

A set of formation water analyses was available from Skagerrak Formation intervals of different fields (Table 7.1). The waters are NaCl- to Na-CaCl-brines with a high content of dissolved solids. The analysis with the highest salinity comes from the Heron Field, north-westerly of the study area. Three selected samples from a relatively large dataset of the Judy Field are given in Table 7.1. One analysis represents high-, one intermediate- and one low salinity, in order to show the range of the data. The lowest salinity was measured in the two samples from Jade Field.

Table 7.1: Analyses of Skagerrak Formation waters.

No. Field	1 Heron Field	2 Judy Field	3 Judy Field	4 Judy Field	5 Jade Field	6 Jade Field
well		P1	P3	P5	30/2c-J08	30/2c-J06
pH	-	-	-	-	-	6.74
unit	mg/l	ppm	ppm	ppm	ppm	ppm
Na	87179	75750	67050	51450	32000	20860
K	11400	6900	7020	5760	3600	2630
Mg	1930	1405	693	520	116	92
Ca	45700	22500	20100	10640	2720	5260
Sr	1140	830	693	666	680	366
Ba	1360	21	24	21	198	140
Fe	8	143	77		65	52
Cl	232749	156870	143193	107503	59000	39409
SO_4	0	-	147	176	12	7
HCO_3^-	245	-	73	-	-	-
source	Sinclair & Weston (1996)	Conoco Phillips	Conoco Phillips	Conoco Phillips	Conoco Phillips	Conoco Phillips

Significant variations in water composition are also known from other North Sea formation waters, intra-formational, as well as within field's scale (Warren & Smalley, 1993). Thus, the observed variations reflect most likely different compositions rather than sampling errors. Nevertheless, sampling and measurement conditions are not known and the data quality can not be assessed here.

The Ca/Na ratio increases with increasing salinity, thus waters with higher salinity (Heron, partly Judy) are the Na-CaCl brines, and waters with lower salinity the NaCl-brines (Jade, partly Judy). This was also observed in other formation waters from the central North Sea province (Warren & Smalley, 1994).

High salinity of formation waters from the Skagerrak Formation was most likely inherited from the depositional to early diagenetic system. Depositional patterns of the Skagerrak Formation are closely linked to structures created by the movement of Zechstein salt (see sections 3 and 5). Dissolution of this salt from salt walls and diapirs, which were already present at the time of deposition, may have acted as source of highly saline pore waters. Different salinity could reflect the proximity to the salt source or the amount of mixing with later infiltrated waters from other sources, like meteoric water or water from adjacent formations.

It is also possible that the pore waters were mixed with water from underlying Zechstein via fluid flow during later diagenesis as suggested by Goldsmith et al. (2003). However, formation waters from Zechstein in the central North Sea seem to have a higher sulphate content (e.g. 1845 mg/l in the Piper Field; Warren & Smalley, 1994), than the waters observed. The low sulphate content in the formation waters, the relatively low amount of sulphates and sulphites in the sandstones points against infiltration of waters from underlying Zechstein.

7.3.2 Detrital composition and diagenetic changes

These input parameters are described in detail in section 5 and only a short summary of the diagenetic changes is given in Table 7.2. A summary of detrital composition can be found in Table 5.1 in section 5.

For modelling a simplified sandstone and mudstone[1] composition was calculated from the petrographic data, in order to get an “average” sandstone composition at the end of eodiagenesis and the beginning of deeper burial (Table 7.3). Average sandstone composition was calculated from data of facies FC/SF from Jade Field. Table 7.3 contains the mineral masses in the system, derived from petrographic data of Table 5.1 and 7.2 re-calculated for 25 % porosity represented by 1 kg of water, since the modelling software uses one kilogram water as system.

The initial K-feldspar content in the models was set using the sum of leached and unleached K-feldspar, secondary porosity due to feldspar leaching and the early feldspar overgrowths.
Quartz content is the total of mono- and polycrystalline quartz, assuming that the main part of quartz cement is mesodiagenetic (and therefore later).
Dolomite content is the sum of dolomite nodules, pore-filling dolomite and detrital dolomite nodules. The amount of cement dissolution porosity must also be added, if these pores were formerly filled with dolomite. However, the total amount of a mineral phase has no effect on the modelling result, as long as it is not completely dissolved.
Hematite content was set to the highest value point counted in sandstones of facies association FC/SF, assuming that the hematite content prior bleaching was higher than the most values observed at present day.
Porosity was set to 25 %, a value relatively close to present days porosity. No porosity loss caused by compaction was considered in the models.

---

[1] Mudstones were only used by R. Ondrak in the sandstone-mudstone-interaction model.

Table 7.2: Average authigenic composition and secondary porosity of samples from the Jade and Judy Fields in volume percent of whole rock. The values given in the table are averages and ranges of values (in brackets) from point-count data (Appendix 2.2).

Field	Jade Field [vol.%]		Judy Field [vol.%]	
Facies	AS	FC/SF	AS/SF	FC/SF
Eodiagenesis and shallow burial:				
Dolomite nodules	6.4 (0...23.5)	3.1 (0...27.7)	5.1 (0...53.7)	1.5 (0...17.0)
Dolomite porefilling/rhombs	0.2 (0...1.7)	4.4 (0...34.3)	0.6 (0...6.3)	2.5 (0...18.3)
Hematite coatings	0.2 (0...0.8)	<0.1 (0...0.3)	1.7 (0...14.0)	0.1 (0...2.0)
Leucoxene/anatase	0.4 (0...1.0)	0.9 (0...3.8)	0.7 (0...2.3)	0.5 (0...1.7)
Illite coatings*	0.4 (0...4.3)	-	0.2 (0...1.3)	<0.1 (0...0.3)
Chlorite coatings*	1.5 (0...13.7)	2.5 (0...6.3)	2.7 (0...8.3)	1.2 (0...6.7)
Chlorite intraclast*	4.3 (0...12.8)	0.5 (0...3.8)	0.7 (0...3.3)	0.2 (0...2.0)
K-feldspar overgrowths	0.4 (0...3.0)	6.0 (0...13.5)	3.7 (0...9.3)	5.9 (0...11.7)
Mesodiagenesis:				
Albite	0.1 (0...0.7)	0.6 (0...1.8)	0.5 (0...4.3)	0.4 (0...2.3)
Quartz overgrowths	0.1 (0...1.2)	3.6 (0...25.0)	1.5 (0...4.7)	2.2 (0...9.0)
Calcite	-	-	0.2 (0...5.0)	0.4 (0...6.7)
Ferrous calcite	-	-	1.6 (0...21.3)	0.4 (0...11.3)
Ankerite	0.1 (0...1.0)	1.1 (0...7.7)	0.1 (0...0.7)	0.4 (0...2.3)
Illite grain replacing**	0.6 (0...4.8)	2.1 (0...5.5)	1.5 (0...4.7)	1.6 (0...5.7)
Chlorite plates (5-10 μm)	0.1 (0...1.5)	2.1 (0...11.8)	0.4 (0...5.3)	tr.
Bitumen	0.2 (0...1.0)	0.3 (0...3.0)	0.3 (0...2.7)	0.6 (0...12.7)
Feldspar leaching	<0.1 (0...0.5)	1.3 (0...3.3)	1.3 (0...3.7)	2.5 (0.3...4.7)
Lithics leaching	<0.1 (0...0.2)	0.7 (0...2.5)	<0.1 (0...0.3)	0.2 (0...1.3)
Oversized pores	-	0.5 (0...8.0)	0.3 (0...1.7)	1.0 (0...6.7)
Cement dissolution	-	1.6 (0...8.0)	0.4 (0...3.3)	3.4 (0...9.7)
Number of analyses	15	35	29	41

*likely initially as smectite and later transformed

**may also be of detrital origin

Table 7.3: Simplified sandstone composition at the end of eodiagenesis as input for modelling (calculated from petrographic data of the Jade Field).

	density	average content	simplified system	
	g/cm³	vol.%	vol. % in system	mass for 1 kg water in g
K-Feldspar total	2.56	27.3	28.9	2953.7
quartz total	2.65	31.8	33.6	3563.0
plagioclase (albite)	2.62	1.9	2.0	210.3
dolomite total	2.87	7.9	8.4	957.7
hematite	5.28	2.0	2.1	446.5
porosity			25.0	

7.4 Modelling results

Different models were composed in order to evaluate different possible ways of fluid rock system evolution during mesodiagenesis of the Triassic Skagerrak Formation. Model 1 was designed to test the behaviour of a closed system without any incoming fluids during burial. Model 2 was used to test the effect of CO_2 influx. The effect of hydrocarbons on hematite was modelled in model 3. Model 4 was constructed to see the effect of organic acids. Interactions with fluids from other formations were evaluated in model 5. The interactions between sandstones and mudstones were modelled by R. Ondrak (GFZ Potsdam). His results are also presented here.

Most of the following models were run with a simplified sandstone composition (Table 7.3) and two different water compositions from Table 7.1. The input data for the modelling software are given in Appendix 7.

7.4.1 Model 1: Closed system – simple heating

The effect of temperature increase with burial was simulated by simply heating up a closed sandstone system. Starting point was the end of eodiagenesis after the system was isolated from groundwater flow (open meteoric system) following the deposition of sealing sediments (mudstone member of Skagerrak Formation, in this case the Jonathan Mudstone for the Joanne Sandstone and the Julius Mudstone for the Judy Sandstone).

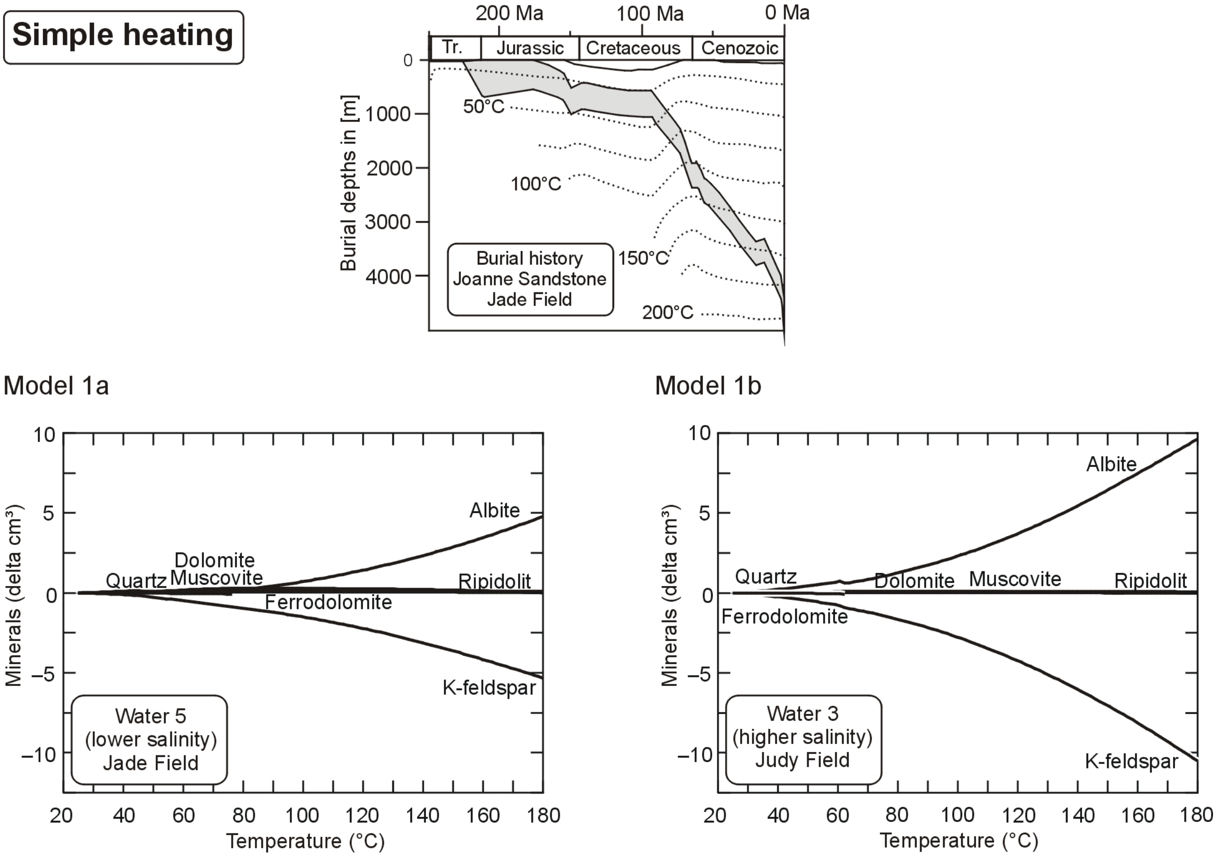

Fig. 7.3: Simple heating of sandstone minerals with different formation waters (Model 1a: Analysis 5, Model 1b: Analysis 3) in order to simulate the effect of temperature increase during burial for the Jade Field Skagerrak Formation sandstone layers.

Temperature was increased in this model from 25°C to 180°C. The K^+ concentration in the initial system was set to be controlled by the equilibrium with K-Feldspar, the Al^{3+} concentration by equilibrium with albite, and the $SiO_{2(aq)}$ concentration by equilibrium with quartz (see input file in Appendix 7).
In real systems the $SiO_{2(aq)}$ concentration would likely be higher, since oversaturation with respect to quartz seems to be common in low temperature natural waters (e.g. Bazin & Brosse, 1997).
The log CO_2 fugacity was set to –3.5 (equilibrium with atmosphere). The precipitation of minerals not observed in the samples and not described in the literature for similar settings was prevented using the suppress option of the software. A lower amount of minerals had to be suppressed if higher CO_2 fugacities, were used. However, the effect of increasing CO_2 is estimated separately in model 2.

Jade Field water (analysis 5 in Table 7.1) with lower salinity was used for model 1a (Fig. 7.3). K-feldspar was dissolved in small amounts and quartz, muscovite[2] and ripidolite (chlorite) were formed in negligible amounts at temperatures < 75°C in the simulation. With temperature increase above 75°C the dissolution of K-feldspar continued, albite became stable and was formed from the dissolution products. The very small amounts of muscovite and quartz[3] were re-dissolved. The model simulated the onset of albite neoformation at higher temperatures than the start of K-feldspar dissolution. This fits to petrographic observations described by Saigal et al. (1988) for different sandstones from offshore Norway.
In summary ~ 5 cm^3 K-feldspar (~ 0.13 vol.% of the fluid-mineral system) were dissolved and nearly the same amount (~ 5 cm^3) of albite was formed from the dissolution products and from Na^+ of the pore water. K^+ content of the pore water increased with increasing temperature from 53 ppm at the beginning to around 1800 ppm at the end of the simulation.

In order to test the effect of the different observed formation waters the same model was restarted with another water composition (analysis 3 from Table 7.1) in model 1b (Fig. 7.3). This formation water has a higher salinity and thus a higher amount of Na^+ was available at the start of the simulation. The effects were generally comparable, but albite formation started at lower temperatures and the amounts of K-feldspar leaching and albite neoformation were higher with ~ 10 cm^3 (~0.26 vol.% of the fluid-mineral system). The K^+ content in the resulting pore water was also higher (3170 ppm).

The average amount of leached K-feldspar observed in thin sections from Skagerrak Formation samples was higher (1.3 to 2.5 vol.%) than predicted by the models. The K^+ content of the modelled final pore water was only the half of that measured in the water analysis, and no secondary porosity was produced by the model. The amount of K-feldspar dissolution is therefore underestimated using only models 1a and 1b for explanation. The amount of albite neoformation is relatively close to the petrographical observed values (observed 0.4 to 0.6 vol.%).

In summary, the simple heating model is too simple to reproduce all observed changes. A completely closed system behaviour is not very likely to have occurred as indicated by the presence of hydrocarbons in the reservoir today. However, this model provides a mechanism for the formation of the observed amount of authigenic albite and the dissolution of a part of the K-feldspar.

---

[2] Since only a Mg-bearing illite is available in the database muscovite was taken as proxy for illite. Leaching of muscovite is not very likely, since detrital muscovite remained relatively unleached in the observed samples.

[3] Quartz dissolution is not likely to have occurred in nature, because the SiO_2 supply by several sources like grain-to-grain contact dissolution is not considered in this model.

Albite formation needs therefore no external Na^+ source and no K^+ sink. Albite neoformation can simply be explained by interaction of sandstone grains with pore water in a closed system with increasing temperatures during burial following the reaction:

K-feldspar[4] + $Na^+ \leftrightarrow K^+$ + Albite (7.1)

Driving force is the changing mineral stability with increasing temperature.

7.4.2 Model 2: The effect of CO_2 influx

Reservoir fluid analysis of the Jade and Judy Fields shows that CO_2 is present in the system. Published values from the Jade Field range between 2.6 and 3.1 mol % (Jones et al., 2005). A number of potential deeper CO_2 sources (e.g. biodegradation, maturation of organic matter in the source rocks, methane oxidation, volcanic gases and dissolution products of carbonates) must be considered. The first charge with hydrocarbons at relatively low temperatures (<40°C) in the Early Cretaceous according to Neumann (2007) and the biogenic stable isotope signature of the CO_2 (M. Lines, pers. communication), points to biodegradation at low temperatures as a major CO_2 sourcing mechanism. CO_2 derived from organic maturation can also have occurred at relatively shallow depths of burial, associated with the first hydrocarbon charge. But CO_2 may also have entered the sandstones at later times, when structurally higher source rocks became mature. The timing of CO_2 generation from source rock maturation predicted by basin modelling (V. Neumann, pers. communication) ranged from Lower Cretaceous (deep basin) to Palaeogene (source rocks at Jade level).

The effect of CO_2 on the given sandstone-pore water system of model 1 was tested using a titration model. Starting point was the model 1a system composition at 30°C. The modelled evolution of mineral composition with increasing CO_2 influx (up to 0.5 mol) is shown in Fig. 7.4. Parts of the K-feldspar (~ 30 cm³ equivalent to 0.8 vol.% of the fluid mineral system) and the largest part of the detrital albite (~ 60 cm³ equivalent to 1.5 vol.%) were dissolved in model 2a (lower salinity pore water). Quartz (~ 40 cm³ equivalent to 1.0 vol.%) and muscovite[5] (~ 40 cm³ equivalent to 1.0 vol.%) were formed from the dissolution products in the model. Small amounts of carbonates, dolomite (~0.4 cm³ equivalent to 0.01 vol.%) and calcite (~ 2.3 cm³ equivalent to 0.06 vol.%) were formed after CO_2 entered the system from the Ca^{2+} and the Mg^{2+} of the pore water and the CO_3^{2-} derived from the reaction set:

$$CO_{2(g)} + H_2O \leftrightarrow H^+ + HCO_3^- \quad (7.2)$$
$$HCO_3^- \leftrightarrow CO_3^{2-} + H^+ \quad (7.3)$$

The dissolution of feldspars (albite and K-feldspar) buffered pH in the model following the reactions:

$$\text{Albite} + 4\,H^+ \leftrightarrow 2\,H_2O + Na^+ + Al^{3+} + 3\,SiO_{2(aq)} \quad (7.4)$$
$$\text{K-feldspar} + 4\,H^+ \leftrightarrow 2\,H_2O + K^+ + Al^{3+} + 3\,SiO_{2(aq)} \quad (7.5)$$

---

[4] Chemical formulas for used minerals are given in Appendix 7.

[5] Muscovite in the model represents the clay mineral illite, since only Mg-bearing illite was available in the dataset.

or written with CO_2:

$$\text{Albite} + 2\ H_2O + 4\ CO_{2(g)} \leftrightarrow Al^{3+} + 3\ SiO_{2(aq)} + Na^{+} + 4\ HCO_3^{-} \qquad (7.6)$$
$$\text{K-feldspar} + 2\ H_2O + 4\ CO_{2(g)} \leftrightarrow Al^{3+} + 3\ SiO_{2(aq)} + K^{+} + 4\ HCO_3^{-} \qquad (7.7)$$

Al^{3+} and $SiO_{2(aq)}$ are known to have relatively low solubilities. A large part of these species was therefore consumed by the neoformation of quartz and muscovite. The main reaction written with quartz and muscovite is:

$$2\ \text{Albite} + \text{K-feldspar} + 2\ H_2O + 2\ CO_{2(g)} \leftrightarrow 2\ Na^{+} + \text{Muscovite} + 6\ \text{Quartz} + 2\ HCO_3^{-} \quad (7.8)$$

With a total volume decrease of solids in the system by 6 cm³ secondary porosity of 0.15 vol.% was created. Assuming that illite was formed in the mudstones and not in the sandstones (see model sandstone mudstone interactions), the amount of secondary porosity created in the sandstone layers would be higher (~ 1.2 vol.%).

The effect of CO_2

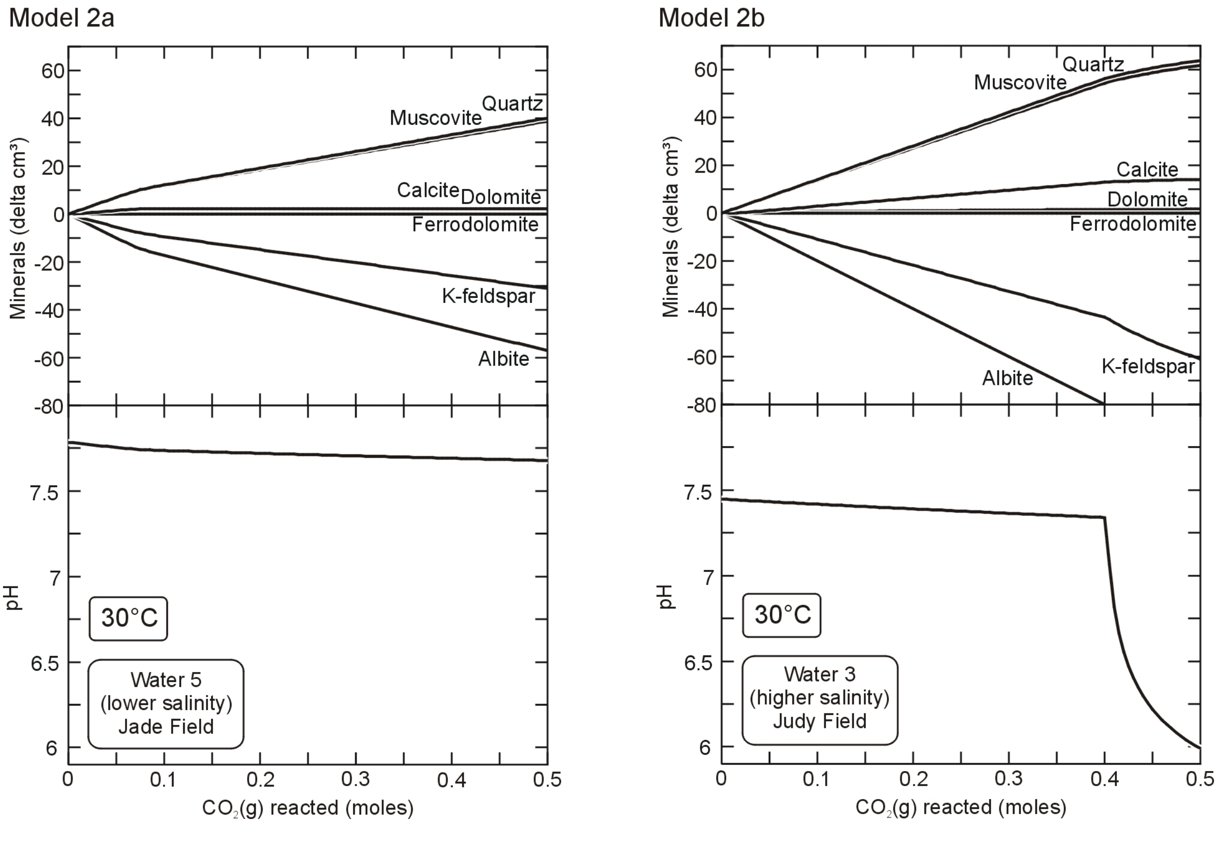

Fig. 7.4: The effect of CO_2 on sandstone mineralogy with different formation waters (Model 2a: Analysis 5, Model 2b: Analysis 3) in order to simulate the effect of infiltrating or biodegradation derived CO_2 on sandstones of the Skagerrak Formation at low temperatures.

The same model was re-run at higher temperatures in order to estimate the effect of temperature on the observed reactions. Generally, the effect of CO_2 on sandstone mineralogy is not as high as at lower temperatures, due to lower CO_2 solubility in the pore water. Ripidolite (chlorite) which was stable in small amounts at higher temperatures initially (see model 1a), dissolved as the first CO_2 entered the system. The euhedral chlorite appears unleached in the investigated sandstone samples. That points against strong effects of CO_2

influx at higher temperatures, but it must be considered that chlorite is covered by thin bitumen coatings and kinetic effects may have retarded dissolution.

The effect of higher salinity in the pore water was tested in model 2b. Albite was leached completely (~ 80 cm^3 equivalent to 2.0 vol.%), more K-feldspar than in model 2a was leached (60 cm^3 equivalent to 1.5 vol.%), and also more quartz (62 cm^3 equivalent to 1.6 vol.%) and illite (64 cm^3 equivalent to 1.6 vol.%), were precipitated. More carbonates have precipitated (1.5 cm^3 equivalent to 0.04 vol.% dolomite, and 14 cm^3 equivalent to 0.36 vol.% calcite) as well.
The precipitation of calcite in some Judy wells can be explained with the influence of CO_2 on higher saline waters (with higher Ca^{2+} content) in contrast to the Jade Field were no calcite could be detected. The average content of calcite observed in the Judy Field (0.4 vol.%) fits very well to the modelled 0.36 vol.%. The high intergranular volume cemented by calcite in the Judy Field samples would indicate CO_2 influx at lower temperatures. However, it must be considered that the observed authigenic calcite is restricted to fracture zones of some wells in the Judy Field.

Despite the enhanced feldspar dissolution, no secondary porosity was created, due to the increasing cementation with carbonates. The increasing reactivity in the model with higher saline pore waters (model 2b) can be explained by the ongoing consumption of CO_2 by carbonate precipitation using the Ca^{2+} and Mg^{2+} from the formation water. Normally, a decreasing CO_2 solubility would be expected with increasing salinity due to the “salting out” effect (e.g. Bethke, 1996)[6].

The CO_2 influx models can explain some of the petrographic observations in thin section. Total feldspar leaching in the models (2.3 to 3.5 vol.%) at low temperatures is close to the observed values (1.3 to 2.5 vol.%). Strong albite dissolution as indicated by both models, was not observed. Detrital albite grains show dissolution traces, but they are not as intensely leached as the K-Feldspar grains.
Dissolution of detrital albite may have been prevented by kinetic effects. However, the simulated enhanced albite dissolution could explain, why authigenic albite was only detected inside of leached K-feldspar grains and not in the open pore space. Neoformed albite may have been protected inside of these grains from leaching fluids in the pore space around. The CO_2 influx models is not able to explain the dissolution of dolomite and the precipitation of ankerite.

Kinetic effects are not considered in these models and the outcome would be probably different if kinetics are considered. For instance, carbonates are known to dissolve more rapidly than silicates in a weathering environment (Gunter et al., 1997 and references therein). Therefore the real system may be buffered rather by carbonates than by feldspars. However, pH in the modelled system is not low enough to force carbonate dissolution.

The presented model did also not consider additional fluid flow. Larger volumes can be dissolved in cases of fluid flow associated with CO_2, as indicated by modelling results of Barclay & Worden (2000a).

---

[6] It must also be considered in all high salinity models that the B-dot equation is not accurate for higher ionic strength (see limitations).

7.4.3 Model 3: Reduction of hematite by hydrocarbons

Petrographic observations in sandstones of the Skagerrak Formation in the Jade and Judy Fields indicate the reduction of former grain-coating hematite. This occurred most likely during the interaction with organic maturation products, which are proven to have entered the reservoir by their recent occurrence. In order to test the effect of hematite reduction by hydrocarbons on the sandstone mineralogy a titration model was used.

Methane forms the largest proportion of the produced hydrocarbons from Jade and Judy Field reservoirs (see Neumann, 2007 and internal industry reports). Therefore methane was used as hydrocarbon phase in the model runs. However, it must be considered that many redox reactions are known to equilibrate very slowly in natural waters at relatively low temperatures, and the oxidation of methane is one of them (Bethke, 1996). The process seems to be inhibited by kinetic factors at lower temperatures. Kinetics were not considered in the presented models, they represent only the thermodynamic equilibrium reactions. Therefore, it may be possible that the reactions calculated by the model do not occur in this way in nature.

Model 3a shows the effect of hematite reduction in formation waters with low salinity (Jade) after the reaction with 0.5 mol CH_4. About 15 cm³ (equivalent to 0.4 vol.% of the fluid mineral system) albite and dolomite, and 5 cm³ (equivalent to 0.1 vol.%) hematite were dissolved. Around 17 cm³ (equivalent to 0.4 vol.%) ripidolite (chlorite), and around 14 cm³ ferrodolomite (equivalent to 0.4 vol.%) were formed from the dissolution products. Quartz and calcite were precipitated in minor amounts (≤ 5 cm³, equivalent to 0.1 vol.%). The pH of the fluid increased during the reaction. The processes seem to cease gradual if the pH exceeds 9.5 (see Fig. 7.5).
Reduction of hematite can be written as:

$$CH_{4(g)} + 15\ H^+ + 4\ \text{Hematite} \leftrightarrow HCO_3^- + 8\ Fe^{2+} + 9\ H_2O \qquad (7.9)$$

If carbonate dissolution and the formation of iron bearing carbonates from HCO_3^- and Fe^{2+} is considered, the reaction is:

$$\begin{aligned} &CH_{4(g)} + 14\ H^+ + 7.5\ \text{Dolomite} + 4\ \text{Hematite} + 0.5\ Ca^{2+} \leftrightarrow \\ &\qquad 9\ H_2O + 8\ \text{Ferrodolomite} + 7.5\ Mg^{2+} \qquad (7.10) \end{aligned}$$

If formation and dissolution of silicates are also involved the reaction becomes more complex:

$$\begin{aligned} &CH_{4(g)} + 3.8\ H_2O + 2.2\ H^+ + 4\ \text{Hematite} + 3.2\ \text{Albite} + 4.8\ \text{Dolomite} \leftrightarrow \\ &\qquad HCO_3^- + 4.8\ \text{Ferrodolomite} + 4.8\ \text{Quartz} + 1.6\ \text{Ripidolite} + 3.2\ Na^+ \qquad (7.11) \end{aligned}$$

If enough Ca^{2+} is in the pore water calcite can be formed from HCO_3^- via the reaction:

$$Ca^{2+} + HCO_3^- \leftrightarrow CaCO_3 + H^+ \qquad (7.12)$$

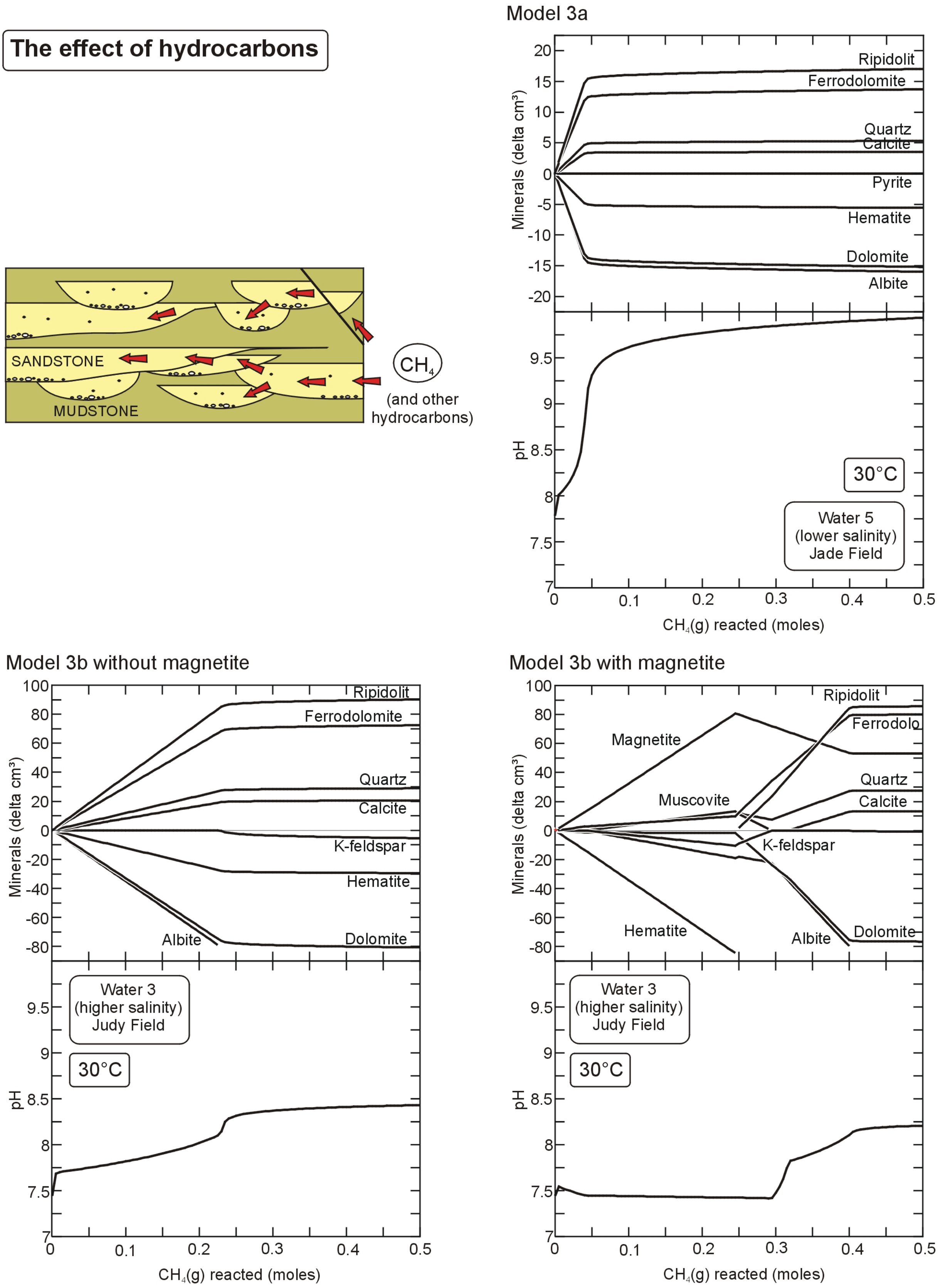

7.5: The effect of hydrocarbons (CH_4 as example) on sandstone mineralogy with different formation waters (Model 3a: Analysis 5, Model 3b: Analysis 3). For explanation see text.

The simulated effect of methane infiltration is much higher in waters with higher salinity (model 3b without magnetite). In model 3b (without magnetite) albite was completely leached (~ 80 cm³ equivalent to 2 vol.% of whole rock fluid system), and K-feldspar started to dissolve after albite was consumed. Moreover, ~ 80 cm³ dolomite (2.0 vol.%) and ~ 29 cm³ hematite (0.7 vol.%) were leached.
The amounts of neoformed products were also higher: ~ 90 cm³ (~ 2.3 vol.%) ripidolite (chlorite), 70 cm³ ferrodolomite (1.8 vol.%), 29 cm³ quartz (0.7 vol.%) and 21 cm³ calcite (0.5 vol.%) were formed (see also Fig. 7.5).
The increase of pH was retarded in the model with higher salinity (model 3b without magnetite) compared to the model with lower salinity. The reason was most likely the higher Ca^{2+} content of the pore water. Ca^{2+} in the pore water allowed the precipitation of carbonates following reaction 7.12. This reactions produced H^+ and prevented the strong increase of pH as long as enough Ca^{2+} was available for carbonate precipitation. Carbonate formation decreased at lower Ca^{2+} contents and pH rose significantly. However, the model was calculated with a ferrodolomite. This mineral has no Mg^{2+} in contrast to the observed ankerite and therefore the role of Mg^{2+} may have been underestimated in all model runs.

The stop of the reaction process at relatively high pH may be, beside kinetic factors, one reason for the observation that methane can be present in recent red bed reservoirs.

The modelled pH-value increased significantly by reactions 7.9 to 7.11 since H^+ was consumed. This favoured the formation of carbonates and chlorite at the one hand (thermodynamically more stable at higher pH), but limited the extent of hematite reduction. This process may explain the high observed pH values reported from some red bed reservoirs (pH>9 reported from red bed brines; see Metcalfe et al., 1994; Schöner, 2006; Warren and Smalley, 1994; and references therein).

Together with H^+ supplying processes (CO_2 or organic acid infiltration/generation) the reduction of hematite by hydrocarbons may be a reaction which is able to explain bleaching, dolomite and feldspar dissolution, as well as ankerite and chlorite formation.
The range of modelled dolomite and feldspar dissolution is only close to observed values of Skagerrak Formation sandstones in the model with high salinity pore waters. Observed cement dissolution average values lie between 1.6 vol.% in Jade Field and 3.4 vol.% in Judy Field and observed feldspar dissolution average values between 1.3 vol.% in Jade Field and 2.5 vol.% in Judy Field. The average observed euhedral chlorite content is 2.1 vol.% in Jade Field. Ankerite is present with average 1.1 vol.% in Jade Field and average 0.4 vol.% in Judy Field.

Several authors suggest the reduction of hematite to magnetite (Barker & Takach, 1992; and others). No magnetite was observed in the samples. Nevertheless, the effect of this reaction was tested in model run 3b with magnetite. Reduction of hematite to magnetite would follow mainly the reaction:

$$CH_{4(g)} + 12\ \text{Hematite} \leftrightarrow H_2O + H^+ + HCO_3^- + 8\ \text{Magnetite} \qquad (7.13)$$

The reduction from hematite to magnetite caused a very minor decrease in pH and no pH increase until hematite was transferred completely into magnetite (Model 3b with magnetite, Fig. 7.5). This reaction produced no Fe^{2+}, which is required for the ankerite/ferrodolomite and chlorite formation.

After all hematite was dissolved, the reduction of the neoformed magnetite started following the equation:

$$CH_{4(g)} + 23\ H^+ + 4\ \text{Magnetite} \leftrightarrow 13\ H_2O + HCO_3^- + 12\ Fe^{2+} \qquad (7.14)$$

This reaction had roughly the same effect as the reduction of hematite without magnetite as intermediate product (see Fig. 7.5).

7.4.4 Model 4: Effect of organic acids on sandstone mineralogy

Effect and occurrence of organic acids as potential leaching agents in sandstones was discussed controversially in the past (see discussion section 11). However, carboxylic acids at concentrations as high as 1000 mmol were observed in recent oilfield brines (Seewald, 2003). Different potential sources for organic acids must be considered, for instance biodegradation of hydrocarbons, organic maturation in source rocks, and the reaction of n-alkanes in the reservoirs (see Seewald, 2001b and Seewald, 2003). Biodegradation and the reactions proposed by Seewald (2001a), Seewald (2001b) and Seewald (2003) are the most likely sources for organic acids in the studied Skagerrak Formation reservoirs.

A titration model was used to estimate the effect of organic acids on the sandstone-water system. The presence or absence of hematite in the sandstones would led to different reactions. Therefore, models were run with and without hematite.

The effect of HCH_3COO was generally comparable to the effect of CO_2 in the model without hematite reduction (see Fig. 7.6 and compare with Fig. 7.4). Albite (23 cm^3 equivalent to 0.6 vol.%) and K-feldspar (12 cm^3 equivalent to 0.3 vol.%) were dissolved after the reaction of 0.2 mol HCH_3COO in the model with low salinity (model 4a). About 16 cm^3 (equivalent to 0.4 vol.%) muscovite (illite proxy) and quartz were formed as main reaction products. Minor amounts of calcite and dolomite were formed additional. The decrease in solid volume was relatively small with 1 cm^3 (equivalent to 0.03 vol.%). Therefore, the gain in porosity can be neglected if illite was precipitated in the sandstones.
Dissociation of acetic acids produced H^+ following the reaction:

$$HCH_3COO \leftrightarrow H^+ + CH_3COO^- \qquad (7.15)$$

and caused the dissolution of feldspars:

$$4\ HCH_3COO + \text{Albite} \leftrightarrow 4\ CH_3COO^- + 2\ H_2O + Na^+ + Al^{3+} + 3\ SiO_{2(aq)} \qquad (7.16)$$
$$4\ HCH_3COO + \text{K-feldspar} \leftrightarrow 4\ CH_3COO^- + 2\ H_2O + K^+ + Al^{3+} + 3\ SiO_{2(aq)} \qquad (7.17)$$

Due to the low solubility of Al^{3+} and $SiO_{2(aq)}$ muscovite and quartz were formed, like in the CO_2 –infiltration model:

$$4\ HCH_3COO + 4\ \text{Albite} + 2\ \text{K-feldspar} \leftrightarrow$$
$$4\ CH_3COO^- + 4\ Na^+ + 2\ \text{Muscovite} + 12\ \text{Quartz} \qquad (7.18)$$

The effect of organic acids

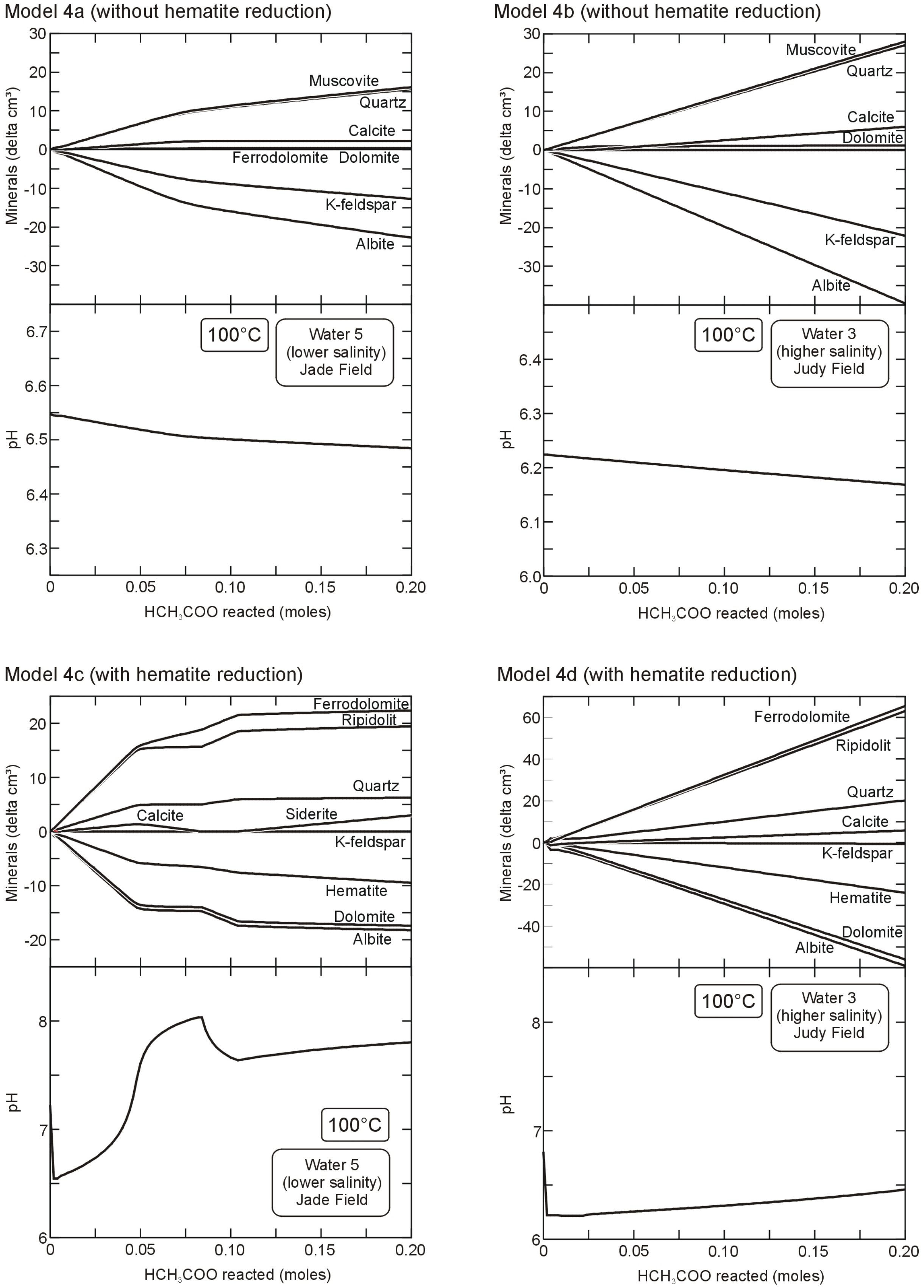

Fig. 7.6: The effect of organic acids on sandstone mineralogy with different formation waters and sandstone mineralogy (model 4a and 4c with analysis 5, model 4b and 4d with analysis 3). For explanation see text.

The effect of 0.2 mol HCH_3COO in higher saline waters was also more intense, comparable to the CO_2 titration model (Fig. 7.6). About 40 cm³ (1.0 vol.%) albite and about 22 cm³ (0.6 vol.%) K-feldspar were leached. 28 cm³ (0.7 vol.%) muscovite and quartz were formed from the dissolution products. Additional 6 cm³ (0.2 vol.%) calcite and minor amounts of dolomite were predicted to precipitate. The effects were slightly lower in model runs at higher temperatures.

The effect of HCH_3COO infiltration was different in a model with hematite in the sandstone (Models 4c and 4d), which considered the reduction of hematite by the organic acid:

$$HCH_3COO + 14\ H^+ + 4\ \text{Hematite} \leftrightarrow 2\ HCO_3^- + 8\ H_2O + 8\ Fe^{2+} \quad (7.19)$$

The results of these models were rather comparable to the infiltration of CH_4 than to the infiltration of CO_2 (see Fig. 7.6 and compare with Fig. 7.5). Increasing Fe^{2+} content forced the precipitation of iron-bearing phases.
In contrast to the CH_4 models the pH showed a different evolution since H^+ was supplied by the organic acid. After initial drop in pH, the reduction of hematite started. This reaction consumed H^+ following reaction 7.9 and the pH rose again comparable to the CH_4 model.

The results of the model run after the infiltration of 0.2 mol HCH_3COO in the low salinity model with hematite were: Dolomite (~ 17 cm³ = 0.4 vol.%), albite (~ 18 cm³ = 0.5 vol.%), hematite (~ 9 cm³ = 0.3 vol.%) and minor amounts of K-feldspar were leached. Ferrodolomite (~ 22 cm³ = 0.6 vol.%), ripidolite (~ 19 cm³ =0.5 vol.%), quartz (7 cm³ = 0.18 vol.%), and minor amounts of siderite (3 cm³ = 0.1 vol.%) and calcite (only in the first phase afterwards with increasing Fe^{2+} content it was replaced by siderite) were precipitated. The total volume of reaction products was by 6 cm³ larger than the initial system. Therefore, net-porosity was destroyed without export of dissolution products.
A summary reaction of this model can be written as:

$$\begin{aligned} &HCH_3COO + 4.5\ \text{Dolomite} + 4\ \text{Hematite} + 6\ H_2O + 0.75\ Mg^{2+} + 3.5\ \text{Albite} \leftrightarrow \\ &\quad 2\ HCO_3^- + 1.75\ \text{Ripidolite} + 4.5\ \text{Ferrodolomite} + 5.25\ SiO_{2(aq)} + 3.5\ Na^+ \quad (7.20) \end{aligned}$$

The effect of HCH_3COO infiltration was higher in the model with hematite and higher salinity (model 4d, Fig. 7.6): Dolomite (~56 cm³ = 1.4 vol.%), albite (~59 cm³ = 1.5 vol.%) and hematite (24 cm³ = 0.6 vol.%) were dissolved. Ripidolite (~63 cm³ = 1.6 vol.%), ferrodolomite (~66 cm³ = 1.6 vol.%), quartz (~21 cm³ = 0.5 vol.%) and calcite (6 cm³ = 0.15 vol.%) were precipitated. The solid reaction products had a higher volume (15 cm³ = 0.4 vol.%) than the initial minerals in the system. Therefore, porosity was also destroyed here.

7.4.5 Model 5: Effect of fluid flow derived from adjacent formations

The effect of water derived from adjacent mudstones on Skagerrak Formation sandstones was tested in this model. The flush option of the Geochemist´s Workbench® was used to displace the existing pore fluid by the new fluid type.
The total amount of fluids derived from the compaction of mudstones was calculated by 3D basin modelling (section 4). These values were compared with the maximum water volume in the reservoir (porosity) to determine how many times the fluid volume of the reservoir can be replaced.
The model was run with some assumptions which resulted in the maximum case for fluid flow: All compactional water from the drainage areas of Jade was focused only through sandstones of the Joanne Sandstone Member, no hydrocarbons are in the pore space (all porosity is water) and the porosity is that of present day level (average ~ 17 % according to Jones et al., 2005). The total amount of compactional fluids from all stratigraphic levels derived from the Jade drainage area (see section 4) would be able to replace the fluids in the sandstones of the Joanne Sandstone Member (if no other fluid migration routes like faults are considered) by 226 times. This number seems to be unrealistic high since most of the compactional fluids would escape via faults. If only the compactional water derived from the Kimmeridge Clay Formation flushes through the Joanne Sandstone the fluid can be replaced by ~ 42 times.

This case was modelled by model 5 (Fig. 7.7) in order to estimate the effect of fluid flushing. Composition of Kimmeridge Clay Formation water was taken from the 211/11-1 well (North Sea formation water atlas; Warren & Smalley, 1994). Two cases were modelled: Constant temperature over the model run for better estimation of fluid effect and increasing temperature (considering increasing burial depths with time).

The first model run with constant temperature (100°C) calculated the dissolution of albite (~50 cm^3 = 1.3 vol.%) and K-feldspar (~57 cm^3 = 1.5 vol.%). Muscovite (48 cm^3 = 1.2 vol.%), quartz (47 cm^3 = 1.2 vol.%) and calcite (13 cm^3 = 0.3 vol.%) were predicted to precipitate.

The model with increasing temperature (30-180°C), which is more realistic, predicted also the dissolution of albite (37 cm^3 = 1.0 vol.%) and K-feldspar (65 cm^3 = 1.7 vol.%), as well as the precipitation of muscovite (45 cm^3 = 1.2 vol.%), quartz (44 cm^3 = 1.1 vol.%) and calcite (13 cm^3 = 0.3 vol.%). The difference between these two models was, that at higher temperatures albite dissolution stopped and re-precipitation started. This effect is comparable to albite precipitation from K-feldspar in the closed system of model 1. The process is controlled by the changing stability of albite vs. K-feldspar with increasing temperature (see equation 7.1).

The infiltrating water from the Kimmeridge Clay Formation contained H^+. This caused feldspar dissolution. Total amount of K-feldspar dissolution is comparable to petrographical observations (see Table 7.4). However, it must be considered that the model represents the maximum case of possible focused fluid flow. In the real system much of the compactional water would escape via faults as indicated by observations of Haszeldine et al. (1999) and bypass the reservoir. Relatively high amounts of Kimmeridge Clay Formation water have to flush the sandstone layers of the Skagerrak Formation to explain some of the observed diagenetic changes.

Fluid flow derived from compaction of mudstones

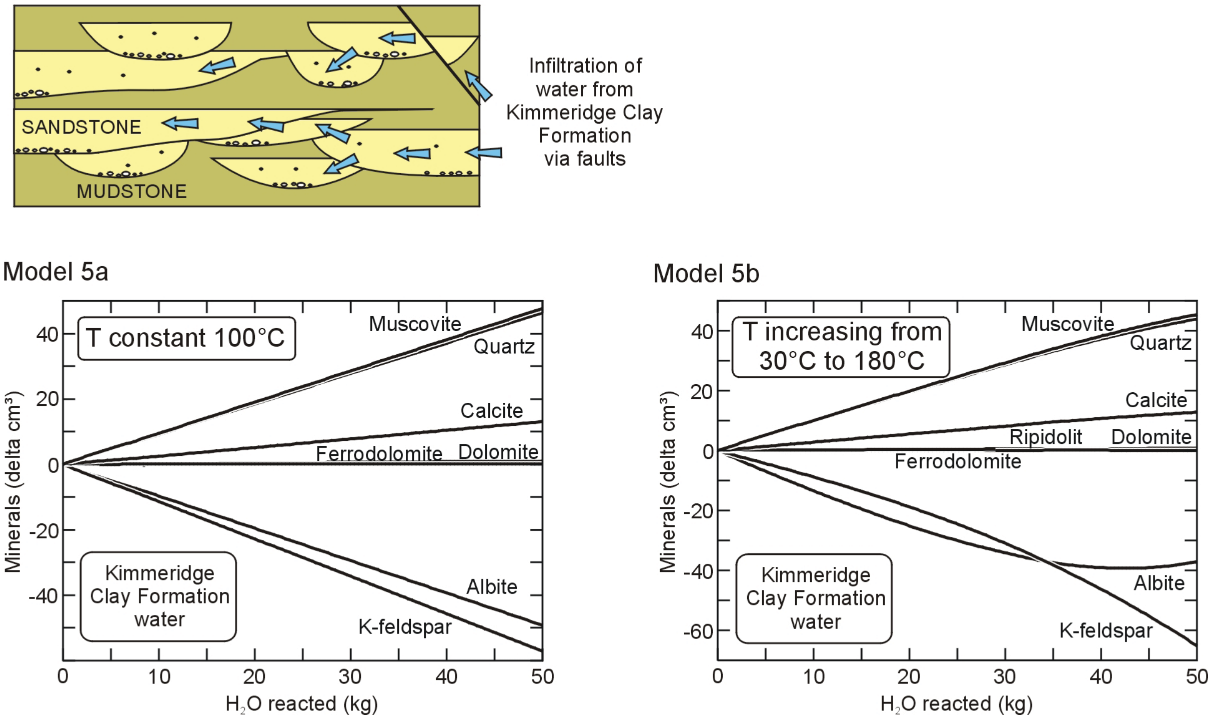

Fig. 7.7: The effect of water derived from the compaction of mudstones in the adjacent Kimmeridge Clay Formation. For explanation see text.

Minor amounts of Kimmeridge Clay Formation water may have infiltrated the Skagerrak Formation sandstones in association with hydrocarbon charge. The relatively high salinity in present days pore waters indicates minor or no exchange with lower saline pore water from the Kimmeridge Clay Formation. Thus, flushing of Skagerrak Formation sandstones with Kimmeridge Clay Formation water is unlikely to have occurred on a regional scale. However, it may have been a local phenomenon close to faults, or in single compartments. The later could be one explanation for the measured differences in Skagerrak Formation water composition today.

Calcite precipitation was the result of infiltration of Ca^{2+} and HCO_3^-. Both species were set to be in equilibrium with calcite in the incoming water, but feldspar dissolution caused a drop in pH by consuming H^+ and calcite was precipitated. This process is another possible explanation for the local occurrence of calcite close to faults in some wells of the Judy Field.

7.4.6 Sandstone mudstone interactions

In some of the presented models illite (modelled as muscovite) was predicted to precipitate in relatively large amounts associated with K-feldspar dissolution. The observed illite in thin sections is represented by illitized clasts and grain coatings only. Fibrous meshwork forming illite was not found in any samples from the Triassic of the Jade and Judy Fields. If the illitized clasts are of detrital origin (not unlikely), then the amount of neoformed illite in sandstones is too low, compared to the amount predicted by the previous models.

There are indications that smectite-to-illite transformation had occurred in the mudstones of the Skagerrak Formation (see section 5 and 9). Significant diffusive mass transfer between adjacent sandstones and shales can occur over distances of 5 to 10 meters and was tested via modelling by Tyne (2001). Smectite-to-illite transformation in the mudstones combined with diffusive mass transport can be an explanation for the apparent lack of authigenic illite in the sandstones as shown by the following model:

A reactive transport model was composed by R. Ondrak (GFZ Potsdam) with CrunchFlow in order to test the effect of sandstone mudstone interactions (see also Schöner et al., 2008). Illite precipitation was kinetically inhibited in sandstones. The initial smectite composition is not known. Beidellite-Mg and Beidellite-Na were used for the model.

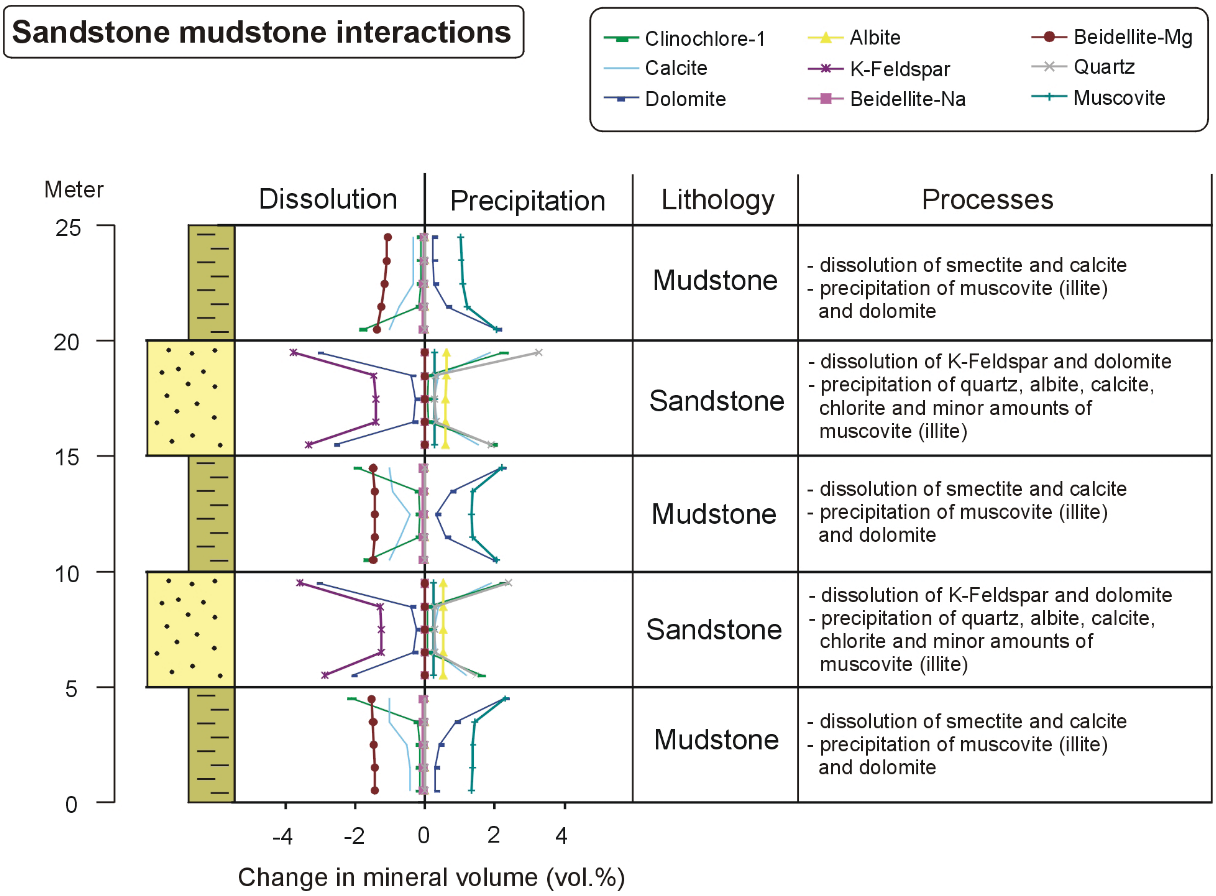

Fig. 7.8: Sandstone mudstone interactions at 135°C modelled with CRUNCH by R. Ondrak (Schöner et al., 2008). Material exchange between sandstones and mudstones is the result of diffusive transport.

Beidellite-Mg, clinochlore and calcite were dissolved in the mudstones, and muscovite (illite) and dolomite precipitated after a number of time steps. The simulated smectite to illite transformation can be expressed with following simplified equation:

$$1.288 \text{ Beidellit-Mg} + K^{+} \leftrightarrow \text{Muscovite} + 1.725\ SiO_{2(aq)} + 0.5751\ H^{+} + 0.2124\ Mg^{2+} \qquad (7.21)$$

K^{+} is required for this reactions and was derived via diffusive transport from the sandstone layers. Here it was released during K-feldspar dissolution.

K-Feldspar and dolomite were dissolved in the sandstone layers, and quartz, calcite, clinochlore and albite were simulated to precipitate in the sandstones. The simulated quartz precipitation in the sandstones showed an increase towards mudstone layers (Fig. 7.8). This distribution of quartz cement is very similar to the petrographic observations made in Jade well 30/2c-4 (see Fig. 5.11, section 5). Parts of the quartz cement were the product of K-feldspar dissolution, but most of the quartz close to mudstones was derived from the smectite-to-illite transformation in the mudstones and transported via diffusion into the sandstones (Fig. 7.8).

Compositional differences between mudstones and sandstones were the driving force for these processes.

This model shows that a diffusive exchange between sandstones and mudstones is generally possible over short distances and can produce distributions of quartz cementation comparable to the observations.

Sandstone-mudstone interaction is an important process which can not only explain the petrographic distribution patterns of quartz cement, but also the apparent illite deficiency in sandstone layers as well as the source of required species for the smectite-to-illite transformation reaction in mudstones of the Skagerrak Formation.

7.4.7 Summary of modelling results

No single model was able to reproduce all observed changes in sandstone mineralogy during diagenesis in the Skagerrak Formation. Nevertheless, important mesodiagenetic changes could be reconstructed quantitatively. The presented models can improve the understanding of diagenetic processes. A comparison of the calculated effects of all models is given in Table 7.4. A more detailed discussion of all processes is included in the following sections.

Table 7.4: Comparison of the different models with petrographic results. The table shows the range of all model runs with different salinity and/or mineralogy for sandstones of the Skagerrak Formation. For details of individual models see text above. Observed values are average values for facies FC/SF taken from Table 7.2. Dissolution is marked by minus and precipitation by plus in front of the numbers in the table. All values are in volume percent of whole rock.

Mineral	Observed		model 1 1a/1b	model 2 2a/2b	model 3** 3a/3b	model 4 4a/4d	model 5 5a/5b	model Ondrak	
	Jade	Judy	Simple heating	CO_2 influx	CH_4 influx	Organic acids	Kimmeridge Clay Formation waters	Sandstone/mudstone interactions	
								mudstones	sandstones
Quartz	+3.6	+2.2		+1.0/+1.6	+0.1/+0.7	+0.4/+0.5	+1.2/+1.1	0	+0.3 to +3.3
Muscovite (Illite)	+2.1*	+1.6*		+1.0/+1.6		+0.4/0	+1.2/+1.2	+1.0 to +2.3	+0.2 to +0.3
Ankerite/Ferrodol.	+1.1	+0.4			+0.4/+1.8	0/+1.6			
Chlorite coatings	+2.5	+1.2			+0.4/+2.3	0/+1.6		-0.1 to -2.1	+0.1 to +2.3
Chlorite euhedral	+2.1	tr							
Albite	+0.6	+0.4	+0.1/+0.3	-1.5/-2	-0.4/-2.0	-0.6/-1.5	-1.3/-1.0	0	+0.5 to +0.6
Calcite	0	+0.4		+tr./+0.4	+0.1/+0.5	+tr./+0.2	+0.3/+0.3	-0.3 to -1.0	+0.3 to +1.9
K-Feldspar	-1.3	-2.5	-0.1/-0.3	-0.8/-1.5	0/-0.1	-0.3/0	-1.5/-1.7	0	-1.2 to -3.8
Dolomite	-1.6	-3.4		+tr./+tr.	-0.4/-2.0	0/-1.4		+0.3 to +2.3	-0.2 to -3.1
Hematite	???	???			-0.1/-0.7	0/-0.6			
Smectite	???	???						-1.2 to -1.6	0

* This is the amount of illite present in the sandstones in form of illitized clasts. They are most likely detrital.

** Models without magnetite

8 Interpretation and discussion of measured stable isotope-values

The interpretation of the stable isotope data is complicated by the low number of samples analysed and the measurement at bulk samples, which often represent more than one carbonate mineral and/or generation. However, despite these circumstances the data can be used to support some of the interpretations.
Roughly five groups of carbonate stable isotope values can be distinguished (see Fig. 8.1).

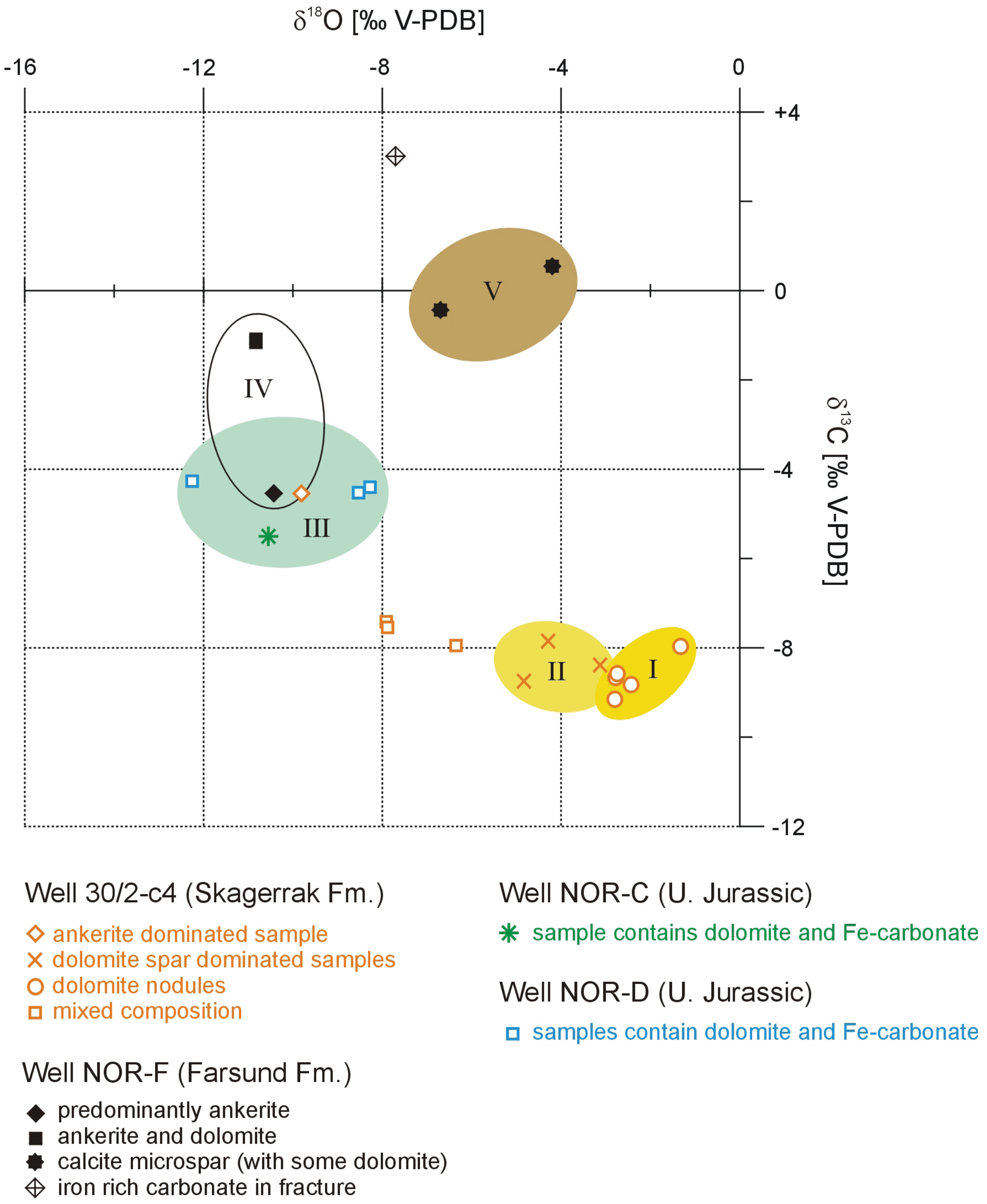

Fig. 8.1: All analysed δ^{13}C- and δ^{18}O-values from the different settings and stratigraphic units together. Data were derived from bulk sample measurements and represent often the signature of more than one carbonate generation. However, five groups can be distinguished (see text for discussion).

The first group consists of samples, which are composed predominantly of dolomite nodules in the Triassic Skagerrak Formation of well 30/2c-4. The second group contains also only samples from well 30/2c-4 and represent samples which are dominated by dolomite spar. The third group contains samples from different wells: the ankerite dominated samples from well 30/2c-4 and also dolomite and Fe-carbonate bearing samples from wells of the Norwegian sector. The values between group II and group III are from samples of the Triassic Skagerrak Formation of well 30/2c-4 and contain both, dolomite and ankerite. They represent most likely a mixing signature between end-members located somewhere in the two groups.
Group IV, which overlaps partly with group III, represents the two sandstone samples from the Intra-Farsund Sandstones of well NOR-F and group V comprises the two analysed microspar samples from the Farsund Formation (well NOR-F), which contain predominantly calcite. The sample of the Fe-carbonate cemented fracture from well NOR-F (Farsund Fm.) has more positive δ^{13}C-values than the rest and δ^{18}O-values between those of samples from group IV and group V.

8.1 Skagerrak Formation (well 30/2c-4)

Samples containing predominantly dolomite spar (group II) have lower δ^{18}O-values than samples dominated by dolomite nodules (group I). The δ^{13}C-values of both groups are comparable and in the range between –7.9 and –9.1‰ and seem to represent isotopically light soil zone carbon. A mixed carbon source composed of atmospheric CO_2 together with carbon from the decay of organic matter and from root-respiration in the soil zone is not unlikely.

The shift in δ^{18}O towards lighter values from dolomite nodules (group I) to the dolomite spar (group II) can be interpreted as slight increase in precipitation temperature in the same formation water. However, an alternative explanation appears to be more plausible: Recharge of groundwater in semi-arid regions with high evapo-transpiration is often confined to periods with heavy rainfall, which tends to have lower δ^{18}O-values than the mean annual rainfall (Vogel & Van Urk, 1975). This may lead to lighter δ^{18}O-values of carbonates precipitated in the groundwater zone compared to pedogenic carbonates (Spötl & Wright, 1992) and references therein). Evaporation in the vadose zone may have enhanced this effect leading to heavier oxygen isotope signatures in the dolomite nodules.

Under the assumption that the present δ^{18}O-values of the dolomite spar in well 30/2c-4 (group I) reflect near surface precipitation temperatures in the groundwater zone it was attempted to estimate δ^{18}O-values for the original water. Using the fractionation equation from Vasconcelos et al. (2005) and a groundwater temperature range from 15 to 25°C[1] a water δ^{18}O-value range from -7.5 to -3.7‰ SMOW was calculated (Fig. 8.2a). This is in consistence with values for eodiagenetic Triassic waters derived from authigenic silica in the Triassic of the Paris Basin (-8.5 to -5.3‰, Spötl & Wright, 1992) and with values published for the δ^{18}O of water in equilibrium with Keuper dolomites (-8.6 to -1.7‰ SMOW, Spötl & Wright, 1992) as well as with assumptions from Morad et al. (1998) for the δ^{18}O-value of pore water during eodiagenesis in the Triassic Lunde Formation of the Snorre Field (-6 to -4‰).

The measured stable isotope values of the sample with the relatively high ankerite content from well 30/2c-4 are comparable to those of dolomite and Fe-carbonate cemented samples

---

[1] Spötl & Wright (1992) assumed a palaeo-groundwater temperature of 20°C for Triassic strata in the Paris Basin and Morad et al. (1998) derived precipitation temperatures between 15 and 30°C from δ^{18}O-values for dolocretes from the Triassic Lunde Formation in the Snorre Field (northernmost North Sea). Cleveland et al. (2008) published mean annual temperatures between 14.6 °C and 26.5°C for Late Triassic strata in New Mexico (USA) derived from pedogenic carbonates, so that 15-25°C seems to be a suitable range.

from Jurassic sandstones in the Norwegian sector (group III, Fig. 8.1). Two explanations are possible for the difference in carbonate isotope signature between diagenetic dolomite and ankerite in well 30/2c-4 of the Triassic Skagerrak Formation:

1.) Ankerite precipitated from the same formation water as the dolomite spar at slightly higher temperatures. That can explain the lighter δ^{18}O-values. The corresponding higher δ^{13}C-values could have been caused by the biodegradation of hydrocarbons. Carbon dioxide in biodegraded oil reservoirs is often isotopically heavy (Larter et al., 2005). Evidence for biodegradation is given by the shallow depth of the reservoir during the first charge with hydrocarbons (see basin modelling in section 4). Under the assumption that the δ^{18}O-value of the water has not changed since dolomite spar formation[2], a precipitation temperature range can be calculated using the fractionation equation for ankerite published by Dutton & Land (1985). The resulting temperatures lie between 43 and 68°C (Fig. 8.2b), in a temperature range were biodegradation is likely to occur (see discussion biodegradation in section 9)[3].

2.) Ankerite may also have precipitated from a formation water which was comparable in isotopic composition to the waters from which authigenic carbonates in the studied Jurassic sandstones of the Norwegian sector were derived. Such a water could have entered the reservoir along with the hydrocarbon charge and could have its origin in the black shales of the source rocks, for instance. The ankerite cemented sample from a thin sandstone bed enclosed into a source rock (sample 5136.20, well NOR-F) plots also in group III. If all carbonates of group III have a common or comparable source, a temperature range can be estimated for the whole group using the equation of Dutton & Land (1985) for ankerite. However, the isotopic composition of the water is not known and so temperatures for two different assumptions were calculated. The first temperature range was calculated for a pore water with the δ^{18}O-value of Jurassic marine water (Fig. 8.2c). A value around –1.2‰ SMOW was used frequently by other authors for Jurassic marine water (Irwin et al., 1977; McCants & Burley, 1996; Haszeldine et al., 1992) and was also applied here. Using the Jurassic marine water a temperature range between 75 and 110°C was calculated. However, it is known from North Sea reservoirs that the δ^{18}O-value of formation waters tend towards heavier values with increasing depth (Bjørlykke et al., 1989; Warren & Smalley, 1994). Girard et al. (2002) reported for instance the formation of ferroan carbonates from isotopically evolved diagenetic waters in the Hild Field (northern North Sea). Therefore, a second temperature was calculated using the δ^{18}O-value of a recent formation water. Values around +3.3‰ SMOW were published for the Gyda (Block 2/1) and Ula Fields (Block 7/12) (Warren & Smalley, 1994). The resulting precipitation temperatures are significantly higher, falling in a range between 115 and 166°C (Fig. 8.2c).

However, both interpretations are based only on few samples and should be verified with more analyses.

---

[2] It seems to be unlikely that the original water remains in-situ unchanged, particularly in permeable sandstones. The water composition and thus the δ^{18}O-value was usually modified during burial by a number of processes, like the dewatering of adjacent shales, dehydration of clay minerals or the influx of hydrocarbons (see also Morad et al., 2003).

[3] It must be considered that this interpretation is based only on one value from one sample.

8.2 Upper Jurassic (wells NOR-C, NOR-D and NOR-F)

The few analysed samples from these two wells plot all in group III. Two diagenetic pathways shall be discussed here shortly for these samples: One possibility is that the carbonates were precipitated from waters derived from Farsund Formation shales and mudstones. This scenario is comparable to the scenario discussed previously for the ankerite dominated sample from well 30/2c-4. Alternatively, the precipitation from meteoric Jurassic waters must be discussed, since a number of reservoirs in the North Sea were affected by the infiltration of meteoric waters (e.g. Bjørlykke et al., 1992; 1989 and others). For Jurassic meteoric waters of the North Sea area a δ^{18}O-value of around –7‰ SMOW is usually inferred (Bjørlykke et al., 1992; Haszeldine et al., 1992). This value was used to calculate temperatures for the case that the analysed carbonates from wells NOR-C and NOR-D were precipitated from pore waters with meteoric isotopic signature (Fig. 8.2d). The resulting temperature range 38 to 62°C is significantly lower than temperatures derived from the other two pore water compositions used previously. However, the lack of authigenic kaolinite in the investigated samples makes the infiltration of meteoric water unlikely. The wide range of possible temperatures (see Fig. 8.2d) dependent on fluid history interpretation shows that this method is not very precise in estimating precipitation temperatures for authigenic ankerites in the investigated Jurassic sandstones of the Norwegian sector.

Carbonate cements in Intra-Farsund sandstones (group IV) were most likely derived by dissolution and reprecipitation from fine-crystalline carbonate rocks in the surrounding Farsund Formation. The calcite dominated samples of well NOR-F (Group V) represent most likely the composition of such a rock. Their isotopic signature is probably not primary, but was changed by different processes like recrystallisation. Recrystallisation for instance would lead to lower δ^{18}O-values than the precursor material (Brand & Morrison, 1987; Morad, 1998). The shift from group V to group IV can be explained by a “typical” diagenesis trend, which is associated with decreasing δ^{18}O-values with increasing temperatures, and a lowering of δ^{13}C-values caused by the influence of isotopically depleted carbon from organic matter. During burial sediments pass different zones of organic matter alteration accompanied by CO_2 production (Irwin et al., 1977). Isotopically light CO_2 can be generated in the bacterial oxidation zone, in the sulphate reduction zone and in the thermal decarboxylation zone. The abundant occurrence of pyrite indicates that at least a part of the isotopically light carbon was derived from the sulphate reduction zone. Further contribution of isotopically light carbon could have been derived from thermal decarboxylation of organic matter. The δ^{13}C-value of the sampled fracture carbonate is the highest and may represent the influence of isotopically heavy methanogenic bicarbonate (see also Irwin et al., 1977). However, data point coverage is too poor to clearly outline any trend.

Temperature estimations for authigenic carbonates based on δ^{18}O-values alone are ambiguous and depend strongly on used fluid evolution scenarios and assumed isotopic compositions of pore water, as illustrated by the calculations above (Fig. 8.2d). Therefore, the calculated temperatures must be interpreted with caution. The uncertainties can be reduced by an evaluation together with petrography and modelling results. This will be addressed in the following sections.

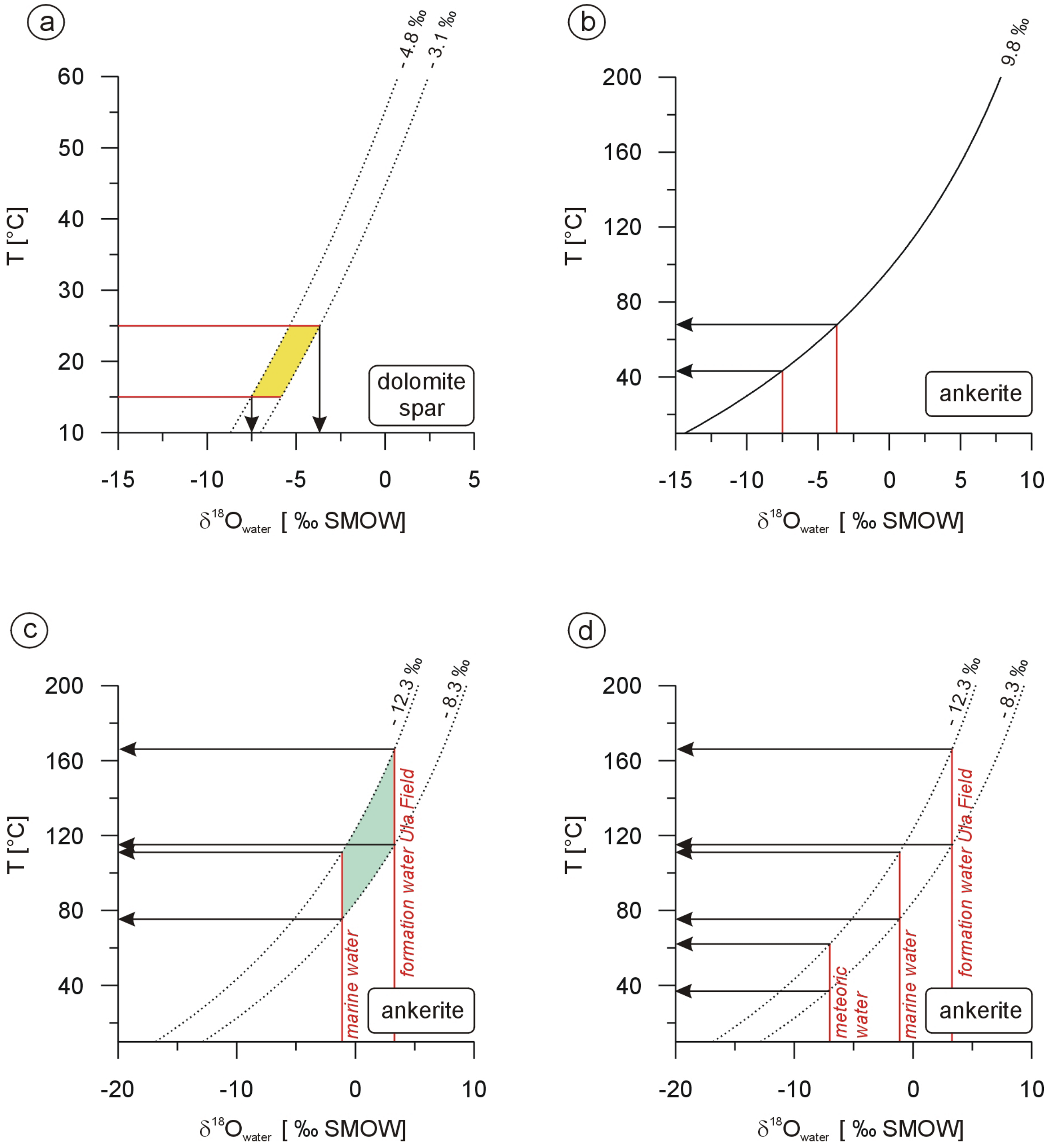

Fig. 8.2: Estimation of precipitation temperature ranges for authigenic carbonates using the temperature dependency of the equilibrium between $\delta^{18}O$ of the carbonate and $\delta^{18}O$ of water. The dotted lines represent constant $\delta^{18}O$-values of ankerite and dolomite, respectively and were calculated using the equation $10^3 \ln \alpha = 2.78 * (10^6 * T^{-2}) + 0.32$ from Dutton & Land (1985) for ankerite and the equation $10^3 \ln \alpha = 2.73 * (10^6 * T^{-2}) + 0.26$ from Vasconcelos et al. (2005) for dolomite. The explanation is given in the text.

9 Interpretation of diagenetic processes in the Jade and Judy Fields

The occurrence of authigenic phases in the Triassic Skagerrak Formation of the Jade and Judy Fields is mainly controlled by depositional facies. In general, fluvial channel and sheetflood sandstones of facies FC and SF show a greater variety of diagenetic phenomena, probably due to their higher permeability for diagenetic fluids, than finer grained silt- and mudstones of the facies AS and LA. Especially the distribution of eodiagenetic phases is related to the depositional environment. The high porosity and permeability zones today are evidently facies controlled.

Detailed descriptions of the geological setting, the petrography and the modelling results are given in sections 5 and 7, respectively.
The paragenetic sequences show only minor differences between the Judy and Jade Fields and the diagenetic evolution of the Triassic Skagerrak Formation seems to be overall comparable in both fields.

9.1 Eodiagenesis

Alterations occurred at or close to the surface during eodiagenesis[1] of the sandstones investigated. The chemistry of pore water was mainly controlled by near surface conditions, which were characterized by an arid to semi-arid climate with seasonal rainfalls and dry periods (e.g. Fisher & Mudge, 1998). The presence of authigenic hematite indicates an at least temporarily strongly oxic environment. Many salt diapirs and walls probably reached the surface during Triassic times and were exposed (Smith et al., 1993). These salt diapirs affected most likely the salinity of the ground water. The groundwater was most likely saline and slightly alkaline. Depositional facies controlled predominantly the distribution of eodiagenetic phases in the Triassic Skagerrak Formation in both investigated fields. So, pore filling dolomite and K-feldspar overgrowths developed mainly in porous sandstones of the fluvial channel and sheetflood facies. Nevertheless, the evaluation of eodiagenetic processes is generally complicated by later mesodiagenetic overprints.

9.1.1 Dolocretes

The occurrence of **dolomite nodules** in argillaceous sandstones or on top of amalgamated sandstone layers together with some of their textures[2] can be used as indicators for a pedogenic origin (vadose dolocrete). Additional evidence can be seen in slightly heavier oxygen isotopes, compared to the pore filling dolomite spar cement, which may show the influence of evapo-transpiration (see section 8). However, pedogenic (or vadose) carbonates are not easy to distinguish from those formed in the groundwater zone (phreatic carbonates) petrographically (see e.g. Alonso-Zarza & Wright, 2010) and many profiles are polygenetic (Khalaf, 2007). Therefore, it cannot be ruled out that some (if not all) of the nodules have been formed below or around the groundwater table. Dolomite nodules developed probably mainly under longer exposed surfaces and were later partly reworked by erosion in the ephemeral fluvial streams, where they have been deposited along with other pebbles as channel lag conglomerates. Here, dolomite nodules acted as nucleation sites for later pore-filling dolomite cementation.

---

[1] Eodiagenesis here is used following the terminology of Schmidt & MacDonald (1979).

[2] The grain rimming dolomite in one sample of well 30/7a-9. Nevertheless, it must be considered that the typical texture is a alpha fabric in sensu Wright (1990) and not diagnostic.

The observed corrosion of framework grains inside the nodules could have provided potassium, silica and aluminium for later K-feldspar precipitation.

Pore filling **coarse dolomite spar** occludes high intergranular porosities (up to 34 vol.%) in some samples. This is evidence for a near surface origin prior to the onset of significant compaction (see also section 5). Patches of coarse dolomite spar were most likely formed in ground water with high magnesium and calcium content nucleating on already existing dolomite nodules and reworked dolomite nodule fragments. Thus, the distribution of coarse dolomite spar cement seems to be bound to already existing nucleation sites. Zoned single dolomite crystals indicate a changing composition of ground water chemistry over time or a periodic precipitation.
The thin dolomite ribbon observed directly at the boundary between sand- and mudstones may have a different origin and can be interpreted as the result of ionic infiltration following smectite-to-illite conversion or the dewatering of shales during a later diagenetic stage[3].

Ancient and modern pedogenic and ground water carbonates consist usually of low-Mg calcite and the occurrence of dolocretes[4] is less common (Spötl & Wright, 1992). Generally, dolocretes were found to develop on Mg-rich host rocks (ultrabasic rocks) or to occur in evaporitic depositional environments (Spötl & Wright, 1992). Down-stream evolution of ground water due to evapo-transpiration associated with an increase in Mg/Ca ratio towards basin centre by precipitation of calcrete in more proximal areas was interpreted to be responsible for the occurrence of dolocretes in inland Australia (Colson & Cojan, 1996 and references therein). Comparable observations were made by Gaupp & Okkerman (2011) in the Rotliegend of the Netherlands, where early pore-filling carbonate cements are mainly composed of calcite in the proximal area close to the hinterland and of dolomite in distal basinal areas. Dolocretes in coastal regions of Kuwait were proposed to have formed from shallow groundwater where the mixing zone with sea water is affected by evaporation (El-Sayed et al., 1991). A comparable model was introduced by Colson & Cojan (1996) for lake margin environments. They attribute the occurrence of dolocretes in the Danian of the Provence Basin to the mixing of groundwater with lake brines that infiltrated the phreatic zone during periods of strong evaporation. The semi-arid to arid depositional environment was most likely the main controlling factor for early diagenetic dolomite formation in the Triassic Skagerrak Formation. Both, the ground water evolution model as well as the mixing with saline brines from ephemeral lakes can explain the dolocrete formation. Weibel (1998) described the occurrence of calcrete from the Triassic Skagerrak Formation in northern Denmark, an area located more proximal to the source of the Fennoscandian Shield. This can be seen as argument for the ground water evolution model.

---

[3] The reactive transport model predicted dolomite to precipitate in mudstones with increasing amounts towards the boundaries to sandstones during mesodiagenetic illitization of smectite (see section 7).

[4] The term dolocrete is used here in sensu Alonso-Zarza & Wright (2010) to describe near-surface dolomites of pedogenic or shallow groundwater origin.

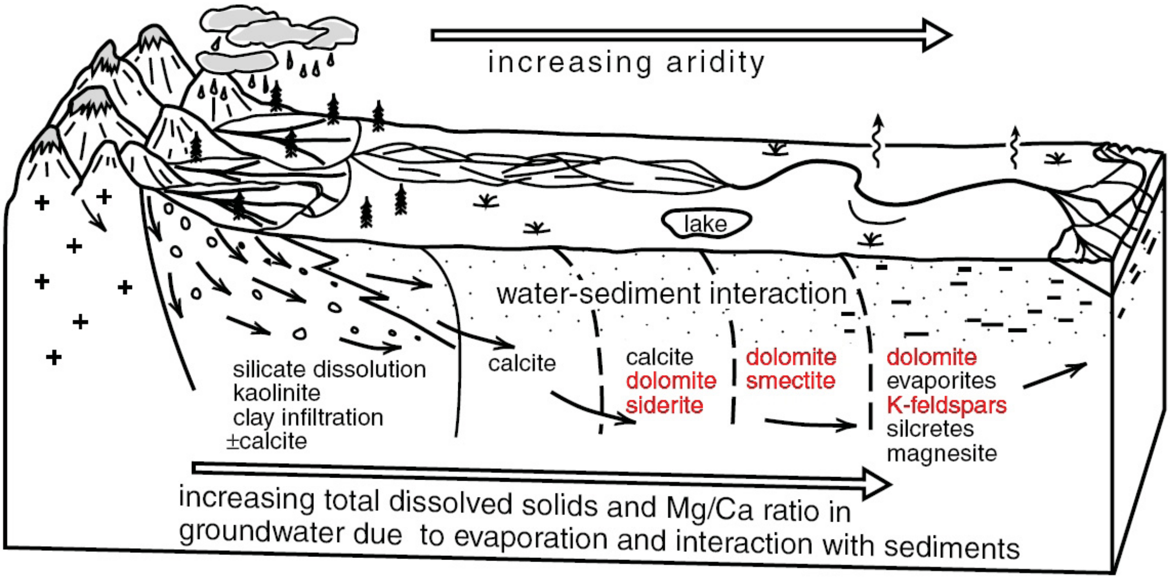

Fig. 9.1: Sketch of spatial distribution of eodiagenetic alterations and regional ground water geochemical modifications in continental settings (Morad et al., 2000). The eodiagenetic phases occurring in the studied samples of the Skagerrak formation are marked red.

9.1.2 Grain coating clays

Tangential **grain coating clay minerals** are present in the form of chlorite (Type I, see section 5) and more seldom in the form of illite today. Grain coating chlorites in the Skagerrak Formation were interpreted by Humphreys et al. (1989)[5] to be an alteration of a precursor swelling chlorite or corrensite, and by Goldsmith et al. (2003) to have formed eodiagenetically in local more reducing environments with high water tables. However, chlorite is known to precipitate not directly during eodiagenesis, but evolves later from eodiagenetic precursor phases (Worden & Morad, 2003). The presence of randomly-interstratified chlorite/smectite in the shallower Gannet Field (Purvis, 1990) suggests a smectite precursor[6] for chlorite type I. The analysis (no. 248, Appendix 3.3) from type I chlorite shows that this chlorite has an iron rich composition today. Nevertheless, this chlorite can also be interpreted as a mesodiagenetic successor of a former more Mg-rich smectite formed later during the release of Fe^{2+} by reduction of iron oxides. Mg-rich precursor clay minerals are more likely under the influence of Mg-bearing ground waters or lake brines. The presence of dolocretes indicates that such Mg-rich eodiagenetic fluids were present.

Iron rich chlorites were described to evolve from berthierine or iron-rich clays of the verdine facies[7], such as odinite (Aagaard et al., 2000; Hillier, 1994; Ryan & Reynolds, 1996). However, the occurrence of these precursor minerals appears to be usually restricted to shallow marine or deltaic environments near river mouths in tropic climates (Ehrenberg, 1993) and this pathway of chlorite formation can be probably ruled out for the Triassic Skagerrak Formation in the Jade and Judy Fields.

Grain coating illite is more abundant in the finer grained facies and may also have been derived from a smectite precursor in a locally slightly different, more potassium-rich, pore

---

[5] The chlorites studied by Humphreys et al. (1989) were with Fe/(Fe+Mg) ratios ~ 0.4 to 0.5 more Mg-rich than chlorites from this study.

[6] The nature of the initial smectite remains speculative. Saponite, for instance, is known to form in sabkha, aeolian and evaporitic environments (Ryan & Hillier, 2002 and references therein).

[7] For definition see Odin (1990) and references therein

water. Smectites can be formed by weathering in arid climates (McKinley et al., 2003). The assumption of a smectite precursor for illite is in consistence with studies of recent sediments in arid regions. Walker et al. (1978) found e.g. early diagenetically formed clay minerals consisting of randomly-interstratified mixed-layer illite-montmorillonite in Cenozoic sediments.

Illites are usually derived from a dioctahedral smectite (such as montmorillonite) and chlorites from a trioctahedral smectite (e.g. saponite) (McKinley et al., 2003). Trioctahedral smectites are known to form in arid settings where evaporation exceeds rainfall and dioctahedral smectites (and illite/smectite mixed layer clay minerals) tend to form in less evaporitic environments (Worden & Morad, 2003)[8]. So, the present distribution of illite vs. chlorite coatings may reflect primary different smectite assemblages controlled by the influence of fresh water and saline lake waters, respectively. Another model was proposed by Hillier et al. (1996) for the Rotliegend in northwest Germany. They suggested that an exposure of the clay coatings to Mg-rich fluids from dewatering evaporitic shales at near surface temperatures promoted the formation of a trioctahedral smectite (as a precursor for later Mg-rich chlorites), while in not affected areas a pore lining dioctahedral clay minerals was formed, which evolved later into illite.

The primary clay coatings, however, developed most likely in the soil zone during infiltration of clay from above, because higher amounts of chlorite coatings can be found frequently at the top of fluvial channel and sheetflood sandstones. Some of the coatings display also faint geopedal structures. Other possible mechanisms are illuvation of clay in the soil zone or in-situ formation by weathering (see also Gaupp et al., 1993). A part of the primary clay coatings may also have been inherited from the source area. However, the typical features of inherited clay coatings (see Wilson,1992 for details), like thicker rims in grain embayments, were not or only rarely observed in the investigated samples of the Skagerrak Formation.

9.1.3 Iron and titanium oxides/hydroxides

Only minor amounts of **iron-oxide coatings** are present in the investigated samples of the Skagerrak Formation. They occur today in the form of thin hematite grain coatings, as thicker crusts probably associated with clay minerals or in intensely reddened mudstones.

Thin iron oxide/hydroxide coats were probably formed in areas with fluctuating ground water tables as a product of periodic wetting and drying or in capillary fringes of the vadose zone (Gaupp, 1996; Gaupp & Okkerman, 2011). Iron was most likely supplied in a dissolved ferrous form by interstital water during wet periods and oxidized and precipitated as ferric iron in dry periods above the water table.

Thicker iron oxide crusts contain frequently a certain amount of clay minerals. They developed most likely when iron oxide/hydroxide precipitation was associated with clay infiltration and/or when the infiltrated detrital clay contained already abundant iron oxides/hydroxides (see also Blodgett et al., 1993).

The breakdown of unstable iron bearing minerals (e.g. biotite, amphibole, pyroxenes, olivine, magnetite) during weathering can be considered as the main source of iron (Walker et al., 1981; Walker et al., 1978; Weibel, 1998). The precipitation of iron oxides/hydroxides occurs in recent soils initially mostly as ferrihydrite ($5\ Fe_2O_3 \cdot 9\ H_2O$) or goethite (α-FeOOH), but ferrihydrite can be altered to fine crystalline hematite (α-Fe_2O_3) during dry periods in warm climates (Schwertmann, 1998). Weibel & Grobety (1999) could show that hematite evolved from early goethite with increasing depth and temperature (onset between 56 and 75°C) in the

---

[8] The type of smectite formed depends also on the mineralogy of the weathered rocks - see e.g. McKinley et al., (2003).

Skagerrak Formation of the Danish Sub-Basin. This may also have been the case in the Central Graben area. The preservation of hematite coatings under K-feldspar and dolomite is evidence for a former more widespread presence. Later bleaching removed most likely a great part of the iron oxides.

Leucoxene and anatase were probably derived from the breakdown of titanium bearing heavy minerals, such as ilmenite or titanomagnetite by weathering in the source area or during eodiagenesis. The euhedral shape of some anatase crystals and their presence in the intergranular pore space is clear evidence for an in-situ growth of at least a part of the titanium oxides. Minor contributions of titanium can also have been added from the dissolution of biotite or feldspars (see Appendix 3.2 for titanium content of feldspars).

9.1.4 K-feldspar

K-feldspar is a common authigenic minerals in arid Cenozoic deposits (Walker et al., 1978) and in Permo-Triassic sandstones in on- and offshore UK (Purvis, 1994; Waugh, 1978). Moreover, the occurrence of authigenic K-feldspar was reported from Jurassic sandstones of the North Sea (e.g. Bjørlykke & Brendsdal, 1986; Bjørlykke et al., 1992; Glasmann, 1992; Harris, 1992; Saigal et al., 1992).

The hydrolysis of detrital silicates could have provided the required ions for the formation of K-feldspar overgrowths (Purvis, 1994; Waugh, 1978). The observed corrosion of framework grains in the dolocrete horizons may have played an important role. Additional K^+ could have been supplied by saline ground waters derived from emerging salt diapirs. That may be an explanation for the predominance of authigenic K-feldspar in former highly permeable fluvial channel and sheetflood sandstones. Fig. 9.2 shows that K-feldspar is thermodynamically stable in waters with high K^+/H^+ ratios. K-feldspar overgrowth formation could have continued also under shallow burial conditions (Dixon et al., 1989; Purvis, 1994). This is also indicated by the textural relationship to hematite (see next section "Reduction of iron oxides/iron hydroxides").

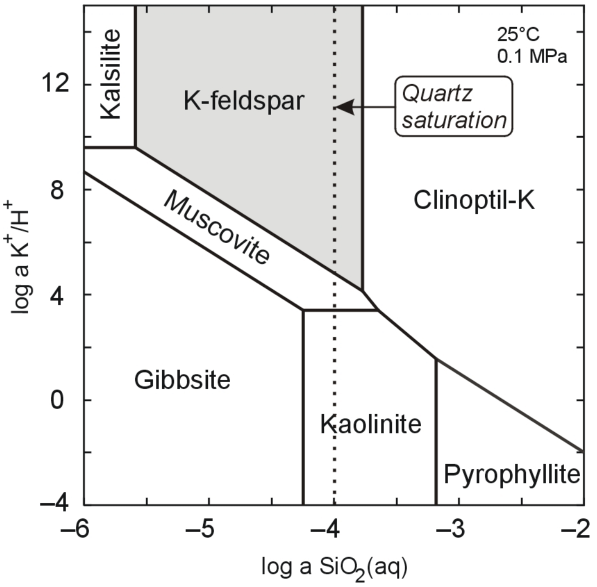

Fig 9.2: Stability field of K-feldspar in the system K_2O-Al_2O_3-SiO_2-H_2O at low temperatures (temperature 25°C, pressure 0.1 MPa) calculated using the program Act2 of the software package Geochemist´s Workbench® Standard Release 6.0 from RockWare Inc. with the LLNL database.

9.2 Mesodiagenesis

With beginning mesodiagenesis, the sandstones were sealed under tight strata from the influence of surface waters by definition (Schmidt & MacDonald, 1979). Temperatures rise during ongoing burial and inorganic/organic diagenetic processes react on changing temperature and pressure conditions. The eodiagenetic and depositional mineralogy of the investigated rocks was certainly more and more overprinted by these later processes and the evolving pore fluids.

9.2.1 Reduction of iron oxides/iron hydroxides

Bleaching may occur in principle already during eodiagenesis in poorly drained, hydric soils or in low eH ground waters (e.g. Blodgett et al., 1993). However, it seems to be more likely that the influence of organic maturation products prior to main quartz cementation was responsible for the bleaching observed in the Triassic Skagerrak Formation. The first influence of hydrocarbons is to expect already at shallow depth (300-500 m) and low temperatures (<30 to 40°C) for both, the Jade and the Judy Fields, as indicated by 3D basin modelling (Neumann, 2007). Microbes which degraded probably the early oil charge in this low temperature environment may have played an active role. Nevertheless, other mesodiagenetic processes can also cause the reduction of iron oxides and it cannot be completely ruled that some of them occurred at deeper burial associated with higher temperatures (see section 11 for other reactions).

The dating of the hematite/goethite[9] reduction in the Skagerrak Formation remains uncertain. Textural evidence points to a timing after K-feldspar and dolomite precipitation but before the onset of significant quartz cementation (since no hematite was found to be preserved under quartz cements). There is no hematite underneath feldspar overgrowths in the deeper Jade Field (in contrast to the Judy Field) which can have two reasons: Either hematite was precipitated not pervasively in the fluvial channel horizons of the Jade Field (but formed only locally under longer exposed surfaces coherent with dolocrete), or bleaching occurred earlier in the Jade Field (before the onset of significant K-feldspar formation) than in the Judy Field. Basin modelling by Neumann (2007) could show that hydrocarbon charge occurred probably earlier in the deeper Jade Field (Early Cretaceous) than in the shallower Judy Field (Late Cretaceous).

A number of the observed mesodiagenetic phases (ankerite, chlorite, pyrite) required Fe^{2+} for their formation and the release of ferrous iron by iron oxide/hydroxide reduction may have triggered the formation of some of these minerals, as indicated by diagenetic modelling (see section 7).

9.2.2 Chloritization of smectite

The grain coating chlorite (Type I) in the sandstones of the Skagerrak Formation is probably the successors of a former smectite as discussed previously. The mudstones contain also certain amounts of chlorite today. A part of this chlorite was most likely detrital, but chloritization of smectite in the mudstones cannot be ruled out. Weibel (1999) mentioned that random smectite/chlorite is converted into ordered smectite/chlorite between 70 and 105°C and chlorite is most abundant at maximum burial temperatures (150°C) in the Skagerrak Formation of the Danish Sub-Basin. Hillier et al. (1996) gave comparable temperature ranges: a temperature close to 100°C for smectite-to-corrensite-transition and temperatures from 150 to 200°C for actual chlorite formation. Typical reaction equations for the formation of chorite from a smectite precursor are given in section 11.

---

[9] It is likely that a certain amount of the former goethite was not transformed into hematite if the reduction occurred at relatively low temperatures.

9.2.3 Chlorite neo-formation

The radial euhedral chlorite plates (chlorite type II) have the typical form of a neo-formed clay mineral and precipitation from pore water seems to be most likely. The occurrence of chlorite II close to fracture zones in the Jade Field indicates a relation to infiltrating fluids which were probably hydrocarbon-bearing. The occurrence of ankerite and iron-bearing chlorite indicates that ferrous iron was available in suitable amounts during mesodiagenesis. Possible sources were the hematite/goethite reduction mentioned previously and the smectite-to-illite transformation in the interbedded mudstones. The required aluminium and silicium species could have been derived from K-feldspar dissolution. A more detailed discussion and reaction equations for the formation of chlorite are given in section 11.

9.2.4 Smectite-to-illite transformation

The observed detrital illite in sand- and mudstones and the tangential grain coatings composed of illite are most likely at least partly the product of smectite-to-illite transformation. Smectite is thermodynamically instable at higher temperatures and is known to transform over mixed layer minerals into illite with increasing burial and temperatures (see detailed discussion and references in section 11). Investigations of Weibel (1999) showed that the conversion of smectite into random smectite/illite took place at temperatures > 47°C and of random smectite/illite into ordered illite/smectite at temperatures > 74°C in the Triassic Skagerrak Formation of the Danish Sub-Basin. This process consumed potassium and aluminium and may explain the fate of major parts of the K-feldspar dissolution products (see reaction equations in sections 7 and 11). Illitization of smectite is known to release potentially significant amounts of Na^+, Ca^{2+}, Fe^{2+}, Mg^{2+} and SiO_2, which can be used by coeval diagenetic reactions (Worden & Morad, 2003). So, released silica was most likely the source for the observed strong quartz cementation in sandstones close to adjacent mudstones as indicated by reactive transport modelling (see section 7). Very thin dolomite ribbons at the contact between sandstones and mudstones can be explained by released Mg^{2+} during the illitization of smectite (e.g. reaction equation 7.21).

9.2.5 Quartz cementation

An early eodiagenetic phase of quartz cementation cannot be completely excluded since early diagenetic quartz cement is frequently associated with K-feldspar overgrowths under semi-arid to arid climate (Walker et al., 1978). However, textural relationship to other diagenetic phases indicates a clear mesodiagenetic origin of most of the present quartz cement and the quartz cement distribution differs from that of authigenic K-feldspar in the investigated sandstones.

Quartz cementation increases toward the interbedded mudstones in the studied sandstones of the Skagerrak Formation. The reason for the high quartz cement content close to the mudstones is probably the release of silica during smectite-to-illite transformation from the mudstones as indicated by results of reactive transport modelling (see section 7). Füchtbauer (1978) described similar cementation patterns but considered dissolution of silt-sized quartz grains to be the main silica source. This process may have provided additional silica for quartz cementation in the contact zone, but reactive transport modelling (section 7) showed that the smectite-to-illite transformation is in principle able to provide enough silica to explain the observed quartz cement patterns. Further silica could have been supplied by the transformation of smectite into chlorite (see reaction 11 for reaction equations, McKinley et al., 2003). Admittedly, in some of the sandbodies of well 30/2c-4 the present quartz cement distribution can also be explained by retardation of silica precipitation by authigenic chlorite (see Fig. 5.11, section 5). The prevention of quartz cementation due to presence of grain

rimming chlorite was observed in numerous sandstones and is known to be an important porosity preserving mechanism in deep burial settings (e.g. Wilkinson et al., 2006).
Dissolution at grain contacts in sandstones is proposed by many authors as main source for deeper burial quartz cementation (see section 11 for discussion and references). Clear evidence for grain-to-grain contact dissolution[10] can be seen in the long and slightly sutured grain contacts observed in the thin sections examined. Therefore, grain-to-grain contact dissolution has certainly provided additional silica. However, mass balances between the amounts of quartz dissolved at grain contacts and precipitated in pore space are critical to establish on thin-sections, because samples taken between stylolites will show for instance only quartz cementation (Bjørlykke & Egeberg, 1993).
The dissolution of K-feldspar was certainly an additional source for silica in the sandstones, since a part of the K-feldspar was removed completely and not replaced by albite (see also modelling results). Extra-formational silica import is not necessary to explain the observed quartz cementation.

Quartz cementation seems to have been a long continuous process with multiple sources down to deep burial in the Skagerrak Formation. The cathodoluminescence investigations showed no zonation (zonation can be indicative for episodic processes). The textural relationship to ankerite (overgrowing and being engulfed by it) indicates continuous quartz cementation interrupted by a shorter period of ankerite precipitation. The bitumen stained chlorite engulfed by later quartz, especially in the contact zone to adjacent mudstones, shows that quartz cementation proceeded after hydrocarbon emplacement at least close to interbedded mudstones. The hydrocarbon bearing fluorescent fluid inclusion is another indicator for ongoing quartz cementation after hydrocarbon charge (see section 5).

The conversion of smectite into random smectite/illite took place at temperatures > 47°C and of random smectite/illite into ordered illite/smectite at temperatures > 74°C in the Triassic Skagerrak Formation of the Danish Sub-Basin (Weibel, 1999). It is likely that quartz cementation sourced by the illitization of smectite started in a comparable temperature range in the settings investigated. Significant mesodiagenetic quartz cement formation occurs in most sedimentary basins at temperatures exceeding 90°C (see discussion and references in section 11). This temperature was reached in the Jade Field in Late Cretaceous times. Fluid inclusion data from the Judy Field indicated the healing of fractures by quartz cements at 115-136°C (Swarbrick et al., 2000).

9.2.6 Carbonate precipitation

Smectite-to-illite or to -chlorite transformation, bleaching of former red beds and the dissolution of dolomite were most likely the sources of metal ions for **ankerite precipitation**. The CO_3^{2-} was probably derived from the dissolution of carbonates or from CO_2 produced by biodegradation or the decarboxylation of organic material. Stable isotope data give evidence for two possible ankerite formation pathways: 1.) the precipitation along with the biodegradation of an early hydrocarbon fill at relatively low temperatures (between 43 and 68°C) or 2.) The precipitation from a hydrocarbon-bearing water coming from Jurassic source rocks. The temperature range, obtained from stable isotopes, is significantly higher for the fluid influx scenario ranging from values between 75 and 110°C for a marine water to values between 115 and 166°C for an evolved pore water (see section 8 for details). The highest temperatures are in the range of present day reservoir temperatures.

---

[10] Also known as “pressure solution” or “chemical compaction” (e.g. Heald, 1956; Renton et al., 1969; Houseknecht, 1987)

Leached dolomites in the reservoir are evidence for carbonate dissolution previous or subsequent to ankerite formation. It may be possible that dolomite dissolution and ankerite formation are linked and that dolomite was leached mainly at the fluid entry points with ankerite precipitating in more distal parts. Ankerite may have formed also with increasing temperature as the leaching capacity of the fluids was exhausted. The post bitumen precipitation shows that enough water was available in the reservoir to transport the required ions even after the first hydrocarbon charge[11]. Diagenetic modelling (section 7) indicates that ankerite formation is linked to the reduction of hematite/goethite by infiltrating hydrocarbons.

Patchy **calcite** cementation around fracture zones in the Judy Field can be explained by the influence of CO_2 or organic acids in higher saline waters (see model 2, section 7) or by the infiltration of Kimmeridge Clay formation waters contemporaneous to hydrocarbon charge (see model 5, section 7). Both processes are likely to have occurred at relatively shallow burial depth in late Cretaceous as indicated by basin modelling (see section 4). Other explanations can be the release of overpressure via these fractures or the influx of hot fluids. Probably is a combination of some of the discussed processes responsible for the observed calcite cementation.

9.2.7 Formation of solid bitumen and bitumen staining

Bitumen was found in different petrographic types (see section 5). Bitumen staining in the Jade Field was found mainly on authigenic chlorite showing that the surfaces of chlorite have attracted the hydrocarbons selectively. This observation indicates that surface processes played an important role in pore-scale.

Different ways of solid bitumen formation are discussed in section 11. Only a short selection is given here. Pyrobitumen is formed by thermal cracking of hydrocarbons at greater burial depths and would indicate a relatively late timing. The cracking of oil, particularly in HPHT settings requires high temperatures in the order of 160 to 200°C (see section 11 for discussion). Only the Jade Field encountered such temperatures during late burial (Neumann, 2007).

Bitumen may have formed by gas stripping and deasphalting but the phase modelling of Neumann (2007) make this scenario not very likely, because no massive gas migration through the reservoir was predicted. Nevertheless, phase separation can also occur without thermal gas generation in biodegraded reservoirs (Larter et al., 2005). The content of carbon dioxide increases most likely during biodegradation and CO_2 can also lead to the precipitation of asphaltenes and other fractions of heavy organics in the reservoir (Monger & Trujillo, 1991).

Biodegradation of an initial hydrocarbon charge was most likely responsible for the observed bitumen formation (Goldsmith et al., 2003; Neumann, 2007). The reservoir was in a relatively shallow position and at temperatures around 30 to 40°C during the first phases of hydrocarbon generation in the deepest kitchen area (see section 4 and Neumann, 2007). Hydrocarbons accumulating in the reservoir at these temperatures were obviously prone to biodegradation. This may have lead to the formation of a heavy residual oil which could wet the mineral surfaces locally, in particular at oil-water contacts (Neumann, 2007; Larter et al., 2005).

It must be considered that high salinities in formation waters were observed to retard methanogenic activity in the Antrim Shale (USA). Nevertheless, deep biodegraded oil fields are often reported to contain saline water (Larter et al., 2005).

---

[11] It is often believed that diagenetic processes stop or be retarded after hydrocarbon charge. Here it may have been that an early hydrocarbon fill at shallow depth has leaked and was replaced with water before a later charge filled the reservoir under deeper burial conditions.

Subsequent hydrocarbon charges during deeper burial filled probably the reservoir at temperatures where biodegradation was inhibited. Present day petroleum composition seems to be rather controlled by the effect of mixing with a fresh charge than by in-reservoir alteration as indicated by organic geochemical data from Jade Field which do no longer point to biodegradation as an important mechanism (Neumann, 2007).

9.2.8 Authigenic albite formation

Authigenic albite is a widespread diagenetic mineral in various sandstones of the North Sea (e.g. Bjørlykke et al., 1992; Saigal et al., 1988). The albite growing inside of leached K-feldspar grains in the Skagerrak Formation shows characteristics, which are typical for authigenic albites: lack of twinning and nearly pure Na-end member composition (see also Deer et al., 2001).

Different scenarios for the formation of authigenic albite are discussed in the literature and a short review is given in section 11. Diagenetic albite in the Triassic Skagerrak Formation of the Jade and Judy Fields is most likely related to K-feldspar dissolution and can be explained by simple heating in a closed system (see section 7). The starting temperature of albite formation seems to depend on pore water composition, as indicated by diagenetic modelling. Albite neoformation started at temperatures >75°C in the model (model 1 section 7) with a Jade Field water and at significantly lower temperatures (<40 °C) using higher saline Judy Field waters. These results suggest that albitization of K-feldspar may have started at varying times in different fields or even compartments, depending on local pore water chemistry.
The Al^{3+} and $SiO_{2(aq)}$ required for albite formation were derived from K-feldspar dissolution. Sufficient Na^+ seems to have been available in the highly saline pore waters. Nevertheless, additional Na^+ may have been released during the transformation of Na-rich smectite into illite during deeper burial as indicated by reactive transport modelling of sandstone-mudstone interactions (see section 7 for details).

9.2.9 Formation of other diagenetic phases

Barite was found in traces in some of the investigated samples. The present volumes are so small that there seems to be no need for an external source of Ba^{2+} and SO_4^{2-}. A suitable amount of barium is present in the formation waters (see Table 7.1). Additional barium can have been released from feldspars and micas during dissolution. The analysed detrital feldspars contain some barium (up to 2.5 wt.%, see Appendix 3.2). The SO_4^{2-} was most likely also derived from pore waters.

Mesodiagenetic **sulphides** are present in negligible amounts in sandstones of the Triassic Skagerrak Formation. Mesodiagenetic pyrite close to faults may indicate the interaction of iron oxides/hydroxides with sulphur-bearing hydrocarbons or pore waters. The sulphur (or better the H_2S) was probably derived either from the degradation of oil or from bacterial sulphate reduction (BSR) and breakdown of kerogen in adjacent source rocks, respectively (see e.g. Worden et al., 2003 and references therein for H_2S sources). Galenite and sphalerite have extremely low solubilities and form even if the respective metals are present only in traces in the formation water (Machel, 2001).

The presence of unleached barite crystals points against a significant influence of thermogenic sulphate reduction (TSR) in the Triassic Skagerrak Formation of the two investigated fields.

9.2.10 Creation of secondary porosity and mesodiagenetic fluid evolution

Dissolution of K-feldspar and dolomite created a notable amount of secondary porosity in the investigated sandstones of the Triassic Skagerrak Formation. It cannot be excluded that some detrital K-feldspars were already partly corroded during transport. However, early leaching of K-feldspar is probably not important as indicated by observations of Walker et al. (1978), who could show that in Cenozoic arid deposits K-feldspar was not discernibly affected by dissolution in contrast to plagioclase. The presence of eodiagenetic to shallow burial K-feldspar overgrowths is also evidence for the stability of K-feldspar in early pore waters. More compacted patchy areas between cement dissolution voids indicate a later leaching event during mesodiagenesis following a certain amount of mechanical compaction.
The creation of secondary porosity in sandstones is a topic that has been discussed intensely and controversially in the past (see section 11). Several processes were thought to be responsible for the dissolution of detrital grains and cements in sandstones after burial. The most important are reviewed in section 11. The development of secondary porosity in Triassic sandstones of the Judy and Jade Fields is interpreted here in the context of the different fluid flow scenarios.

Five fluid evolution scenarios may be able to explain at least parts of the observed leaching in the context of other diagenetic alterations. These scenarios are partly comparable to those modelled in section 7.

1. Closed system re-equilibration of mineral phases with increasing temperatures
2. Meteoric water leaching
3. Focused fluid flow from dewatering of adjacent or underlying sediments
4. Leaching by aggressive organic maturation products like CO_2 and organic acids brought into the reservoir from adjacent source rocks
5. Leaching by biodegradation related CO_2 and organic acids
6. The influence of organic acids created during the oxidation of n-alkanes in the reservoir in-situ

Closed system diagenesis is driven by the disequilibrium between detrital minerals and the interstital pore water. A once attained equilibrium is disturbed by increasing temperatures and some phases become thermodynamically unstable and will be replaced by more stable ones. Such an isochemical model was suggested for instance by Bjørkum & Gjelsvik (1988) for Jurassic sandstones of the North Sea.
The effect of temperature increase with burial in a closed sandstone-pore water system was simulated in model 1 (see section 7 for details). This simple model simulated a closed system in sandbody scale and was able to reproduce the albitization of K-feldspar and a part of the K-feldspar dissolution in a closed system. Another typical (not modelled) reaction, which works also in a closed system is the grain-to-grain-contact dissolution of quartz with subsequent precipitation of quartz cement (see section 11 for details). However, most of the diagenetic changes could not be reproduced by the simple model in sandbody scale.
A reactive transport model (see modelling section for details) composed of sandstone and mudstone layers representing a closed system in reservoir scale was able to reproduce a remarkable number of the petrographic observations. Driving force was the compositional difference between sandstones and mudstones which caused a disequilibrium during illitization of smectite. However, all processes which require ferrous iron (e.g. chlorite and ankerite formation) could not be modelled adequately without an additional reducing agent. Moreover, the presence of liquid hydrocarbons and solid bitumen is clear evidence for an open system with respect to migrating hydrocarbons.

Meteoric water leaching is often favoured to explain secondary porosity in North Sea reservoir sandstones. It must be considered that meteoric waters are known to percolate deep into sedimentary basins. So, meteoric waters were found in more than 2 km depth in the Great Artesian Basin of Australia and tens of kilometres off the south-eastern coast of the USA (Giles, 1997; Worden & Burley, 2003 and references therein). Nevertheless, it seems to be unlikely that meteoric waters infiltrate into sandstones deeper than 3 km (Morad et al., 2000).
Jurassic northern North Sea reservoirs show clear evidence for the influence of meteoric water flushing (e.g. Bjørlykke et al., 1992; Bjørlykke et al., 1989; Glasmann, 1992) and the telodiagenetic influence of meteoric water in the Triassic of the Central Graben cannot be completely negated due to the frequent occurrence of unconformities on top of Triassic strata. So, Goldsmith et al. (2003) assumed that meteoric water flushing during the late Mid-Jurassic uplift was responsible for widespread secondary porosity creation in the Skagerrak Formation. However, there are some objections to be raised against the meteoric water leaching scenario. The climate in Jurassic to Cretaceous times was more humid than in the Triassic and typical Jurassic meteoric waters will most likely have been dilute and acidic. Such meteoric waters cause K-feldspar dissolution associated with typical authigenic minerals, such as kaolinite (Worden & Morad, 2003). Hence, authigenic kaolinite can be found in the many northern North Sea reservoirs which were affected by meteoric water leaching (Bjørlykke et al., 1992; Blanche & Whitaker, 1978; Glasmann, 1992; Ketzer et al., 2003). However, no authigenic kaolinite was detected in the investigated samples of the Skagerrak Formation from Jade and Judy Fields. This observation indicates that the formation water composition at the time of K-feldspar dissolution was probably not in the stability field of kaolinite. The lack of authigenic kaolinite can be seen as evidence for K-feldspar dissolution in a non-meteoric water, which was probably in equilibrium with illite (see also section 7 modelling). It must be considered that authigenic kaolinite was described for other Skagerrak Formation reservoirs, for instance the Claymore Field (Spark & Trewin, 1986) and the Gannet Field (Purvis, 1994). Meteoric water flushing may have occurred in these places, and the points discussed above must not be generalized for all Skagerrak Formation reservoirs.
Finally, the architecture of the reservoir argues against an easy infiltration of meteoric water from above at shallow burial depths in the whole reservoir. The widespread mudstone layers and the layer cake structure would act as multiple vertical barriers preventing the water from penetrating to greater depths. This is supported by investigations of Jones et al. (2005) who showed that the pore fluids are non-communicating in sandstone units separated by thicker mudstones in the Jade Field today.

The lack of authigenic fibrous/flaky illite and authigenic kaolinite in Skagerrak Formation sandstones of the Jade and Judy Fields may indicate feldspar leaching in a temperature range where smectite-to-illite transformation in mudstones was active as sink for aluminium species. Another explanation may be restricted mass transport due to hydrocarbon fill (see section 11).

Jurassic source rocks lie spatially close to the Josephine High in the graben and they are considered to be the major source for the hydrocarbons in the Jade and Judy Fields (see section 4). The possible influx of **hydrocarbon associated aggressive fluids** must therefore be taken into account.
The role of such fluids for the creation of secondary porosity was discussed controversially in the past (see section 11). The leaching potential of organic acids and CO_2 was probably largely neutralized by carbonates (and feldspars) within the source rock or during transport (Bjørlykke, 1983; Giles & Marshall, 1986). Evidence for this is given by the studied intra-Farsund sandstones (see section 6 and 10).

Nevertheless, organic acids and/or CO_2 may have played an active role during mesodiagenesis in the Skagerrak formation of the Jade and Judy Fields, as indicated by bleaching and the recent presence of CO_2 in the reservoir fluids. Therefore, an in-situ origin of these agents by biodegradation of an early hydrocarbon charge or the decomposition of n-alkanes seems to be more likely than the import from adjacent source rocks.
The agents were probably consumed instantly or shortly after generation so that no significant drop in pH could occur (see modelling section 7). This is indicated by the presence of chlorite, which is not stable in acidic waters.

Focused fluid flow derived from overpressure release during the compaction of sediments in deeper basin parts is discussed to have affected diagenesis by several authors (e.g. (Haszeldine et al., 1999). Overpressure leak-off through faults and fractures can cause focused vertical and lateral fluid flow.
The present day variability in pore water composition together with the compartmentalization of the investigated reservoirs can be seen as evidence against a large scale fluid flow scenario connected with the exchange of the entire pore water. Nevertheless, the effect was tested by model 5 (see section 7). The model indicates that some of the petrographic observation can be explained by a focused fluid flow model. However, it must be considered that relatively high (up to unrealistic high) amounts of water have to flush the sandstone to do this and it seems to be more likely that this scenario is only locally important, for instance close to faults or in fracture zones.

Organic acids and CO_2 can also have been generated by **biodegradation** of hydrocarbons (e.g. Bennett et al., 2000). The shallow burial during first charge is indicated by 3D basin modelling and makes biodegradation of an early hydrocarbon charge very likely (see section 4). Moreover, the $\delta^{13}C$-values of the ankerite cemented sample in well 30/2c-4 can be interpreted as being influenced by biodegradation (see section 8).

Seewald (2001a) demonstrated via laboratory experiments that the **decomposition of n-alkanes** can generate organic acids in the reservoir itself at elevated temperatures. Organic acids, in particular acetic and oxalic acids are considered to increase the solubility of aluminium in water significantly (Surdam et al., 1984), thus increasing its mobility. The effect of organic acids was modelled (section 7 model 4) and leaching by organic acids can explain some of the observed alterations. However, it remains speculative if this process has taken place or not.

In summary, a number of diagenetic processes can be explained by a more or less closed system behaviour. Nevertheless, the presence of hydrocarbons today and the reduction of iron oxides/hydroxides along with the occurrence of Fe^{2+}-bearing mesodiagenetic phases which require the influence of hydrocarbons, indicate an at least partial open system. Leaching by organic maturation or alteration products such as organic acids and CO_2 seems to be efficient and a good interpretation to explain some observations as indicated by modelling results. Three possible sources for the origin of these reactants exist: the adjacent source rocks, the oxidation of n-alkanes or the biodegradation of an early hydrocarbon charge. Stable isotope data can be used to support the biodegradation scenario and the infiltration of source rock related water. However, pervasively flushing of the reservoirs seems to be unlikely due to high salinities, varying compositions of the encountered formation waters and compartmentalization today. Decomposition of n-alkanes may have occurred at higher temperatures in the reservoirs. Finally, it must be considered that no net-gain in porosity was achieved by reactions of the reservoir sandstones with organic acids as indicated by diagenetic modelling (see section 7).

9.2.11 The interaction of mesodiagenetic processes

Numerical modelling of diagenesis indicates that several of the diagenetic processes which caused the observed alterations occurred not independently, but were related or connected to each other. The products of one process were often directly consumed by other reactions. This shows clearly that individual process like quartz cementation may have multiple sources and should not considered independently. Some of the mesodiagenetic reactions were probably triggered by initial hydrocarbon charge and subsequent biodegradation.
A sketch displaying the major process and interactions during mesodiagenesis is given in Fig. 9.3.

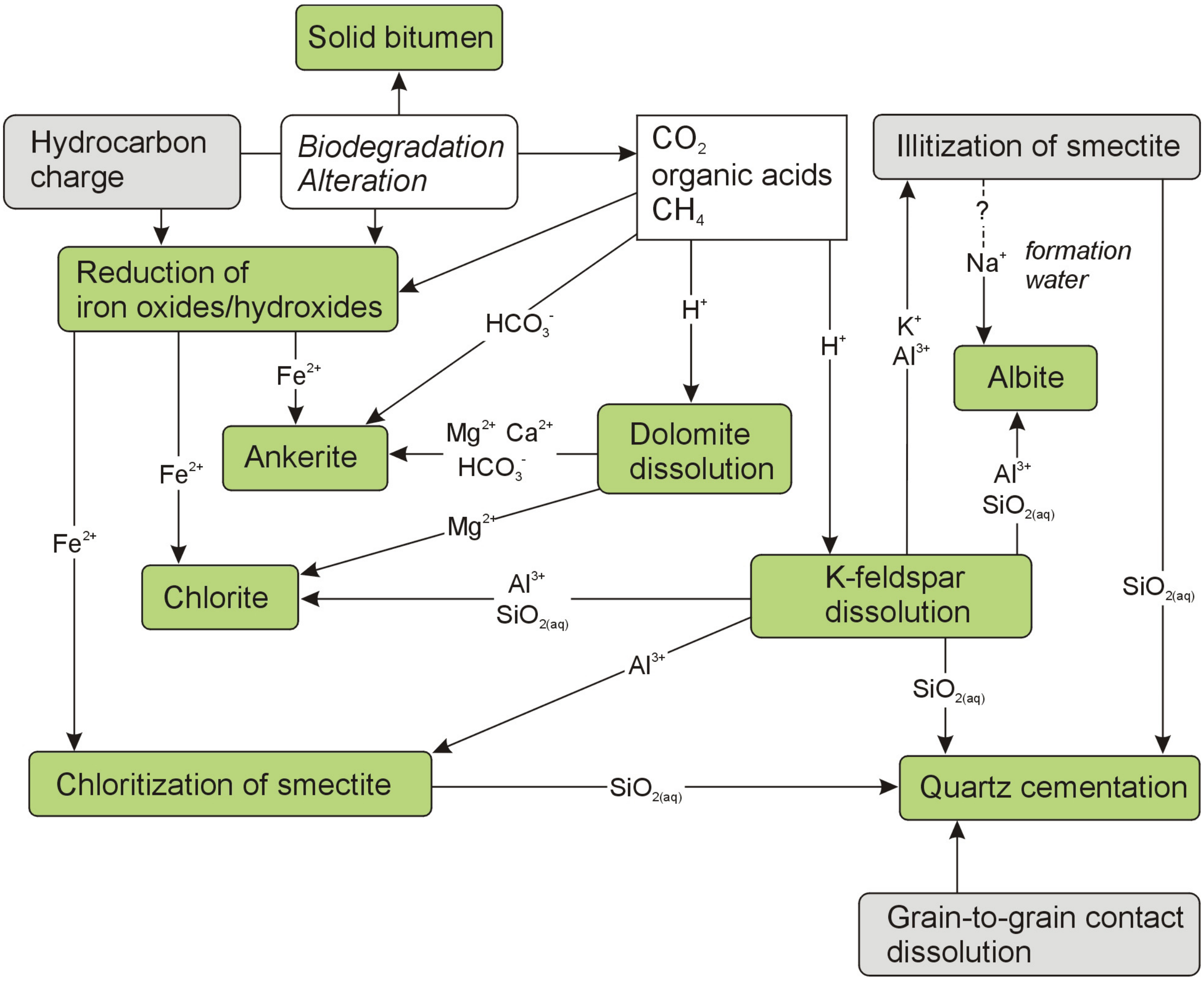

Fig. 9.3: Major mesodiagenetic processes and their interactions in the Triassic Skagerrak Formation of the Jade and Judy Fields as indicated by numerical modelling and petrographic observations.

The high pressure and temperature conditions observed today, had probably little effect on most diagenetic processes in the Jade and Judy Fields since these conditions were established after most of the observed diagenetic processes were already completed.
The filling with hydrocarbons occurred already at relatively shallow burial depth (see section 4 and Neumann, 2007). After final hydrocarbon filling many diagenetic processes were probably retarded and only quartz cementation may have continued in the presence of oil in remarkable amounts as indicated also by a number of other studies (e.g. Barclay & Worden,

2000b). Minor amount of ankerite were also observed to be precipitated after bitumen formation. Quartz cementation sourced by grain-to-grain contact dissolution may have been reduced by late overpressure (Bjørlykke, 1983). Osborne & Swarbrick (1999) observed more quartz cement in wells with high effective stress at present day. However, to evaluate the effect of overpressure exactly, a comparison with wells of the Triassic Skagerrak Formation without overpressure from the same depth and temperature range is necessary.

High porosities are known to be preserved in sandstones with grain framework stabilizing cements and in reservoirs with hydrocarbon fill and overpressure, respectively (e.g. Morad et al., 2000 and references therein). Nevertheless, Ehrenberg & Nadeau (2005) compiled core measurements from the North Sea and found no significant support for the porosity preservation by petroleum in sandstones. So, grain framework stabilizing cements and former pore-filling cements were most likely responsible for the high porosities in the reservoirs today. The role of overpressure remains uncertain, but the high overpressures observed today were probably developed too late to have significant influence on the compaction behaviour (see also discussion section 11).

10 Interpretation and discussion - wells of the Norwegian sector

The interpretation of diagenesis in studied wells of the Norwegian sector are based on petrographic observations and geochemical analyses of a relatively small number of samples (see section 2). Petrographic descriptions and an overview of available material are given in sections 2 and 6, respectively. A detailed discussion of mesodiagenetic processes and their interactions is given in the following section 11.

10.1 Interpretation of diagenetic processes - Rotliegend (wells NOR-A and NOR-B)

The Rotliegend in both wells was found to be water-bearing. Relatively high porosities but low permeabilities were reported from core data. Both investigated Rotliegend reservoirs have documented inorganic diagenesis down to deep burial conditions in contrast to investigated hydrocarbon-filled reservoirs (like the Skagerrak Formation in Jade and Judy Fields), where many late diagenetic processes have been terminated or at least restricted after charging with hydrocarbons.

10.1.1 Eodiagenesis

The eodiagenetic phase assemblage from both wells is overall comparable and contains authigenic phases which are typical for continental settings in an arid to semi-arid climate. Walker et al. (1978) found for instance hematite, quartz, K-feldspar overgrowths and smectite coatings in Cenozoic sediments deposited under comparable climatic conditions. Grain coating clays and iron oxides are also typical eodiagenetic authigenic phases in other Rotliegend sandstones (e.g. Gaupp et al., 1993). Grain coating hematite and illite may have been derived from precursor phases as described for the Triassic Skagerrak Formation in section 9. A large part of the hematite coats (or its precursors[1]) seems to have been inherited from the source area as indicated by its occurrence in grain indentations (see Wilson, 1992 for criteria of inherited clay). Thinner crust/films may have been precipitated in-situ by Fe-bearing ground waters (see also discussion in section 9).

Authigenic K-feldspar was detected in minor amounts only in samples from well NOR-A and the amount is significantly lower than in samples from the Triassic Skagerrak Formation. The reason may be the initial detrital composition: Investigated Rotliegend sandstones contain more quartz and less detrital feldspar and muscovite than Triassic sandstones from the Jade and Judy Fields. Weathering of these silicates was probably the major source for K-feldspar overgrowths.

Dolomite occurs pore-filling or as isolated rhomb-shaped crystals and was most likely formed in the groundwater zone (see discussion for eodiagenetic dolomites in section 9). The weak zonation indicates changing ground water composition. Early diagenetic dolomite is very common in Rotliegend sandstones of the North Sea and adjacent areas (Ziegler, 2006; Gaupp & Okkerman, 2011). Barite was found in samples from both wells and anhydrite only in well NOR-B. Some petrographic indications (e.g. large occupied intergranular volumes) point to an early diagenetic origin. Eodiagenetic sulphates (anhydrite and barite) are common in the Rotliegend of northwest Germany (Gaupp et al., 1993). Anhydrite, gypsum, barite, calcite and dolomite are characteristic early diagenetic cements in coastal sabkha, evaporitic sandflat and playa margin environments (Gaupp, 1996; Morad et al., 2000). However, a later precipitation cannot completely be ruled out, at least for some of the observed crystals. Late diagenetic sulphates were reported from other Rotliegend settings as well. Gluyas et al. (1997) described for instance pervasive (up to 20 %) late barite and anhydrite cementation in Rotliegend sandstones of the southern North Sea (Amethyst Field) with oxygen and sulphur isotopic compositions comparable to overlying Zechstein anhydrites. Late diagenetic authigenic

---

[1] *see discussion section 9*

sulphates (anhydrite and barite) are also known from the Rotliegend in NW-Germany (Gaupp, 1996; Gaupp et al., 1993).

Leucoxene was most likely derived from the breakdown of titanium bearing heavy minerals during eodiagenesis.

10.1.2 Mesodiagenesis

Two episodes of quartz cementation could be observed in well NOR-A. One before (quartz I) and one after (quartz II) the precipitation of fibrous/flaky illite meshworks. Quartz cement predating authigenic illite was not observed in well NOR-B. However, the amounts of both, fibrous/flaky illite and authigenic quartz are significantly lower in well NOR-B than in well NOR-A and the textural relationship between illite and quartz is not clear in this well. So, the presence of an early quartz cannot be ruled out for well NOR-B. The timing of quartz I in well NOR-A remains uncertain. It may be an early mesodiagenetically or even eodiagenetically formed cement. The high intergranular volume occupied locally by this cement suggest early precipitation. Early soil zone silica cementation is known from silcretes in recent arid to semi-arid areas, such as the Kalahari (Watts, 1980). The occurrence of early quartz overgrowths was also described for Rotliegend sandstones in Northwest Germany (e.g. Gaupp et al., 1993). However, it must be considered that large cement dissolution pores are also present today and quartz I could have formed in such pores under deep burial conditions.

The higher amount of quartz cement in well NOR-A compared to well NOR-B is accompanied by a larger proportion of corroded K-feldspar grains. This indicates that feldspar dissolution or alteration to illite following reaction 11.9 was responsible for a significant part of the quartz cement. Additional contributions to quartz cementation came most likely from grain-to-grain contact dissolution.

Diagenetic modelling (section 7) indicates that minor amounts of authigenic albite can be formed by interaction of K-feldspar grains with saline pore waters with increasing temperatures. Thus, the albite crystals present in K-feldspar grains seem to be the product of changing mineral stability with increasing temperature.

A remarkable difference between investigated samples of the two wells is the more pronounced development of mesodiagenetic alterations in well NOR-A. This is expressed by local bleaching[2], cement- and feldspar dissolution along with the formation of pervasive fibrous illite meshworks and the precipitation of Fe-dolomite cement. Fe-dolomite is completely absent in well NOR-B, while cement dissolution is not as intensive here. The pore-filling dolomite is still present in well NOR-B (only relicts were found in well NOR-A). Pervasive fibrous illite is restricted to the deepest sample in well NOR-B. The morphology of the illite seems to reflect growth time, starting with single fibres evolving into a more flaky/platy type with time (see e.g. discussion in Wilkinson et al., 2006). A more detailed discussion of illite formation is given in section 11.

Formation of Fe-dolomite overgrowths is most likely the product of increasing Fe^{2+} content in the pore water probably sourced from the reduction of iron oxides/hydroxides. The dissolution and enhanced corrosion of detrital K-feldspar in well NOR-A seems to be linked to the growth of fibrous/flaky illite meshwork following reaction 11.9 (see following section 11).

Leaching of the early diagenetic cement was probably simultaneous and the process may be comparable to ankerite formation in the investigated wells of the Triassic Skagerrak Formation. Smectite-to-illite transformation occurred most likely in grain-coating clay minerals. However, this process was volumetrically not as important as the smectite-to-illite transformation in the mudstones of the Triassic Skagerrak Formation. Therefore, quartz

---

[2] The cm-sized local bleaching zone should not be over-interpreted. Nevertheless, whitish pale colours reported from the upper 25m of the Rotliegend section in well NOR-A may be seen as further evidence for bleaching of red beds in this well.

cementation is controlled predominantly by other factors, such as grain-to-grain contact dissolution, the dissolution at stylolites and feldspar leaching.

Recent works from Schöner & Gaupp (2005) show that pervasive meshwork illite and Fe-rich cements are related to organic maturation products in the Rotliegend of northwest Germany. The petrographic difference between samples of the two wells investigated here may be explained by a stronger influence of organic maturation products in well NOR-A. However, both reservoirs were encountered water-bearing (with very faint hydrocarbon indications) and the influence of organic maturation products was probably significantly weaker than in the investigated Triassic Skagerrak Formation samples. Bleaching was most likely restricted to local areas close to fluid pathways.

Mesodiagenetic processes are linked also here and produce a typical petrographic pattern. Interpreted main reaction pathways are given in Fig 10.1.

In summary, the studied Rotliegend reservoirs were found to be water-bearing, but an influence of organic maturation products seems to be likely. The most significant difference to studied Skagerrak Formation reservoirs is the occurrence of permeability destroying fibrous/flaky illite. Other mesodiagenetic processes, such as quartz cementation, dolomite dissolution and albite formation also occur in the Triassic. Nevertheless, controlling factors for the individual processes were partly different (e.g. quartz cementation related to smectite-to-illite transformation in the Skagerrak Formation).

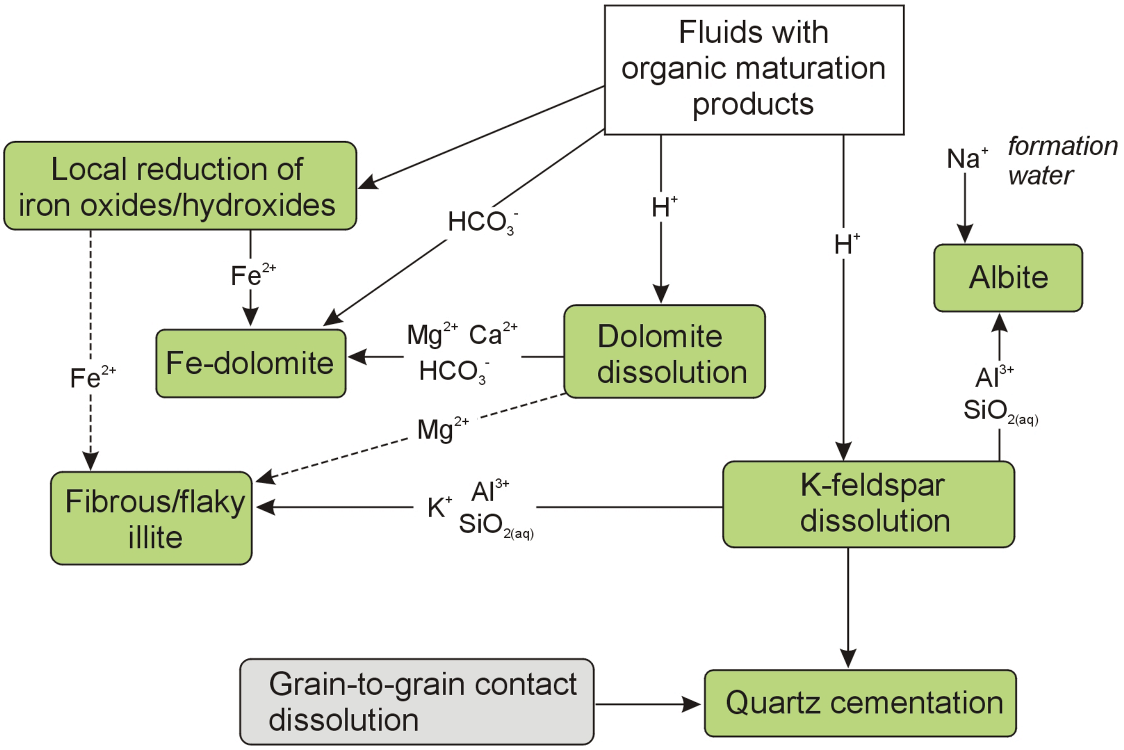

Fig. 10.1: Major mesodiagenetic processes and their interactions in Rotliegend sandstones of well NOR-A as indicated by petrographic observations. Reduction of iron oxides was not as pervasive as in the Triassic Skagerrak Formation of the Jade and Judy Fields in the UK sector.

10.2 Interpretation of diagenesis in the Triassic of well NOR-E

The seven samples from well NOR-E represent a more distal facies in a mud-richer depositional environment, than the investigated samples from the Triassic Skagerrak Formation of the Jade and Judy Fields. The thin sandstone layers may have been deposited as sheetfloods in the distal part of a braid plain (Prestholm & Walderhaug, 1994). The overall poorer reservoir quality (compared to the Jade and Judy Fields) is most likely controlled by depositional facies (only sheetflood sands present) and eodiagenetic dolomite cementation.

Diagenesis is partly facies controlled, comparable to the studied wells of the UK-sector. Authigenic quartz, bitumen and euhedral chlorite occur dominantly in sheetflood sands or in sandy parts of the facies AS. Grain coating chlorite is present predominantly in the finer grained facies AS. Authigenic dolomite is abundant in all samples.

10.2.1 Eodiagenesis

Eodiagenetic phases and their evolution are overall comparable to the Jade and Judy Fields in the UK-sector: Grain coating chlorites were probably derived from a smectite precursor, hematite evolved likely from goethite and dolomite was formed as dolocrete (see discussion in section 9 for details). The significantly lower amount of K-feldspar overgrowths is most likely related to the quartz richer detrital composition as previously discussed for the Rotliegend in the Norwegian sector.

10.2.2 Mesodiagenesis

Some of the mesodiagenetic alterations observed in the UK-sector occurred here too. However, they are not as pronounced. This may be related to the lower primary porosity which goes along with a lower available pore-water volume during burial diagenesis. Thus, pore water-rock interactions were most likely limited in the studied Triassic interval of well NOR-E.

The infiltration of petroleum is proven by the observed bitumen. Hydrocarbon induced iron oxide/hydroxide reduction may have provided ferrous iron for the neo-formation of chlorite or for the smectite-to-chlorite transformation. Only minor amounts of ankerite were detected and no indication for pervasive dolomite leaching was found. This indicates that the dolomite dissolution – ankerite precipitation process was not significant here. Small volumes of ankerite were probably formed coeval or subsequent to chlorite.

High present day reservoir temperatures (190°C) indicate that the observed bitumen is the relict of thermally altered petroleum (pyrobitumen).

Authigenic quartz was predominantly sourced from grain-to-grain contact dissolution and from smectite-to-illite or chlorite transformation (see also section 9). Significant import of silica from mudstones into the thin sand layers, comparable to well 30/2c-4 seems to be likely. Quartz crystals overgrowing bitumen indicate that at least a part of the authigenic quartz is of late diagenetic origin, probably following a rise in the oil water contact.

Another difference to the UK-Fields is the lack of authigenic albite in the investigated samples. All samples were visually tight and had only negligible amounts of thin section porosity (see Appendix 2.3). This suggests that probably not enough pore water was available to supply sufficient Na^+ when the temperature was reached for the start of albitization (see also section 9 for discussion of starting temperatures).

In summary, eodiagenetic processes in the Triassic of well NOR-E are comparable to those in finer grained lithologies of the Jade and Judy Fields, except for the minor occurrence of K-feldspar overgrowths. Mesodiagenetic alterations are not as intensive as in the two investigated fields from the UK-sector. This is related to the low initial porosity along with restricted amounts of pore water available for mass transport. A remarkable difference to the Jade and Judy Fields is the lower amount of dolomite dissolution and ankerite formation, which may be related to the lack of biodegradation in well NOR-E, were hydrocarbon charge occurred not until deep burial (the seven samples from well NOR-E represent diagenesis in a deep graben settings, while Judy/Jade represent a morphological high). The bitumen present is assumed to be related to thermal cracking of hydrocarbons (pyrobitumen).

10.3 Interpretation of diagenesis in the Triassic of well NOR-C

Well NOR-C represents Triassic and Jurassic sandstones close to a fault separating both stratigraphic units from each other (Jysereid et al., 1994) and is therefore suitable to assess the effects of fault associated fluids.

The eodiagenetic evolution of the Triassic Skagerrak Formation in well NOR-C is comparable to the other Triassic wells studied and the reader is referred to section 9 for detailed discussion. The observed pyrite may be an eodiagenetic phase precipitated under locally reducing conditions (Weibel, 1998) or be related to fluids that percolated into the Triassic sandstone from the fault.

Bleaching of red beds seems to have occurred also in the Triassic of well NOR-C as indicated by hematite remains in the dolocrete sample. Ferrous iron-bearing mesodiagenetic phases are also present, predominantly in the form of different types of chlorite. Ferroan carbonates were not observed in the studied samples, but occur together with barite in feldspar dissolution pores as described by Prestholm & Walderhaug (1994) for samples from the Triassic interval of the same well.

Samples from well NOR-C show some different mesodiagenetic pattern compared to samples from the Jade and Judy Fields in the UK-sector. The most significant difference is the occurrence of minor amounts of illite fibres and flakes, which may be attributed to the lack of a hydrocarbon fill, and the rosette shape and larger size of authigenic chlorite plates. Smaller euhedral chlorite plates were also found in the proximity of fractures in the Jade Field indicating the influence of fault related fluids there. The illite fibres may have grown also under the influence of hydrocarbon-bearing fluids entering the reservoir via the fault. This wells shows that minor illite precipitation is also possible in the Triassic. Nevertheless, the minor local illite observed in well NOR-C is not comparable to the pervasive meshworks in the Rotliegend of well NOR-A.

All investigated sandstone samples show intense K-feldspar dissolution as well as some faint traces of cement dissolution. The timing of this leaching event remains unclear. Prestholm & Walderhaug (1994) interpreted the feldspar leaching in well NOR-C as being caused by meteoric waters. However, the lack of authigenic kaolinite can be seen as evidence against the meteoric water leaching scenario (see also discussion in section 9). All investigated samples were taken very close to a major fault and the two Jurassic sandstone samples above the fault showed intense feldspar leaching too. Fluids circulating along this fault may have been responsible for the leaching. Main source rocks in the area are located in the Jurassic Farsund Formation. They are fairly mature and thought to have generated significant quantities of oil and gas (Jysereid et al., 1994). Traces of bitumen staining in samples from the overlying Jurassic sandstones show that at least minor hydrocarbon migration took place. Different possible ways for feldspar dissolution are discussed in section 11. The available data and the amount of samples from this well are to insufficient to allow a more detailed evaluation.

Sutured grain contacts and stylolites were observed in the investigated Triassic samples from well NOR-C and indicate that a certain amount of silica was derived from stylolites and grain-to-grain-contact dissolution additionally to feldspar dissolution and sandstone-mudstone interactions. Sandstones containing detrital clay bands or grain coating clays were observed to be more affected by grain-to-grain contact dissolution.

In summary, The Triassic in well NOR-C shows diagenetic alterations close to a fault zone. Extensive K-feldspar dissolution was probably caused by aggressive fault related fluids. A significant difference to other Triassic reservoirs studied is the presence of minor amounts of illite fibres/flakes and a different morphology of the authigenic chlorite here. The Triassic in well NOR-C was found to be water-bearing and the presence of this local illite may be attributed to the lack of a hydrocarbon fill.

10.4 Interpretation of diagenesis in Jurassic sandstones of wells NOR-C and NOR-D

Well NOR-C represents Triassic and Jurassic sandstones close to a fault. Well NOR-D was drilled as a site track of well NOR-C and documents the same Jurassic sandstones as well NOR-C, but further away from the fault zone.

The eodiagenesis of the Jurassic in wells NOR-C and NOR-D is comparable with other Jurassic sandstones. A typical eodiagenesis for Upper Jurassic Sandstones in the North Sea is discussed in more detail later for well NOR-G. The observed minor K-feldspar overgrowths may have been inherited if the sand was supplied from erosion of Triassic sediments in the hinterland. Nevertheless, authigenic K-feldspar was also reported as eodiagenetic to shallow burial cement from other Jurassic sandstones in the North Sea (e.g. Bjørlykke & Brendsdal, 1986; Weibel & Keulen, 2008), so it may have formed in-situ as well.
Framboidal pyrite is typical for marine eodiagenesis and was usually formed by pseudomorphing greigite (Fe_3S_4) framboids (which are derived from initial mackinawite - FeS) in the sulphate reduction zone (Berner, 1981, Wignall, 1994). Chloritic clay rims in marine settings are known to be derived mesodiagenetically from an iron-rich precursor phase such as berthierne or odinite (e.g. Odin, 1990; Hillier, 1994; Worden & Morad, 2003).

Authigenic carbonate formation started probably with non-ferrous dolomite grading later into Fe-dolomite. Part of the dolomite may have been precipitated in the sulphate reduction zone triggered by microbial activity (e.g. Morad, 1998 and references therein). Nevertheless, stable isotope data suggest a mesodiagenetic origin from waters containing carbon derived from thermal maturation of organic matter in the source rocks (see section 8). Two precipitation temperature ranges were calculated using the δ^{18}O-values from the authigenic carbonates of group III (see section 8 for details). The first temperature range was estimated for a pore water with the δ^{18}O-value of Jurassic marine water resulting in temperatures between 75 and 110°C. A second temperature range was derived from an isotopically evolved pore water resulting in significantly higher temperatures between 115 and 166°C. Fluid inclusion measurements at this dolomite type in other Central Graben wells suggested precipitation temperatures between 90 and 130°C (Prestholm & Walderhaug, 1994). Thus, a mesodiagenetic origin at temperatures exceeding 100°C is likely.
Vermicular kaolinite was found only in one sample from well NOR-D in very small amounts. Pervasive occurrence of authigenic kaolinite (comparable to well NOR-G) could not be observed in any of the two wells. So, meteoric water is probably not responsible for the intense feldspar dissolution in well NOR-C. The iron-rich coarse euhedral chlorite plates occurring in well NOR-C (and also in well NOR-D) are comparable to those found in the Triassic of well NOR-C. Similar chlorite types were not detected in the other studied Jurassic wells. Their occurrence may be a local feature related to mesodiagenetic fluids entering the

reservoir via faults. Ferrous iron may have been derived from the reduction of hematite in adjacent Triassic strata.
Silica sourced from stylolites and grain-to-grain contact dissolution together with feldspar leaching products seems to be responsible for the late quartz cement.
Late diagenetic barite may have formed from barium released by feldspars (Prestholm & Walderhaug, 1994).

In summary, The Jurassic samples of well NOR-C document the influence of mesodiagenetic fault related fluids causing feldspar dissolution probably associated with chlorite neo-formation. The present carbonates are interpreted to be of mesodiagenetic origin and precipitated at temperatures exceeding 100°C.

10.5 Interpretation of diagenesis in Intra-Farsund sandstones of well NOR-F

The thin sandstone layers interbedded into organic rich shales, mudstones and fine crystalline carbonates of the Farsund Formation provide a good example for deep burial sandstone diagenesis in very close vicinity of a source rock. They are suited to study the interaction of organic maturation products with inorganic compounds of sandstones.

10.5.1 Eodiagenesis

The eodiagenetic phase assemblage probably reflects depositional conditions in a restricted basin with partial anoxic bottom waters. The predominant eodiagenetic mineral is ubiquitous pyrite. It occurs mainly in euhedral form in the thin sandstones and in framboidal form in the mudstones and black shales. The framboidal form is indicator for greigite and mackinawite precursors (Berner, 1981; Wignall, 1994).
The small amounts of calcite and dolomite cement may also be of eodiagenetic origin. Carbonate supersaturation may for instance have been caused by bacterial fermentation of organic material (Cowan, 1989). Calcite is a typical cement in marine eodiagenesis and dolomite is known to precipitate in the sulphate reduction zone under microbial influence (Morad, 1998; Morad et al., 2000). Mg^{2+} required for dolomite formation in the sulphate reduction zone (and later also for ankerite preciptation) may have been derived from sea water with additional contributions from the recrystallization of high-Mg calcite in the carbonate layers of the Farsund Formation or from Mg^{2+} adsorbed to organic matter (see also Lawrence, 1991).
However, it must be considered that the whole texture is heavily overprinted by later mesodiagenetic processes and so the evaluation of early diagenesis is limited.

10.5.2 Mesodiagenesis

Mesodiagenesis in the thin sandstone layers is dominated by the close relationship to maturing organic rich black shales. CO_2 and organic acids are known to be generated during burial and thermal maturation of organic material (e.g. Kharaka et al., 1986; Snowdon, 1989). Dissolved organic species are prone to be degraded to CO_2 and hydrocarbon gases by bacteria at temperatures lower than 80°C (Kharaka et al., 1986). The organic acid concentration was most likely at maximum between 80 and 120°C (e.g. Surdam et al., 1989b). Carboxylic acids begin to decarboxylate at temperatures exceeding 100°C accompanied by an increase in pCO_2 (Surdam et al., 1989b). This pCO_2 increase may rather enhance carbonate precipitation than dissolution (Morad, 1998) as indicated also by the abundant ankerite cementation in well NOR-F.
The fluids associated with source rock maturation percolated most likely into the thin interbedded sandstones and affected their mineralogy. The paragenetic sequence derived from the textural relationship indicates that the process has started with the breakdown of detrital

feldspar grains and the precipitation of kaolinite and quartz. It is very unlikely that this phase assemblage is the result of meteoric water infiltration, since the thin sandstone layers are completely enclosed into tight shale lithologies. Kaolinite is most likely the product of low pH-waters derived from the thermal alteration of organic material in the adjacent black shales. However, McMahon et al. (1992) described the link between microbial organic acid production (via fermentation) in clays and microbial organic acid consumption (via sulphate reduction) in interbedded sands at relatively shallow depths for the Black Creek Formation in South Carolina. The influence of microbial organic acids may have been responsible for kaolinite formation too.

A part of the kaolinite transformed probably into dickite with increasing temperatures as indicated by SEI (secondary electron images).

A large part of the kaolinite was later replaced by authigenic chlorite, as suggested by the occurrence of pseudomorphous replacements and the relatively high aluminium content of the chlorite (see section 6). The presence of liquid hydrocarbons may have blocked late diagenetic ferrous iron-bearing waters from alterating kaolinite in areas were it is still present. This is indicated by bitumen staining of kaolinite/dickite. The phase of chloritization and chlorite neoformation was associated with a contemporaneous or following phase of pervasive pore occluding ankerite cementation. The replacement of kaolinite by chlorite can be explained by changing minerals stabilities with increasing temperature (see Fig. 10.2). However, only small amounts of chlorite can be formed from the iron dissolved in the interstital pore water. A simple temperature increase under closed system conditions in the sandstones cannot explain the pervasive chlorite and ankerite formation. Both were most likely initiated by a significant change in pore water chemistry together with increasing temperatures, probably connected to the smectite-to-illite transformation in the surrounding black shales.

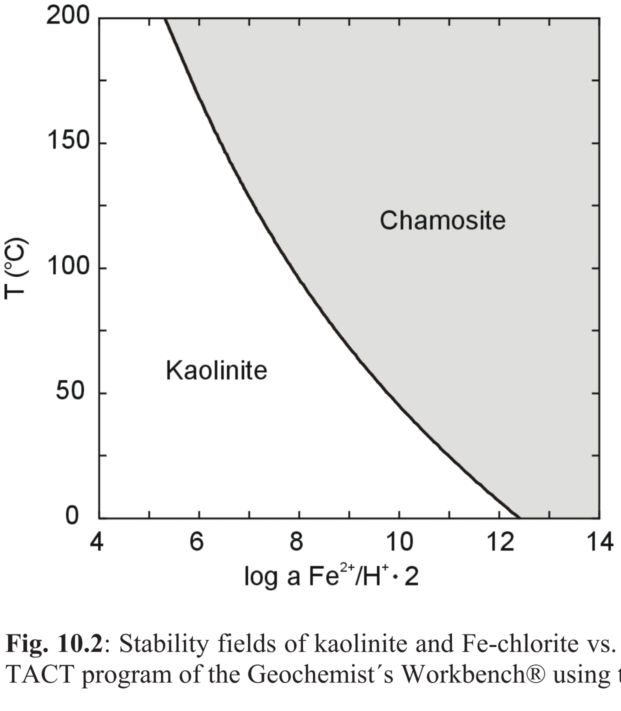

Fig. 10.2: Stability fields of kaolinite and Fe-chlorite vs. temperature in the presence of quartz (created with the TACT program of the Geochemist´s Workbench® using thermo.dat).

Late diagenetic pore waters must have experienced a significant increase in Fe^{2+}. The source of the ferrous iron is not entirely clear, but was most likely the illitization of smectite in the thick adjacent clay rich lithologies of the Farsund Formation with increasing temperatures at deeper burial (see section 11 for reaction equations). This process may also have liberated additional Mg^{2+}.

The ions required for late diagenetic ankerite precipitation in the sandstones were most likely sourced by dissolution of fine-crystalline calcite and from illite-to-smectite transformation in the source rocks. Ankerite-filled fractures in the source rocks can be seen as evidence for leaching and reprecipitation of carbonates. The studied ankerite-bearing sandstone samples have lower $\delta^{13}C$-values than the fine-crystalline calcite of the source rock. A shift towards lighter carbon isotopes is frequently associated with two diagenetic processes in marine sediments: sulphate reduction and thermal decarboxylation (see Irwin et al., 1977). Authigenic carbonates formed in the sulphate reduction zone contain usually no ferrous iron, since this is predominantly consumed by the precipitation of pyrite from cogenerated H_2S (e.g. Morad, 1998). Therefore, the shift was most likely caused by the incorporation of isotopically light carbon from thermal maturation of organic matter. This is consistent with the lighter $\delta^{18}O$-values indicating higher temperatures. The temperature range calculated for type III carbonates (the ankerite of well NOR-F plots in this field – see section 8 for details) using a Jurassic marine water signature (T between 75 and 110°C) is compatible with the interpretation that ankerite formation started after the onset (and beginning Mg^{2+} and Fe^{2+} release) of smectite-to-illite transformation. Thus, ankerite formation was probably triggered by organic maturation and mobilization of carbonates by leaching agents at higher temperatures.

Albite may have formed from Na^+ of the pore water and K-feldspar dissolution with increasing temperatures, but can also have been triggered by Na^+ release after the onset of smectite-to-illite transformation in adjacent mudstones and black shales.

The present quartz cement was most likely precipitated from multiple sources during burial and not restricted to one single event as indicated by textural relationship to other phases (see section 6). The breakdown of feldspars must have released a remarkable amount of silica. The dissolution of detrital quartz grains at grain contacts and clay lamina has most likely added further silica with increasing compaction. Clay mineral transformations, such as the illitization of smectite in the surrounding mudstones have probably generated a significant amount of silica. Reactive transport modelling (see section 7) has shown that the silica transport is possible over short distances by diffusion. The import from other formations can be completely neglected, since the thin sand layers are completely sealed by surrounding tight lithologies. Quartz cemented areas seem to preserve a lower intergranular volume than ankerite cemented areas. So, late quartz cement may have occluded the entire remaining porosity subsequent to ankerite cementation.

Diagenesis ceased most likely with complete occlusion of interstital pore space by ankerite and quartz cement, leaving only small amounts of microporosity.

In summary, the mesodiagenesis of the thin intra-Farsund sandstone layers is dominated by the close relationship to maturing organic rich source rocks. Mesodiagenetic alterations started with the breakdown of detrital feldspar grains to kaolinite and quartz. A large part of the kaolinite was probably later replaced by authigenic chlorite and a minor part by dickite. Chloritization and chlorite neoformation were accompanied by pervasive ankerite cementation. The replacement of kaolinite by chlorite can be explained by changing minerals stabilities with increasing temperature together with smectite-to-illite transformation in the surrounding source rocks. The ions required for late diagenetic ankerite precipitation were most likely mobilised in the source rocks and transported into the thin sandstones destroying a significant proportion of the porosity. Thus, the influence of organic maturation products brought no gain in porosity in the studied intra-Farsund sandstones.

10.6 Interpretation of diagenesis in Jurassic sandstones of well NOR-G

The investigated samples of the Upper Jurassic Ula Formation from well NOR-G represent hydrocarbon bearing sandstones deposited in a shoreface and lagoonal environment.

10.6.1 Eodiagenesis

Eodiagenetic alterations and processes are generally related to the depositional environment and the present phase assemblage is typical for marine settings. Authigenic pyrite was probably formed in the sulphate reduction zone beneath the sediment water interface (Berner, 1981; Wignall, 1994).

Grain coating iron-rich clays are typical for deltaic settings in subtropical to tropical seas were they form close to river mouths from flocculating clay minerals (Ehrenberg, 1993; Odin, 1990; Worden & Morad, 2003; Ryan & Hillier, 2002). They are abundant in Jurassic sediments of the North Sea (Ehrenberg, 1993). The early origin of these clay coats is indicated by textural observations (see also section 6 and Prestholm & Walderhaug, 1994). The former shape of dissolved feldspar grains is often outlined by such clay rims. The early diagenetic iron-rich clays were most likely transformed into chlorite with increasing burial (Worden & Morad, 2003).

Early diagenetic corrosion of unstable feldspars cannot be excluded. However, the main episode of feldspar leaching is most likely associated with later telodiagenetic kaolinite formation.

Early pore-lining illite in North Sea sandstones can be interpreted as early diagenetic clay (most likely smectite or smectite-rich illite) or infiltrated detrital clay (Wilkinson et al., 2006).

10.6.2 Telodiagenesis

Crestal parts of the structure were probably subject to erosion in Upper Jurassic times, since an unconformity is present between the Oxfordian- to lower Kimmeridgian and the overlying marine Volgian mudstones (Bray, 1992). Pervasive feldspar dissolution and kaolinite precipitation (along with quartz quartz cementation) were most likely caused by the infiltration of meteoric waters (Prestholm & Walderhaug, 1994). Percolation of meteoric waters and the resulting leaching associated with kaolinite formation is well known from many Jurassic North Sea reservoir, particularly from the Brent Group (Bjørlykke & Brendsdal, 1986; Bjørlykke et al., 1992; Bjørlykke et al., 1989; Bray, 1992; Glasmann, 1992). It cannot be excluded that a short phase of burial occurred before the meteoric water flushed the reservoir, but most mesodiagenetic phases were observed to postdate kaolinite formation. A major part of the initial marine pore fluid was most likely replaced by meteoric waters relatively early. Meteoric waters are known to percolate deep into sedimentary basins as mentioned previously in section 9 (Giles, 1997; Worden & Burley, 2003 and references therein).

10.6.3 Mesodiagenesis

The timing of dolomite formation remains uncertain and the textural relationship observed in the samples is ambiguous (see section 6.3). The ferroan carbonates were most likely precipitated during deeper burial as indicated by the paragenetic sequence. Bray (1992) and Prestholm & Walderhaug (1994) interpreted also the dolomite in well NOR-G as being of late diagenetic origin. Nevertheless, dolomite can also form at relatively shallow depths in the sulphate reduction zone or when marine waters mix with waters of meteoric origin (e.g. (Morad, 1998; Morad et al., 2000). Nevertheless, early carbonate cements in marine sediments are often dominated by calcite (Morad et al., 2000). Late diagenetic dolomite and ankerite could have formed from Mg^{2+} and Fe^{2+} bearing compactional fluids. The Mg^{2+} in these fluids can for instance be derived from the illitization of smectite in clay-rich lithologies, as proposed for some of the dolomites in the Triassic Skagerrak Formation of the Jade Field (see section 9) and for the ankerite in well NOR-F. Prestholm & Walderhaug (1994) reported precipitation temperatures between 90-130°C for a comparable type of dolomite in other Central Graben wells derived from homogenisation temperatures of aqueous fluid inclusions. This temperature range is consistent with the temperatures calculated from $\delta^{18}O$-values of group III carbonates using a Jurassic marine water signature (T between 75 and 110°C) as well as with the lower boundary of the temperature range calculated using an evolved formation water from the Ula Field (T between 115 and 166°C) (see section 8 for details). 3D basin modelling by Neumann (2007) indicated a hydrocarbon charge at temperatures between 80 and 90°C in the Oxfordian Sands.

These points indicate a regional comparable precipitation process for mesodiagenetic dolomites and ferroan carbonates in Upper Jurassic sandstones of the Central Graben, probably associated with infiltrating waters enriched with organic maturation products from the source rocks (e.g. Farsund Formation).

Illite fibres growing locally on kaolinite crystals or in leached feldspars were most likely formed at increasing temperatures. Minor amounts of authigenic albite located in leached K-feldspars formed most likely with Na^+ taken from the pore water (see also sections 9 and 11 for discussion).

The mass of quartz cement was probably formed during late diagenesis. Stylolites and zones with enhanced grain-to-grain contact dissolution in mica- and clay-rich layers are most likely the major sources for the late authigenic quartz observed. Prestholm & Walderhaug (1994) state that fluid inclusions data from the Ula Formation in the Ula Field and in another unnamed well suggest the onset of significant quartz cementation at temperatures exceeding 80 to 100°C.

Small amounts of barite are most likely of late diagenetic origin. They can be explained by barium from feldspar dissolution and SO_4^{2-} from pore water (as discussed in section 9 for the Triassic). Evidence for a feldspar source of the barium is given by the authigenic barite inside of feldspar dissolution pores.

The charge with hydrocarbons probably terminated most diagenetic processes in well NOR-G. However, quartz overgrowing bitumen indicates continued minor quartz cementation close to grain contacts subsequent to hydrocarbon fill.

In summary, well NOR-G shows a typical marine eodiagenesis. Meteoric water influx probably caused feldspar dissolution along with kaolinite and quartz cementation after shallow burial. The mesodiagenetic evolution is characterized by carbonate and quartz cementation together with illite, chlorite, barite and albite precipitation. Mesodiagenetic processes, such as carbonate cementation may have been influenced by organic maturation products. The reservoir is filled with hydrocarbons today. This hydrocarbon fill has terminated many diagenetic processes.

11 Comparison and synthesis

This section contains an attempt to bring the observations from all investigated settings together and to put them into a larger framework. It contains a detailed discussion to major aspects and processes which were identified in the studied samples.

Diagenesis is generally driven by a broad range of physical, chemical and also biological processes (Worden & Burley, 2003). During burial the rock and the interstitial pore water try to reach equilibrium and react on changing temperature and pressure conditions, as well as on the influx of fluids and changes in chemical composition of pore fluid caused by diffusively transported ions (Worden & Burley, 2003).

11.1 Comparison of eodiagenesis in the studied wells

Eodiagenetic modifications and the chemistry of the early diagenetic pore waters are predominantly controlled by depositional environment and palaeoclimate (see also Worden & Burley, 2003). Nevertheless, the detrital composition of the sandstones has played also a certain role. So, the amount of K-feldspar overgrowths is most likely controlled by the proportion of detrital K-feldspar as indicated by a lower amount of K-feldspar overgrowths in Rotliegend and Triassic sandstones of the Norwegian sector compared to Triassic sandstones in the UK-sector (see section 10).

However, eodiagenetic processes are generally heavily overprinted by later alterations in the studied deep basinal settings. Eodiagenesis is easier to study in shallower wells or in recent analogous settings. Thus, the focus of the following discussion is on burial diagenesis.

The eodiagenetic evolution in the studied Rotliegend and Triassic sediments was more or less comparable and detailed discussions are given in the previous sections 9 and 10, respectively. The arid to semi-arid climate with highly oxic conditions resulted in iron oxide/hydroxide formation. K-feldspar overgrowths were formed mainly in higher permeable sediments, probably under shallow burial conditions. Early grain coating smectitic clay minerals were abundant in some of the investigated sandstones. They were transformed into more stable phases, such as chlorite and illite during burial. Dolocrete formation was probably caused by a down-slope evolution of groundwater or by the mixing of groundwater with playa lake brines.

The eodiagenesis of the studied Jurassic sandstones was dominated by the marine depositional environment. The pore waters were less oxic, partially even sub-oxic to anoxic (e.g. the Intra-Farsund sandstones). This resulted in a different suite of iron-bearing eodiagenetic minerals, such as pyrite. The eodiagenetic clay coatings, which evolved later into chlorite, had probably also a different composition (more likely to be odinite) compared to those from the Permo-Triassic.

11.2 Comparison of meso- and telodiagenetic alterations in the studied wells

The studied settings were isolated from the influence of surface waters with increasing burial and mesodiagenetic processes overprinted the eodiagenetic framework. Porosity was reduced significantly by mechanical compaction and cementation. The largest amount of porosity reduction was attributed to mechanical compaction (see Ajdukiewicz & Lander, 2010). One of the studied wells (NOR-G) was affected by telodiagenetic alterations caused by meteoric water influence. This is discussed in detail in section 10.

The mineral assemblages present (related to depositional composition and varying eodiagenetic alterations) controlled along with burial history and fluid inflow the later mesodiagenetic evolution in the investigated sandstones. Overall, two mesodiagenetic evolution pathways can be derived from the studied wells. The mesodiagenesis of Permo-

Triassic sediments was influenced by the presence or former presence of iron oxides/hydroxides, which were partially reduced during mesodiagenesis. This source of ferrous iron played no significant role in the investigated Jurassic sandstones.
All of the investigated wells were drilled for hydrocarbon exploration. Therefore, it is not surprising that all of them have a significant "risk" of having been affected by organic maturation products, despite the fact that some of them were found water-bearing. Organic maturation products, particularly petroleum and its alteration products, played an important role in the mesodiagenesis of all studied sandstones.

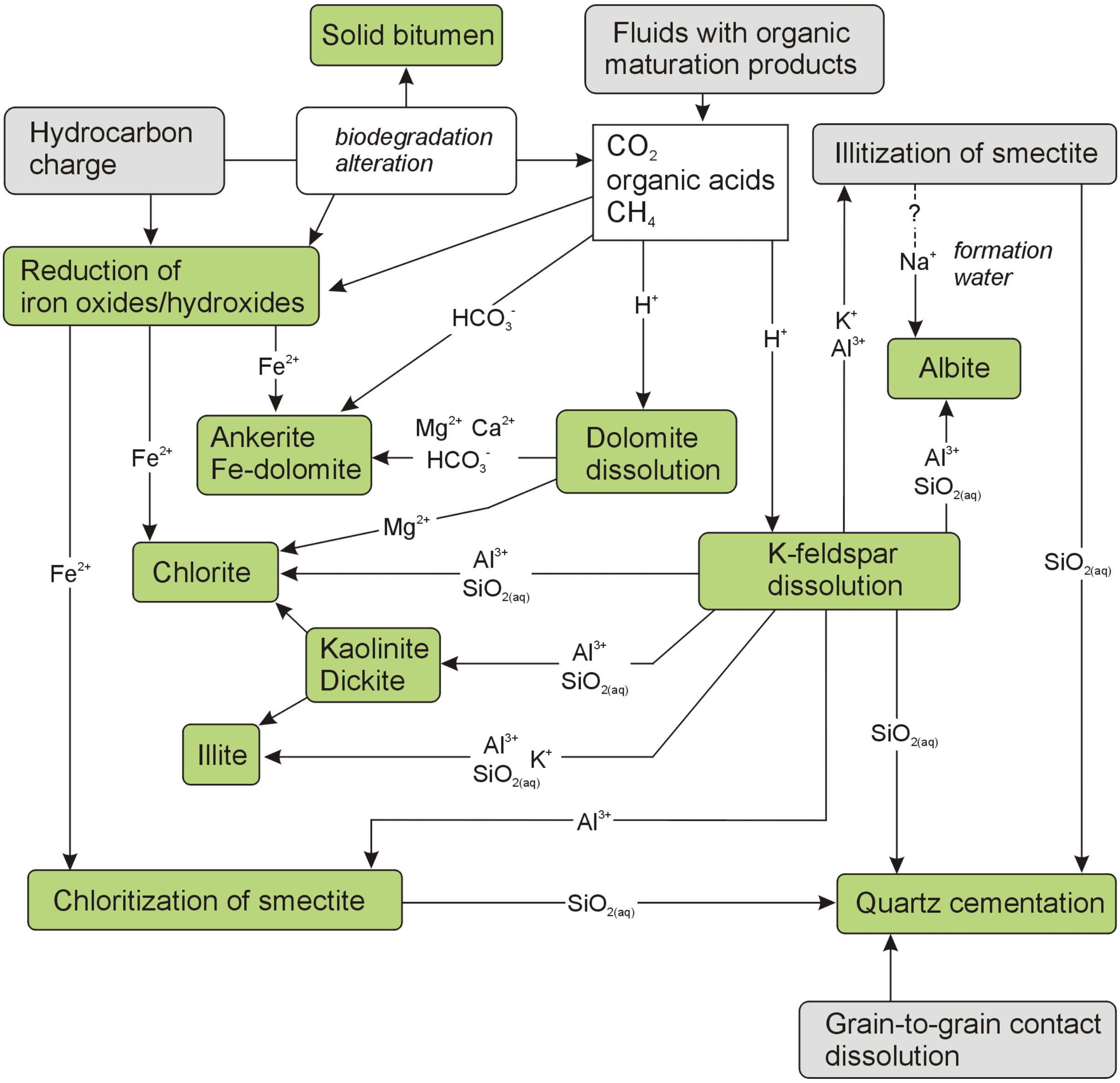

Fig. 11.1: Simplified flow chart of the main mesodiagenetic pathways and process interactions in the studied Triassic and Rotliegend reservoirs. Not all of these processes occurred together in one reservoir. Please see text for details.

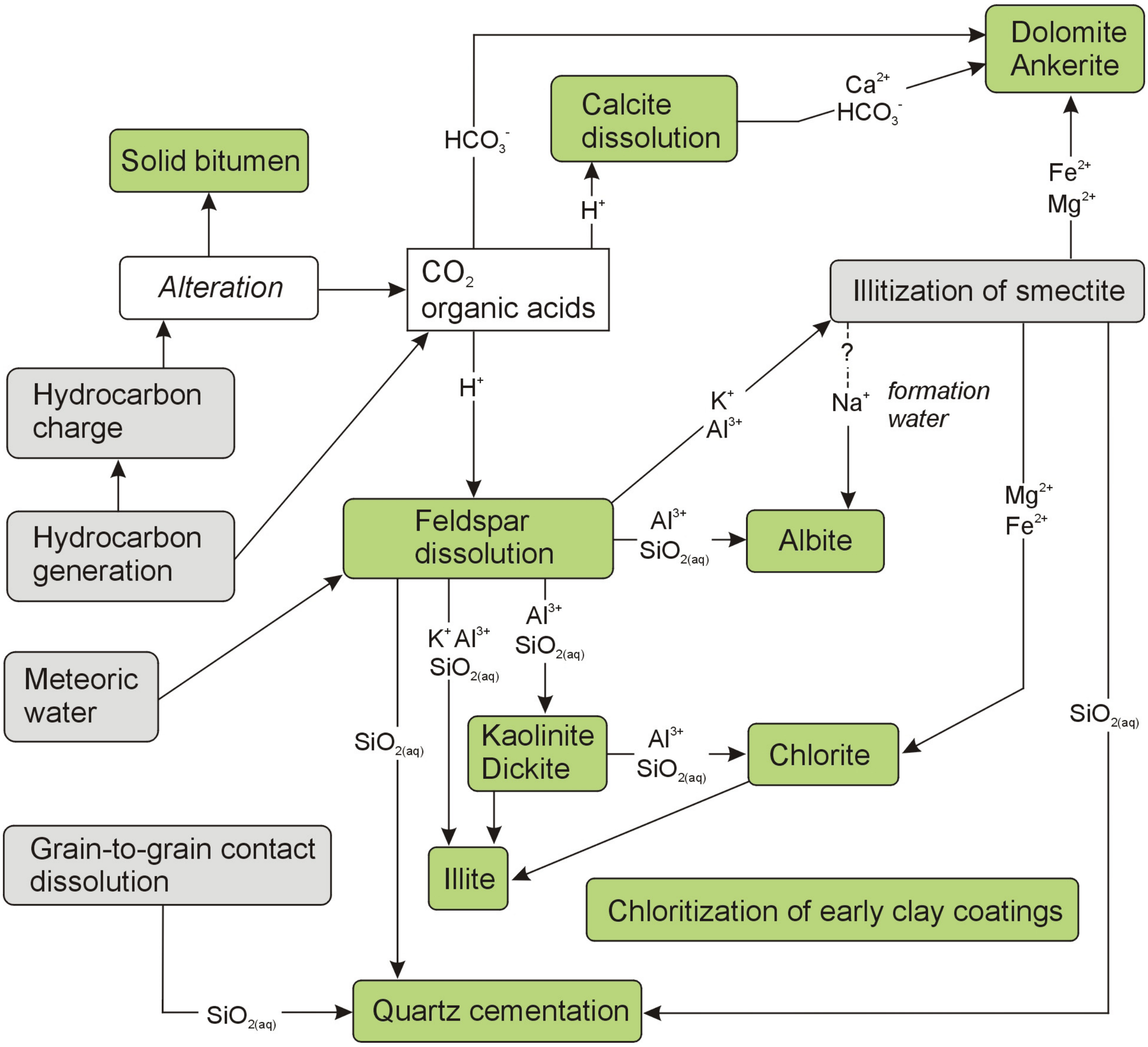

Fig. 11.2: Simplified flow chart of the main mesodiagenetic and telodiagenetic pathways and process interactions in the studied Jurassic reservoirs of the Central North Sea. Not all of these processes occurred together in one reservoir. Please see text for detailed discussion.

Numerical modelling of some of the mesodiagenetic processes in sandstones of the Triassic Skagerrak Formation shows that different diagenetic reactions (such as bleaching and chlorite formation) are connected and do not occur independently from each other. Therefore, one reaction provides often the agents required for other reactions and removes the reaction product. The later is particularly important to keep reactions running where the reaction products have low solubilities (e.g. Al^{3+} and SiO_2) and saturation with these species is reached quickly.

Some of the processes may occur together with others in a more or less closed system, while other require the influx of agents from outside. A sketch of the relationship between the individual processes is given in Fig. 11.1 and 11.2.

Most of the mesodiagenetic processes were found to occur in more than one of the studied wells and some selected processes and their main controlling factors shall be reviewed briefly on the following pages. The reaction equations were created with help of the Rxn modul of the software package Geochemist´s Workbench® Standard Release 6.0 from RockWare Inc where no other reference is given.

11.2.1 Albite and the albitization of K-feldspar

Albite is a widespread diagenetic mineral in various sandstones in the North Sea and other sedimentary basins. Saigal et al. (1988) described for instance the albitization of detrital K-feldspar from Jurassic, Lower Cretaceous and Tertiary reservoir sandstones from offshore Norway, and Hancock (1978) the occurrence of albite overgrowths and cements in Rotliegend sandstones of northwest Germany. Diagenetic albite was also observed in the form of pore-filling cement and overgrowths on plagioclase grains in the Huldra Field in the northern Viking Graben (Bjørlykke et al., 1992 and references therein).

Nevertheless, authigenic albite is not restricted to sandstones and can also occur in other sedimentary rocks. Spötl et al. (1999) reported for instance authigenic albite which formed under high temperature (> 150°C) diagenetic to low grade metamorphic conditions in carbonates. The occurrence of authigenic albite in solid bitumen from different localities was described by Parnell et al. (1994).

Authigenic albite crystals typically lack twinning and have nearly pure Na-end member composition (Deer et al., 2001).

Different scenarios for the formation of authigenic albite are discussed in the literature. The simplest way is direct precipitation from infiltrating pore water or during evaporation (Reaction 11.1).

$$Na^+ + Al^{3+} + 3\ SiO_{2(aq)} + 2\ H_2O \leftrightarrow NaAlSi_3O_8 + 4\ H^+ \qquad (11.1)$$

However, it must be considered that the availability of Al^{3+} and SiO_2 is usually limited in natural waters due to the low solubility of these species. For the precipitation of remarkable amounts of albite large fluid volumes are required. Sufficient amounts of Na^+ are likely to be present in higher saline waters. Therefore, direct albite precipitation from pore waters is most likely in early diagenetic settings with inflow of saline ground waters supplying Na^+ where Al^{3+} and SiO_2 are released by weathering of aluminosilicates.

In deeper burial settings with limited fluid circulation often an internal source of Al^{3+} and SiO_2 is required. It was often observed that the precipitation of authigenic albite goes along with K-feldspar dissolution following the reaction:

$$KAlSi_3O_8 + Na^+ \leftrightarrow K^+ + NaAlSi_3O_8 \qquad (11.2)$$

This process is a dissolution-precipitation mechanism and referred to as albitization of K-feldspar in the literature (e.g. Saigal et al., 1988). It seems to be a major source for late diagenetic albite. The starting time (temperature) of the albitization process is related to the aNa^+/aK^+ ratio of the pore water (Fig. 11.3) and may differ from setting to setting dependent on initial pore water composition (see also diagenetic modelling section 7).

Saigal et al. (1988) for instance, found that this process starts at 65°C (2.2 km depth) and reaches a maximum at 105°C (3.4 km) in reservoir sandstones offshore Norway. They found that K-feldspar grains at shallower depths (2.2 to 3.0 km, 65 to 90°C) were not completely leached and contained numerous tiny albite crystals with abundant microporosity, while at greater depths (>3.5 km, >90°C) authigenic albite occurred as larger blocky euhedral crystals replacing K-feldspar grains pseudomorphically without any dissolution porosity. These petrographic observations indicate that the dissolution of K-feldspar is more intense at shallower depths than the precipitation of albite and that the proportion of albite precipitation increases with depth and temperature (Saigal et al., 1988). This is also supported by the results of diagenetic modelling in this study (see section 7 for details).

Aagaard et al. (1990) concluded from kinetic data that the dissolution of K-feldspar is faster than albite precipitation at temperatures below 145°C. They found that albitization of K-feldspar occurs in the range between 65 and 125°C in sandstones offshore Norway. A broader range from 60 to 150°C was obtained from modelling results by Baccar et al. (1993). Nevertheless, temperature is not the only controlling factor and albitization of K-feldspar may be triggered also by increasing salinity of formation water during burial (Worden & Burley, 2003).

Different starting temperatures of albitization of K-feldspar appear to reflect different pore water compositions in the investigated settings of this study. Albite neoformation started at temperatures > 75°C with Jade Field water and at significantly lower temperatures using Judy Field waters with higher salinities in the models used here (see section 7). Eodiagenetic albite formed at lower temperatures was reported from Rotliegend sandstones of northwest Germany (e.g. Gaupp et al., 1993) and is additional evidence for possible diagenetic albite formation below 65°C.

While Al^{3+} and SiO_2 are derived from the K-feldspar during albitization, additional input of Na^+ is required. Sufficient Na^+ seems to be available in pore waters with high salinity as indicated by the modelling results from Jade and Judy Fields (see modelling section 7), which show that albitization of K-feldspar can be explained by simple heating of a closed system. However, in many settings there is not enough Na^+ available in the initial pore water and external sources are required. Waters with high sodium contents may have been derived from evaporitic sediments in other stratigraphic levels or some Na^+ may remain in connate marine pore waters (Saigal et al., 1988). Na^+ may also be released by the transformation of Na-rich smectite into illite during burial. Some published starting temperatures for albitization of K-feldspar and smectite-to-illite transformation coincide more or less and may be evidence for the triggering of albitization by the release of Na^+ by illitization of smectite (Aagaard et al., 1990). The formation of minor amounts of albite in sandstones during illtization in adjacent mudstones was modelled with CRUNCH by R. Ondrak (see modelling section 7) for the Triassic Skagerrak Formation and showed that mudstones may be able to provide sufficient Na^+ for the albitization of K-feldspar. Another possible source for Na^+ is the dissolution of sodium rich plagioclases (e.g. Walker, 1984).

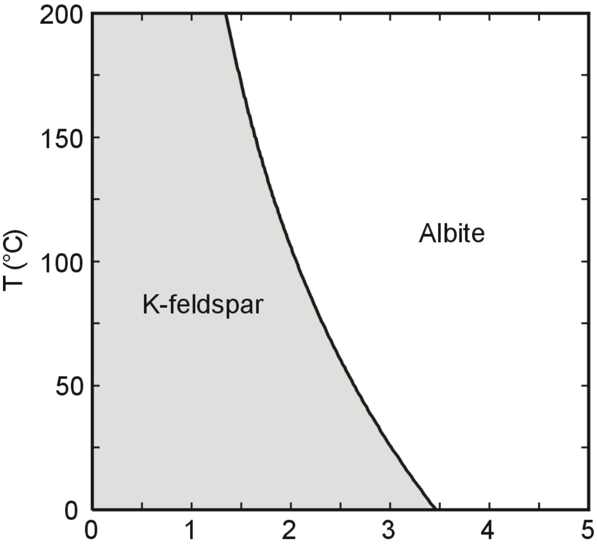

Fig. 11.3: Stability fields of albite and K-feldspar vs. temperature (created with the TACT program of the Geochemist´s Workbench® using thermo.dat).

The conversion of K-feldspar to albite is not always straightforward. It may involve intermediate phases like anhydrite or calcite. Walker (1984) found petrographic evidence for a two step replacement in sandstones of Fountain Formation (Colorado, USA) and presented the following set of reactions:

Replacement of potassium feldspar by anhydrite:

$$KAlSi_3O_8 + Ca^{2+} + SO_4^{2-} + 8\ H_2O \leftrightarrow CaSO_4 + 3\ H_4SiO_4^0 + Al(OH)_4^- + K^+ \quad (11.3)$$

Replacement of potassium feldspar by calcite:

$$KAlSi_3O_8 + Ca^{2+} + HCO_3^- + 8\ H_2O \leftrightarrow CaCO_3 + 3\ H_4SiO_4^0 + Al(OH)_4^- + K^+ + H^+ \quad (11.4)$$

Replacement of anhydrite by albite:

$$CaSO_4 + 3\ H_4SiO_4^0 + Na^+ + Al(OH)_4^- \leftrightarrow NaAlSi_3O_8 + Ca^{2+} + SO_4^{2-} + 8\ H_2O \quad (11.5)$$

Replacement of calcite by albite:

$$CaCO_3 + 3\ H_4SiO_4^0 + Na^+ + Al(OH)_4^- + H^+ \leftrightarrow NaAlSi_3O_8 + Ca^{2+} + HCO_3^- + 8\ H_2O \quad (11.6)$$

The replacement of detrital plagioclase by nearly pure albite is also a common diagenetic process and referred as the albitization of plagioclase (e.g. Morad et al., 2000). Baccar et al. (1993) inferred from thermodynamic and kinetic modelling that plagioclase albitization decreases with increasing temperature and is therefore more likely to occur during eodiagenesis and shallow burial.

Albite neoformation dependents on the supply of ions such as Na^+. Albitization of K-feldspar (or plagioclases) seems to be additionally sensitive to the removal of K^+ (Aagaard et al., 1990; Saigal et al., 1992). Therefore, these processes are most likely stopped by the emplacement of hydrocarbons (Saigal et al., 1988).

11.2.2 The dissolution of feldspar and carbonates and the creation of secondary porosity

Feldspars were often observed to be leached or at least to be partly corroded during mesodiagenesis in the investigated wells. Most of the leached feldspars are K-feldspars, while plagioclases were lesser affected. Moreover, the existence of authigenic albite in many studied samples shows that at least Na-plagioclase was thermodynamically stable under mesodiagenetic conditions in many cases. It is a common observation in the North Sea that the K-feldspar content decreases with increasing burial depth (Wilkinson et al., 2001). The dissolution of K-feldspar can be expressed by the following reaction:

$$KAlSi_3O_8 + 4\ H^+ \leftrightarrow 2\ H_2O + K^+ + Al^{3+} + 3\ SiO_{2(aq)} \quad (11.7)$$

Some of the reaction products (particularly Al^{3+}) have very low solubilities in most diagenetic pore waters. So, the dissolution of feldspar is frequently accompanied by quartz and clay mineral precipitation. Nevertheless, export of aluminium from sandstones by pore fluids was also interpreted by some authors, e.g. by Haszeldine et al. (1999) for the Fulmar Sandstones.
Which clay mineral is formed from the dissolution products depends on water chemistry and temperature. Fig. 11.4 displays the stability diagrams at HPHT conditions. A low temperature stability diagram for the system K_2O-Al_2O_3-SiO_2-H_2O is given in section 9 (Fig. 9.2) and the

temperature dependency of the boundary between the kaolinite and Fe-chlorite stability field is given in section 10 (Fig. 10.2).

Kaolinite for instance is the typical clay mineral at low temperatures and in waters with low K^+/H^+ ratios (e.g. Beaufort et al., 1998; Lanson et al., 2002). It forms following the reaction:

$$2\ KAlSi_3O_8 + H_2O + 2\ H^+ \leftrightarrow 2\ K^+ + Al_2Si_2O_5(OH)_4 + 4\ SiO_{2(aq)} \qquad (11.8)$$

Probably only small amounts of the released silica will form quartz cements, since meteoric waters are normally supersaturated with respect to quartz and significant quartz cementation is usually observed at higher temperatures as discussed in a following section.

In waters with higher K^+ content and at higher temperatures the formation of illite[1] is favoured:

$$3\ KAlSi_3O_8 + 2\ H^+ \leftrightarrow 2\ K^+ + KAl_3Si_3O_{10}(OH)_2 + 6\ SiO_{2(aq)} \qquad (11.9)$$

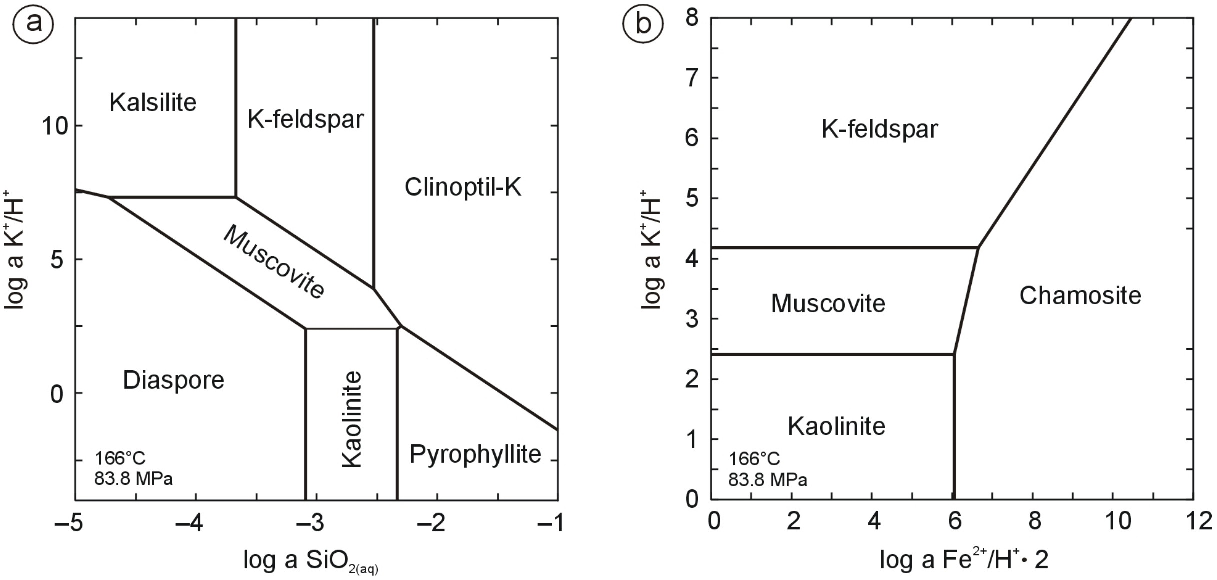

Fig. 11.4a: Stability field of K-feldspar in the system K_2O-Al_2O_3-SiO_2-H_2O at reservoir conditions of the Jade Field and **b:** Stability fields in the system K_2O-Al_2O_3-SiO_2-H_2O-FeO in the presence of quartz. Both diagrams were calculated using the program Act2 of the software package Geochemist´s Workbench® Standard Release 6.0 from RockWare Inc. using the LLNL database.

Both reactions require a source of H^+ and therefore they are expected to be associated with H^+ generating processes or low pH pore waters. The direct formation of an iron-rich chlorite from the breakdown of K-feldspar is slightly different:

$$2\ KAlSi_3O_8 + 8\ H_2O + 3\ Fe^{2+} + 2\ Mg^{2+} \leftrightarrow$$
$$2\ K^+ + Fe_3Mg_2Al_2Si_3O_{10}(OH)_8 + 3\ SiO_{2(aq)} + 8\ H^+ \qquad (11.10)$$

This reaction produces H^+ and can only proceed if the protons are taken up by other processes, such as the coeval reduction of iron oxides (reactions 11.14 and 11.15), since chlorite is not stable in acidic waters and the system will reach equilibrium soon without producing significant amounts of chlorite. Diagenetic modelling of these processes shows clearly that the individual reactions are connected and should be considered together. K-feldspar dissolution products were most likely exported into adjacent mudstones and used for illitization of smectite in the studied Triassic Skagerrak Formation as indicated by reactive

---

[1] Written as muscovite in the formula

transport modelling (see section 7). K-feldspar leaching can also be associated with albite formation as mentioned previously.

Leached dolomite crystals were observed in some of the wells and calcite dissolution was interpreted to have taken place during organic matter maturation in the Farsund Formation (see section 10) following the reactions:

$$CaMg(CO_3)_2 + 2\ H^+ \leftrightarrow Ca^{2+} + Mg^{2+} + 2\ HCO_3^- \qquad (11.11)$$

$$CaCO_3 + H^+ \leftrightarrow Ca^{2+} + HCO_3^- \qquad (11.12)$$

The dissolution products were observed to have been re-precipitated as iron-rich carbonates in the investigated settings.

The debate about secondary porosity is long and can be summarized by illustrating the key positions. This issue is further complicated by the fact that secondary porosity can only be quantified by more or less subjective petrographic methods (see for instance section 5). Following mechanisms were proposed for secondary porosity generation:

- Meteoric water leaching (e.g. Giles & Marshall, 1986)
- Mixing corrosion (e.g. Giles & Marshall, 1986)
- Acidic fluids generated by CO_2 from source rocks (Schmidt & MacDonald, 1979)
- Carboxylic acids generated in source rocks (Surdam et al., 1984)
- Acidic fluids generated by clay mineral reactions in shales (Bjørlykke, 1983)
- CO_2 and organic acids produced during biodegradation of oil (see later)
- Organic acids produced by alteration of n-alkanes (e.g. Seewald, 2001a)
- Cooling of fluids in equilibrium with carbonates (Giles, 1997)
- Heating of fluids in equilibrium with minerals showing increasing solubility with increasing temperature (Giles, 1997)

While there is relatively broad consensus about the possible creation of secondary porosity by percolating meteoric waters or mixing corrosion at shallow burial, the amount of mesodiagenetic dissolution and mass transport processes in the deep subsurface are under debate. The creation of secondary porosity by organic acids and CO_2 derived from maturing source rocks was mentioned to be an important mesodiagenetic process by Schmidt & MacDonald (1979) and Surdam et al. (1984). Bjørlykke (1983) and Giles & Marshall (1986) argued that the amounts of produced CO_2 and organic acids from kerogen are insufficient to create significant secondary porosities and that the acidic fluids produced would tend to be neutralized within the source rock formation itself. The petrographic observations of the studied well NOR-F support this objection. As argued by Giles & de Boer (1990), the formation of porosity at one place will be associated with the precipitation of pore occluding minerals in other places, due to the low solubility of many (especially aluminium) species in natural waters. Particularly, deep burial settings are characterized by low fluid rock ratios and low flow rates of moving pore waters. The low amounts of fluid have a limited capacity in taking up dissolution products. The amount of secondary porosity which can be created is limited if no extensive flush with undersaturated fluids takes place. Most of the observed secondary porosity in the sandstones is probably related to the export of dissolution products into adjacent lithologies, where they may form pore occluding cements. Thus, the porosity was only re-distributed (Giles & de Boer, 1990). This is supported by petrographic observations of this study (Ankerite and Fe-carbonate formation in settings with carbonate cement dissolution) and by the results of the diagenetic modelling in section 7, where no or

only a small gain in net-porosity was calculated. A significant net-gain in porosity can only be attained if dissolution products are exported from the system (and precipitated elsewhere). This may have been the case in investigated sandstones of the Triassic Skagerrak Formation, where K-feldspar dissolution products were probably taken up by the illitization of smectite in interbedded mudstones (see section 9).
Vertical fluid flow via faults may produce typical cementation - dissolution patterns caused by temperature related changes in mineral stability. So, carbonates dissolve and silicates (e.g. quartz and clay minerals) precipitate during the cooling of hot fluids in the reservoir adjacent to fault zones (e.g. McCants & Burley, 1996).

11.2.3 The influence of organic maturation products or of alteration products of petroleum

The role of organic maturation products from source rocks (especially organic acids and CO_2) during diagenesis was discussed controversially in the past. Schmidt & MacDonald (1979) and Surdam et al. (1984) suggested that such organic maturation products are responsible for the creation of secondary porosity. Barclay & Worden (2000a) showed via diagenetic modelling that the influx of source rock derived CO_2 can lead to K-feldspar dissolution and simultaneous precipitation of quartz, ankerite and illite. It was demonstrated by experiments that carboxylic acids enhance the solubility and thus the mobility of aluminium by formation of organic complexes (Franklin et al., 1994; Surdam et al., 1984; Surdam et al., 1989b). The organic acid concentration is at a maximum in many formation waters between 80 and 120°C (Surdam et al., 1989b). Below this temperature range organic species are prone to be degraded to CO_2 and hydrocarbon gases by bacteria. Above 100° carboxylic acids begin to decarboxylate resulting in pCO_2 increase (Kharaka et al., 1986; Surdam et al., 1989a). The "organic acid temperature windows" falls together with the typical oil window. So, the assumption was formulated that aggressive fluids associated with migrating hydrocarbons may create enhanced porosity on fluid pathways and in the reservoirs (e.g. Burley, 1993).

Opposing views were discussed e.g. by Giles & de Boer (1990) and Bjørlykke et al. (1989). Giles & de Boer (1990) argued that carboxylic acids will not only complex with aluminium, but also with other ions such as Ca^{2+} and Mg^{2+}. So, the increase in aluminium solubility will be limited by such competing ions, which are ubiquitous in most natural waters. However, the main argument against the influence of CO_2 and organic acids from maturing source rocks remains the problem of the transport of aggressive agents from source rock to reservoir sandstone. While Surdam et al. (1989a) made the assumption that enough carboxylic and difunctional carboxylic acids are present in formation waters for diagenetic reactions, Giles & Marshall (1986) and Bjørlykke et al. (1989) negated any significant effect of organic acids or CO_2 from the source rocks on sandstone diagenesis. They argued, that the limited amount of generated organic acids and CO_2 must first react with minerals in the place of generation and no leaching potential remains when these waters enter sandstones after cross formational fluid flow. Therefore much of the CO_2 generated ends up as authigenic carbonate in the source rock itself. This is indeed a strong argument and the petrographic observations from studied intra-source rock sandstones of well NOR-F support this argumentation (see section 6 and 10 for details).

However, several processes of in-reservoir alteration of petroleum are known to produce CO_2 and organic acids as well. So, organic acids and CO_2 present in recent oil field waters may derive from other processes than from organic maturation in the source rocks. Seewald (2001a), for instance could demonstrate via laboratory experiments that the decomposition of n-alkanes can generate organic acids in the reservoir itself. This process is probably responsible for the post-illite porosity enhancement in the Rotliegend of northwestern Germany as indicated by experiments of A. Meier (personal communication R. Gaupp).

Biodegradation of hydrocarbons can produce CO_2 and organic acids (Bennett et al., 2000; Ehrenberg & Jakobsen, 2001; Larter et al., 2005). So, no external source for these agents is required.

The infiltration (or in-situ) generation of CO_2 may have different effects: Shiraki & Dunn (2000) reported e.g. dolomite dissolution and K-feldspar alteration to kaolinite during experimental flooding of sandstones. Diagenetic modelling in this study (model 2, section 7) shows that in pore waters with high Ca^{2+} and Mg^{2+} contents the infiltration of CO_2 may cause carbonate cementation.

Diagenetic modelling in section 7 showed that the equilibrium of the system is disturbed by the infiltration of hydrocarbons and a number of mesodiagenetic reactions, such as bleaching of red beds (see later), dissolution of grains and cements as well as chlorite formation and carbonate cementation are triggered. In reservoir alteration of hydrocarbons may have been an important source for aggressive agents and diagenetic alteration during mesodiagenesis in the investigated settings.

11.2.4 Solid bitumen and the alteration of petroleum

Bitumen staining (very thin layers on clay minerals) or the occurrence of thick pore-lining (or filling) solid bitumen crusts were observed in thin sections from Jade and Judy field wells, (Triassic) as well as in the wells NOR-C (Jurassic), NOR-G (Jurassic), NOR-E (Triassic) and NOR-F (Jurassic). The occurrence of bitumen indicates the presence or former presence of petroleum in these rocks.

A number of synonyms are in use (mostly in the oil and gas industry) for solid bitumen in reservoirs: solid hydrocarbons, pyrobitumen, dead oil, black sands, asphaltic sands, tar mats, solid reservoir bitumen, and migrabitumen (Jacob, 1989; Lomando, 1992). Solid bitumen can be classified using their reflectance, intensity of fluorescence, micro-solubility and micro-flowpoint (Jacob, 1989). The term impsonite, for instance, is restricted to solid bitumen with reflectances higher than 0.7 %[2].

Solid bitumen in reservoirs or migration carrier beds is the solid (or highly viscous) residue of natural or artificial petroleum alteration (Lomando, 1992). Secondary alteration processes can also be linked to inorganic diagenesis such as bleaching of red beds or creation of secondary porosity.

The most important physico-chemical or biological processes which can alter and degrade petroleum in a reservoir are described here briefly (for details see e.g. Blanc & Connan, 1994). Most of them result in the formation of heavy oil or solid bitumen.

Thermal degradation or oil cracking: Oil is cracked to gaseous and light hydrocarbons and a black solid residue (pyrobitumen) by this process. Thermal cracking leads to an increase in GOR. Published temperatures for the deepest oil occurrence vary broadly between 90 and 200°C in different regional studies (Horsfield et al., 1992; Schenk et al., 1997 and references therein). 150°C is commonly used as mean value for the limit of oil stability (Blanc & Connan, 1994; Horsfield et al., 1992). Nevertheless, the cracking process may be retarded by high pressures, and liquid fluids can also be present in deep hot settings. Gas generation from oil in the Norwegian North Sea Central Graben occurred between 160 to 190°C as estimated with closed-system pyrolysis and kinetic modelling by Horsfield et al. (1992). The picture in the UK-sector of the central North Sea is comparable: Isaksen (2004) reported cracking temperatures for light oils and gas condensates in fields northwest of the study area (Heron,

---

[2] For details of the classification see (Jacob, 1989)

Egret, Puffin, well 22/30A-1, Shearwater, Elgin and Franklin) ranging from 163 to 193°C. Neumann (2007) mentioned that the experimental cracking of oil requires temperatures in the order of 180-200°C.
Therefore, thermal cracking of oil is limited to the deepest and hottest fields in the investigated area (e.g. well NOR-E, see also Isaksen, 2004). Thermal cracking can occur together with deasphalting initiated by the generated gas or the influx of natural gas as discussed by Littke et al. (1996) for the Rotliegend in northwest Germany or by Spötl et al. (1996) for the Spiro sandstone in the Arkoma Basin (USA). As cracking occurs in the entire oil column the resulting bitumen staining is expected to be present in the whole oil zone and not only in discrete zones (like the bitumen generated by biodegradation or deasphalting).

Water washing means the removal of more water-soluble compounds by flowing water and goes frequently along with biodegradation (Blanc & Connan, 1994).

Biodegradation affects the hydrocarbon properties and results in the creation of heavy oil or solid bitumen and a dry gas (Blanc & Connan, 1994; Larter et al., 2005). Therefore, phase separation can occur also in biodegraded reservoirs without thermal gas generation (Larter et al., 2005). Biodegradation is a low temperature process. It decreases with increasing temperature and stops around 80°C (Larter et al., 2005). In deeper petroleum reservoirs biodegradation takes place rather via anaerobic microbial metabolism, than via aerobic (Larter et al., 2005). Biodegradation occurs commonly at the base of the oil column (Larter et al., 2005) and thus the solid bitumen lines out the former oil-water contacts. Biodegradation has occurred probably in the Jade and Judy Field during first charge with hydrocarbons at shallow depth (see section 4 and Neumann, 2007). Biodegradation of hydrocarbons produces CO_2 and organic acids (Bennett et al., 2000; Ehrenberg & Jakobsen, 2001; Larter et al., 2005). A large part of the CO_2 produced during oil biodegradation is probably often consumed by subsequent methanogenesis (Larter et al., 2005).

Oxidation and evaporation is an extreme form of oil alteration at the surface (for instance in oil seeps) which leads usually to degradation from extra-heavy oil to solid bitumen (Blanc & Connan, 1994). These processes are unlikely for the studied settings.

Gravity segregation is a process were larger molecules sink towards the bottom of an oil column and lead to the occurrence of heavier oils at the base of some reservoirs (Blanc & Connan, 1994).

Dysmigration can create heavy oils and is related the efficiency of sealing rocks. Usually, it is a two step process connected with leakage. First, the single phase system is converted in a two phase system by pressure release and afterwards the gas and the light oil is lost through the leak and may form a new hydrocarbon pool leaving the heavy residual oil behind (Blanc & Connan, 1994 and references therein).

Deasphalting can be initiated by the generation of gas due to oil cracking (Horsfield et al., 1992 and references therein) or the injection of natural gas (or very light oil) into a reservoir and results in the formation of light oil and a solid residue composed of asphaltenes (Blanc & Connan, 1994). The asphaltene precipitates are often concentrated in zones with the best pre-oil-entrapment reservoir properties (Lomando, 1992).

CO_2-flooding can cause the precipitation of asphaltenes and other fractions of heavy organics in the reservoir (Monger & Trujillo, 1991). The process is comparable to the precipitation of heavy residues by low-molecular-weight paraffins as mentioned in the section deasphalting, but the chemical composition of the precipitates is broader and the process seem to be more complex (Monger & Trujillo, 1991).

Thermochemical sulphate reduction (TSR) may also form bitumen (Machel, 2001). Indications for TSR such as corroded sulphates were not found in any of the investigated wells (see also next section).

Bitumen staining in the Jade Field was found mainly on authigenic chlorite platelets indicating that the surfaces of chlorite attracted the hydrocarbons selectively. This shows that surface processes play an important role in pore-scale. The infiltration of liquid hydrocarbons will have a number of effects on the sandstone pore system including hydrophobisation of mineral surfaces as well as the reduction of specific internal surface area by impregnation of clay aggregates and pore-lining clays by bitumen (Gaupp & Okkerman, 2011).

Solid bitumen can have different effects on reservoir properties. Thin pore-lining bitumen may inhibit cementation and preserve pore space as observed by Littke et al. (1996) in Rotliegend reservoirs of northwest Germany. Conversely, thicker crusts or pore-filling solid bitumen can reduce porosity and permeability significantly. In reservoir scale, solid bitumen cementation can form permeability barriers independent of initial depositional facies and reservoir quality (Lomando, 1992). Therefore, Isaksen (2004) addressed the in-reservoir formation of pyrobitumen as a significant risk for reservoir quality in Jurassic and Triassic reservoirs of the central North Sea.

11.2.5 The bleaching of red beds

The reduction of iron oxides/hydroxides is often directly related to organic matter or organisms (see Blodgett et al., 1993). Several processes are known to cause the bleaching of red beds. Early diagenetic bleaching can occur in poorly drained, hydric soils or in low eH ground waters (e.g. Blodgett et al., 1993), while iron oxide reduction during deeper burial is frequently associated with the migration of organic rich fluids (Schöner, 2006; Schöner & Gaupp, 2005). A typical process in petroleum reservoirs which is often discussed in the literature is the interaction of iron oxides with petroleum. Shebl & Surdam (1996) observed the reduction of iron oxides, the dissolution of framework grains and the oxidation of hydrocarbons to oxygenated compounds (e.g. CO_2 and organic acids) during experimental heating of hematitic sandstones with oil and water. Following reaction equation was given by Surdam et al. (1993) for the interaction of iron oxides with sulphur-rich oil:

$$0.15\ C_9H_{20} + 0.5\ Fe_2O_3 + 2\ S \leftrightarrow 0.675\ CH_3COOH + FeS_2 + 0.15\ H_2O \qquad (11.13)$$

The produced organic acids can cause feldspar and carbonate dissolution and create secondary porosity. Organic acids are also known to be agents for the reduction of iron oxides (see also section 7 model 4). Aqueous acetic acid and acetate were observed to decompose by decarboxylation and oxidation in hydrothermal experiments (McCollom & Seewald, 2003). The oxidation reaction is promoted when hematite is present. In this case organic acids are likely to react with iron oxides to form CO_2 and water following the equation:

$$CH_3COOH + 16\ H^+ + 4\ Fe_2O_3 \leftrightarrow 2\ CO_2 + 10\ H_2O + 8\ Fe^{2+} \qquad (11.14)$$

Organic acids can also be formed by other processes such as the biodegradation of oil or the oxidation of n-alkanes within the reservoir, as discussed previously.

The oxidation of methane is known to equilibrate very slowly in natural waters at low temperatures. This process seems to take place only at deep burial, since it is kinetically inhibited at low temperatures (Bethke, 1996; Schöner, 2006).

$$CH_4 + 15\ H^+ + 4\ Fe_2O_3 \leftrightarrow 9\ H_2O + HCO_3^- + 8\ Fe^{2+} \tag{11.15}$$

The coexistence of hematite with methane in many Rotliegend gas reservoirs in northwest Germany and elsewhere is clear evidence that this reaction cannot be significant in these settings. Besides from kinetic factors, a major reason probably is the relatively high amount of H^+ consumed by the process, which leads to a strong rise in pH (see also model 3 section 7). This can together with a lacking Fe^{2+} sink force the reaction to cease, if no H^+ producing coeval process takes place (such as chlorite formation from K-feldspar dissolution – see reaction 11.10).

Iron oxides/hydroxides can also be reduced by microbial activity (Schöner, 2006 and references therein). H_2S produced by bacterial sulphate reduction (BSR) can reduce ferric iron and produce authigenic pyrite following the reaction:

$$Fe_2O_3 + 2\ H^+ + 2\ H_2S \leftrightarrow 3\ H_2O + Fe^{2+} + FeS_2 \tag{11.16}$$

Bacterial sulphate reduction occurs in near surface or shallow burial diagenetic settings with temperatures from about 0 to 80°C and will abate with increasing temperatures or decreasing sulphate content of the pore waters (Machel, 2001). However, H_2S can also be generated without microbes at higher temperatures. The process is known as thermochemical sulphate reduction (TSR) and produces H_2S and solid bitumen by the interaction of sulphates with hydrocarbons usually at temperatures between 100 and 140°C (160 to 180°C may be necessary in some settings, Machel, 2001). Machel (2001) gives following reaction equation:

$$\begin{aligned}&\text{hydrocarbons} + SO_4^{2-} \leftrightarrow\\ &\text{altered hydrocarbons} + \text{solid bitumen} + H_2S + HCO_3^- + H_2O\end{aligned} \tag{11.17}$$

The reduction of hematite by H_2S was written by (Metcalfe et al., 1994) as:

$$4Fe_2O_3 + H_2S + 14H^+ \leftrightarrow 8\ Fe^{2+} + SO_4^{2-} + 8\ H_2O \tag{11.18}$$

Nevertheless, the presence of unleached late authigenic barite in most of the studied wells and the lack of typical petrographic features for thermochemical sulphate reduction (e.g. leached sulphates with partial pyrite replacement) indicates that thermochemical sulphate reduction was not significant in the studied reservoirs.
H_2S and CO_2 originating from thermochemical sulphate reduction in deeper basin parts can also be brought into the reservoir sandstones by migrating fluids (e.g. Haszeldine et al., 2005).

11.2.6 The formation of mesodiagenetic ferroan carbonates

The textural relationship indicates a late diagenetic formation of ferroan carbonates for most investigated wells and the mesodiagenetic origin is relatively certain. Ankerite and Fe-dolomite were frequently found to overgrow earlier dolomite. Formula 11.19 gives an example for an ankerite forming reaction:

$$1.0\ Ca^{2+} + 0.6\ Mg^{2+} + 0.4\ Fe^{2+} + 2\ HCO_3^- \leftrightarrow Ca_{1.0}Mg_{0.6}Fe_{0.4}(CO_3)_2 + 2\ H^+ \tag{11.19}$$

The precipitation of ankerite seems to be connected to dolomite leaching in the studied wells of the Triassic Skagerrak Formation from Jade and Judy Fields and in the studied Rotliegend wells. The required Fe^{2+} was most likely derived from the reduction of iron oxides/hydroxides. The stable carbon isotopes of the Skagerrak Formation samples indicate that a part of the incorporated CO_3^{2-} was derived from biodegradation related CO_2. Worden & Morad (2000) postulated a link between carbonate precipitation and the formation of quartz and kaolinite or illite during feldspar dissolution. The observed dissolution of feldspar along with the precipitation of authigenic clays (reaction 11.8 or 11.9) consumed probably the H^+ produced by reaction 11.19.

The picture is not so obvious in the investigated Jurassic sandstones. Pervasive ankerite formation in the intra-Farsund sandstones seems to be related to calcite dissolution in the surrounding source rocks coeval with the maturation of organic matter. The required ferrous iron and magnesium may have been derived from the transformation of smectite into illite in the adjacent mudstones. Part of the HCO_3^- may have also originated from maturing source rocks as indicated by isotopically lighter carbon in the sample from well NOR-F. Dolomite in the Ula Formation is probably also mesodiagenetic and its occurrence may indicate a lesser available amount of Fe^{2+}, compared to settings were ankerite has formed.

Exact precipitation temperatures of ferroan carbonates in the investigated settings remain uncertain. Temperatures estimated with aid of stable isotope measurements cover a wide range (43 – 166°C) dependent on assumed isotopic water composition and fluid evolution scenario (see section 8 for details). Relatively high temperatures for Fe-carbonate formation are also known from other settings. Temperatures of about 125°C were published by Boles (1978) for the replacement of calcite cement by ankerite in Wilcox Sandstone (Texas) and temperatures > 110°C were reported for ankerite formation in the Triassic Sherwood Sandstone in the Corrib Field (Ireland) by Schmid et al. (2004). However, a well defined starting temperature does not exist and the onset of the process is probably controlled by water composition and triggering processes, such as bleaching of red beds in the studied settings. Carbonate cementation can also be associated with the infiltration of CO_2 as indicated by diagenetic modelling (model 2, section 7). Barclay & Worden (2000a) could show (also by diagenetic modelling) that authigenic quartz, illite and ankerite were potentially formed by the infiltration of CO_2 from petroleum source rocks in the Magnus Sandstone (Upper Jurassic, North Sea).

11.2.7 Quartz cementation

Quartz is one of the volumetrically most important cement minerals in deeply buried sandstones (Worden & Morad, 2000) and present in all investigated wells. Mesodiagenetic quartz cement forms from aqueous silica following the reaction:

$$SiO_{2(aq)} \leftrightarrow SiO_2 \qquad (11.20)$$

The solubility of quartz increases with increasing temperatures (Giles et al., 2000) and so it would be to expect that quartz is rather dissolved than precipitated during ongoing burial in a closed system. However, the silica content of the pore water is overbalanced by additional aqueous silica from a number of diagenetic reactions and processes. So, the silica content of most oilfield brines is in equilibrium or slightly oversaturated with respect to alpha quartz (Giles & de Boer, 1990). Such reactions are e.g. the dissolution of feldspars (reaction 11.7) and amorphous silica, as well as the illitization or chloritization of smectite (reaction 11.21 and 11.24) and the remobilisation of silica from silt and clay sized quartz grains via Oswald ripening (Giles et al., 2000; Worden & Morad, 2000). The illitization of smectite in mudstones together with diffusive silica transport, for instance, can explain a large part of the quartz cement in adjacent sandstones of the studied Triassic Skagerrak Formation of the Jade and Judy Fields (see sections 5 and 9). Mudstones can also export silica derived from the dissolution of silt-sized grains (Füchtbauer, 1978).

Another major source of silica under deep burial conditions is the dissolution of quartz grains at grain contacts and/or stylolites (e.g. Füchtbauer, 1978 or Worden & Morad, 2000). This process is also known as "pressure solution" or "chemical compaction[3]" (e.g. Heald, 1956; Renton et al., 1969; Bjørlykke et al., 1989; Houseknecht, 1987). The process can provide significant amounts of silica and is thought by some workers to be responsible for most of the quartz cement in deep burial settings (e.g. Bjørlykke & Egeberg, 1993; Oelkers et al., 2000; Walderhaug, 1996; Walderhaug et al., 2000, Buller et al., 2005). Grain coating illite as well as detrital muscovite and biotite are known to enhance this effect, while authigenic chlorite and microcrystalline quartz coatings prevent quartz precipitation (Aase et al., 1996; Houseknecht, 1988; Worden & Morad, 2000). The later block probably nucleation sites and lead to a high degree of silica saturation which may inhibit further quartz dissolution. Finer grained sediments were more affected by grain-to-grain contact dissolution than coarse-grained in experiments (Renton et al., 1969). This effect was also observed in numerous field studies (e.g. Heald, 1956; Houseknecht, 1984; Houseknecht, 1988). The effect of grain-to-grain contact dissolution increases with increasing temperature (Houseknecht, 1984). The dissolution of quartz grains at grain contacts and/or stylolites has certainly provided significant amounts of silica in some of the investigated settings (see section 9 and 10 for detailed discussion).

Cooling of hot fluids or of the entire reservoir during uplift may cause significant quartz cementation since the solubility of quartz increases with temperature. However, the import of larger amounts of silica over longer distances into a sandstone by advective large scale fluid flow is still a matter of debate (see Bjørlykke & Egeberg, 1993; Worden & Morad, 2000; Giles et al., 2000 for discussion). The major problem is the low solubility of silica and thus the (unrealistic) huge volume of fluids required to transport significant amounts of dissolved SiO_2 over longer distances into a sandstone under deep burial conditions. This is difficult to explain, especially in relatively tight lithologies. Therefore, silica is rather transported by diffusive processes than by advection (Worden & Morad, 2000). Aplin et al. (1993) mentioned that quartz cements in sandstones from the central North Sea precipitated from fluids with an extremely diverse compositional range which can be seen as additional evidence against large scale fluid flow in the area of interest.

The formation of thermal convection cells (with quartz cementation in the upper part) requires relative thick permeable sandstones and modelling of fluid flow in sandstone/shale sequences suggests that the conditions are seldom suitable for Rayleigh convection in most natural sedimentary systems (Bjørlykke et al., 1989). Thermal convection may be locally important where relatively steep isothermes are developed (e.g. around igneous intrusions and salt diapirs, Bjørlykke et al., 1989).

Mesodiagenetic quartz cementation is largely controlled by temperature, probably via a number of linked reactions (Giles et al., 2000). There is a relatively wide agreement based on numerous observations that significant mesodiagenetic quartz cement formation occurs in most sedimentary basins at higher temperatures, typically > 80-90°C (e.g. Giles et al., 2000; Worden & Morad, 2000; Ajdukiewicz & Lander, 2010). Earlier phases of quartz cementation are usually volumetrically less important. Quartz cement formation temperatures derived from

---

[3] irreversible dissolution of grains at points of contact - for definition see e.g. Houseknecht (1987)

fluid inclusion measurements of North Sea and Haltenbanken sandstones cover, for instance, a range between 70°C and 170°C (Bjørlykke & Egeberg, 1993). Nevertheless, lower temperatures (40-60°C) were also reported for some settings (Boles & Franks, 1979; Worden & Morad, 2000 and references therein).

Quartz cementation is likely to be inhibited by oil emplacement in the oil impregnated zone (degree depends on wettability – see Barclay & Worden, 2000c) compared to the underlying water bearing zone (Worden & Morad, 2000). Some of the samples investigated in this study show quartz cement precipitation subsequent to bitumen formation (see sections 5 and 6). There are also a number of other studies which showed continued quartz cementation after oil emplacement (e.g. Molenaar et al., 2008). Therefore, Taylor et al. (2010) argued that retardation of quartz cementation in the presence of hydrocarbons will not be significant. Haszeldine et al. (2003) worked out that oil stops quartz cementation in reservoirs containing less than 20% water.

Aqueous silica-organic complexations seems to have no significant effect on silica mobility during deeper burial as indicated by experimental evidence (Fein, 2000; Franklin et al., 1994).

11.2.8 The formation of chlorite

Authigenic chlorite can be formed in two principle ways: by the transformation from a precursor phase or by direct precipitation from pore water. Worden & Morad (2003) mentioned that both processes are typically mesodiagenetic and that the early diagenetic chlorite coatings described in some publications were most likely derived from eodiagenetic precursor phases, such as odinite or smectite.

Hillier (2003) described the occurrence of dioctahedral chlorites in hydrothermal alterations or pervasive in some red beds where they might have evolved from a kaolin precursor or aluminous (beidellitic) smectite. Some chlorites are known to be the product of smectite-to-chlorite transformation (e.g. McKinley et al., 2003). The precursor phase is mostly a trioctahedral smectite (e.g. saponite) (Hillier et al., 1996; Worden & Morad, 2003).

Two reaction equations were published by Chang et al. (1986) for the transformation of saponite into chlorite. One needs an external source of Al^{3+} and the other is neutral in respect of aluminium supply.

$$Ca_{0.1}Na_{0.2}Fe_{1.1}MgAlSi_{3.6}O_{10}(OH)_2 + 1.5\ Fe^{2+} + 1.2\ Mg^{2+} + 1.4\ Al^{3+} + 7.6\ H_2O \leftrightarrow \\ Fe_{2.6}Mg_{2.2}Al_{2.4}Si_{2.8}O_{10}(OH)_8 + 0.1\ Ca^{2+} + 0.2\ Na^+ + 0.8\ SiO_2 + 9.2\ H^+ \qquad (11.21)$$

$$2.4\ Ca_{0.1}Na_{0.2}Fe_{1.1}MgAlSi_{3.6}O_{10}(OH)_2 + 0.88\ H_2O + 1.44\ H^+ \leftrightarrow \\ Fe_{2.6}Mg_{2.2}Al_{2.4}Si_{2.8}O_{10}(OH)_8 + 0.24\ Ca^{2+} + 0.48\ Na^+ + 0.04\ Fe^{2+} \\ + 0.20\ Mg^{2+} + 5.84\ SiO_2 \qquad (11.22)$$

It is assumed that the smectite-to-chlorite transformation is a progressive dissolution-reprecipitation process which starts with a trioctahedral smectite and takes place via an intermediate mixed-layer chlorite-smectite phase (Hillier et al., 1996; Worden & Morad, 2003).

The evolution from a smectite precursor seems to be likely for the tangential grain rimming chlorites in the Triassic Skagerrak Formation. Weibel (1999) described that random smectite/chlorite is converted into ordered smectite/chlorite between 70 and 105°C, and that chlorite is most abundant at maximum burial temperatures of 150°C in the Skagerrak Formation of the Danish Subbasin. Hillier et al. (1996) published comparable temperature ranges for another setting: A temperature close to 100°C for the smectite to corrensite transition and temperatures from 150 to 200°C for actual chlorite formation.

The grain coatings chlorites in the Upper Jurassic sandstones had probably another precursor, which is more common in shallow marine to deltaic settings, such as odinite or berthierine (see also section 10). Aagaard et al. (2000) showed via hydrothermal experiments that grain coating chlorite can be produced from a Fe-rich berthierine. A large part of the chlorites observed in the Intra-Farsund sandstones of well NOR-F are probably the result of the replacement of kaolinite as discussed later.

The direct precipitation from solution seems to have occurred predominantly close to fluid entry points such as faults in the investigated wells. This is for instance indicated by the distribution of euhedral iron-rich chlorite plates in well 30/2c-4 and well NOR-C. The direct precipitation of an iron-rich chlorite from pore water can be expressed as:

$$3\ Fe^{2+} + 3\ SiO_{2(aq)} + 2\ Al^{3+} + 2\ Mg^{2+} + 12\ H_2O \leftrightarrow Fe_3Mg_2Al_2Si_3O_{10}(OH)_8 + 16\ H^+ \qquad (11.23)$$

The infiltrating fluids probably brought some of the required agents such as silica, iron and magnesium whereas Al^{3+} is known to be relatively immobile due to its very low solubility. Large fluid volumes would have been required to supply sufficient amounts of Al^{3+}. Another possible pathway without any Al^{3+} import is the contemporaneous dissolution of feldspar following reaction 11.7.

The chlorite formation following reaction 11.23 is not likely to occur alone because it produces excess H^+, which must be taken up by other reactions such as the reduction of iron oxides (see reactions 11.14 and 11.15) or the dissolution of carbonates (reactions 11.11 and 11.12). The coeval leaching of feldspars for aluminium supply can take up also some of the produced H^+ (see reaction 11.7).

Authigenic chlorites in sandstones are known to be often related to bleaching by hydrocarbons (e.g. Morad et al., 2000). Leveille et al. (1997) suggested that the iron in the chlorites of the Jupiter Fields (Southern North Sea, Rotliegendes) was derived from the reduction of hematite triggered by the influx of hydrocarbons. They found a similar whole-rock iron content in hematite and in chlorite dominated sandstones.

Grain coating chlorite is known to preserve high porosities down to deep burial conditions (e.g. Wilkinson et al., 2006) and so its presence is important for the quality of hydrocarbon reservoirs.

11.2.9 The illitization of smectite

Smectite is transformed into illite involving a smectite-illite-mixed layer intermediate phase. A progressive increase in the illite content of illite/smectite with increasing depths of burial can be seen as clear evidence for smectite-to-illite transformation in Jurassic and Triassic mudrocks of the North Sea and adjacent areas (e.g. Weibel, 1999; Wilkinson et al., 2006). It is known that this process takes place with increasing temperatures. Published temperatures for the transformation of smectite to illite cover nearly the entire diagenetic regime from 20 to 200°C, but range mostly from 70 to 110°C (e.g. Bjørlykke et al., 1992; van de Kamp, 2008; Worden & Burley, 2003; Dypvik, 1983). The disappearance of discrete smectite in the Wilcox Sandstone (Texas) was observed by Boles & Franks (1979) at temperatures higher than 70°C and the transition from randomly interlayered to ordered interlayered structures at 95 to 100°C. Weibel (1999) mentioned that the transformation of smectite into illite starts at temperatures higher than 47 °C with the conversion of smectite into random smectite-illite in the Triassic Skagerrak Formation in Denmark. Random smectite-illite is later converted into ordered illite-smectite at temperatures exceeding 74°C there.

K-, Ca- and Na-rich smectites are usually the precursor phases for illite, while Mg- and Fe-rich smectites are prone to be chloritized (Worden & Morad, 2000).

The reaction for the conversion of smectite into illite was expressed by Boles & Franks (1979) with:

$$4.5\ K^+ + 8\ Al^{3+}\ KNaCa_2Mg_4Fe_4Al_{14}Si_{38}O_{100}(OH)_{20}\cdot 10\ H_2O \leftrightarrow K_{5.5}Mg_2Fe_{1.5}Al_{22}Si_{35}O_{100}(OH)_{20} + Na^+ + 2\ Ca^{2+} + 2.5\ Fe^{3+} + 2\ Mg^{2+} + 3\ Si^{4+} + 10\ H_2O \tag{11.24}$$

The reaction equation can (similar to those of smectite chloritization) also be written neutral in terms of aluminium consumption (Boles & Franks, 1979):

$$3.93\ K^+ + 1.57\ KNaCa_2Mg_4Fe_4Al_{14}Si_{38}O_{100}(OH)_{20}\cdot 10\ H_2O \leftrightarrow K_{5.5}Mg_2Fe_{1.5}Al_{22}Si_{35}O_{100}(OH)_{20} + 1.57\ Na^+ + 3.14\ Ca^{2+} + 4.28\ Mg^{2+} + 4.78\ Fe^{3+} + 24.66\ Si^{4+} + 57\ O^{2-} + 11.40\ OH^- + 15.7\ H_2O \tag{11.25}$$

The illitization of smectite produces significant amounts of silica, which can lead to increased quartz cementation in sandstones close to mudstones (see modelling section 7). This process can explain the observed quartz cementation in sandstones of the Triassic Skagerrak Formation in the Jade Field (see section 9). Illitization of smectite and some of the related reactions could be reproduced by reactive transport modelling in this study (see section 7).

A number of other ions such as Ca^{2+}, Mg^{2+}, Fe^{2+} and Na^+ is usually liberated along with silica during illitization of smectite depending on the composition of the smectite precursor (e.g. Worden & Burley, 2003). The products of smectite-to-illite transformation are important reagents for other process, particularly in sandstones adjacent to or enclosed into thick mudstone packages. Ankerite and chlorite formation in thin sandstones of the Farsund Formation were probably sourced by this process and modelling (section 7) showed that albitization of K-feldspar as well as quartz neoformation in the Triassic Skagerrak Formation can be explained by ions sourced from the illitization of smectite in adjacent mudstones.

Since the reaction needs supply of certain reagents (at least K^+) it is coupled and limited by other reactions such as the breakdown of K-Feldspar.

The conversion of smectite into illite may be promoted by microbes (Kim et al., 2004).

11.2.10 The precipitation of illite

Pervasive meshworks composed of fibrous/flaky illite were found only in the Rotliegend samples in this study. Illite is also an important authigenic phase in other Rotliegend sandstones of the North Sea and adjacent areas (Ziegler, 2006). The fibrous/flaky illite is clearly authigenic and was most likely formed during late diagenesis. Early grain coating illite was observed to provide nuclei for this late illite (Giles et al., 1992; Gaupp et al., 1993). There appears to be a dependency between crystallisation temperature and morphological and structural characteristics of illite (Lanson et al., 2002 and references therein). Even small amounts of pore bridging fibrous/flaky illite can reduce the permeability in sandstones significantly (e.g. Wilkinson et al., 2006; Lander & Bonnell, 2010; Gaupp & Okkerman, 2011). Therefore, this illite type is very important for the quality of hydrocarbon reservoirs. However, significant quantities of dense pore-filling meshworks of fibrous/flaky illite are usually restricted to aeolian sandstones close (< 1 km) to major faults in the southern North Sea, the onshore Netherlands and in northwest Germany (Gaupp et al., 1993; Gaupp & Okkerman, 2011). When the permeability is reduced by illite meshworks, any subsequent fluid flow is most likely limited. Diagenetic fluids which are able to infiltrate the sandstones after significant fibrous illite precipitation will preferably use other, higher permeable, fluid pathways and their effect on the reservoir is to expect to be minor (e.g. Ziegler, 2006).

Pervasive illite meshwork formation was observed to occur usually in deeply buried reservoirs of the North Sea. In shallow North Sea reservoirs authigenic illite is generally rare and a lower threshold temperature between 70 and 140°C due to the presence of a kinetic barrier was derived for illite growth from this observation (e.g. Burley, 1993; Ehrenberg & Nadeau, 1989). The formation of fibrous illite seems to need higher temperatures than the illitization of smectite (Lander & Bonnell, 2010).
However, a wide range of illite growth temperatures was published for the North Sea and offshore Norway, starting from 15-20°C ranging up to 130-150°C (Girard et al., 2002; Wilkinson et al., 2006; Ziegler, 2006 and references therein). Lander & Bonnell (2010) gave a relatively narrow range from 120 to 140°C for the transition from incipient to pervasive illitization in Jurassic sandstones of the North Sea and Haltenbanken. Wilkinson et al. (2006) concluded from the wide temperature range that there is no real lower threshold temperature for illite growth, and it is more likely that illite formation is triggered by a change in physico-chemical conditions such as hydrocarbon charge or overpressure release. Gaupp et al. (1993), for instance, worked out that illite ages in the Rotliegend of northwest Germany correspond to a period of regional tectonic activity. Gaupp & Okkerman (2011) reviewed data from a number of Rotliegend gas fields in the Netherlands and proposed that illite formation is triggered by tectonically released fluids from the Carboniferous there. The event-hypothesis is also supported by K-Ar ages from Brent Group sandstones which cover an age interval from c. 60 to 17 Ma, indicating that no illite is formed at present day (Hamilton et al., 1992; Wilkinson et al., 2006). Illite ages can be used to date the hydrocarbon charge using the event assumption and the presence of significant amounts of illite can be seen as evidence for the influence of hydrocarbons (Hamilton et al., 1992; Haszeldine et al., 2003). Other workers could also show the connection between hydrocarbon fill and illite growth (e.g. Schöner & Gaupp, 2005).

Authigenic illite formation can be expressed by following reaction equations:

$$6\ H_2O + K^+ + 3\ Al^{3+} + 3\ SiO_{2(aq)} \leftrightarrow KAl_3Si_3O_{10}(OH)_2 + 10\ H^+ \qquad (11.26)$$

Due to the low solubility of Al^{3+} it seems to be likely, particularly for larger amounts of neoformed illite, that the process is associated with the breakdown of other silicates, such as K-feldspar (reaction 11.9 above) or kaolinite (reaction 11.27).

$$2\ K^+ + 3\ Al_2Si_2O_5(OH)_4 \leftrightarrow 2\ KAl_3Si_3O_{10}(OH)_2 + 3\ H_2O + 2\ H^+ \qquad (11.27)$$

Kaolin is known as precursor for fibrous illite in Jurassic sandstones of the North Sea (e.g. Bjørlykke & Aagaard, 1992). Bauer et al. (2000) showed experimentally that illite can be precipitated from kaolinite in KOH solutions in a relatively short time at low temperatures (35°C). However, significant illitization of kaolin was not observed in any of the investigated samples and so reaction 11.27 is of minor importance in the investigated settings.

The required K^+ can be derived from the breakdown of K-Feldspars or KCl-Bines from adjacent evaporites (Ziegler, 2006). Formation waters of deeply buried North Sea reservoirs may also contain suitable amounts of K^+ (see e.g. Table 7.1 Judy/Jade Fields).

An interesting point is the lack of pervasive fibrous illite in the studied Triassic Skagerrak Formation of the Jade and Judy Fields. This may have two reasons: Either illitization of smectite in adjacent and interbedded mudstones (see section 9 for details) consumed all reagents which are required for illite neo-formation, or the hydrocarbon fill at relatively low temperatures left only a small amount of interstital pore water for mass transport at temperatures (and depths) were illite precipitation may have started. Some fibrous illite was found in water-bearing samples of the Skagerrak Formation in well NOR-C showing that illite formation is generally possible in the Triassic. Nevertheless, even the water-filled Triassic reservoir shows only few amounts of fibrous illite compared to the studied Rotliegend wells. The studied Triassic reservoirs are characterized by interbedded mudstones. So, the smectite-to-illite transformation in mudstones may limit fibrous illite formation in interbedded sandstones.

11.2.11 Authigenic kaolin[4]

Detailed reviews about the origin and occurrence of authigenic kaolin in sandstones are given by Beaufort et al. (1998), Lanson et al. (2002) and Wilkinson et al. (2006). Kaolin formation is usually favoured at acidic and low salinity conditions (Ziegler, 2006).

Mainly two pathways are discussed for kaolin neoformation in sandstones: early kaolinite formation caused by the infiltration of meteoric water at low temperatures (surface to ~ 40°C) or late diagenetic kaolin precipitation related to maturation products of organic matter, e.g. CO_2 or organic acids (see Lanson et al., 2002). While there is a general agreement concerning the role of meteoric water in early kaolin formation in North Sea sandstones, the second hypothesis is not accepted by all workers. Wilkinson et al. (2006) argued, for instance, that this hypothesis is not supported by stable isotope data.

Usually, the species necessary for kaolin neoformation are sourced by in reservoir alteration of aluminium-bearing detrital silicates, mainly feldspars. Nevertheless, the cross-formational import of aluminium and silica is also under discussion (e.g. Haszeldine et al., 1999). However, in the later case the low solubility of the aluminium species is a major limiting factor. The ongoing formation of authigenic kaolin connected to the dissolution of K-feldspar needs a constant supply of H^+ and removal of K^+ in an open system. Gaupp et al. (1993) observed kaolin formation in the Rotliegend of northwest Germany close to coal bearing Carboniferous fault blocks (the zone is few hundred meters wide). More distant from the faults late diagenetic illite was favoured as the H^+ in the fluids was exhausted and K^+ activity increased due to ongoing K-feldspar dissolution.

The formation of the kaolinite polytype occurs in acidic and/or diluted waters at low temperatures and dickite is the stable polytype in deeply buried sandstones (e.g. Beaufort et al., 1998; Lanson et al., 2002).

As the kaolinite polytype is not stable under deeper burial conditions it is usually altered following one of tree pathways discussed in the literature with increasing burial depth (and temperature):

1. Transformation into dickite in systems with low K^+/H^+ activity ratio (e.g. Beaufort et al., 1998; Lanson et al., 2002 and references therein)
2. Conversation into illite in systems with high K^+/H^+ activity ratio (Bjørkum & Gjelsvik, 1988; Bjørlykke & Aagaard, 1992) at temperatures between 50 and 150°C
3. Replacement by chlorite as observed in well NOR-F (see also Bjørlykke & Aagaard, 1992)

---

[4] The term kaolin is used here to describe kaolin-group minerals

A common observation in North Sea sandstones is that early diagenetic vermiform kaolinite is progressively replaced by coarse blocky dickite with increasing depth and temperature (Beaufort et al., 1998; Lanson et al., 2002). However, it remains unclear if all observed blocky kaolin crystals observed in North Sea sandstones are composed of the dickite polytype, since some of the blocky crystals may have formed at relatively low temperatures (Wilkinson et al., 2006). A relatively wide temperature range is proposed for the growth of blocky kaolin in North Sea sandstones by different workers starting from 45-70°C (Wilkinson et al., 2004) and going up to 110-130°C for neoformed dickite in the Hild field (Girard et al., 2002). Wilkinson et al. (2006) noted that dickite is stable above ca. 100°C.

Dickite (and blocky kaolin) is not exclusively derived from kaolinite transformation but can also precipitate from solution (Lanson et al., 2002). The charge with hydrocarbons may inhibit or retard the kaolinite-to-dickite reaction (Lanson et al., 2002). The kaolinite to dickite transformation is kinetically controlled and may be related to acidic fluids of organic origin (Lanson et al., 2002). Kaolin recrystallization may also be linked to hydrocarbon emplacement as assumed for the Cormorant Field (northern North Sea) by Wilkinson et al. (2004).

Illitization of kaolinite in the presence of K-feldspar can be explained by thermodynamics in a closed system following the reaction:

$$KAlSi_3O_8 + Al_2Si_2O_5(OH)_4 \leftrightarrow KAl_3Si_3O_{10}(OH)_2 + 2\ SiO_2(aq) + H_2O \qquad (11.28)$$

Illitization of kaolinite was observed to occur usually at elevated temperatures (120-150°C), but thermodynamical calculations indicated that also temperatures as low as 50°C are sufficient (Bjørkum & Gjelsvik, 1988; Bjørlykke et al., 1992; Lanson et al., 2002). Dickite has a better ordered crystal lattice and seems to be less susceptible to illitization than kaolinite (Morad et al., 2000).

Kaolinite can also be altered to chlorite as observed in well NOR-F. A reaction equation for the chloritization of kaolinite was given by Boles & Franks (1979):

$$3.5\ Fe^{2+} + 3.5\ Mg^{2+} + 9\ H_2O + 3\ Al_2Si_2O_5(OH)_4 \leftrightarrow$$
$$Fe_{3.5}Mg_{3.5}Al_{6.0}Si_{6.0}O_{20}(OH)_{16} + 14\ H^+ \qquad (11.29)$$

Bjørlykke & Aagaard (1992) mentioned that the replacement of kaolinite by chlorite starts at about 90 to 100°C in the North Sea. Gaupp & Okkerman (2011) discuss a higher temperature (> 150°C) for the formation of chlorite from kaolin. However, thermodynamic data (Fig. 10.2) indicate that the transformation temperature is a function of fluid composition (e.g. the Fe^{2+}/H^+ ratio).

All kaolinite (or dickite) aggregates found in the investigated wells were observed to replace former grains, probably feldspars. So, the precipitation of kaolinite took place following a reaction comparable to reaction 11.8. Two different water types seem to have been responsible for the formation of kaolin in well NOR-F and NOR-G respectively: The influence of acidic waters derived from maturing organic matter in the adjacent black shales in well NOR-F and meteoric waters in well NOR-G (see section 10 for details).
No kaolinite was observed in the investigated samples from the Triassic Skagerrak Formation. This was interpreted as evidence for the lack of telodiagenetic meteoric water influence in the studied sandstones. Early diagenetic pore waters were most likely not in the stability field of kaolinite (see section 9) and late diagenetic fluids were probably not acidic enough to reach it.

11.3 A note to effect of overpressure on diagenesis in the studied settings

Overpressure is pressure above hydrostatic pressure at a given depth, by definition (e.g. Isaksen, 2004; Osborne & Swarbrick, 1997). Highly overpressured reservoirs are typical for the central North Sea. Most important overpressure generating processes for the studied settings are disequilibrium compaction and gas generation in combination with lateral pressure transfer, especially during the latest burial phase (Neumann, 2007; di Primio & Neumann, 2008).

Buller et al. (2005) mentioned that rapid quartz cementation at temperatures exceeding 120°C can generate high overpressures in areas with limited drainage. However, Osborne & Swarbrick (1999) argued that diagenetic reactions, such as smectite-to-illite transformation and quartz cementation have most likely not contributed to observed overpressures, since the rates of volume increase are too slow and the seal permeabilities are usually too high to built up significant overpressures.

Overpressure development started in late Cretaceous and accelerated significantly during the extremely rapid burial in the last million years in the study area (Swarbrick et al., 2000; Neumann, 2007; di Primio & Neumann, 2008).

Overpressure can preserve enhanced intergranular porosity when overpressures developed early during burial before the onset of significant mechanical compaction and cementation (Burley, 1993; Ajdukiewicz & Lander, 2010; Gaupp & Okkerman, 2011). Late overpressure development has only small or negligible effect on porosity (Taylor et al., 2010). High overpressure in the study area developed late, so its effect on porosity was probably minor. However, overpressure may have helped to hold some secondary pores open.

Generally, all diagenetic reactions, where the reaction products have a higher volume than the reagents, should be retarded by overpressure following Le Chatelier´s principle. Thus, the temperature of smectite dehydration increases with increasing pore fluid pressure (Colten-Bradley, 1987).

It is also important that the effective stress at grain contacts decreases in overpressured sandstones (e.g. Worden & Morad, 2000). Therefore, overpressure is thought to reduce grain-to-grain-contact dissolution and affects the amount of quartz cement (Bjørlykke, 1983). The retardation of quartz cementation by overpressure was reported by Osborne & Swarbrick (1999). Buller et al. (2005) mentioned that diagenesis is mainly controlled by temperature and the influence of effective stress is not significant. Fracture healing by quartz cement was described to have occurred in the Judy Field under overpressure conditions during the late phase of rapid burial (Aplin et al., 2000; Swarbrick et al., 2000). However, the effect of overpressure was most likely obscured by other more dominant controls on quartz cementation, such as detrital composition, the degree of feldspar leaching or the interactions with mudstones in most of the investigated settings. Numerical modelling of diagenetic reactions indicates that the observed quartz cements and their distribution can be mostly explained by other processes than grain-to-grain contact dissolution in the Triassic Skagerrak Formation.

Periods of regional overpressure are commonly characterized by a scarcity of diagenetic alterations because of the lack of significant fluid flow due to absence of internal pressure potential and the reduction of quartz cementation due to high pore pressures (Swarbrick, 1994). Fluid flow is initiated again when overpressured fluids are released. Therefore, diagenesis (in particular quartz and illite precipitation) was observed to be enhanced in phases of lower pressure following high pressure periods in the northern North Sea (Swarbrick, 1994). The hard overpressure in the study area is the result of the latest burial phase in the last million years. There are no indication from basin modelling for a significant phase of lower pressure in the study area. The modelling of gas generation together with disequilibrium compaction shows some minor fluctuations of excess hydraulic pressure (see section 4 and Neumann, 2007) but the magnitude of these fluctuations is significantly lower than those modelled by Swarbrick (1994) for some northern North Sea fields.

Fluid flow triggered by overpressure release via faults was described to be responsible for a number of diagenetic alterations. So, carbonates can precipitate due to a decrease of pCO_2 during fault-valving (e.g. McCants & Burley, 1996; Morad et al., 2000) and growth zonation seen in the quartz overgrowths in the South Brae sandstone (North Sea) was attributed to episodic quartz cementation related to overpressure release (McLaughlin et al., 1996). Wilkinson et al. (1997) and Haszeldine et al. (1999) postulated the creation of secondary porosity at leak-off points along with the removal of Si, Al and K from the sandstones by vertical leakage of overpressured pore fluids for the Fulmar Formation in the Central Graben. Haszeldine et al. (1999) and Wilkinson et al. (2006) proposed overpressure release as trigger for illite growth. However, the relationship between fibrous illite present in the studied Rotliegend sandstones and overpressure cannot be assessed by the available data.

The major problem in assessing the influence of overpressure on diagenesis in the studied sandstones is that a large number of the samples come from hydrocarbon filled reservoirs. Hydrocarbon fill can limit if not completely prevent many diagenetic reactions (e.g. Burley, 1993; Haszeldine et al., 2003; Wilkinson et al., 2004). The development of high overpressures occurred after the fill with hydrocarbons in most of the investigated reservoirs. Bitumen formation is often one of the latest phases in the studied diagenetic sequences and many observed diagenetic alterations were most likely completed at this time. So, the high pressure and temperature conditions today were probably not responsible for most of the observed diagenetic alterations in the studied reservoirs. Quartz and Fe-carbonates were the only phases which were found to postdate bitumen locally. Quartz cementation is known to proceed also after oil emplacement (see e.g. Taylor et al., 2010). Albite and local sulphides may have also a timing subsequent to bitumen formation, but their petrographic relationship to other authigenic phase remains unclear (see section 5 and 6 for details).

12 Conclusions

Aim of this thesis was to study the diagenetic evolution of important clastic HPHT reservoirs of Rotliegend, Triassic and Jurassic age in the North Sea Central Graben. Focus was on the Triassic Skagerrak Formation of Jade and Judy Fields in the UK sector, because most data and sample material was available from these two fields. The study used petrographic analyses, geochemical investigations and diagenetic modelling in order to identify major diagenetic processes in the investigated reservoirs.

12.1 Triassic Skagerrak Formation diagenesis: Summary

The studied diagenesis in the Triassic Skagerrak Formation of the Jade and Judy Fields (UK sector) can be summarized with following points:

1.) Diagenesis and reservoir properties are strongly facies controlled. Fluvial channel and sheetflood sandstones have the best reservoir properties. The relatively high permeability of these sandstones stimulated the infiltration of hydrocarbon-bearing mesodiagenetic fluids.

2.) Detrital feldspar grains and eodiagenetic cements were corroded by aggressive fluids during mesodiagenesis. These fluids were probably associated with in-reservoir alteration of hydrocarbons by biodegradation at relatively shallow burial depth causing dissolution of dolomite and K-feldspar in sandstones. The dissolution products were mainly consumed by illitization of smectite in interbedded mudstones and the local precipitation of Fe-carbonates and chlorite in the sandstones. The transport occurred via diffusion. A small increase in bulk porosity can only be achieved when dissolution products are exported from sandstones, for instance, into adjacent mudstones. If the dissolution products remain in the sandstones, the porosity net-gain is negligible or even a loss of porosity is very likely.

3.) Quartz cement is not distributed uniformly in the individual sandstone bodies, but shows an increase towards the contacts to over- and underlying mudstones. This distribution can be explained best by smectite-to-illite transformation in the interbedded mudstones releasing excessive SiO_2 into the sandstones. Diagenetic modelling shows that diffusive mass transport is possible over these short distances. Nevertheless, quartz cementation appears to be also partly controlled by the distribution of authigenic chlorite in the sandstones.

4.) Authigenic chlorite occurs in two different types. Platy euhedral chlorite is more common in the Jade Field and can be found in higher amounts close to fractured core sections. The precipitation of authigenic chlorite was probably associated with the reduction of hematite/goethite by hydrocarbons as indicated by diagenetic modelling. Grain coating chlorite may have a smectite precursor.

5.) Widespread hematite is restricted to few single beds, but the occurrence of preserved hematite beneath K-feldspar overgrowths and in carbonate nodules suggest a larger occurrence in former times. The reduction of hematite was probably caused by hydrocarbon infiltration.

6.) Ankerite occurs predominantly as euhedral overgrowth on dolomite and was formed subsequent to partial dolomite leaching. Carbon and oxygen isotopic signature of one sample is similar to ankerites in the Jurassic Intra-Farsund sandstones. This can be interpreted as indication for a common source for this type of carbonate cement. Nevertheless, the isotopic signature may also be the result of biodegradation of an early hydrocarbon charge. Diagenetic modelling indicates that ankerite formation (along with chlorite precipitation) is linked to the reduction of hematite/goethite by infiltrating hydrocarbons.

7.) The apparent lack of significant quantities of fibrous illite despite significant K-Feldspar dissolution is probably related to the preferred consumption of feldspar dissolution products by illitization of smectite in adjacent mudstones and/or the early hydrocarbon fill of the reservoir. Thus, smectite-to-illite transformation in mudstones may limit pervasive fibrous illite formation in interbedded sandstones.

8.) Diagenetic albite in the Triassic Skagerrak Formation of the Jade and Judy Fields is most likely related to K-feldspar dissolution. The formation of authigenic albite needs no external Na^+ source here and can be explained by heating the sandstone with its saline formation water during increasing burial. Minor contribution of Na^+ may also have been derived from mudstones as indicated by diagenetic modelling. The modelled onset temperature of albite formation is related to pore water compositions. Therefore, albitization of K-feldspar has most likely started at varying times in different fields or even compartments, depending on local pore water chemistry.

9.) The late overpressure had no significant effect on inorganic diagenesis, since most volumetrically important processes occurred earlier and the early filling with hydrocarbons prevented most diagenetic reactions (excepting quartz cementation). However, the available samples are not suitable for an exact evaluation of overpressure influence on mineral alteration.

Eodiagenetic processes in the Triassic of well NOR-E from the Norwegian sector are overall comparable to those in finer grained lithologies of the Jade and Judy Fields, except for the marginal occurrence of K-feldspar overgrowths. Mesodiagenetic alterations are not as intensive as in the two investigated fields from the UK sector. This is probably related to the low initial porosity which goes along with restricted amounts of pore water available for mass transport. A remarkable difference to the Jade and Judy Fields is the comparable lower amount of dolomite dissolution and ankerite formation, which may be related to the lack of biodegradation in well NOR-E, where hydrocarbon charge occurred not until deep burial (the seven samples from well NOR-E represent diagenesis in a deep graben settings, while Judy/Jade represent a morphological high). The present bitumen is most likely related to thermal cracking of hydrocarbons in well NOR-E.

The Triassic in well NOR-C of the Norwegian sector shows diagenesis close to a fault zone. Extensive K-feldspar dissolution was probably caused by aggressive fault related fluids. A significant difference to other Triassic reservoirs studied is the presence of some illite fibres/flakes and a different morphology of the authigenic chlorite. The Triassic sandstones in well NOR-C were found to be water-bearing and the presence of this minor illite occurrence may be attributed to the lack of a hydrocarbon fill.

12.2 Rotliegend diagenesis: Summary

Limited sample material was available from two Rotliegend wells in the Norwegian sector of the North Sea. They represent also red bed sandstones, but deposited in a different environment than the Triassic samples. The studied Rotliegend reservoirs are water-bearing, but an influence of organic maturation products is likely. The most significant difference to the studied Skagerrak Formation reservoirs is the partly pervasive occurrence of pore-filling permeability destroying fibrous/flaky illite. Other mesodiagenetic processes, such as quartz cementation, dolomite dissolution and albite formation occur in the Triassic too. Authigenic chlorite was not as abundant in the Rotliegend sandstones. However, controlling factors for the individual diagenetic processes were partly different. Quartz cementation was not predominantly controlled by smectite-to-illite transformation because of the lack of thicker interbedded mudstones in the Rotliegend sandstones and the biodegradation of hydrocarbons played most likely no significant role in the Rotliegend.

12.3 Jurassic Intra-Farsund sandstone diagenesis: Summary

The Intra-Farsund sandstones from well NOR-F in the Norwegian sector represent thin sandstones completely enclosed into source rocks. They provided a good opportunity to study the effect of organic maturation related fluids on sandstone diagenesis.

The mesodiagenesis of the thin (cm- to dm-thick) Intra-Farsund sandstone layers is dominated by the close relationship to thick maturing organic rich source rocks. Mesodiagenetic alterations started with the breakdown of detrital feldspar grains into kaolinite and quartz. A large part of the kaolinite was later replaced by authigenic chlorite and a minor part by dickite. The phase of chloritization and chlorite neoformation was accompanied by pervasive ankerite cementation. The replacement of kaolinite by chlorite can be explained by changing mineral stabilities with increasing temperature along with smectite-to-illite transformation in the surrounding source rocks. A major part of the ions required for late diagenetic ankerite precipitation was most likely mobilised in the source rocks by leaching of carbonates and transported into the thin sandstones destroying a significant proportion of the porosity. Therefore, the influence of organic maturation products brought no gain in porosity in the studied Intra-Farsund sandstones. Diagenesis ceased with complete occlusion of interstital pore space by ankerite and quartz cement, leaving only small amounts of microporosity.

12.4 Jurassic Ula Formation diagenesis: Summary

Well NOR-G shows a typical marine eodiagenesis. Meteoric water influx caused probably feldspar dissolution along with kaolinite and quartz cementation after shallow burial. The mesodiagenetic evolution is characterized by carbonate and quartz cementation together with some illite (but not as widespread as in the Rotliegend samples), chlorite, barite and albite precipitation. Organic maturation products may have influenced mesodiagenetic processes, such as carbonate cementation. The reservoir is filled with hydrocarbons today. This hydrocarbon fill has terminated a number of diagenetic processes, excepting quartz cementation.

12.5 Diagenetic modelling: Summary

Diagenetic modelling is a powerful tool to test different fluid flow scenarios and can help to understand diagenetic processes in reservoir sandstones and their effect on porosity evolution. Nevertheless, the results of diagenetic modelling are strongly affected by the defined initial system and many input parameters are unknown. Therefore, it is necessary to use petrographic and geochemical data to fill the gaps. No single model of this study was able to reproduce all observed changes in sandstone mineralogy during diagenesis of the Skagerrak Formation, but important mesodiagenetic changes could be reconstructed quantitatively. Diagenetic modelling shows also that the infiltration of hydrocarbons is able to trigger a number of mesodiagenetic reactions, such as bleaching of red beds, dissolution of grains and cements as well as chlorite formation and carbonate cementation. Alteration of hydrocarbons in the reservoirs may have been an important source for aggressive agents during mesodiagenesis in the Skagerrak Formation. All models show no or only a very small gain in net-porosity. All secondary porosity created was most likely plugged elsewhere by authigenic phases.

Generally, all modelled reactions depend strongly on the chemistry of the used formation water. Therefore, the use of formation water analyses is essential for interpreting diagenesis. Despite a number of restrictions provide theses numerical models important input for the understanding of diagenetic processes and the development of concepts, also in other settings.

In summary, all studied settings show that eodiagenesis is controlled by sedimentary facies and depositional environment. Eodiagenetic authigenic phases together with detrital components provided the framework for later burial diagenesis and were overprinted by it.

The mesodiagenesis of Permo-Triassic sediments was influenced by the presence of iron oxides/hydroxides, which were partially reduced during mesodiagenesis. This source of ferrous iron played no significant role in the investigated Jurassic sandstones.

Organic maturation products, particularly petroleum and its alteration products, played an important role in the mesodiagenesis of all studied sandstones. Diagenetic modelling shows that most mesodiagenetic reactions are linked to others via various species which are produced or consumed during the individual processes. This is supported by petrographic observations from all studied wells. Diffusive mass transfer allows the interaction between diagenetic reactions in different lithologies, such as sandstones and mudstones. This is an important process which can explain the dissolution of feldspars and dolomite, the distribution patterns of quartz cement and the apparent illite deficiency in sandstone layers of the Skagerrak Formation. Moreover, ankerite formation and chloritization of kaolinite in Upper Jurassic Intra-Farsund sandstones are most likely related to mass transfer from adjacent source rocks. Mesodiagenetic processes (such as quartz cementation) should therefore not be considered separately but examined quantitatively in the context of all possibly linked reactions.

References

Aagaard, P.; Egeberg, P. K.; Saigal, G. C.; Morad, S. & Bjørlykke, K. (1990): Diagenetic albitization of detrital K-feldspar in Jurassic, Lower Cretaceous, and Tertiary clastic reservoir rocks from offshore Norway, II. formation water chemistry and kinetic considerations.- Journal of Sedimentary Petrology, 60 (4): 575-581.

Aagaard, P.; Jahren, J. S.; Harstad, A. O.; Nilsen, O. & Ramm, M. (2000): Formation of grain-coating chlorite in sandstones. Laboratory synthesized vs. natural occurrences.- Clay Minerals, 35: 261-269.

Aase, N. E.; Bjørkum, P. A. & Nadeau, P. H. (1996): The effect of grain-coating microquartz on preservation of reservoir porosity.- American Association of Petroleum Geologists Bulletin, 80 (10): 1654-1673.

Ajdukiewicz, J. M. & Lander, R. H. (2010): Sandstone reservoir quality prediction: The state of the art.- American Association of Petroleum Geologists Bulletin, 94 (8): 1083-1091.

Alonso-Zarza, A. M. & Wright, V. P. (2010): Calcretes.- In: Alonso-Zarza, A. M. & Tanner, L. H. (Editors): Carbonates in continental settings - facies, environments and processes. Developments in Sedimentology, 61. Elsevier, pp. 225-267.

Aplin, A. C.; Larter, S. R.; Bigge, M. A.; Macleod, G.; Swarbrick, R. E. & Grunberger, D. (2000): PVTX history of the North Sea´s Judy oilfield.- Journal of Geochemical Exploration, 69-70: 641-644.

Aplin, A. C.; Warren, E. A.; Grant, S. M. & Robinson, A. G. (1993): Mechanisms of quartz cementation in North Sea reservoir sandstones: Constraints from fluid compositions.- In: Horbury, A. D. & Robinson, A. G. (Editors): Diagenesis and Basin Development. AAPG Studies in Geology 36, pp. 7-22.

Baccar, M. B.; Fritz, B. & Madé, B. (1993): Diagenetic albitization of K-feldspar and plagioclase in sandstone reservoirs: thermodynamic and kinetic modeling.- Journal of Sedimentary Petrology, 63 (6): 1100-1109.

Barclay, S. A. & Worden, R. H. (2000a): Geochemical modelling of diagenetic reactions in a sub-arkosic sandstone.- Clay Minerals, 35: 57-67.

Barclay, S. A. & Worden, R. H. (2000b): Petrophysical and petrographical analysis of quartz cement volumes across oil-water contacts in the Magnus Field, northern North Sea.- In: Worden, R. H. & Morad, S. (Editors): Quartz cementation in sandstones, pp. 147-161.

Barclay, S. A. & Worden, R. H. (2000c): Effects of reservoir wettability on quartz cementation in oil fields.- In: Worden, R. H. & Morad, S. (Editors): Quartz cementation in sandstones, pp. 103-117.

Barker, C. & Takach, N. E. (1992): Prediction of natural gas composition in ultradeep sandstone reservoirs.- American Association of Petroleum Geologists Bulletin, 76(12): 1859-1873.

Bassett, M. G. (2003): Sub-Devonian geology.- In: Evans, D., Graham, C., Armour, A. & Bathurst, P. (Editors): The Millennium Atlas: petroleum geology of the central and northern North Sea. The Geological Society, London, pp. 61-63.

Bauer, A.; Velde, B. & Gaupp, R. (2000): Experimental constraints on illite crystal morphology.- Clay Minerals, 35: 587-597.

Bazin, B. & Brosse, É. (1997): Chemistry of oil-field brines in relation to diagenesis of reservoirs - 1. Use of mineral stability fields to reconstruct in situ water composition. Example of the Mahakam basin.- Marine and Petroleum Geology, 14(5): 481-495.

Beard, D. C. & Weyl, P. K. (1973): Influence of texture on porosity and permeability of unconsolidated sand.- American Association of Petroleum Geologists Bulletin, 57 (2): 349-369.

Beaufort, D.; Cassagnabere, A.; Petit, S.; Lanson, B.; Berger, G.; Lacharpagne, J. C. & Johansen, H. (1998): Kaolinite-to-dickite reaction in sandstone reservoirs.- Clay Minerals, 33: 297-316.

Bennett, P. C.; Hiebert, F. K. & Rogers, J. (2000): Microbial control of mineral-groundwater equilibria: Macroscale to microscale.- Hydrogeology Journal, 8: 47-62.

Berner, R. A. (1981): Authigenic mineral formation resulting from organic matter decomposition in modern sediments.- Fortschritte der Mineralogie, 59 (1): 117-135.

Bethke, C. M. (1996): Geochemical reaction modeling: Concepts and applications.- Oxford University Press, Oxford, 389 pp.

Bishop, D. J. (1996): Regional distributions and geometry of salt diapirs and supra-Zechstein Group faults in the western and central North Sea.- Marine and Petroleum Geology, 13 (4): 355-364.

Bjørkum, P. A. & Gjelsvik, N. (1988): An isochemical model for formation of authigenic kaolinite, K-feldspar and illite in sediments.- Journal of Sedimentary Petrology, 58 (3): 506-511.

Bjørlykke, K. (1983): Diagenetic reactions in sandstones.- In: Parker, A. & Sellwood, B. W. (Editors): Sediment diagenesis. NATO ASI series. D. Reidel Publishing Company, pp. 169-213.

Bjørlykke, K. & Brendsdal, A. (1986): Diagenesis of the Brent Sandstone in the Statfjord Field, North Sea.- In: Gautier, D. L. (Editor): Roles of Organic Matter in Sediment Diagenesis. Society of Economic Paleontologists and Mineralogists Special Publication, 38, pp. 157-167.

Bjørlykke, K. & Aagaard, P. (1992): Clay minerals in North Sea sandstones.- In: Houseknecht, D. W. & Pittman, E. D. (Editors): Origin, Diagenesis, and Petrophysics of Clay Minerals in Sandstones, SEPM Special Publication No. 47, pp. 65-80.

Bjørlykke, K. & Egeberg, P. K. (1993): Quartz cementation in sedimentary basins.- American Association of Petroleum Geologists Bulletin, 77 (9): 1538-1548.

Bjørlykke, K.; Nedkvitne, T.; Ramm, M. & Saigal, G. C. (1992): Diagenetic processes in the Brent Group (Middle Jurassic) reservoirs of the North Sea: an overview.- In: Morton, A. C., Haszeldine, R. S., Giles, M. R. & Brown, S. (Editors): Geology of the Brent Group. The Geological Society Special Publication No. 61. The Geological Society, London, pp. 263-287.

Bjørlykke, K.; Ramm, M. & Saigal, G. C. (1989): Sandstone diagenesis and porosity modification during basin evolution.- Geologische Rundschau, 78 (1): 243-268.

Blanc, P. & Connan, J. (1994): Preservation, degradation and destruction of trapped Oil.- In: Magoon, L. B. & Dow, W. G. (Editors): The petroleum system - from source to trap: AAPG Memoir 60, pp. 237-247.

Blanche, J. B. & Whitaker, J. H. (1978): Diagenesis of part of the Brent Sand Formation (Middle Jurassic) of the northern North Sea Basin.- Journal of the Geological Society, 135: 73-82.

Blodgett, R. H.; Crabaugh, J. P. & McBride, E. F. (1993): The color of red beds - a geologic perspective.- Soil Science Society of America Special Publication, 31: 127-159.

Boles, J. R. (1978): Active ankerite cementation in the subsurface Eocene of southwest Texas.- Contributions to Mineralogy and Petrology, 68: 13-22.

Boles, J. R. & Franks, S. G. (1979): Clay diagenesis in Wilcox sandstones of southwest Texas: implications of smectite diagenesis on sandstone cementation.- Journal of Sedimentary Petrology, 49 (1): 55-70.

Brand, U. & Morrison, J. O. (1987): Paleoscene #6. Biogeochemistry of fossil marine invertebrates.- Geoscience Canada, 14 (2): 85-107.

Bray, A. A. (1992): Sedimentology and petrography of the Ula Formation, Phillips Norway NOR-G.- Internal Industry Report, 7077/Id/17787 (Simon-Robertson): 99 pp.

Brosse, É.; Margueron, T.; Cassou, C.; Sanjuan, B.; Canham, A.; Girard, J. P.; Lacharpagne, J. C. & Sommer, F. (2003): The formation and stability of kaolinite in Brent sandstone reservoirs: a modelling approach.- International Association of Sedimentologist Special Publication, 34: 383-408.

Bruce, D. & Stemmerik, L. (2003): Carboniferous.- In: Evans, D., Graham, C., Armour, A. & Bathurst, P. (Editors): The Millennium Atlas: petroleum geology of the central and northern North Sea. The Geological Society, London, pp. 83-89.

Bulach, A. G. (1970): Berechnung von Mineralformeln.- VEB Deutscher Verlag für Grundstoffindustrie, Leipzig, 167 pp.

Buller, A. T.; Bjørkum, P. A.; Nadeau, P. & Walderhaug, O. (2005): Distribution of hydrocarbons in sedimentary basins - the importance of temperature.- Statoil Research & Technology Memoir, 7: 1-15.

Burley, S. D. (1993): Models of burial diagenesis for deep exploration plays in Jurassic fault traps of the Central and Northern North Sea.- In: Parker, J. R. (Editor): Petroleum Geology of Northwest Europe: Proceedings of the 4th Conference. The Geological Society, London, pp. 1353-1375.

Burley, S. D. & MacQuaker, J. H. S. (1992): Authigenic clays, diagenetic sequences and conceptual diagenetic models in contrasting basin-margin and basin-center North Sea Jurassic sandstones and mudstones.- In: Houseknecht, D. W. & Pittman, E. D. (Editors): Origin, Diagenesis, and Petrophysics of Clay Minerals in Sandstones, SEPM Special Publication No. 47, pp. 81-110.

Cayley, G.T., 1986. Hydrocarbon migration in the central North Sea, Petroleum geology of northwest Europe: Proceedings of the 3rd conference. The Geological Society, London, pp. 549-556.

Chang, H. K.; Mackenzie, F. T. & Schoonmaker, J. (1986): Comparisons between the diagenesis of dioctahedral and trioctahedral smectite, Brazilian offshore basins.- Clays and Clay Minerals, 34 (4): 407-423.

Cleveland, D. M.; Nordt, L. C.; Dworkin, S. I. & Atchley, S. C. (2008): Pedogenic carbonate isotopes as evidence for extreme climatic events preceding the Triassic-Jurassic boundary: Implications for the biotic crisis?- Geological Society of America Bulletin, 120 (11/12): 1408-1415.

Colson, J. & Cojan, I. (1996): Groundwater dolocretes in a lake-marginal environment: an alternative model for dolocrete formation in continental settings (Danian of the Provence Basin, France).- Sedimentology, 43: 175-188.

Colten-Bradley, V. A. (1987): Role of pressure in smectite dehydration - effects on geopressure and smectite-to-illite transformation.- American Association of Petroleum Geologists Bulletin, 71 (11): 1414-1427.

Core-Laboraties (1992): Reservoir fluid study for Phillips Petroleum Company Norway, well NOR-G, North Sea.- Internal Industry Report, RFLA 920029: 49 pp.

Cornford, C. (1994): Mandal-Ekofisk Petroleum System in the Central Graben of the North Sea.- In: Magoon, L. B. & Dow, W. G. (Editors): The petroleum system - from source to trap: AAPG Memoir 60, pp. 537-571.

Cowan, G. (1989): Diagenesis of Upper Carboniferous sandstones: southern North Sea Basin.- In: Whateley, M. K. G. & Pickering, K. T. (Editors): Deltas: Sites and Traps for Fossil Fuels. Geological Society Special Publication No. 41, pp. 57-73.

Coward, M. P. (1995): Structural and tectonic setting of the Permo-Triassic basins of northwest Europe.- In: Boldy, S. A. R. (Editor): Permian and Triassic Rifting in Northwest Europe. Geological Society Special Publications, 91. The Geological Society, London, pp. 7-39.

Coward, M. P.; Dewey, J.; Hempton, M. & Holroyd, J. (2003): Tectonic evolution.- In: Evans, D., Graham, C., Armour, A. & Bathurst, P. (Editors): The Millennium Atlas: petroleum geology of the central and northern North Sea. The Geological Society, London, pp. 17-33.

Davies, R. J.; O´Donnell, D.; Bentham, P. N.; Gibson, J. P. C.; Curry, M. R.; Dunay, R. E. & Maynard, J. R. (1999): The origin and genesis of major Jurassic unconformities within the triple junction area of the North Sea, UK.- In: Fleet, A. J. & Boldy, S. A. R. (Editors): Petroleum Geology of Northwest Europe: Proceedings of the 5th Conference, 1. The Geological Society, London, pp. 117-131.

De Boer, L.; Harris, R.; Frimann-Dahl, C.; Lambertersen, A. M.; Kingsley, M.; Kennedy, C. & Mogensen, R. (1992): Final well report NOR-G.- Internal Industry Report, 50.92.D\RM1019 (Phillips Petroleum Co. Norway): 294 pp.

Deer, W. A.; Howie, R. A. & Zussman, J. (1992): An introduction to the rock-forming minerals.- Longman, 696 pp.

Deer, W. A.; Howie, R. A. & Zussman, J. (2001): Rock forming minerals - framework silicates: feldspars.- Vol. 4A, The geological society, London, 972 pp.

di Primio, R. & Neumann, V. (2008): HPHT reservoir evolution: a case study from Jade and Judy fields, Central Graben, UK North Sea.- International Journal of Earth Sciences, 97: 1101-1114.

Dixon, S. A.; Summers, D. M. & Surdam, R. C. (1989): Diagenesis and preservation of porosity in Norphlet Formation (Upper Jurassic), southern Alabama.- American Association of Petroleum Geologists Bulletin, 73 (6): 707-728.

Dunham, R. J. (1962): Classification of carbonate rocks according to depositional texture.- In Ham, W. E. (Editor): Classification of carbonate rocks, American Association of Petroleum Geologists Memoir. 1. pp. 108-121.

Dutton, S. P. & Land, L. S. (1985): Meteoric burial diagenesis of Pennsylvanian arkosic sandstones, southwestern Anadarko Basin, Texas.- American Association of Petroleum Geologists Bulletin, 69 (1): 22-38.

Dypvik, H. (1983): Clay mineral transformations in Tertiary and Mesozoic sediments from North Sea.- American Association of Petroleum Geologists Bulletin, 67 (1): 160-165.

Ehrenberg, S. N. (1993): Preservation of anomalously high porosity in deeply buried sandstones by grain-coating chlorite: examples from the Norwegian Continental Shelf.- American Association of Petroleum Geologists Bulletin, 77 (7): 1260-1286.

Ehrenberg, S. N. (1995): Measuring sandstone compaction from modal analyses of thin sections: how to do it and what the results mean.- Journal of Sedimentary Research, A65 (2): 369-379.

Ehrenberg, S. N. & Jakobsen, K. G. (2001): Plagioclase dissolution related to biodegradation of oil in Brent Group sandstones (Middle Jurassic) of Gullfaks Field, northern North Sea.- Sedimentology, 48: 703-721.

Ehrenberg, S. N. & Nadeau, P. H. (1989): Formation of diagenetic illite in sandstones of the Garn Formation, Haltenbanken area, Mid-Norwegian continental shelf.- Clay Minerals, 24: 233-253.

Ehrenberg, S. N. & Nadeau, P. H. (2005): Sandstone vs. carbonate petroleum reservoirs: A global perspective on porosity-depth and porosity-permeability relationships.- American Association of Petroleum Geologists Bulletin, 89 (4): 435-445.

El-Sayed, M. I.; Fairchild, I. J. & Spiro, B. (1991): Kuwaiti dolocrete: petrology, geochemistry and groundwater origin.- Sedimentary Geology, 73: 59-75.

Erratt, D.; Thomas, G. M. & Wall, G. R. T. (1999): The evolution of the Central North Sea Rift.- In: Fleet, A. J. & Boldy, S. A. R. (Editors): Petroleum Geology of Northwest Europe: Proceedings of the 5th Conference, 1. The Geological Society, London, pp. 65-82.

Faimon, J. (1996): Oscillatory silicon and aluminium aqueous concentrations during experimental aluminosilicate weathering.- Geochimica et Cosmochimica Acta, 60(15): 2901-2907.

Fein, J. B. (2000): Experimental and field constraints on the role of silica-organic complexation and silica-microbial interactions during sediment diagenesis.- In: Worden, R. H. & Morad, S. (Editors): Quartz cementation in sandstones, pp. 119-127.

Fisher, M. J. & Mudge, D. C. (1998): Triassic.- In: Glennie, K. W. (Editor): Petroleum Geology of the North Sea. Blackwell Science, Oxford, pp. 212-244.

Franklin, S. P.; Hajash, A.; Dewers, T. A. & Tieh, T. T. (1994): The role of carboxylic acids in albite and quartz dissolution: An experimental study under diagenetic conditions.- Geochimica et Cosmochimica Acta, 58 (20): 4259-4279.

Fraser, S.; Robinson, A.; Johnson, H.; Underhill, J. & Kadolsky, D. (2003): Upper Jurassic.- In: Evans, D., Graham, C., Armour, A. & Bathurst, P. (Editors): The Millennium Atlas: petroleum geology of the central and northern North Sea. The Geological Society, London, pp. 157-189.

Füchtbauer, H. (1978): Zur Herkunft des Quarzzements. Abschätzung der Quarzauflösung in Silt- und Sandsteinen.- Geologische Rundschau, 67 (3): 991-1008.

Gatliff, R. W.; Richards, P. C.; Smith, K.; Graham, C. C.; McCormac, M.; Smith, N. J. P.; Long, D.; Cameron, T. D. J.; Evans, D.; Stevenson, A. G.; Bulat, J. & Ritchie, J. D. (1994): The geology of the central North Sea.- United Kingdom Offshore Regional Report, British Geological Survey, London, 119 pp.

Gaupp, R. (1996): Diagenesis types and their application in diagenesis mapping.- Zentralblatt für Geologie und Paläontologie Teil I, 1994 (11/12): 1183-1199.

Gaupp, R.; Matter, A.; Platt, J.; Ramseyer, K. & Walzebuck, J. (1993): Diagenesis and Fluid Evolution of Deeply Buried Permian (Rotliegende) Gas Reservoirs, Northwest Germany.- American Association of Petroleum Geologists Bulletin, 77 (7): 1111-1128.

Gaupp, R. & Okkerman, J. A. (2011): Diagenesis and reservoir quality of Rotliegend sandstones in the northern Netherlands - a review.- In: Grötsch, J. & Gaupp, R. (Editors): The Permian Rotliegend of the Netherlands, SEPM Special Publication No. 98, Tulsa (Oklahoma), pp. 193-226.

Giles, M. R. (1997): Diagenesis: A quantitative perspective.- Kluwer Academic Publishers, Dordrecht, 526 pp.

Giles, M. R. & de Boer, R. B. (1990): Origin and significance of redistributional secondary porosity.- Marine and Petroleum Geology, 7: 378-397.

Giles, M. R.; Indrelid, S. L.; Beynon, G. V. & Amthor, J. (2000): The origin of large-scale quartz cementation: evidence from large data sets and coupled heat-fluid mass transport modelling.- In: Worden, R. H. & Morad, S. (Editors): Quartz cementation in sandstones, pp. 21-38.

Giles, M. R. & Marshall, J. D. (1986): Constraints on the development of secondary porosity in the subsurface: re-evaluation of processes.- Marine and Petroleum Geology, 3: 243-255.

Giles, M. R.; Stevenson, S.; Martin, S. V.; Cannon, S. J. C.; Hamilton, P. J.; Marshall, J. D. & Samways, G. M. (1992): The reservoir properties and diagenesis of the Brent Group: a regional perspective.- In: Morton, A. C., Haszeldine, R. S., Giles, M. R. & Brown, S. (Editors): Geology of the Brent Group. The Geological Society Special Publication No. 61. The Geological Society, London, pp. 289-327.

Girard, J.-P.; Munz, I. A.; Johansen, H.; Lacharpagne, J.-C. & Sommer, F. (2002): Diagenesis of the Hild Brent Sandstones, northern North Sea: Isotopic evidence for the prevailing influence of deep basinal water.- Journal of Sedimentary Research, 72 (6): 746-759.

Glasmann, J. R. (1992): The fate of feldspar in Brent Group reservoirs, North Sea: a regional synthesis of diagenesis in shallow, intermediate, and deep burial environments.- In: Morton, A. C., Haszeldine, R. S., Giles, M. R. & Brown, S. (Editors): Geology of the Brent Group. The Geological Society Special Publication No. 61. The Geological Society, London, pp. 329-350.

Glasmann, J. R. & Wilkinson, G. C. (1993): Clay mineral stratigraphy of Mesozoic and Paleozoic red beds, Northern North Sea.- In: Parker, J. R. (Editor): Petroleum geology of Northwest Europe: proceedings of the 4th Conference. The Geological Society, London, pp. 625-636.

Glennie, K.; Higham, J. & Stemmerik, L. (2003): Permian.- In: Evans, D., Graham, C., Armour, A. & Bathurst, P. (Editors): The Millennium Atlas: petroleum geology of the central and northern North Sea. The Geological Society, London, pp. 91-103.

Glennie, K. W. (1998): Lower Permian-Rotliegend.- In: Glennie, K. W. (Editor): Petroleum geology of the North Sea. Blackwell science, Petroleum geology of the North Sea, pp. 137-173.

Glennie, K. W. (2001): Exploration activities in the Netherlands and North-West Europe since Groningen.- Geologie en Mijnbouw, 80 (1): 33-52.

Glennie, K. W. & Underhill, J. R. (1998): Origin, development and evolution of structural styles.- In: Glennie, K. W. (Editor): Petroleum geology of the North Sea. Blackwell science, Oxford, pp. 42-84.

Gluyas, J.; Jolley, L. & Primmer, T. (1997): Element mobility during diagenesis: sulphate cementation of Rotliegend sandstones, Southern North Sea.- Marine and Petroleum Geology, 14 (7/8): 1001-1011.

Goldsmith, P. J.; Hudson, G. & Van Veen, P. (2003): Triassic.- In: Evans, D., Graham, C., Armour, A. & Bathurst, P. (Editors): The Millennium Atlas: petroleum geology of the central and northern North Sea. The Geological Society, London, pp. 105-127.

Goldsmith, P. J.; Rich, B. & Standring, J. (1995): Triassic correlation and stratigraphy in the South Central Graben, UK North Sea.- In: Boldy, S. A. R. (Editor): Permian and Triassic Rifting in Northwest Europe. Geological Society, London, pp. 123-143.

Gowers, M. B.; Holtar, E. & Swensson, E. (1993): The structure of the Norwegian Central Trough (Central Graben area).- In: Parker, J. R. (Editor): Petroleum Geology of Northwest Europe: Proceedings of the 4th Conference. The Geological Society, London, pp. 1245-1254.

Gunter, W. D.; Wiwchar, B. & Perkins, E. H. (1997): Aquifer disposal of CO_2-rich greenhouse gases: extension of the time scale of experiment for CO_2-sequestering reactions by geochemical modelling.- Mineralogy and Petrology, 59: 121-140.

Hamilton, P. J.; Giles, M. R. & Ainsworth, P. (1992): K-Ar dating of illites in Brent Group reservoirs: a regional perspective.- In: Morton, A. C., Haszeldine, R. S., Giles, M. R. & Brown, S. (Editors): Geology of the Brent Group. The Geological Society Special Publication No. 61. The Geological Society, London, pp. 377-400.

Hancock, N. J. (1978): Possible causes of Rotliegend sandstone diagenesis in northern West Germany.- Journal of the Geological Society, 135: 35-40.

Haq, B. U.; Hardenbol, J.; Vail & R., P. (1987): Chronology of fluctuating sea levels since the Triassic.- Science, 235: 1156-1167.

Harrel, J. A. & Eriksson, K. A. (1979): Empirical conversion equations for thin-section and sieve derived size distribution parameters.- Journal of Sedimentary Petrology, 49 (1): 273-280.

Harris, N. B. (1992): Burial diagenesis of Brent sandstones: a study of Statjord, Hutton and Lyell fields.- In: Morton, A. C., Haszeldine, R. S., Giles, M. R. & Brown, S. (Editors): Geology of the Brent Group. The Geological Society Special Publication No. 61. The Geological Society, London, pp. 351-375.

Haszeldine, R. S.; Brint, J. F.; Fallick, A. E.; Hamilton, P. J. & Brown, S. (1992): Open and restricted hydrologies in Brent Group diagenesis: North Sea.- In: Morton, A. C., Haszeldine, R. S., Giles, M. R. & Brown, S. (Editors): Geology of the Brent Group. The Geological Society Special Publication No. 61. The Geological Society, London, pp. 401-419.

Haszeldine, R. S.; Cavanagh, A. J. & England, G. L. (2003): Effects of oil charge on illite dates and stopping quartz cement: calibration of basin models.- Journal of Geochemical Exploration, 78-79: 373-376.

Haszeldine, R. S.; Quinn, O.; England, G.; Wilkinson, M.; Shipton, Z. K.; Evans, J. P.; Heath, J.; Crossey, L.; Ballentine, C. J. & Graham, C. M. (2005): Natural geochemical analogues for carbon dioxide storage in deep geological porous reservoirs, a United Kingdom perspective.- Oil & Gas Science and Technology - Rev. IFP, 60: 33-49.

Haszeldine, R. S.; Wilkinson, M.; Darby, D.; Macaulay, C. I.; Couples, G. D.; Fallick, A. E.; Fleming, C. G.; Stewart, R. N. T. & McAulay, G. (1999): Diagenetic porosity creation in an overpressured graben.- In: A. J. Fleet & S. A. R. Boldy (Editors), Petroleum Geology of Northwest Europe: Proceedings of the 5th Conference. The Geological Society, London, pp. 1339-1350.

Heald, M. T. (1956): Cementation of Simpson and St. Peter Sandstones in parts of Oklahoma, Arkansas, and Missouri.- Journal of Geology, 64: 16-30.

Hillier, S. (1994): Pore-lining chlorites in siliciclastic reservoir sandstones: Electron microprobe, SEM and XRD data, and implications for their origin.- Clay Minerals, 29: 665-679.

Hillier, S. (2003): Chlorite in sediments.- In: Middleton, G. V. (Editor): Encyclopedia of Sediments and Sedimentary Rocks. Kluwer, pp. 123-126.

Hillier, S.; Fallick, A. E. & Matter, A. (1996): Origin of pore-lining chlorite in the aeolian Rotliegend of northern Germany.- Clay Minerals, 31: 153-171.

Hodgson, N. A.; Farnsworth, J. & Fraser, A. J. (1992): Salt-related tectonics, sedimentation and hydrocarbon plays in the Central Graben, North Sea, UKCS.- In: Hardman, R. F. P. (Editor): Exploration Britain: Geological insights for the next decade. The Geological Society Special Publication No. 67, pp. 31-63.

Horsfield, B.; Schenk, H. J.; Mills, N. & Welte, D. H. (1992): An investigation of the in-reservoir conversion of oil to gas: compositional and kinetic findings from closed-system programmed-temperature pyrolysis.- Organic Geochemistry, 19 (1-3): 191-204.

Houseknecht, D. W. (1984): Influence of grain size and temperature on intergranular pressure solution, quartz cementation, and porosity in a quartzose sandstone.- Journal of Sedimentary Petrology, 54 (2): 348-361.

Houseknecht, D. W. (1987): Assessing the relative importance of compaction processes and cementation to reduction of porosity in sandstones.- American Association of Petroleum Geologists Bulletin, 71 (6): 633-642.

Houseknecht, D. W. (1988): Intergranular pressure solution in four quartzose sandstones.- Journal of Sedimentary Petrology, 58 (2): 228-246.

Howarth, R. J. (1998): Improved estimators of uncertainty in proportions, point-counting, and pass-fail test results.- American Journal of Science, 298: 594-607.

Humphreys, B.; Smith, S. A. & Strong, G. E. (1989): Authigenic chlorite in Late Triassic sandstones from the Central Graben, North Sea.- Clay Minerals, 24: 427-444.

Irwin, H.; Curtis, C. & Coleman, M. (1977): Isotopic evidence for source of diagenetic carbonates formed during burial of organic - rich sediments.- Nature, 269: 209-213.

Isaksen, G. H. (2004): Central North Sea hydrocarbon systems: Generation, migration, entrapment, and thermal degradation of oil and gas.- American Association of Petroleum Geologists Bulletin, 88 (11): 1545-1572.

Jacob, H. (1989): Classification, structure, genesis and practical importance of natural solid oil bitumen ("migrabitumen").- International Journal of Coal Geology, 11: 65-79.

Jensen, H.; Ferriday, I. L. & Bharati, S. (1992): Geochemical report for well NOR-G.- Internal Industry Report (Geolab NOR A/S): 445 pp.

Johnson, H. D. & Fisher, M. J. (1998): North Sea Plays: Geological Controls on Hydrocarbon Distribution.- In: Glennie, K. W. (Editor): Petroleum geology of the North Sea. Blackwell science, pp. 463-547.

Jones, A. D.; Auld, H. A.; Carpenter, T. J.; Fetkovich, E.; Palmer, I. A.; Rigatos, E. N. & Thompson, M. W. (2005): Jade Field: an innovative approach to high-pressure, high-temperature field development.- In: Doré, A. G. & Vining, B. A. (Editors): Petroleum Geology: North-West Europe and Global Perspectives-Proceedings of the 6th Geology Conference. Petroleum Geology Conferences Ltd. Published by the Geological Society, London, pp. 269-283.

Jysereid, G.; Bassetti, A.; Schjerverud, K. & Tarran, S. P. (1994): Well NOR-C Final Well Report.- Internal Industry Report, 01/03/94 (Norsk Agip): 341 pp.

Keller, T.; Bayes, R.; Auld, H. & Lines, M. (2005): Judy Field: rejuvenation through a second phase of drilling.- In: Doré, A. G. & Vining, B. A. (Editors): Petroleum Geology: North-West Europe and Global Perspectives-Proceedings of the 6th Geology Conference. Petroleum Geology Conferences Ltd. Published by the Geological Society, London, pp. 651-661.

Ketzer, J. M.; Morad, S.; Nystuen, J. P. & De Ros, L. F. (2003): The role of the Cimmerian Unconformity (Early Cretaceous) in the kaolinitization and related reservoir-quality evolution in Triassic sandstones of the Snorre Field, North Sea.- International Association of Sedimentologist Special Publication, 34: 361-382.

Khalaf, F. I. (2007): Occurrences and genesis of calcrete and dolocrete in the Mio-Pleistocene fluviatile sequence in Kuwait, northeast Arabian Peninsula.- Sedimentary Geology, 199: 129-139.

Kharaka, Y. K.; Law, L. M.; Carothers, W. W. & Goerlitz, D. F. (1986): Role of organic species dissolved in formation waters from sedimentary basins in mineral diagenesis.- In: Gautier, D. L. (Editor): Roles of Organic Matter in Sediment Diagenesis. Society of Economic Paleontologists and Mineralogists Special Publication, 38, pp. 111-122.

Kim, J.; Dong, H.; Seabaugh, J.; Newell, S. W. & Eberl, D. D. (2004): Role of microbes in the smectite-to-illite reaction.- Science, 303: 830-832.

Kimber, R. N. & Mathieson, F. (1997): Reservoir Geology of the Triassic Joanne Sandstone Member in Jade well 30/2c-4, and correlation to adjacent well 30/2c-3, British North Sea.- Internal Industry Report, No. RB/97/1008 (Project No. RB 142).

Kirste, D.M.; Watson, M. N. & Tingate, P. R. (2004): Geochemical modelling of CO_2-water-rock interaction in the Pretty Hill Formation, Otway Basin.- In: P. J. Boult, D. R. Johns & S. C. Lang (Editors), Eastern Australasian Basins Symposium II. Petroleum Exploration Society of Australia, Special Publication. Petroleum Exploration Society of Australia, Adelaide, pp. 403-411.

KPUI/1 (1993): Exploration final well report well NOR-E.- Internal Industry Report (Norske-Shell): 118 pp.

Krumbein, W. C. & Sloss, L. L. (1963): Stratigraphy and Sedimentation.- W. H. Freeman, San Francisco, pp. 198.

Kvadsheim, E. & Aga, D. (1985): Geological completion report, NOCS well NOR-B.- Internal Industry Report, No. SASR8515768 (BP Petroleum Development Ltd. Norway): 36 pp.

Laier, T. & Nielsen, B. L. (1989): Cementing halite in Triassic Bunter Sandstone (Tønder, southwest Denmark) as a result of hyperfiltration of brines.- Chemical Geology, 76: 353-363.

Lander, R. H. & Bonnell, L. M. (2010): A model for fibrous illite nucleation and growth in sandstones.- American Association of Petroleum Geologists Bulletin, 94 (8): 1161-1187.

Lanson, B.; Beaufort, D.; Berger, G.; Bauer, A.; Cassagnabére, A. & Meunier, A. (2002): Authigenic kaolin and illitic minerals during burial diagenesis of sandstones: a review.- Clay Minerals, 37: 1-22.

Larter, S. R.; Head, I. M.; Huang, H.; Bennett, B.; M., J.; Aplin, A. C.; Murray, A.; Erdmann, M.; Wilhelms, A. & di Primio, R. (2005): Biodegradation, gas destruction and methane generation in deep subsurface petroleum reservoirs: an overview.- In: Doré, A. G. & Vining, B. A. (Editors): Petroleum Geology: North-West Europe and Global Perspectives-Proceedings of the 6th Geology Conference. Petroleum Geology Conferences Ltd. Published by the Geological Society, London, pp. 633-639.

Lawrence, M. J. F. (1991): Early diagenetic dolomite concretions in late Cretaceous Herring Formation, eastern Marlborough, New Zealand.- Sedimentary Geology, 75: 125-140.

Legler, B. & Schneider, J. W. (2008): Marine ingressions into the Middle/Late Permian saline lake of the Southern Permian Basin (Rotliegend, Northern Germany) possibly linked to sea-level highstands in the Arctic rift system.- Palaeogeography, Palaeoclimatology, Palaeoecology, 267: 102-114.

Leveille, G. P.; Primmer, T. J.; Dudley, G.; Ellis, D. & Allinson, G. J. (1997): Diagenetic controls on reservoir quality in Permian Rotliegendes sandstones, Jupiter Fields area, southern North Sea.- In: Ziegler, K., Turner, P. & Daines, S. R. (Editors): Petroleum Geology of the Southern North Sea: Future Potential, Geological Society Special Publication No. 123, pp. 105-122.

Lines, M. D. & Auld, H. A. (2004): A petroleum charge model for the Judy and Joanne Fields, Central North Sea: application to exploration and field development.- In: Cubitt, J. M., England, W. A. & Larter, S. (Editors): Understanding petroleum reservoirs: towards an integrated reservoir engineering and geochemical approach. Geological Society Special Publications 237, The Geological Society, London, pp. 175-206.

Littke, R.; Brauckmann, F. J.; Radke, M. & Schaefer, R. G. (1996): Solid bitumen in Rotliegend gas reservoirs in northern Germany: implications for their thermal and filling history.- Zentralblatt für Geologie und Paläontologie Teil I, 11/12: 1275-1291.

Lomando, A. J. (1992): The Influence of Solid Reservoir Bitumen on Reservoir Quality.- American Association of Petroleum Geologists Bulletin, 76 (8): 1137-1152.

Machel, H. G. (2001): Bacterial and thermochemical sulfate reduction in diagenetic settings - old and new insights.- Sedimentary Geology, 140: 143-175.

Marshall, J. & Hewett, T. (2003): Devonian.- In: Evans, D., Graham, C., Armour, A. & Bathurst, P. (Editors): The Millennium Atlas: petroleum geology of the central and northern North Sea. The Geological Society, London, pp. 65-81.

McBride, E. F. (1963): A classification of common sandstones.- Journal of Sedimentary Petrology, 33 (3): 664-669.

McCants, C. Y. & Burley, S. D. (1996): Reservoir architecture and diagenesis in downthrown fault block plays: the Lowlander Prospect of block 14/20b, Witch Ground Graben, Outer Moray Firth, UK North Sea.- In: Hurst, A., Johnson, H. D., Burley, S. D., Canham, A. C. & Mackertich, D. S. (Editors): Geology of the Humber Group: Central Graben and Moray Firth, UKCS. Geological Society Special Publication No. 114. The Geological Society, London, pp. 251-285.

McCollom, T. M. & Seewald, J. S. (2003): Experimental study of the hydrothermal reactivity of organic acids and acid anions: II. Acetic acid, acetate, and valeric acid.- Geochimica et Cosmochimica Acta, 67 (19): 3645-3664.

McDougall, N. D. & Kimber, R. N. (1994): Sedimentology of Phillips well 30/7a-P3, Judy Field, British North Sea.- Internal Industry Report, No. 7400/Id (Project No. Id/17847): 76 pp.

McKinley, J. M.; Worden, R. H. & Ruffell, A. H. (2003): Smectite in sandstones: a review of the controls on occurrence and behaviour during diagenesis.- In: Worden, R. H. & Morad, S. (Editors): Clay Mineral Cements in Sandstones, International Association of Sedimentologist Special Publication 34. Blackwell Publishing, pp. 109-128.

McLaughlin, O. M.; Haszeldine, R. S. & Fallick, A. E. (1996): Quartz diagenesis in layered fluids in the south Brae Oilfield, North Sea.- In: Crossey, L., Loucks, R. & Totten, M. (Editors): Siliciclastic diagenesis and fluid flow: concepts and applications. SEPM Special Publication, no. 55. SEPM, pp. 103-113.

McMahon, P. B.; Chapelle, F. H.; Fred Falls, W. & Bradley, P. M. (1992): Role of microbial processes in linking sandstone diagenesis with organic-rich clays.- Journal of Sedimentary Petrology, 62 (1): 1-10.

McManus, J. (1996): Korngrößenanalyse und ihre Interpretation.- In: Tucker, M. (Editor): Methoden der Sedimentologie. Enke, Stuttgart, pp. 58-79.

Menning, M. & German Stratigraphic Commission (2002): A geologic time scale 2002.- In: German Stratigraphic Commission (Editor): Stratigraphic table of Germany. German Stratigraphic Commission, Potsdam.

Metcalfe, R.; Rochelle, C. A.; Savage, D. & Higgo, J.W. (1994): Fluid-rock interactions during continental red bed diagenesis: implications for theoretical models of mineralization in sedimentary basins.- In: J. Parnell (Editor), Geofluids: Origin, migration and evolution of fluids in sedimentary basins, pp. 301-324.

Molenaar, N.; Cyziene, J.; Sliaupa, S. & Craven, J. (2008): Lack of inhibiting effect of oil emplacement on quartz cementation: Evidence from Cambrian reservoir sandstones, Paleozoic Baltic Basin.- Geological Society of America Bulletin, 120 (9/10): 1280-1295.

Monger, T. G. & Trujillo, D. E. (1991): Organic deposition during CO_2 and rich-gas flooding.- SPE Reservoir Evaluation & Engineering, 6: 17-24.

Morad, S. (1998): Carbonate cementation in sandstones: distribution patterns and geochemical evolution.- In: Morad, S. (Editor): Carbonate cementation in sandstones; distribution patterns and geochemical evolution. Special Publication of the International Association of Sedimentologists 26. Blackwell, Oxford, pp. 1-26.

Morad, S.; De Ros, L. F.; Nystuen, J. P. & Bergan, M. (1998): Carbonate diagenesis and porosity evolution in sheet-flood sandstones: evidence from the Middle and Lower Lunde Members (Triassic) in the Snorre Field, Norwegian North Sea.- In: Morad, S. (Editor): Carbonate cementation in sandstones; distribution patterns and geochemical evolution. Special Publication of the International Association of Sedimentologists 26. Blackwell, Oxford, pp. 53-85.

Morad, S.; Ketzer, J. M. & De Ros, L. F. (2000): Spatial and temporal distribution of diagenetic alterations in siliciclastic rocks: implications for mass transfer in sedimentary basins.- Sedimentology, 47 (1): 95-120.

Morad, S.; Worden, R. H. & Ketzer, J. M. (2003): Oxygen and hydrogen isotopic composition of diagenetic clay minerals in sandstones: a review of the data and controls.- International Association of Sedimentologist Special Publication, 34: 63-91.

Neumann, V. (2007): Numerical modeling and phase prediction in deep overpressured basinal settings of the Central Graben, North Sea.- PhD Thesis, Technische Universität Berlin, 191 pp.

Norske-Shell (1985): Exploration well resume, well NOR-A.- Internal Industry Report, NSEP 246 (Norske Shell): 70 pp.

Oakman, C. D. & Partington, M. A. (1998): Cretaceous.- In: Glennie, K. W. (Editor): Petroleum Geology of the North Sea. Blackwell Science, Oxford, pp. 294-349.

Odin, G. S. (1990): Clay mineral formation at the continent-ocean boundary: The Verdine facies.- Clay Minerals, 25: 477-483.

Oelkers, E. H.; Bjørkum, P. A.; Walderhaug, O.; Nadeau, P. H. & Murphy, W. M. (2000): Making diagenesis obey thermodynamics and kinetics: the case of quartz cementation in sandstones from offshore mid-Norway.- Applied Geochemistry, 15: 295-309.

Osborne, M. J. & Swarbrick, R. E. (1997): Mechanisms for Generating Overpressure in Sedimentary Basins: A Reevaluation.- American Association of Petroleum Geologists Bulletin, 81: 1023-1041.

Osborne, M. J. & Swarbrick, R. E. (1999): Diagenesis in North Sea HPHT clastic reservoirs-consequences for porosity and overpressure prediction.- Marine and Petroleum Geology, 16: 337-353.

Parnell, J.; Carey, P. F. & Bottrell, S. H. (1994): The occurrence of authigenic minerals in solid bitumens.- Journal of Sedimentary Research, A64 (1): 95-100.

Penge, J.; Munns, J. W.; Taylor, B. & Windle, T. M. F. (1999): Rift-raft tectonics: examples of gravitational tectonics from the Zechstein basins of northwest Europe.- In: Fleet, A. J. & Boldy, S. A. R. (Editors): Petroleum Geology of Northwest Europe: Proceedings of the 5th Conference, 1. The Geological Society, London, pp. 201-213.

Palmer, I. & Kelman, J. (1997): Geological Well Report 30/2c-4.- Internal Industry Report, Phillips Petroleum (UK) Ltd, 78 pp.

Pittman, E. D.; Larese, R., E. & Heald, M. T. (1992): Clay coats: occurrence and relevance to preservation of porosity in sandstones.- In: Houseknecht, D. W. & Pittman, E. D. (Editors): Origin, Diagenesis, and Petrophysics of Clay Minerals in Sandstones, SEPM Special Publication No. 47, pp. 241-255.

Pooler, J. & Amory, M. (1999): A subsurface perspective on ETAP - an integrated development of seven Central North Sea fields.- In: Fleet, A. J. & Boldy, S. A. R. (Editors): Petroleum Geology of Northwest Europe: Proceedings of the 5th Conference, 2. The Geological Society, London, pp. 993-1006.

Prestholm, E. & Walderhaug, O. (1994): Jurassic and Pre-Jurassic sandstones in and around the XXXX-License area - provenance, diagenesis and depositional settings.- Internal Industry Report, RF-112/94 (Rogaland Research): 278 pp.

Purvis, K. (1990): The clay mineralogy of the Upper Triassic Skagerrak Formation, central North Sea.- In: Farmer, V. C. & Tardy, Y. (Editors), 9th International Clay Conference 1989, Strasbourg, pp. 125-134.

Purvis, K. (1994): Extensive albite dissolution in Triassic reservoir sandstones from Gannet field, UK North Sea.- Marine and Petroleum Geology, 11 (5): 624-630.

Renton, J. J.; Heald, M. T. & Cecil, C. B. (1969): Experimental investigation of pressure solution of quartz.- Journal of Sedimentary Petrology, 39 (3): 1107-1117.

Rimstidt, J. D. & Barnes, H. L. (1980): The kinetics of silica-water reactions.- Geochimica et Cosmochimica Acta, 44: 1683-1699.

Ryan, P. C. & Hillier, S. (2002): Berthierine/chamosite, corrensite, and discrete chlorite from evolved verdine and evaporite-associated facies in the Jurassic Sundance Formation, Wyoming.- American Mineralogist, 87: 1607-1615.

Ryan, P. C. & Reynolds, R. C. (1996): The origin and diagenesis of grain-coating serpentine-chlorite in Tuscaloosa Formation sandstone, U.S. Gulf Coast.- American Mineralogist, 81: 213-225.

Rose, J. (1994): Block 2/X basin modelling study.- Internal Industry Report (Valebridge Exploration Consultants Ltd.): 125 pp.

Rosenbaum, J. & Sheppard, S. M. F. (1986): An isotopic study of siderites, dolomites and ankerites at high temperatures.- Geochimica et Cosmochimica Acta, 50: 1147-1150.

Saga-Petroleum (1994): Final well report NOR-F.- Internal Industry Report (Saga Petroleum): 203 pp.

Saigal, G. C.; Bjørlykke, K. & Larter, S. (1992): The effects of oil emplacement on diagenetic processes - Example from Fulmar reservoir sandstones, Central North Sea.- American Association of Petroleum Geologists Bulletin, 76 (7): 1024-1033.

Saigal, G. C.; Morad, S.; Bjørlykke, K.; Egeberg, P. K. & Aagaard, P. (1988): Diagenetic albitization of detrital K-feldspar in Jurassic, Lower Cretaceous, and Tertiary clastic reservoir rocks from offshore Norway, I. textures and origin.- Journal of Sedimentary Petrology, 58 (6): 1003-1013.

Schenk, H. J.; di Primio, R. & Horsfield, B. (1997): The conversion of oil into gas in petroleum reservoirs. Part 1: Comparative kinetic investigation of gas generation from crude oils of lacustrine, marine and fluviodeltaic origin by programmed-temperature closed-system pyrolysis.- Organic Geochemistry, 26 (7/8): 467-481.

Schmid, S.; Worden, R. H. & Fisher, Q. J. (2004): Diagenesis and reservoir quality of the Sherwood Sandstone (Triassic), Corrib Field, Slyne Basin, west of Ireland.- Marine and Petroleum Geology, 21: 299-315.

Schmidt, V. & MacDonald, D. A. (1979): The role of secondary porosity in the course of sandstone diagenesis.- SEPM Special Publication, 26: 175-207.

Schöner, R. (2006): Comparison of Rotliegend sandstone diagenesis from northern and southern margin of the North German Basin, and implications for the importance of organic maturation and migration.- PhD Thesis, Friedrich Schiller Universität, Jena, 222 pp.

Schöner, R. & Gaupp, R. (2005): Contrasting red bed diagenesis: the southern and northern margin of the Central European Basin.- International Journal of Earth Sciences, 94: 897-916.

Schöner, R.; Lüders, V.; Ondrak, R.; Gaupp, R. & Möller, P. (2008): Fluid-rock interactions.- In: Littke, R., Bayer, U., Gajewski, D. & Nelskamp, S. (Editors): Dynamics of Complex Intracontinental Basins: The Central European Basin System. Springer, pp. 389-410.

Schulze, B.; Wirth, C.; Linke, P.; Brand, W. A.; Kuhlmann, I.; Horna, V. & Schulze, E. D. (2004): Laser ablation-combustion-GC-IRMS - a new method for online analysis of intra-annual variation of $\delta^{13}C$ in tree rings, Tree Physiology, pp. 1193-1201.

Schwertmann, U. (1998): Anorganische Komponenten der Böden - Minerale und Gesteine.- In: Schachtschabel, P., Blume, H. P., Brümmer, G., Hartge, K. H. & Schwertmann, U. (Editors): Scheffer/Schachtschabel Lehrbuch der Bodenkunde. Enke Verlag, Stuttgart, pp. 5-44.

Seewald, J. S. (2001a): Aqueous geochemistry of low molecular weight hydrocarbons at elevated temperatures and pressures: Constraints from mineral buffered laboratory experiments.- Geochimica et Cosmochimica Acta, 65 (10): 1641-1664.

Seewald, J. S. (2001b): Model for origin of carboxylic acids in basinal brines.- Geochimica et Cosmochimica Acta, 65(21): 3779-3789.

Seewald, J. S. (2003): Organic-inorganic interactions in petroleum-producing sedimentary basins.- Nature, 426: 327-333.

Shebl, M. A. & Surdam, R. C. (1996): Redox reactions in hydrocarbon clastic reservoirs: experimental validation of this mechanism for porosity enhancement.- Chemical Geology, 132: 103-117.

Shiraki, R. & Dunn, T. L. (2000): Experimental study on water-rock interactions during CO_2 flooding in the Tensleep Formation, Wyoming, USA.- Applied Geochemistry, 15: 265-279.

Simon Petroleum Technology limited (1994): Geological evolution of the Central Graben during the Early Cretaceous and Jurassic.- Internal Industry Report, EM057: 265 pp.

Sinclair, R. & Weston, R. (1996): Application of sulphate removal technology in Heron cluster field, Internal Industry Report (Natco Group), 18 pp.

Smith, R. I.; Hodgson, N. & Fulton, M. (1993): Salt control on Triassic reservoir distribution, UKCS Central North Sea.- In: Parker, J. R. (Editor): Petroleum geology of Northwest Europe: proceedings of the 4th Conference. The Geological Society, London, pp. 547-557.

Snowdon, L. R. (1989): Organic mater properties and thermal evolution.- In: Hutcheon, I. E. (Editor): Short Course in Burial Diagenesis. Mineralogical Association of Canada, Montreal, pp. 39-60.

Spark, I. S. C. & Trewin, N. H. (1986): Facies-related diagenesis in the Main Claymore oilfield sandstones.- Clay Minerals, 21: 479-496.

Spencer, A. M.; Leckie, G. G. & Chew, K. J. (1996): North Sea hydrocarbon plays and their resources.- First Break, 14 (9): 345-357.

Spötl, C.; Houseknecht, D. W. & Burns, S. J. (1996): Diagenesis of an ´overmature´ gas reservoir: the Spiro sand of the Arkoma Basin, USA.- Marine and Petroleum Geology, 13 (1): 25-40.

Spötl, C.; Longstaffe, F. J.; Ramseyer, K. & Rüdingers, B. (1999): Authigenic albite in carbonate rocks - a tracer for deep burial brine migration?- Sedimentology, 46: 649-666.

Spötl, C. & Wright, V. P. (1992): Groundwater dolocretes from the Upper Triassic of the Paris Basin, France: a case study of an arid, continental diagenetic facies.- Sedimentology, 39: 1119-1136.

Surdam, R. C.; Boese, S. W. & Crossey, L. J. (1984): The Chemistry of Secondary Porosity.- In: McDonald, D. A. & Surdam, R. C. (Editors): Clastic Diagenesis. AAPG, pp. 127-149.

Surdam, R. C.; Crossey, L. J.; Hagen, E. S. & Heasler, H. P. (1989a): Organic-inorganic interactions and sandstone diagenesis.- American Association of Petroleum Geologists Bulletin, 73 (1): 1-23.

Surdam, R. C.; Dunn, T. L.; Heasler, H. P. & MacGowan, D. B. (1989b): Porosity evolution in sandstone/shale systems.- In: Hutcheon, I. E. (Editor): Short Course in Burial Diagenesis. Mineralogical Association of Canada, Montreal, pp. 61-134.

Surdam, R. C.; Jiao, Z. S. & MacGowan, D. B. (1993): Redox reactions involving hydrocarbons and mineral oxidants: a mechanism for significant porosity enhancement in sandstones.- American Association of Petroleum Geologists Bulletin, 77 (9): 1509-1518.

Sutherland, N.; Flemming, S.; Keeble, P. J. & Slater, A. C. (1985): Drilling completion report well NOR-B.- Internal Industry Report, No. 01.R.SS.004 (Statoil): 222 pp.

Swarbrick, R. E. (1994): Reservoir diagenesis and hydrocarbon migration under hydrostatic palaeopressure conditions.- Clay Minerals, 29: 463-473.

Swarbrick, R. E.; Osborne, M. J.; Grunberger, D.; Yardley, G. S.; Macleod, G.; Aplin, A. C.; Larter, S. R.; Knight, I. & Auld, H. A. (2000): Integrated study of the Judy Field (Block 30/7a) - an overpressured Central North Sea oil/gas field.- Marine and Petroleum Geology, 17: 993-1010.

Taylor, J. C. M. (1978): Control of diagenesis by depositional environment within a fluvial sandstone sequence in the northern North Sea Basin.- Journal of the Geological Society, 135: 83-91.

Taylor, J. C. M. (1998): Upper Permian-Zechstein.- In: Glennie, K. W. (Editor): Petroleum geology of the North Sea. Blackwell science, Oxford, pp. 174-211.

Taylor, J. M. (1950): Pore-space reduction in sandstones.- American Association of Petroleum Geologists Bulletin, 34 (4): 701-716.

Taylor, T. R.; Giles, M. R.; Hathon, L. A.; Diggs, T. N.; Braunsdorf, N. R.; Birbiglia, G. V.; Kittridge, M. G.; Macaulay, C. I. & Espejo, I. S. (2010): Sandstone diagenesis and reservoir quality prediction: Models, myths, and reality.- American Association of Petroleum Geologists Bulletin, 94 (8): 1093-1132.

Thyne, G. (2001): A model for diagenetic mass transfer between adjacent sandstone and shale.- Marine and Petroleum Geology, 18: 743-755.

Underhill, J. R. (1998): Jurassic.- In: Glennie, K. W. (Editor): Petroleum geology of the North Sea. Blackwell science, Oxford, pp. 245-293.

van de Kamp, P. (2008): Smectite-illite-muscovite transformations, quartz dissolution, and silica release in shales.- Clays and Clay Minerals, 56 (1): 66-81.

Vasconcelos, C.; McKenzie, J. A.; Warthmann, R. & Bernasconi, S. M. (2005): Calibration of the $\delta^{18}O$ paleothermometer for dolomite precipitated in microbial cultures and natural environments.- Geology, 33 (4): 317-320.

Veevers, J. J. & Powell, C. M. (1987): Late Paleozoic glacial episodes in Gondwanaland reflected in transgressive-regressive depositional sequences in Euramerica.- Geological Society of America Bulletin, 98: 475-487.

Vogel, J. C. & Van Urk, H. (1975): Isotopic composition of groundwater in semi-arid regions of southern Africa.- Journal of Hydrology, 25: 23-36.

Wachter, E. & Hayes, J. M. (1985): Exchange of oxygen isotopes in carbon-dioxide - phosphoric acid systems.- Chemical Geology, 52: 365-374.

Walderhaug, O. (1996): Kinetic modelling of quartz cementation and porosity loss in deeply buried sandstone reservoirs.- American Association of Petroleum Geologists Bulletin, 80 (5): 731-745.

Walderhaug, O.; Lander, R. H.; Bjørkum, P. A.; Oelkers, E. H.; Bjørlykke, K. & Nadeau, P. H. (2000): Modelling quartz cementation and porosity in reservoir sandstones: examples from the Norwegian continental shelf.- In: Worden, R. H. & Morad, S. (Editors): Quartz cementation in sandstones, pp. 39-49.

Walker, T. R. (1984): 1984 SEPM Presidential address: Diagenetic albitization of potassium feldpar in arkosic sandstones.- Journal of Sedimentary Petrology, 54 (1): 3-16.

Walker, T. R.; Larson, E. E. & Hoblitt, R. P. (1981): Nature and origin of hematite in the Moenkopi Formation (Triassic), Colorado Plateau: A contribution to the origin of magnetism in red beds.- Journal of Geophysical Research, 86 (B1): 317-333.

Walker, T. R.; Waugh, B. & Grone, A. J. (1978): Diagenesis in first-cycle desert alluvium of Cenozoic age, southwestern United States and northwestern Mexico.- Geological Society of America Bulletin, 89: 19-32.

Warren, E. A. & Smalley, P. C. (1993): The chemical composition of North Sea formation waters: a review of their heterogeneity and potential applications.- In: J. R. Parker (Editor), Petroleum Geology of Northwest Europe: Proceedings of the 4th Conference. The Geological Society, London, pp. 1347-1352.

Warren, E. A. & Smalley, P. C. (Editors), (1994): North Sea formation water atlas.- Memoir No. 15. The Geological Society, London, 200 pp.

Watts, N. L. (1980): Quaternary pedogenic calcretes from the Kalahari (southern Africa): mineralogy, genesis and diagenesis.- Sedimentology, 27: 661-686.

Waugh, B. (1978): Authigenic K-feldspar in British Permo-Triassic sandstones.- Journal of the Geological Society, 135: 51-56.

Weibel, R. (1998): Diagenesis in oxidising and locally reducing conditions - an example from the Triassic Skagerrak Formation, Denmark.- Sedimentary Geology, 121: 259-276.

Weibel, R. (1999): Effects of burial on the clay assemblages in the Triassic Skagerrak Formation, Denmark.- Clay Minerals, 34: 619-635.

Weibel, R. & Grobety, B. (1999): Note: Pseudomorphous transformation of goethite needles into hematite in sediments of the Triassic Skagerrak Formation, Denmark.- Clay Minerals, 34: 657-660.

Weibel, R. & Keulen, N. (2008): Diagenesis influencing the porosity of Upper Jurassic reservoir sandstones, Danish North Sea.- Geological Survey of Denmark and Greenland Bulletin, 15: 9-12.

Wieser, M. E. & Brand, W. A. (1999): A laser extraction/combustion technique for in situ $\delta^{13}C$ analysis of organic and inorganic materials.- Rapid Communications in Mass Spectrometry, 13: 1218-1225.

Wignall, P. B. (1994): Black Shales.- Oxford Monographs on Geology and Geophysics, Vol. 30, Clarendon Press, Oxford, 127 pp.

Wilkinson, M.; Darby, D.; Haszeldine, R. S. & Couples, G. D. (1997): Secondary Porosity Generation During Deep Burial Associated with Overpressure Leak-Off: Fulmar Formation, United Kingdom Central Graben.- American Association of Petroleum Geologists Bulletin, 81 (5): 803-813.

Wilkinson, M.; Haszeldine, R. S.; Ellam, R. M. & Fallick, A. (2004): Hydrocarbon filling history from diagenetic evidence: Brent Group, UK North Sea.- Marine and Petroleum Geology, 21: 443-455.

Wilkinson, M.; Haszeldine, R. S. & Fallick, A. E. (2006): Jurassic and Cretaceous clays of the northern and central North Sea hydrocarbon reservoirs reviewed.- Clay Minerals, 41: 151-186.

Wilkinson, M.; Milliken, K. L. & Haszeldine, R. S. (2001): Systematic destruction of K-feldspar in deeply buried rift and passive margin sandstones.- Journal of the Geological Society, 158: 675-683.

Wilson, M. D. (1992): Inherited grain-rimming clays in sandstones from eolian and shelf environments: their origin and control on reservoir properties.- In: Houseknecht, D. W. & Pittman, E. D. (Editors): Origin, Diagenesis, and Petrophysics of Clay Minerals in Sandstones, SEPM Special Publication No. 47, pp. 209-225.

Worden, R. H. & Burley, S. D. (2003): Sandstone diagenesis: the evolution of sand to stone.- In: Burley, S. D. & Worden, R. H. (Editors): Sandstone diagenesis: recent and ancient, pp. 3-44.

Worden, R. H. & Morad, S. (2000): Quartz cementation in oil field sandstones: a review of the key controversies.- In: Worden, R. H. & Morad, S. (Editors): Quartz cementation in sandstones, pp. 1-20.

Worden, R. H. & Morad, S. (2003): Clay minerals in sandstones: controls on formation, distribution and evolution.- International Association of Sedimentologist Special Publication, 34: 3-41.

Worden, R. H.; Smalley, P. C. & Barclay, S. A. (2003): H_2S and diagenetic pyrite in North Sea sandstones: due to TSR or organic sulphur compound cracking?- Journal of Geochemical Exploration, 78-79: 487-491.

Wright, V. P. (1990): Meteoric diagenesis.- In: Tucker, M. E. & Wright, V. P. (Editors): Carbonate Sedimentology. Blackwell Science, pp. 336-348.

Xu, T.; Apps, J. A. & Pruess, K. (2000): Analysis of mineral trapping for CO_2 disposal in deep aquifers.- LBNL-46992, Lawrence Berkeley National Laboratory Report, Berkeley, California, 61 pp.

Zanella, E. & Coward, M. P. (2003): Structural framework.- In: Evans, D., Graham, C., Armour, A. & Bathurst, P. (Editors): The Millennium Atlas: petroleum geology of the central and northern North Sea. The Geological Society, London, pp. 45-59.

Zanella, E.; Coward, M. P. & McGrandle, A. (2003): Crustal structure.- In: Evans, D., Graham, C., Armour, A. & Bathurst, P. (Editors): The Millennium Atlas: petroleum geology of the central and northern North Sea. The Geological Society, London, pp. 35-43.

Ziegler, K. (2006): Clay minerals of the Permian Rotliegend Group in the North Sea and adjacent areas.- Clay Minerals, 41: 355-393.

Ziegler, P. A. (1990): Geological Atlas of Western and Central Europe.- Shell Internationale Petroleum Maatschappij B.V., The Hague, 239 pp.

Appendix

Appendix 1: Table samples and methods
Appendix 2.1: Table petrographic data Rotliegend (Norwegian sector)
Appendix 2.2: Table petrographic data Triassic and overlying strata (UK sector)
Appendix 2.3: Table petrographic data Triassic and Jurassic (Norwegian sector)
Appendix 3.1: Table electron microprobe data of authigenic carbonates
Appendix 3.2: Table electron microprobe data of feldspars
Appendix 3.3: Table electron microprobe data of clay minerals
Appendix 4.1: Table minerals found by XRD-analysis in well 30/2c-4
Appendix 4.2: Example XRD patterns
Appendix 5.1: Carbonate stable isotope analysis of bulk rock samples
Appendix 5.2: Table δ^{13}C-values of samples from well 30/2c-4 measured by UV laser-system
Appendix 6: Table grain contacts
Appendix 7: Input scripts for Geochemist´s Workbench

Appendix 1: Table samples and methods

Abbreviations: BEI...backscatter electron images, CL...cathodoluminescence, congl...conglomerate, E...in Erlangen, EMP...electron microprobe, J...in Jena, L...Laser, MD...measured depth, OM...optical microscopy, Oxf...Oxfordian, PC...pointcount analysis, SEM...scanning electron microscopy, Skag. Fm...Skag. Fm. Formation, strat...stratigraphy, TVD...true vertical depth, W...by M. Wrobel in Warszawa, XRD...X-ray diffraction analysis

well	sample	strat.	MD [m]	TVD [m]	lithology	material	OM	PC	EMP	BEI	SEM	CL	δ18O	δ13C	XRD
Norwegian sector (1 and 2)															
NOR-A	4805.6	Rotliegend	4805.60		sandstone	sample	x	x							
NOR-A	4808.8	Rotliegend	4808.80		sandstone	sample	x	x	x	x					
NOR-A	4810.9	Rotliegend	4810.90		sandstone	sample	x	x			J				
NOR-A	4812.1	Rotliegend	4812.10		sandstone	sample	x	x	x	x					
NOR-A	4812.8	Rotliegend	4812.80		sandstone	sample	x	x			W				
NOR-B	5115.4	Rotliegend	5115.40	5114.46	sandstone	sample	x	x							
NOR-B	5116.7	Rotliegend	5116.70	5115.76	sandstone	sample	x	x							
NOR-B	5119.4	Rotliegend	5119.40	5118.46	sandstone	sample	x	x	x	x					
NOR-B	5121.6	Rotliegend	5121.60	5120.66	sandstone	sample	x	x							
NOR-B	5124.6	Rotliegend	5124.60	5123.66	sandstone	sample	x	x							
NOR-B	5126.7	Rotliegend	5126.70	5125.76	sandstone	sample	x	x							
NOR-B	5152.8	Rotliegend	5152.80	5151.86	sandstone	sample	x								
NOR-B	5164.6	Rotliegend	5164.60	5163.65	sandstone	sample	x	x							
NOR-C	4575.55	Oxf. sands	4575.55	4562.00	sandstone	sample	x	x					E	E	
NOR-C	4576.1	Oxf. sands	4576.10	4562.55	sandstone	sample	x	x							
NOR-C	4577.5	Skag. Fm.	4577.50	4563.95	sandstone	sample	x	x							
NOR-C	4578.4	Skag. Fm.	4578.40	4564.85	sandstone	sample	x	x							
NOR-C	4579.5	Skag. Fm.	4579.50	4565.95	sandstone	sample	x	x							
NOR-C	4582.45	Skag. Fm.	4582.45	4568.90	sandstone	sample	x	x							
NOR-C	4583.7	Skag. Fm.	4583.70	4570.15	sandstone	sample	x								
NOR-C	4584.65	Skag. Fm.	4584.65	4571.10	sandstone	sample	x	x							
NOR-C	4585.5	Skag. Fm.	4585.50	4571.95	sandstone	sample	x	x							
NOR-C	4587.2	Skag. Fm.	4587.20	4573.65	sandstone	sample	x								
NOR-C	4589.6	Skag. Fm.	4589.60	4576.05	sandstone	sample	x	x	x	x	J, W				
NOR-C	4590.5	Skag. Fm.	4590.50	4576.95	sandstone	sample	x								
NOR-D	4612.1	Oxf. sands	4612.10		sandstone	sample	x								
NOR-D	4613.5	Oxf. sands	4613.50		sandstone	sample	x						E	E	
NOR-D	4616.75	Oxf. sands	4616.75		sandstone	sample	x								
NOR-D	4617.45	Oxf. sands	4617.45		sandstone	sample	x								
NOR-D	4618.5	Oxf. sands	4618.50		sandstone	sample							E	E	
NOR-D	4622.25	Oxf. sands	4622.25		sandstone	sample	x						E	E	
NOR-D	4628.45	Oxf. sands	4628.45		sandstone	sample	x								
NOR-D	4630.25	Oxf. sands	4630.25		sandstone	sample	x								
NOR-D	4632.6	Oxf. sands	4632.60		sandstone	sample	x								
NOR-D	4636.9	Oxf. sands	4636.90		sandstone	sample	x								
NOR-D	4638.5	Oxf. sands	4638.50		sandstone	sample	x								
NOR-E	5555.85	Triassic	5555.85	5527.90	sandstone	sample	x	x							
NOR-E	5556.45	Triassic	5556.45	5528.49	sandstone	sample	x	x							
NOR-E	5558.4	Triassic	5558.40	5530.43	sandstone	sample	x	x							
NOR-E	5558.5	Triassic	5558.50	5530.53	sandstone	sample	x	x							
NOR-E	5559.35	Triassic	5559.35	5531.38	sandstone	sample	x	x							
NOR-E	5563.5	Triassic	5563.50	5535.51	sandstone	sample	x	x							
NOR-E	5564.35	Triassic	5564.35	5536.35	sandstone	sample	x	x	x						
NOR-F	5108.55	Farsund	5108.55	5105.55	source rock	sample	x	x					E	E	
NOR-F	5108.7	Farsund	5108.70	5105.70	source rock	sample	x	x					E	E	
NOR-F	5109.4	Farsund	5109.40	5106.40	source rock	sample	x	x							
NOR-F	5109.65	Farsund	5109.65	5106.65	source rock	sample	x	x							
NOR-F	5113.65	Farsund	5113.65	5110.65	source rock	sample	x	x							
NOR-F	5134.35	Farsund	5134.35	5131.05	sandstone	sample	x	x					E	E	

Appendix 1: Table samples and methods

Abbreviations: BEI...backscatter electron images, CL...cathodoluminescence, congl...conglomerate, E...in Erlangen, EMP...electron microprobe, J...in Jena, L...Laser, MD...measured depth, OM...optical microscopy, Oxf...Oxfordian, PC...pointcount analysis, SEM...scanning electron microscopy, Skag. Fm...Skag. Fm. Formation, strat...stratigraphy, TVD...true vertical depth, W...by M. Wrobel in Warszawa, XRD...X-ray diffraction analysis

well	sample	strat.	MD [m]	TVD [m]	lithology	material	OM	PC	EMP	BEI	SEM	CL	δ18O	δ13C	XRD
NOR-F	5134.95	Farsund	5134.95	5131.65	sandstone	sample	x	x					E	E	
NOR-F	5135.6	Farsund	5135.60	5132.30	sandstone	sample	x	x	x						
NOR-F	5136.2	Farsund	5136.20	5132.90	sandstone	sample	x	x	x	x			E	E	
NOR-F	5136.55	Farsund	5136.55	5133.25	source rock	sample	x	x							
NOR-F	5136.85	Farsund	5136.85	5133.55	sandstone	sample	x	x			W				
NOR-G	5006.34	Rotliegend	5006.34	5003.01	-	cuttings	x								
NOR-G	5009	Rotliegend	5009.00	5005.67	-	cuttings	x								
NOR-G	5178.55	Rotliegend	5178.55	5175.11	-	cuttings	x								
NOR-G	14237	Ula Fm	4339.44	4337.58	sandstone	thin section	x	x							
NOR-G	14246	Ula Fm	4342.18	4340.32	sandstone	thin section	x	x							
NOR-G	14249.2	Ula Fm	4343.16	4341.29	sandstone	thin section	x	x							
NOR-G	14254	Ula Fm	4344.62	4342.76	sandstone	thin section	x	x							
NOR-G	14260.1	Ula Fm	4346.48	4344.61	sandstone	thin section	x	x							
NOR-G	14265	Ula Fm	4347.97	4346.11	sandstone	thin section	x	x							
NOR-G	14269	Ula Fm	4349.19	4347.33	sandstone	thin section	x	x							
NOR-G	14274	Ula Fm	4350.72	4348.85	sandstone	thin section	x	x							
NOR-G	14282	Ula Fm	4353.15	4351.29	sandstone	thin section	x	x							
UK sector (30)															
30/2c-4	15584	Skag. Fm.	4750.00	4631.25	mudstone	sample	x	x					E	E	x
30/2c-4	15593	Skag. Fm.	4752.72	4633.90	siltstone	sample	x	x							x
30/2c-4	15598	Skag. Fm.	4754.24	4635.38	sandstone	sample	x	x							
30/2c-4	15604	Skag. Fm.	4756.10	4637.20	sandstone	sample	x	x	x			x	E	E	
30/2c-4	15608	Skag. Fm.	4757.26	4638.33	sandstone	sample	x	x					E	E, L	
30/2c-4	15613	Skag. Fm.	4758.84	4639.87	sandstone	sample	x	x	x	x		x			
30/2c-4	15615	Skag. Fm.	4759.21	4640.23	sandstone	sample	x	x			W				
30/2c-4	15616	Skag. Fm.	4759.79	4640.79	sandstone	sample	x	x	x	x	J				
30/2c-4	15624.5	Skag. Fm.	4762.38	4643.32	sandstone	sample	x	x							
30/2c-4	15628	Skag. Fm.	4763.38	4644.30	siltstone	sample	x	x					E	E	
30/2c-4	15631.5	Skag. Fm.	4764.51	4645.40	sandstone	sample	x	x							
30/2c-4	15634.3	Skag. Fm.	4765.37	4646.23	sandstone	sample	x	x							x
30/2c-4	15639	Skag. Fm.	4766.74	4647.57	siltstone	sample	x	x							x
30/2c-4	15645	Skag. Fm.	4768.60	4649.38	sandstone	sample	x	x							
30/2c-4	15646.3	Skag. Fm.	4769.02	4649.80	sandstone	sample	x	x							
30/2c-4	15647.5	Skag. Fm.	4769.30	4650.06	sandstone	sample	x	x							
30/2c-4	15651.5	Skag. Fm.	4770.49	4651.22	sandstone	sample	x	x							
30/2c-4	15654.5	Skag. Fm.	4771.40	4652.12	sandstone	sample	x	x	x	x	W				x
30/2c-4	15655.3	Skag. Fm.	4771.80	4652.50	sandstone	sample	x	x					E	E	x
30/2c-4	15660	Skag. Fm.	4773.08	4653.75	sandstone	sample	x	x							
30/2c-4	15665	Skag. Fm.	4774.78	4655.41	mudstone	sample	x	x					E	E	
30/2c-4	15671.5	Skag. Fm.	4776.67	4657.26	sandstone	sample	x	x					E	E	
30/2c-4	15676	Skag. Fm.	4778.14	4658.68	sandstone	sample	x	x							
30/2c-4	15680	Skag. Fm.	4779.26	4659.78	sandstone	sample	x	x	x	x					
30/2c-4	15685	Skag. Fm.	4780.76	4661.24	sandstone	sample	x	x							
30/2c-4	15688	Skag. Fm.	4781.79	4662.25	sandstone	sample	x	x							
30/2c-4	15691	Skag. Fm.	4782.31	4662.75	sandstone	sample	x	x		x	J				
30/2c-4	15691.5	Skag. Fm.	4782.49	4662.93	sandstone	sample	x	x							
30/2c-4	15704	Skag. Fm.	4786.58	4666.91	sandstone	sample	x	x							x
30/2c-4	15715	Skag. Fm.	4789.90	4670.15	sandstone	sample	x	x	x	x			E	E, L	x
30/2c-4	15716	Skag. Fm.	4790.24	4670.48	sandstone	sample	x	x					E	E	
30/2c-4	15718.5	Skag. Fm.	4790.97	4671.19	sandstone	sample	x	x							
30/2c-4	15722.2	Skag. Fm.	4792.19	4672.38	mudstone	sample	x	x							x
30/2c-4	15739	Skag. Fm.	4797.25	4677.32	sandstone	sample	x	x					E	E, L	
30/2c-4	15741	Skag. Fm.	4797.92	4677.97	sandstone	sample	x	x							
30/2c-4	15743	Skag. Fm.	4798.47	4678.50	sandstone	sample	x	x							

Abbreviations: BEI...backscatter electron images, CL...cathodoluminescence, congl...conglomerate, E...in Erlangen, EMP...electron microprobe, J...in Jena, L...Laser, MD...measured depth, OM...optical microscopy, Oxf...Oxfordian, PC...pointcount analysis, SEM...scanning electron microscopy, Skag. Fm...Skag. Fm. Formation, strat...stratigraphy, TVD...true vertical depth, W...by M. Wrobel in Warszawa, XRD...X-ray diffraction analysis

well	sample	strat.	MD [m]	TVD [m]	lithology	material	OM	PC	EMP	BEI	SEM	CL	δ18O	δ13C	XRD
30/2c-4	15745	Skag. Fm.	4799.14	4679.16	sandstone	sample	x	x					E	E	
30/2c-4	15747	Skag. Fm.	4800.57	4680.56	sandstone	sample	x	x	x			x		L	
30/2c-4	15747.5	Skag. Fm.	4800.90	4680.88	mudstone	sample	x	x							x
30/2c-4	15752	Skag. Fm.	4800.30	4680.29	sandstone	sample	x	x					E	E	
30/2c-4	15757	Skag. Fm.	4802.70	4682.64	mudstone	sample	x	x							
30/2c-4	15768.5	Skag. Fm.	4806.27	4686.11	mudstone	sample	x	x	x	x					x
30/2c-4	15792.5	Skag. Fm.	4813.55	4693.22	sandstone	sample	x	x							
30/7a-6	12209.5	Jurassic?	3721.46	3721.46	mudstone	thin section	x	x							
30/7a-6	12217	Jurassic?	3723.74	3723.74	sandstone	thin section	x	x							
30/7a-7	9480.1	Lista	2889.53	2889.53	mudstone	thin section	x	x							
30/7a-7	9490.1	Andrew	2892.58	2892.58	mudstone	thin section	x	x							
30/7a-7	9506.1	Andrew	2897.46	2897.46	sandstone	thin section	x	x							
30/7a-7	9513.1	Andrew	2899.59	2899.59	sandstone	thin section	x	x							
30/7a-7	11291	Skag. Fm.	3441.50	3441.50	sandstone	thin section	x	x							
30/7a-7	11308	Skag. Fm.	3446.68	3446.68	sandstone	thin section	x	x							
30/7a-7	11316	Skag. Fm.	3449.12	3449.12	sandstone	thin section	x	x							
30/7a-7	11333	Skag. Fm.	3454.30	3454.30	sandstone	thin section	x	x							
30/7a-7	11344	Skag. Fm.	3457.65	3457.65	sandstone	thin section	x	x							
30/7a-7	11363.4	Skag. Fm.	3463.56	3463.56	congl.	thin section	x	x							
30/7a-7	11367.1	Skag. Fm.	3464.69	3464.69	sandstone	thin section	x	x							
30/7a-7	11433.2	Skag. Fm.	3484.84	3484.84	sandstone	thin section	x	x							
30/7a-7	11443.1	Skag. Fm.	3487.86	3487.86	sandstone	thin section	x	x							
30/7a-7	11468	Skag. Fm.	3495.45	3495.45	sandstone	thin section	x	x							
30/7a-7	11488	Skag. Fm.	3501.54	3501.54	sandstone	thin section	x	x							
30/7a-7	11512.1	Skag. Fm.	3508.89	3508.89	sandstone	thin section	x	x							
30/7a-7	11527.1	Skag. Fm.	3513.46	3513.46	sandstone	thin section	x	x							
30/7a-7	11529	Skag. Fm.	3514.04	3514.04	sandstone	thin section	x								
30/7a-7	11531	Skag. Fm.	3514.65	3514.65	sandstone	thin section	x	x							
30/7a-7	11531.3	Skag. Fm.	3514.74	3514.74	siltstone	thin section	x	x							
30/7a-7	11544.7	Skag. Fm.	3518.82	3518.82	siltstone	thin section	x	x							
30/7a-8	9531-8	Lista Fm	2905.05	2905.05	marl	thin section	x	x							
30/7a-8	9573	Andrew	2917.85	2917.85	sandstone	thin section	x	x							
30/7a-8	9988.75	Ekofisk	3044.57	3044.57	chalk	thin section	x	x							
30/7a-8	10012.4	Ekofisk	3051.78	3051.78	chalk	thin section	x	x							
30/7a-8	10037.8	Ekofisk	3059.52	3059.52	chalk	thin section	x	x							
30/7a-8	11429	Devils hole	3483.56	3483.56	sandstone	thin section	x	x							
30/7a-8	11444	Devils hole	3488.13	3488.13	sandstone	thin section	x	x							
30/7a-8	11455	Devils hole	3491.48	3491.48	sandstone	thin section	x	x							
30/7a-8	11681	Skag. Fm.	3560.37	3560.37	sandstone	thin section	x	x							
30/7a-8	11808	Skag. Fm.	3599.08	3599.08	sandstone	thin section	x	x							
30/7a-8	11834	Skag. Fm.	3607.00	3607.00	sandstone	thin section	x	x							
30/7a-8	11928	Skag. Fm.	3635.65	3635.65	sandstone	thin section	x	x							
30/7a-8	11963	Skag. Fm.	3646.32	3646.32	siltstone	thin section	x	x							
30/7a-9	9869	Andrew	3008.07	2978.11	siltstone	thin section	x	x							
30/7a-9	9876	Andrew	3010.21	2980.23	sandstone	thin section	x	x							
30/7a-9	9881	Andrew	3011.73	2981.74	marl	thin section	x	x							
30/7a-9	11850	Andrew	3611.88	3575.91	sandstone	cuttings	x								
30/7a-9	12097	Skag. Fm.	3687.17	3650.45	sandstone	thin section	x	x							
30/7a-9	12099.5	Skag. Fm.	3687.93	3651.20	sandstone	thin section	x	x	x	x					
30/7a-9	12099.7	Skag. Fm.	3687.99	3651.26	sandstone	thin section	x	x							
30/7a-9	12105	Skag. Fm.	3689.60	3652.86	sandstone	thin section	x	x							
30/7a-9	12110	Skag. Fm.	3691.13	3654.37	siltstone	thin section	x	x							
30/7a-9	12117	Skag. Fm.	3693.26	3656.48	siltstone	thin section	x	x							

Appendix 1: Table samples and methods

Abbreviations: BEI...backscatter electron images, CL...cathodoluminescence, congl...conglomerate, E...in Erlangen, EMP...electron microprobe, J...in Jena, L...Laser, MD...measured depth, OM...optical microscopy, Oxf...Oxfordian, PC...pointcount analysis, SEM...scanning electron microscopy, Skag. Fm...Skag. Fm. Formation, strat...stratigraphy, TVD...true vertical depth, W...by M. Wrobel in Warszawa, XRD...X-ray diffraction analysis

well	sample	strat.	MD [m]	TVD [m]	lithology	material	OM	PC	EMP	BEI	SEM	CL	δ18O	δ13C	XRD
30/7a-9	12124	Skag. Fm.	3695.40	3658.59	siltstone	thin section	x	x							
30/7a-9	12131	Skag. Fm.	3697.53	3660.71	sandstone	thin section	x	x							
30/7a-9	1235.5	Skag. Fm.	3698.90	3662.06	mudstone	thin section	x	x							
30/7a-9	12142	Skag. Fm.	3700.88	3664.03	siltstone	thin section	x	x							
30/7a-9	12152	Skag. Fm.	3703.93	3667.04	sandstone	thin section	x	x							
30/7a-9	12160	Skag. Fm.	3706.37	3669.46	sandstone	thin section	x	x							
30/7a-9	12160.4	Skag. Fm.	3706.49	3669.58	sandstone	thin section	x	x							
30/7a-9	12168	Skag. Fm.	3708.81	3671.87	sandstone	thin section	x	x							
30/7a-9	12174	Skag. Fm.	3710.64	3673.68	sandstone	thin section	x	x							
30/7a-9	12186	Skag. Fm.	3714.29	3677.30	sandstone	thin section	x	x							
30/7a-9	12194	Skag. Fm.	3716.73	3679.72	sandstone	thin section	x	x							
30/7a-11z	11424	Skag. Fm.	3482.04	3457.17	sandstone	thin section	x	x							
30/7a-11z	11427.6	Skag. Fm.	3483.13	3458.26	siltstone	thin section	x	x							
30/7a-11z	11430	Skag. Fm.	3483.86	3458.99	sandstone	thin section	x	x							
30/7a-11z	11439	Skag. Fm.	3486.61	3461.71	sandstone	thin section	x	x							
30/7a-11z	11446	Skag. Fm.	3488.74	3463.83	congl.	thin section	x	x							
30/7a-11z	11446.3	Skag. Fm.	3488.83	3463.92	congl.	thin section	x	x							
30/7a-11z	11454	Skag. Fm.	3491.18	3466.25	sandstone	thin section	x	x							
30/7a-11z	11468	Skag. Fm.	3495.45	3470.49	sandstone	thin section	x	x							
30/7a-11z	11483	Skag. Fm.	3500.02	3475.03	sandstone	thin section	x	x							
30/7a-11z	11491	Skag. Fm.	3502.46	3477.45	sandstone	thin section	x	x							
30/7a-11z	11503	Skag. Fm.	3506.11	3481.08	sandstone	thin section	x	x							
30/7a-11z	11510	Skag. Fm.	3508.25	3483.20	sandstone	thin section	x	x							
30/7a-11z	11519	Skag. Fm.	3510.99	3485.92	sandstone	thin section	x	x							
30/7a-11z	11533	Skag. Fm.	3515.26	3490.16	sandstone	thin section	x	x							
30/7a-11z	11546	Skag. Fm.	3519.22	3494.09	sandstone	thin section	x	x							
30/7a-11z	11557	Skag. Fm.	3522.57	3497.42	congl.	thin section	x	x							
30/7a-11z	11573	Skag. Fm.	3527.45	3502.27	sandstone	thin section	x	x							
30/7a-11z	11579.5	Skag. Fm.	3529.43	3504.23	sandstone	thin section	x	x							
30/7a-11z	11588	Skag. Fm.	3532.02	3506.81	sandstone	thin section	x	x							
30/7a-11z	11602	Skag. Fm.	3536.29	3511.04	sandstone	thin section	x	x							
30/7a-11z	11607.2	Skag. Fm.	3537.87	3512.62	sandstone	thin section	x	x							
30/7a-11z	11621	Skag. Fm.	3542.08	3516.79	sandstone	thin section	x	x							
30/7a-11z	11626.5	Skag. Fm.	3543.76	3518.46	sandstone	thin section	x	x							
30/7a-11z	11627	Skag. Fm.	3543.91	3518.61	sandstone	thin section	x	x							
30/7a-11z	11632	Skag. Fm.	3545.43	3520.12	sandstone	thin section	x	x							
30/7a-11z	11641	Skag. Fm.	3548.18	3522.84	sandstone	thin section	x	x							
30/7a-11z	11647.8	Skag. Fm.	3550.25	3524.90	sandstone	thin section	x	x							
30/7a-11z	11655.1	Skag. Fm.	3552.47	3527.11	sandstone	thin section	x	x							
30/7a-11z	11682	Skag. Fm.	3560.67	3535.25	sandstone	thin section	x	x							
30/7a-11z	11682.75	Skag. Fm.	3560.90	3535.48	sandstone	thin section	x	x							
30/7a-P7	14331.5	Skag. Fm.	4368.24	3596.18	sandstone	thin section	x	x							
30/7a-P7	(17)14341	Skag. Fm.	4371.14	3598.57	sandstone	thin section	x	x							
30/7a-P7	(24)14348	Skag. Fm.	4373.27	3600.32	sandstone	thin section	x	x							

Appendix 2 petrographic tables

Appendix 2.1: Table petrographic data Rotliegend (Norwegian sector)
Appendix 2.2: Table petrographic data Triassic and overlying strata (UK sector)
Appendix 2.3: Table petrographic data Triassic and Jurassic (Norwegian sector)

Following abbreviations were used in the tables:

Andrew	Andrew Formation
AS	argillaceous sandflat facies association
biocl.	Bioclasts
c. plates	coarse plates
D zone	dolomite cemented zone
detr.	Detrital
Devils H.	Lower Tithonian - Devils Hole Formation
Ekofisk.	Ekofisk Formation
FC	fluvial channel facies association
H.	Haugesund Formation
Heavy-min.	heavy minerals
Joanne	Joanne Sandstone Member
Jos. U.	Josephine Upper Sandstone Member
Jura	Jurassic
Lista	Lista Formation
L2	shallow lagoonal facies (see section 6 for details)
MD	measured depth
MSF	middle shoreface facies (see section 6 for details)
mst/sst.	mixed layers of mm thick sand layers and mudstone layers
mudst.	mudstone
Palaeoc.	Palaeocene
pol.	polished
polycr.	polycrystalline
Q zone	quartz cemented zone
Rotlieg.	Rotliegend
s. plates	small plates radial around grains
sandst.	sandstone
SF	sheetflood facies association
source	source rock
Skag. F.	Skagerrak Formation
tr.	traces
U. Oxf.	Upper Oxfordian
USF	upper shoreface fazies (see section 6 for details)

Remark: The percent values in the tables were calculated from point count values and rounded. The rounding error may have the effect that the total of all percent values may differ somewhat from 100.

Appendix 2.1: Table petrographic data Rotliegend (Norwegian sector)

Well			NOR-A	NOR-A	NOR-A	NOR-A	NOR-A
Thin section no.			**4805.6**	**4808.8**	**4810.9**	**4812.1**	**4812.8**
Depth MD [m]			4805.60	4808.80	4810.90	4812.10	4812.80
Stratigraphy			Rotlieg.	Rotlieg.	Rotlieg.	Rotlieg.	Rotlieg.
Detrital grains [%]	Quartz	Monocrystalline quartz	51.3	53.0	52.7	52.0	55.3
		Polycr. quartz and quartzite	6.0	4.0	5.3	9.3	6.7
	Lithics	Metamorphics	0.3	0.3	1.0	0.7	0.0
		Quartz feldspar aggregates	2.0	2.7	2.7	1.0	2.3
		Sedimentary extraclasts	0.0	0.0	0.0	0.3	0.0
		Volcanic	0.0	tr.	0.0	0.0	0.0
		Indeterminate	0.0	2.0	0.7	0.3	0.3
	Feldspar	Plagioclase	0.7	2.0	1.0	1.3	1.0
		K-feldspar (uncorroded)	5.7	5.7	4.7	4.0	5.7
		K-feldpar (partly dissolved)	1.0	1.0	1.7	1.7	1.3
	Sheet-silicates	Light mica	0.0	0.3	0.0	0.0	0.0
		Biotite	0.0	0.0	0.0	0.0	0.0
		Chlorite	0.0	0.0	0.0	0.0	0.0
	Intraclasts	Shale/Siltstone	0.7	0.0	0.7	0.0	0.7
		Detr. dolomite nodules	0.0	0.0	0.0	0.0	0.0
		Glauconite	0.0	0.0	0.0	0.0	0.0
		Bioclasts	0.0	0.0	0.0	0.0	0.0
		Black shale clasts	0.0	0.0	0.0	0.0	0.0
		Chert	0.0	0.0	0.0	0.0	0.0
		Microspar/micrite with biocl.	0.0	0.0	0.0	0.0	0.0
	Heavy minerals		tr.	tr.	tr.	tr.	tr.
Mud [%]		Clay matrix	0.0	0.0	0.0	0.0	0.0
		Black shale	0.0	0.0	0.0	0.0	0.0
		Micrite/microspar	0.0	0.0	0.0	0.0	0.0
Authigenic minerals [%]	Carbonate	Dolomite nodules	0.0	0.0	0.0	0.0	0.0
		Dolomite pore filling+rhombi	2.0	4.3	2.0	5.0	2.0
		Clast replacing	0.0	0.0	0.0	0.0	0.0
		Calcite	0.0	0.0	0.0	0.0	0.0
		Ferrous calcite	0.0	0.0	0.0	0.0	0.0
		Ankerite	0.0	0.0	0.0	0.0	0.0
	Quartz overgrowths		1.3	2.3	0.3	1.3	4.3
	Feldspar	K-feldspar overgrowths	tr.	tr.	0.0	tr.	0.0
		Albite in K-feldspar grains	0.0	0.0	0.3	0.3	0.0
	Hematite coatings		9.3	10.3	9.0	0.0	6.3
	Leucoxene/Anatase		tr.	0.3	0.0	0.0	0.0
	Anhydrite		0.0	0.0	0.0	0.0	0.0
	Barite		tr.	0.0	0.0	0.0	0.0
	Halite		0.0	0.0	0.0	0.7	0.0
	Clay minerals	Replacement of grains	2.0	2.0	1.3	1.0	0.7
		Illite coatings	tr.	1.0	tr.	1.0	1.0
		Illite meshwork	8.3	5.0	6.3	11.3	8.7
		Chlorite coatings and shreds	0.0	0.0	0.0	0.0	0.0
		Chlorite s. plates (5-10μm)	0.0	0.0	0.0	0.0	0.0
		Chlorite c. plates (>10μm)	0.0	0.0	0.0	0.0	0.0
		Clorite intraclast	0.0	0.0	0.0	0.0	0.0
		Kaolinite	0.0	0.0	0.0	0.0	0.0
	Bitumen	Massive in cracks or pores	0.0	0.0	0.0	0.0	0.0
Porosity [%]	Intergranular without secondary pores		3.0	2.3	5.0	3.3	2.3
	Secondary	Feldspar-leaching	0.3	tr.	0.7	0.3	0.3
		Lithics-leaching	0.0	0.0	0.0	0.0	0.0
		Heavy-min.-leaching	0.0	0.0	0.0	0.0	0.0
		Oversized pores	1.0	0.3	0.7	0.0	0.0
		Cement diss. voids	5.0	1.0	4.0	5.0	1.0
Granulometry		grainsize [mm]	0.25	0.20	0.25	0.25	0.25
		sorting	1.2	1.4	1.1	1.3	1.3
		rounding	0.7	0.7	0.8	0.5	0.7
		sphericity	0.7	0.5	0.7	0.7	0.7
Number of counts			300	300	300	300	300

Appendix 2.1: Table petrographic data Rotliegend (Norwegian sector)

Well			NOR-B	NOR-B	NOR-B	NOR-B	NOR-B	NOR-B	NOR-B
Thin section no.			**5115.4**	**5116.7**	**5119.4**	**5121.6**	**5124.6**	**5126.7**	**5164.6**
Depth MD [m]			5115.40	5116.70	5119.40	5121.60	5124.60	5126.70	5164.60
Stratigraphy			Rotlieg.	Rotlieg.	Rotlieg.	Rotlieg.	Rotlieg.	Rotlieg.	Rotlieg.
Detrital grains [%]	Quartz	Monocrystalline quartz	49.3	37.7	46.7	38.7	54.0	56.7	47.0
		Polycr. quartz and quartzite	9.3	7.7	8.0	11.3	6.3	6.0	11.7
	Lithics	Metamorphics	1.3	0.3	2.0	3.7	1.0	1.0	2.0
		Quartz feldspar aggregates	2.3	3.0	3.3	1.7	1.3	1.0	1.7
		Sedimentary extraclasts	0.0	0.0	0.0	0.0	0.0	0.0	0.0
		Volcanic	1.0	0.3	1.0	1.0	0.7	0.3	0.0
		Indeterminate	0.7	2.7	1.0	0.7	0.7	0.7	0.3
	Feldspar	Plagioclase	1.3	3.7	0.7	3.0	2.3	0.7	0.3
		K-feldspar (uncorroded)	8.3	8.0	3.7	2.3	3.0	6.7	4.3
		K-feldpar (partly dissolved)	0.0	0.3	tr.	0.0	0.0	0.3	0.0
	Sheet-silicates	Light mica	0.0	0.3	1.0	0.3	tr.	tr.	0.7
		Biotite	0.0	0.0	0.3	0.0	0.0	0.3	0.0
		Chlorite	0.0	0.0	0.0	0.0	0.3	0.0	0.0
	Intraclasts	Shale/Siltstone	0.0	0.7	1.7	2.3	1.0	0.0	0.3
		Detr. dolomite nodules	0.0	0.0	0.0	0.0	0.0	0.0	0.0
		Glauconite	0.0	0.0	0.0	0.0	0.0	0.0	0.0
		Bioclasts	0.0	0.0	0.0	0.0	0.0	0.0	0.0
		Black shale clasts	0.0	0.0	0.0	0.0	0.0	0.0	0.0
		Chert	0.0	0.0	0.0	0.0	0.0	0.0	0.0
		Microspar/micrite with biocl.	0.0	0.0	0.0	0.0	0.0	0.0	0.0
	Heavy minerals		0.0	0.7	0.3	0.0	0.3	0.3	0.0
Mud [%]		Clay matrix	0.0	0.0	3.0	1.0	0.0	0.0	0.0
		Black shale	0.0	0.0	0.0	0.0	0.0	0.0	0.0
		Micrite/microspar	0.0	0.0	0.0	0.0	0.0	0.0	0.0
Authigenic minerals [%]	Carbonate	Dolomite nodules	0.0	0.0	0.0	0.0	0.0	0.0	0.0
		Dolomite pore filling+rhombi	7.0	0.3	3.7	1.0	1.0	1.7	0.7
		Clast replacing	0.3	0.0	0.0	0.0	0.0	0.0	0.0
		Calcite	0.0	0.0	0.0	0.0	0.0	0.0	0.0
		Ferrous calcite	0.0	0.0	0.0	0.0	0.0	0.0	0.0
		Ankerite	0.0	0.0	0.0	0.0	0.0	0.0	0.0
	Quartz overgrowths		0.3	0.0	0.3	tr.	0.7	0.3	0.7
	Feldspar	K-feldspar overgrowths	0.0	0.0	0.0	0.0	0.0	0.0	0.0
		Albite in K-feldspar grains	0.0	0.0	tr.	0.0	0.0	0.0	0.3
	Hematite coatings		6.7	18.7	16.0	20.0	16.0	9.7	14.0
	Leucoxene/Anatase		0.3	0.3	tr.	0.0	0.0	0.3	0.0
	Anhydrite		tr.	tr.	0.0	0.0	0.0	0.0	0.0
	Barite		0.3	0.0	tr.	0.0	0.0	0.0	tr.
	Halite		0.0	0.0	tr.	0.0	0.0	0.0	0.0
	Clay minerals	Replacement of grains	0.0	0.3	2.0	1.0	2.0	0.0	1.0
		Illite coatings	0.0	0.0	0.0	tr.	0.3	0.0	0.7
		Illite meshwork	0.0	0.0	tr.	0.0	0.0	0.3	7.3
		Chlorite coatings and shreds	0.0	0.0	0.0	0.0	0.0	0.0	0.0
		Chlorite s. plates (5-10μm)	0.0	0.0	tr.	0.0	0.0	0.0	0.0
		Chlorite c. plates (>10μm)	0.0	0.0	0.0	0.0	0.0	0.0	0.0
		Clorite intraclast	0.0	0.0	0.0	0.0	0.0	0.0	0.0
		Kaolinite	0.0	0.0	0.0	0.0	0.0	0.0	0.0
	Bitumen	Massive in cracks or pores	0.0	0.0	0.0	0.0	0.0	0.0	0.0
Porosity [%]	Intergranular without secondary pores		8.7	13.7	5.0	11.7	8.3	10.0	6.0
	Secondary	Feldspar-leaching	0.0	0.3	0.3	0.0	0.0	0.7	0.0
		Lithics-leaching	0.0	0.3	0.0	0.0	0.0	0.0	0.0
		Heavy-min.-leaching	0.0	0.0	0.0	0.0	0.0	0.0	0.0
		Oversized pores	0.7	0.7	0.0	0.3	0.7	1.0	0.3
		Cement diss. voids	2.0	tr.	0.0	tr.	0.0	2.0	0.7
Granulometry		grainsize [mm]	0.30	0.15	0.15	0.15	0.15	0.25	0.20
		sorting	1.7	1.7	2.0	2.0	2.0	1.4	1.8
		rounding	0.5	0.5	0.3	0.5	0.5	0.7	0.7
		sphericity	0.7	0.7	0.7	0.7	0.7	0.7	0.7
Number of counts			300	300	300	300	300	300	300

Well			30/2c4	30/2c4	30/2c4	30/2c4	30/2c4	30/2c4	30/2c4	30/2c4	30/2c4
Thin section no.			**15584**	**15593**	**15598 B**	**15604 B**	**15608B**	**15613 B**	**15615**	**15616 B**	**15624.5**
Depth TVDSS [m]			4631.25	4633.90	4635.38	4637.20	4638.33	4639.87	4640.23	4640.79	4643.32
Stratigraphy			Skag. F.	Skag. F.	Skag. F.	Skag. F.	Skag. F.	Skag. F.	Skag. F.	Skag. F.	Skag. F.
			Joanne	Joanne	Joanne	Joanne	Joanne	Joanne	Joanne	Joanne	Joanne
Facies			AS	AS	AS	AS	FC	FC	FC	FC	FC
Detrital grains [%]	Quartz	Monocrystalline quartz	12.2	33.5	32.0	29.5	28.5	22.5	21.3	23.7	25.3
		Polycr. quartz and quartzite	0.5	5.2	6.8	6.8	6.5	12.0	9.5	14.0	13.3
	Lithics	Metamorphics	0.0	0.3	1.7	0.7	0.7	1.2	1.2	1.8	0.8
		Quartz feldspar aggregates	0.2	0.8	0.3	0.5	0.2	0.5	3.5	1.3	2.0
		Sedimentary extraclasts	0.0	0.0	0.0	0.0	0.0	0.0	0.0	0.0	0.0
		Volcanic	0.0	0.0	0.0	0.0	0.0	0.0	0.0	0.0	0.0
		Indeterminate	0.0	0.7	0.2	0.7	0.3	1.5	0.0	1.3	1.2
	Feldspar	Plagioclase	0.2	1.3	0.2	0.2	0.3	0.5	3.2	1.5	2.0
		K-feldspar (uncorroded)	8.0	17.0	23.3	26.3	19.2	14.7	15.3	12.7	8.8
		K-feldpar (partly dissolved)	0.0	1.7	2.5	3.2	7.3	7.3	5.2	8.5	7.7
	Sheet-silicates	Light mica	0.5	3.0	1.8	1.2	1.7	1.2	1.2	1.0	2.5
		Biotite	0.2	0.0	0.0	0.0	0.0	0.0	0.0	0.0	0.0
		Chlorite	0.0	0.5	0.3	0.2	0.2	0.0	0.0	0.3	0.3
	Intraclasts	Shale/Siltstone	0.3	0.0	0.0	0.0	0.0	0.2	0.0	0.0	0.0
		Detr. dolomite nodules	0.0	0.0	0.0	0.2	0.0	0.0	0.0	0.0	0.0
		Glauconite	0.0	0.0	0.0	0.0	0.0	0.0	0.0	0.0	0.0
		Bioclasts	0.0	0.0	0.0	0.0	0.0	0.0	0.0	0.0	0.0
		Black shale clasts	0.0	0.0	0.0	0.0	0.0	0.0	0.0	0.0	0.0
		Chert	0.0	0.0	0.0	0.0	0.0	0.0	0.0	0.0	0.0
		Microspar/micrite with biocl.	0.0	0.0	0.0	0.0	0.0	0.0	0.0	0.0	0.0
	Heavy minerals		0.2	0.7	0.2	0.0	0.0	0.2	0.2	0.2	0.2
Mud [%]		Clay matrix	50.8	30.3	21.5	14.2	13.5	0.0	0.0	0.0	0.0
		Black shale	0.0	0.0	0.0	0.0	0.0	0.0	0.0	0.0	0.0
		Micrite/microspar	0.0	0.0	0.0	0.0	0.0	0.0	0.0	0.0	0.0
Authigenic minerals [%]	Carbonate	Dolomite nodules	19.8	0.0	3.5	6.5	1.7	0.0	0.0	0.0	0.0
		Dolomite pore filling+rhombi	0.0	0.0	0.0	0.5	5.7	0.2	0.0	0.0	0.0
		Clast replacing	1.5	0.0	0.5	1.3	1.8	0.0	0.0	0.0	0.0
		Calcite	0.0	0.0	0.0	0.0	0.0	0.0	0.0	0.0	0.0
		Ferrous calcite	0.0	0.0	0.0	0.0	0.0	0.0	0.0	0.0	0.0
		Ankerite	0.0	0.0	0.0	0.3	1.2	0.0	0.0	0.0	0.0
	Quartz overgrowths		0.0	0.0	0.0	0.0	0.0	3.7	1.3	4.5	5.8
	Feldspar	K-feldspar overgrowths	0.0	0.5	0.2	0.5	0.7	7.0	9.2	7.5	7.3
		Albite in K-feldspar grains	0.0	0.2	0.7	0.5	0.2	0.2	0.0	1.0	0.0
	Hematite coatings		0.2	0.0	0.2	0.0	0.0	0.0	0.0	0.0	0.0
	Leucoxene/Anatase		0.0	0.7	0.7	0.8	1.0	0.5	1.2	0.3	1.0
	Anhydrite		0.0	0.0	0.0	0.0	0.0	0.0	0.0	0.0	0.0
	Barite		0.0	0.0	0.0	0.0	0.0	0.0	0.0	0.0	0.0
	Sulphides		0.0	0.0	0.0	0.0	0.0	0.2	0.0	0.0	0.0
	Clay minerals	Replacement of grains	0.0	0.3	0.2	1.5	2.0	1.5	3.2	2.5	2.5
		Illite coatings	0.0	1.3	0.0	0.0	0.0	0.0	0.0	0.0	0.0
		Illite meshwork	0.0	0.0	0.0	0.0	0.0	0.0	0.0	0.0	0.0
		Chlorite coatings and shreds	0.0	0.5	1.3	1.2	2.3	2.0	4.5	0.7	0.5
		Chlorite s. plates (5-10μm)	0.0	0.2	0.0	0.3	2.2	0.0	0.2	0.2	0.0
		Chlorite c. plates (>10μm)	0.0	0.0	0.0	0.0	0.0	0.0	0.0	0.0	0.0
		Clorite intraclast	5.5	1.0	0.8	2.3	1.2	0.0	0.0	0.2	0.0
		Kaolinite	0.0	0.0	0.0	0.0	0.0	0.0	0.0	0.0	0.0
	Bitumen	Massive in cracks or pores	0.0	0.3	1.0	0.5	0.8	0.0	0.0	0.0	1.8
Porosity [%]	Intergranular without secondary pores		0.0	0.0	0.2	0.2	0.8	3.2	11.0	3.2	9.3
	Secondary	Feldspar-leaching	0.0	0.0	0.0	0.0	0.2	2.8	2.0	2.0	2.3
		Lithics-leaching	0.0	0.0	0.0	0.0	0.0	1.2	1.0	1.7	2.3
		Heavy-min.-leaching	0.0	0.0	0.0	0.0	0.0	0.0	0.2	0.0	0.2
		Oversized pores	0.0	0.0	0.0	0.0	0.0	8.0	3.3	5.0	0.2
		Cement diss. voids	0.0	0.0	0.0	0.0	0.0	8.0	2.5	5.0	2.5
Granulometry		grainsize [mm]	<0.02	0.08	0.16	0.12	0.13	0.31	0.24	0.34	0.24
		sorting	-	1.2	1.2	1.1	1.3	1.2	1.3	1.3	1.8
		rounding	-	0.4	0.4	0.4	0.4	0.4	0.4	0.4	0.4
		sphericity	-	0.6	0.7	0.7	0.7	0.6	0.6	0.6	0.6
Number of counts			600	600	600	600	600	600	600	600	600

Appendix 2.2: Table petrographic data Triassic and overlying strata (UK sector)

Well			30/2c4	30/2c4	30/2c4	30/2c4	30/2c4	30/2c4	30/2c4	30/2c4	30/2c4
Thin section no.			**15628**	**15631.5**	**15634.3 B**	**15639 B**	**15645**	**15646**	**15647.5**	**15651.5**	**15654.5 B**
Depth TVDSS [m]			4644.30	4645.40	4646.23	4647.57	4649.38	4649.80	4650.07	4651.22	4652.12
Stratigraphy			Skag. F.	Skag. F.	Skag. F.	Skag. F.	Skag. F.	Skag. F.	Skag. F.	Skag. F.	Skag. F.
			Joanne	Joanne	Joanne	Joanne	Joanne	Joanne	Joanne	Joanne	Joanne
Facies			AS	AS	AS	AS	SF	SF	FC/SF	FC/SF	FC/SF
Detrital grains [%]	Quartz	Monocrystalline quartz	10.5	34.7	28.0	20.5	28.3	23.0	27.7	26.3	28.2
		Polycr. quartz and quartzite	0.8	3.8	1.7	3.0	10.8	9.5	5.0	2.7	2.7
	Lithics	Metamorphics	0.0	0.0	0.0	0.3	2.5	0.5	1.3	0.8	0.5
		Quartz feldspar aggregates	0.0	0.2	0.3	0.0	0.3	1.5	1.0	2.3	0.2
		Sedimentary extraclasts	0.0	0.0	0.0	0.0	0.0	0.0	0.0	0.0	0.0
		Volcanic	0.0	0.0	0.0	0.0	0.0	0.0	0.0	0.0	0.0
		Indeterminate	0.0	0.8	0.2	0.2	0.5	0.8	1.0	1.8	0.7
	Feldspar	Plagioclase	0.0	0.8	0.3	0.2	4.5	1.5	1.3	2.2	1.0
		K-feldspar (uncorroded)	7.5	23.8	16.8	7.7	14.5	13.3	9.7	14.8	16.5
		K-feldpar (partly dissolved)	0.0	4.0	3.3	0.0	4.7	4.5	3.0	8.2	7.8
	Sheet-silicates	Light mica	1.7	0.7	2.5	6.3	1.7	0.8	2.3	1.5	1.0
		Biotite	0.2	0.0	0.0	0.0	0.0	0.0	0.0	0.0	0.0
		Chlorite	1.0	0.0	0.3	0.7	0.0	1.0	0.0	0.7	0.5
	Intraclasts	Shale/Siltstone	0.0	0.0	0.0	3.5	0.0	0.5	0.0	0.0	0.0
		Detr. dolomite nodules	0.0	0.0	0.0	0.0	0.0	0.0	0.0	0.0	0.0
		Glauconite	0.0	0.0	0.0	0.0	0.0	0.0	0.0	0.0	0.0
		Bioclasts	0.0	0.0	0.0	0.0	0.0	0.0	0.0	0.0	0.0
		Black shale clasts	0.0	0.0	0.0	0.0	0.0	0.0	0.0	0.0	0.0
		Chert	0.0	0.0	0.0	0.0	0.0	0.0	0.0	0.0	0.0
		Microspar/micrite with biocl.	0.0	0.0	0.0	0.0	0.0	0.0	0.0	0.0	0.0
	Heavy minerals		0.5	0.5	0.2	0.2	0.3	0.0	0.0	2.0	0.8
Mud [%]		Clay matrix	59.3	0.0	42.2	39.3	0.0	0.0	7.7	0.0	0.3
		Black shale	0.0	0.0	0.0	0.0	0.0	0.0	0.0	0.0	0.0
		Micrite/microspar	0.0	0.0	0.0	0.0	0.0	0.0	0.0	0.0	0.0
Authigenic minerals [%]	Carbonate	Dolomite nodules	7.0	0.0	0.0	2.7	0.0	0.0	27.7	0.7	0.3
		Dolomite pore filling+rhombi	0.0	0.7	0.7	1.7	0.0	0.0	4.3	0.0	0.5
		Clast replacing	0.0	0.2	0.0	0.5	0.0	0.0	1.7	0.0	0.2
		Calcite	0.0	0.0	0.0	0.0	0.0	0.0	0.0	0.0	0.0
		Ferrous calcite	0.0	0.0	0.0	0.0	0.0	0.0	0.0	0.0	0.0
		Ankerite	0.0	0.5	1.0	tr.	0.0	0.0	tr.	0.0	0.5
	Quartz overgrowths		0.0	1.2	0.3	0.0	7.2	3.2	0.0	0.3	0.0
	Feldspar	K-feldspar overgrowths	0.0	3.0	0.5	0.0	7.2	6.3	0.3	8.2	11.2
		Albite in K-feldspar grains	0.0	0.7	0.0	0.0	1.5	0.0	0.0	1.3	0.5
	Hematite coatings		0.3	0.0	0.0	0.3	0.0	0.0	0.0	0.0	0.0
	Leucoxene/Anatase		0.5	0.8	0.3	0.2	0.2	0.8	0.3	3.8	1.7
	Anhydrite		0.0	0.0	0.0	0.0	0.0	0.0	0.0	0.0	0.0
	Barite		0.0	0.0	0.0	0.0	0.0	0.0	0.0	0.0	0.0
	Sulphides		0.0	0.0	0.0	0.0	0.0	0.0	0.0	0.0	0.3
	Clay minerals	Replacement of grains	0.0	4.8	0.3	0.0	1.8	2.7	0.3	2.5	3.3
		Illite coatings	0.0	0.0	0.0	0.0	0.0	0.0	0.0	0.0	0.0
		Illite meshwork	0.0	0.0	0.0	0.0	0.0	0.0	0.0	0.0	0.0
		Chlorite coatings and shreds	0.0	13.7	0.0	0.0	4.7	6.2	2.7	5.7	1.3
		Chlorite s. plates (5-10μm)	0.0	1.5	0.2	0.0	1.7	0.2	0.3	2.5	11.8
		Chlorite c. plates (>10μm)	0.0	0.0	0.0	0.0	0.0	0.0	0.0	0.0	0.0
		Clorite intraclast	10.7	0.2	0.0	12.8	0.0	1.3	0.0	0.0	1.2
		Kaolinite	0.0	0.0	0.0	0.0	0.0	0.0	0.0	0.0	0.0
	Bitumen	Massive in cracks or pores	0.0	0.2	0.7	0.0	0.0	0.0	0.0	0.0	0.0
Porosity [%]	Intergranular without secondary pores		0.0	2.5	0.2	0.0	6.8	17.7	1.7	10.8	5.2
	Secondary	Feldspar-leaching	0.0	0.5	0.0	0.0	0.5	2.2	0.0	0.7	1.0
		Lithics-leaching	0.0	0.2	0.0	0.0	0.2	1.3	0.0	0.0	0.0
		Heavy-min.-leaching	0.0	0.2	0.0	0.0	0.0	0.0	0.0	0.2	0.2
		Oversized pores	0.0	0.0	0.0	0.0	0.2	0.5	0.0	0.0	0.0
		Cement diss. voids	0.0	0.0	0.0	0.0	0.0	0.7	0.7	0.0	0.7
Granulometry		grainsize [mm]	<0.02	0.12	0.11	<0.02	0.21	0.19	0.17	0.11	0.14
		sorting	-	1.2	1.3	-	1.3	1.2	1.4	1.3	1.5
		rounding	-	0.3	0.4	-	0.4	0.4	0.4	0.4	0.4
		sphericity	-	0.6	0.7	-	0.6	0.6	0.6	0.6	0.7
Number of counts			600	600	600	600	600	600	300	600	600

Appendix 2.2: Table petrographic data Triassic and overlying strata (UK sector)

Well			30/2c4	30/2c4	30/2c4	30/2c4	30/2c4	30/2c4	30/2c4	30/2c4	30/2c4
Thin section no.			**15655.3**	**15655.3 B**	**15660**	**15665**	**15671.5**	**15676**	**15680**	**15680 B**	**15685**
Depth TVDSS [m]			4652.50	4652.50	4653.75	4655.41	4657.26	4658.68	4659.78	4659.78	4661.24
Stratigraphy			Skag. F.	Skag. F.	Skag. F.	Skag. F.	Skag. F.	Skag. F.	Skag. F.	Skag. F.	Skag. F.
			Joanne	Joanne	Joanne	Joanne	Joanne	Joanne	Joanne	Joanne	Joanne
Facies			FC/SF	FC/SF	FC/SF	AS	FC/SF	FC	FC	FC	FC
Detrital grains [%]	Quartz	Monocrystalline quartz	23.2	24.3	22.5	21.7	28.7	28.0	30.0	24.3	20.7
		Polycr. quartz and quartzite	12.7	12.2	9.8	1.0	3.0	7.3	6.2	8.7	5.2
	Lithics	Metamorphics	1.7	1.7	0.3	0.0	2.0	1.5	1.0	0.7	0.8
		Quartz feldspar aggregates	1.3	1.3	2.0	0.0	0.0	1.0	0.8	0.2	1.7
		Sedimentary extraclasts	0.0	0.0	0.0	0.0	0.0	0.0	0.0	0.0	0.0
		Volcanic	0.0	0.0	0.0	0.0	0.0	0.0	0.0	0.0	tr.
		Indeterminate	0.7	1.2	0.8	0.7	2.7	0.5	0.5	1.5	1.5
	Feldspar	Plagioclase	2.7	2.2	2.7	0.0	1.7	3.2	1.5	0.8	2.2
		K-feldspar (uncorroded)	13.8	14.7	15.0	11.0	23.3	12.3	13.7	13.8	17.3
		K-feldpar (partly dissolved)	4.8	2.3	7.2	0.0	4.3	7.2	3.2	2.8	8.7
	Sheet-silicates	Light mica	1.2	0.8	0.8	7.3	3.0	0.3	0.3	0.5	2.0
		Biotite	0.0	0.0	0.0	0.0	0.0	0.0	0.0	0.0	0.0
		Chlorite	0.0	0.0	0.5	1.0	1.0	0.3	0.7	0.2	0.5
	Intraclasts	Shale/Siltstone	0.2	0.2	0.5	0.0	0.0	0.0	0.7	0.0	0.0
		Detr. dolomite nodules	0.5	0.0	0.0	0.0	0.0	0.0	7.3	0.7	0.0
		Glauconite	0.0	0.0	0.0	0.0	0.0	0.0	0.0	0.0	0.0
		Bioclasts	0.0	0.0	0.0	0.0	0.0	0.0	0.0	0.0	0.0
		Black shale clasts	0.0	0.0	0.0	0.0	0.0	0.0	0.0	0.0	0.0
		Chert	0.0	0.0	0.0	0.0	0.0	0.0	0.0	0.0	0.0
		Microspar/micrite with biocl.	0.0	0.0	0.0	0.0	0.0	0.0	0.0	0.0	0.0
	Heavy minerals		0.2	0.2	0.2	1.0	0.3	0.0	0.2	0.8	0.3
Mud [%]		Clay matrix	0.0	0.2	0.0	23.3	4.7	0.0	0.0	0.0	0.7
		Black shale	0.0	0.0	0.0	0.0	0.0	0.0	0.0	0.0	0.0
		Micrite/microspar	0.0	0.0	0.0	0.0	0.0	0.0	0.0	0.0	0.0
Authigenic minerals [%]	Carbonate	Dolomite nodules	0.2	0.2	0.0	18.0	0.0	0.0	1.5	0.5	0.0
		Dolomite pore filling+rhombi	0.3	0.2	0.7	0.0	4.0	0.2	1.0	0.8	0.5
		Clast replacing	0.0	0.2	0.0	0.3	1.0	0.0	0.0	0.7	0.2
		Calcite	0.0	0.0	0.0	0.0	0.0	0.0	0.0	0.0	0.0
		Ferrous calcite	0.0	0.0	0.0	0.0	0.0	0.0	0.0	0.0	0.0
		Ankerite	1.0	1.7	1.5	0.0	1.3	0.0	0.0	0.5	0.3
	Quartz overgrowths		3.7	3.2	6.3	0.0	1.3	4.3	0.8	0.8	0.7
	Feldspar	K-feldspar overgrowths	6.2	6.2	8.2	0.7	8.0	6.8	8.3	11.3	7.5
		Albite in K-feldspar grains	0.0	0.5	0.0	0.0	0.7	0.0	0.2	0.5	1.2
	Hematite coatings		0.0	0.0	0.0	0.3	0.0	0.0	0.0	0.0	0.0
	Leucoxene/Anatase		0.8	0.5	0.0	1.0	0.7	0.8	2.5	3.8	0.3
	Anhydrite		0.0	0.0	0.0	0.0	0.0	0.0	0.0	0.0	0.0
	Barite		0.0	0.0	0.0	0.0	0.0	0.0	0.0	0.0	0.0
	Sulphides		0.0	0.0	0.0	0.0	0.0	0.0	0.0	0.0	0.0
	Clay minerals	Replacement of grains	2.3	1.8	3.0	1.3	2.3	2.0	1.5	2.2	5.5
		Illite coatings	0.0	0.0	0.0	0.0	0.0	0.0	0.0	0.0	0.0
		Illite meshwork	0.0	0.0	0.0	0.0	0.0	0.0	0.0	0.0	0.0
		Chlorite coatings and shreds	4.5	1.5	1.3	5.3	3.7	1.5	3.2	0.8	6.3
		Chlorite s. plates (5-10μm)	1.2	0.7	0.0	0.0	0.3	0.2	9.3	11.8	8.5
		Chlorite c. plates (>10μm)	0.0	0.0	0.0	0.0	0.0	0.0	0.0	0.0	0.0
		Clorite intraclast	0.2	0.3	0.5	5.7	0.0	0.5	1.0	1.3	0.5
		Kaolinite	0.0	0.0	0.0	0.0	0.0	0.0	0.0	0.0	0.0
	Bitumen	Massive in cracks or pores	0.0	0.2	0.0	0.3	0.0	0.0	0.2	0.0	0.2
Porosity [%]	Intergranular without secondary pores		6.0	12.0	10.3	0.0	1.7	12.3	1.8	5.3	4.8
	Secondary	Feldspar-leaching	2.7	2.0	3.3	0.0	0.3	2.8	0.2	0.8	0.8
		Lithics-leaching	2.5	1.2	1.2	0.0	0.0	1.5	0.8	0.8	0.2
		Heavy-min.-leaching	0.0	0.0	0.0	0.0	0.0	0.0	0.0	1.2	0.0
		Oversized pores	0.0	0.0	0.0	0.0	0.0	0.7	0.0	0.0	0.0
		Cement diss. voids	5.7	6.7	1.3	0.0	0.0	4.7	1.7	1.7	1.0
Granulometry		grainsize [mm]	0.28	0.30	0.24	<0.02	0.11	0.24	0.23	0.23	0.18
		sorting	1.2	1.3	1.3	-	1.8	1.3	1.3	1.3	1.4
		rounding	0.4	0.4	0.4	-	0.4	0.4	0.4	0.4	0.4
		sphericity	0.6	0.6	0.6	-	0.6	0.6	0.7	0.7	0.6
Number of counts			600	600	600	300	300	600	600	600	600

Well			30/2c4	30/2c4	30/2c4	30/2c4	30/2c4	30/2c4	30/2c4	30/2c4	30/2c4
Thin section no.			**15688**	**15691 B**	**15691.5**	**15704**	**15715**	**15715 B**	**15716**	**15716 B**	**15718.5**
Depth TVDSS [m]			4662.25	4662.75	4662.93	4666.91	4670.15	4670.15	4670.48	4670.48	4671.19
Stratigraphy			Skag. F. Joanne	Skag. F. Joanne	Skag. F. Joanne	Skag. F. Joanne	Skag. F. Joanne	Skag. F. Joanne	Skag. F. Joanne	Skag. F. Joanne	Skag. F. Joanne
Facies			FC	FC	FC	AS	FC	FC	FC	FC	FC
Detrital grains [%]	Quartz	Monocrystalline quartz	23.8	27.2	26.5	35.5	20.2	18.7	20.3	24.2	15.8
		Polycr. quartz and quartzite	5.2	5.0	9.7	4.0	4.7	4.7	7.2	5.5	6.7
	Lithics	Metamorphics	1.3	2.0	3.3	0.3	0.2	0.7	1.7	0.5	1.5
		Quartz feldspar aggregates	1.2	1.0	1.2	0.0	0.3	0.0	1.2	0.3	1.3
		Sedimentary extraclasts	0.0	0.0	0.0	0.0	0.0	0.0	0.0	0.0	0.0
		Volcanic	0.0	0.0	0.0	0.0	0.0	0.0	0.0	0.0	0.0
		Indeterminate	1.0	1.7	3.3	1.5	0.2	0.3	0.7	1.2	0.5
	Feldspar	Plagioclase	2.0	3.8	2.8	0.5	2.0	1.0	1.2	2.8	2.5
		K-feldspar (uncorroded)	16.5	16.0	17.7	12.3	12.5	8.7	14.8	7.7	12.3
		K-feldpar (partly dissolved)	9.0	9.0	6.3	0.8	0.7	2.7	5.7	13.8	10.0
	Sheet-silicates	Light mica	2.7	0.8	2.3	4.3	1.7	0.7	0.3	1.2	1.7
		Biotite	0.0	0.0	0.0	0.0	0.0	0.0	0.0	0.0	0.0
		Chlorite	0.5	0.7	0.8	0.8	0.0	0.3	0.2	0.2	0.2
	Intraclasts	Shale/Siltstone	0.3	0.0	0.0	0.0	1.0	2.3	0.2	0.0	0.2
		Detr. dolomite nodules	0.0	0.0	0.0	0.0	0.0	0.0	0.2	0.0	0.0
		Glauconite	0.0	0.0	0.0	0.0	0.0	0.0	0.0	0.0	0.0
		Bioclasts	0.0	0.0	0.0	0.0	0.0	0.0	0.0	0.0	0.0
		Black shale clasts	0.0	0.0	0.0	0.0	0.0	0.0	0.0	0.0	0.0
		Chert	0.0	0.0	0.0	0.0	0.0	0.0	0.0	0.0	0.0
		Microspar/micrite with biocl.	0.0	0.0	0.0	0.0	0.0	0.0	0.0	0.0	0.0
	Heavy minerals		0.2	0.0	0.0	0.2	0.0	0.0	0.2	0.2	0.0
Mud [%]		Clay matrix	0.0	2.2	0.0	30.5	2.2	1.0	1.2	0.0	0.0
		Black shale	0.0	0.0	0.0	0.0	0.0	0.0	0.0	0.0	0.0
		Micrite/microspar	0.0	0.0	0.0	0.0	0.0	0.0	0.0	0.0	0.0
Authigenic minerals [%]	Carbonate	Dolomite nodules	0.7	0.0	0.0	1.0	0.3	2.0	0.3	0.2	0.0
		Dolomite pore filling+rhombi	2.0	0.5	0.2	0.2	30.3	34.3	4.8	3.7	0.0
		Clast replacing	0.0	0.2	0.2	0.0	9.0	15.0	0.2	0.8	0.0
		Calcite	0.0	0.0	0.0	0.0	0.0	0.0	0.0	0.0	0.0
		Ferrous calcite	0.0	0.0	0.0	0.0	0.0	0.0	0.0	0.0	0.0
		Ankerite	1.5	0.3	tr.	0.0	7.5	2.0	5.3	3.2	0.0
	Quartz overgrowths		1.8	0.2	0.2	0.2	0.3	0.0	3.3	4.5	7.8
	Feldspar	K-feldspar overgrowths	8.7	2.8	3.2	1.2	1.0	1.3	10.2	7.7	13.5
		Albite in K-feldspar grains	0.0	1.2	1.2	0.0	1.5	0.7	1.2	0.3	1.2
	Hematite coatings		0.0	0.0	0.0	0.2	0.0	0.0	0.0	0.0	0.0
	Leucoxene/Anatase		0.5	1.2	0.2	1.0	0.7	0.0	1.7	1.2	0.0
	Anhydrite		0.0	0.0	0.0	0.0	0.0	0.0	0.0	0.0	0.0
	Barite		0.2	0.0	0.0	0.0	0.0	0.0	0.0	0.0	0.0
	Sulphides		0.0	0.0	0.0	0.0	0.0	0.0	0.0	0.0	0.0
	Clay minerals	Replacement of grains	2.8	1.8	0.8	0.2	0.7	1.3	1.5	2.8	2.0
		Illite coatings	0.0	0.0	0.0	4.3	0.0	0.0	0.0	0.0	0.0
		Illite meshwork	0.0	0.0	0.0	0.0	0.0	0.0	0.0	0.0	0.0
		Chlorite coatings and shreds	4.7	2.3	3.8	0.0	1.8	1.0	3.3	1.2	2.7
		Chlorite s. plates (5-10μm)	1.3	11.7	7.5	0.0	0.0	0.0	0.2	0.2	0.2
		Chlorite c. plates (>10μm)	0.0	0.0	0.0	0.0	0.0	0.0	0.0	0.0	0.0
		Clorite intraclast	0.0	1.0	0.8	1.0	0.7	0.0	0.8	0.2	1.3
		Kaolinite	0.0	0.0	0.0	0.0	0.0	0.0	0.0	0.0	0.0
	Bitumen	Massive in cracks or pores	3.0	0.2	0.2	0.0	0.0	0.0	0.0	0.2	0.0
Porosity [%]	Intergranular without secondary pores		5.0	4.0	7.7	0.0	0.2	1.3	7.2	9.7	12.3
	Secondary	Feldspar-leaching	1.8	1.3	0.2	0.0	0.0	0.0	1.3	2.5	2.8
		Lithics-leaching	1.0	0.7	0.0	0.0	0.2	0.0	1.2	0.7	0.7
		Heavy-min.-leaching	0.0	0.0	0.0	0.0	0.0	0.0	0.0	0.3	0.2
		Oversized pores	0.0	0.3	0.0	0.0	0.0	0.0	0.0	0.0	0.0
		Cement diss. voids	1.3	1.0	0.0	0.0	0.3	0.0	2.7	3.3	2.7
Granulometry		grainsize [mm]	0.20	0.16	0.18	0.13	0.19	0.20	0.16	0.17	0.19
		sorting	1.6	1.6	1.4	1.4	1.3	1.3	1.3	1.3	1.4
		rounding	0.4	0.4	0.4	0.3	0.3	0.4	0.4	0.4	0.4
		sphericity	0.6	0.7	0.6	0.6	0.6	0.7	0.7	0.7	0.6
Number of counts			600	600	600	600	300	600	600	600	600

Well			30/2c4	30/2c4	30/2c4	30/2c4	30/2c4	30/2c4	30/2c4	30/2c4	30/2c4
Thin section no.			**15722.2**	**15739**	**15741**	**15743**	**15745**	**15747B** sandst.	**15747B** Q zone	**15747B** D zone	**15747B** mudst.
Depth TVDSS [m]			4672.38	4677.32	4677.97	4678.50	4679.16	4680.56	4680.56	4680.56	4680.56
Stratigraphy			Skag. F. Joanne	Skag. F. Joanne	Skag. F. Joanne	Skag. F. Joanne	Skag. F. Joanne	Skag. F. Joanne	Skag. F. Joanne	Skag. F. Joanne	Skag. F. Joanne
Facies			AS	FC?	FC?	FC?	FC?	FC	FC	FC	AS
Detrital grains [%]	Quartz	Monocrystalline quartz	16.7	24.7	26.7	24.7	28.7	19.5	19.0	19.0	9.0
		Polycr. quartz and quartzite	0.8	6.0	7.3	8.5	11.2	9.8	4.0	7.0	1.0
	Lithics	Metamorphics	0.2	1.3	2.0	1.5	1.3	1.0	1.0	1.0	0.0
		Quartz feldspar aggregates	0.0	1.2	2.2	1.7	0.5	0.5	1.0	2.0	0.0
		Sedimentary extraclasts	0.0	0.0	0.0	0.0	0.0	0.0	0.0	0.0	0.0
		Volcanic	0.0	0.0	0.0	0.0	0.0	0.0	0.0	0.0	0.0
		Indeterminate	0.7	1.7	0.7	0.7	1.0	0.3	0.0	1.0	0.0
	Feldspar	Plagioclase	0.5	1.5	1.8	1.5	1.8	0.5	2.0	0.0	0.0
		K-feldspar (uncorroded)	5.5	10.0	21.0	13.7	11.7	15.0	11.0	15.0	5.0
		K-feldpar (partly dissolved)	0.0	0.7	4.7	9.0	3.8	5.8	5.0	2.0	0.0
	Sheet-silicates	Light mica	1.2	5.3	4.5	2.2	1.5	0.3	0.0	2.0	4.0
		Biotite	0.0	0.0	0.0	0.0	0.0	0.0	0.0	0.0	0.0
		Chlorite	0.5	0.5	0.5	0.3	0.0	0.0	0.0	1.0	1.0
	Intraclasts	Shale/Siltstone	0.0	0.0	0.3	0.0	0.0	1.0	4.0	0.0	0.0
		Detr. dolomite nodules	0.0	0.0	0.0	0.0	0.0	1.3	0.0	0.0	0.0
		Glauconite	0.0	0.0	0.0	0.0	0.0	0.0	0.0	0.0	0.0
		Bioclasts	0.0	0.0	0.0	0.0	0.0	0.0	0.0	0.0	0.0
		Black shale clasts	0.0	0.0	0.0	0.0	0.0	0.0	0.0	0.0	0.0
		Chert	0.0	0.0	0.0	0.0	0.0	0.0	0.0	0.0	0.0
		Microspar/micrite with biocl.	0.0	0.0	0.0	0.0	0.0	0.0	0.0	0.0	0.0
	Heavy minerals		0.5	0.5	0.5	0.3	0.2	0.0	0.0	0.0	2.0
Mud [%]		Clay matrix	64.0	7.3	0.7	0.0	0.0	0.0	0.0	0.0	68.0
		Black shale	0.0	0.0	0.0	0.0	0.0	0.0	0.0	0.0	0.0
		Micrite/microspar	0.0	0.0	0.0	0.0	0.0	0.0	0.0	0.0	0.0
Authigenic minerals [%]	Carbonate	Dolomite nodules	7.3	25.0	3.5	0.5	8.3	4.5	5.0	21.0	5.0
		Dolomite pore filling+rhombi	0.0	0.0	1.0	0.8	3.7	13.3	14.0	21.0	0.0
		Clast replacing	0.0	6.5	0.0	0.0	1.5	0.3	0.0	6.0	0.0
		Calcite	0.0	0.0	0.0	0.0	0.0	0.0	0.0	0.0	0.0
		Ferrous calcite	0.0	0.0	0.0	0.0	0.0	0.0	0.0	0.0	0.0
		Ankerite	0.0	0.0	0.8	0.8	2.5	0.0	0.0	0.0	0.0
	Quartz overgrowths		0.0	0.0	1.2	1.0	2.2	16.0	25.0	1.0	0.0
	Feldspar	K-feldspar overgrowths	0.0	0.5	4.8	5.3	3.5	4.0	4.0	0.0	0.0
		Albite in K-feldspar grains	0.0	0.5	1.8	0.5	0.8	0.0	0.0	1.0	0.0
	Hematite coatings		0.2	0.0	0.0	0.0	0.0	0.3	0.0	0.0	0.0
	Leucoxene/Anatase		0.2	1.5	0.5	0.7	0.3	0.0	1.0	0.0	0.0
	Anhydrite		0.0	0.0	0.0	0.0	0.0	0.0	0.0	0.0	0.0
	Barite		0.0	0.2	0.0	0.0	0.0	0.0	0.0	0.0	0.0
	Sulphides		0.3	0.0	0.0	0.0	0.0	0.0	0.0	0.0	0.0
	Clay minerals	Replacement of grains	0.0	0.8	3.8	4.3	1.3	1.0	0.0	0.0	0.0
		Illite coatings	0.0	0.0	0.0	0.0	0.0	0.0	0.0	0.0	0.0
		Illite meshwork	0.0	0.0	0.0	0.0	0.0	0.0	0.0	0.0	0.0
		Chlorite coatings and shreds	0.0	0.3	3.7	5.5	1.0	0.0	0.0	0.0	0.0
		Chlorite s. plates (5-10μm)	0.0	0.0	0.2	1.3	0.0	0.0	0.0	0.0	0.0
		Chlorite c. plates (>10μm)	0.0	0.0	0.0	0.0	0.0	0.0	0.0	0.0	0.0
		Clorite intraclast	1.5	3.8	0.2	0.2	0.0	0.0	1.0	0.0	5.0
		Kaolinite	0.0	0.0	0.0	0.0	0.0	0.0	0.0	0.0	0.0
	Bitumen	Massive in cracks or pores	0.0	0.2	0.2	0.2	0.8	0.3	0.0	0.0	0.0
Porosity [%]	Intergranular without secondary pores		0.0	0.0	4.7	11.7	8.5	4.5	2.0	0.0	0.0
	Secondary	Feldspar-leaching	0.0	0.0	0.8	1.2	1.0	1.3	0.0	0.0	0.0
		Lithics-leaching	0.0	0.0	0.0	1.5	0.8	0.0	1.0	0.0	0.0
		Heavy-min.-leaching	0.0	0.0	0.0	0.0	0.0	0.0	0.0	0.0	0.0
		Oversized pores	0.0	0.0	0.0	0.2	0.0	0.0	0.0	0.0	0.0
		Cement diss. voids	0.0	0.0	0.0	0.3	2.0	0.0	0.0	0.0	0.0
Granulometry		grainsize [mm]	<0.02	0.11	0.16	0.18	0.27	-	-	-	-
		sorting	-	1.8	1.6	1.6	1.3	-	-	-	-
		rounding	-	0.7	0.4	0.4	0.4	-	-	-	-
		sphericity	-	0.6	0.6	0.6	0.6	-	-	-	-
Number of counts			600	600	600	600	600	400	100	100	100

Appendix 2.2: Table petrographic data Triassic and overlying strata (UK sector)

Well			30/2c4	30/2c4	30/2c4	30/2c4	30/2c4	30/7a-6	30/7a-6	30/7a-7
Thin section no.			**15747.5 B**	**15752**	**15757**	**15768.5**	**15792.5 B**	**12209.5**	**12217**	**9480.1**
Depth TVDSS [m]			4680.88	4680.29	4682.64	4686.11	4693.22	3721.46	3723.74	2889.53
Stratigraphy			Skag. F.	Skag. F.	Skag. F.	Skag. F.	Skag. F.	Jura?	?	Palaeoc.
			Joanne	Joanne	Joanne	Joanne	Joanne			
Facies			AS	FC?	AS	AS	SF		Dolcret?	
Detrital grains [%]	Quartz	Monocrystalline quartz	7.5	23.7	11.7	4.5	24.2	25.3	16.0	48.7
		Polycr. quartz and quartzite	0.3	8.8	2.2	0.2	6.8	2.0	0.7	6.3
	Lithics	Metamorphics	0.0	2.2	0.3	0.0	0.8	0.0	0.0	0.3
		Quartz feldspar aggregates	0.0	1.2	0.2	0.0	0.2	0.0	0.3	0.3
		Sedimentary extraclasts	0.0	0.0	0.0	0.0	0.0	0.0	0.0	0.0
		Volcanic	0.0	0.0	0.0	0.0	0.0	0.0	0.0	0.0
		Indeterminate	0.0	0.3	0.0	0.0	0.5	0.0	0.0	0.3
	Feldspar	Plagioclase	0.0	1.8	0.5	0.0	0.8	2.0	1.7	1.3
		K-feldspar (uncorroded)	3.0	10.5	10.2	0.5	12.5	5.3	1.7	1.7
		K-feldpar (partly dissolved)	0.0	3.0	0.0	0.0	13.2	0.3	0.0	3.3
	Sheet-silicates	Light mica	1.5	0.8	5.0	4.2	1.3	5.0	1.0	0.3
		Biotite	0.0	0.0	1.0	0.0	0.0	2.0	0.0	0.0
		Chlorite	0.2	0.0	0.5	0.3	0.7	4.0	0.0	0.3
	Intraclasts	Shale/Siltstone	0.0	0.5	0.2	0.2	0.2	0.0	0.0	0.7
		Detr. dolomite nodules	0.0	5.3	0.0	0.0	0.0	0.0	0.0	0.0
		Glauconite	0.0	0.0	0.0	0.0	0.0	0.0	0.0	0.0
		Bioclasts	0.0	0.0	0.0	0.0	0.0	0.0	0.0	0.0
		Black shale clasts	0.0	0.0	0.0	0.0	0.0	0.0	0.0	0.3
		Chert	0.0	0.0	0.0	0.0	0.0	0.0	0.0	0.0
		Microspar/micrite with biocl.	0.0	0.0	0.0	0.0	0.0	0.0	0.0	0.0
	Heavy minerals		0.2	0.3	0.3	0.2	0.3	0.0	0.0	0.0
Mud [%]		Clay matrix	58.0	0.0	61.2	81.5	0.2	44.3	10.7	25.7
		Black shale	0.0	0.0	0.0	0.0	0.0	0.0	0.0	0.0
		Micrite/microspar	0.0	0.0	0.0	0.0	0.0	0.0	0.0	0.0
Authigenic minerals [%]	Carbonate	Dolomite nodules	23.5	3.3	0.0	2.2% Mg-siderite	0.0	1.0	27.7	0.0
		Dolomite pore filling+rhombi	0.0	6.2	0.0		0.0	1.7	26.7	0.0
		Clast replacing	0.0	1.3	0.0		0.0	0.0	0.3	0.0
		Calcite	0.0	0.0	0.0		0.0	0.0	0.0	0.0
		Ferrous calcite	0.0	0.0	0.0		0.0	0.0	0.0	0.0
		Ankerite	0.0	7.7	0.0		0.0	0.3	7.7	0.0
	Quartz overgrowths		0.0	6.2	0.0	0.0	8.0	0.0	0.0	0.0
	Feldspar	K-feldspar overgrowths	0.0	3.2	0.0	0.0	10.7	0.3	0.0	0.0
		Albite in K-feldspar grains	0.0	1.7	0.0	0.0	1.5	0.0	0.0	0.0
	Hematite coatings		0.0	0.0	0.2	0.8	0.0	tr.	tr.	0.0
	Leucoxene/Anatase		0.0	0.2	0.3	0.0	0.5	0.3	0.0	0.0
	Anhydrite		0.0	0.0	0.0	0.0	0.0	0.0	0.0	0.0
	Barite		0.0	0.0	0.0	0.0	0.0	0.0	0.0	0.0
	Sulphides		0.0	0.2	0.0	0.2	0.0	1.3	4.3	2.0
	Clay minerals	Replacement of grains	0.0	0.7	0.0	0.0	4.7	0.0	0.0	3.3
		Illite coatings	0.0	0.0	0.0	0.0	0.0	0.0	0.0	0.0
		Illite meshwork	0.0	0.0	0.0	0.0	0.0	0.0	0.0	0.0
		Chlorite coatings and shreds	0.0	0.7	0.0	0.0	1.8	2.0	0.0	0.0
		Chlorite s. plates (5-10μm)	0.0	0.0	0.0	0.0	0.8	0.0	0.0	0.0
		Chlorite c. plates (>10μm)	0.0	0.0	0.0	0.0	0.0	0.0	0.0	0.0
		Clorite intraclast	5.8	0.0	6.3	5.2	0.0	0.3	0.3	0.0
		Kaolinite	0.0	0.0	0.0	0.0	0.0	0.0	0.0	1.0
	Bitumen	Massive in cracks or pores	0.0	0.7	0.0	0.0	0.0	0.0	0.0	0.0
Porosity [%]	Intergranular without secondary pores		0.0	7.7	0.0	0.0	6.8	1.7	1.0	2.3
	Secondary	Feldspar-leaching	0.0	0.8	0.0	0.0	2.7	0.7	0.0	1.7
		Lithics-leaching	0.0	0.2	0.0	0.0	0.5	0.0	0.0	0.0
		Heavy-min.-leaching	0.0	0.0	0.0	0.0	0.0	0.0	0.0	0.0
		Oversized pores	0.0	0.0	0.0	0.0	0.0	0.0	0.0	0.0
		Cement diss. voids	0.0	1.0	0.0	0.0	0.3	0.0	0.0	0.0
Granulometry		grainsize [mm]	<0.02	0.32	<0.02	<0.02	0.19	<0.06	0.09	0.12
		sorting	-	1.3	-	-	1.4	-	1.3	1.6
		rounding	-	0.5	-	-	0.4	-	0.4	0.4
		sphericity	-	0.6	-	-	0.6	-	0.6	0.6
Number of counts			600	600	600	600	600	300	300	300

Appendix 2.2: Table petrographic data Triassic and overlying strata (UK sector)

Well			30/7a-7	30/7a-7	30/7a-7	30/7a-7	30/7a-7	30/7a-7	30/7a-7	30/7a-7	30/7a-7
Thin section no.			**9490.1 B-2**	**9506.1 C-3**	**9513.1 O-4**	**9513.1 O-4(2)**	**11291 R- 5**	**11308**	**11316**	**11333 6-1**	**11344**
Depth TVDSS [m]			2892.58	2897.46	2899.59	2899.59	3441.50	3446.68	3449.12	3454.30	3457.65
Stratigraphy			Palaeoc.	Palaeoc.	Palaeoc.	Palaeoc.	Skag. F.	Skag. F.	Skag. F.	Skag. F.	Skag. F.
							Judy	Judy	Judy	Judy	Judy
Facies							AS?	AS/SF?	AS/SF?	AS/SF?	AS/SF?
Detrital grains [%]	Quartz	Monocrystalline quartz	52.7	43.0	54.0	55.0	36.0	30.0	31.0	35.3	29.0
		Polycr. quartz and quartzite	3.3	0.7	4.7	4.7	1.7	4.0	2.3	2.3	1.3
	Lithics	Metamorphics	0.3	0.0	0.0	0.0	0.3	1.3	1.0	0.3	1.0
		Quartz feldspar aggregates	0.7	0.0	0.0	0.0	0.7	1.3	0.3	0.0	1.7
		Sedimentary extraclasts	0.0	0.0	0.0	0.0	0.0	0.0	0.0	0.0	0.0
		Volcanic	0.0	0.0	0.0	0.0	0.0	0.0	0.0	0.0	0.0
		Indeterminate	1.0	0.0	0.0	0.0	0.0	0.3	0.0	0.0	1.0
	Feldspar	Plagioclase	1.7	2.3	1.0	1.0	4.7	5.3	9.7	3.7	2.7
		K-feldspar (uncorroded)	5.7	1.3	1.7	0.7	3.3	9.7	9.0	7.3	15.7
		K-feldpar (partly dissolved)	2.7	0.3	0.0	0.0	10.0	8.3	4.0	11.7	10.0
	Sheet-silicates	Light mica	0.7	1.3	0.0	tr.	7.3	2.3	1.3	2.0	1.7
		Biotite	0.7	0.0	0.0	0.0	0.7	1.0	0.0	0.0	0.3
		Chlorite	0.0	0.0	0.0	0.0	2.7	2.0	1.7	3.0	4.0
	Intraclasts	Shale/Siltstone	2.0	3.7	2.0	0.0	0.0	1.0	2.3	0.0	1.0
		Detr. dolomite nodules	0.0	0.0	0.0	0.0	0.0	0.0	0.0	0.0	0.0
		Glauconite	0.0	1.0	0.0	tr.	0.0	0.0	0.0	0.0	0.0
		Bioclasts	0.0	3.7	0.3	1.3	0.0	0.0	0.0	0.0	0.0
		Black shale clasts	0.7	0.0	0.0	0.0	0.0	0.0	0.0	0.0	0.0
		Chert	1.3	0.0	0.0	0.3	0.0	0.0	0.0	0.0	0.0
		Microspar/micrite with biocl.	0.0	4.3	2.3	1.3	0.0	0.0	0.0	0.0	0.0
	Heavy minerals		0.0	0.3	0.0	0.3	0.0	0.3	0.3	0.0	0.0
Mud [%]		Clay matrix	16.7	0.7	0.0	0.0	1.3	1.0	1.0	0.0	1.7
		Black shale	0.0	0.0	0.0	0.0	0.0	0.0	0.0	0.0	0.0
		Micrite/microspar	0.0	0.7	0.7	2.0	0.0	0.0	0.0	0.0	0.0
Authigenic minerals [%]	Carbonate	Dolomite nodules	0.0	0.0	0.0	0.0	0.0	0.0	0.0	1.3	0.0
		Dolomite pore filling+rhombi	0.0	1.0	1.7	2.0	0.0	0.0	0.0	0.0	0.0
		Clast replacing	0.7	0.0	0.7	0.3	0.0	0.0	0.0	0.0	0.0
		Calcite	0.0	0.0	0.0	0.0	0.0	0.0	0.0	0.0	0.0
		Ferrous calcite	0.0	0.0	0.0	0.0	0.0	0.0	0.0	0.0	0.0
		Ankerite	0.0	0.0	0.0	0.0	0.0	0.0	0.0	0.0	0.0
	Quartz overgrowths		0.3	6.3	14.7	11.3	2.3	1.3	4.0	1.7	1.7
	Feldspar	K-feldspar overgrowths	0.0	0.0	0.0	0.0	4.0	1.7	4.7	2.7	4.3
		Albite in K-feldspar grains	0.7	1.0	0.3	0.0	1.3	tr.	1.7	1.0	0.0
	Hematite coatings		0.0	0.0	0.0	0.0	0.0	tr.	0.0	0.0	tr.
	Leucoxene/Anatase		0.0	0.0	0.0	0.0	tr.	1.3	2.3	1.0	0.7
	Anhydrite		0.0	0.0	0.0	0.0	0.0	0.0	0.0	0.0	0.0
	Barite		0.0	0.3	0.3	0.0	0.0	0.0	0.0	0.0	0.0
	Sulphides		0.0	0.0	0.7	0.3	0.0	0.0	0.0	0.0	0.0
	Clay minerals	Replacement of grains	2.7	4.3	0.0	0.0	2.3	3.0	1.7	2.3	2.3
		Illite coatings	0.0	0.0	0.0	0.0	0.0	0.0	0.0	0.0	0.0
		Illite meshwork	0.0	0.0	0.0	0.0	0.0	0.0	0.0	0.0	0.0
		Chlorite coatings and shreds	0.0	0.0	0.0	0.0	2.0	2.3	5.0	1.7	4.0
		Chlorite s. plates (5-10μm)	0.0	0.0	0.0	0.0	0.0	5.3	0.0	0.0	1.3
		Chlorite c. plates (>10μm)	0.0	0.0	0.0	0.0	0.0	0.0	0.0	0.0	0.0
		Clorite intraclast	0.0	0.0	0.0	0.0	0.3	2.0	1.3	0.3	0.3
		Kaolinite	1.3	6.0	4.3	1.0	0.0	0.0	0.0	0.0	0.0
	Bitumen	Massive in cracks or pores	0.0	tr.	0.0	0.0	2.3	0.0	1.3	2.7	0.0
Porosity [%]	Intergranular without secondary pores		3.3	14.7	7.3	15.0	12.0	11.3	10.0	15.0	10.3
	Secondary	Feldspar-leaching	1.0	0.7	1.0	0.0	2.7	3.7	0.7	1.3	3.0
		Lithics-leaching	0.0	0.3	0.0	0.0	0.3	0.0	0.0	0.0	0.0
		Heavy-min.-leaching	0.0	0.0	0.0	0.0	0.0	0.0	0.0	0.0	0.0
		Oversized pores	0.0	1.3	1.3	2.0	0.7	0.0	1.7	1.7	0.7
		Cement diss. voids	0.0	0.7	1.0	1.3	1.0	0.0	1.7	1.7	0.3
Granulometry		grainsize [mm]	0.11	0.12	0.29	0.29	0.08	0.09	0.09	0.08	0.09
		sorting	2.0	1.4	1.2	1.2	1.2	1.3	1.6	1.2	1.4
		rounding	0.4	0.5	0.7	0.7	0.7	0.7	0.5	0.5	0.5
		sphericity	0.6	0.7	0.7	0.7	0.7	0.5	0.5	0.5	0.5
Number of counts			300	300	300	300	300	300	300	300	300

Well			30/7a-7	30/7a-7	30/7a-7	30/7a-7	30/7a-7	30/7a-7	30/7a-7	30/7a-7	30/7a-7
Thin section no.			**11363.4 H-8**	**11367.1 I-9**	**11433.2 J-10**	**11443.1 K-11**	**11468 - 12**	**11488 7-13**	**11512.1 N-14**	**11512.1 N-14(II)**	**11527.1 O-15**
Depth TVDSS [m]			3463.56	3464.69	3484.84	3487.86	3495.45	3501.54	3508.89	3508.89	3513.46
Stratigraphy			Skag. F.	Skag. F.	Skag. F.	Skag. F.	Skag. F.	Skag. F.	Skag. F.	Skag. F.	Skag. F.
			Judy	Judy	Judy	Judy	Judy	Judy	Judy	Judy	Judy
Facies			FC?	AS/SF?	AS/SF?	FC/SF?	FC/SF?	FC/SF?	FC/SF?	FC/SF?	AS?
Detrital grains [%]	Quartz	Monocrystalline quartz	8.7	31.0	33.7	37.0	29.3	35.3	22.7	26.7	33.7
		Polycr. quartz and quartzite	0.3	0.7	1.0	2.0	2.0	2.7	6.3	3.0	3.0
	Lithics	Metamorphics	0.3	0.3	0.0	0.3	0.7	1.3	1.3	1.3	1.7
		Quartz feldspar aggregates	0.0	0.0	0.3	0.7	1.0	1.7	1.3	1.3	0.0
		Sedimentary extraclasts	0.0	0.0	0.0	0.0	0.0	0.0	0.0	0.0	0.0
		Volcanic	0.0	0.0	0.0	0.0	0.0	0.0	0.0	0.0	0.0
		Indeterminate	0.0	0.0	0.0	0.0	0.0	0.0	0.3	0.3	1.3
	Feldspar	Plagioclase	0.0	5.3	3.0	4.0	2.0	5.0	6.7	5.3	3.7
		K-feldspar (uncorroded)	2.0	14.7	8.3	11.0	15.0	10.3	12.3	14.0	10.7
		K-feldpar (partly dissolved)	0.7	9.3	8.0	6.3	5.0	8.3	4.0	3.7	6.0
	Sheet-silicates	Light mica	tr.	1.3	2.3	0.7	1.0	1.7	2.0	3.0	8.0
		Biotite	0.0	0.0	0.0	0.0	0.0	0.3	1.0	0.3	4.3
		Chlorite	tr.	2.0	2.0	1.0	1.3	1.3	1.7	1.0	2.3
	Intraclasts	Shale/Siltstone	39.3	0.7	tr.	0.0	0.7	0.3	0.0	0.0	2.3
		Detr. dolomite nodules	23.7	0.0	0.0	0.0	0.0	0.3	0.0	0.0	0.0
		Glauconite	0.0	0.0	0.0	0.0	0.0	0.0	0.0	0.0	0.0
		Bioclasts	0.0	0.0	0.0	0.0	0.0	0.0	0.0	0.0	0.0
		Black shale clasts	0.0	0.0	0.0	0.0	0.0	0.0	0.0	0.0	0.0
		Chert	0.0	0.0	0.0	0.0	0.0	0.0	0.0	0.0	0.0
		Microspar/micrite with biocl.	0.0	0.0	0.0	0.0	0.0	0.0	0.0	0.0	0.0
	Heavy minerals		0.0	0.7	0.3	0.3	1.0	0.3	0.0	0.0	0.0
Mud [%]		Clay matrix	0.0	0.3	3.0	1.3	2.7	0.0	0.0	0.0	0.7
		Black shale	0.0	0.0	0.0	0.0	0.0	0.0	0.0	0.0	0.0
		Micrite/microspar	0.0	0.0	0.0	0.0	0.0	0.0	0.0	0.0	0.0
Authigenic minerals [%]	Carbonate	Dolomite nodules	7.7	0.0	0.0	0.0	0.0	0.3	0.0	0.0	0.0
		Dolomite pore filling+rhombi	14.7	0.0	0.0	0.0	0.0	0.3	0.0	0.0	0.0
		Clast replacing	0.7	0.0	0.0	0.0	0.0	0.7	0.0	0.0	0.3
		Calcite	0.0	0.0	0.0	0.0	0.0	0.0	0.0	0.0	0.0
		Ferrous calcite	0.0	0.0	0.0	0.0	0.0	0.0	0.0	0.0	0.0
		Ankerite	0.0	0.0	0.0	0.0	0.0	0.0	0.0	0.0	0.0
	Quartz overgrowths		0.0	4.0	3.3	5.7	9.0	4.3	6.3	7.3	3.7
	Feldspar	K-feldspar overgrowths	0.0	4.7	2.3	3.7	2.7	3.3	5.0	6.0	4.7
		Albite in K-feldspar grains	tr.	1.3	0.7	1.0	2.3	2.0	2.0	1.7	4.3
	Hematite coatings		0.0	0.0	0.0	0.0	0.0	0.0	0.0	0.0	0.0
	Leucoxene/Anatase		0.0	0.7	0.7	0.3	1.0	0.7	0.7	0.3	tr.
	Anhydrite		0.0	0.0	0.0	0.0	0.0	0.0	0.0	0.0	0.0
	Barite		0.0	0.0	0.0	0.0	0.0	0.0	0.0	0.0	0.0
	Sulphides		0.3	0.0	0.0	0.0	0.0	0.0	0.0	0.0	0.3
	Clay minerals	Replacement of grains	0.3	2.0	1.7	1.0	1.3	1.3	0.7	1.7	1.3
		Illite coatings	0.0	0.0	tr.	0.3	0.0	0.0	0.0	0.0	1.3
		Illite meshwork	0.0	0.0	0.0	0.0	0.0	0.0	0.0	0.0	0.0
		Chlorite coatings and shreds	0.0	0.7	6.3	3.3	0.3	0.0	0.3	0.0	0.3
		Chlorite s. plates (5-10μm)	0.0	0.0	0.0	0.0	0.0	0.0	0.0	0.0	0.0
		Chlorite c. plates (>10μm)	0.0	0.0	0.0	0.0	0.0	0.0	0.0	0.0	0.0
		Clorite intraclast	0.0	0.0	0.7	0.0	0.0	0.0	0.0	0.3	0.3
		Kaolinite	0.0	0.0	0.0	0.0	0.0	0.0	0.0	0.0	0.0
	Bitumen	Massive in cracks or pores	0.0	tr.	0.3	tr.	1.7	0.0	tr.	tr.	tr.
Porosity [%]	Intergranular without secondary pores		0.7	16.0	18.3	15.0	9.7	13.0	15.7	14.0	4.7
	Secondary	Feldspar-leaching	0.7	3.3	2.7	3.0	3.0	3.0	3.7	3.0	1.0
		Lithics-leaching	0.0	0.0	0.0	0.0	1.3	0.0	0.0	0.3	0.0
		Heavy-min.-leaching	0.0	0.0	0.0	0.0	0.0	0.0	0.0	0.0	0.0
		Oversized pores	0.0	0.3	0.7	0.3	1.3	0.0	1.3	0.7	0.0
		Cement diss. voids	0.0	0.7	0.3	1.7	4.7	2.0	4.7	4.7	0.0
Granulometry		grainsize [mm]	-	0.08	0.08	0.09	0.16	0.13	0.15	0.15	0.06
		sorting	-	1.4	1.4	1.4	1.3	1.6	1.4	1.4	1.8
		rounding	-	0.5	0.5	0.5	0.5	0.3	0.3	0.3	0.3
		sphericity	-	0.7	0.7	0.7	0.7	0.7	0.5	0.5	0.4
Number of counts			300	300	300	300	300	300	300	300	300

Appendix 2.2: Table petrographic data Triassic and overlying strata (UK sector)

Well			30/7a-7	30/7a-7	30/7a-7	30/7a-P7	30/7a-P7	30/7a-P7	30/7a-8	30/7a-8
Thin section no.			**11531 R-17**	**11531.3 R-18**	**11544.7 5-19**	**14331.5**	**(17) 14341**	**(24) 14348**	**9531-8**	**9573**
Depth TVDSS [m]			3514.65	3514.74	3518.82	3596.18	3598.57	3600.32	2905.05	2917.85
Stratigraphy			Skag. F.	Skag. F.	Skag. F.	Skag. F.	Skag. F.	Skag. F.	Paleoc.	Paleoc.
			Judy	Judy	Judy	Joanne	Joanne	Joanne	Lista	Andrew
Facies			FC/SF?	AS?	AS?	AS?	AS?	AS/SF?		
Detrital grains [%]	Quartz	Monocrystalline quartz	32.0	20.3	36.0	24.3	29.0	26.7	0.0	39.7
		Polycr. quartz and quartzite	4.7	1.3	4.0	9.3	2.3	2.7	0.0	2.3
	Lithics	Metamorphics	1.0	0.0	0.7	0.3	1.0	1.0	0.0	1.0
		Quartz feldspar aggregates	0.3	0.0	0.0	1.3	0.3	2.0	0.0	0.0
		Sedimentary extraclasts	0.0	0.0	0.0	0.0	0.0	0.0	0.0	1.0
		Volcanic	0.0	0.0	0.0	0.0	0.0	0.0	0.0	1.3
		Indeterminate	0.7	0.3	1.7	1.7	0.3	0.7	0.0	0.7
	Feldspar	Plagioclase	1.7	1.0	2.0	3.0	1.7	3.0	0.0	1.3
		K-feldspar (uncorroded)	15.7	6.0	10.3	16.3	20.0	17.0	0.0	5.3
		K-feldpar (partly dissolved)	2.0	0.0	5.0	2.3	1.0	7.7	0.0	2.0
	Sheet-silicates	Light mica	5.3	4.7	2.7	1.3	4.7	1.3	0.0	1.3
		Biotite	1.0	0.7	1.0	0.3	1.0	0.0	0.0	0.7
		Chlorite	0.7	0.7	0.7	0.7	4.7	1.3	0.0	0.3
	Intraclasts	Shale/Siltstone	0.0	0.0	0.0	7.7	0.0	0.7	0.0	0.0
		Detr. dolomite nodules	0.0	0.0	0.0	0.0	0.0	0.0	0.0	0.0
		Glauconite	0.0	0.0	0.0	0.0	0.0	0.0	0.0	0.0
		Bioclasts	0.0	0.0	0.0	0.0	0.0	0.0	14.7	3.7
		Black shale clasts	0.0	0.0	0.0	0.0	0.0	0.0	0.0	0.0
		Chert	0.0	0.0	0.0	0.0	0.0	0.0	0.0	0.0
		Microspar/micrite with biocl.	0.0	0.0	0.0	0.0	0.0	0.0	0.0	2.7
	Heavy minerals		0.3	0.3	0.0	0.0	0.0	0.0	0.0	1.0
Mud [%]		Clay matrix	0.3	7.0	6.0	0.3	28.3	1.3	0.0	20.7
		Black shale	0.0	0.0	0.0	0.0	0.0	0.0	0.0	0.0
		Micrite/microspar	0.0	0.0	0.0	0.0	0.0	0.0	82.7	0.0
Authigenic minerals [%]	Carbonate	Dolomite nodules	0.3	53.7	0.0	0.0	0.0	0.0	0.0	0.0
		Dolomite pore filling+rhombi	0.3	0.7	tr.	0.0	0.0	0.0	0.0	0.0
		Clast replacing	0.3	1.7	0.0	0.0	0.0	0.0	0.0	0.0
		Calcite	0.0	0.0	0.0	0.0	0.0	0.0	0.0	1.7
		Ferrous calcite	0.0	0.0	0.0	4.0	0.0	2.7	1.0	1.7
		Ankerite	0.0	0.0	0.0	15.3	0.0	0.7	0.0	0.0
	Quartz overgrowths		4.7	0.0	0.7	1.0	0.0	0.0	0.0	2.3
	Feldspar	K-feldspar overgrowths	3.7	0.3	1.0	3.0	0.7	6.3	0.0	0.0
		Albite in K-feldspar grains	1.0	0.0	0.3	0.0	0.0	0.3	0.0	0.0
	Hematite coatings		0.0	0.0	0.0	tr.	0.0	tr.	0.0	0.0
	Leucoxene/Anatase		0.0	0.0	0.7	0.3	tr.	2.3	0.0	0.0
	Anhydrite		0.0	0.0	0.0	0.0	0.0	0.0	0.0	0.0
	Barite		0.0	0.0	0.0	0.0	0.0	0.0	0.0	tr.
	Sulphides		0.0	0.0	0.0	tr.	0.3	0.0	0.0	0.7
	Clay minerals	Replacement of grains	0.3	0.0	2.3	1.0	0.0	1.0	1.0	4.7
		Illite coatings	0.3	0.0	1.0	0.0	0.7	0.0	0.0	0.0
		Illite meshwork	0.0	0.0	0.0	0.0	0.0	0.0	0.0	0.0
		Chlorite coatings and shreds	6.7	0.0	6.7	2.3	1.7	8.3	0.0	1.0
		Chlorite s. plates (5-10μm)	0.0	0.0	0.0	0.3	1.0	2.3	0.0	0.0
		Chlorite c. plates (>10μm)	0.0	0.0	0.0	0.0	0.0	0.0	0.0	0.0
		Clorite intraclast	2.0	1.3	3.3	0.3	0.7	1.0	0.0	0.0
		Kaolinite	0.0	0.0	0.0	0.0	0.0	0.0	0.0	1.0
	Bitumen	Massive in cracks or pores	0.0	0.0	0.0	0.0	0.0	0.0	0.0	0.3
Porosity [%]	Intergranular without secondary pores		11.7	0.0	10.3	2.7	0.7	7.0	0.7	1.7
	Secondary	Feldspar-leaching	2.0	0.0	1.0	0.3	0.0	2.3	0.0	0.0
		Lithics-leaching	0.0	0.0	0.3	0.0	0.0	0.0	0.0	0.0
		Heavy-min.-leaching	0.0	0.0	0.0	0.0	0.0	0.0	0.0	0.0
		Oversized pores	0.0	0.0	1.7	0.3	0.0	0.0	0.0	0.0
		Cement diss. voids	1.0	0.0	0.7	0.0	0.0	0.3	0.0	0.0
Granulometry		grainsize [mm]	0.10	0.02	0.05	0.26	0.08	0.13	<0.02	0.08
		sorting	1.6	2.0	1.6	1.3	1.6	1.4	-	1.6
		rounding	0.3	-	0.3	0.3	0.3	0.3	-	0.4
		sphericity	0.5	-	0.7	0.7	0.3	0.7	-	0.6
Number of counts			300	300	300	300	300	300	300	300

Appendix 2.2: Table petrographic data Triassic and overlying strata (UK sector)

Well			30/7a-8	30/7a-8	30/7a-8	30/7a-8	30/7a-8	30/7a-8	30/7a-8	30/7a-8	30/7a-8
Thin section no.			**9988.75**	**10012.4**	**10037.8**	**11429**	**11455**	**11681**	**11808**	**11834**	**11928**
Depth TVDSS [m]			3044.57	3051.78	3059.52	3483.56	3491.48	3560.37	3599.08	3607.00	3635.65
Stratigraphy			Ekofisk	Ekofisk	Ekofisk	Jurassic	Jurassic	Skag. F.	Skag. F.	Skag. F.	Skag. F.
			Chalk	Chalk	Chalk	Devils H.	Devils H.	Joanne	Joanne	Joanne	Joanne
Facies								FC?	AS/SF?	AS/SF?	FC?
Detrital grains [%]	Quartz	Monocrystalline quartz	0.0	0.0	0.0	4.7	28.0	26.7	32.0	38.0	26.3
		Polycr. quartz and quartzite	0.0	0.0	0.0	1.0	4.7	3.3	3.3	7.7	11.3
	Lithics	Metamorphics	0.0	0.0	0.0	0.7	1.7	2.0	1.7	1.7	2.0
		Quartz feldspar aggregates	0.0	0.0	0.0	0.0	2.0	3.3	0.3	1.7	3.3
		Sedimentary extraclasts	0.0	0.0	0.0	0.0	0.0	0.0	0.0	0.0	0.0
		Volcanic	0.0	0.0	0.0	0.0	0.0	0.0	0.0	0.0	0.0
		Indeterminate	0.0	0.0	0.0	0.0	0.3	0.3	0.7	0.3	2.0
	Feldspar	Plagioclase	0.0	0.0	0.0	tr.	4.0	4.0	3.7	4.0	6.7
		K-feldspar (uncorroded)	0.0	0.0	0.0	2.7	12.3	13.3	15.0	14.0	13.0
		K-feldpar (partly dissolved)	0.0	0.0	0.0	0.0	4.7	6.0	2.7	1.3	3.3
	Sheet-silicates	Light mica	0.0	0.0	0.0	0.0	1.7	1.7	3.0	1.7	1.0
		Biotite	0.0	0.0	0.0	0.0	0.0	0.0	0.7	0.0	0.0
		Chlorite	0.0	0.0	0.0	0.0	1.0	0.3	0.7	0.7	0.0
	Intraclasts	Shale/Siltstone	0.0	0.0	0.0	0.3	0.7	0.0	0.0	0.0	0.0
		Detr. dolomite nodules	0.0	0.0	0.0	0.0	0.0	0.0	0.0	0.0	0.0
		Glauconite	0.0	0.0	0.0	0.0	0.0	0.0	0.0	0.0	0.0
		Bioclasts	5.3	5.3	15.7	0.0	0.0	0.0	0.0	0.0	0.0
		Black shale clasts	0.0	0.0	0.0	0.0	0.0	0.0	0.0	0.0	0.0
		Chert	0.0	0.0	0.0	0.0	0.0	0.0	0.0	0.0	0.0
		Microspar/micrite with biocl.	0.0	0.0	0.0	0.0	0.0	0.0	0.0	0.0	0.0
	Heavy minerals		0.0	0.0	0.0	0.0	0.3	0.7	0.3	0.0	0.0
Mud [%]		Clay matrix	0.0	0.0	0.0	4.3	2.3	0.7	0.7	10.7	0.0
		Black shale	0.0	0.0	0.0	0.0	0.0	0.0	0.0	0.0	0.0
		Micrite/microspar	93.0	94.3	83.0	0.0	0.0	0.0	0.0	0.0	0.0
Authigenic minerals [%]	Carbonate	Dolomite nodules	0.0	0.0	0.0	29.0	0.0	0.0	0.0	0.0	0.0
		Dolomite pore filling+rhombi	0.0	0.0	0.0	29.0	0.0	0.0	0.0	0.0	0.0
		Clast replacing	0.0	0.0	0.0	0.3	0.0	0.0	0.0	0.0	0.0
		Calcite	0.0	0.0	0.0	0.0	0.0	0.0	0.0	0.0	0.0
		Ferrous calcite	1.7	0.3	1.3	0.0	0.0	0.0	0.0	0.0	0.0
		Ankerite	0.0	0.0	0.0	15.3	0.0	0.0	0.0	0.0	0.0
	Quartz overgrowths		0.0	0.0	0.0	0.7	3.3	0.7	4.7	1.0	0.7
	Feldspar	K-feldspar overgrowths	0.0	0.0	0.0	0.0	7.3	3.3	9.3	1.0	2.7
		Albite in K-feldspar grains	0.0	0.0	0.0	0.0	0.0	0.3	0.0	1.3	0.3
	Hematite coatings		0.0	0.0	0.0	0.0	0.0	1.0	tr.	0.0	tr.
	Leucoxene/Anatase		0.0	0.0	0.0	0.0	tr.	0.7	1.0	0.3	0.3
	Anhydrite		0.0	0.0	0.0	0.0	0.0	0.0	0.0	0.0	0.0
	Barite		0.0	0.0	0.0	0.0	0.0	0.0	0.0	0.0	0.0
	Sulphides		0.0	0.0	0.0	6.7	6.0	0.0	0.3	0.0	0.0
	Clay minerals	Replacement of grains	0.0	0.0	0.0	0.0	2.3	5.7	1.3	2.3	4.3
		Illite coatings	0.0	0.0	0.0	0.0	0.0	0.0	0.3	0.0	0.0
		Illite meshwork	0.0	0.0	0.0	0.0	0.0	0.0	0.0	0.0	0.0
		Chlorite coatings and shreds	0.0	0.0	0.0	0.0	0.3	4.7	5.7	6.0	1.7
		Chlorite s. plates (5-10µm)	0.0	0.0	0.0	0.0	0.0	0.0	tr.	tr.	0.0
		Chlorite c. plates (>10µm)	0.0	0.0	0.0	0.0	0.0	0.0	0.0	0.0	0.0
		Clorite intraclast	0.0	0.0	0.0	0.0	0.0	0.0	1.0	3.0	0.7
		Kaolinite	0.0	0.0	0.0	0.0	0.0	0.0	0.0	0.0	0.0
	Bitumen	Massive in cracks or pores	0.0	0.0	0.0	0.0	tr.	0.0	0.0	0.0	12.7
Porosity [%]	Intergranular without secondary pores		0.0	0.0	0.0	4.3	15.3	15.3	9.7	3.0	5.3
	Secondary	Feldspar-leaching	0.0	0.0	0.0	0.0	1.0	3.0	1.3	0.3	1.3
		Lithics-leaching	0.0	0.0	0.0	0.0	0.3	0.0	0.0	0.0	0.3
		Heavy-min.-leaching	0.0	0.0	0.0	0.0	0.0	0.0	0.0	0.0	0.0
		Oversized pores	0.0	0.0	0.0	1.0	0.3	0.0	0.3	0.0	0.3
		Cement diss. voids	0.0	0.0	0.0	0.0	0.0	3.0	0.3	0.0	0.3
Granulometry		grainsize [mm]	<0.02	<0.02	<0.02	0.10	0.18	0.19	0.09	0.09	0.27
		sorting	-	-	-	2.0	1.4	1.3	1.6	1.3	1.2
		rounding	-	-	-	0.4	0.4	0.4	0.4	0.4	0.4
		sphericity	-	-	-	0.6	0.6	0.6	0.6	0.6	0.6
Number of counts			300	300	300	300	300	300	300	300	300

Well			30/7a-8	30/7a-9	30/7a-9	30/7a-9	30/7a-9	30/7a-9	30/7a-9	30/7a-9	30/7a-9
Thin section no.			**11963**	**9869**	**9876**	**9881**	**12097**	**12099.5** **pol.**	**12099.7** **pol.**	**12105**	**12110** **pol.**
Depth TVDSS [m]			3646.32	2978.12	2980.23	2981.74	3650.45	3651.20	3651.26	3652.86	3654.37
Stratigraphy			Skag. F.	Paleoc.	Paleoc.	Paleoc.	Skag. F.	Skag. F.	Skag. F.	Skag. F.	Skag. F.
			Joanne	Andrew	Andrew	Andrew	Joanne	Joanne	Joanne	Joanne	Joanne
Facies			AS (red)				AS?	FC/SF?	AS?	FC?	FC?
Detrital grains [%]	Quartz	Monocrystalline quartz	18.0	25.7	37.0	44.7	22.7	27.7	19.7	22.3	18.0
		Polycr. quartz and quartzite	3.3	4.3	3.7	3.0	2.3	2.0	0.7	2.3	1.7
	Lithics	Metamorphics	0.0	0.0	0.0	0.0	1.0	0.3	0.0	1.7	0.7
		Quartz feldspar aggregates	0.7	0.3	0.7	0.3	1.3	1.7	0.0	0.7	2.0
		Sedimentary extraclasts	0.0	0.3	tr.	0.3	0.0	0.0	0.0	0.0	0.0
		Volcanic	0.0	0.0	tr.	0.0	0.0	0.0	0.0	0.0	0.0
		Indeterminate	1.0	0.0	0.0	0.7	0.0	0.0	0.3	0.0	0.3
	Feldspar	Plagioclase	1.3	0.3	1.0	1.3	2.0	3.3	1.3	4.0	3.3
		K-feldspar (uncorroded)	7.0	5.0	2.3	2.3	18.7	15.3	14.7	23.3	10.3
		K-feldpar (partly dissolved)	1.3	0.3	0.0	0.0	3.3	5.0	4.3	2.0	4.3
	Sheet-silicates	Light mica	4.7	2.7	1.7	1.3	4.0	2.3	0.3	3.7	3.7
		Biotite	0.0	0.7	0.7	0.3	0.0	0.0	0.0	0.0	0.0
		Chlorite	2.0	0.7	0.3	0.0	2.0	0.7	0.0	2.0	0.3
	Intraclasts	Shale/Siltstone	0.0	0.3	9.7	5.7	0.0	0.0	tr.	0.3	7.0
		Detr. dolomite nodules	0.0	0.0	0.0	0.0	0.0	1.0	0.0	0.7	0.0
		Glauconite	0.0	0.0	0.0	0.0	0.0	0.0	0.0	0.0	0.0
		Bioclasts	0.0	2.0	4.0	2.0	0.0	0.0	0.0	0.0	0.0
		Black shale clasts	0.0	0.0	0.0	0.0	0.0	0.0	0.0	0.0	0.0
		Chert	0.0	0.0	0.0	0.0	0.0	0.0	0.0	0.0	0.0
		Microspar/micrite with biocl.	0.0	0.0	1.0	1.0	0.0	0.0	0.0	0.0	0.0
	Heavy minerals		0.3	0.3	0.3	0.0	0.3	0.3	0.3	0.0	0.0
Mud [%]		Clay matrix	49.7	23.8	9.7	16.3	1.0	0.0	0.0	0.3	23.0
		Black shale	0.0	0.0	0.0	0.0	0.0	0.0	0.0	0.0	0.0
		Micrite/microspar	0.0	23.9	4.0	2.0	0.0	0.0	0.0	0.0	0.0
Authigenic minerals [%]	Carbonate	Dolomite nodules	2.3	0.0	0.0	0.0	20.0	9.3	27.7	1.0	0.0
		Dolomite pore filling+rhombi	0.3	0.0	0.0	0.0	0.0	0.3	6.3	0.3	0.3
		Clast replacing	0.0	0.7	0.3	0.3	2.0	1.3	3.7	0.0	0.0
		Calcite	0.0	0.7	1.3	1.0	0.0	1.3	0.0	0.0	1.3
		Ferrous calcite	0.0	2.0	0.7	0.7	no stain	no stain	no stain	no stain	no stain
		Ankerite	tr.	0.0	0.0	0.0	no stain	no stain	no stain	no stain	no stain
	Quartz overgrowths		0.3	tr.	4.7	4.3	0.3	0.7	tr.	3.0	tr.
	Feldspar	K-feldspar overgrowths	1.0	0.0	0.0	0.0	5.7	3.0	4.0	6.3	5.0
		Albite in K-feldspar grains	0.3	0.0	0.0	0.0	0.0	0.3	0.3	1.0	0.0
	Hematite coatings		5.3	0.0	0.0	0.0	tr.	tr.	tr.	0.0	tr.
	Leucoxene/Anatase		0.3	0.0	0.3	0.0	0.7	tr.	0.7	0.3	tr.
	Anhydrite		0.0	0.0	0.0	0.0	0.0	0.0	0.0	0.0	0.0
	Barite		0.0	0.0	0.0	0.0	0.0	0.0	0.0	0.0	0.0
	Sulphides		0.0	3.7	0.3	0.3	0.3	tr.	1.0	0.0	0.0
	Clay minerals	Replacement of grains	0.3	1.3	0.7	0.3	0.3	1.0	0.7	2.3	1.0
		Illite coatings	0.0	0.0	0.0	0.0	0.0	0.0	0.0	0.0	0.0
		Illite meshwork	0.0	0.0	0.0	0.0	0.0	0.0	0.0	0.0	0.0
		Chlorite coatings and shreds	0.0	0.0	0.0	0.0	0.7	0.0	0.0	0.7	0.0
		Chlorite s. plates (5-10μm)	0.0	0.0	0.0	0.0	0.0	0.0	0.0	0.0	0.0
		Chlorite c. plates (>10μm)	0.0	0.0	0.0	0.0	0.0	0.0	0.0	0.0	0.0
		Clorite intraclast	0.0	0.0	0.3	0.0	0.0	0.0	0.0	tr.	0.0
		Kaolinite	0.0	0.0	2.7	2.7	0.0	0.0	0.0	0.0	0.0
	Bitumen	Massive in cracks or pores	0.0	0.0	0.0	0.0	0.0	tr.	0.0	0.0	0.0
Porosity [%]	Intergranular without secondary pores		0.3	1.0	11.3	8.7	9.0	19.7	11.3	15.7	11.0
	Secondary	Feldspar-leaching	0.0	0.0	0.0	0.0	2.3	1.3	2.0	3.3	2.7
		Lithics-leaching	0.0	0.0	0.0	0.0	0.0	0.0	0.0	0.0	0.0
		Heavy-min.-leaching	0.0	0.0	0.0	0.0	0.0	0.0	0.0	0.0	0.0
		Oversized pores	0.0	0.0	0.3	0.0	0.0	0.0	0.3	0.7	0.0
		Cement diss. voids	0.0	0.0	1.0	0.3	0.0	2.0	0.3	2.0	4.0
Granulometry		grainsize [mm]	<0.06	0.06	0.13	0.15	0.08	0.12	0.12	0.08	0.15
		sorting	2.4	1.8	1.6	1.2	2.0	1.6	1.6	1.8	3.0
		rounding	-	0.4	0.4	0.4	0.4	0.4	0.4	0.3	0.4
		sphericity	-	0.6	0.6	0.7	0.5	0.6	0.6	0.4	0.6
Number of counts			300	300	300	300	300	300	300	300	300

Appendix 2.2: Table petrographic data Triassic and overlying strata (UK sector)

Well			30/7a-9	30/7a-9	30/7a-9	30/7a-9	30/7a-9	30/7a-9	30/7a-9	30/7a-9	30/7a-9
Thin section no.			**12117**	**12124**	**12131**	**12135.5**	**12142**	**12152**	**12160**	**12160.4 (I)**	**12168**
Depth TVDSS [m]			3656.48	3658.59	3660.71	3662.06	3664.03	3667.04	3669.46	3669.58	3671.87
Stratigraphy			Skag. F.	Skag. F.	Skag. F.	Skag. F.	Skag. F.	Skag. F.	Skag. F.	Skag. F.	Skag. F.
			Joanne	Joanne	Joanne	Joanne	Joanne	Joanne	Joanne	Joanne	Joanne
Facies			AS (red)	AS (red)	FC?	AS (red)	AS?	FC?	Dolcrete	Dolcrete	FC?
Detrital grains [%]	Quartz	Monocrystalline quartz	27.0	27.7	27.0	13.0	29.3	23.7	15.3	15.0	24.3
		Polycr. quartz and quartzite	1.3	1.3	2.0	0.3	2.3	4.0	1.3	11.3	6.0
	Lithics	Metamorphics	1.3	0.3	0.3	tr.	0.3	2.0	0.0	2.3	1.3
		Quartz feldspar aggregates	0.3	0.3	0.3	0.0	1.0	1.3	0.7	2.3	5.0
		Sedimentary extraclasts	0.0	0.3	0.0	0.0	0.3	0.0	0.0	0.0	0.0
		Volcanic	0.0	0.0	0.0	0.0	0.0	0.0	0.0	0.0	0.0
		Indeterminate	0.0	0.0	0.7	0.0	0.7	2.0	0.0	0.7	1.3
	Feldspar	Plagioclase	3.0	3.0	2.3	1.3	2.7	1.0	1.3	2.7	2.7
		K-feldspar (uncorroded)	11.7	11.7	9.0	8.7	10.0	14.7	11.7	10.3	11.7
		K-feldpar (partly dissolved)	4.7	4.0	6.3	0.0	0.3	7.0	1.7	1.3	6.7
	Sheet-silicates	Light mica	8.0	3.7	1.3	1.0	2.3	2.7	0.3	0.0	0.3
		Biotite	0.0	0.0	0.0	0.0	0.0	0.3	0.0	0.0	0.0
		Chlorite	1.3	0.0	1.0	tr.	0.3	0.0	1.0	0.7	0.0
	Intraclasts	Shale/Siltstone	2.7	0.0	0.0	0.0	0.0	0.3	0.0	0.0	1.3
		Detr. dolomite nodules	0.0	0.3	0.0	0.0	0.0	0.0	0.0	0.0	0.0
		Glauconite	0.0	0.0	0.0	0.0	0.0	0.0	0.0	0.0	0.0
		Bioclasts	0.0	0.0	0.0	0.0	0.0	0.0	0.0	0.0	0.0
		Black shale clasts	0.0	0.0	0.0	0.0	0.0	0.0	0.0	0.0	0.0
		Chert	0.0	0.0	0.0	0.0	0.0	0.0	0.0	0.0	0.0
		Microspar/micrite with biocl.	0.0	0.0	0.0	0.0	0.0	0.0	0.0	0.0	0.0
	Heavy minerals		1.0	0.3	0.3	0.0	0.0	0.7	0.0	0.3	0.0
Mud [%]		Clay matrix	4.7	17.0	0.3	45.7	28.3	0.0	0.0	0.0	0.0
		Black shale	0.0	0.0	0.0	0.0	0.0	0.0	0.0	0.0	0.0
		Micrite/microspar	0.0	0.0	0.0	0.0	0.0	0.0	0.0	0.0	0.0
Authigenic minerals [%]	Carbonate	Dolomite nodules	0.0	14.3	0.0	0.0	14.3	0.0	57.7	37.3	0.0
		Dolomite pore filling+rhombi	0.0	2.0	0.0	0.0	0.0	0.0	2.7	9.0	0.0
		Clast replacing	0.0	1.3	0.7	1.7	2.0	0.0	0.7	0.3	0.0
		Calcite	0.0	0.0	2.0	0.0	1.3	0.0	0.0	0.0	0.3
		Ferrous calcite	0.0	0.7	2.7	21.3	0.3	0.0	0.0	0.0	0.0
		Ankerite	0.0	tr.	0.0	0.0	tr.	0.0	tr.	5.0	0.0
	Quartz overgrowths		0.3	0.7	3.7	0.0	0.0	2.3	0.0	0.0	0.7
	Feldspar	K-feldspar overgrowths	2.3	1.0	6.7	tr.	0.0	7.3	1.0	0.0	4.7
		Albite in K-feldspar grains	0.0	tr.	0.0	0.0	0.0	0.3	0.0	0.0	0.3
	Hematite coatings		14.0	1.3	2.0	6.7	tr.	tr.	0.0	tr.	tr.
	Leucoxene/Anatase		tr.	1.3	0.3	0.0	tr.	1.0	0.3	0.3	0.3
	Anhydrite		0.0	0.0	0.0	0.0	0.0	0.0	0.0	0.0	0.0
	Barite		0.0	0.0	tr.	0.0	0.0	0.0	0.0	0.0	0.0
	Sulphides		0.0	0.0	0.0	0.0	0.0	0.0	0.3	0.3	0.0
	Clay minerals	Replacement of grains	3.3	1.0	2.0	0.3	3.3	0.7	0.0	0.0	0.3
		Illite coatings	0.0	tr.	0.0	0.0	0.7	0.0	0.0	0.0	0.0
		Illite meshwork	0.0	0.0	0.0	0.0	0.0	0.0	0.0	0.0	0.0
		Chlorite coatings and shreds	6.0	1.0	0.7	0.0	0.0	0.7	0.0	0.0	0.0
		Chlorite s. plates (5-10μm)	0.3	0.0	tr.	0.0	0.0	0.0	0.0	0.0	0.0
		Chlorite c. plates (>10μm)	0.0	0.0	0.0	0.0	0.0	0.0	0.0	0.0	0.0
		Clorite intraclast	0.0	0.0	0.0	0.0	0.0	0.0	0.3	0.0	0.0
		Kaolinite	0.0	0.0	0.0	0.0	0.0	0.0	0.0	0.0	0.0
	Bitumen	Massive in cracks or pores	0.0	0.0	tr.	0.0	0.0	0.0	0.0	0.0	0.0
Porosity [%]	Intergranular without secondary pores		5.0	3.7	15.0	0.0	0.0	19.7	3.0	0.7	23.7
	Secondary	Feldspar-leaching	1.7	1.0	2.0	0.0	0.0	3.7	0.7	0.0	3.3
		Lithics-leaching	0.0	0.0	0.3	0.0	0.0	0.3	0.0	0.0	0.7
		Heavy-min.-leaching	0.0	0.0	0.0	0.0	0.0	0.0	0.0	0.0	0.0
		Oversized pores	0.0	0.3	6.7	0.0	0.0	0.0	0.0	0.0	0.3
		Cement diss. voids	0.0	0.3	4.3	0.0	0.0	4.3	0.0	0.0	4.7
Granulometry		grainsize [mm]	0.05	0.06	0.10	<0.02	<0.02	0.11	0.12	0.20	0.29
		sorting	1.6	1.8	1.6	-	-	1.6	1.6	1.3	1.2
		rounding	-	0.4	0.4	-	-	0.4	0.4	0.4	0.4
		sphericity	-	0.6	0.6	-	-	0.6	0.6	0.6	0.6
Number of counts			300	300	300	300	300	300	300	300	300

Appendix 2.2: Table petrographic data Triassic and overlying strata (UK sector)

Well			30/7a-9	30/7a-9	30/7a-9	30/7a-11z	30/7a-11z	30/7a-11z	30/7a-11z	30/7a-11z	30/7a-11z
Thin section no.			**12174**	**12186**	**12194**	**11424 (92)**	**11427.6**	**11430 (98)**	**11439 (107)**	**11446 (114)**	**11446.3**
Depth TVDSS [m]			3673.68	3677.30	3679.72	3457.17	3458.26	3458.99	3461.71	3463.83	3463.92
Stratigraphy			Skag. F.	Skag. F.	Skag. F.	Skag. F.	Skag. F.	Skag. F.	Skag. F.	Skag. F.	Skag. F.
			Joanne	Joanne	Joanne	Joanne	Joanne	Joanne	Joanne	Joanne	Joanne
Facies			FC?	FC?	FC?	FC	AS	FC	FC	FC	Dolcrete
Detrital grains [%]	Quartz	Monocrystalline quartz	21.7	23.3	18.7	29.3	14.7	21.3	24.7	11.0	7.3
		Polycr. quartz and quartzite	2.3	5.3	2.3	10.7	1.7	3.0	9.7	1.0	0.0
	Lithics	Metamorphics	1.3	1.7	0.3	1.7	0.3	2.0	1.3	0.7	0.0
		Quartz feldspar aggregates	0.7	2.3	2.0	0.7	0.0	0.3	1.0	0.3	0.0
		Sedimentary extraclasts	0.0	0.0	0.0	0.0	0.0	0.0	0.0	0.0	0.0
		Volcanic	0.0	0.0	0.0	0.0	0.0	0.0	0.0	0.0	0.0
		Indeterminate	0.3	0.3	0.3	0.0	0.3	0.3	0.3	0.0	0.0
	Feldspar	Plagioclase	4.7	1.7	3.7	3.3	0.3	3.0	2.7	2.0	0.3
		K-feldspar (uncorroded)	18.7	12.7	20.7	8.7	8.0	17.7	12.0	10.3	8.0
		K-feldpar (partly dissolved)	5.7	5.0	6.0	4.3	0.3	7.3	7.3	4.0	0.0
	Sheet-silicates	Light mica	1.7	1.7	1.0	0.0	4.3	1.0	1.7	1.0	0.3
		Biotite	tr.	0.0	0.0	0.0	0.3	0.0	0.3	tr.	0.0
		Chlorite	0.3	0.0	0.7	0.0	1.7	0.0	1.0	1.7	0.0
	Intraclasts	Shale/Siltstone	0.3	2.7	0.0	tr.	0.0	0.0	0.0	12.3	0.0
		Detr. dolomite nodules	0.0	0.0	0.0	0.0	0.0	0.0	0.0	13.7	0.0
		Glauconite	0.0	0.0	0.0	0.0	0.0	0.0	0.0	0.0	0.0
		Bioclasts	0.0	0.0	0.0	0.0	0.0	0.0	0.0	0.0	0.0
		Black shale clasts	0.0	0.0	0.0	0.0	0.0	0.0	0.0	0.0	0.0
		Chert	0.0	0.0	0.0	0.0	0.0	0.0	0.0	0.0	0.0
		Microspar/micrite with biocl.	0.0	0.0	0.0	0.0	0.0	0.0	0.0	0.0	0.0
	Heavy minerals		0.3	0.0	0.0	0.7	0.3	0.7	0.3	0.0	0.0
Mud [%]		Clay matrix	0.3	2.0	0.0	0.0	46.7	1.0	0.3	2.3	12.3
		Black shale	0.0	0.0	0.0	0.0	0.0	0.0	0.0	0.0	0.0
		Micrite/microspar	0.0	0.0	0.0	0.0	0.0	0.0	0.0	0.0	0.0
Authigenic minerals [%]	Carbonate	Dolomite nodules	0.0	9.0	5.3	tr.	15.0	0.0	0.0	3.0	47.3
		Dolomite pore filling+rhombi	tr.	tr.	6.0	5.3	0.7	tr.	1.3	14.0	20.7
		Clast replacing	0.0	2.0	2.7	0.0	0.3	0.0	0.3	0.7	0.0
		Calcite	0.0	0.0	0.0	0.0	0.0	0.0	0.0	0.0	0.0
		Ferrous calcite	0.0	0.0	0.0	0.0	0.0	0.0	0.0	0.0	0.0
		Ankerite	0.0	1.3	2.3	1.0	tr.	tr.	0.3	0.3	1.0
	Quartz overgrowths		1.3	0.3	0.3	2.0	0.0	2.7	0.3	2.7	0.0
	Feldspar	K-feldspar overgrowths	8.3	6.3	6.0	4.7	0.0	8.0	4.7	4.0	0.0
		Albite in K-feldspar grains	0.0	0.3	0.0	0.3	0.0	0.0	1.0	0.0	0.0
	Hematite coatings		tr.	0.3	tr.	0.0	0.3	0.0	0.0	tr.	tr.
	Leucoxene/Anatase		1.7	1.0	0.7	0.0	0.0	0.7	0.7	0.0	0.7
	Anhydrite		0.0	0.0	0.0	0.0	0.0	0.0	0.0	0.0	0.0
	Barite		0.0	0.0	0.0	0.0	0.0	0.0	0.0	0.0	0.0
	Sulphides		tr.	tr.	tr.	0.0	0.0	tr.	0.0	0.7	tr.
	Clay minerals	Replacement of grains	1.7	0.3	1.0	1.3	1.3	1.3	3.3	1.0	0.0
		Illite coatings	0.0	0.0	0.0	0.0	0.0	0.0	0.0	0.0	0.0
		Illite meshwork	0.0	0.0	0.0	0.0	0.0	0.0	0.0	0.0	0.0
		Chlorite coatings and shreds	0.0	2.3	0.0	0.0	0.7	1.7	2.3	0.7	0.0
		Chlorite s. plates (5-10μm)	0.0	0.0	0.0	0.0	0.0	0.0	0.0	0.0	0.0
		Chlorite c. plates (>10μm)	0.0	0.0	0.0	0.0	0.0	0.0	0.0	0.0	0.0
		Clorite intraclast	0.0	0.7	0.3	0.0	2.7	0.0	0.7	0.0	0.0
		Kaolinite	0.0	0.0	0.0	0.0	0.0	0.0	0.0	0.0	0.0
	Bitumen	Massive in cracks or pores	0.0	0.0	0.0	0.0	0.0	0.0	0.0	0.3	tr.
Porosity [%]	Intergranular without secondary pores		20.3	13.3	16.3	12.7	0.0	22.0	14.3	8.7	2.0
	Secondary	Feldspar-leaching	2.7	1.0	2.0	0.7	0.0	2.0	3.7	2.7	0.0
		Lithics-leaching	0.3	0.0	0.0	0.3	0.0	0.7	0.3	0.0	0.0
		Heavy-min.-leaching	0.0	0.3	0.0	0.0	0.0	0.0	0.3	0.0	0.0
		Oversized pores	0.3	0.7	0.0	4.3	0.0	0.3	0.7	0.0	0.0
		Cement diss. voids	5.0	2.0	1.3	8.0	0.0	3.0	3.0	1.0	0.0
Granulometry		grainsize [mm]	0.14	0.13	0.17	0.34	0.03	0.12	0.18	0.14	-
		sorting	1.3	1.4	2.0	1.2	1.4	1.4	1.3	2.0	-
		rounding	0.4	0.4	0.4	0.4	0.4	0.4	0.3	0.4	-
		sphericity	0.6	0.6	0.6	0.6	0.6	0.6	0.6	0.6	-
Number of counts			300	300	300	300	300	300	300	300	300

Well			30/7a-11z	30/7a-11z	30/7a-11z	30/7a-11z	30/7a-11z	30/7a-11z	30/7a-11z	30/7a-11z	30/7a-11z
Thin section no.			**11454 (122)**	**11468 (136)**	**(136)**	**11483 (151)**	**11491**	**11503 (171)**	**11510 (178)**	**11519**	**11533 (201)**
Depth TVDSS [m]			3466.25	3470.49	3470.49	3475.03	3477.45	3481.08	3483.20	3485.92	3490.16
Stratigraphy			Skag. F.	Skag. F.	Skag. F.	Skag. F.	Skag. F.	Skag. F.	Skag. F.	Skag. F.	Skag. F.
			Joanne	Joanne	Joanne	Joanne	Joanne	Joanne	Joanne	Joanne	Joanne
Facies			SF	SF	SF	AS	SF	SF	SF	FC	SF
Detrital grains [%]	Quartz	Monocrystalline quartz	22.3	28.0	20.3	18.3	17.0	27.7	24.0	35.3	20.7
		Polycr. quartz and quartzite	3.3	7.3	5.0	1.0	2.0	3.3	6.0	5.0	3.3
	Lithics	Metamorphics	1.3	1.3	1.7	1.0	2.3	0.7	1.3	1.7	1.3
		Quartz feldspar aggregates	0.0	1.7	1.3	0.7	1.7	0.3	1.3	3.3	1.3
		Sedimentary extraclasts	0.0	0.3	0.0	0.0	0.0	0.0	0.0	0.0	0.0
		Volcanic	0.0	0.0	0.0	0.0	0.0	0.0	0.0	0.0	0.0
		Indeterminate	0.7	0.3	0.3	0.7	0.3	0.3	0.3	0.0	1.0
	Feldspar	Plagioclase	4.3	1.3	4.0	2.0	4.7	3.3	3.0	3.0	3.0
		K-feldspar (uncorroded)	10.3	9.7	12.3	21.0	13.0	13.0	10.0	7.3	11.0
		K-feldpar (partly dissolved)	7.7	6.0	6.7	4.7	7.3	4.3	10.0	4.0	10.0
	Sheet-silicates	Light mica	2.3	1.0	1.0	4.0	1.0	1.7	0.7	1.0	3.3
		Biotite	tr.	tr.	0.0	0.7	tr.	0.0	0.0	0.0	0.3
		Chlorite	0.7	0.3	0.3	3.3	0.3	1.3	0.3	0.3	4.7
	Intraclasts	Shale/Siltstone	0.0	0.0	1.0	0.0	1.0	5.0	4.3	0.3	2.3
		Detr. dolomite nodules	0.0	0.0	0.3	0.0	0.0	0.0	0.0	0.0	0.0
		Glauconite	0.0	0.0	0.0	0.0	0.0	0.0	0.0	0.0	0.0
		Bioclasts	0.0	0.0	0.0	0.0	0.0	0.0	0.0	0.0	0.0
		Black shale clasts	0.0	0.0	0.0	0.0	0.0	0.0	0.0	0.0	0.0
		Chert	0.0	0.0	0.0	0.0	0.0	0.0	0.0	0.0	0.0
		Microspar/micrite with biocl.	0.0	0.0	0.0	0.0	0.0	0.0	0.0	0.0	0.0
	Heavy minerals		1.0	0.0	0.0	0.0	0.0	0.3	0.3	0.0	0.3
Mud [%]		Clay matrix	0.3	5.0	2.0	14.7	1.0	12.7	1.0	0.0	0.0
		Black shale	0.0	0.0	0.0	0.0	0.0	0.0	0.0	0.0	0.0
		Micrite/microspar	0.0	0.0	0.0	0.0	0.0	0.0	0.0	0.0	0.0
Authigenic minerals [%]	Carbonate	Dolomite nodules	0.0	0.3	1.3	0.0	0.0	0.0	0.0	0.0	0.0
		Dolomite pore filling+rhombi	1.3	7.0	6.3	0.7	0.0	0.3	0.0	0.0	0.0
		Clast replacing	0.3	2.0	3.0	0.7	0.0	0.0	1.7	0.0	0.0
		Calcite	0.0	0.0	0.0	0.0	0.0	0.0	6.7	2.7	0.0
		Ferrous calcite	0.0	0.0	0.0	0.0	0.0	0.0	0.7	0.3	0.0
		Ankerite	0.7	1.7	0.0	tr.	0.0	tr.	0.0	0.0	0.3
	Quartz overgrowths		2.0	tr.	1.7	tr.	2.3	1.0	4.0	1.3	1.0
	Feldspar	K-feldspar overgrowths	11.0	7.3	6.7	8.0	11.7	6.3	6.3	4.3	5.7
		Albite in K-feldspar grains	0.0	tr.	0.0	0.0	tr.	0.0	0.0	0.0	0.0
	Hematite coatings		tr.	0.0	0.3	tr.	tr.	tr.	tr.	tr.	0.3
	Leucoxene/Anatase		0.3	0.3	tr.	0.0	1.3	0.7	0.3	tr.	0.3
	Anhydrite		0.0	0.0	0.0	0.0	0.0	0.0	0.0	0.0	0.0
	Barite		0.0	0.0	0.0	0.0	0.0	0.0	0.0	0.0	0.0
	Sulphides		0.0	0.0	0.0	0.0	0.0	0.0	0.0	0.0	0.0
	Clay minerals	Replacement of grains	4.0	4.3	1.0	0.3	2.3	0.7	1.0	0.3	1.0
		Illite coatings	0.0	0.0	0.0	0.3	0.0	tr.	0.0	0.0	0.0
		Illite meshwork	0.0	0.0	0.0	0.0	0.0	0.0	0.0	0.0	0.0
		Chlorite coatings and shreds	1.7	1.3	1.3	6.3	1.0	3.7	0.3	0.7	2.0
		Chlorite s. plates (5-10μm)	0.0	0.0	0.0	0.0	0.0	0.0	0.0	0.0	0.0
		Chlorite c. plates (>10μm)	0.0	0.0	0.0	0.0	0.0	0.0	0.0	0.0	0.0
		Clorite intraclast	0.0	0.0	0.3	2.3	0.0	0.3	0.0	0.0	0.7
		Kaolinite	0.0	0.0	0.0	0.0	0.0	0.0	0.0	0.0	0.0
	Bitumen	Massive in cracks or pores	0.0	0.0	0.0	0.0	tr.	0.0	tr.	tr.	tr.
Porosity [%]	Intergranular without secondary pores		14.7	7.0	12.3	8.3	15.3	12.0	10.7	16.7	20.7
	Secondary	Feldspar-leaching	3.0	2.3	4.7	0.7	2.3	0.3	1.7	2.3	3.7
		Lithics-leaching	0.3	0.0	0.7	0.0	0.3	0.0	0.0	0.0	0.0
		Heavy-min.-leaching	0.3	0.0	0.0	0.0	0.0	0.0	0.0	0.0	0.0
		Oversized pores	0.3	1.3	0.0	0.3	2.0	0.0	0.7	2.7	0.7
		Cement diss. voids	5.7	2.7	4.0	0.0	9.7	0.7	3.3	7.3	1.0
Granulometry		grainsize [mm]	0.13	0.20	-	0.07	0.13	0.09	0.18	0.24	0.11
		sorting	1.3	1.4	-	1.6	1.4	3.0	1.3	1.3	1.4
		rounding	0.4	0.4	-	0.4	0.4	0.4	0.4	0.4	0.4
		sphericity	0.6	0.6	-	0.4	0.6	0.6	0.6	0.6	0.6
Number of counts			300	300	300	300	300	300	300	300	300

Appendix 2.2: Table petrographic data Triassic and overlying strata (UK sector)

Well			30/7a-11z	30/7a-11z	30/7a-11z	30/7a-11z	30/7a-11z	30/7a-11z	30/7a-11z	30/7a-11z	30/7a-11z
Thin section no.			**11546 (214)**	**11557 (225)**	**11573 (241)**	**11579.5**	**11588 (256)**	**(256)**	**11602 (270)**	**11607.2 (275)**	**11621 (289)**
Depth TVDSS [m]			3494.09	3497.42	3502.27	3504.23	3506.81	3506.81	3511.04	3512.62	3516.79
Stratigraphy			Skag. F.	Skag. F.	Skag. F.	Skag. F.	Skag. F.	Skag. F.	Skag. F.	Skag. F.	Skag. F.
			Joanne	Joanne	Joanne	Joanne	Joanne	Joanne	Joanne	Joanne	Joanne
Facies			SF	SF	FC	AS?	SF	SF	SF	SF	AS
Detrital grains [%]	Quartz	Monocrystalline quartz	21.7	12.7	16.3	17.3	23.0	21.0	21.0	22.0	19.3
		Polycr. quartz and quartzite	1.7	1.3	4.0	5.3	4.3	6.3	0.7	4.0	3.7
	Lithics	Metamorphics	1.0	0.0	0.3	1.0	1.3	2.0	1.3	0.0	1.0
		Quartz feldspar aggregates	1.3	0.3	0.0	0.7	1.0	1.3	1.3	1.3	1.3
		Sedimentary extraclasts	0.3	0.0	0.0	0.0	0.3	0.0	0.3	0.0	0.0
		Volcanic	0.0	0.0	0.0	0.0	0.0	0.0	0.0	0.0	0.0
		Indeterminate	0.7	0.0	0.0	1.3	1.7	2.3	1.7	0.3	1.3
	Feldspar	Plagioclase	2.3	0.3	3.3	5.7	5.3	2.7	4.3	4.7	4.0
		K-feldspar (uncorroded)	7.7	7.0	15.0	12.3	14.0	10.0	16.7	13.3	15.7
		K-feldpar (partly dissolved)	10.7	0.0	3.7	4.0	4.0	5.0	5.7	5.3	8.0
	Sheet-silicates	Light mica	2.3	0.0	1.7	0.7	1.0	1.7	1.7	1.0	3.3
		Biotite	1.0	0.0	0.3	0.0	tr.	0.3	0.0	tr.	0.0
		Chlorite	1.0	0.3	3.3	0.3	1.3	0.3	1.3	0.3	3.7
	Intraclasts	Shale/Siltstone	1.7	7.0	4.7	2.0	0.0	2.0	2.0	0.3	0.7
		Detr. dolomite nodules	0.0	31.0	0.7	tr.	0.0	0.0	0.0	0.0	0.0
		Glauconite	0.0	0.0	0.0	0.0	0.0	0.0	0.0	0.0	0.0
		Bioclasts	0.0	0.0	0.0	0.0	0.0	0.0	0.0	0.0	0.0
		Black shale clasts	0.0	0.0	0.0	0.0	0.0	0.0	0.0	0.0	0.0
		Chert	0.0	0.0	0.0	0.0	0.0	0.0	0.0	0.0	0.0
		Microspar/micrite with biocl.	0.0	0.0	0.0	0.0	0.0	0.0	0.0	0.0	0.0
	Heavy minerals		0.0	0.0	0.0	0.0	1.0	0.0	0.3	0.0	0.0
Mud [%]		Clay matrix	0.0	0.7	5.0	15.7	0.3	0.0	0.0	0.0	2.7
		Black shale	0.0	0.0	0.0	0.0	0.0	0.0	0.0	0.0	0.0
		Micrite/microspar	0.0	0.0	0.0	0.0	0.0	0.0	0.0	0.0	0.0
Authigenic minerals [%]	Carbonate	Dolomite nodules	0.0	17.0	7.3	0.0	0.0	0.3	0.0	0.0	0.0
		Dolomite pore filling+rhombi	0.3	18.3	8.7	0.0	0.7	1.7	tr.	1.3	0.0
		Clast replacing	0.0	2.0	0.7	0.3	0.0	0.0	0.0	0.3	0.0
		Calcite	0.0	0.0	0.0	0.0	0.0	0.0	0.7	0.0	0.0
		Ferrous calcite	0.0	0.0	0.0	3.7	0.0	0.0	1.0	0.0	0.0
		Ankerite	tr.	0.3	0.7	tr.	tr.	0.0	0.0	0.3	0.7
	Quartz overgrowths		0.7	tr.	tr.	4.0	1.3	0.3	0.3	5.3	1.7
	Feldspar	K-feldspar overgrowths	9.3	0.7	7.0	7.3	7.7	7.0	6.0	7.3	7.3
		Albite in K-feldspar grains	0.0	0.0	0.0	0.0	0.0	0.0	0.0	0.0	0.3
	Hematite coatings		tr.	tr.	tr.	tr.	tr.	tr.	tr.	0.0	tr.
	Leucoxene/Anatase		0.3	0.0	0.3	0.3	tr.	0.3	1.0	0.7	0.3
	Anhydrite		0.0	0.0	0.0	0.0	0.0	0.0	0.0	0.0	0.0
	Barite		0.0	0.0	0.0	0.0	0.0	0.0	0.0	0.0	0.0
	Sulphides		0.0	0.0	0.0	0.0	0.0	0.0	0.0	0.0	0.0
	Clay minerals	Replacement of grains	3.0	0.0	0.3	1.0	2.7	1.3	1.0	4.3	4.7
		Illite coatings	0.0	0.0	0.0	0.0	0.0	0.0	0.0	0.0	0.0
		Illite meshwork	0.0	0.0	0.0	0.0	0.0	0.0	0.0	0.0	0.0
		Chlorite coatings and shreds	4.3	0.0	1.0	0.0	0.3	0.3	2.7	0.0	1.7
		Chlorite s. plates (5-10μm)	0.0	0.0	0.0	0.3	0.0	0.0	0.0	0.0	0.0
		Chlorite c. plates (>10μm)	0.0	0.0	0.0	0.0	0.0	0.0	0.0	0.0	0.0
		Clorite intraclast	tr.	0.0	0.0	0.0	0.0	0.0	1.0	0.0	0.0
		Kaolinite	0.0	0.0	0.0	0.0	0.0	0.0	0.0	0.0	0.0
	Bitumen	Massive in cracks or pores	tr.	0.0	tr.	1.3	tr.	0.0	0.0	4.3	0.3
Porosity [%]	Intergranular without secondary pores		23.7	0.7	12.0	10.7	17.0	20.7	20.0	17.3	16.7
	Secondary	Feldspar-leaching	2.3	0.3	1.7	1.0	3.0	4.3	3.7	2.0	1.3
		Lithics-leaching	0.0	0.0	0.3	0.0	0.3	0.0	1.0	0.7	0.0
		Heavy-min.-leaching	0.0	0.0	0.0	0.0	0.0	0.0	0.0	0.0	0.0
		Oversized pores	1.3	0.0	0.3	0.3	1.7	1.7	0.7	0.7	0.0
		Cement diss. voids	1.3	0.0	1.3	3.3	6.7	7.0	2.7	2.7	0.3
Granulometry		grainsize [mm]	0.09	0.29	0.13	0.17	0.15	0.12	0.12	0.16	0.09
		sorting	1.4	2.2	2.0	1.3	1.4	1.3	1.3	1.4	1.4
		rounding	0.4	0.5	0.5	0.4	0.4	0.4	0.4	0.4	0.4
		sphericity	0.6	0.7	0.4	0.6	0.6	0.6	0.6	0.6	0.5
Number of counts			300	300	300	300	300	300	300	300	300

Appendix 2.2: Table petrographic data Triassic and overlying strata (UK sector)

Well			30/7a-11z	30/7a-11z	30/7a-11z	30/7a-11z	30/7a-11z	30/7a-11z	30/7a-11z	30/7a-11z
Thin section no.			**11626.5**	**11627 (295)**	**11632 (300)**	**11641 (309)**	**11647.8 (316)**	**11655.1 (323)**	**11682 (350)**	**11682.75**
Depth TVDSS [m]			3518.46	3518.61	3520.12	3522.84	3524.90	3527.11	3535.25	3535.48
Stratigraphy			Skag. F.	Skag. F.	Skag. F.	Skag. F.	Skag. F.	Skag. F.	Skag. F.	Skag. F.
			Joanne	Joanne	Joanne	Joanne	Joanne	Joanne	Joanne	Joanne
Facies				FC	FC	FC	AS	AS?	FC	AS?
Detrital grains [%]	Quartz	Monocrystalline quartz	20.3	19.7	20.7	22.3	29.0	26.7	23.3	24.7
		Polycr. quartz and quartzite	4.3	3.7	5.0	6.7	1.7	0.3	4.3	3.7
	Lithics	Metamorphics	3.7	1.0	0.7	1.7	1.3	0.7	0.3	0.0
		Quartz feldspar aggregates	1.3	1.0	1.3	3.3	1.7	0.7	1.3	2.7
		Sedimentary extraclasts	0.0	0.0	0.0	0.0	0.0	0.0	0.0	0.3
		Volcanic	0.0	0.0	0.0	0.0	0.0	0.0	0.0	0.0
		Indeterminate	0.3	1.0	0.3	0.0	0.3	1.0	0.3	0.3
	Feldspar	Plagioclase	5.3	6.3	7.0	4.0	3.3	5.7	8.0	4.7
		K-feldspar (uncorroded)	14.3	12.3	8.0	7.7	12.3	15.7	12.3	12.0
		K-feldpar (partly dissolved)	5.0	6.7	5.7	4.3	7.0	7.0	4.0	3.3
	Sheet-silicates	Light mica	1.3	1.3	2.0	0.7	1.7	1.7	2.0	3.0
		Biotite	tr.	0.0	0.0	0.0	tr.	0.0	0.3	0.0
		Chlorite	0.3	0.0	1.0	0.0	0.7	1.0	1.3	0.3
	Intraclasts	Shale/Siltstone	0.0	0.3	0.7	3.0	3.3	9.3	0.7	1.3
		Detr. dolomite nodules	0.0	0.0	0.0	3.3	0.0	0.0	0.0	0.0
		Glauconite	0.0	0.0	0.0	0.0	0.0	0.0	0.0	0.0
		Bioclasts	0.0	0.0	0.0	0.0	0.0	0.0	0.0	0.0
		Black shale clasts	0.0	0.0	0.0	0.0	0.0	0.0	0.0	0.0
		Chert	0.0	0.0	0.0	0.0	0.0	0.0	0.0	0.0
		Microspar/micrite with biocl.	0.0	0.0	0.0	0.0	0.0	0.0	0.0	0.0
	Heavy minerals		0.0	0.0	0.3	0.0	0.3	0.3	1.0	0.0
Mud [%]		Clay matrix	0.0	0.0	0.0	0.0	4.3	11.7	0.7	11.7
		Black shale	0.0	0.0	0.0	0.0	0.0	0.0	0.0	0.0
		Micrite/microspar	0.0	0.0	0.0	0.0	0.0	0.0	0.0	0.0
Authigenic minerals [%]	Carbonate	Dolomite nodules	0.0	0.0	0.0	0.0	0.0	0.0	0.0	0.0
		Dolomite pore filling+rhombi	0.0	0.0	5.0	4.0	4.3	0.0	3.0	1.0
		Clast replacing	2.7	0.3	0.0	0.3	0.3	0.0	0.3	0.7
		Calcite	1.7	2.0	0.0	0.0	0.0	0.0	0.0	5.0
		Ferrous calcite	17.3	11.3	0.0	0.0	0.0	0.0	0.0	10.0
		Ankerite	0.0	0.0	1.3	0.7	0.3	0.0	1.0	0.0
	Quartz overgrowths		tr.	1.0	1.7	5.3	2.0	tr.	0.7	0.7
	Feldspar	K-feldspar overgrowths	9.7	7.3	10.3	4.7	6.0	3.7	9.0	6.3
		Albite in K-feldspar grains	0.0	0.0	0.0	0.3	0.0	1.0	0.0	0.0
	Hematite coatings		tr.	tr.	tr.	tr.	0.0	tr.	0.0	tr.
	Leucoxene/Anatase		0.7	0.3	0.3	0.7	1.0	0.0	0.7	tr.
	Anhydrite		0.0	0.0	0.0	0.0	0.0	0.0	0.0	0.0
	Barite		0.0	0.0	0.0	0.0	0.0	0.0	0.0	0.0
	Sulphides		0.0	0.0	0.0	0.0	0.0	0.0	0.0	0.0
	Clay minerals	Replacement of grains	1.0	1.3	2.3	0.0	1.3	0.7	1.7	1.0
		Illite coatings	0.0	0.0	0.0	0.0	0.0	0.0	0.0	tr.
		Illite meshwork	0.0	0.0	0.0	0.0	0.0	0.0	0.0	0.0
		Chlorite coatings and shreds	0.3	0.3	0.0	0.0	4.0	4.7	0.7	1.3
		Chlorite s. plates (5-10μm)	0.0	0.0	0.0	0.0	0.0	0.0	0.0	0.0
		Chlorite c. plates (>10μm)	0.0	0.0	0.0	0.0	0.0	0.0	0.0	0.0
		Clorite intraclast	0.0	0.0	0.3	0.0	0.0	0.7	0.3	0.0
		Kaolinite	0.0	0.0	0.0	0.0	0.0	0.0	0.0	0.0
	Bitumen	Massive in cracks or pores	0.0	0.0	tr.	5.0	0.7	0.3	0.0	0.0
Porosity [%]	Intergranular without secondary pores		7.3	14.0	13.0	13.3	10.0	6.3	14.7	4.3
	Secondary	Feldspar-leaching	0.7	2.0	4.7	3.3	1.7	1.0	2.3	0.7
		Lithics-leaching	0.3	0.3	0.3	0.0	0.0	0.0	0.3	0.0
		Heavy-min.-leaching	0.3	0.0	0.0	0.0	0.0	0.0	0.0	0.0
		Oversized pores	0.0	5.0	1.3	1.0	0.7	0.0	1.3	0.0
		Cement diss. voids	1.7	1.3	6.7	4.3	0.7	0.0	4.0	1.0
Granulometry		grainsize [mm]	0.16	0.17	0.18	0.22	0.08	0.09	0.10	0.12
		sorting	1.6	1.4	1.2	1.3	1.6	1.8	1.6	1.8
		rounding	0.4	0.4	0.4	0.4	0.4	0.4	0.4	0.4
		sphericity	0.6	0.6	0.6	0.6	0.6	0.6	0.6	0.6
Number of counts			300	300	300	300	300	300	300	300

Appendix 2.3: Table petrographic data Triassic and Jurassic (Norwegian sector)

Well			NOR-E	NOR-E	NOR-E	NOR-E	NOR-E	NOR-E	NOR-E
Thin section no.			**5555.85** **sandst.**	**5556.45**	**5558.4**	**5558.5** **sandst.**	**5559.35** **sandst.**	**5563.5** **sandst.**	**5564.35**
Depth MD [m]			5555.85	5556.45	5558.40	5558.50	5559.35	5563.50	5564.35
Stratigraphy			Triassic	Triassic	Triassic	Triassic	Triassic	Triassic	Triassic
Facies			SF/AS?	SF?	Dolcrete	AS?	AS?	AS?	SF?
Detrital grains [%]	Quartz	Monocrystalline quartz	40.7	37.0	30.3	31.3	38.0	35.7	43.3
		Polycr. quartz and quartzite	5.0	6.7	7.0	6.0	4.0	3.7	6.3
	Lithics	Metamorphics	0.3	0.7	3.3	6.7	0.7	0.3	0.3
		Quartz feldspar aggregates	2.7	5.3	3.7	3.3	2.7	5.7	4.3
		Sedimentary extraclasts	0.0	0.0	0.3	0.0	0.0	0.0	0.0
		Volcanic	0.0	0.3	0.0	0.3	0.3	0.0	tr.
		Indeterminate	1.7	0.0	1.7	0.7	3.3	2.0	1.7
	Feldspar	Plagioclase	0.3	1.0	0.3	0.7	tr.	0.3	0.0
		K-feldspar (uncorroded)	4.3	9.7	7.3	6.3	8.7	5.3	7.3
		K-feldpar (partly dissolved)	0.7	1.0	1.7	1.0	0.3	1.0	0.7
	Sheet-silicates	Light mica	1.7	tr.	0.7	0.3	6.3	4.0	tr.
		Biotite	0.0	0.0	0.0	0.0	0.0	0.0	0.0
		Chlorite	0.7	0.0	0.0	0.0	1.0	0.7	0.7
	Intraclasts	Shale/Siltstone	0.0	0.0	2.0	0.0	0.0	0.0	0.0
		Detr. dolomite nodules	0.0	0.0	0.0	0.3	0.0	0.0	0.0
		Glauconite	0.0	0.0	0.0	0.0	0.0	0.0	0.0
		Bioclasts	0.0	0.0	0.0	0.0	0.0	0.0	0.0
		Black shale clasts	0.0	0.0	0.0	0.0	0.0	0.0	0.0
		Chert	0.0	0.0	0.3	0.3	0.7	0.7	0.0
		Microspar/micrite with biocl.	0.0	0.0	0.0	0.0	0.0	0.0	0.0
	Heavy minerals		1.0	0.0	0.3	0.0	0.7	0.3	0.3
Mud [%]		Clay matrix	3.3	0.7	4.0	7.7	11.7	11.3	1.3
		Black shale	0.0	0.0	0.0	0.0	0.0	0.0	0.0
		Micrite/microspar	0.0	0.0	1.0	0.7	0.0	0.0	0.0
Authigenic minerals [%]	Carbonate	Dolomite nodules	tr.	5.3	11.7	1.7	0.0	0.0	tr.
		Dolomite pore filling+rhombi	18.0	12.4	17.6	18.0	14.7	20.7	22.7
		Clast replacing	2.0	1.0	4.0	0.0	0.0	1.7	1.3
		Calcite	0.0	0.0	0.0	0.0	0.0	0.0	0.0
		Ferrous calcite	0.0	0.0	0.0	0.0	0.0	0.0	0.0
		Ankerite/Fe-dolomite	0.0	tr.	tr.	0.0	0.0	tr.	no stain
	Quartz overgrowths		3.3	3.7	1.0	0.7	0.0	0.0	2.0
	Feldspar	K-feldspar overgrowths	0.0	0.0	0.0	0.0	0.0	tr.	tr.
		Albite in K-feldspar grains	0.0	0.0	0.0	0.0	0.0	0.0	0.0
	Hematite		tr.	tr.	0.0	tr.	0.0	tr.	tr.
	Leucoxene/Anatase		tr.	0.0	0.0	0.0	0.0	0.0	tr.
	Anhydrite		0.0	0.0	0.0	0.0	0.0	0.0	0.0
	Barite		0.0	0.0	0.0	0.0	0.0	0.0	0.0
	Sulphides		0.0	0.0	0.0	0.0	0.0	0.0	0.0
	Clay minerals	Replacement of grains	0.0	0.3	1.0	1.0	0.0	0.0	0.7
		Illite coatings	0.0	0.0	0.0	0.0	0.0	0.0	0.0
		Illite meshwork	0.0	0.0	0.0	0.0	0.0	0.0	0.0
		Chlorite coatings and shreds	4.0	0.7	0.3	9.7	5.0	6.3	0.0
		Chlorite s. plates (5-10μm)	0.0	0.0	0.0	0.0	0.0	0.0	tr.
		Chlorite c. plates (>10μm)	0.0	0.0	0.0	0.0	0.0	0.0	0.0
		Clorite intraclast	1.0	0.0	0.0	3.0	2.0	0.3	0.0
		Kaolinite	0.0	0.0	0.0	0.0	0.0	0.0	0.0
	Bitumen		9.3	14.3	tr.	0.0	0.0	tr.	7.0
Porosity [%]	Intergranular without secondary pores		0.0	tr.	0.3	tr.	0.0	0.0	tr.
	Secondary	Feldspar-leaching	0.0	0.0	tr.	0.0	0.0	0.0	tr.
		Lithics-leaching	0.0	0.0	0.0	0.0	0.0	0.0	0.0
		Heavy-min.-leaching	0.0	0.0	0.0	0.0	0.0	0.0	0.0
		Oversized pores	0.0	0.0	tr.	0.3	0.0	0.0	0.0
		Cement diss. voids	0.0	0.0	0.0	0.0	0.0	0.0	0.0
Granulometry		grainsize [mm]	0.10	0.15	0.15	0.20	0.10	0.07	0.15
		sorting	1.6	1.8	1.4	2.0	1.2	1.4	1.6
		rounding	0.3	0.3	0.3	0.5	0.5	0.3	0.3
		sphericity	0.7	0.7	0.7	0.9	0.9	0.7	0.7
Number of counts			300	300	300	300	300	300	300

Well			NOR-G	NOR-G	NOR-G	NOR-G	NOR-G	NOR-G	NOR-G	NOR-G	NOR-G
Thin section no.			**14237**	**14246**	**14249.2**	**14254**	**14260.1**	**14265**	**14269**	**14274**	**14282**
Depth MD [m]			4339.44	4342.18	4343.16	4344.62	4346.48	4347.97	4349.19	4350.72	4353.15
Stratigraphy			Jurassic	Jurassic	Jurassic	Jurassic	Jurassic	Jurassic	Jurassic	Jurassic	Jurassic
			H./Ula	Ula Fm.	Ula Fm.	Ula Fm.	Ula Fm.	Ula Fm.	Ula Fm.	Ula Fm.	Ula Fm.
Facies			L2	USF	USF	USF	USF	USF	MSF	USF	MSF
Detrital grains [%]	Quartz	Monocrystalline quartz	57.7	54.8	56.8	54.0	58.7	54.0	52.0	59.0	62.2
		Polycr. quartz and quartzite	2.8	4.0	4.3	6.5	4.8	5.5	6.7	5.7	5.2
	Lithics	Metamorphics	0.0	0.0	0.3	0.2	0.2	0.0	0.2	0.2	0.0
		Quartz feldspar aggregates	0.0	0.2	0.0	0.2	0.0	0.0	0.0	0.0	0.0
		Sedimentary extraclasts	0.0	0.0	0.0	0.0	0.0	0.0	0.0	0.0	0.0
		Volcanic	0.0	0.0	0.0	0.0	0.0	0.0	0.0	0.0	0.0
		Indeterminate	0.8	0.5	0.5	0.3	0.0	0.5	0.5	0.2	0.3
	Feldspar	Plagioclase	0.3	0.0	tr.	0.0	0.0	0.0	tr.	tr.	tr.
		K-feldspar (uncorroded)	0.0	0.0	0.0	0.0	0.0	0.0	0.0	0.0	0.0
		K-feldpar (partly dissolved)	1.2	1.2	0.7	1.0	0.3	0.2	0.2	0.7	0.2
	Sheet-silicates	Light mica	3.3	0.8	0.3	0.0	0.0	0.5	1.7	0.3	1.0
		Biotite	tr.	0.0	tr.	0.0	0.0	0.0	0.5	0.0	0.5
		Chlorite	0.0	0.2	0.0	0.0	0.0	0.0	0.0	0.0	0.0
	Intraclasts	Shale/Siltstone	tr.	0.0	tr.	0.0	0.0	0.2	0.0	tr.	tr.
		Detr. dolomite nodules	0.0	0.0	0.0	0.0	0.0	0.0	0.0	0.0	0.0
		Glauconite	0.0	0.0	0.0	0.0	0.0	0.0	0.0	0.0	0.0
		Bioclasts	0.0	0.0	0.0	0.0	0.0	0.0	0.0	0.0	0.0
		Black shale clasts	0.0	0.0	0.0	0.0	0.0	0.0	0.0	0.0	0.0
		Chert	0.0	0.0	0.0	0.0	0.0	0.0	0.0	0.0	0.0
		Microspar/micrite with biocl.	0.0	0.0	0.0	0.0	0.0	0.0	0.0	0.0	0.0
	Heavy minerals		0.5	0.2	0.3	0.0	0.0	0.0	0.3	0.0	0.2
Mud [%]		Clay matrix	4.0	27.7	0.0	0.0	0.5	0.8	8.3	1.2	2.5
		Black shale	0.0	0.0	0.0	0.0	0.0	0.0	0.0	0.0	0.0
		Micrite/microspar	0.0	0.0	0.0	0.0	0.0	0.0	0.0	0.0	0.0
Authigenic minerals [%]	Carbonate	Dolomite nodules	0.0	0.0	0.0	0.0	0.0	0.0	0.0	0.0	0.0
		Dolomite pore filling+rhombi	0.5	0.0	0.2	0.0	0.0	0.0	0.3	tr.	0.2
		Clast replacing	0.0	0.0	0.0	0.0	0.0	0.0	0.0	0.0	0.0
		Calcite	0.0	0.0	0.0	0.0	0.0	0.0	0.0	0.0	0.0
		Ferrous calcite	0.0	0.0	0.0	0.0	0.0	0.0	0.0	0.0	0.0
		Ankerite/Fe-dolomite	0.7	0.0	0.3	0.5	0.3	0.3	0.5	tr.	1.3
	Quartz overgrowths		5.0	0.7	11.3	10.7	11.3	13.3	7.7	8.0	6.0
	Feldspar	K-feldspar overgrowths	0.0	0.0	0.0	0.0	0.0	0.0	0.0	0.0	0.0
		Albite in K-feldspar grains	0.0	0.0	tr.	0.0	0.0	0.0	0.0	tr.	0.2
	Hematite		0.0	0.0	0.0	0.0	0.0	0.0	0.0	0.0	0.0
	Leucoxene/Anatase		0.0	0.0	0.0	0.0	0.0	0.0	0.0	0.0	0.0
	Anhydrite		0.0	0.0	0.0	0.0	0.0	0.0	0.0	0.0	0.0
	Barite		0.0	0.0	0.0	0.0	0.0	0.0	0.0	0.0	0.2
	Sulphides		0.8	3.2	1.0	0.8	1.2	2.3	1.3	1.0	0.8
	Clay minerals	Replacement of grains	4.5	2.7	3.0	2.2	2.5	3.7	8.5	1.8	4.7
		Illite coatings	0.0	0.0	0.3	0.2	0.7	0.3	1.2	1.0	1.5
		Illite meshwork	tr.	tr.	tr.	tr.	tr.	tr.	tr.	tr.	tr.
		Chlorite coatings and shreds	1.0	0.2	1.0	1.2	0.5	1.3	0.8	1.3	0.8
		Chlorite s. plates (5-10μm)	0.0	0.0	0.0	0.0	0.0	0.0	0.0	0.0	0.0
		Chlorite c. plates (>10μm)	0.0	0.0	0.0	0.0	0.0	0.0	0.0	0.0	0.0
		Clorite intraclast	0.0	0.0	0.0	0.0	0.0	0.0	0.0	0.0	0.0
		Kaolinite	0.8	0.3	1.8	1.8	3.0	3.0	1.7	3.0	2.3
	Bitumen		5.3	0.0	0.3	0.0	0.5	0.0	1.2	0.0	0.2
Porosity [%]	Intergranular without secondary pores		6.0	0.3	15.2	18.2	12.5	9.0	4.2	13.3	5.8
	Secondary	Feldspar-leaching	4.2	2.7	2.2	1.8	2.2	4.5	2.2	3.3	4.0
		Lithics-leaching	0.3	0.5	0.0	0.3	0.2	0.2	0.0	0.0	0.0
		Heavy-min.-leaching	0.0	0.0	0.0	0.0	0.0	0.0	0.0	0.0	0.0
		Oversized pores	0.2	0.0	0.0	0.2	0.7	0.3	0.2	0.0	0.0
		Cement diss. voids	0.0	0.0	tr.	0.0	tr.	tr.	0.0	0.0	0.0
Granulometry		grainsize [mm]	0.07	0.17	0.18	0.21	0.19	0.18	0.11	0.18	0.12
		sorting	1.3	1.1	1.2	1.2	1.3	1.2	1.4	1.1	1.4
		rounding	0.4	0.4	0.5	0.6	0.5	0.5	0.4	0.4	0.4
		sphericity	0.7	0.7	0.7	0.7	0.7	0.7	0.6	0.7	0.6
Number of counts			600	600	600	600	600	600	600	600	600

Appendix 2.3: Table petrographic data Triassic and Jurassic (Norwegian sector)

Well			NOR-F	NOR-F	NOR-F	NOR-F	NOR-F	NOR-F	NOR-F	NOR-F	NOR-F
Thin section no.			**5108.55**	**5108.7**	**5109.4**	**5109.65**	**5113.65**	**5134.35**	**5134.35**	**5134.95**	**5135.6**
Depth MD [m]			5108.55	5108.70	5109.40	5109.65	5113.65	5134.35	5134.35	5134.95	5135.60
Stratigraphy			Jurassic	Jurassic	Jurassic	Jurassic	Jurassic	Jurassic	Jurassic	Jurassic	Jurassic
			Farsund	Farsund	Farsund	Farsund	Farsund	Farsund	Farsund	Farsund	Farsund
Facies			source.	source.	source.	source.	source.	sandst.	sandst.	sandst.	sandst.
Detrital grains [%]	Quartz	Monocrystalline quartz	0.7	0.7	2.3	3.3	tr.	31.3	41.7	34.0	50.3
		Polycr. quartz and quartzite	0.0	0.0	0.0	0.0	0.0	6.3	6.0	9.0	7.7
	Lithics	Metamorphics	0.0	0.0	0.0	0.0	tr.	0.3	1.3	0.7	tr.
		Quartz feldspar aggregates	0.0	0.0	tr.	0.0	0.0	0.7	tr.	1.3	0.3
		Sedimentary extraclasts	0.3	0.0	0.0	1.0	0.0	tr.	0.7	0.3	0.0
		Volcanic	0.0	0.0	0.0	0.0	0.0	0.0	0.3	tr.	tr.
		Indeterminate	0.0	0.0	0.0	0.0	0.0	0.7	1.0	0.7	1.3
	Feldspar	Plagioclase	0.0	0.0	0.0	0.3	0.0	1.0	1.3	2.3	1.3
		K-feldspar (uncorroded)	0.0	0.3	0.0	0.0	0.0	2.3	0.0	0.7	0.3
		K-feldpar (partly dissolved)	0.0	0.0	0.0	0.0	0.0	0.0	0.0	0.3	0.0
	Sheet-silicates	Light mica	0.0	0.0	0.7	0.7	0.0	0.7	0.0	0.0	0.0
		Biotite	0.0	0.0	0.0	0.0	0.0	0.0	0.0	0.0	0.0
		Chlorite	0.0	0.0	0.0	0.0	0.0	0.0	0.0	0.0	0.0
	Intraclasts	Shale/Siltstone	0.0	0.0	0.0	0.0	0.0	0.0	0.0	0.0	0.0
		Detr. dolomite nodules	0.0	0.0	0.0	0.0	0.0	0.0	0.0	0.0	0.0
		Glauconite	0.0	0.0	0.0	0.0	0.0	0.0	0.0	tr.	0.0
		Bioclasts	0.0	0.0	tr.	0.0	0.0	0.0	0.0	0.0	0.0
		Black shale clasts	0.0	0.0	0.0	0.0	0.0	0.0	0.0	0.0	0.0
		Chert	0.0	0.0	0.0	0.0	0.0	0.0	0.0	0.0	0.0
		Microspar/micrite with biocl.	0.0	0.0	0.0	0.0	0.0	0.0	0.0	0.0	0.0
	Heavy minerals		0.0	0.0	0.0	0.0	0.0	0.0	0.0	0.0	0.3
Mud [%]		Clay matrix	tr.	tr.	0.0	0.0	0.0	35.7	36.7	0.0	0.0
		Black shale	0.0	0.0	96.7	94.7	0.0	0.0	0.0	1.0	0.0
		Micrite/microspar	78.0	85.7	0.0	0.0	87.3	0.0	0.0	0.0	0.0
Authigenic minerals [%]	Carbonate	Dolomite nodules	0.0	0.0	0.0	0.0	0.0	0.0	0.0	0.0	0.0
		Dolomite pore filling+rhombi	0.0	0.0	0.0	0.0	0.0	0.0	0.3	3.7	2.7
		Clast replacing	0.0	0.0	0.0	0.0	0.0	tr.	0.3	14.3	6.7
		Calcite	0.0	0.0	0.0	0.0	0.0	0.0	0.0	0.0	tr.
		Ferrous calcite	0.0	0.0	0.0	0.0	0.0	0.0	0.0	0.0	0.0
		Ankerite/Fe-dolomite	0.0	0.0	0.3	0.0	0.0	2.7	0.0	22.6	17.3
	Quartz overgrowths		0.0	0.0	0.0	0.0	0.0	4.3	4.3	1.0	4.0
	Feldspar	K-feldspar overgrowths	0.0	0.0	0.0	0.0	0.0	0.0	0.0	0.0	0.0
		Albite in K-feldspar grains	0.0	0.0	0.0	0.0	0.0	tr.	0.3	0.0	0.0
	Hematite		0.0	0.0	0.0	0.0	0.0	0.0	0.0	0.0	0.0
	Leucoxene/Anatase		0.0	0.0	0.0	0.0	0.0	0.0	0.0	0.0	0.0
	Anhydrite		0.0	0.0	0.0	0.0	0.0	0.0	0.0	0.0	0.0
	Barite		0.0	0.0	0.0	0.0	0.0	0.0	0.0	0.0	0.0
	Sulphides		21.0	13.3	0.0	0.0	12.7	5.0	0.3	2.3	1.0
	Clay minerals	Replacement of grains	0.0	0.0	0.0	0.0	0.0	6.0	0.0	0.7	0.0
		Illite coatings	0.0	0.0	0.0	0.0	0.0	0.0	tr.	0.0	0.0
		Illite meshwork	0.0	0.0	0.0	0.0	0.0	0.0	0.0	0.0	0.0
		Chlorite coatings and shreds	0.0	0.0	0.0	0.0	0.0	0.0	0.0	0.0	0.0
		Chlorite s. plates (5-10μm)	0.0	0.0	0.0	0.0	0.0	0.0	0.0	0.0	0.0
		Chlorite c. plates (>10μm)	0.0	0.0	0.0	0.0	0.0	0.0	0.0	0.0	0.0
		Clorite intraclast	0.0	0.0	0.0	0.0	0.0	0.3	0.0	4.3	6.0
		Kaolinite	0.0	0.0	0.0	0.0	0.0	0.3	2.7	0.7	0.0
	Bitumen		0.0	tr.	0.0	0.0	0.0	2.0	2.0	0.0	0.7
Porosity [%]	Intergranular without secondary pores		0.0	0.0	0.0	0.0	0.0	0.3	0.0	0.0	0.0
	Secondary	Feldspar-leaching	0.0	0.0	0.0	0.0	0.0	0.0	0.7	0.0	0.0
		Lithics-leaching	0.0	0.0	0.0	0.0	0.0	0.0	0.0	0.0	0.0
		Heavy-min.-leaching	0.0	0.0	0.0	0.0	0.0	0.0	0.0	0.0	0.0
		Oversized pores	0.0	0.0	0.0	0.0	0.0	0.0	0.0	0.0	0.0
		Cement diss. voids	0.0	0.0	0.0	0.0	0.0	0.0	0.0	0.0	0.0
Granulometry		grainsize [mm]	<0.01	<0.01	<0.01	<0.01	<0.01	0.25	0.25	0.15	0.15
		sorting	-	-	-	-	-	1.3	1.3	1.3	1.4
		rounding	-	-	-	-	-	0.5	0.5	0.7	0.5
		sphericity	-	-	-	-	-	0.7	0.7	0.7	0.7
Number of counts			300	300	300	300	300	300	300	300	300

Appendix 2.3: Table petrographic data Triassic and Jurassic (Norwegian sector)

Well			NOR-F	NOR-F	NOR-F	NOR-F	NOR-F
Thin section no.			**5135.6**	**5136.2B**	**5136.2**	**5136.55**	**5136.85**
Depth MD [m]			5135.60	5136.20	5136.20	5136.55	5136.85
Stratigraphy			Jurassic	Jurassic	Jurassic	Jurassic	Jurassic
			Farsund	Farsund	Farsund	Farsund	Farsund
Facies			sandst.	sandst.	sandst.	source.	sandst.
Detrital grains [%]	Quartz	Monocrystalline quartz	40.0	37.0	39.3	2.7	47.0
		Polycr. quartz and quartzite	8.0	8.7	7.3	0.0	9.7
	Lithics	Metamorphics	tr.	0.3	0.3	0.3	1.0
		Quartz feldspar aggregates	0.7	0.7	1.7	0.0	2.0
		Sedimentary extraclasts	0.7	0.0	0.3	0.0	tr.
		Volcanic	0.0	0.0	0.0	0.0	0.0
		Indeterminate	1.0	0.0	0.3	0.0	1.0
	Feldspar	Plagioclase	1.7	2.3	1.3	0.0	1.7
		K-feldspar (uncorroded)	1.0	0.0	1.3	0.0	0.3
		K-feldpar (partly dissolved)	0.3	1.3	0.3	0.0	0.3
	Sheet-silicates	Light mica	0.7	tr.	0.3	0.7	0.7
		Biotite	0.0	0.0	0.0	0.0	0.0
		Chlorite	0.0	0.0	0.0	0.0	0.0
	Intraclasts	Shale/Siltstone	0.0	0.0	0.0	0.0	0.0
		Detr. dolomite nodules	0.0	0.0	0.0	0.0	0.0
		Glauconite	0.0	tr.	tr.	tr.	tr.
		Bioclasts	0.0	0.0	0.0	0.0	0.0
		Black shale clasts	0.0	0.0	0.0	0.0	0.0
		Chert	0.0	0.0	0.0	0.0	0.0
		Microspar/micrite with biocl.	0.0	0.0	0.0	0.0	0.0
	Heavy minerals		0.0	0.0	0.0	0.0	0.0
Mud [%]		Clay matrix	0.0	0.0	0.0	0.0	0.0
		Black shale	0.0	1.3	5.0	96.0	5.7
		Micrite/microspar	0.0	0.0	0.0	0.0	0.0
Authigenic minerals [%]	Carbonate	Dolomite nodules	0.0	0.0	0.0	0.0	0.0
		Dolomite pore filling+rhombi	tr.	tr.	tr.	0.3	1.3
		Clast replacing	9.7	13.3	10.0	0.0	0.7
		Calcite	tr.	0.0	0.0	0.0	0.0
		Ferrous calcite	0.0	0.0	0.0	no stain	no stain
		Ankerite/Fe-dolomite	20.7	21.7	17.0		
	Quartz overgrowths		6.0	1.7	4.3	0.0	6.3
	Feldspar	K-feldspar overgrowths	tr.	0.0	0.0	0.0	0.0
		Albite in K-feldspar grains	0.0	tr.	0.0	0.0	0.0
	Hematite		0.0	0.0	0.0	0.0	0.0
	Leucoxene/Anatase		0.0	0.0	0.0	0.0	0.0
	Anhydrite		0.0	0.0	0.0	0.0	0.0
	Barite		0.0	0.0	0.0	0.0	0.0
	Sulphides		2.7	0.7	1.0	0.0	0.3
	Clay minerals	Replacement of grains	0.3	0.7	0.3	0.0	0.7
		Illite coatings	0.0	0.0	0.0	0.0	0.0
		Illite meshwork	0.0	0.0	0.0	0.0	0.0
		Chlorite coatings and shreds	0.0	0.0	0.0	0.0	0.0
		Chlorite s. plates (5-10μm)	0.0	0.0	0.0	0.0	0.0
		Chlorite c. plates (>10μm)	0.0	0.0	0.0	0.0	0.0
		Clorite intraclast	6.0	7.7	7.0	0.0	3.3
		Kaolinite	0.0	2.0	1.7	0.0	12.7
	Bitumen		0.7	0.7	1.0	0.0	5.3
Porosity [%]	Intergranular without secondary pores		0.0	0.0	0.0	0.0	0.0
	Secondary	Feldspar-leaching	0.0	tr.	0.0	0.0	0.0
		Lithics-leaching	0.0	0.0	0.0	0.0	0.0
		Heavy-min.-leaching	0.0	0.0	0.0	0.0	0.0
		Oversized pores	0.0	0.0	0.0	0.0	0.0
		Cement diss. voids	0.0	0.0	0.0	0.0	0.0
Granulometry		grainsize [mm]	0.15	0.20	0.20	<0.01	0.15
		sorting	1.4	1.4	1.4	-	1.8
		rounding	0.5	0.5	0.5	-	0.5
		sphericity	0.7	0.7	0.7	-	0.7
Number of counts			300	300	300	300	300

Appendix 2.3: Table petrographic data Triassic and Jurassic (Norwegian sector)

Well			NOR-C	NOR-C	NOR-C	NOR-C	NOR-C	NOR-C	NOR-C	NOR-C	NOR-C
Thin section no.			**4575.55**	**4576.1**	**4577.5**	**4578.4**	**4579.5**	**4582.45**	**4584.65**	**4585.5B**	**4589.6**
Depth MD [m]			4575.55	4576.10	4577.50	4578.40	4579.50	4582.45	4584.65	4585.50	4589.60
Stratigraphy			Jurassic	Jurassic	Triassic	Triassic	Triassic	Triassic	Triassic	Triassic	Triassic
			U. Oxf.	U. Oxf.	Skg. Fm	Skg. Fm	Skg. Fm	Skg. Fm	Skg. Fm	Skg. Fm	Skg. Fm
Facies			sandst.	sandst.	sandst.	sandst.	sandst.	sandst.	sandst.	Dolcrete	sandst.
Detrital grains [%]	Quartz	Monocrystalline quartz	58.7	65.7	40.0	32.0	39.7	42.0	42.0	8.7	40.3
		Polycr. quartz and quartzite	7.3	10.0	7.7	6.0	7.0	2.7	15.0	0.3	10.3
	Lithics	Metamorphics	0.0	0.0	1.0	1.7	1.7	0.3	0.3	0.0	2.7
		Quartz feldspar aggregates	2.3	0.7	1.3	1.3	1.7	0.0	1.3	0.0	1.3
		Sedimentary extraclasts	0.0	0.0	0.7	0.3	tr.	0.0	0.0	0.0	tr.
		Volcanic	0.0	0.0	0.0	0.0	0.0	0.0	0.0	0.0	0.0
		Indeterminate	0.0	0.3	0.3	1.0	1.7	0.7	0.0	0.0	0.7
	Feldspar	Plagioclase	0.7	0.0	3.3	4.3	1.7	1.3	2.7	tr.	3.3
		K-feldspar (uncorroded)	1.7	1.3	2.0	4.3	2.0	4.7	3.3	1.0	4.0
		K-feldpar (partly dissolved)	2.3	4.0	10.7	12.7	16.7	9.0	8.3	0.3	12.3
	Sheet-silicates	Light mica	1.0	0.0	6.0	10.3	8.7	7.3	0.0	0.7	2.3
		Biotite	0.0	0.0	1.0	1.7	2.0	1.0	0.0	0.0	tr.
		Chlorite	0.0	0.0	3.0	2.3	2.3	2.0	0.0	0.0	1.3
	Intraclasts	Shale/Siltstone	0.0	0.0	0.0	0.0	0.0	0.0	0.0	0.0	0.0
		Detr. dolomite nodules	0.0	0.0	0.0	0.0	0.0	0.0	0.0	0.0	0.0
		Glauconite	0.0	0.0	0.0	0.0	0.0	0.0	0.0	0.0	0.0
		Bioclasts	0.0	0.0	0.0	0.0	0.0	0.0	0.0	0.0	0.0
		Black shale clasts	0.0	0.0	0.0	0.0	0.0	0.0	0.0	0.0	0.0
		Chert	0.0	0.0	0.0	0.0	0.0	0.0	0.0	0.0	0.0
		Microspar/micrite with biocl.	0.0	0.0	0.0	0.0	0.0	0.0	0.0	0.0	0.0
	Heavy minerals		0.7	0.3	0.7	0.0	0.0	0.0	0.0	0.3	0.3
Mud [%]		Clay matrix	2.7	7.3	14.7	1.3	3.7	25.3	2.0	8.3	1.0
		Black shale	0.0	0.0	0.0	0.0	0.0	0.0	0.0	0.0	0.0
		Micrite/microspar	0.0	0.0	0.0	0.0	0.0	0.0	0.0	0.0	0.0
Authigenic minerals [%]	Carbonate	Dolomite nodules	0.0	0.0	0.0	0.0	0.0	0.0	0.0	0.0	0.0
		Dolomite pore filling+rhombi	5.7	tr.	0.0	0.0	0.0	0.0	tr.	80.0	tr.
		Clast replacing	0.3	0.0	0.0	0.0	0.0	0.0	tr.	0.0	tr.
		Calcite	0.0	0.0	0.0	0.0	0.0	0.0	0.0	0.0	0.0
		Ferrous calcite	tr.	no stain	no stain	no stain	no stain	no stain	no stain	no stain	no stain
		Ankerite/Fe-dolomite									
	Quartz overgrowths		9.3	7.7	1.7	5.7	0.7	0.0	6.3	0.0	7.7
	Feldspar	K-feldspar overgrowths	0.0	0.0	0.0	1.3	0.7	0.0	2.0	0.0	1.7
		Albite in K-feldspar grains	0.0	0.0	0.0	0.0	0.0	0.0	0.0	0.0	0.0
	Hematite		0.0	0.0	0.0	0.0	0.0	0.0	0.0	tr.	0.0
	Leucoxene/Anatase		0.0	0.0	tr.	0.0	tr.	0.0	0.7	0.0	0.3
	Anhydrite		0.0	0.0	0.0	0.0	0.0	0.0	0.0	0.0	0.0
	Barite		0.3	0.0	0.0	0.0	0.0	0.0	0.0	0.0	tr.
	Sulphides		0.3	0.0	0.0	0.0	tr.	0.3	0.0	0.3	0.0
	Clay minerals	Replacement of grains	1.7	0.0	3.7	3.3	3.0	1.3	1.7	0.0	2.3
		Illite coatings	0.0	0.0	0.0	0.0	0.0	0.0	0.0	0.0	0.3
		Illite meshwork	0.0	0.0	0.0	0.0	0.0	0.0	0.3	0.0	0.0
		Chlorite coatings and shreds	0.0	0.0	0.7	tr.	tr.	tr.	tr.	0.0	0.0
		Chlorite s. plates (5-10μm)	0.0	0.0	0.0	0.0	0.0	0.0	0.0	0.0	0.0
		Chlorite c. plates (>10μm)	0.7	tr.	0.3	1.7	3.0	0.7	0.7	0.0	2.3
		Clorite intraclast	0.0	0.0	0.7	0.0	0.3	0.0	0.0	0.0	0.3
		Kaolinite	0.0	0.0	0.0	0.0	0.0	0.0	0.0	0.0	0.0
	Bitumen		tr.	tr.	0.0	0.0	0.0	0.0	0.0	0.0	0.0
Porosity [%]	Intergranular without secondary pores		3.0	1.7	0.3	3.3	1.0	1.0	10.3	0.0	2.7
	Secondary	Feldspar-leaching	1.3	1.0	0.3	5.0	2.7	0.3	2.7	0.0	2.3
		Lithics-leaching	0.0	0.0	0.0	0.0	0.0	0.0	0.0	0.0	0.0
		Heavy-min.-leaching	0.0	0.0	0.0	0.0	0.0	0.0	0.3	0.0	0.0
		Oversized pores	0.0	0.0	0.0	0.3	0.0	0.0	tr.	0.0	tr.
		Cement diss. voids	0.0	0.0	0.0	0.0	0.0	0.0	tr.	0.0	0.0
Granulometry		grainsize [mm]	0.10	0.15	0.06	0.09	0.08	<0.06	0.25	<0.06	0.15
		sorting	1.4	1.2	1.6	1.6	1.7	1.4	1.4	-	1.4
		rounding	0.7	0.4	0.3	0.4	0.4	0.4	0.4	-	0.4
		sphericity	0.7	0.6	0.3	0.6	0.6	0.6	0.6	-	0.6
Number of counts			300	300	300	300	300	300	300	300	300

Appendix 3.1: Table electron microprobe analyses of authigenic carbonates

no.	well	stratigraphy	sample	mineral	Chemical composition [wt%]								Ions in structural formula on the basis of 6 oxygen							
					MgO	CaO	FeO	SrO	BaO	MnO	SiO_2	total	Mg	Ca	Fe	Sr	Ba	Mn	Si	total
1	NOR-A	Rotliegend	4808.8	dolomite	21.17	30.21	0.07	-	-	0.69	0.05	52.18	0.97	0.99	0.00	0.00	0.00	0.02	0.00	1.99
2	NOR-A	Rotliegend	4808.8	dolomite	20.18	28.64	0.31	0.04	-	0.82	1.24	51.22	0.91	0.93	0.01	0.00	0.00	0.02	0.04	1.91
3	NOR-A	Rotliegend	4808.8	Fe-dolomite	17.05	29.46	4.13	0.03	-	2.47	0.30	53.44	0.80	1.00	0.11	0.00	0.00	0.07	0.01	1.98
4	NOR-A	Rotliegend	4808.8	dolomite	21.65	30.32	0.04	0.04	0.00	0.62	0.06	52.71	0.99	1.00	0.00	0.00	0.00	0.02	0.00	2.02
5	NOR-A	Rotliegend	4808.8	dolomite	21.67	30.11	0.09	0.03	0.06	1.41	0.10	53.47	1.00	1.00	0.00	0.00	0.00	0.04	0.00	2.05
6	NOR-A	Rotliegend	4808.8	Fe-dolomite	17.23	29.63	3.97	0.01	-	2.63	0.21	53.69	0.81	1.00	0.11	0.00	0.00	0.07	0.01	2.00
7	NOR-A	Rotliegend	4812.1	dolomite	20.61	29.67	0.07	0.00	0.02	1.03	0.07	51.48	0.94	0.97	0.00	0.00	0.00	0.03	0.00	1.94
8	NOR-A	Rotliegend	4812.1	Fe-dolomite	17.28	27.49	3.98	0.03	0.00	1.34	0.04	50.16	0.79	0.90	0.10	0.00	0.00	0.03	0.00	1.83
9	NOR-A	Rotliegend	4812.1	dolomite	20.19	29.06	0.59	0.03	0.00	1.65	0.01	51.53	0.92	0.96	0.02	0.00	0.00	0.04	0.00	1.94
10	NOR-A	Rotliegend	4812.1	Fe-dolomite	17.78	29.45	4.06	0.01	0.02	1.76	0.00	53.08	0.83	0.99	0.11	0.00	0.00	0.05	0.00	1.98
11	NOR-A	Rotliegend	4812.1	dolomite	21.46	29.62	0.06	0.03	0.00	0.52	0.03	51.73	0.98	0.97	0.00	0.00	0.00	0.01	0.00	1.97
12	NOR-A	Rotliegend	4812.1	Fe-dolomite	17.76	29.00	3.65	0.00	0.00	1.99	0.08	52.49	0.83	0.97	0.10	0.00	0.00	0.05	0.00	1.95
13	NOR-A	Rotliegend	4812.1	Fe-dolomite	17.96	29.18	3.60	0.03	0.01	2.07	0.05	52.88	0.84	0.98	0.09	0.00	0.00	0.05	0.00	1.97
14	NOR-B	Rotliegend	5119.4	dolomite	20.71	29.71	0.00	0.00	0.00	0.69	0.05	51.17	0.94	0.97	0.00	0.00	0.00	0.02	0.00	1.93
15	NOR-B	Rotliegend	5119.4	dolomite	20.57	29.72	0.07	0.00	0.03	1.47	0.00	51.87	0.94	0.98	0.00	0.00	0.00	0.04	0.00	1.96
16	NOR-B	Rotliegend	5119.4	dolomite	20.65	29.72	0.08	0.00	0.00	1.54	0.02	52.01	0.95	0.98	0.00	0.00	0.00	0.04	0.00	1.97
17	NOR-B	Rotliegend	5119.4	dolomite	20.31	29.88	0.16	0.00	0.04	1.63	0.06	52.08	0.93	0.99	0.00	0.00	0.00	0.04	0.00	1.97
18	NOR-B	Rotliegend	5119.4	dolomite	20.66	29.67	0.08	0.00	0.05	1.51	0.03	52.00	0.95	0.98	0.00	0.00	0.00	0.04	0.00	1.97
19	NOR-B	Rotliegend	5119.4	dolomite	20.84	29.95	0.06	0.00	0.00	0.73	0.00	51.58	0.95	0.98	0.00	0.00	0.00	0.02	0.00	1.95
20	NOR-E	Triassic	5564.35	dolomite	20.60	31.09	0.19	0.02	0.00	0.88	0.04	52.81	0.95	1.03	0.01	0.00	0.00	0.02	0.00	2.01
21	NOR-E	Triassic	5564.35	dolomite	20.79	30.92	0.14	0.01	0.00	0.59	0.04	52.49	0.96	1.02	0.00	0.00	0.00	0.02	0.00	2.00
22	NOR-E	Triassic	5564.35	dolomite	19.71	31.75	0.73	0.00	0.00	0.76	0.02	52.97	0.91	1.06	0.02	0.00	0.00	0.02	0.00	2.01
23	NOR-E	Triassic	5564.35	dolomite	21.43	30.69	0.00	0.04	0.03	0.40	0.09	52.67	0.98	1.01	0.00	0.00	0.00	0.01	0.00	2.01
24	NOR-F	Jurassic	5135.6	ankerite	11.25	30.60	12.92	0.03	-	0.17	0.03	54.99	0.55	1.07	0.35	0.00	0.00	0.00	0.00	1.98
25	NOR-F	Jurassic	5135.6	ankerite	5.36	40.75	8.92	0.07	0.01	0.17	0.01	55.29	0.26	1.44	0.25	0.00	0.00	0.00	0.00	1.96
26	NOR-F	Jurassic	5135.6	calcite	1.13	52.51	2.60	0.03	0.04	0.16	0.03	56.50	0.06	1.88	0.07	0.00	0.00	0.00	0.00	2.02
27	NOR-F	Jurassic	5135.6	dolomite	21.45	29.73	0.29	0.00	-	0.38	0.02	51.86	0.98	0.98	0.01	0.00	0.00	0.01	0.00	1.97
28	NOR-F	Jurassic	5135.6	ankerite	9.78	31.31	14.55	-	0.05	0.25	0.01	55.95	0.48	1.11	0.40	0.00	0.00	0.01	0.00	2.01
29	NOR-F	Jurassic	5135.6	ankerite	9.36	30.00	16.78	0.05	0.01	0.25	0.08	56.53	0.47	1.08	0.47	0.00	0.00	0.01	0.00	2.02
30	NOR-F	Jurassic	5135.6	ankerite	8.22	29.24	16.05	0.06	0.04	0.19	0.28	54.08	0.40	1.03	0.44	0.00	0.00	0.01	0.01	1.88
31	NOR-F	Jurassic	5135.6	ankerite	9.06	29.72	16.62	0.03	0.03	0.26	0.05	55.77	0.45	1.06	0.46	0.00	0.00	0.01	0.00	1.98
32	NOR-F	Jurassic	5136.2	ankerite	10.72	32.26	12.28	0.00	0.02	0.15	0.02	55.45	0.52	1.14	0.34	0.00	0.00	0.00	0.00	2.00
33	NOR-F	Jurassic	5136.2	ankerite	10.41	32.89	12.51	0.01	0.03	0.12	0.00	55.97	0.51	1.16	0.35	0.00	0.00	0.00	0.00	2.03
34	NOR-F	Jurassic	5136.2	ankerite	10.09	32.59	12.94	0.00	0.05	0.19	0.00	55.87	0.50	1.15	0.36	0.00	0.00	0.01	0.00	2.02
35	NOR-F	Jurassic	5136.2	ankerite	8.51	28.93	16.20	0.03	0.05	0.23	2.86	56.82	0.42	1.03	0.45	0.00	0.00	0.01	0.09	2.00
36	NOR-F	Jurassic	5136.2	ankerite	9.04	32.61	13.73	0.04	0.00	0.21	0.01	55.65	0.45	1.16	0.38	0.00	0.00	0.01	0.00	1.99

Appendix 3.1: Table electron microprobe analyses of authigenic carbonates

no.	well	stratigraphy	sample	mineral	Chemical composition [wt%]								Ions in structural formula on the basis of 6 oxygen							
					MgO	CaO	FeO	SrO	BaO	MnO	SiO_2	total	Mg	Ca	Fe	Sr	Ba	Mn	Si	total
37	NOR-F	Jurassic	5136.2	ankerite	9.16	33.10	13.43	0.00	0.00	0.22	0.00	55.91	0.45	1.18	0.37	0.00	0.00	0.01	0.00	2.01
38	NOR-F	Jurassic	5136.2	ankerite	10.18	32.72	12.32	0.02	0.00	0.15	0.03	55.41	0.50	1.15	0.34	0.00	0.00	0.00	0.00	2.00
39	NOR-F	Jurassic	5136.2	ankerite	9.95	29.66	16.22	0.02	0.03	0.26	0.00	56.15	0.49	1.06	0.45	0.00	0.00	0.01	0.00	2.01
40	NOR-F	Jurassic	5136.2	ankerite	9.31	33.08	13.75	0.02	0.00	0.24	0.00	56.40	0.46	1.18	0.38	0.00	0.00	0.01	0.00	2.03
41	NOR-F	Jurassic	5136.2	ankerite	9.90	33.16	12.82	0.03	0.00	0.20	0.02	56.14	0.49	1.18	0.36	0.00	0.00	0.01	0.00	2.03
42	NOR-F	Jurassic	5136.2	ankerite	10.42	33.49	11.76	0.02	0.03	0.15	0.00	55.86	0.51	1.18	0.32	0.00	0.00	0.00	0.00	2.02
43	NOR-F	Jurassic	5136.2	ankerite	9.90	33.01	12.64	0.03	0.00	0.17	0.01	55.75	0.49	1.17	0.35	0.00	0.00	0.00	0.00	2.01
44	30/2c-4	Skagerrak Fm.	15604	dolomite	20.95	29.81	0.48	0.00	0.00	0.47	0.62	52.34	0.96	0.98	0.01	0.00	0.00	0.01	0.02	1.98
45	30/2c-4	Skagerrak Fm.	15604	dolomite	21.40	31.00	0.08	0.00	0.05	0.30	0.00	52.83	0.99	1.03	0.00	0.00	0.00	0.01	0.00	2.02
46	30/2c-4	Skagerrak Fm.	15654.5	dolomite	21.56	30.65	0.18	0.05	-	0.40	0.00	52.83	0.99	1.01	0.00	0.00	0.00	0.01	0.00	2.02
47	30/2c-4	Skagerrak Fm.	15654.5	dolomite	20.90	31.31	0.07	0.02	-	0.53	0.01	52.83	0.96	1.04	0.00	0.00	0.00	0.01	0.00	2.02
48	30/2c-4	Skagerrak Fm.	15654.5	ankerite	5.93	30.03	16.70	0.02	0.05	4.55	0.04	57.31	0.30	1.10	0.48	0.00	0.00	0.13	0.00	2.01
49	30/2c-4	Skagerrak Fm.	15654.5	ankerite	11.36	30.64	12.15	0.15	-	1.02	0.00	55.32	0.56	1.08	0.33	0.00	0.00	0.03	0.00	2.00
50	30/2c-4	Skagerrak Fm.	15654.5	ankerite	11.76	29.74	13.25	0.18	0.03	1.05	0.00	56.01	0.58	1.05	0.37	0.00	0.00	0.03	0.00	2.03
51	30/2c-4	Skagerrak Fm.	15680	ankerite	9.71	29.59	15.88	0.14	0.02	1.24	0.19	56.76	0.48	1.06	0.45	0.00	0.00	0.04	0.01	2.04
52	30/2c-4	Skagerrak Fm.	15680	ankerite	11.65	29.19	14.01	0.16	0.00	1.25	0.03	56.29	0.58	1.04	0.39	0.00	0.00	0.04	0.00	2.04
53	30/2c-4	Skagerrak Fm.	15680	dolomite	21.48	30.41	0.09	0.01	0.00	0.37	0.03	52.40	0.99	1.00	0.00	0.00	0.00	0.01	0.00	2.00
54	30/2c-4	Skagerrak Fm.	15680	dolomite	21.64	30.42	0.09	0.00	0.00	0.37	0.01	52.53	0.99	1.00	0.00	0.00	0.00	0.01	0.00	2.01
55	30/2c-4	Skagerrak Fm.	15715	dolomite	21.48	30.62	0.05	0.00	0.01	0.32	0.01	52.48	0.99	1.01	0.00	0.00	0.00	0.01	0.00	2.01
56	30/2c-4	Skagerrak Fm.	15715	dolomite	21.41	30.62	0.01	0.00	0.02	0.38	0.01	52.47	0.98	1.01	0.00	0.00	0.00	0.01	0.00	2.00
57	30/2c-4	Skagerrak Fm.	15715	dolomite	21.34	30.14	0.04	0.00	0.00	0.62	0.01	52.15	0.98	0.99	0.00	0.00	0.00	0.02	0.00	1.99
58	30/2c-4	Skagerrak Fm.	15715	dolomite	20.84	30.30	0.15	0.00	0.01	1.08	0.04	52.42	0.96	1.00	0.00	0.00	0.00	0.03	0.00	1.99
59	30/2c-4	Skagerrak Fm.	15715	dolomite	20.85	29.71	0.09	0.01	0.02	1.35	0.04	52.08	0.96	0.98	0.00	0.00	0.00	0.04	0.00	1.97
60	30/2c-4	Skagerrak Fm.	15715	dolomite	20.14	28.83	0.06	0.03	0.00	3.11	0.01	52.18	0.93	0.95	0.00	0.00	0.00	0.08	0.00	1.97
61	30/2c-4	Skagerrak Fm.	15715	dolomite	21.22	30.15	0.06	0.01	0.03	0.97	0.05	52.48	0.97	1.00	0.00	0.00	0.00	0.03	0.00	2.00
62	30/2c-4	Skagerrak Fm.	15715	ankerite	12.32	28.51	12.09	0.14	0.00	2.10	0.01	55.17	0.60	1.00	0.33	0.00	0.00	0.06	0.00	1.99
63	30/2c-4	Skagerrak Fm.	15715	ankerite	10.96	28.82	13.04	0.13	0.03	2.56	0.01	55.56	0.54	1.02	0.36	0.00	0.00	0.07	0.00	1.99
64	30/2c-4	Skagerrak Fm.	15715	dolomite	20.72	29.84	0.01	0.02	0.01	1.52	0.01	52.13	0.95	0.98	0.00	0.00	0.00	0.04	0.00	1.98
65	30/2c-4	Skagerrak Fm.	15715	dolomite	20.16	29.65	0.05	0.02	0.00	2.63	0.00	52.52	0.93	0.98	0.00	0.00	0.00	0.07	0.00	1.99
66	30/2c-4	Skagerrak Fm.	15715	dolomite	21.44	29.67	0.05	0.00	0.02	1.23	0.00	52.41	0.98	0.98	0.00	0.00	0.00	0.03	0.00	2.00
67	30/2c-4	Skagerrak Fm.	15715	ankerite	11.79	29.65	11.66	0.08	0.00	2.10	0.05	55.33	0.58	1.04	0.32	0.00	0.00	0.06	0.00	2.00
68	30/2c-4	Skagerrak Fm.	15715	dolomite	21.65	30.40	0.00	0.02	0.00	0.45	0.02	52.55	0.99	1.00	0.00	0.00	0.00	0.01	0.00	2.01
69	30/2c-4	Skagerrak Fm.	15715	dolomite	21.47	30.48	0.06	0.03	0.00	1.14	0.15	53.33	0.99	1.01	0.00	0.00	0.00	0.03	0.00	2.04
70	30/2c-4	Skagerrak Fm.	15715	dolomite	21.33	30.47	0.05	0.01	0.00	0.46	0.00	52.32	0.98	1.00	0.00	0.00	0.00	0.01	0.00	2.00
71	30/2c-4	Skagerrak Fm.	15715	dolomite	21.34	30.93	0.01	0.01	0.00	0.34	0.02	52.64	0.98	1.02	0.00	0.00	0.00	0.01	0.00	2.01
72	30/2c-4	Skagerrak Fm.	15715	dolomite	20.49	29.89	0.47	0.02	0.00	0.39	1.86	53.11	0.94	0.99	0.01	0.00	0.00	0.01	0.06	2.00
73	30/2c-4	Skagerrak Fm.	15715	ankerite	10.79	28.96	13.06	0.12	0.00	2.63	0.03	55.59	0.53	1.02	0.36	0.00	0.00	0.07	0.00	1.99

Appendix 3.1: Table electron microprobe analyses of authigenic carbonates

no.	well	stratigraphy	sample	mineral	Chemical composition [wt%]								Ions in structural formula on the basis of 6 oxygen							
					MgO	CaO	FeO	SrO	BaO	MnO	SiO_2	total	Mg	Ca	Fe	Sr	Ba	Mn	Si	total
74	30/2c-4	Skagerrak Fm.	15715	dolomite	21.24	28.65	0.07	0.03	0.00	1.51	0.02	51.54	0.97	0.94	0.00	0.00	0.00	0.04	0.00	1.95
75	30/2c-4	Skagerrak Fm.	15715	dolomite	19.89	32.29	0.05	0.05	0.00	0.35	0.03	52.65	0.92	1.07	0.00	0.00	0.00	0.01	0.00	2.00
76	30/2c-4	Skagerrak Fm.	15715	ankerite	10.59	29.66	13.24	0.15	0.02	2.42	0.06	56.14	0.52	1.06	0.37	0.00	0.00	0.07	0.00	2.02
77	30/2c-4	Skagerrak Fm.	15715	dolomite	21.02	30.10	0.13	0.00	0.00	1.12	0.08	52.45	0.97	0.99	0.00	0.00	0.00	0.03	0.00	2.00
78	30/2c-4	Skagerrak Fm.	15715	dolomite	21.42	31.13	0.11	0.01	0.00	0.42	0.02	53.11	0.99	1.03	0.00	0.00	0.00	0.01	0.00	2.04
79	30/2c-4	Skagerrak Fm.	15715	dolomite	20.57	30.19	0.06	0.00	0.00	1.34	0.02	52.18	0.94	1.00	0.00	0.00	0.00	0.04	0.00	1.98
80	30/2c-4	Skagerrak Fm.	15715	ankerite	10.12	29.57	13.51	0.13	0.00	2.70	0.00	56.04	0.50	1.05	0.38	0.00	0.00	0.08	0.00	2.01
81	30/2c-4	Skagerrak Fm.	15715	ankerite	11.63	29.15	12.45	0.12	0.02	2.45	0.00	55.83	0.57	1.03	0.34	0.00	0.00	0.07	0.00	2.02
82	30/2c-4	Skagerrak Fm.	15715	dolomite	20.60	30.64	0.08	0.01	0.00	0.92	0.00	52.25	0.95	1.01	0.00	0.00	0.00	0.02	0.00	1.98
83	30/2c-4	Skagerrak Fm.	15715	dolomite	21.55	31.18	0.05	0.03	0.00	0.37	0.01	53.19	0.99	1.03	0.00	0.00	0.00	0.01	0.00	2.04
84	30/2c-4	Skagerrak Fm.	15715	dolomite	20.89	30.33	0.01	0.00	0.05	1.46	0.04	52.78	0.96	1.01	0.00	0.00	0.00	0.04	0.00	2.01
85	30/2c-4	Skagerrak Fm.	15715	dolomite	20.50	30.35	0.00	0.00	0.00	1.39	0.00	52.24	0.94	1.00	0.00	0.00	0.00	0.04	0.00	1.98
86	30/2c-4	Skagerrak Fm.	15715	dolomite	20.15	30.92	0.10	0.01	0.00	0.84	0.01	52.02	0.92	1.02	0.01	0.00	0.00	0.02	0.00	1.97
87	30/2c-4	Skagerrak Fm.	15747	dolomite	20.89	30.67	0.17	0.03	0.00	0.37	0.06	52.19	0.96	1.01	0.00	0.00	0.00	0.01	0.00	1.98
88	30/2c-4	Skagerrak Fm.	15747	dolomite	21.28	30.09	0.04	0.03	0.02	0.78	0.03	52.28	0.98	0.99	0.00	0.00	0.00	0.02	0.00	1.99
89	30/2c-4	Skagerrak Fm.	15747	dolomite	21.86	30.48	0.07	0.00	0.00	0.44	0.10	52.96	1.01	1.01	0.00	0.00	0.00	0.01	0.00	2.03
90	30/2c-4	Skagerrak Fm.	15768.5	Mg-siderite	4.75	0.08	54.01	-	0.03	1.09	0.02	59.98	0.26	0.00	1.67	0.00	0.00	0.03	0.00	1.97
91	30/2c-4	Skagerrak Fm.	15768.5	Mg-siderite	5.18	0.11	53.80	-	0.01	0.96	0.01	60.07	0.28	0.00	1.66	0.00	0.00	0.03	0.00	1.98
92	30/2c-4	Skagerrak Fm.	15768.5	Mg-siderite	4.48	0.04	53.77	0.03	-	1.18	0.42	59.92	0.25	0.00	1.66	0.00	0.00	0.04	0.02	1.96
93	30/2c-4	Skagerrak Fm.	15768.5	Mg-siderite	5.01	0.75	52.39	0.04	0.01	1.21	0.58	59.98	0.27	0.03	1.61	0.00	0.00	0.04	0.02	1.97
94	30/7a-9	Skagerrak Fm.	12099.5	calcite	0.05	56.52	0.16	0.03	-	0.54	0.12	57.42	0.00	2.04	0.00	0.00	0.00	0.02	0.00	2.07
95	30/7a-9	Skagerrak Fm.	12099.5	calcite	0.13	56.47	0.23	0.03	-	0.46	0.05	57.36	0.01	2.04	0.01	0.00	0.00	0.01	0.00	2.07
96	30/7a-9	Skagerrak Fm.	12099.5	dolomite	21.61	31.02	0.15	0.02	-	0.00	0.00	52.80	0.99	1.03	0.00	0.00	0.00	0.00	0.00	2.02
97	30/7a-9	Skagerrak Fm.	12099.5	dolomite	21.59	31.07	0.11	0.01	-	0.01	0.00	52.80	0.99	1.03	0.00	0.00	0.00	0.00	0.00	2.02
98	30/7a-9	Skagerrak Fm.	12099.5	Fe-dolomite	17.33	30.52	3.20	0.00	-	0.82	0.17	52.04	0.80	1.02	0.08	0.00	0.00	0.02	0.01	1.93
99	30/7a-9	Skagerrak Fm.	12099.5	Fe-dolomite	19.43	30.36	2.17	0.04	-	0.83	0.04	52.87	0.90	1.01	0.06	0.00	0.00	0.02	0.00	1.99
100	30/7a-9	Skagerrak Fm.	12099.5	Fe-dolomite	18.94	31.00	3.11	0.04	-	0.44	0.07	53.60	0.89	1.04	0.08	0.00	0.00	0.01	0.00	2.02
101	30/7a-9	Skagerrak Fm.	12099.5	calcite	0.12	55.33	0.24	0.02	-	0.47	0.03	56.21	0.01	1.98	0.01	0.00	0.00	0.01	0.00	2.01
102	30/7a-9	Skagerrak Fm.	12099.5	dolomite	19.65	30.36	1.22	0.04	-	0.32	0.49	52.07	0.90	1.00	0.03	0.00	0.00	0.01	0.01	1.96
103	30/7a-9	Skagerrak Fm.	12099.5	dolomite	20.45	29.21	1.32	0.04	-	0.22	0.99	52.22	0.94	0.96	0.03	0.00	0.00	0.01	0.03	1.97
104	30/7a-9	Skagerrak Fm.	12099.5	Fe-dolomite	19.30	29.60	1.86	0.04	-	0.36	1.27	52.43	0.89	0.98	0.05	0.00	0.00	0.01	0.04	1.96
105	30/7a-9	Skagerrak Fm.	12099.5	Fe-dolomite	19.86	29.42	1.85	0.04	-	0.54	0.80	52.51	0.91	0.97	0.05	0.00	0.00	0.01	0.02	1.97
106	30/7a-9	Skagerrak Fm.	12099.5	Fe-dolomite	16.15	28.56	5.12	0.03	-	2.04	1.35	53.23	0.76	0.96	0.13	0.00	0.00	0.05	0.04	1.95
107	30/7a-9	Skagerrak Fm.	12099.5	Fe-dolomite	17.96	30.02	3.09	0.03	-	1.12	0.80	53.02	0.84	1.00	0.08	0.00	0.00	0.03	0.02	1.97
108	30/7a-9	Skagerrak Fm.	12099.5	Fe-dolomite	18.37	29.46	2.77	0.02	-	1.29	0.95	52.86	0.85	0.98	0.07	0.00	0.00	0.03	0.03	1.97
109	30/7a-9	Skagerrak Fm.	12099.5	Fe-dolomite	17.30	30.09	4.03	0.01	-	1.03	0.54	53.00	0.81	1.01	0.11	0.00	0.00	0.03	0.02	1.97

Appendix 3.2: Table electron microprobe data of feldspars

no.	well	stratigraphy	sample	mineral	Chemical composition [wt%]											
					SiO_2	Al_2O_3	Na_2O	K_2O	CaO	SrO	FeO	MgO	TiO_2	MnO	BaO	total
110	NOR-A	Rotliegend	4808.8	detrital albite	67.22	18.71	11.52	0.10	0.07	0.01	0.02	0.00	0.03	0.00	0.00	97.68
111	NOR-A	Rotliegend	4808.8	detrital albite	67.43	19.10	11.33	0.05	0.28	0.07	0.02	0.00	0.02	0.00	0.02	98.32
112	NOR-A	Rotliegend	4808.8	detrital albite	66.91	19.21	11.57	0.04	0.15	0.00	0.05	0.00	0.01	0.02	0.00	97.97
113	NOR-A	Rotliegend	4808.8	detrital K-feldspar	62.85	17.75	0.40	15.83	0.00	0.12	0.06	0.03	0.00	0.00	0.42	97.46
114	NOR-A	Rotliegend	4808.8	detrital K-feldspar	62.85	18.05	0.73	15.17	0.03	0.04	0.07	0.01	0.01	0.01	0.16	97.13
115	NOR-A	Rotliegend	4808.8	detrital K-feldspar	63.24	18.01	1.22	14.51	0.02	0.04	0.04	0.00	0.02	0.01	0.35	97.46
116	NOR-A	Rotliegend	4808.8	detrital K-feldspar	62.54	18.06	0.37	15.64	0.00	0.00	0.04	0.01	0.00	0.01	0.78	97.46
117	NOR-A	Rotliegend	4808.8	detrital K-feldspar	62.40	18.34	0.63	15.78	0.00	0.00	0.04	0.00	0.01	0.00	0.00	97.20
118	NOR-A	Rotliegend	4808.8	detrital K-feldspar	63.28	17.94	0.78	15.41	0.02	0.00	0.00	0.00	0.00	0.00	0.24	97.67
119	NOR-A	Rotliegend	4808.8	authigenic albite	67.29	18.73	11.87	0.07	0.00	0.00	0.04	0.00	0.00	0.00	0.03	98.03
120	NOR-A	Rotliegend	4812.1	authigenic albite	67.82	18.58	12.09	0.10	0.08	0.07	0.04	0.00	0.04	0.00	0.00	98.82
121	NOR-A	Rotliegend	4812.1	detrital K-feldspar	58.49	14.87	0.41	15.54	0.06	0.03	0.03	0.03	0.00	0.03	0.03	89.52
122	NOR-A	Rotliegend	4812.1	detrital K-feldspar	63.88	17.95	0.91	15.22	0.01	0.06	0.03	0.00	0.03	0.02	0.26	98.38
123	NOR-A	Rotliegend	4812.1	detrital K-feldspar	64.23	17.95	0.63	15.82	0.00	0.00	0.04	0.00	0.01	0.00	0.51	99.19
124	NOR-A	Rotliegend	4812.1	detrital K-feldspar	63.52	17.94	0.59	15.81	0.00	0.07	0.00	0.02	0.00	0.02	0.09	98.05
125	NOR-A	Rotliegend	4812.1	detrital K-feldspar	64.06	17.60	0.43	16.29	0.00	0.02	0.00	0.00	0.01	0.00	0.13	98.54
126	NOR-A	Rotliegend	4812.1	detrital K-feldspar	63.86	18.13	1.30	14.84	0.01	0.00	0.00	0.00	0.00	0.02	0.19	98.34
127	NOR-A	Rotliegend	4812.1	authigenic albite	67.74	18.64	11.63	0.18	0.04	0.01	0.00	0.02	0.01	0.03	0.00	98.30
128	NOR-A	Rotliegend	4812.1	detrital albite	67.72	18.85	11.96	0.13	0.05	0.04	0.00	0.01	0.00	0.03	0.00	98.79
129	NOR-A	Rotliegend	4812.1	detrital albite	66.44	19.36	11.42	0.09	0.58	0.00	0.00	0.01	0.01	0.00	0.05	97.97
130	NOR-A	Rotliegend	4812.1	detrital albite	67.00	19.04	11.88	0.04	0.01	0.00	0.00	0.00	0.02	0.00	0.00	98.00
131	NOR-A	Rotliegend	4812.1	detrital albite	67.96	18.37	11.91	0.08	0.02	0.00	0.04	0.01	0.00	0.02	0.01	98.41
132	NOR-A	Rotliegend	4812.1	detrital albite	67.21	18.85	11.64	0.59	0.07	0.00	0.06	0.04	0.02	0.04	0.03	98.55
133	NOR-A	Rotliegend	4812.1	detrital albite	66.85	19.45	11.71	0.06	0.55	0.02	0.01	0.00	0.01	0.01	0.00	98.68
134	NOR-A	Rotliegend	4812.1	albite	66.11	19.01	11.38	0.44	0.07	0.00	0.09	0.09	0.02	0.00	0.00	97.22
135	NOR-E	Triassic	5564.35	detrital K-feldspar	62.46	18.28	0.69	15.22	0.00	0.04	0.02	0.00	0.01	0.01	0.91	97.63
136	NOR-E	Triassic	5564.35	detrital K-feldspar (Perthite)	62.80	18.14	0.70	14.98	0.02	0.01	0.00	0.00	0.03	0.03	0.83	97.54
137	NOR-E	Triassic	5564.35	albite lamellae in no. 136	66.39	18.15	10.59	1.98	0.12	0.06	0.24	0.14	0.03	0.00	0.00	97.70
138	NOR-E	Triassic	5564.35	detrital albite	66.14	19.41	11.26	0.25	0.79	0.00	0.02	0.03	0.00	0.01	0.00	97.90
139	NOR-E	Triassic	5564.35	detrital K-feldspar	62.34	18.07	0.45	15.45	0.00	0.06	0.12	0.00	0.00	0.00	0.36	96.85
140	NOR-E	Triassic	5564.35	detrital K-feldspar	62.66	18.07	0.40	15.77	0.00	0.00	0.10	0.02	0.00	0.00	0.02	97.04
141	NOR-E	Triassic	5564.35	detrital K-feldspar	63.90	18.06	0.54	15.80	0.00	0.03	0.02	0.00	0.03	0.00	0.15	98.54
142	NOR-F	Jurassic	5135.6	detrital albite	66.55	20.06	11.66	0.08	0.32	0.03	0.23	0.03	-	-	0.09	99.05
143	NOR-F	Jurassic	5135.6	detrital albite	67.65	19.80	11.03	0.10	0.53	-	0.38	0.13	-	-	-	99.62
144	NOR-F	Jurassic	5135.6	detrital albite	68.02	19.90	11.55	0.10	0.29	0.03	0.07	0.02	-	-	-	99.98
145	NOR-F	Jurassic	5135.6	detrital albite	66.93	19.97	11.57	0.09	0.22	0.01	0.13	-	-	-	0.02	98.94

Appendix 3.2: Table electron microprobe data of feldspars

no.	well	stratigraphy	sample	mineral	Ions in structural formula on the basis of 24 oxygen											
					Si	Al	Na	K	Ca	Sr	Fe	Mg	Ti	Mn	Ba	total at
110	NOR-A	Rotliegend	4808.8	detrital albite	9.02	2.96	3.00	0.02	0.01	0.00	0.00	0.00	0.00	0.00	0.00	15.01
111	NOR-A	Rotliegend	4808.8	detrital albite	8.99	3.00	2.93	0.01	0.04	0.01	0.00	0.00	0.00	0.00	0.00	14.98
112	NOR-A	Rotliegend	4808.8	detrital albite	8.96	3.03	3.00	0.01	0.02	0.00	0.01	0.00	0.00	0.00	0.00	15.03
113	NOR-A	Rotliegend	4808.8	detrital K-feldspar	8.98	2.99	0.11	2.89	0.00	0.01	0.01	0.01	0.00	0.00	0.02	15.02
114	NOR-A	Rotliegend	4808.8	detrital K-feldspar	8.97	3.04	0.20	2.76	0.00	0.00	0.01	0.00	0.00	0.00	0.01	14.99
115	NOR-A	Rotliegend	4808.8	detrital K-feldspar	8.98	3.01	0.33	2.63	0.00	0.00	0.01	0.00	0.00	0.00	0.02	14.99
116	NOR-A	Rotliegend	4808.8	detrital K-feldspar	8.95	3.05	0.10	2.86	0.00	0.00	0.01	0.00	0.00	0.00	0.04	15.01
117	NOR-A	Rotliegend	4808.8	detrital K-feldspar	8.92	3.09	0.17	2.88	0.00	0.00	0.01	0.00	0.00	0.00	0.00	15.06
118	NOR-A	Rotliegend	4808.8	detrital K-feldspar	8.99	3.00	0.21	2.79	0.00	0.00	0.00	0.00	0.00	0.00	0.01	15.01
119	NOR-A	Rotliegend	4808.8	authigenic albite	9.01	2.96	3.08	0.01	0.00	0.00	0.00	0.00	0.00	0.00	0.00	15.06
120	NOR-A	Rotliegend	4812.1	authigenic albite	9.02	2.91	3.12	0.02	0.01	0.01	0.00	0.00	0.00	0.00	0.00	15.09
121	NOR-A	Rotliegend	4812.1	detrital K-feldspar	9.13	2.74	0.12	3.10	0.01	0.00	0.00	0.01	0.00	0.00	0.00	15.11
122	NOR-A	Rotliegend	4812.1	detrital K-feldspar	9.00	2.98	0.25	2.74	0.00	0.01	0.00	0.00	0.00	0.00	0.01	15.00
123	NOR-A	Rotliegend	4812.1	detrital K-feldspar	9.01	2.97	0.17	2.83	0.00	0.00	0.00	0.00	0.00	0.00	0.03	15.01
124	NOR-A	Rotliegend	4812.1	detrital K-feldspar	8.99	2.99	0.16	2.86	0.00	0.01	0.00	0.00	0.00	0.00	0.00	15.02
125	NOR-A	Rotliegend	4812.1	detrital K-feldspar	9.04	2.93	0.12	2.93	0.00	0.00	0.00	0.00	0.00	0.00	0.01	15.02
126	NOR-A	Rotliegend	4812.1	detrital K-feldspar	8.98	3.01	0.35	2.66	0.00	0.00	0.00	0.00	0.00	0.00	0.01	15.02
127	NOR-A	Rotliegend	4812.1	authigenic albite	9.04	2.93	3.01	0.03	0.01	0.00	0.00	0.00	0.00	0.00	0.00	15.02
128	NOR-A	Rotliegend	4812.1	detrital albite	9.00	2.95	3.08	0.02	0.01	0.00	0.00	0.00	0.00	0.00	0.00	15.07
129	NOR-A	Rotliegend	4812.1	detrital albite	8.91	3.06	2.97	0.02	0.08	0.00	0.00	0.00	0.00	0.00	0.00	15.05
130	NOR-A	Rotliegend	4812.1	detrital albite	8.97	3.01	3.08	0.01	0.00	0.00	0.00	0.00	0.00	0.00	0.00	15.07
131	NOR-A	Rotliegend	4812.1	detrital albite	9.06	2.89	3.08	0.01	0.00	0.00	0.00	0.00	0.00	0.00	0.00	15.05
132	NOR-A	Rotliegend	4812.1	detrital albite	8.98	2.97	3.02	0.10	0.01	0.00	0.01	0.01	0.00	0.00	0.00	15.09
133	NOR-A	Rotliegend	4812.1	detrital albite	8.91	3.05	3.03	0.01	0.08	0.00	0.00	0.00	0.00	0.00	0.00	15.08
134	NOR-A	Rotliegend	4812.1	albite	8.94	3.03	2.99	0.08	0.01	0.00	0.01	0.02	0.00	0.00	0.00	15.07
135	NOR-E	Triassic	5564.35	detrital K-feldspar	8.92	3.08	0.19	2.77	0.00	0.00	0.00	0.00	0.00	0.00	0.05	15.02
136	NOR-E	Triassic	5564.35	detrital K-feldspar (Perthite)	8.95	3.05	0.19	2.73	0.00	0.00	0.00	0.00	0.00	0.00	0.05	14.98
137	NOR-E	Triassic	5564.35	albite lamellae in no. 136	9.00	2.90	2.78	0.34	0.02	0.00	0.03	0.03	0.00	0.00	0.00	15.11
138	NOR-E	Triassic	5564.35	detrital albite	8.89	3.08	2.94	0.04	0.11	0.00	0.00	0.01	0.00	0.00	0.00	15.06
139	NOR-E	Triassic	5564.35	detrital K-feldspar	8.95	3.06	0.12	2.83	0.00	0.01	0.01	0.00	0.00	0.00	0.02	15.00
140	NOR-E	Triassic	5564.35	detrital K-feldspar	8.96	3.05	0.11	2.88	0.00	0.00	0.01	0.00	0.00	0.00	0.00	15.01
141	NOR-E	Triassic	5564.35	detrital K-feldspar	9.00	3.00	0.15	2.84	0.00	0.00	0.00	0.00	0.00	0.00	0.01	15.00
142	NOR-F	Jurassic	5135.6	detrital albite	8.85	3.14	3.01	0.01	0.05	0.00	0.03	0.01	0.00	0.00	0.00	15.09
143	NOR-F	Jurassic	5135.6	detrital albite	8.91	3.08	2.82	0.02	0.08	0.00	0.04	0.03	0.00	0.00	0.00	14.97
144	NOR-F	Jurassic	5135.6	detrital albite	8.93	3.08	2.94	0.02	0.04	0.00	0.01	0.00	0.00	0.00	0.00	15.01
145	NOR-F	Jurassic	5135.6	detrital albite	8.88	3.13	2.98	0.02	0.03	0.00	0.01	0.00	0.00	0.00	0.00	15.05

Appendix 3.2: Table electron microprobe data of feldspars

no.	well	stratigraphy	sample	mineral	Chemical composition [wt%]											
					SiO_2	Al_2O_3	Na_2O	K_2O	CaO	SrO	FeO	MgO	TiO_2	MnO	BaO	total
146	NOR-F	Jurassic	5136.2	detrital plagioclase	64.03	20.97	10.24	0.17	2.75	0.08	0.12	0.01	0.02	0.04	0.00	98.43
147	NOR-F	Jurassic	5136.2	detrital albite	67.30	19.00	12.03	0.05	0.05	0.00	0.07	0.00	0.02	0.03	0.04	98.59
148	NOR-F	Jurassic	5136.2	detrital albite	66.25	19.11	11.86	0.17	0.05	0.07	0.09	0.00	0.00	0.00	0.00	97.59
149	NOR-F	Jurassic	5136.2	detrital albite	67.35	19.24	11.89	0.20	0.45	0.03	0.05	0.00	0.00	0.01	0.01	99.22
150	NOR-F	Jurassic	5136.2	detrital albite	67.30	19.01	12.23	0.02	0.08	0.00	0.04	0.01	0.00	0.02	0.01	98.71
151	NOR-F	Jurassic	5136.2	authigenic albite with traces of chlorite	64.93	18.93	11.61	0.02	0.03	0.00	1.94	0.33	0.01	0.00	0.00	97.80
152	NOR-F	Jurassic	5136.2	detrial albite	68.02	18.73	12.07	0.02	0.18	0.00	0.11	0.01	0.00	0.00	0.00	99.14
153	NOR-F	Jurassic	5136.2	detrital albite	67.60	19.57	11.75	0.05	0.08	0.00	0.05	0.01	0.00	0.00	0.01	99.13
154	NOR-F	Jurassic	5136.2	detrital albite	67.28	19.85	11.95	0.06	0.18	0.00	0.10	0.02	0.00	0.00	0.00	99.43
155	NOR-F	Jurassic	5136.2	detrital albite	67.69	19.48	11.92	0.05	0.19	0.04	0.10	0.02	0.01	0.00	0.00	99.49
156	NOR-F	Jurassic	5136.2	detrital albite	69.09	19.64	11.89	0.02	0.03	0.01	0.08	0.01	0.02	0.00	0.00	100.79
157	NOR-C	Skagerrak Fm.	4589.6	detrital plagioclase	65.41	20.04	10.89	0.07	1.43	0.00	0.07	0.01	0.00	0.02	0.05	97.99
158	NOR-C	Skagerrak Fm.	4589.6	detrital K-feldspar	61.40	17.92	0.59	15.47	0.00	0.13	0.09	0.00	0.00	0.00	0.36	95.95
159	NOR-C	Skagerrak Fm.	4589.6	detrital albite	67.35	19.05	11.88	0.06	0.03	0.00	0.03	0.00	0.00	0.01	0.08	98.49
160	NOR-C	Skagerrak Fm.	4589.6	detrital K-feldspar	62.90	18.44	0.88	14.77	0.00	0.12	0.01	0.00	0.00	0.01	0.91	98.04
161	NOR-C	Skagerrak Fm.	4589.6	detrital albite	65.37	19.13	11.74	0.07	0.26	0.02	0.02	0.00	0.02	0.00	0.03	96.66
162	NOR-C	Skagerrak Fm.	4589.6	detrital albite	66.21	19.37	11.61	0.09	0.45	0.07	0.08	0.00	0.00	0.00	0.07	97.95
163	30/2c-4	Skagerrak Fm.	15604	detrital plagioclase	67.57	19.50	11.70	0.11	0.32	0.07	0.02	0.01	0.00	0.03	0.00	99.32
164	30/2c-4	Skagerrak Fm.	15604	authigenic K-feldspar	63.66	18.15	0.04	16.24	0.00	0.01	0.05	0.01	0.00	0.00	0.02	98.19
165	30/2c-4	Skagerrak Fm.	15613	detrital K-feldspar	63.55	17.88	0.06	16.69	0.00	0.01	0.00	0.01	0.05	0.00	0.02	98.26
166	30/2c-4	Skagerrak Fm.	15613	detrital K-feldspar	63.88	18.29	0.05	16.76	0.00	0.00	0.05	0.01	0.00	0.04	0.05	99.13
167	30/2c-4	Skagerrak Fm.	15613	detrital K-feldspar	63.46	18.05	0.06	17.28	0.00	0.00	0.03	0.00	0.05	0.02	0.00	98.94
168	30/2c-4	Skagerrak Fm.	15613	detrital K-feldspar	63.12	18.61	1.27	14.69	0.19	0.17	0.10	0.01	0.00	0.03	0.76	98.95
169	30/2c-4	Skagerrak Fm.	15613	albite patches in no. 173	66.42	20.33	10.76	0.33	1.10	0.11	0.09	0.00	0.00	0.00	0.05	99.18
170	30/2c-4	Skagerrak Fm.	15613	detrital K-feldspar (Perthite)	63.72	18.71	1.31	15.04	0.00	0.11	0.03	0.00	0.00	0.00	0.54	99.47
171	30/2c-4	Skagerrak Fm.	15613	detrital K-feldspar (Perthite)	64.08	18.03	0.05	16.75	0.00	0.00	0.00	0.00	0.03	0.00	0.06	99.00
172	30/2c-4	Skagerrak Fm.	15613	detrital K-feldspar	63.48	18.16	0.03	16.82	0.00	0.00	0.02	0.00	0.00	0.00	0.02	98.53
173	30/2c-4	Skagerrak Fm.	15613	detrital K-feldspar	63.57	18.37	0.64	15.29	0.00	0.01	0.00	0.00	0.02	0.00	0.23	98.13
174	30/2c-4	Skagerrak Fm.	15613	authigenic K-feldspar	63.23	18.00	0.05	16.65	0.00	0.00	0.00	0.00	0.00	0.00	0.03	97.96
175	30/2c-4	Skagerrak Fm.	15613	detrital K-feldspar	63.07	18.06	0.02	16.41	0.00	0.00	0.02	0.00	0.00	0.00	0.00	97.58
176	30/2c-4	Skagerrak Fm.	15616	detrital albite	67.40	19.80	11.58	0.25	0.08	-	-	-	-	0.01	0.01	99.13
177	30/2c-4	Skagerrak Fm.	15616	detrital K-feldspar	63.98	18.81	0.51	15.94	-	-	0.02	0.01	-	-	0.32	99.59
178	30/2c-4	Skagerrak Fm.	15616	detrital K-feldspar	63.36	19.05	1.22	14.37	0.02	0.15	0.01	-	-	-	1.33	99.51
179	30/2c-4	Skagerrak Fm.	15616	detrital K-feldspar	63.64	19.06	0.55	15.76	-	-	0.03	-	0.02	0.01	0.11	99.18
180	30/2c-4	Skagerrak Fm.	15616	detrital albite	67.56	19.71	11.90	0.02	0.04	-	-	-	0.01	-	0.04	99.28
181	30/2c-4	Skagerrak Fm.	15616	authigenic albite	68.31	19.65	11.57	0.05	0.02	-	-	0.02	0.02	0.01	-	99.66
182	30/2c-4	Skagerrak Fm.	15616	detrital K-feldspar	64.06	18.96	0.74	15.64	-	0.12	0.04	0.01	-	0.03	0.43	100.03

Appendix 3.2: Table electron microprobe data of feldspars

no.	well	stratigraphy	sample	mineral	Ions in structural formula on the basis of 24 oxygen											
					Si	Al	Na	K	Ca	Sr	Fe	Mg	Ti	Mn	Ba	total at
146	NOR-F	Jurassic	5136.2	detrital plagioclase	8.62	3.33	2.67	0.03	0.40	0.01	0.01	0.00	0.00	0.00	0.00	15.07
147	NOR-F	Jurassic	5136.2	detrital albite	8.97	2.98	3.11	0.01	0.01	0.00	0.01	0.00	0.00	0.00	0.00	15.10
148	NOR-F	Jurassic	5136.2	detrital albite	8.93	3.04	3.10	0.03	0.01	0.01	0.01	0.00	0.00	0.00	0.00	15.12
149	NOR-F	Jurassic	5136.2	detrital albite	8.93	3.01	3.06	0.03	0.06	0.00	0.01	0.00	0.00	0.00	0.00	15.11
150	NOR-F	Jurassic	5136.2	detrital albite	8.96	2.98	3.16	0.00	0.01	0.00	0.00	0.00	0.00	0.00	0.00	15.12
151	NOR-F	Jurassic	5136.2	authigenic albite with traces of chlorite	8.82	3.03	3.06	0.00	0.01	0.00	0.22	0.07	0.00	0.00	0.00	15.20
152	NOR-F	Jurassic	5136.2	detrial albite	9.01	2.93	3.10	0.00	0.03	0.00	0.01	0.00	0.00	0.00	0.00	15.08
153	NOR-F	Jurassic	5136.2	detrital albite	8.95	3.05	3.02	0.01	0.01	0.00	0.01	0.00	0.00	0.00	0.00	15.04
154	NOR-F	Jurassic	5136.2	detrital albite	8.89	3.09	3.06	0.01	0.03	0.00	0.01	0.00	0.00	0.00	0.00	15.10
155	NOR-F	Jurassic	5136.2	detrital albite	8.94	3.03	3.05	0.01	0.03	0.00	0.01	0.00	0.00	0.00	0.00	15.07
156	NOR-F	Jurassic	5136.2	detrital albite	8.98	3.01	3.00	0.00	0.00	0.00	0.01	0.00	0.00	0.00	0.00	15.01
157	NOR-C	Skagerrak Fm.	4589.6	detrital plagioclase	8.79	3.18	2.84	0.01	0.21	0.00	0.01	0.00	0.00	0.00	0.00	15.04
158	NOR-C	Skagerrak Fm.	4589.6	detrital K-feldspar	8.92	3.07	0.16	2.87	0.00	0.01	0.01	0.00	0.00	0.00	0.02	15.06
159	NOR-C	Skagerrak Fm.	4589.6	detrital albite	8.98	2.99	3.07	0.01	0.00	0.00	0.00	0.00	0.00	0.00	0.00	15.07
160	NOR-C	Skagerrak Fm.	4589.6	detrital K-feldspar	8.93	3.08	0.24	2.67	0.00	0.01	0.00	0.00	0.00	0.00	0.05	14.99
161	NOR-C	Skagerrak Fm.	4589.6	detrital albite	8.90	3.07	3.10	0.01	0.04	0.00	0.00	0.00	0.00	0.00	0.00	15.12
162	NOR-C	Skagerrak Fm.	4589.6	detrital albite	8.90	3.07	3.03	0.02	0.07	0.01	0.01	0.00	0.00	0.00	0.00	15.09
163	30/2c-4	Skagerrak Fm.	15604	detrital plagioclase	8.94	3.04	3.00	0.02	0.04	0.01	0.00	0.00	0.00	0.00	0.00	15.05
164	30/2c-4	Skagerrak Fm.	15604	authigenic K-feldspar	8.99	3.02	0.01	2.93	0.00	0.00	0.01	0.00	0.00	0.00	0.00	14.96
165	30/2c-4	Skagerrak Fm.	15613	detrital K-feldspar	9.00	2.98	0.02	3.02	0.00	0.00	0.00	0.00	0.01	0.00	0.00	15.02
166	30/2c-4	Skagerrak Fm.	15613	detrital K-feldspar	8.97	3.03	0.01	3.00	0.00	0.00	0.01	0.00	0.00	0.00	0.00	15.02
167	30/2c-4	Skagerrak Fm.	15613	detrital K-feldspar	8.96	3.00	0.02	3.11	0.00	0.00	0.00	0.00	0.00	0.00	0.00	15.10
168	30/2c-4	Skagerrak Fm.	15613	detrital K-feldspar	8.89	3.09	0.35	2.64	0.03	0.01	0.01	0.00	0.00	0.00	0.04	15.06
169	30/2c-4	Skagerrak Fm.	15613	albite patches in no. 173	8.82	3.18	2.77	0.06	0.16	0.01	0.01	0.00	0.00	0.00	0.00	15.00
170	30/2c-4	Skagerrak Fm.	15613	detrital K-feldspar (Perthite)	8.91	3.08	0.36	2.68	0.00	0.01	0.00	0.00	0.00	0.00	0.03	15.07
171	30/2c-4	Skagerrak Fm.	15613	detrital K-feldspar (Perthite)	9.00	2.99	0.01	3.00	0.00	0.00	0.00	0.00	0.00	0.00	0.00	15.01
172	30/2c-4	Skagerrak Fm.	15613	detrital K-feldspar	8.97	3.02	0.01	3.03	0.00	0.00	0.00	0.00	0.00	0.00	0.00	15.04
173	30/2c-4	Skagerrak Fm.	15613	detrital K-feldspar	8.97	3.05	0.17	2.75	0.00	0.00	0.00	0.00	0.00	0.00	0.01	14.96
174	30/2c-4	Skagerrak Fm.	15613	authigenic K-feldspar	8.98	3.01	0.01	3.02	0.00	0.00	0.00	0.00	0.00	0.00	0.00	15.03
175	30/2c-4	Skagerrak Fm.	15613	detrital K-feldspar	8.98	3.03	0.01	2.98	0.00	0.00	0.00	0.00	0.00	0.00	0.00	15.00
176	30/2c-4	Skagerrak Fm.	15616	detrital albite	8.92	3.09	2.97	0.04	0.01	0.00	0.00	0.00	0.00	0.00	0.00	15.04
177	30/2c-4	Skagerrak Fm.	15616	detrital K-feldspar	8.93	3.09	0.14	2.84	0.00	0.00	0.00	0.00	0.00	0.00	0.02	15.02
178	30/2c-4	Skagerrak Fm.	15616	detrital K-feldspar	8.87	3.14	0.33	2.57	0.00	0.01	0.00	0.00	0.00	0.00	0.07	15.01
179	30/2c-4	Skagerrak Fm.	15616	detrital K-feldspar	8.90	3.14	0.15	2.81	0.00	0.00	0.00	0.00	0.00	0.00	0.01	15.01
180	30/2c-4	Skagerrak Fm.	15616	detrital albite	8.93	3.07	3.05	0.00	0.01	0.00	0.00	0.00	0.00	0.00	0.00	15.06
181	30/2c-4	Skagerrak Fm.	15616	authigenic albite	8.97	3.04	2.95	0.01	0.00	0.00	0.00	0.00	0.00	0.00	0.00	14.98
182	30/2c-4	Skagerrak Fm.	15616	detrital K-feldspar	8.91	3.11	0.20	2.77	0.00	0.01	0.00	0.00	0.00	0.00	0.02	15.03

Appendix 3.2: Table electron microprobe data of feldspars

no.	well	stratigraphy	sample	mineral	Chemical composition [wt%]											
					SiO_2	Al_2O_3	Na_2O	K_2O	CaO	SrO	FeO	MgO	TiO_2	MnO	BaO	total
183	30/2c-4	Skagerrak Fm.	15616	detrital plagioclase	64.54	21.01	10.27	0.23	1.68	0.13	0.10	-	0.01	-	-	97.96
184	30/2c-4	Skagerrak Fm.	15616	authigenic K-feldspar	63.11	18.64	0.05	16.62	-	-	-	-	-	-	0.01	98.43
185	30/2c-4	Skagerrak Fm.	15616	authigenic K-feldspar	63.10	18.37	0.07	16.49	-	0.01	-	0.02	0.04	-	-	98.09
186	30/2c-4	Skagerrak Fm.	15616	authigenic K-feldspar	63.25	18.72	0.53	15.82	-	-	-	-	0.02	0.01	0.06	98.40
187	30/2c-4	Skagerrak Fm.	15616	detrital K-feldspar	63.94	18.44	0.06	16.84	-	-	-	-	-	0.01	0.03	99.31
188	30/2c-4	Skagerrak Fm.	15616	authigenic albite	67.79	19.46	11.97	0.07	0.01	-	0.02	0.01	-	0.01	0.03	99.37
189	30/2c-4	Skagerrak Fm.	15616	detrital K-feldspar	63.60	18.14	-	16.82	-	-	0.01	-	-	0.01	-	98.58
190	30/2c-4	Skagerrak Fm.	15616	authigenic albite	67.73	19.86	11.65	0.07	0.01	-	0.02	0.01	-	0.02	0.05	99.42
191	30/2c-4	Skagerrak Fm.	15616	detrital K-feldspar	63.95	18.46	0.05	16.49	-	-	0.01	-	-	-	0.01	98.97
192	30/2c-4	Skagerrak Fm.	15654.5	detrital K-feldspar	63.34	18.17	1.56	14.01	0.10	0.10	0.07	0.00	0.02	0.00	0.53	97.90
193	30/2c-4	Skagerrak Fm.	15654.5	authigenic albite	66.95	18.94	11.89	0.09	0.01	0.00	0.02	0.00	0.03	0.00	0.01	97.93
194	30/2c-4	Skagerrak Fm.	15654.5	authigenic albite	66.87	18.93	11.71	0.06	0.00	0.01	0.02	0.00	0.01	0.00	0.00	97.60
195	30/2c-4	Skagerrak Fm.	15654.5	detrital albite	65.40	18.85	11.83	0.09	0.03	0.00	0.01	0.00	0.05	0.01	0.02	96.29
196	30/2c-4	Skagerrak Fm.	15654.5	authigenic albite	66.81	19.00	11.65	0.05	0.00	0.04	0.00	0.00	0.00	0.00	0.00	97.56
197	30/2c-4	Skagerrak Fm.	15654.5	detrital K-feldspar	63.61	17.84	0.07	16.52	0.00	0.02	0.04	0.00	0.01	0.00	0.00	98.11
198	30/2c-4	Skagerrak Fm.	15654.5	detrital K-feldspar	63.30	17.77	0.11	16.41	0.02	0.00	0.05	0.00	0.01	0.00	0.07	97.74
199	30/2c-4	Skagerrak Fm.	15715	authigenic K-feldspar	63.43	18.07	0.04	16.64	0.00	0.00	0.04	0.00	0.00	0.00	0.01	98.22
200	30/2c-4	Skagerrak Fm.	15715	authigenic K-feldspar	63.94	18.33	0.01	16.95	0.00	0.02	0.08	0.00	0.01	0.04	0.06	99.44
201	30/2c-4	Skagerrak Fm.	15715	detrital K-feldspar	63.95	18.34	0.62	15.75	0.00	0.13	0.06	0.00	0.04	0.01	0.24	99.13
202	30/2c-4	Skagerrak Fm.	15715	detrital K-feldspar	63.78	18.52	1.19	14.98	0.02	0.06	0.06	0.00	0.00	0.01	0.43	99.04
203	30/2c-4	Skagerrak Fm.	15715	authigenic K-feldspar	63.81	18.46	0.55	15.82	0.00	0.00	0.04	0.00	0.00	0.02	0.63	99.32
204	30/2c-4	Skagerrak Fm.	15715	detrital K-feldspar	63.73	18.40	0.57	16.14	0.00	0.10	0.14	0.00	0.00	0.03	0.24	99.34
205	30/2c-4	Skagerrak Fm.	15715	detrital albite	67.33	19.19	11.95	0.06	0.05	0.00	0.02	0.00	0.02	0.00	0.01	98.63
206	30/2c-4	Skagerrak Fm.	15747	detrital albite	67.06	19.71	11.89	0.04	0.23	0.03	0.00	0.00	0.01	0.00	0.00	98.98
207	30/2c-4	Skagerrak Fm.	15768.5	authigenic K-feldspar	63.44	18.52	0.03	16.18	-	0.02	-	0.01	0.02	-	0.01	98.23
208	30/2c-4	Skagerrak Fm.	15768.5	detrital K-feldspar	63.48	18.94	0.47	15.90	0.01	-	-	-	0.02	0.02	0.49	99.33
209	30/2c-4	Skagerrak Fm.	15768.5	authigenic? K-feldspar	63.67	18.42	0.07	16.52	-	-	0.40	0.01	0.01	-	0.02	99.12
210	30/2c-4	Skagerrak Fm.	15768.5	authigenic? K-feldspar	62.79	18.59	0.05	16.16	-	0.02	0.74	0.20	-	0.01	0.07	98.63
211	30/2c-4	Skagerrak Fm.	15768.5	authigenic? K-feldspar	63.33	18.51	0.11	16.28	-	-	0.20	0.01	0.01	-	-	98.44
212	30/7a-9	Skagerrak Fm.	12099.5	detrital K-feldspar	63.07	19.75	1.67	13.03	0.31	0.57	0.04	0.00	0.08	0.00	2.51	101.02
213	30/7a-9	Skagerrak Fm.	12099.5	authigenic K-feldspar	64.72	18.64	0.07	16.86	0.04	0.01	0.03	0.00	0.00	0.00	0.00	100.36

Appendix 3.2: Table electron microprobe data of feldspars

no.	well	stratigraphy	sample	mineral	Ions in structural formula on the basis of 24 oxygen											
					Si	Al	Na	K	Ca	Sr	Fe	Mg	Ti	Mn	Ba	total at
183	30/2c-4	Skagerrak Fm.	15616	detrital plagioclase	8.69	3.33	2.68	0.04	0.24	0.01	0.01	0.00	0.00	0.00	0.00	15.00
184	30/2c-4	Skagerrak Fm.	15616	authigenic K-feldspar	8.92	3.10	0.01	3.00	0.00	0.00	0.00	0.00	0.00	0.00	0.00	15.03
185	30/2c-4	Skagerrak Fm.	15616	authigenic K-feldspar	8.94	3.07	0.02	2.98	0.00	0.00	0.00	0.00	0.00	0.00	0.00	15.02
186	30/2c-4	Skagerrak Fm.	15616	authigenic K-feldspar	8.92	3.11	0.15	2.84	0.00	0.00	0.00	0.00	0.00	0.00	0.00	15.02
187	30/2c-4	Skagerrak Fm.	15616	detrital K-feldspar	8.96	3.05	0.01	3.01	0.00	0.00	0.00	0.00	0.00	0.00	0.00	15.03
188	30/2c-4	Skagerrak Fm.	15616	authigenic albite	8.95	3.03	3.07	0.01	0.00	0.00	0.00	0.00	0.00	0.00	0.00	15.07
189	30/2c-4	Skagerrak Fm.	15616	detrital K-feldspar	8.98	3.02	0.00	3.03	0.00	0.00	0.00	0.00	0.00	0.00	0.00	15.03
190	30/2c-4	Skagerrak Fm.	15616	authigenic albite	8.93	3.09	2.98	0.01	0.00	0.00	0.00	0.00	0.00	0.00	0.00	15.02
191	30/2c-4	Skagerrak Fm.	15616	detrital K-feldspar	8.97	3.05	0.01	2.95	0.00	0.00	0.00	0.00	0.00	0.00	0.00	14.99
192	30/2c-4	Skagerrak Fm.	15654.5	detrital K-feldspar	8.96	3.03	0.43	2.53	0.02	0.01	0.01	0.00	0.00	0.00	0.03	15.00
193	30/2c-4	Skagerrak Fm.	15654.5	authigenic albite	8.97	2.99	3.09	0.02	0.00	0.00	0.00	0.00	0.00	0.00	0.00	15.08
194	30/2c-4	Skagerrak Fm.	15654.5	authigenic albite	8.98	3.00	3.05	0.01	0.00	0.00	0.00	0.00	0.00	0.00	0.00	15.05
195	30/2c-4	Skagerrak Fm.	15654.5	detrital albite	8.93	3.03	3.13	0.01	0.01	0.00	0.00	0.00	0.00	0.00	0.00	15.12
196	30/2c-4	Skagerrak Fm.	15654.5	authigenic albite	8.98	3.01	3.04	0.01	0.00	0.00	0.00	0.00	0.00	0.00	0.00	15.04
197	30/2c-4	Skagerrak Fm.	15654.5	detrital K-feldspar	9.01	2.98	0.02	2.99	0.00	0.00	0.00	0.00	0.00	0.00	0.00	15.00
198	30/2c-4	Skagerrak Fm.	15654.5	detrital K-feldspar	9.01	2.98	0.03	2.98	0.00	0.00	0.01	0.00	0.00	0.00	0.00	15.01
199	30/2c-4	Skagerrak Fm.	15715	authigenic K-feldspar	8.98	3.02	0.01	3.01	0.00	0.00	0.00	0.00	0.00	0.00	0.00	15.02
200	30/2c-4	Skagerrak Fm.	15715	authigenic K-feldspar	8.96	3.03	0.00	3.03	0.00	0.00	0.01	0.00	0.00	0.00	0.00	15.04
201	30/2c-4	Skagerrak Fm.	15715	detrital K-feldspar	8.96	3.03	0.17	2.82	0.00	0.01	0.01	0.00	0.00	0.00	0.01	15.01
202	30/2c-4	Skagerrak Fm.	15715	detrital K-feldspar	8.93	3.06	0.32	2.68	0.00	0.00	0.01	0.00	0.00	0.00	0.02	15.03
203	30/2c-4	Skagerrak Fm.	15715	authigenic K-feldspar	8.95	3.05	0.15	2.83	0.00	0.00	0.00	0.00	0.00	0.00	0.03	15.02
204	30/2c-4	Skagerrak Fm.	15715	detrital K-feldspar	8.94	3.04	0.15	2.89	0.00	0.01	0.02	0.00	0.00	0.00	0.01	15.06
205	30/2c-4	Skagerrak Fm.	15715	detrital albite	8.96	3.01	3.08	0.01	0.01	0.00	0.00	0.00	0.00	0.00	0.00	15.08
206	30/2c-4	Skagerrak Fm.	15747	detrital albite	8.90	3.08	3.06	0.01	0.03	0.00	0.00	0.00	0.00	0.00	0.00	15.09
207	30/2c-4	Skagerrak Fm.	15768.5	authigenic K-feldspar	8.95	3.08	0.01	2.91	0.00	0.00	0.00	0.00	0.00	0.00	0.00	14.96
208	30/2c-4	Skagerrak Fm.	15768.5	detrital K-feldspar	8.89	3.13	0.13	2.84	0.00	0.00	0.00	0.00	0.00	0.00	0.03	15.02
209	30/2c-4	Skagerrak Fm.	15768.5	authigenic? K-feldspar	8.94	3.05	0.02	2.96	0.00	0.00	0.05	0.00	0.00	0.00	0.00	15.02
210	30/2c-4	Skagerrak Fm.	15768.5	authigenic? K-feldspar	8.88	3.10	0.01	2.92	0.00	0.00	0.09	0.04	0.00	0.00	0.00	15.04
211	30/2c-4	Skagerrak Fm.	15768.5	authigenic? K-feldspar	8.94	3.08	0.03	2.93	0.00	0.00	0.02	0.00	0.00	0.00	0.00	15.00
212	30/7a-9	Skagerrak Fm.	12099.5	detrital K-feldspar	8.76	3.23	0.45	2.31	0.05	0.05	0.00	0.00	0.01	0.00	0.14	14.99
213	30/7a-9	Skagerrak Fm.	12099.5	authigenic K-feldspar	8.96	3.04	0.02	2.98	0.01	0.00	0.00	0.00	0.00	0.00	0.00	15.01

Appendix 3.3: Table electron microprobe data of clay minerals

no.	well	stratigraphy	sample	mineral	Chemical composition [wt%]											
					SiO_2	Al_2O_3	Na_2O	K_2O	CaO	SrO	FeO	MgO	TiO_2	MnO	BaO	total
214	NOR-A	Rotliegend	4808.8	authigenic illite	33.34	17.60	0.04	6.02	0.23	0.00	1.41	1.75	0.01	0.00	0.00	60.40
215	NOR-F	Jurassic	5136.2	authigenic Fe-chlorite	24.71	23.18	0.01	0.01	0.26	0.00	30.81	6.70	0.00	0.01	0.00	85.69
216	NOR-F	Jurassic	5136.2	authigenic Fe-chlorite	24.78	23.01	0.01	0.00	0.08	0.03	31.05	7.29	0.00	0.01	0.05	86.31
217	NOR-F	Jurassic	5136.2	authigenic Fe-chlorite	24.14	23.09	0.01	0.01	0.09	0.00	30.64	7.73	0.05	0.03	0.00	85.79
218	NOR-F	Jurassic	5136.2	authigenic Fe-chlorite	24.94	23.26	0.00	0.02	0.10	0.00	29.93	7.41	0.05	0.00	0.00	85.71
219	NOR-F	Jurassic	5136.2	authigenic Fe-chlorite	25.95	24.17	0.12	0.10	0.14	0.01	29.51	6.33	0.04	0.00	0.02	86.39
220	NOR-F	Jurassic	5136.2	authigenic Fe-chlorite	24.55	22.81	0.06	0.00	0.09	0.02	31.22	7.27	0.00	0.02	0.00	86.04
221	NOR-F	Jurassic	5136.2	authigenic Fe-chlorite	25.35	23.73	0.02	0.01	0.03	0.00	30.93	6.09	0.02	0.00	0.00	86.18
222	NOR-F	Jurassic	5136.2	authigenic Fe-chlorite	24.75	23.05	0.02	0.02	0.20	0.01	30.23	7.73	0.02	0.00	0.00	86.03
223	NOR-F	Jurassic	5136.2	authigenic chlorite (coarse plates)	24.48	23.23	0.05	0.02	0.04	0.00	30.40	7.54	0.02	0.02	0.00	85.80
224	NOR-F	Jurassic	5136.2	authigenic kaolinite group mineral	45.22	40.09	0.04	0.07	0.22	0.01	0.39	0.14	0.00	0.00	0.04	86.22
225	NOR-F	Jurassic	5136.2	authigenic Fe-chlorite	25.12	23.99	0.00	0.05	0.06	0.00	31.92	6.62	0.00	0.04	0.00	87.80
226	NOR-F	Jurassic	5136.2	authigenic kaolinite group mineral	45.39	41.09	0.03	0.07	0.16	0.00	0.32	0.13	0.01	0.01	0.00	87.21
227	NOR-F	Jurassic	5136.2	authigenic kaolinite group mineral	44.80	40.07	0.05	0.07	0.21	0.00	0.52	0.16	0.00	0.03	0.03	85.95
228	NOR-F	Jurassic	5136.2	authigenic Fe-chlorite (after kaolinite?)	24.36	23.83	0.02	0.00	0.08	0.00	33.52	5.95	0.02	0.01	0.00	87.78
229	NOR-F	Jurassic	5136.2	authigenic Fe-chlorite	24.88	23.88	0.02	0.01	0.11	0.00	31.82	7.11	0.02	0.00	0.04	87.88
230	NOR-F	Jurassic	5136.2	authigenic Fe-chlorite	25.30	24.36	0.00	0.00	0.11	0.00	30.97	7.34	0.05	0.00	0.03	88.16
231	NOR-F	Jurassic	5136.2	authigenic Fe-chlorite	24.73	23.86	0.00	0.02	0.09	0.00	32.27	6.60	0.03	0.00	0.00	87.60
232	NOR-F	Jurassic	5136.2	authigenic Fe-chlorite	25.58	24.52	0.00	0.02	0.16	0.02	31.13	6.63	0.05	0.05	0.00	88.15
233	NOR-C	Skagerrak Fm.	4589.6	authigenic chlorite (coarse plates)	22.67	16.35	0.03	1.55	0.34	0.00	16.12	6.35	0.16	0.03	0.02	63.62
234	NOR-C	Skagerrak Fm.	4589.6	authigenic chlorite (coarse plates)	24.20	21.50	0.03	0.06	0.02	0.00	28.98	9.47	0.03	0.03	0.02	84.34
235	NOR-C	Skagerrak Fm.	4589.6	authigenic chlorite (coarse plates)	25.24	20.43	0.01	0.85	0.11	0.00	24.25	9.05	0.00	0.01	0.03	79.97
236	NOR-C	Skagerrak Fm.	4589.6	authigenic chlorite (coarse plates)	25.25	22.00	0.03	0.09	0.07	0.00	29.19	9.24	0.00	0.04	0.00	85.90
237	NOR-C	Skagerrak Fm.	4589.6	detrital chlorite	29.95	15.05	0.17	0.43	0.15	0.04	27.40	11.52	0.02	0.12	0.05	84.91
238	30/2c-4	Skagerrak Fm.	15604	authigenic chlorite	13.64	8.90	0.03	0.46	0.03	0.03	10.77	4.11	0.00	0.03	0.01	38.02
239	30/2c-4	Skagerrak Fm.	15604	detrital chlorite	25.47	20.76	0.05	0.02	0.03	0.02	21.84	17.49	0.08	0.25	0.00	86.00
240	30/2c-4	Skagerrak Fm.	15613	detrital chlorite	24.92	20.33	0.03	0.00	0.08	0.00	29.40	9.90	0.05	0.03	0.00	84.74
241	30/2c-4	Skagerrak Fm.	15613	detrital chlorite	37.97	26.00	1.33	4.37	0.08	0.00	12.86	5.49	0.90	0.07	0.02	89.08
242	30/2c-4	Skagerrak Fm.	15616	detrital chlorite	25.52	20.19	0.03	0.04	0.06	-	30.08	10.01	0.02	0.05	0.01	86.01
243	30/2c-4	Skagerrak Fm.	15654.5	authigenic Fe-chlorite	14.88	11.05	0.02	0.07	0.12	0.01	14.58	5.56	0.01	0.02	0.00	46.33
244	30/2c-4	Skagerrak Fm.	15654.5	authigenic Fe-chlorite	11.99	8.78	0.00	0.04	0.08	0.05	11.72	4.94	0.00	0.03	0.02	37.66
245	30/2c-4	Skagerrak Fm.	15654.5	authigenic Fe-chlorite	18.95	13.87	0.04	0.13	0.11	0.08	20.35	8.17	0.02	0.03	0.00	61.75
246	30/2c-4	Skagerrak Fm.	15654.5	authigenic Fe-chlorite	16.43	10.65	0.14	0.58	0.10	0.01	14.18	5.85	0.53	0.01	0.01	48.49
247	30/2c-4	Skagerrak Fm.	15654.5	detrital chlorite	23.96	19.56	0.00	0.03	0.02	0.01	31.85	10.37	0.18	0.45	0.06	86.48
248	30/2c-4	Skagerrak Fm.	15654.5	authigenic Fe-chlorite (coatings)	24.64	17.11	0.15	0.79	0.13	0.00	24.08	8.52	0.06	0.04	0.02	75.53
249	30/2c-4	Skagerrak Fm.	15768.5	authigenic? Fe-chlorite	25.47	18.26	-	0.09	0.01	-	33.68	9.34	-	0.04	0.01	86.90
250	30/2c-4	Skagerrak Fm.	15768.5	authigenic? Fe-chlorite	25.44	17.99	0.04	0.07	0.02	-	33.88	9.02	0.04	0.06	-	86.55

Appendix 3.3: Table electron microprobe data of clay minerals

no.	well	stratigraphy	sample	mineral	Ions in structural formula on the basis of 14 O equivalents (analyses 224, 226, 227); 22 O equivalents (analysis 214) and 28 O equivalents (analyses 215 to 223, 225 and 228 to 250)													
					Si	Al (total)	*Al(IV)*	*Al(VI)*	Na	K	Ca	Sr	Fe	Mg	Ti	Mn	Ba	total at
214	NOR-A	Rotliegend	4808.8	authigenic illite	6.94	4.32	*1.06*	*3.25*	0.01	1.60	0.05	0.00	0.25	0.54	0.00	0.00	0.00	13.71
215	NOR-F	Jurassic	5136.2	authigenic Fe-chlorite	5.47	6.05	*2.53*	*3.52*	0.00	0.00	0.06	0.00	5.71	2.21	0.00	0.00	0.00	19.51
216	NOR-F	Jurassic	5136.2	authigenic Fe-chlorite	5.45	5.97	*2.55*	*3.42*	0.00	0.00	0.02	0.00	5.72	2.39	0.00	0.00	0.00	19.56
217	NOR-F	Jurassic	5136.2	authigenic Fe-chlorite	5.34	6.03	*2.66*	*3.37*	0.01	0.00	0.02	0.00	5.67	2.55	0.01	0.01	0.00	19.64
218	NOR-F	Jurassic	5136.2	authigenic Fe-chlorite	5.49	6.03	*2.51*	*3.52*	0.00	0.01	0.02	0.00	5.51	2.43	0.01	0.00	0.00	19.49
219	NOR-F	Jurassic	5136.2	authigenic Fe-chlorite	5.63	6.18	*2.37*	*3.80*	0.05	0.03	0.03	0.00	5.35	2.05	0.01	0.00	0.00	19.32
220	NOR-F	Jurassic	5136.2	authigenic Fe-chlorite	5.43	5.95	*2.57*	*3.38*	0.03	0.00	0.02	0.00	5.78	2.40	0.00	0.00	0.00	19.61
221	NOR-F	Jurassic	5136.2	authigenic Fe-chlorite	5.56	6.13	*2.44*	*3.69*	0.01	0.00	0.01	0.00	5.67	1.99	0.00	0.00	0.00	19.38
222	NOR-F	Jurassic	5136.2	authigenic Fe-chlorite	5.44	5.97	*2.56*	*3.42*	0.01	0.01	0.05	0.00	5.56	2.53	0.00	0.00	0.00	19.58
223	NOR-F	Jurassic	5136.2	authigenic chlorite (coarse plates)	5.40	6.04	*2.60*	*3.45*	0.02	0.01	0.01	0.00	5.61	2.48	0.00	0.00	0.00	19.58
224	NOR-F	Jurassic	5136.2	authigenic kaolinite group mineral	3.90	4.08	*0.10*	*3.98*	0.01	0.01	0.02	0.00	0.03	0.02	0.00	0.00	0.00	8.06
225	NOR-F	Jurassic	5136.2	authigenic Fe-chlorite	5.44	6.12	*2.56*	*3.56*	0.00	0.01	0.01	0.00	5.78	2.14	0.00	0.01	0.00	19.51
226	NOR-F	Jurassic	5136.2	authigenic kaolinite group mineral	3.87	4.13	*0.13*	*4.00*	0.00	0.01	0.01	0.00	0.02	0.02	0.00	0.00	0.00	8.07
227	NOR-F	Jurassic	5136.2	authigenic kaolinite group mineral	3.88	4.09	*0.12*	*3.98*	0.01	0.01	0.02	0.00	0.04	0.02	0.00	0.00	0.00	8.08
228	NOR-F	Jurassic	5136.2	authigenic Fe-chlorite (after kaolinite?)	5.33	6.15	*2.67*	*3.48*	0.01	0.00	0.02	0.00	6.14	1.94	0.00	0.00	0.00	19.59
229	NOR-F	Jurassic	5136.2	authigenic Fe-chlorite	5.38	6.09	*2.62*	*3.48*	0.01	0.00	0.03	0.00	5.76	2.29	0.00	0.00	0.00	19.57
230	NOR-F	Jurassic	5136.2	authigenic Fe-chlorite	5.42	6.15	*2.58*	*3.57*	0.00	0.00	0.03	0.00	5.55	2.34	0.01	0.00	0.00	19.50
231	NOR-F	Jurassic	5136.2	authigenic Fe-chlorite	5.38	6.12	*2.62*	*3.51*	0.00	0.00	0.02	0.00	5.87	2.14	0.01	0.00	0.00	19.55
232	NOR-F	Jurassic	5136.2	authigenic Fe-chlorite	5.48	6.19	*2.52*	*3.67*	0.00	0.00	0.04	0.00	5.58	2.12	0.01	0.01	0.00	19.42
233	NOR-C	Skagerrak Fm.	4589.6	authigenic chlorite (coarse plates)	6.42	5.46	*1.58*	*3.88*	0.01	0.56	0.10	0.00	3.82	2.68	0.03	0.01	0.00	19.10
234	NOR-C	Skagerrak Fm.	4589.6	authigenic chlorite (coarse plates)	5.42	5.68	*2.58*	*3.10*	0.01	0.02	0.00	0.00	5.43	3.16	0.01	0.01	0.00	19.75
235	NOR-C	Skagerrak Fm.	4589.6	authigenic chlorite (coarse plates)	5.84	5.57	*2.16*	*3.41*	0.00	0.25	0.03	0.00	4.69	3.12	0.00	0.00	0.00	19.50
236	NOR-C	Skagerrak Fm.	4589.6	authigenic chlorite (coarse plates)	5.53	5.68	*2.47*	*3.22*	0.01	0.02	0.02	0.00	5.35	3.02	0.00	0.01	0.00	19.64
237	NOR-C	Skagerrak Fm.	4589.6	detrital chlorite	6.58	3.90	*1.42*	*2.48*	0.07	0.12	0.04	0.01	5.04	3.77	0.00	0.02	0.00	19.56
238	30/2c-4	Skagerrak Fm.	15604	authigenic chlorite	6.52	5.02	*1.48*	*3.54*	0.03	0.28	0.02	0.01	4.31	2.93	0.00	0.01	0.00	19.13
239	30/2c-4	Skagerrak Fm.	15604	detrital chlorite	5.39	5.17	*2.61*	*2.56*	0.02	0.00	0.01	0.00	3.86	5.51	0.01	0.04	0.00	20.03
240	30/2c-4	Skagerrak Fm.	15613	detrital chlorite	5.57	5.35	*2.43*	*2.92*	0.01	0.00	0.02	0.00	5.49	3.30	0.01	0.00	0.00	19.75
241	30/2c-4	Skagerrak Fm.	15613	detrital chlorite	7.26	5.86	*0.74*	*5.12*	0.49	1.07	0.02	0.00	2.06	1.57	0.13	0.01	0.00	18.46
242	30/2c-4	Skagerrak Fm.	15616	detrital chlorite	5.63	5.25	*2.37*	*2.87*	0.01	0.01	0.01	0.00	5.55	3.29	0.00	0.01	0.00	19.76
243	30/2c-4	Skagerrak Fm.	15654.5	authigenic Fe-chlorite	5.95	5.21	*2.05*	*3.16*	0.02	0.04	0.05	0.00	4.88	3.31	0.00	0.01	0.00	19.47
244	30/2c-4	Skagerrak Fm.	15654.5	authigenic Fe-chlorite	5.91	5.10	*2.09*	*3.00*	0.00	0.02	0.04	0.01	4.83	3.63	0.00	0.01	0.00	19.56
245	30/2c-4	Skagerrak Fm.	15654.5	authigenic Fe-chlorite	5.77	4.98	*2.23*	*2.75*	0.02	0.05	0.04	0.01	5.18	3.71	0.00	0.01	0.00	19.77
246	30/2c-4	Skagerrak Fm.	15654.5	authigenic Fe-chlorite	6.24	4.77	*1.76*	*3.01*	0.10	0.28	0.04	0.00	4.51	3.31	0.15	0.00	0.00	19.41
247	30/2c-4	Skagerrak Fm.	15654.5	detrital chlorite	5.35	5.15	*2.65*	*2.51*	0.00	0.01	0.01	0.00	5.95	3.45	0.03	0.08	0.01	20.04
248	30/2c-4	Skagerrak Fm.	15654.5	authigenic Fe-chlorite (coatings)	6.09	4.98	*1.91*	*3.07*	0.07	0.25	0.03	0.00	4.98	3.14	0.01	0.01	0.00	19.57
249	30/2c-4	Skagerrak Fm.	15768.5	authigenic? Fe-chlorite	5.69	4.80	*2.31*	*2.49*	0.00	0.03	0.00	0.00	6.29	3.11	0.00	0.01	0.00	19.92
250	30/2c-4	Skagerrak Fm.	15768.5	authigenic? Fe-chlorite	5.71	4.76	*2.29*	*2.48*	0.02	0.02	0.00	0.00	6.36	3.02	0.01	0.01	0.00	19.92

Appendix 4.1: Minerals found by XRD analysis in well 30/2c-4

sample	facies	minerals
15584	AS	dolomite, illite, quartz, chlorite, albite, K-feldspar
15593	AS	quartz, illite, chlorite, albite, K-feldspar
15634.3	AS	quartz,albite, K-feldspar, illite, chlorite
15639	AS	quartz, chlorite, illite, albite, K-feldspar, dolomite
15654.5	FC/SF	quartz, albite, K-feldspar, chlorite, illite, ankerite
15655.3	FC/SF	quartz, albite, K-feldspar
15704	AS	quartz, albite, illite, chlorite, K-feldspar
15715	FC	quartz, dolomite, K-feldspar, albite, illite
15722.2	AS	quartz, illite, chlorite, albite
15747.5	AS	illite, dolomite, chlorite, albite, K-feldspar
15768.5	AS	illite, chlorite

Appendix 4.2: Example XRD-patterns

Skagerrak Formation
facies FC

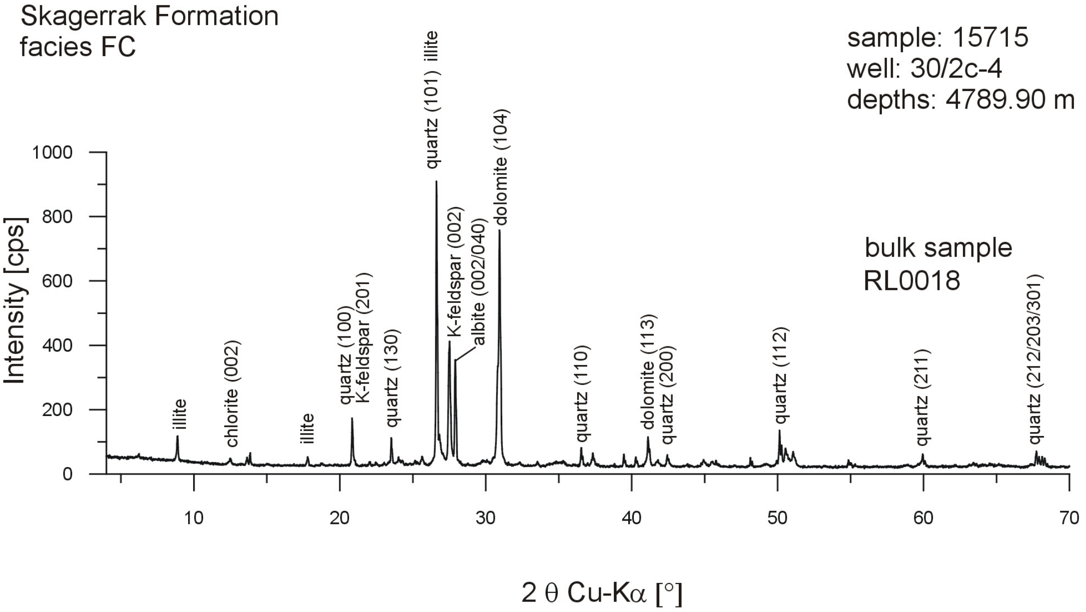

Appendix 4.2: Example XRD-patterns

Skagerrak Formation
facies AS

sample: 15593
well: 30/2c-4
depths: 4752.72 m

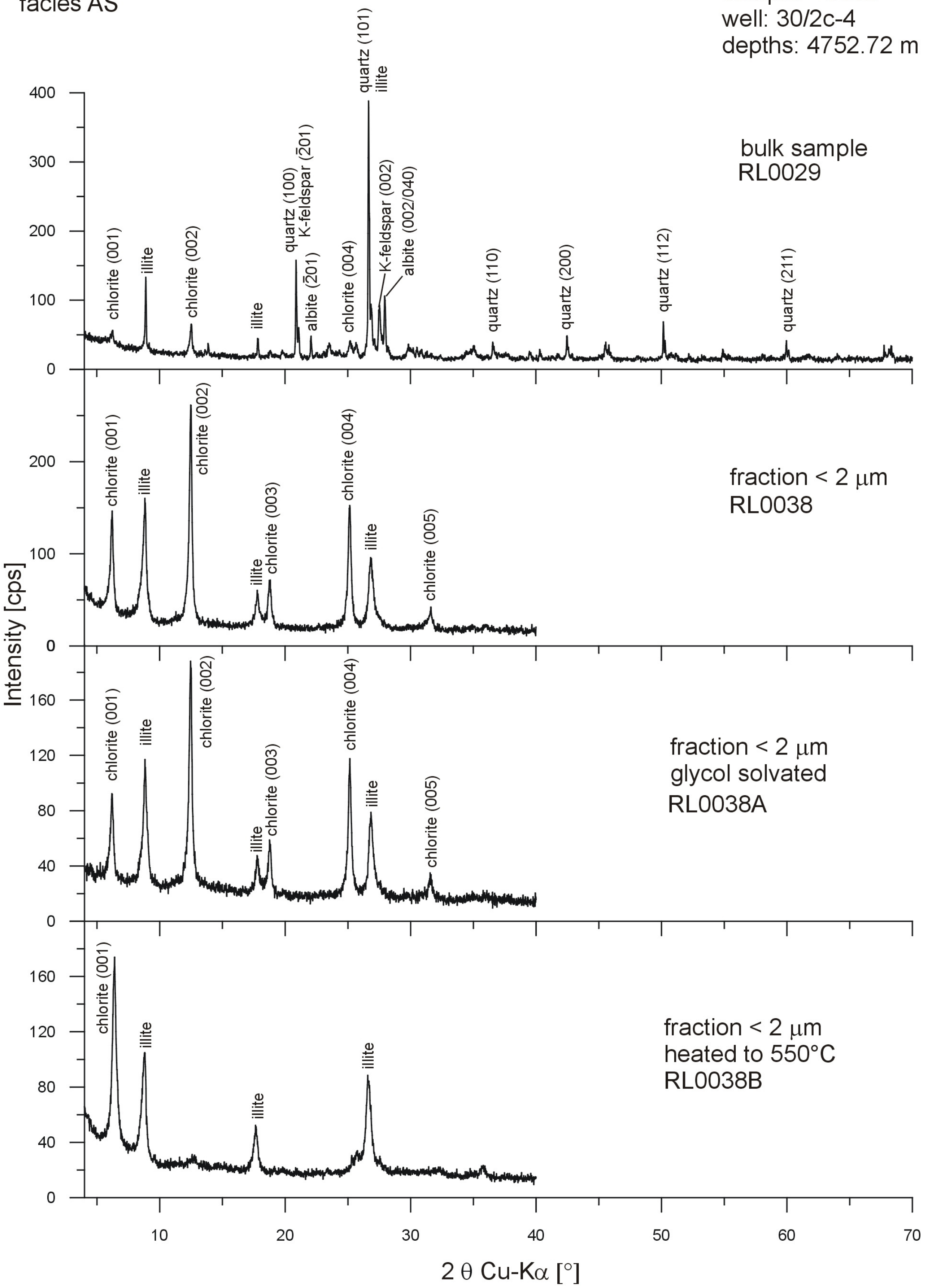

Appendix 4.2: Example XRD-patterns

Skagerrak Formation
facies AS

sample: 15768.5
well: 30/2c-4
depths: 4806.27 m

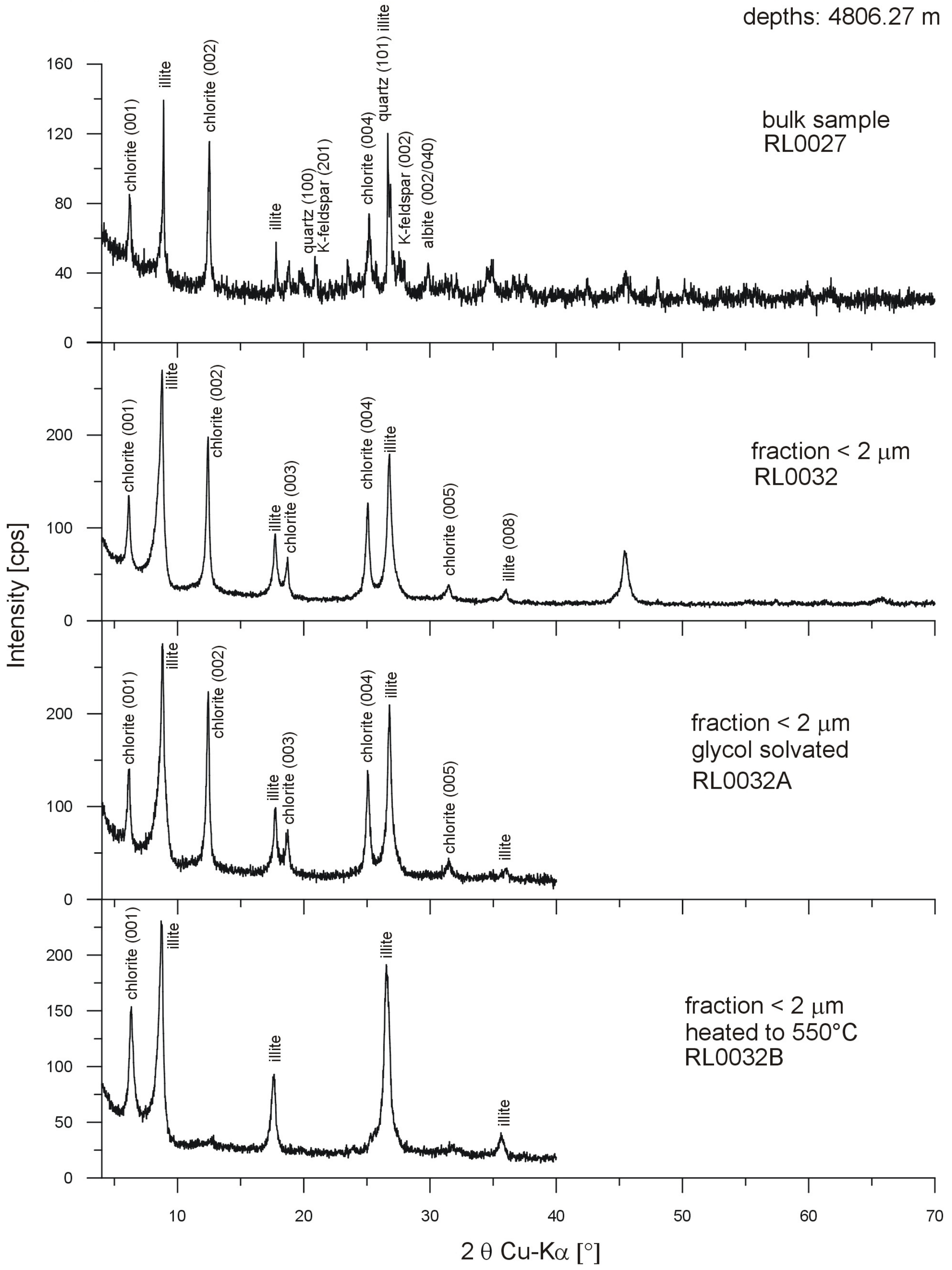

Appendix 5.1: Carbonate stable isotope analysis of bulk rock samples

no.	**well**	**sample**	**material**	**carbonates in sample** (see Appendix 2 for details)	δ^{13}**C [‰ V-PDB]**	δ^{18}**O [‰ V-PDB]**	δ^{18}O **Dolomite acid fractionation corrected [‰ V-PDB]**
1	NOR-F	5108.55	microspar	calcite, dolomite	-0.43	-6.69	-8.31
2	NOR-F	5108.7	microspar	calcite, dolomite	0.55	-4.18	-5.80
3	NOR-F	5108.7	fissure filling	Fe-carbonate	3.00	-6.11	-7.73
4	NOR-F	5134.35	sandstone carbonate cemented	ankerite, dolomite	-1.09	-9.21	-10.82
5	NOR-F	5134.95	sandstone carbonate cemented	ankerite, dolomite	-1.14	-9.21	-10.83
6	NOR-F	5136.2	sandstone carbonate cemented	ankerite	-4.54	-8.81	-10.43
7	NOR-C	4575.55	sandstone carbonate cemented	Fe-carb./dolomite	-5.50	-8.93	-10.55
8	NOR-D	4613.5	sandstone carbonate cemented	Fe-carb./dolomite	-4.40	-6.66	-8.28
9	NOR-D	4618.5	sandstone carbonate cemented	Fe-carb./dolomite	-4.53	-6.89	-8.51
10	NOR-D	4622.25	sandstone carbonate cemented	Fe-carb./dolomite	-4.28	-10.65	-12.26
11	30/2c-4	15584	sandstone carbonate cemented	dolomite	-7.97	0.31	-1.33
12	30/2c-4	15604	sandstone carbonate cemented	dolomite, ankerite	-8.67	-1.14	-2.77
13	30/2c-4	15608	sandstone carbonate cemented	dolomite, ankerite	-7.85	-2.66	-4.29
14	30/2c-4	15628	sandstone carbonate cemented	dolomite	-8.81	-0.79	-2.42
15	30/2c-4	15655.3	sandstone carbonate cemented	ankerite, dolomite	-4.55	-8.19	-9.81
16	30/2c-4	15665	sandstone carbonate cemented	dolomite	-8.59	-1.10	-2.73
17	30/2c-4	15671.5	sandstone carbonate cemented	dolomite, ankerite	-8.74	-3.20	-4.83
18	30/2c-4	15715	sandstone carbonate cemented	dolomite, ankerite	-8.38	-1.50	-3.13
19	30/2c-4	15716	sandstone carbonate cemented	ankerite, dolomite	-7.45	-6.30	-7.92
20	30/2c-4	15739	sandstone carbonate cemented	dolomite	-9.14	-1.17	-2.80
21	30/2c-4	15745	sandstone carbonate cemented	dolomite, ankerite	-7.95	-4.72	-6.35
22	30/2c-4	15752	sandstone carbonate cemented	ankerite, dolomite	-7.54	-6.26	-7.88
23	Standard material for UV laser system			dolomite	1.93	0.23	-1.40

Appendix 5.2: Table δ^{13}C-values of samples from well 30/2c-4 measured by UV laser system

sample	line	spot no.	analysis	sample material (on the surface)	δ^{13}C	amplitude mass 45	crater diameter [μm]
15608	1	3	2971	do	-10.99	205	64
15608	1	4	2971	do (ank)	-10.43	216	48
15608	1	5	2971	do	-10.39	152	50.8
15608	1	6	2971	do (ank + bit)	-12.80	132	63.1
15608	1	7	2971	bit	-19.18	61	48.3
15608	1	8	2971	do (ank)	-9.57	364	67
15608	2	4	2981	do	-9.99	487	64
15608	2	5	2981	do (ank)	-10.15	381	66
15608	2	6	2981	do (ank)	-10.47	428	58
15608	2	7	2981	do + ank	-11.21	424	54
15608	2	8	2981	ank + bit	-19.88	70	82
15608	2	9	2981	do	-10.83	457	50
15608	3	4	2986	do (ank)	-10.81	255	148
15608	3	5	2986	do (ank)	-9.53	525	143
15608	3	6	2986	do (ank)	-11.21	348	138
15608	3	7	2986	do (ank)	-12.67	213	105
15608	3	8	2986	bit	-14.71	157	134
15608	3	9	2986	quartz+fsp	-13.84	181	113
15608	4	5	2991	ank + bit	-17.99	98	56
15608	4	6	2991	do (ank)	-10.95	447	70
15608	4	7	2991	do (ank)	-10.98	474	75
15608	4	8	2991	do + ank	-10.34	575	40
15608	4	9	2991	do (ank)	-10.55	420	72
15608	5	4	3000	bit	-15.27	150	86
15608	5	5	3000	do + ank + bit	-13.06	224	89
15608	5	6	3000	do (ank)	-10.42	453	85
15608	5	7	3000	do + ank	-11.16	453	82
15608	5	8	3000	do + ank + bit	-11.23	343	89
15608	5	9	3000	do (ank)	-10.65	340	87
15608	5	10	3000	do (ank)	-11.38	419	89
15608	5	11	3000	do (ank)	-11.17	347	76
15608	5	12	3000	do (ank)	-12.79	148	86
15608	6	4	3011	do (ank)	-17.49	94	86
15608	6	5	3011	do (ank + bit)	-11.15	246	81
15608	6	6	3011	do (ank + bit)	-11.50	290	78
15608	6	7	3011	do (ank + bit)	-10.76	273	84
15608	6	8	3011	do (ank)	-10.48	360	70
15608	6	9	3011	do	-10.25	441	85
15608	6	10	3011	do	-11.38	290	83
15608	6	11	3011	do	-10.28	405	78
15608	6	12	3011	do	-10.31	323	96
15608	6	13	3011	do (ank)	-11.21	300	74
15608	7	6	3015	ank + bit	-18.82	63	60
15608	7	7	3015	bit	-13.05	249	58
15608	7	9	3015	do (bit)	-12.25	212	51
15608	7	10	3015	do	-10.90	229	54
15608	7	11	3015	do (ank)	-10.86	237	58
15608	7	12	3015	do + ank	-12.19	321	53
15715	1	4	3033	do + bit (ank)	-11.28	360	61
15715	1	5	3033	do (ank)	-12.19	227	49
15715	1	6	3033	bit	-11.60	358	47
15715	1	7	3033	do	-9.68	385	58
15715	1	8	3033	do	-9.45	476	61
15715	1	9	3033	do (ank)	-11.60	334	51
15715	1	10	3033	do (ank)	-9.47	429	49
15715	1	11	3033	do	-9.04	586	63
15715	1	12	3033	do	-9.73	477	57
15715	2	4	3036	do	-10.64	394	34
15715	2	5	3036	do + ank + bit	-10.64	537	51
15715	2	6	3036	crack	-12.63	400	59

Appendix 5.2: Table δ^{13}C-values of samples from well 30/2c-4 measured by UV laser system

sample	line	spot no.	analysis	sample material (on the surface)	δ^{13}C	amplitude mass 45	crater diameter [μm]
15715	2	7	3036	crack	-14.56	232	86
15715	2	8	3036	crack	-10.95	444	71
15715	2	9	3036	do	-8.58	669	54
15715	2	10	3036	do (ank)	-9.27	553	39
15715	2	11	3036	do + ank	-9.23	759	27
15715	2	12	3036	do	-8.56	667	52
15715	3	4	3037	do (ank + bit)	-10.98	388	53
15715	3	5	3037	do	-9.59	469	67
15715	3	6	3037	do	-9.65	461	66
15715	3	7	3037	quartz	-12.18	165	64
15715	3	8	3037	do + ank + bit	-9.95	420	54
15715	3	9	3037	do	-10.57	316	53
15715	3	10	3037	do (ank)	-9.40	427	57
15715	3	11	3037	do (ank)	-8.97	391	59
15715	3	12	3037	ank (do)	-9.14	443	56
15739	1	4	3044	do	-7.63	671	50
15739	1	5	3044	do + ank + bit	-11.43	300	34
15739	1	6	3044	do + ank (bit)	-9.37	427	41
15739	1	7	3044	ank (bit)	-8.54	550	33
15739	1	8	3044	do (ank)	-8.93	472	43
15739	1	9	3044	do	-8.73	488	40
15739	1	10	3044	do + ank	-8.65	467	36
15739	1	11	3044	do (ank)	-9.21	435	25
15739	1	12	3044	do	-8.38	552	36
15739	2	4	3045	do	-8.55	532	43
15739	2	5	3045	do	-8.33	517	50
15739	2	6	3045	do	-7.70	627	28
15739	2	7	3045	do (ank)	-8.90	357	43
15739	2	8	3045	do (ank + bit)	-9.39	345	28
15739	2	9	3045	do	-7.16	661	34
15739	2	10	3045	do	-7.91	509	46
15739	2	11	3045	do	-9.27	404	33
15739	2	12	3045	fsp	-10.42	241	32
15739	3	4	3048	do + ank + bit	-15.35	144	-
15739	3	5	3048	ank + bit (do)	-12.89	236	-
15739	3	6	3048	bit (ank)	-13.95	221	-
15739	3	7	3048	bit (ank)	-14.61	217	-
15739	3	8	3048	bit	-15.59	173	-
15739	3	9	3048	ank + bit	-18.21	92	-
15739	3	10	3048	bit	-18.62	64	-
15739	3	12	3048	ank + bit (do)	-12.93	263	-
15747	1	4	3021	do + ank	-10.46	479	89
15747	1	5	3021	do	-11.19	496	72
15747	1	6	3021	ank (do)	-12.42	281	51
15747	1	7	3021	fsp	-10.87	513	43
15747	1	8	3021	fsp	-14.22	101	47
15747	2	4	3023	do	-10.23	370	71
15747	2	5	3023	do (ank)	-10.85	372	69
15747	2	6	3023	ank (do)	-11.53	392	63
15747	2	7	3023	do + ank	-12.72	193	61
15747	2	8	3023	do (ank + bit)	-12.76	288	-
15747	2	9	3023	do (ank + bit)	-11.19	211	63
15747	3	4	3028	do (ank)	-11.06	268	47
15747	3	5	3028	do (ank)	-11.52	272	63
15747	3	6	3028	ank (do)	-12.20	215	46
15747	3	7	3028	do + ank	-12.72	143	42
15747	3	8	3028	do (ank + bit)	-12.05	223	40
15747	3	9	3028	ank (do + bit)	-12.40	215	39

abbreviations: do = dolomite, ank = ankerite, bit = bitumen, fsp = feldspar, ( ) = minor

Appendix 6: Table grain contacts

Well	Thin section no.	Depth TVDSS [m]	Stratigraphy	Facies	Graincontacts [%]						level of compaction	IGV	grainsize [mm]
					0	1	2	3	4	5			
					floating grains	point contacts	short longitudinal	long longitudinal	concave-convex	slightly sutured			
30/2c4	15593	4633.90	Skag. F.	AS	0	0	0	62	13	25	3.63	2.8	0.08
30/2c4	15604B	4637.20	Skag. F.	AS	0	0	14	64	9	13	3.21	3.5	0.12
30/2c4	15608B	4638.33	Skag. F.	FC	0	3	28	65	1	3	2.73	13.7	0.13
30/2c4	15613B	4639.87	Skag. F.	FC	3	29	52	15	1	0	1.82	24.2	0.31
30/2c4	15615	4640.23	Skag. F.	FC	1	10	54	35	0	0	2.23	28.7	0.24
30/2c4	15616B	4640.79	Skag. F.	FC	1	12	70	17	0	0	2.03	21.0	0.34
30/2c4	15624.5	4643.32	Skag. F.	FC	0	3	49	48	0	0	2.45	27.3	0.24
30/2c4	15631.5	4645.40	Skag. F.	AS	0	0	44	50	4	2	2.64	23.2	0.12
30/2c4	15634.3B	4646.23	Skag. F.	AS	0	0	22	71	2	5	2.90	3.5	0.11
30/2c4	15645	4649.38	Skag. F.	SF	0	0	20	69	3	8	2.99	27.5	0.21
30/2c4	15646	4649.80	Skag. F.	SF	1	16	55	24	2	2	2.16	34.2	0.19
30/2c4	15647.5	4650.07	Skag. F.	FC/SF	0	1	30	59	10	0	2.78	10.0	0.17
30/2c4	15651.5	4651.22	Skag. F.	FC/SF	0	2	38	59	1	0	2.59	27.5	0.11
30/2c4	15654.5B	4652.12	Skag. F.	FC/SF	0	1	47	50	1	1	2.54	31.5	0.14
30/2c4	15655.3	4652.50	Skag. F.	FC/SF	1	13	64	22	0	0	2.07	28.5	0.28
30/2c4	15655.3B	4652.50	Skag. F.	FC/SF	1	15	61	22	1	0	2.07	32.2	0.3
30/2c4	15660	4653.75	Skag. F.	FC/SF	1	10	50	39	0	0	2.27	29.7	0.24
30/2c4	15671.5	4657.26	Skag. F.	FC/SF	0	0	22	51	19	8	3.13	20.3	0.11
30/2c4	15676	4658.68	Skag. F.	FC	1	13	61	24	0	1	2.12	30.0	0.24
30/2c4	15680	4659.78	Skag. F.	FC	0	7	61	31	1	0	2.26	26.3	0.23
30/2c4	15680B	4659.78	Skag. F.	FC	0	5	50	44	0	1	2.42	33.2	0.23
30/2c4	15685	4661.24	Skag. F.	FC	0	1	48	45	2	4	2.60	29.8	0.18
30/2c4	15688	4662.25	Skag. F.	FC	0	5	35	59	0	1	2.57	29.5	0.2
30/2c4	15691B	4662.75	Skag. F.	FC	0	0	40	60	0	0	2.60	23.0	0.16
30/2c4	15691.5	4662.93	Skag. F.	FC	0	2	46	46	4	2	2.58	22.7	0.18
30/2c4	15704	4666.91	Skag. F.	AS	0	0	9	31	9	51	4.02	6.0	0.13
30/2c4	15715	4670.15	Skag. F.	FC	27	31	39	3	0	0	1.18	41.5	0.19
30/2c4	15715B	4670.15	Skag. F.	FC	44	40	14	2	0	0	0.74	40.0	0.2
30/2c4	15716	4670.48	Skag. F.	FC	0	7	45	48	0	0	2.41	37.0	0.16
30/2c4	15716B	4670.48	Skag. F.	FC	0	13	66	19	2	0	2.10	33.5	0.17
30/2c4	15718.5	4671.19	Skag. F.	FC	0	21	57	21	1	0	2.02	39.2	0.19
30/2c4	15739	4677.32	Skag. F.	FC?	0	0	14	55	15	16	3.33	1.2	0.11
30/2c4	15741	4677.97	Skag. F.	FC?	0	1	16	74	4	5	2.96	16.5	0.16
30/2c4	15743	4678.50	Skag. F.	FC?	0	2	35	59	3	1	2.66	27.0	0.18
30/2c4	15745	4679.16	Skag. F.	FC?	0	2	32	61	2	3	2.72	24.2	0.27
30/2c4	15752	4680.29	Skag. F.	FC?	2	38	54	6	0	0	1.64	33.3	0.32
30/2c4	15792.5B	4693.22	Skag. F.	SF	0	2	28	60	7	3	2.81	28.5	0.19

texture in dolomite nodules

30/2c4	15647.5	4650.07	Skag. F.		63	28	9	0	0	0	0.46
30/2c4	15745	4679.16	Skag. F.		85	8	7	0	0	0	0.22

Appendix 7: Input scripts for Geochemist´s Workbench

Chemical formula of minerals in LLNL Database applied in the presented models

Albite	$NaAlSi_3O_8$
Beidellite-Mg	$Mg_{0.165}Al_{2.33}Si_{3.67}O_{10}(OH)_2$
Beidellite-Na	$Na_{0.33}Al_{2.33}Si_{3.67}O_{10}(OH)_2$
Calcite	$CaCO_3$
Clinochlore	$Mg_5Al_2Si_3O_{10}(OH)_8$
Chamosite	$Fe_2Al_2SiO_5(OH)_4$
Dolomite	$CaMg(CO_3)_2$
Ferrodolomite*	$CaFe(CO_3)_2$
Goethite	$FeOOH$
Hematite	Fe_2O_3
Illite	$K_{0.6}Mg_{0.25}Al_{2.3}Si_{3.5}O_{10}(OH)_2$
K-feldspar	$KAlSi_3O_8$
Kaolinite	$Al_2Si_2O_5(OH)_4$
Magnetite	Fe_3O_4
Muscovite	$KAl_3Si_3O_{10}(OH)_2$
Pyrite	FeS_2
Quartz	SiO_2
Ripidolit	$Fe_2Mg_3Al_2Si_3O_{10}(OH)_8$
Siderite	$FeCO_3$

* not in LLNL Database – taken from D. M. Kirste (Australian National University)

Appendix 7: Input scripts for Geochemist´s Workbench

Model 1a:

```
temperature initial = 25, final = 180
swap Albite for Al+++
swap Quartz for SiO2(aq)
swap Dolomite for HCO3-
swap K-feldspar for K+
swap CO2(g) for H+
1 kg H2O
210.3 free gram Albite
3563 free gram Quartz
957.7 free gram Dolomite
2953.7 free gram K-feldspar
-3.5 log fugacity CO2(g)
32000 mg/kg Na+
2720 mg/kg Ca++
116 mg/kg Mg++
65 mg/kg Fe++
balance on Cl-
59000 mg/kg Cl-
12 mg/kg SO4--
suppress ALL
unsuppress  Albite Ferrodolomite Calcite Chamosite-7A
unsuppress  Dolomite Goethite Hematite Illite
unsuppress  K-feldspar Kaolinite Muscovite Pyrite
unsuppress  Quartz Ripidolit-14A Ripidolit-7A Siderite
```

Model 1b:

```
temperature initial = 25, final = 180
swap Albite for Al+++
swap Quartz for SiO2(aq)
swap Dolomite for HCO3-
swap K-feldspar for K+
swap CO2(g) for H+
1 kg H2O
210.3 free gram Albite
3563 free gram Quartz
957.7 free gram Dolomite
2953.7 free gram K-feldspar
-3.5 log fugacity CO2(g)
67050 mg/kg Na+
20100 mg/kg Ca++
693 mg/kg Mg++
77 mg/kg Fe++
balance on Cl-
143193 mg/kg Cl-
147 mg/kg SO4--
suppress ALL
unsuppress  Albite Ferrodolomite Calcite Chamosite-7A
unsuppress  Dolomite Goethite Hematite Illite
unsuppress  K-feldspar Kaolinite Muscovite Pyrite
unsuppress  Quartz Ripidolit-14A Ripidolit-7A Siderite
```

Appendix 7: Input scripts for Geochemist´s Workbench

Model 2a:

```
temperature = 30
swap Albite for Al+++
swap Quartz for SiO2(aq)
swap Dolomite for HCO3-
swap K-feldspar for K+
swap CO2(g) for H+
1 kg H2O
210.3 free gram Albite
3563 free gram Quartz
957.7 free gram Dolomite
2953.7 free gram K-feldspar
-3.5 log fugacity CO2(g)
32000 mg/kg Na+
2720 mg/kg Ca++
116 mg/kg Mg++
65 mg/kg Fe++
balance on Cl-
59000 mg/kg Cl-
12 mg/kg SO4--
react .5 mol of CO2(g)
suppress ALL
unsuppress  Albite Ferrodolomite Calcite Chamosite-7A
unsuppress  Dolomite Goethite Hematite Illite
unsuppress  K-feldspar Kaolinite Muscovite Pyrite
unsuppress  Quartz Ripidolit-14A Ripidolit-7A Siderite
```

Model 2b:

```
temperature = 30
swap Albite for Al+++
swap Quartz for SiO2(aq)
swap Dolomite for HCO3-
swap K-feldspar for K+
swap CO2(g) for H+
1 kg H2O
210.3 free gram Albite
3563 free gram Quartz
957.7 free gram Dolomite
2953.7 free gram K-feldspar
-3.5 log fugacity CO2(g)
67050 mg/kg Na+
20100 mg/kg Ca++
693 mg/kg Mg++
77 mg/kg Fe++
balance on Cl-
143193 mg/kg Cl-
147 mg/kg SO4--
react .5 mol of CO2(g)
suppress ALL
unsuppress  Albite Ferrodolomite Calcite Chamosite-7A
unsuppress  Dolomite Goethite Hematite Illite
unsuppress  K-feldspar Kaolinite Muscovite Pyrite
unsuppress  Quartz Ripidolit-14A Ripidolit-7A Siderite
```

Appendix 7: Input scripts for Geochemist´s Workbench

Model 3a:

```
temperature = 30
swap Albite for Al+++
swap Quartz for SiO2(aq)
swap Dolomite for HCO3-
swap K-feldspar for K+
swap Hematite for O2(aq)
1 kg H2O
210.3 free gram Albite
3563 free gram Quartz
957.7 free gram Dolomite
2953.7 free gram K-feldspar
7 pH
32000 mg/kg Na+
2720 mg/kg Ca++
116 mg/kg Mg++
65 mg/kg Fe++
balance on Cl-
59000 mg/kg Cl-
12 mg/kg SO4--
446.5 free gram Hematite
react .5 mol of CH4(g)
suppress ALL
unsuppress  Albite Ferrodolomite Calcite Chamosite-7A
unsuppress  Dolomite Goethite Hematite Illite
unsuppress  K-feldspar Kaolinite Muscovite Pyrite
unsuppress  Quartz Ripidolit-14A Ripidolit-7A Siderite
```

Model 3b without magnetite:

```
temperature = 30
swap Albite for Al+++
swap Quartz for SiO2(aq)
swap Dolomite for HCO3-
swap K-feldspar for K+
swap Hematite for O2(aq)
1 kg H2O
210.3 free gram Albite
3563 free gram Quartz
957.7 free gram Dolomite
2953.7 free gram K-feldspar
7 pH
446.5 free gram Hematite
67050 mg/kg Na+
20100 mg/kg Ca++
693 mg/kg Mg++
77 mg/kg Fe++
balance on Cl-
143193 mg/kg Cl-
react .5 mol of CH4(g)
suppress ALL
unsuppress  Albite Ferrodolomite Calcite Chamosite-7A
unsuppress  Dolomite Goethite Hematite Illite
unsuppress  K-feldspar Kaolinite Muscovite Pyrite
unsuppress  Quartz Ripidolit-14A Ripidolit-7A Siderite
```

Appendix 7: Input scripts for Geochemist´s Workbench

Model 3b with magnetite:

```
temperature = 30
swap Albite for Al+++
swap Quartz for SiO2(aq)
swap Dolomite for HCO3-
swap K-feldspar for K+
swap Hematite for O2(aq)
1 kg H2O
210.3 free gram Albite
3563 free gram Quartz
957.7 free gram Dolomite
2953.7 free gram K-feldspar
446.5 free gram Hematite
7 pH
67050 mg/kg Na+
20100 mg/kg Ca++
693 mg/kg Mg++
77 mg/kg Fe++
balance on Cl-
143193 mg/kg Cl-
react .5 mol of CH4(g)
suppress ALL
unsuppress  Albite Ferrodolomite Calcite Chamosite-7A
unsuppress  Dolomite Goethite Hematite Illite
unsuppress  K-feldspar Kaolinite Magnetite Muscovite
unsuppress  Pyrite Quartz Ripidolit-14A Ripidolit-7A
unsuppress  Siderite
```

Appendix 7: Input scripts for Geochemist´s Workbench

Model 4a:

```
temperature = 100
swap Albite for Al+++
swap Quartz for SiO2(aq)
swap Dolomite for HCO3-
swap K-feldspar for K+
swap CO2(g) for H+
swap Pyrite for O2(aq)
1 kg H2O
210.3 free gram Albite
3563 free gram Quartz
957.7 free gram Dolomite
2953.7 free gram K-feldspar
-3.5 log fugacity CO2(g)
0 free gram Pyrite
32000 mg/kg Na+
2720 mg/kg Ca++
116 mg/kg Mg++
65 mg/kg Fe++
balance on Cl-
59000 mg/kg Cl-
12 mg/kg SO4--
react .2 mol of HCH3COO
suppress ALL
unsuppress  Albite Ferrodolomite Calcite Chamosite-7A
unsuppress  Dolomite Goethite Hematite Illite
unsuppress  K-feldspar Kaolinite Muscovite Pyrite
unsuppress  Quartz Ripidolit-14A Ripidolit-7A Siderite
```

Model 4b:

```
temperature = 100
swap Albite for Al+++
swap Quartz for SiO2(aq)
swap Dolomite for HCO3-
swap K-feldspar for K+
swap CO2(g) for H+
swap Pyrite for O2(aq)
1 kg H2O
210.3 free gram Albite
3563 free gram Quartz
957.7 free gram Dolomite
2953.7 free gram K-feldspar
-3.5 log fugacity CO2(g)
0 free gram Pyrite
67050 mg/kg Na+
20100 mg/kg Ca++
693 mg/kg Mg++
77 mg/kg Fe++
balance on Cl-
143193 mg/kg Cl-
147 mg/kg SO4--
react .2 mol of HCH3COO
suppress ALL
unsuppress  Albite Ferrodolomite Calcite Chamosite-7A
unsuppress  Dolomite Goethite Hematite Illite
unsuppress  K-feldspar Kaolinite Muscovite Pyrite
unsuppress  Quartz Ripidolit-14A Ripidolit-7A Siderite
```

Appendix 7: Input scripts for Geochemist´s Workbench

Model 4c:

```
temperature = 100
swap Albite for Al+++
swap Quartz for SiO2(aq)
swap Dolomite for HCO3-
swap K-feldspar for K+
swap CO2(g) for H+
swap Pyrite for O2(aq)
swap Hematite for Fe++
1 kg H2O
210.3 free gram Albite
3563 free gram Quartz
957.7 free gram Dolomite
2953.7 free gram K-feldspar
-3.5 log fugacity CO2(g)
0 free gram Pyrite
32000 mg/kg Na+
2720 mg/kg Ca++
116 mg/kg Mg++
446.5 free gram Hematite
balance on Cl-
59000 mg/kg Cl-
12 mg/kg SO4--
react .2 mol of HCH3COO
suppress ALL
unsuppress  Albite Ferrodolomite Calcite Chamosite-7A
unsuppress  Dolomite Goethite Hematite Illite
unsuppress  K-feldspar Kaolinite Muscovite Pyrite
unsuppress  Quartz Ripidolit-14A Ripidolit-7A Siderite
```

Model 4d:

```
temperature = 100
swap Albite for Al+++
swap Quartz for SiO2(aq)
swap Dolomite for HCO3-
swap K-feldspar for K+
swap CO2(g) for H+
swap Pyrite for O2(aq)
swap Hematite for Fe++
1 kg H2O
210.3 free gram Albite
3563 free gram Quartz
957.7 free gram Dolomite
2953.7 free gram K-feldspar
-3.5 log fugacity CO2(g)
0 free gram Pyrite
67050 mg/kg Na+
20100 mg/kg Ca++
693 mg/kg Mg++
446.5 free gram Hematite
balance on Cl-
143193 mg/kg Cl-
147 mg/kg SO4--
react .2 mol of HCH3COO
suppress ALL
unsuppress  Albite Ferrodolomite Calcite Chamosite-7A
unsuppress  Dolomite Goethite Hematite Illite
unsuppress  K-feldspar Kaolinite Muscovite Pyrite
unsuppress  Quartz Ripidolit-14A Ripidolit-7A Siderite
```

Appendix 7: Input scripts for Geochemist´s Workbench

Model 5a:

```
temperature = 100
swap Albite for Al+++
swap Quartz for SiO2(aq)
swap Dolomite for HCO3-
swap K-feldspar for K+
swap CO2(g) for H+
1 kg H2O
210.3 free gram Albite
3563 free gram Quartz
957.7 free gram Dolomite
2953.7 free gram K-feldspar
-3.5 log fugacity CO2(g)
32000 mg/kg Na+
2720 mg/kg Ca++
116 mg/kg Mg++
65 mg/kg Fe++
balance on Cl-
59000 mg/kg Cl-
12 mg/kg SO4--
reactants times 50
react 55.5035665 of H2O
react .00607210413 of H+
react .390172958 of Na+
react 2.55765596e-9 of K+
react .000374623755 of Mg++
react .0103887499 of Ca++
react .408029849 of Cl-
react .000301902192 of SO4--
react .00913895289 of HCO3-
react 2.64819924e-7 of Al+++
react .00102803988 of SiO2(aq)
flush
suppress ALL
unsuppress  Albite Ferrodolomite Calcite Chamosite-7A
unsuppress  Dolomite Goethite Hematite Illite
unsuppress  K-feldspar Kaolinite Muscovite Pyrite
unsuppress  Quartz Ripidolit-14A Ripidolit-7A Siderite
```

Appendix 7: Input scripts for Geochemist´s Workbench

Model 5b:

```
temperature initial = 30, final = 180
swap Albite for Al+++
swap Quartz for SiO2(aq)
swap Dolomite for HCO3-
swap K-feldspar for K+
swap CO2(g) for H+
1 kg H2O
210.3 free gram Albite
3563 free gram Quartz
957.7 free gram Dolomite
2953.7 free gram K-feldspar
-3.5 log fugacity CO2(g)
32000 mg/kg Na+
2720 mg/kg Ca++
116 mg/kg Mg++
65 mg/kg Fe++
balance on Cl-
59000 mg/kg Cl-
12 mg/kg SO4--
reactants times 50
react 55.5035665 of H2O
react .00607210413 of H+
react .390172958 of Na+
react 2.55765596e-9 of K+
react .000374623755 of Mg++
react .0103887499 of Ca++
react .408029849 of Cl-
react .000301902192 of SO4--
react .00913895289 of HCO3-
react 2.64819924e-7 of Al+++
react .00102803988 of SiO2(aq)
flush
suppress ALL
unsuppress  Albite Ferrodolomite Calcite Chamosite-7A
unsuppress  Dolomite Goethite Hematite Illite
unsuppress  K-feldspar Kaolinite Muscovite Pyrite
unsuppress  Quartz Ripidolit-14A Ripidolit-7A Siderite
```

Selbständigkeitserklärung

Ich erkläre, dass ich die vorliegende Arbeit selbständig und unter Verwendung der angegebenen Hilfsmittel, persönlichen Mitteilungen und Quellen angefertigt habe.

Winsen (Aller), 30.11.2011 Robert Lippmann